ORNL-3360
UC-34 – Physics
TID-4500 (17th ed., Rev.)

NEUTRON PHYSICS DIVISION

ANNUAL PROGRESS REPORT

FOR PERIOD ENDING SEPTEMBER 1, 1962

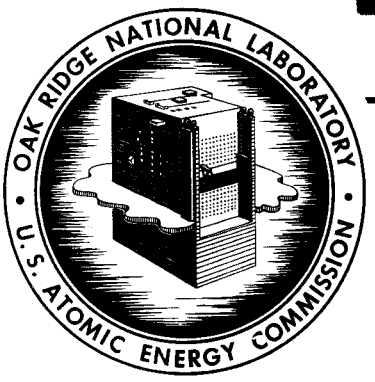

OAK RIDGE NATIONAL LABORATORY
operated by
UNION CARBIDE CORPORATION
for the
U.S. ATOMIC ENERGY COMMISSION

Printed in USA. Price: $4.00 Available from the
Office of Technical Services
U. S. Department of Commerce
Washington 25, D. C.

ORNL-3360
UC-34 – Physics
TID-4500 (17th ed., Rev.)

Contract No. W-7405-eng-26

NEUTRON PHYSICS DIVISION

ANNUAL PROGRESS REPORT

for Period Ending September 1, 1962

E. P. Blizard, Director
A. D. Callihan, Associate Director
F. C. Maienschein, Associate Director

DATE ISSUED

OCT 8 1962

OAK RIDGE NATIONAL LABORATORY
Oak Ridge, Tennessee
operated by
UNION CARBIDE CORPORATION
for the
U. S. ATOMIC ENERGY COMMISSION

TABLE OF CONTENTS AND SUMMARY

1. RESEARCH FOR LIGHT-WATER-MODERATED REACTORS

1.1. *PRELIMINARY REPORT ON THE MEASURED GAMMA-RAY SPECTRA FROM A STAINLESS STEEL REACTOR*

G. T. Chapman, K. M. Henry, J. D. Jarrard, and R. L. Cowperthwaite 1

The gamma-ray spectrum from a stainless steel reactor core has been studied with various thicknesses of water separating the core and the air-filled, 6-ft-long spectrometer acceptance cone. Data were obtained with the acceptance cone normal to the core face and also at several angles to the normal. It was found that above an energy of 5 Mev the principal contribution to the spectrum comes from capture gamma rays born in the steel of the reactor core. Below 5 Mev the predominant peak comes from thermal-neutron captures in the water. Data are presented as pulse-height distributions.

1.2. *EXPERIMENTS AND CALCULATIONS ON THE REACTIVITY EFFECTS OF SMALL FUEL DISPLACEMENTS*

E. G. Silver, Z. M. Bartolome, K. M. Henry, and J. D. Kington 12

The reactivity effects associated with the motion of reactor fuel are being investigated in a calculational and experimental program at the BSF. The experiments performed to date indicate that negative reactivities result from all perturbations that decrease the homogeneity of the core, except when the perturbation adds fuel to high-importance regions, such as those adjacent to interior water volumes. The calculational methods appear to be inadequate to cope with the kind of small-dimension, large-magnitude perturbations represented by the experiments; however, experiments are being designed which can be more accurately represented in the calculations.

2. RADIATION DETECTOR STUDIES

2.1. *APPLICATIONS OF SOME INSTRUMENT-RESPONSE UNFOLDING METHODS*

W. R. Burrus 19

Codes OPTIMO and SLOP have been written for the IBM-7090 computer to unfold experimental data. Both are designed to take account of a priori information such as nonnegativity or smoothness. OPTIMO has been used to unfold a neutron spectrum from the Tower Shielding Reactor II, and SLOP has been applied to the unfolding of a capture-gamma-ray spectrum measured with a large NaI(Tl) crystal.

2.2. *THE SLOP CODE FOR THE UNFOLDING OF INSTRUMENT RESPONSE*

V. D. Bogert and W. R. Burrus 22

A variation of the ordinary method of least squares has been utilized in the construction of a computer code (identified as SLOP) for the unfolding of the response of instruments such as scintillation spectrometers. The code takes advantage of a priori knowledge of the solutions sought, such as nonnegativity, knowledge that a particular spectrum may be smoothly varying, etc. The result of the application of the code is the determination of a statistical confidence interval for the unknown spectrum. A sample problem is computed for demonstration.

3. CRITICAL EXPERIMENTS

3.1. CRITICAL EXPERIMENTS WITH MIXTURES OF AQUEOUS U^{235}-ENRICHED URANYL NITRATE SOLUTIONS AND BOROSILICATE GLASS RINGS

J. K. Fox and J. T. Thomas 35

Several critical experiments were performed with mixtures of aqueous 92.6% U^{235}-enriched uranyl nitrate and borosilicate glass Raschig rings to provide information for nuclear safety applications. The mixtures were contained in 20-, 30-, and 48-in.-ID aluminum or stainless steel cylinders, and two concentrations of uranyl nitrate solutions were used, one containing 415 g of uranium per liter and the other 279 g of uranium per liter. The glass rings varied in size, the largest having a 1.52-in. inside diameter, a 1.85-in. outside diameter, and a 1.89-in. length. Their boron content was 0.5 to 5.7 wt %. It was found that for solutions having a uranium concentration $\leq$415 g/liter, k_∞ will be less than 1 if the glass rings contain 5.7 wt % natural boron and occupy 24.1 vol % of the mixture. For solutions having a uranium concentration of $\leq$279 g/liter, the corresponding values are 4.0 wt % natural boron and 24.1 vol % glass.

3.2. CRITICAL CUBIC ARRAYS OF NEUTRON-INTERACTING UNITS OF AQUEOUS URANYL NITRATE SOLUTION

J. T. Thomas and J. K. Fox 37

Critical experiments with 5-liter units of 92.6% U^{235}-enriched uranyl nitrate solution in cubic arrays have shown that the number of units required for criticality as a function of their spacing and reflector obeys the relation $N = N_0 F^{-s}$, where N_0 and s are constants and F is the ratio of the average uranium density in the array to that in a unit. Values of the constants are given for various reflector conditions.

3.3. PROMPT-NEUTRON LIFETIME IN HYDROGEN-MODERATED 3% U^{235}-ENRICHED URANIUM CRITICAL ASSEMBLIES

J. T. Mihalczo 37

Prompt-neutron decay constants in unreflected and reflected delayed-critical parallelepipeds of a homogeneous mixture of UF_4 and paraffin were determined by the pulsed-neutron technique. The fuel mixture had a density of 4.5 g/cc and contained 92 wt % UF_4 in which the U^{235} enrichment was 3%. The reflector was a 15-cm thickness of paraffin ($C_{25}H_{52}$) with a density of 0.93 g/cc. With the resulting values of the decay constants, together with the effective delayed-neutron fractions obtained from critical measurements and transport theory calculations, the prompt-neutron mean lifetime was found to be 2.17×10^{-5} sec and 2.88×10^{-5} sec for the unreflected and reflected critical assemblies, respectively.

3.4. PROMPT-NEUTRON DECAY CONSTANTS FOR UNMODERATED URANIUM METAL CRITICAL ASSEMBLIES WITH LARGE GAPS

J. T. Mihalczo 39

Experiments in which the large metal faces of two 8 by 10 in. uranium (93.2 wt % U^{235}) metal slabs were separated by various distances have shown that the critical thickness of each slab varies from 1.87 in. at a separation distance of 0.11 in. to 3.12 in. at a separation distance of 5 in. The prompt-neutron decay constants, measured by the Rossi-α technique, varied from 1.07×10^6 sec^{-1} to $\sim 8.9 \times 10^5$ sec^{-1} for separation distances from 0 to 1 in. and was then constant between 1 and 5 in.

3.5. CRITICAL EXPERIMENTS WITH THE HEALTH PHYSICS RESEARCH REACTOR

J. T. Mihalczo 41

A series of critical experiments were performed with the Health Physics Research Reactor both at zero power and under superprompt-critical conditions. In the zero-power experiments fission-rate distributions were measured, reactivity calibrations of various movable parts were made, and the reactivity effects of the presence of neutron-reflecting materials adjacent to the reactor were determined. Also, the static temperature coefficient of reactivity was found to be 0.31 ¢/°C. In the study of the superprompt-critical conditions of the reactor, reactivity increases

up to 11¢ above prompt critical resulted in bursts yielding as many as 1.8×10^{17} fissions with reactor periods as short as 16 μsec and temperature increases as large as 400°C. Pressure waves generated in a portion of the core held in position by an electromagnet for bursts greater than $\sim 6 \times 10^{16}$ fissions initiated the removal of this section of the core about 225 μsec after the peak of the burst.

3.6. CRITICAL EXPERIMENTS WITH ROVER REACTOR FUEL ELEMENTS

E. B. Johnson and J. K. Fox 43

Critical and safe conditions for Rover fuel were defined under conditions characteristic of both its fabrication and storage. Since the work is classified, the results are presented elsewhere.

3.7. HIGH-FLUX ISOTOPE REACTOR CRITICAL EXPERIMENT NO. 2

D. W. Magnuson 44

Recent critical experiments in support of the nuclear design of the High-Flux Isotope Reactor have been principally concerned with evaluation of the proposed reactor control devices and their effects on the power distribution. The results of the experiments led to changes in the original design of the controls. Since the data were unique to a particular design, they are not reported in detail, but the experimental method is described and typical results of control plate calibrations are given. Experimental values of the critical neutron decay constant are shown to be in general agreement with calculations. A preliminary investigation of possible safety devices to augment the control plates in the event of an emergency shutdown is described.

4. NUCLEAR AND REACTOR PHYSICS – EXPERIMENTAL

4.1. THE MEASUREMENT OF α AS A FUNCTION OF ENERGY

G. deSaussure, L. W. Weston, J. D. Kington, R. D. Smiddie, and W. S. Lyon 51

The ratio, α, of the capture cross section to the fission cross section of U^{235} was measured at neutron energies of 30 and 65 kev. The results, $\alpha = 0.372 \pm 0.026$ at 30 ± 8 kev and $\alpha = 0.315 \pm 0.06$ at 64 ± 20 kev, are in agreement with previously measured values. The capture cross section of U^{238} was also determined – 0.531 barn at 30 kev and 0.340 barn at 64 kev, values which are in agreement with published data.

4.2. STATUS OF PULSED-NEUTRON MEASUREMENTS IN LIGHT-WATER ICE

E. G. Silver 63

An experiment is in progress to measure the temperature dependence of neutron diffusion parameters in light-water ice, over the range −5 to −90°C. A pulsed-neutron source, yielding 2.4-Mev neutrons by the (D,D) reaction, is being used. Results obtained from a single ice cylinder with buckling $B^2 = 0.300$ cm^{-2} are given for temperatures of −5 and −90°C. From these results it appears that an asymptotic value of the decay constant λ is attained soon enough to permit accurate measurement over the entire temperature range of the experiment. Decay data have been taken for eight cylinders from 8 to 12 in. in diameter and from 6.5 to 12 in. in height. Future experiments will extend the data to small assemblies over the same temperature range.

4.3. MANGANESE BATH MEASUREMENTS OF η OF Pu^{239}

R. L. Macklin, G. deSaussure, J. D. Kington, and W. S. Lyon 67

The result of a manganese bath measurement of η of Pu^{239} is given as 2.058 ± 0.010 for a black sample in the thermal spectrum used and as $2.143 \, ^{+0.010}_{-0.020}$ for 2200-m/sec neutrons.

4.4. THE NEUTRON ASYMPTOTIC DECAY CONSTANT IN A SMALL CRYSTALLINE MODERATOR ASSEMBLY

G. deSaussure 68

Methods previously reported have been used to compute upper and lower bounds for the asymptotic decay constant for neutrons in a graphite moderating assembly.

4.5. AN APPLICATION OF PILE NOISE ANALYSIS TO MEASUREMENTS OF KINETICS PARAMETERS OF A POOL-TYPE REACTOR

M. N. Alam, A. L. Colomb, and K. M. Henry 68

The spectral densities of a BSR-II stainless-steel-clad reactor core and two BSR-I aluminum-clad reactor cores have been measured using pile noise analysis techniques. From these data values of the neutron lifetime divided by the delayed-neutron effective fraction, l/β_{eff}, have been computed and show good agreement with published values obtained by the pulsed-neutron technique. The methods used in assigning standard deviations to the data are briefly outlined. It is concluded that the experiments demonstrate the adequacy of reactor spectral density measurements for providing knowledge of various reactor kinetics parameters.

5. NUCLEAR AND REACTOR PHYSICS – THEORETICAL

5.1. ISOPERIMETRIC AND OTHER INEQUALITIES IN THE THEORY OF NEUTRON TRANSPORT, II

Lawrence Dresner 75

It is shown that certain theorems regarding five quantities of interest in the one-velocity theory of neutron transport, previously proved for bare, homogeneous, convex solids with isotropic scattering, can in some cases be proved for the same solids with linearly anisotropic scattering. The present paper summarizes work previously published as an ORNL report.

5.2. A REMARK ON THE SECOND FUNDAMENTAL THEOREM IN ONE-VELOCITY TRANSPORT THEORY

Lawrence Dresner 76

It was previously shown that, in one-velocity transport theory with isotropic scattering, the second fundamental theorem of reactor theory always gave a lower limit, P_∞, to the nonescape probability if the buckling corresponded to zero extrapolation. In the work summarized here, this proof is extended to the case of linearly anisotropic scattering for slabs, spheres, and infinite cylinders.

5.3. RESONANCE SELF-SHIELDING IN THE MEASUREMENT OF RADIATIVE CAPTURE CROSS SECTIONS

Lawrence Dresner 78

The calculation of the resonance self-shielding correction, required for application to experimental values of average neutron capture cross sections in the kilovolt range of energies, can be made by slightly altering the procedure commonly used for calculating the resonance self-shielding factor in reactor calculations. An expression for the part of the correction due to absorption of uncollided neutrons is given; formulas by which it may be evaluated in the absense of Doppler broadening are given, as well as a number of functions in terms of which it can be estimated in the presence of Doppler broadening. An expression for the fraction of the correction due to absorption of already collided neutrons is also given.

5.4. AN EXTENSION OF O5R MONTE CARLO CALCULATIONS TO THE THERMAL-NEUTRON RANGE

G. R. Dalton and R. R. Coveyou 81

The O5R code has been extended to give a detailed treatment of collisions between neutrons and nuclei having a Maxwell-Boltzmann distribution of energy. The new work takes into account the thermal motion of the nuclei, the anisotropic scattering, the variation of temperature as it affects the nuclei, and the dependence of cross sections on the neutron speed. The code does not treat nonisotropic media, nor does it take account of the energy states of a nucleus bound in a crystal or a molecule. The code is being tested on some simple calculations.

5.5. EXCITATION OF TWO PHONON STATES BY INELASTIC α-PARTICLE SCATTERING

B. Buck 82

Recent experiments on inelastic scattering of 40-Mev α-particles have shown that the angular distributions from the excitation of some known 4^+ states in medium-weight nuclei are not in accord with the Blair phase rule. Calculations are reported which indicate that the anomaly arises as an interference effect between two possible mechanisms for exciting the first 4^+ state, that is, a direct transition and a multiple transition. This conclusion is contrary to previous interpretations based on plane-wave perturbation calculations.

5.6. *EFFECT OF NUCLEAR COLLECTIVE MOTIONS ON S- AND P-WAVE STRENGTH FUNCTIONS*
B. Buck and F. Perey 82
Consideration of dynamical distortions of the nucleus in addition to permanent distortions previously considered has resulted in a more satisfactory agreement between theory and experiment in a calculation of *S*- and *P*-wave strength functions.

5.7. *THE CALCULATION OF ELASTIC AND INELASTIC PROTON SCATTERING WITH A GENERALIZED OPTICAL MODEL*
B. Buck 83
This is an extremely brief summary of a paper which is to be submitted to *Physical Review*.

5.8. *OPTICAL MODEL ANALYSIS OF PROTON ELASTIC SCATTERING IN THE RANGE OF 9 TO 22 Mev*
F. G. Perey 84
This is a brief summary of a paper to be reported more fully at a later date.

5.9. *OPTICAL MODEL ANALYSIS OF DEUTERON SCATTERING IN THE RANGE OF 10 TO 27 Mev*
C. M. Perey and F. G. Perey 84a
This is a brief summary of a paper to be reported more fully at a later date.

5.10. *CORRESPONDENCE BETWEEN NONLOCAL AND LOCAL OPTICAL POTENTIALS*
F. G. Perey 84a
This is a brief summary of a paper to be reported more fully at a later date.

6. REACTOR SHIELDING

6.1. *THE RADIATION LEAKAGE SURVEY OF THE SHIELD OF THE NUCLEAR SHIP "SAVANNAH"*
E. P. Blizard, T. V. Blosser, and R. M. Freestone, Jr. 87
This paper consists of an abstract of a paper previously issued as a Laboratory report (ORNL-3336).

6.2. *A STUDY OF THE SHIELD OF THE UNIVERSITY OF ILLINOIS TRIGA MARK II RESEARCH REACTOR*
T. V. Blosser, R. M. Freestone, Jr., and J. M. Miller 87
This paper consists of an abstract of a paper previously issued as a Laboratory technical memorandum (ORNL TM-178).

6.3. *A STUDY OF THE SHIELD OF THE VIRGINIA POLYTECHNIC INSTITUTE UTR-10 REACTOR*
T. V. Blosser and R. M. Freestone, Jr. 88
This paper consists of an abstract of a paper to be issued as a Laboratory technical memorandum (ORNL TM-290).

6.4. *A RADIATION STUDY OF THE WESTINGHOUSE TESTING REACTOR*
T. V. Blosser and R. M. Freestone, Jr. 88
This paper consists of an abstract of a paper to be issued as a Laboratory technical memorandum (ORNL TM-332).

6.5. *A SYSTEM FOR GENERATING GAMMA-RAY CROSS-SECTION DATA FOR USE WITH THE IBM-7090 COMPUTER*
S. K. Penny, M. B. Emmett, and D. K. Trubey 89
A system for generating detailed tables of gamma-ray cross-section data has been devised for use on the IBM-7090 computer. This system obviates the preparation of large amounts of cross-section data and provides a scheme for rapid access to the tabulated values.

6.6. OGRE – A MONTE CARLO SYSTEM FOR THE CALCULATION OF GAMMA-RAY TRANSPORT
S. K. Penny, D. K. Trubey, and M. B. Emmett 90
OGRE is a skeleton IBM-7090 computer program consisting of a number of subroutines that provide the basic structure repeated in every Monte Carlo code dealing with gamma-ray transport. Its advantage lies in the fact that most types of codes can be "manufactured" by writing a few special subroutines.

6.7. OGRE-P1 – A MONTE CARLO PROGRAM FOR COMPUTING GAMMA-RAY TRANSMISSION THROUGH LAMINATED SLABS (MONOENERGETIC SOURCE)
D. K. Trubey, S. K. Penny, and M. B. Emmett 90
A Monte Carlo IBM-7090 program, called OGRE-P1, has been written for the calculation of the dose rate on one side of a slab due to an isotropic, cosine, or collimated monoenergetic gamma-ray source on the other side of the slab. Up to 50 homogeneous regions are permitted.

6.8. OGRE-P2 – A MONTE CARLO PROGRAM FOR COMPUTING GAMMA-RAY LEAKAGE FROM LAMINATED SLABS CONTAINING DISTRIBUTED SOURCES
D. K. Trubey, S. K. Penny, and M. B. Emmett 91
A Monte Carlo IBM-7090 program, called OGRE-P2, has been written for the calculation of dose rate on one side of a slab due to gamma-ray sources distributed in energy and space within the slab. The code, except for the source routine, is similar to OGRE-P1.

6.9. MONTE CARLO CODE FOR CALCULATION OF ENERGY DEPOSITION BY GAMMA RAYS IN A LAMINATED INFINITE SLAB
S. K. Penny, D. K. Trubey, and M. B. Emmett 94
A Monte Carlo code has been written in the OGRE system to compute energy deposition by gamma rays in an infinite slab, consisting of as many as 50 laminations, which in turn may consist of as many as 13 distinct mixtures of elements. The source is a monoenergetic current incident on one face of the slab. It may be monodirectional or have an isotropic or cosine angular distribution about the slab normal.

6.10. USE OF RENUPAK AND NIOBE NEUTRON TRANSPORT CODES
D. K. Trubey and S. K. Penny 94
The IBM-7090 neutron transport codes RENUPAK and NIOBE have been obtained from United Nuclear Corporation and are in use on the Oak Ridge IBM-7090 machine. In order to use these codes effectively, auxiliary codes, including a response function code suitable for use with either code and a RENUPAK tape edit, have been prepared. Some difficulties experienced with RENUPAK are discussed.

6.11. TRANSFUSION – A NUMERICAL METHOD FOR COMPUTING LOW-ENERGY NEUTRON SPATIAL DISTRIBUTIONS
D. K. Trubey and S. K. Penny 96
A technique for calculating neutron slowing down in shields has been developed which uses transport theory for high energies and diffusion theory for low energies. Preliminary results for a point fission source in water show that the technique, which is called the Transfusion method, gives much better predictions of thermal-neutron fluxes at large distances from the source than are given by the diffusion theory.

6.12. IBM-7090 GAUSSIAN INTEGRATION PACKAGE WITH OPTIONAL POINT QUADRATURE
S. K. Penny 98
A Gaussian integration package has been written for the IBM-7090 computer. This package allows for the possibility of performing a four-fold integral and for an optional number of points in the Gaussian quadrature.

6.13. A FORTRAN SUBROUTINE FOR TABLE GENERATION BY DATA INTERPOLATION
S. K. Penny 98
A Fortran subroutine has been written for the purpose of generating a table of data by interpolation in a smaller table of data. There are four options for the interpolation scheme. The purpose is to provide information for a "table look-up" which is usually much less costly than direct computation.

6.14. ENØFX – AN IBM-7090 ROUTINE FOR COMPUTING THE EXPONENTIAL INTEGRALS, $E_n(x)$

D. K. Trubey 99

An IBM-7090 subroutine has been written in FAP language to compute the exponential integrals

$$E_n(x) = x^{n-1} \int_x^\infty \frac{e^{-y}}{y^n}\, dy \ .$$

The code will give accurate answers for arguments as small as 10^{-35}. It has been written to be compatible with Fortran and the ORGDP IBM-7090 monitor system.

6.15. AN IBM-7090 ROUTINE FOR READING O5R TAPES

D. K. Trubey 100

An IBM-7090 subroutine, called REDØ5R, has been written to expedite use of the O5R neutron Monte Carlo code. The routine, which is compatible with Fortran and the ORGDP IBM-7090 monitor system, has a buffered input so that the machine may process the neutron histories and read tape simultaneously.

6.16. SHIELDING RESEARCH FOR NUCLEAR SPACE POWER PLANTS

C. E. Clifford 102

Shielding research in direct support of the Space Nuclear Auxiliary Power (SNAP) program wherein reactors are utilized as the power source for space vehicles has been initiated. It includes studies of neutron penetration through lithium hydride (see Secs. 6.17 and 6.18) and investigations of structure scattering of radiation, both aimed at assisting in the development of an efficient technique for shaping shadow shields on space vehicles.

6.17. TRANSPORT OF FAST NEUTRONS THROUGH LITHIUM HYDRIDE. PART I: NEUTRON SPECTRA

V. V. Verbinski, T. A. Love, R. D. Smiddie, H. A. Todd, and T. Fuse 105

Time-of-flight techniques have been used to obtain the spectra of near-fission neutrons transported through a 20-cm-thick slab of lithium hydride and emerging at angles of 0 and 30° to the normal. NIOBE calculations in which the measured source spectrum was used as input show good gross agreement with the experimental results, although in detail the 0° calculations are low by up to 45% in the region from 4 to 5 Mev and high by about the same fraction from 2.5 to 3.5 Mev.

6.18. TRANSPORT OF FAST NEUTRONS THROUGH LITHIUM HYDRIDE. PART II: ANGULAR DISTRIBUTIONS

V. V. Verbinski, T. Fuse, J. D. Kington, and K. M. Henry 111

Integral-type measurements of the angular variation of neutron fluxes leaking from a lithium hydride slab were made with threshold detectors and the results compared with the predictions of a neutron transport calculation. The computed spectrum for each angle was weighted with the activation cross section of the detector to obtain the predicted angular variations of detector activation. The detectors were Pu^{240}, Np^{237}, U^{238}, sulfur and aluminum, having effective thresholds of approximately 0.001, 0.75, 1.5, 3.5, and 7 Mev, respectively. Two components of leakage neutrons were apparent; a collimated and a diffuse component. The former is the uncollided plus small-angle-scattered flux. The diffuse component appears to have an angular distribution that is invariant with depth of penetration; however, above a few Mev its slope increases with energy.

6.19. SHIELDING AGAINST PROMPT WEAPONS RADIATION

L. B. Holland, V. R. Cain, R. E. Maerker, H. E. Stern, F. H. Clark, J. L. Hull, J. J. Manning, and D. R. Ward 122

An experimental and calculational program relating to the penetration of prompt weapons radiation into shielded and open underground configurations has been carried out. The source of radiation was the Tower Shielding Reactor II modified to give a radiation leakage similar to that from a weapon, and the underground installations to be studied were simulated by vertical concrete-lined cylindrical holes, 4 ft in diameter and 20 ft in depth, dug in the ground at distances of 53, 161, and 435 ft from the reactor pool. A horizontal tunnel 10 ft below ground level was connected with the hole nearest the reactor. Measurements were made at positions within the holes while they were covered with various thicknesses of iron or concrete shields. Typical results are reported.

7. SHIELDING AGAINST HIGH-ENERGY RADIATIONS

7.1. *MONTE CARLO CALCULATIONS ON INTRANUCLEAR CASCADES FOR INCIDENT-PARTICLE ENERGIES FROM ABOUT 50 TO 350 Mev*

H. W. Bertini 137

Calculations have been made for nucleons and pions incident on complex nuclei at energies where pion production is not likely (≈350 Mev). The interaction with the nucleus as a whole is represented by individual particle-particle collisions within the nucleus where the history of each particle involved in the collision is traced. Extensive comparisons with experiment are made to examine the limits of validity of the model. The effect of a diffuse nuclear edge is examined for certain reactions. It is demonstrated that the model can be used to predict a broad range of experimental results for incident nucleons, whereas the predictions for incident pions are not as reliable as those for nucleons when detailed information is required. It is shown that the bulk of the effects which result when a diffuse nuclear edge is used comes from the increased nuclear dimensions rather than from the edge itself.

7.2. *COMPILATION OF REACTIONS CALCULATED FOR PARTICLES WITH ENERGIES FROM ABOUT 50 TO 350 Mev*

H. W. Bertini and L. Dresner 182

A compilation is being prepared that will give the calculated results of incident nucleons and pions on complex nuclei. This will include the results of the cascade phase and the evaporation phase of the reaction. The compilation itself will contain graphs and tables of representative cases for incident protons and neutrons with energies from 25 to 400 Mev on nuclei from carbon to uranium, and for incident π^+ and π^- with energies from 25 to 300 Mev on nuclei in the same range. Some preliminary results are given here, and the data that will be available on request is listed. It is estimated that the completion time of the compilation is three or four months.

7.3. *MONTE CARLO CALCULATIONS ON INTRANUCLEAR CASCADES FOR INCIDENT-PARTICLE ENERGIES FROM ABOUT 50 Mev TO 2 Gev*

H. W. Bertini 199

The intranuclear cascade calculation which has been completed for incident particles with energies below the region where pion production is likely is now being extended to include pion production. The basic premises of the calculation remain the same. The isobar model is being used to determine the collision products when pion production occurs. It is assumed that the $T = {}^3/_2$ isobar alone is involved in any production collision, so that single and double pion production will be permitted in nucleon-nucleon collisions while single production only will be allowed in pion-nucleon collisions. When some of the required data for use with the isobar model are not available, simplifying assumptions are made in order that the data can be calculated. The calculation is now in the coding and debugging stage, and it is estimated that the code will be ready for production in about six months.

7.4. *A MONTE CARLO CALCULATION OF SCATTERED NEUTRON FLUXES AT AN AIR-GROUND INTERFACE DUE TO POINT ISOTROPIC SOURCES ON THE INTERFACE*

W. E. Kinney 203

Scattered neutron fluxes on the interface between SiO_2 ground and air due to 1- to 19-Mev point isotropic monoenergetic sources located on the interface have been calculated by the Monte Carlo method at distances out to 4×10^5 cm from the source. The validity of the method was established by comparing Monte Carlo results for an infinite air medium with moments-method results. The two methods were found to yield fluxes that were in good agreement out to 8 source mean free paths for a 2-Mev source. At higher source energies the treatment of inelastic scattering as isotropic elastic scattering overestimated the high-energy flux and underestimated the low-energy flux, while allowing only P_1 anisotropic elastic scattering overestimated the flux near the source and underestimated it far from the source. Scattered neutron fluxes at the interface of black ground and air, which is a useful limiting case, were also calculated.

7.5. A CODE GROUP APPLYING THE MONTE CARLO METHOD TO THE COMPUTATION OF THE TRANSPORT OF NUCLEONS OF ENERGY LESS THAN 400 Mev

W. E. Kinney, R. R. Coveyou, and C. D. Zerby 204

The interaction of a high-energy proton with the material of a radiation shield initiates a complex avalanche of lower-energy secondary particles, which then proceed through the shield. A knowledge of the behavior of this cascade is necessary in the design of shielding for space vehicles or high-energy accelerators. A code grouping of existing codes with newly devised codes now enables the calculation of the events, including cascades and nuclear particle evaporation from excited nuclei, which result from the interaction of <400-Mev nucleons with shield materials. Flow charts and an example of typical results are shown.

7.6. ENERGY DEPOSITION BY HIGH-ENERGY NUCLEONS AS A FUNCTION OF DEPTH IN TISSUE

W. E. Kinney, C. D. Zerby, and R. P. Leinius 213

A description is given of a program to calculate the energy deposition in tissue by high-energy incident nucleons as a function of depth. Preliminary results for 400-Mev incident protons are presented.

7.7. AN IMPROVED CODE FOR THE NUMERICAL ANALYSIS OF A NUCLEON-MESON CASCADE

R. G. Alsmiller, Jr., F. S. Alsmiller, and J. E. Murphy 215

An IBM-7090 code is being written to solve the nucleon-meson cascade equations in the straight-ahead approximation. The equations which are to be solved are discussed and the manner in which these equations differ from those we have used previously is described.

7.8. TWO CATEGORIES OF SOLUBLE NUCLEON-MESON CASCADE EQUATIONS

F. S. Alsmiller and R. G. Alsmiller, Jr. 221

Analytic solutions to the one-dimensional nucleon-meson cascade equations are given for two classes of separable secondary energy distributions under the conditions that the slowing down of charged particles and the energy dependence of the nonelastic cross sections may be neglected.

7.9. SPACE VEHICLE SHIELDING STUDIES: CALCULATIONS OF THE ATTENUATION OF A MODEL SOLAR FLARE AND MONOENERGETIC PROTON BEAMS BY ALUMINUM SHIELDS

R. G. Alsmiller, Jr., and J. E. Murphy 224

Nucleon-meson cascade calculations have been carried out, with the straight-ahead approximation, for a typical proton flare spectrum incident on a shield and for approximately monoenergetic incident proton beams. The shield material considered has very approximately the properties of aluminum. The results from the monoenergetic beams may be used to obtain shielding information for any incident proton spectrum.

7.10. COMPARISON OF PRIMARY PROTON DOSE WITH THE DOSE FROM GAMMA RAYS PRODUCED BY INELASTIC SCATTERING OF SOLAR FLARE PROTONS

F. S. Alsmiller, R. G. Alsmiller, Jr., and D. K. Trubey 225

The primary proton dose resulting from solar flare (May 10, 1959) protons incident on an aluminum shield is compared with the dose from gamma rays produced by inelastic collisions of the primary protons. Both spherical shell and slab shields are considered.

7.11. COMPUTER ROUTINE FOR TREATING COMPLEX GEOMETRIES IN MONTE CARLO AND OTHER TYPES OF CALCULATIONS

D. Irving 230

A general-purpose geometry routine for use in Monte Carlo and other calculations is described. The routine treats straight-line paths in complex geometrical configurations and determines through which media the path passes and the length of the path segment in each medium.

7.12. *TISSUE DOSE RATE FROM BREMSSTRAHLUNG RADIATION BEHIND AN IDEALIZED APOLLO VEHICLE WALL EXPOSED TO ELECTRONS IN THE EARTH'S OUTER RADIATION BELT*

C. D. Zerby, H. S. Moran, S. K. Penny, and D. K. Trubey 231

Calculations were performed to obtain the tissue dose rate from bremsstrahlung radiation behind an idealized Apollo vehicle wall exposed to electrons in the most intense part of the earth's outer radiation belt. The wall thickness was assumed to be 2.75 g/cm^2, and the resulting tissue dose rate was 8.58×10^{-3} rad/hr.

7.13. *TISSUE DOSE RATE FROM BREMSSTRAHLUNG RADIATION BEHIND AN IDEALIZED APOLLO VEHICLE WALL EXPOSED TO ELECTRONS IN THE ARTIFICIAL RADIATION BELT*

C. D. Zerby and H. S. Moran 236

Calculations were performed to obtain the first-order estimate of the tissue dose rate from bremsstrahlung radiation behind an idealized Apollo vehicle wall exposed to electrons in the most intense part of the earth's artificial radiation belt. The calculation followed the methods described in Sec. 7.12. The resulting calculated tissue dose rate is 1.91 rads/hr.

7.14. *NUCLEON-MESON CASCADE CALCULATIONS: TRANSVERSE SHIELDING FOR A 45-Gev ELECTRON ACCELERATOR*

R. G. Alsmiller, Jr., F. S. Alsmiller, and J. E. Murphy..... 238

Nucleon-meson cascade calculations have been carried out in the straight-ahead approximation to provide a check on other estimates of the thickness of earth shielding required for the 45-Gev electron accelerator to be built at Stanford University.

7.15. *NUCLEON-MESON CASCADE CALCULATIONS: SHIELDING AGAINST AN 800-Mev PROTON BEAM*

R. G. Alsmiller, Jr., and J. E. Murphy..... 239

Nucleon-meson cascade calculations have been carried out and the dose as a function of depth has been obtained for an 800-Mev proton beam incident on a shield. The physical properties used for the shielding medium are only a rough approximation to the properties of any particular medium.

7.16. *NUCLEON-MESON CASCADE CALCULATIONS: THE STAR DENSITY PRODUCED BY A 24-Gev PROTON BEAM IN HEAVY CONCRETE*

R. G. Alsmiller, Jr., and J. E. Murphy..... 240

The nuclear star density produced by a 24-Gev proton beam in a material having only approximately the properties of heavy concrete has been calculated. A comparison has been made with experimental measurements made at CERN, but, since the quantity which could be calculated is not the same as that which was measured, no firm conclusions can be drawn.

7.17. *PRELIMINARY RESULTS FROM EMULSIONS EMBEDDED IN A CONCRETE SHIELD EXPOSED TO A NARROW 9-Gev/c INCIDENT PROTON BEAM*

R. L. Childers..... 241

Preliminary measurements have been made on a set of nuclear emulsions exposed at various depths in barytes concrete on which an incident beam of 9-Gev/c protons impinged. The plates were exposed along the center line of the nuclear cascade only. Measurements of both the star density and track density indicate an attenuation length of about 165 g/cm^2 along the center line. The presence of μ-mesons is made evident by the nonexponential drop-off of the track density at great depths.

7.18. *A MONTE CARLO CALCULATION OF THE THREE-DIMENSIONAL DEVELOPMENT OF HIGH-ENERGY ELECTRON-PHOTON CASCADE SHOWERS*

C. D. Zerby..... 248

A general-purpose Monte Carlo program for study of the three-dimensional development of high-energy electron-photon cascade showers in a homogeneous medium is described.

7.19. *COLLIMATOR STUDIES FOR HIGH-ENERGY ELECTRON BEAMS*
C. D. Zerby and H. S. Moran 256
Calculations to determine the effectiveness of collimators in high-energy electron beams are described. Numerical results for 5-Gev electron beams incident on two aluminum collimators with inside radii of 0.3175 and 0.7239 cm are reported.

7.20. *POSITRON SOURCE STUDIES FOR A HIGH-ENERGY POSITRON ACCELERATOR*
C. D. Zerby and H. S. Moran 261
The positron flux resulting from the bombardment of a gold target by high-energy electrons has been calculated for incident-electron energies of 300, 1000, and 5000 Mev. Target thickness was 10 radiation lengths. The computational method was the same as that described in Sec. 7.18.

7.21. *A COMPILATION OF DATA CONCERNING SECONDARY PARTICLES RESULTING FROM PARTICLE-PARTICLE INTERACTIONS AT HIGH ENERGIES*
J. A. Elder 262
This paper is a brief summary of a paper to be published as an ORNL technical memorandum (ORNL TM-374).

8. EXPERIMENTAL TECHNIQUES FOR THE MEASUREMENT OF SECONDARY NUCLEAR PARTICLES FROM THE INTERACTIONS OF HIGH-ENERGY PROTONS

8.1. *PROTON INTENSITY MEASUREMENTS*
R. T. Santoro, R. W. Peelle, W. A. Gibson, W. R. Burrus, and R. J. Scroggs 272
Equipment and methods developed to accurately position target and detector equipment for experiments employing a synchrocyclotron are described, as are experiments leading to a detailed knowledge of beam profile, beam monitoring methods, and time distribution of protons within the beam.

8.2. *PROTON-RECOIL TELESCOPES FOR SPECTRAL MEASUREMENTS OF NEUTRONS AND PROTONS WITH ENERGIES > 10 Mev*
W. A. Gibson, W. R. Burrus, and C. F. Johnson 281
Two proton-recoil telescopes have been constructed, the first to measure spectra of neutrons having energies in the range from ~8 to 50 Mev and the second to measure those in the range from 50 to 150 Mev. Tests with neutrons produced by bombarding a copper target with 156-Mev protons indicate that modification of the low-energy telescope is needed to reduce backgrounds. Similar tests show essentially satisfactory performance of the high-energy telescope. The telescopes, with minor modifications, can also be used for proton spectral measurements.

8.3. *FLIGHT-TIME SPECTROSCOPY FOR NEUTRON AND PROTON YIELDS FROM NUCLEI BOMBARDED BY PROTONS*
R. W. Peelle, T. A. Love, and G. A. Luce 286
Flight-time spectroscopy is to be employed for measurements of thick-target yields and differential cross sections for interactions of 50- to 700-Mev protons with nuclei. The spectrometer design includes provision for counting individual protons incident upon the target, detection of target-produced neutrons, and identification of events caused by protons scattered from the primary beam. Modifications to the original equipment, made as a result of preliminary tests using a 25.2-g/cm^2-thick copper target and 156-Mev protons, are discussed. Some preliminary results are also shown.

8.4. *BONNER SPHERES AND THRESHOLD DETECTORS FOR NEUTRON SPECTROSCOPY*
W. R. Burrus 296
The application of so-called "Bonner spheres" to the measurement of neutron spectra over the energy range from thermal to ~10 Mev was investigated in preliminary experiments at the Harvard synchrocyclotron. The feasibility of augmenting the Bonner sphere data above 10 Mev with threshold detector data was also examined. Bonner spheres appear to be useful and will be studied further; the use of threshold detectors has been abandoned.

8.5. *SPECTROMETRY FOR GAMMA RAYS FROM PROTON-BOMBARDED NUCLEI*
W. Zobel 306

A three-crystal gamma-ray spectrometer has been constructed for the measurement of secondary gamma rays resulting from the bombardment of various nuclei by ~156-Mev protons. It will be used as a total-absorption spectrometer for low-energy gamma rays (<2 Mev) and as a pair spectrometer for higher energies. Preliminary experiments in which accelerator targets of aluminum and copper were used indicate that the design must be modified to reduce backgrounds caused by target-neutron interactions in the spectrometer shield.

8.6. *DOSIMETRY*
F. C. Maienschein and T. V. Blosser 310

During preliminary experiments at the Harvard synchrocyclotron an attempt was made to obtain very approximate dose rates with fast-neutron and gamma-ray dosimeters designed for measurements of reactor radiations. Most of their use came in investigating extraneous room background. Because of their high-energy proton response, the dosimeters will not be used in future work. One dose measurement will be attempted, however – the measurement of the physical dose due to all secondaries, regardless of type, in the interior of a 45-cm-diam spherical water-filled phantom.

9. ORNL DESALINATION STUDIES – THEORETICAL

9.1. *ION EXCLUSION IN POROUS-BED SALT FILTERS*
Lawrence Dresner 315

Ionic exclusion in packed beds of surface-charged particles has been studied with two special models of the fixed-charge distribution for which the Poisson-Boltzmann equation is exactly soluble. In the case of good co-ion exclusion, simple formulas have been obtained for the equilibrium co- and counter-ion concentrations.

9.2. *ELECTROKINETIC PHENOMENA IN CHARGED MICROCAPILLARIES*
Lawrence Dresner 317

Electrokinetic phenomena in small surface-charged capillaries have been studied. Fluid flow has been described by the Navier-Stokes equations, the ionic diffusion by the Planck-Henderson equation, and the electric field by Poisson's equation. In the case of good co-ion exclusion from the capillary, the coefficients in the linear laws relating water flow and counter-ion current to pressure, concentration, and electrical gradients have been explicitly calculated. Some numerical calculations of electrokinetic quantities have been carried out.

1. Research for Light-Water-Moderated Reactors

1.1. PRELIMINARY REPORT ON THE MEASURED GAMMA-RAY SPECTRA FROM A STAINLESS STEEL REACTOR

G. T. Chapman, K. M. Henry, J. D. Jarrard,
and R. L. Cowperthwaite [1]

A series of measurements of the gamma-ray leakage spectra from a stainless steel reactor core has been completed at the Bulk Shielding Facility (BSF). The measurements were made in the water surrounding the reactor core, through several different thicknesses of water. In addition, spectra were taken at various angles to the reactor normal at two points in the water away from the reactor face. The data are presented in this report as pulse-height distributions, pending the completion of the "unscrambling" of the data to obtain the gamma-ray spectra. Before the data can be completely analyzed the absolute neutron flux distribution in the reactor must also be determined.

For this experiment, the Pool Critical Assembly (PCA) was loaded with a 5×4 array of stainless steel fuel elements.[2] This resulted in an active core measuring 15 in. high by 15 in. wide by 12 in. deep. The minimum core thickness sufficient to maintain a critical assembly and a simple geometry was used to minimize the effects of core-scattered gamma rays on the spectra. The reactor was maintained at a nominal 2-w power level throughout the experiment to retard the buildup of fission-product gamma-ray emitters in the core.

In addition to the usual reactor control instruments, the reactor power was further monitored by means of a 3-in.-diam fission plate detector located at the east face of the reactor and by the activation induced in a gold foil exposed in the core during each run. A 50-cc ion chamber located adjacent to the fission-plate detector was used to monitor the gamma-ray intensity during each run. The reactor was operated at the 2-w power level for a minimum of 1 hr prior to any gamma-ray data being taken, and then the data were taken only if the ion chamber indicated an equilibrium gamma-ray condition. Figure 1.1.1 is a block diagram of the reactor monitor system.

The data were obtained with the Model IV gamma-ray spectrometer.[3] Figure 1.1.2 is a drawing of the spectrometer shield and the crystal, showing the collimator-acceptance cone arrangement. The acceptance cone was an air-filled, aluminum-walled, conical section with an acceptance angle slightly larger than the solid angle defined by the tungsten-lead collimator of the spectrometer. The length of the cone was 72 in.

---

[1] Co-operative student from the Missouri School of Mines and Metallurgy, Rolla, Missouri.

[2] E. G. Silver and J. Lewin, *Safeguard Report for a Stainless Steel Research Reactor for the BSF (BSR-II)*, ORNL-2470 (July 16, 1958).

[3] G. T. Chapman and T. A. Love, *Neutron Phys. Div. Ann. Progr. Rept. Sept. 1, 1958*, ORNL-2609, p 133.

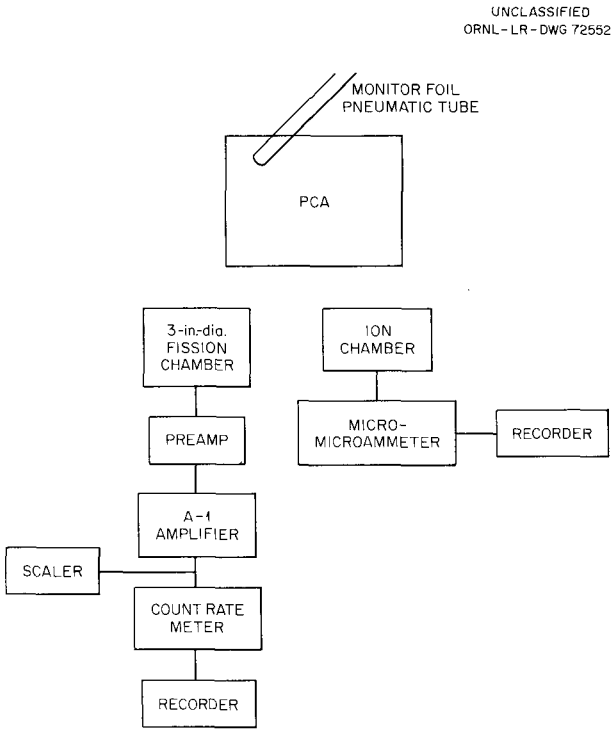

Fig. 1.1.1. Block Diagram of Reactor Monitoring System Electronics.

and the diameter of its end was 2 in. With the cone in place, a minimum of 72 in. of water was maintained between the spectrometer shield and the reactor. It was shown previously[4] that 72 in. of water is sufficient to prevent contamination of the measured spectra by neutron-capture gamma rays born in the materials of the spectrometer shield.

Figure 1.1.3 shows a block diagram of the electronics for the gamma-ray spectrometer. By means of a pneumatically controlled heating-cooling system, the internal temperature, as measured by an iron-constantan thermocouple, was maintained at a constant 75 $\pm$ 0.5°F. Both input and storage of the 256-channel analyzer are monitored by count-rate meters to assure a knowledge of count-rate behavior during each run. The system was calibrated before and after each run with the gamma rays from Na^{22} (0.511 and 1.274 Mev), Na^{24} (1.368 and 2.754 Mev), Y^{88} (0.855 and 1.840 Mev), Cs^{137} (0.662 Mev), and Pr^{144} (0.697, 1.487, and 2.186 Mev). In addition, a calibration at the beginning and end of each day was made with the 6.13-Mev gamma ray from the N^{16} of activated water. A standard test pulse generator was used as an additional check on the gain and linearity of the whole spectrometer system.

Figure 1.1.4 shows the pulse-height distribution of gamma rays obtained with the spectrometer oriented so that the axis of the acceptance cone was normal to the face of the reactor. The distributions indicate

---

[4]G. T. Chapman, *Neutron Phys. Div. Ann. Progr. Rept. Sept. 1, 1961*, ORNL-3193, p 197.

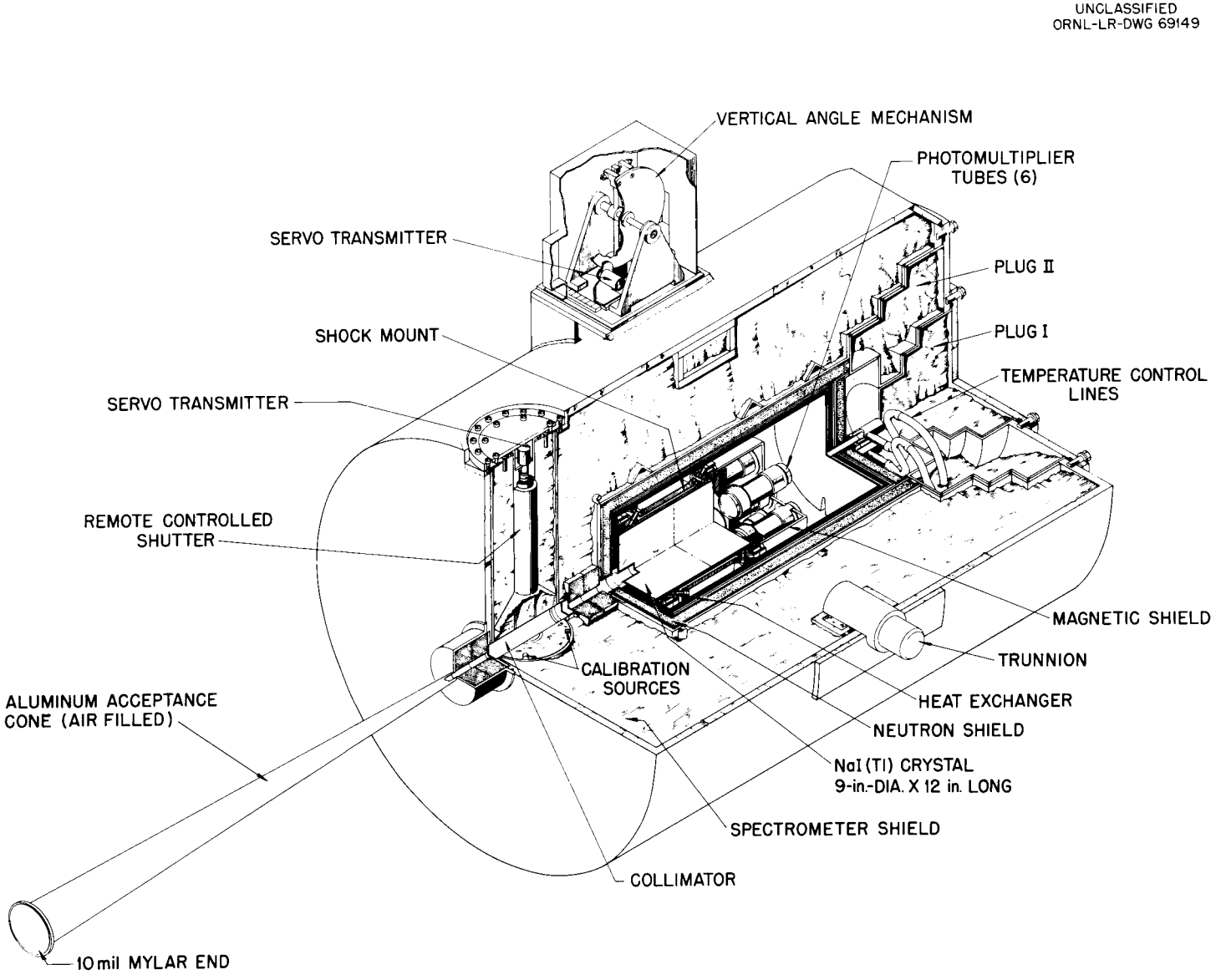

Fig. 1.1.2. Model IV Gamma-Ray Spectrometer, Showing Aluminum Acceptance Tube Used in Spectral Measurements on a Stainless Steel Reactor Core.

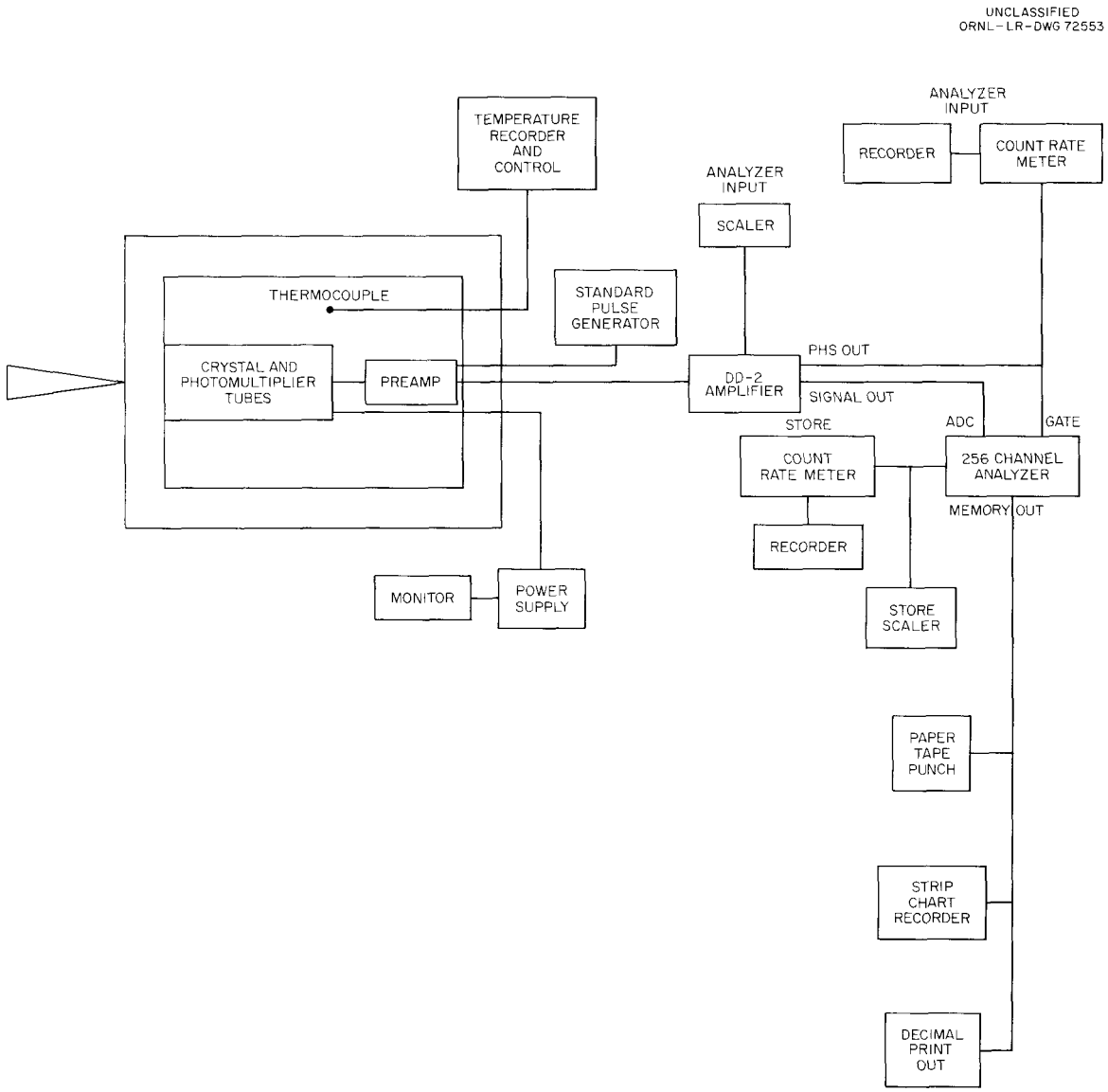

Fig. 1.1.3. Block Diagram of Spectrometer Electronics for Measurement of Spectra from a Stainless Steel Reactor Core.

that above 5 Mev the spectrum is composed primarily of the gamma rays resulting from the capture of thermal neutrons in the elements of the stainless steel. This is demonstrated by the histogram of photons per Mev vs energy, where the relative numbers of capture gamma rays were weighted by the relative amount of the capturing elements in the stainless steel. This histogram is based on the compilations of Groshev *et al.*[5] and Troubetzkoy and Goldstein.[6] The predominant peak below 5 Mev is due to the capture of thermal neutrons in the reactor pool water. An examination of the spectra below 3 Mev with a greater amplifier gain (see Fig. 1.1.5) confirmed that no significant structure in the spectra is evident below 2 Mev.

---

[5]L. V. Groshev *et al.*, *Atlas of Gamma-Ray Spectra from Radiative Capture of Thermal Neutrons*, International Series of Monographs on Nuclear Energy, Pergamon, New York, 1959.

[6]E. Troubetzkoy and H. Goldstein, *A Compilation of Information on Gamma-Ray Spectra Resulting from Thermal-Neutron Capture*, ORNL-2904 (May 17, 1960).

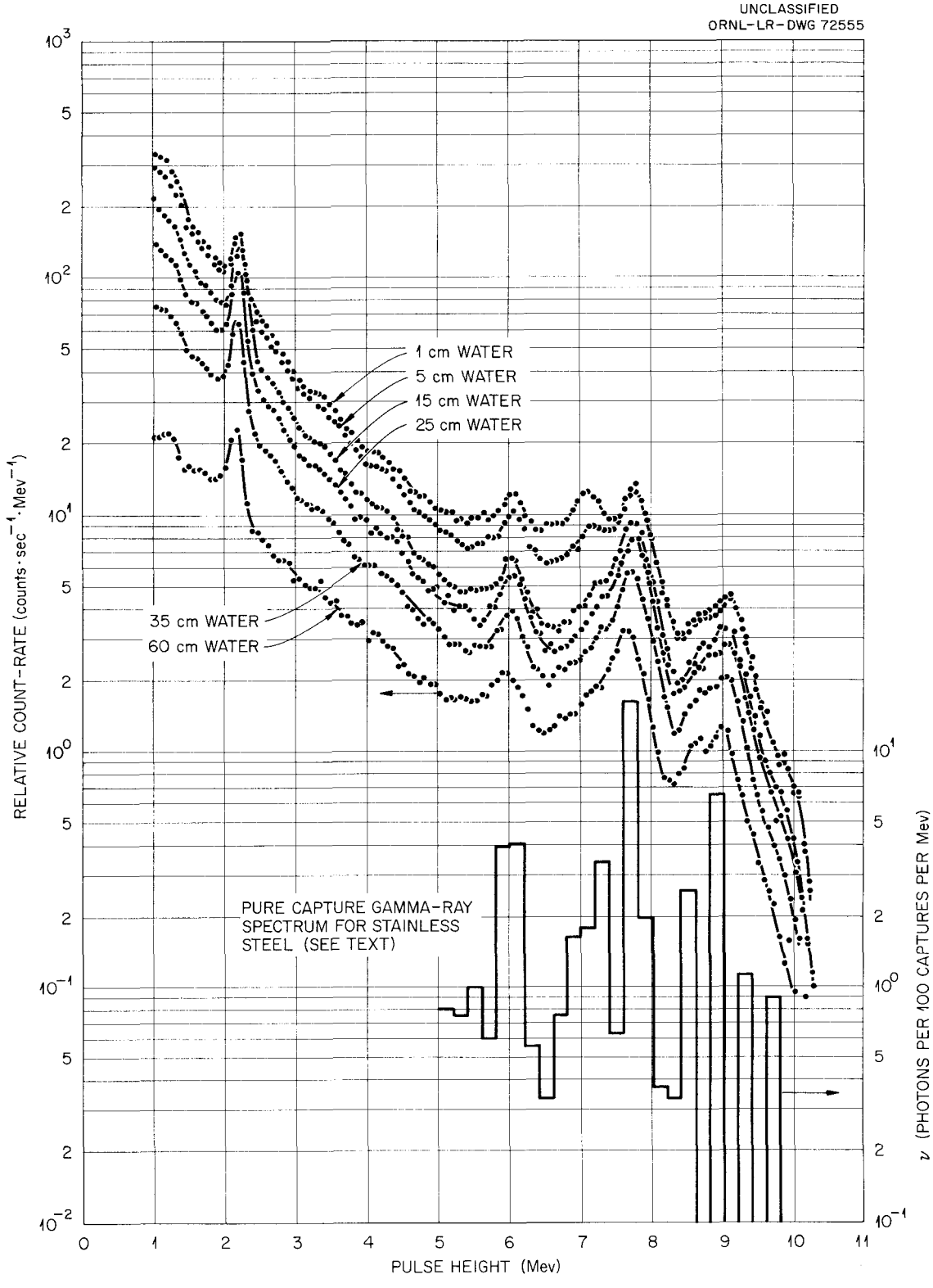

Fig. 1.1.4. Pulse-Height Distribution of Gamma Rays Emitted Normal to the Surface of a Stainless Steel Reactor Core Through Various Thicknesses of Water.

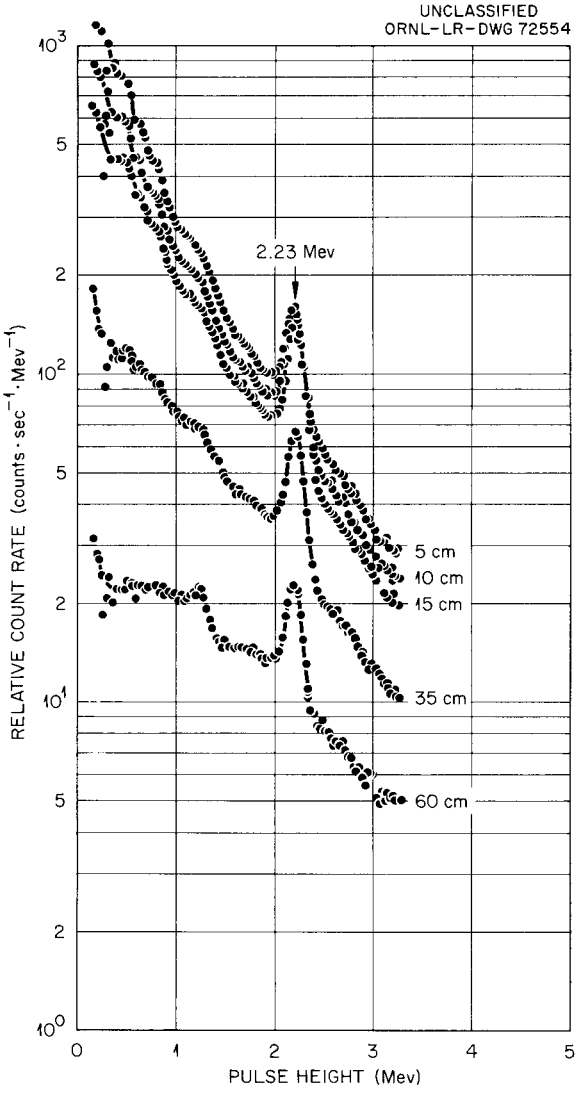

Fig. 1.1.5. Pulse-Height Distribution of Gamma Rays of Energies Less Than 3 Mev Emitted Normal to the Surface of a Stainless Steel Reactor Core Through Various Thicknesses of Water.

Figures 1.1.6 and 1.1.7 show the pulse-height distributions obtained at various angles as the spectrometer was rotated in a horizontal plane about points in the water at 10 and 25 cm from the surface of the reactor. The coordinate scheme to which the data were referenced is diagrammed in Fig. 1.1.8. A more detailed study of these data is required, and it may only be said at present that the general shape of the distributions is not greatly changed except at the extreme angles, where the spectrometer saw essentially none of the active core. The intensities may be modified when the data are corrected for the change in source strength, due to the change in reactor thickness, as the spectrometer was rotated away from the normal axis.

A number of programs for the IBM-7090 have been written to facilitate the handling of the original data as delivered on punched paper tape by the pulse-height analyzer. Initially, a nonlinear least-squares fit is made on the peaks which occur in the calibration spectra to determine the location of the peak centers for each energy. These data are then fitted by means of a bivariant-polynomial least-squares fit, that is,

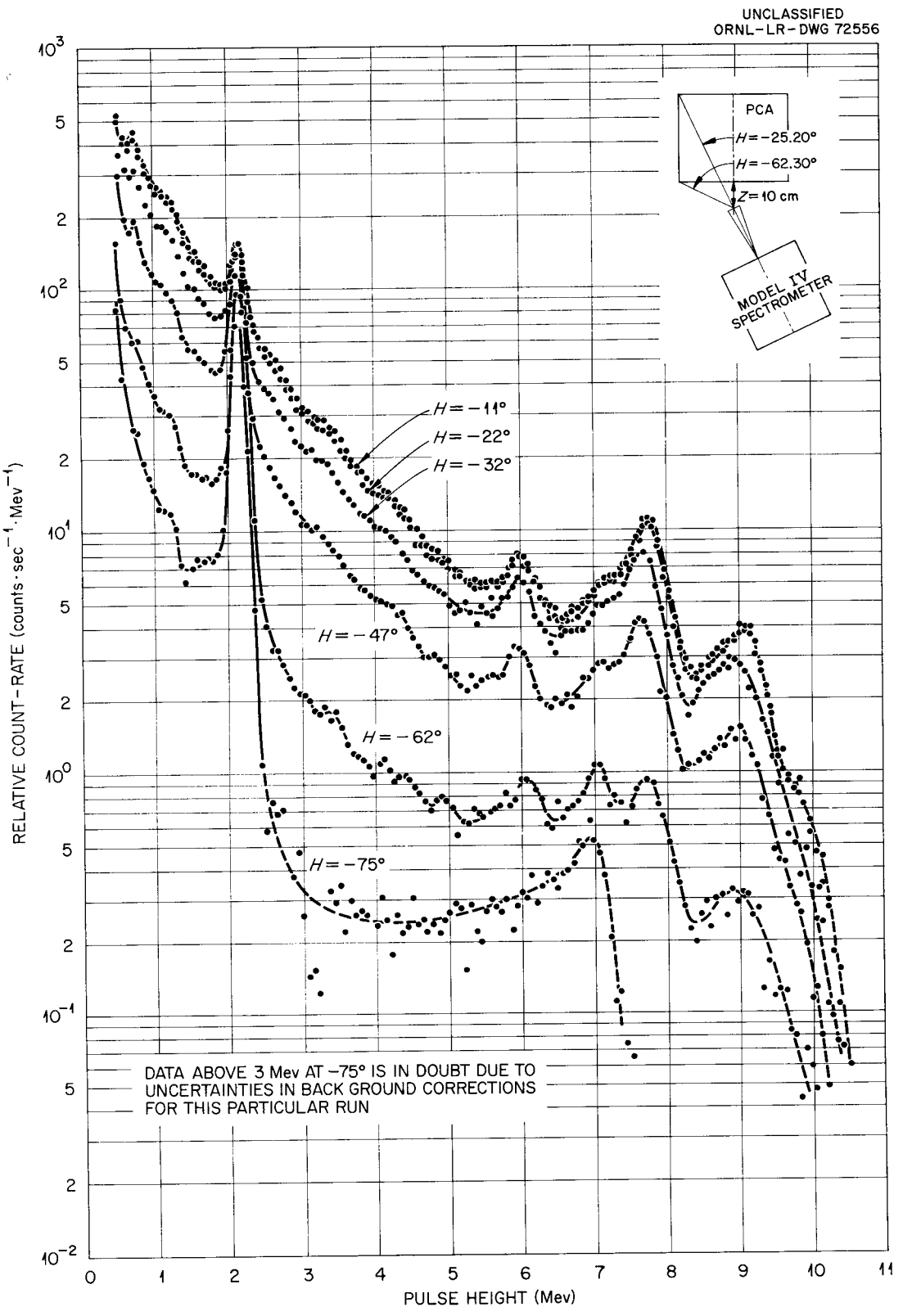

Fig. 1.1.6. Pulse-Height Distribution of Gamma Rays from a Stainless Steel Reactor Core at Various Angles About a Point in Water 10 cm from Core Surface.

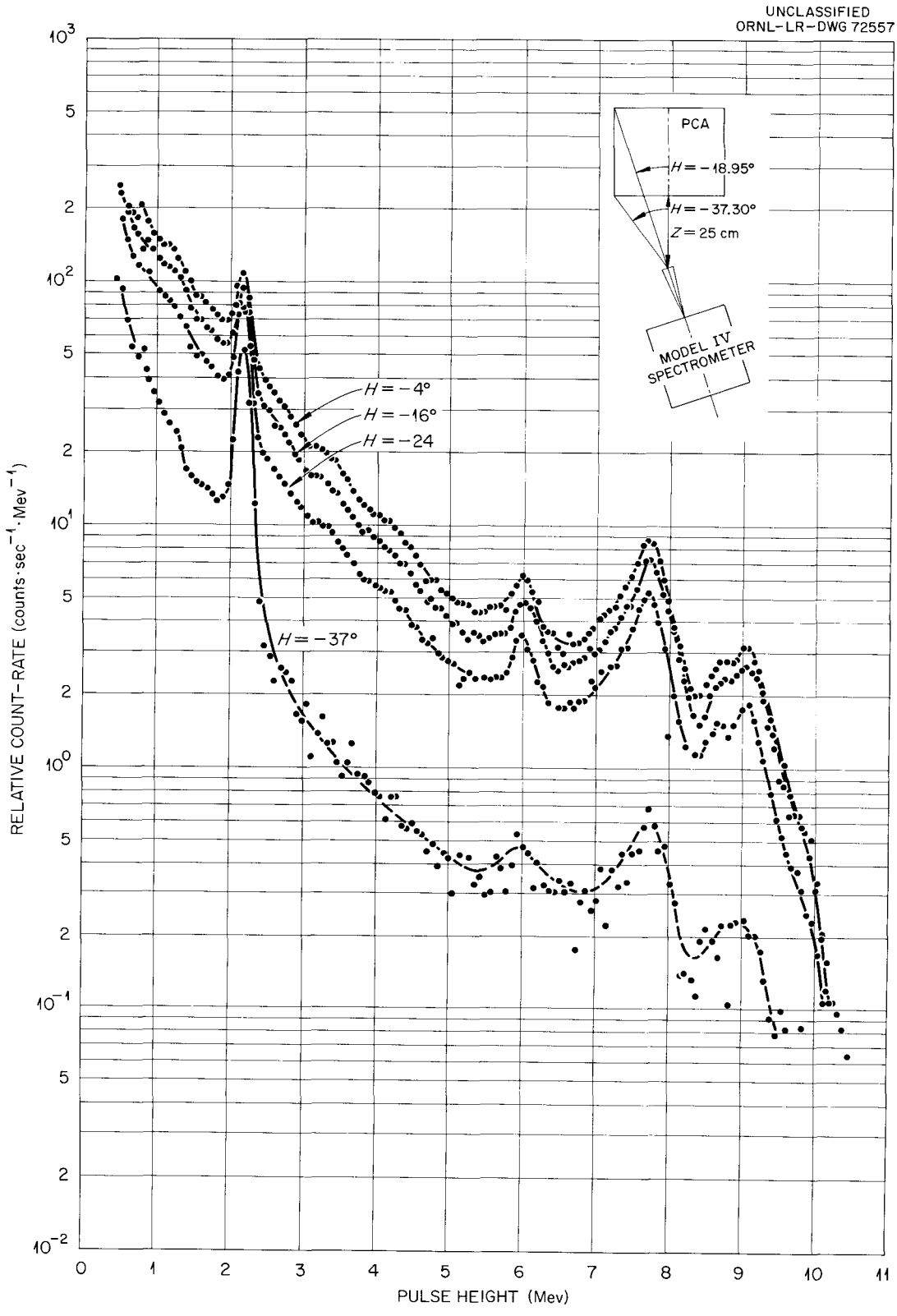

Fig. 1.1.7. Pulse-Height Distribution of Gamma Rays from Stainless Steel Reactor Core at Various Angles About a Point in Water 25 cm from Core Surface.

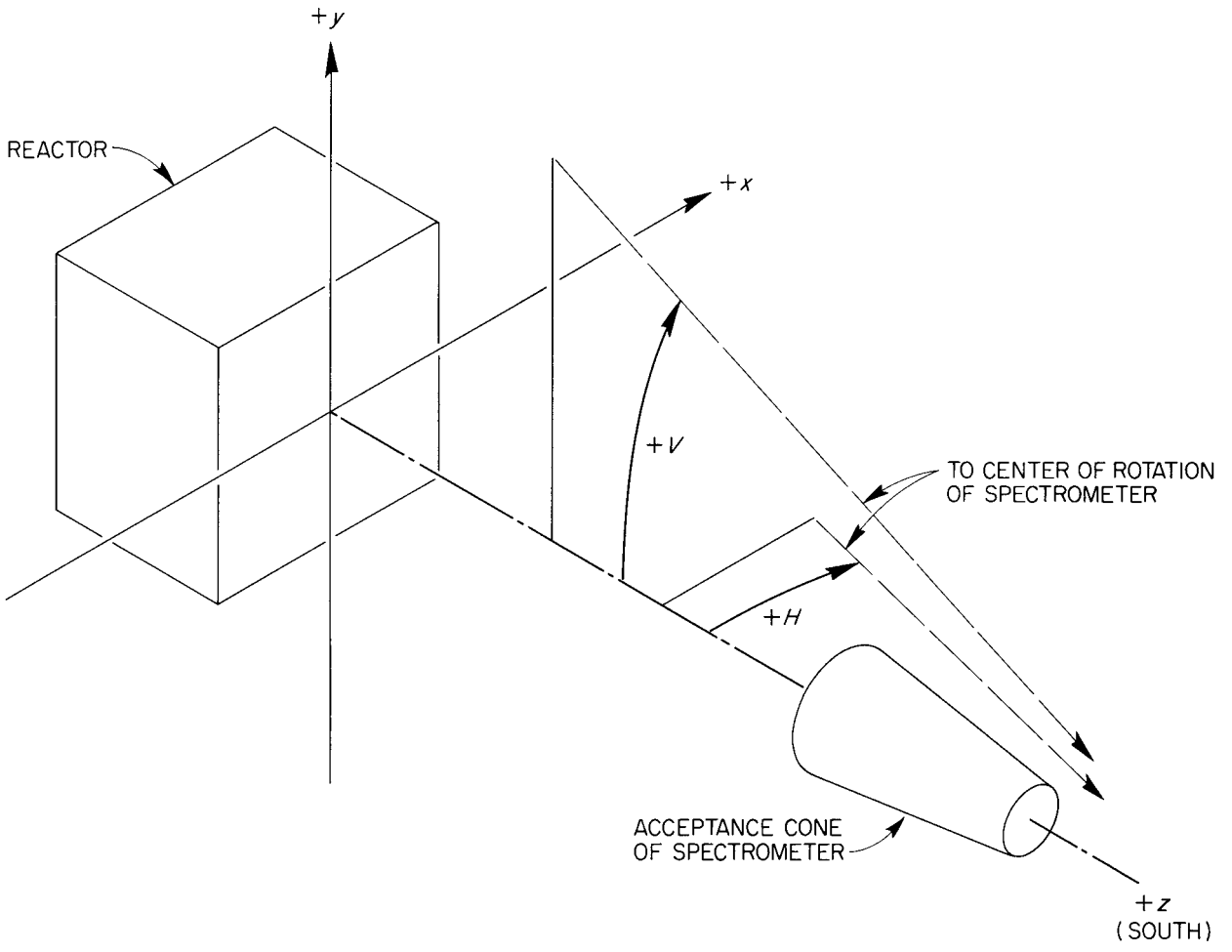

Fig. 1.1.8. Coordinate Scheme Used in Measurement of Gamma-Ray Spectra at Various Angles from Reactor Normal.

a fit weighted by the error in both the abscissa and the ordinate, to determine the energy-vs-channel relation and the estimated errors of the fit. A group of experimental spectra is then read into the computer and converted, at the option of the operator, into count rate vs channel and/or count rate per Mev vs Mev. The background for each run may be subtracted individually, or as many as five runs may be accumulated before the background subtraction is done. The output may be in printed form, on magnetic tape suitable for use on the CALCOMP curve plotter, or both. Programs are being written to fit semianalytic functions to the energy-response curves in preparation for the unscrambling phase of the analysis and to correct for systematic errors that are now known to have existed. For example, it may be noticed in Fig. 1.1.4 that the spectra are shifted slightly toward higher energy as the spectrometer approached the reactor. This was found to be due to an effective shift in the lower level of the analog-to-digital converter circuit of the 256-channel analyzer as the input count rate was increased.

1.2. EXPERIMENTS AND CALCULATIONS ON THE REACTIVITY EFFECTS OF SMALL FUEL DISPLACEMENTS

E. G. Silver, Z. M. Bartolome,[1] K. M. Henry, and J. D. Kington

One of the various mechanisms affecting the reactivity during a reactor power transient is the motion of fuel, such as that due to pressure or temperature-gradient effects. A program is in progress at the Bulk Shielding Facility to determine the reactivity effects of certain small fuel displacements in the BSR-I by experiment, to find calculation methods for computing such effects, and to check the adequacy of the calculational methods by the experimental results.

Experiments

A basic 25-element loading of the BSR-I reactor was perturbed by making compensating changes in the three center elements shown in Fig. 1.2.1. By "compensating changes" is meant that as a fuel plate was removed two other specially made plates, each containing one-half the amount of fuel that was in the removed plate, were inserted in a water channel elsewhere in the three-element experimental region. Thus the total amount of fuel remained unaltered by the perturbation. In order to determine the effect of the proximity of a control-rod water-well, some loadings incorporated a 9-plate space in the center of the reactor core. In the majority of cases the perturbations were so designed as to maintain as nearly as possible the symmetry of the core with respect to two mutually perpendicular planes (as shown in Fig. 1.2.1) in order to facilitate comparison with the calculations. The quoted uncertainties in the results include possible errors in reading the regulating-rod position, uncertainties in the parameters of the inhour equation, and, most important, errors due to free play in the fuel element positions and orientations. The last mentioned error was determined by several repetitions of measurements with intervening unloading and reloading of many fuel elements in order to introduce random changes.

The reactivity effects were measured by the use of a calibrated regulating rod (one of the four rods shown in Fig. 1.2.1) with a total worth of approximately 0.35% $\delta k/k$. This rod was calibrated by the use of the inhour method, using the shim rods to compensate for the reactivity of the rod being calibrated. In some cases the reactor configuration was subcritical with the 5×5 loading. In such cases two additional elements were added as needed in the positions indicated in Fig. 1.2.1, and the regulating rod was recalibrated to avoid errors due to changes in its importance. The results of all measurements are shown in Fig. 1.2.2.

Calculations

Several reactor codes which in the past had given satisfactory results for the critical mass of unperturbed reactors were used to calculate some of the loadings tested by experiment. A one-dimensional calculation in cylindrical geometry was performed with the MODRIC code,[2] a one-dimension, 32-group diffusion theory code for treating the hydrogen scattering in the Goertzel-Selengut approximation. The energy

---

[1] Affiliated with the Philippine Atomic Energy Commission; formerly on loan to ORNL.

[2] *MODRIC: A One-Dimensional Neutron Diffusion Code for the IBM-7090*, private unpublished material by the Central Data Processing Group, Oak Ridge.

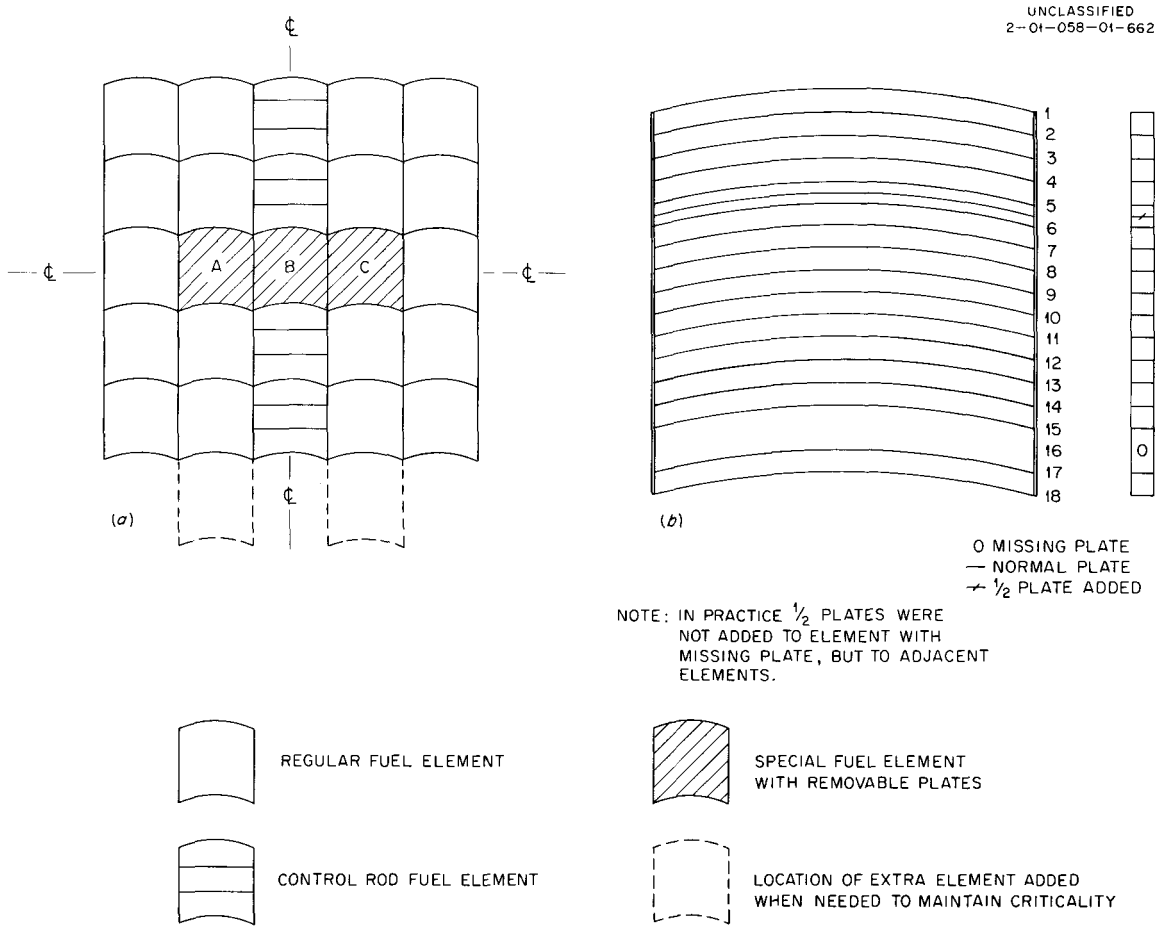

Fig. 1.2.1. Bulk Shielding Reactor I Core Configuration for Investigation of Fuel Displacement Reactivity Effects. (*a*) Top view of core configuration. (*b*) End view of special fuel element showing one plate removed and a one-half plate added. The representation of this element, as used in Fig. 1.2.2, is shown at the right.

fluxes yielded by this code are used to produce energy-weighted few-group cross sections and diffusion coefficients. These few-group parameters (four groups) were used as input to the two-dimensional PDQ-2 code,[3] an IBM-704 code adapted for use with the IBM-7090 computer, which is a straight diffusion theory few-group code that solves the reactor equation in two cartesian or cylindrical dimensions. In order to improve the energy weighting in regions near discontinuities in the core, regions of homogeneous composition were subdivided into separate regions surrounding each interface; thus the cross-section computation is separately carried out in the vicinity of such discontinuities.

In most cases, several MODRIC calculations were used to assemble the input parameters for the PDQ-2 calculation in order to take proper account of the effect of the eccentric location of some of the regions, which could not be adequately handled in a single one-dimensional calculation.

---

[3]G. G. Bilodeau *et al.*, PDQ – *An IBM-704 Code to Solve the Two-Dimensional Few-Group Neutron-Diffusion Equations*, WAPD-TM-70 (August 1957).

UNCLASSIFIED
2-01-058-01-663

EXPERIMENT NUMBER	PLATE NUMBER (1 2 3 4 5 6 7 8 9 10 11 12 13 14 15 16 17 18)	δk/k (%) MEASURED	δk/k (%) CALCULATED
1	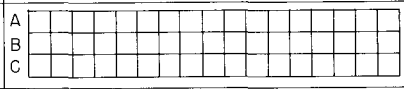	(UNPERTURBED)	(UNPERTURBED)
2	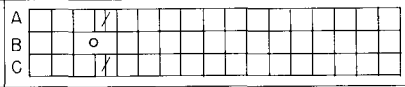	−0.092 ± 0.005	
3	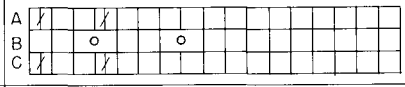	−0.207 ± 0.005	
4	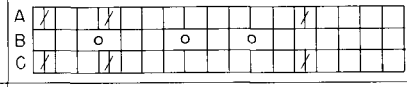	−0.314 ± 0.005	
5	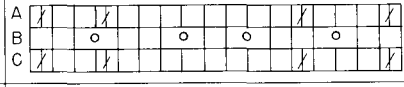	−0.422 ± 0.005	−0.381
6	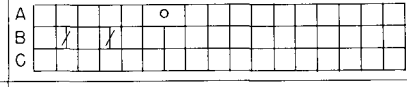	−0.061 ± 0.005	
7		−0.140 ± 0.005	
7a	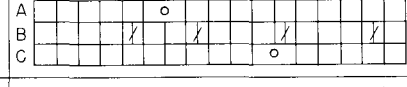	−0.142 ± 0.005	
8		−0.231 ± 0.005	
9	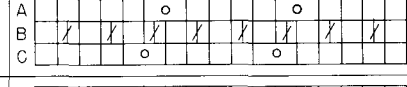	−0.305 ± 0.005	−0.580
10		UNPERTURBED WITH WATER SPACE	UNPERTURBED WITH WATER SPACE
11		+0.025 ± 0.005	
12		+0.081 ± 0.005	−0.158
13		+0.056 ± 0.005	
14		+0.016 ± 0.005	−0.163

CODE OF SYMBOLS

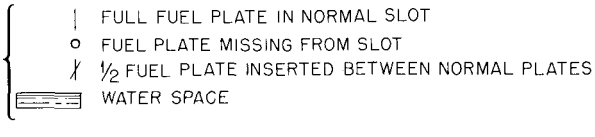

Fig. 1.2.2. Measured and Calculated Changes in Reactivity Due to Fuel Displacements in Various BSR-I Core Configurations.

The computed multiplication agreed with the experimental one within 1.5% in all cases, the calculated values lying systematically lower than the experimental results. Although this agreement is reasonably good, the interest here was in the relative differences between the perturbed and unperturbed reactor configurations. These differences as calculated are also shown in Fig. 1.2.2, and it can be seen that although the agreement seems reasonably good in some cases, it is quite poor in others.

Further calculations to determine the cause of the disagreement were performed. The results suggest strongly that the problem involves the transport effects that may be expected to be important close to region boundaries and in small regions of highly different composition from that of the adjacent regions. The perturbations do constitute such regions. A one-dimensional S_n-method calculation was performed for comparison with the MODRIC result. Figure 1.2.3 shows the two thermal flux shapes as obtained by the MODRIC and DSN codes (the latter is a one-dimensional, 18-energy-group transport code using four direction groups; it was used with the same mesh and input as the MODRIC case with which it is being compared). It is apparent that the effect of the water space and of the extra-fuel region is much larger in the S_n calculation.

Since there are as yet no transport-theory codes available in two dimensions that are comparable to PDQ-2 in geometric sophistication and coded for the IBM-7090, no direct testing of this hypothesis as to the source for the disagreement between the measured and calculated effects of these perturbations has been possible.

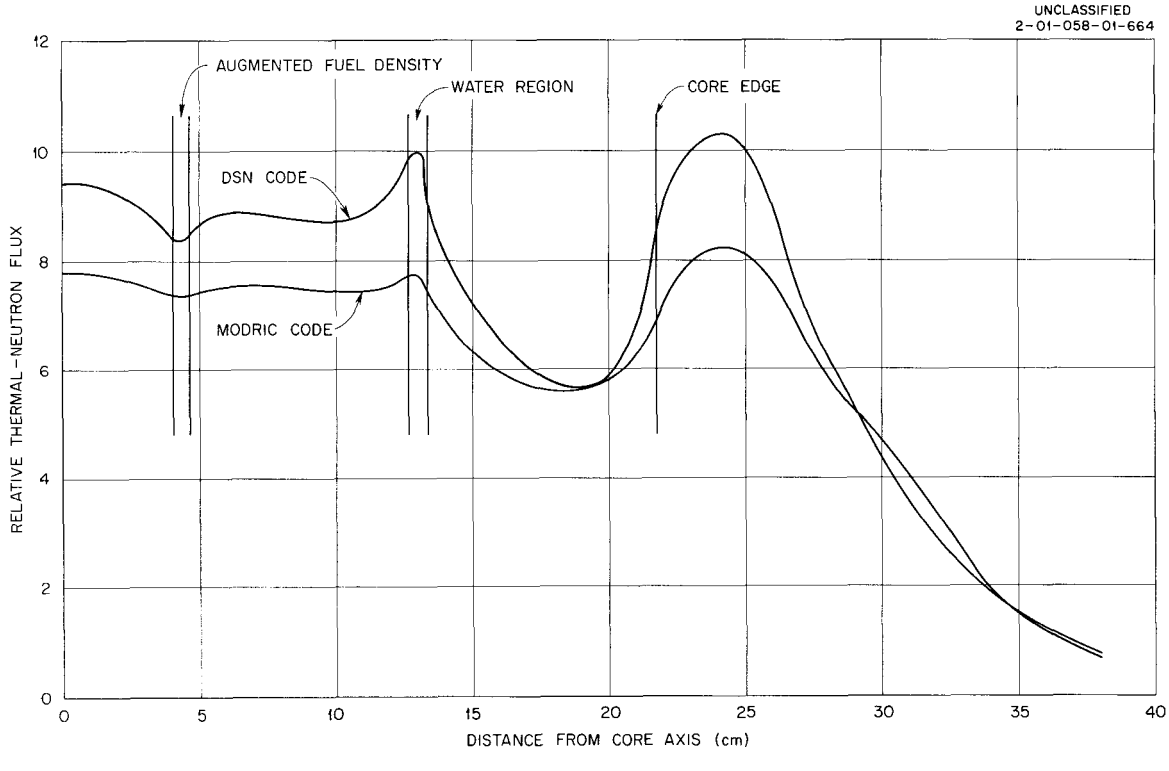

Fig. 1.2.3. Comparison of Thermal-Neutron Fluxes Calculated by DSN and MODRIC Codes for Cylindrical Model of a BSR-I Configuration.

Conclusions and Plans

The experiments indicated that negative reactivities result from all perturbations that decrease the homogeneity of the core, except when the perturbation adds fuel to high-importance regions, such as those adjacent to interior water volumes. However, there is not yet enough evidence to establish this supposition as a conclusion. Further experimental work, including larger regions of the core, is needed to accomplish this.

The calculational methods used appear to be inadequate to cope with the kind of small-dimension, large-magnitude perturbations represented by the experiments. No direct method of calculating these perturbations seems available in the absence of a two-dimensional transport code of sufficient scope to deal simultaneously with multigroup, many-mesh-point, multiangle problems, at least with acceptable computing times.

Preliminary preparations are in progress on two types of experiments designed to substantiate the inferences drawn as to the cause of the discrepancies in the results. First, a number of "one-dimensional" slab reactor experiments will be performed with fuel plates with effective dimensions of 30 by 60 in. reflected only along the slab axis. The cores so formed will be perturbed by the removal and addition of single fuel plates and the results will be rigorously compared with calculations by the one-dimensional transport theory (the DSN code). It is hoped that the DSN code will result in agreement between calculations and experiment sufficiently satisfactory to explain the causes of the present discrepancies.

Following these experiments, it is intended to perform measurements in a "two-dimensional" core, that is, a reactor of normal BSR-type shape, using variable fuel-plate spacings, so that realistic perturbations can be simulated; diffusion-theory code methods should be applicable for comparison.

2. Radiation Detector Studies

2.1. APPLICATIONS OF SOME INSTRUMENT-RESPONSE UNFOLDING METHODS

W. R. Burrus

It is usually essential in making use of experimental data to calculate a set of desired quantities from a set of instrument readings. The set of desired quantities is called the "solution" and the instrument readings are called the "observations." Underlying the solution and the observation is the "hidden spectrum," which is usually unobtainable because of the effects of instrument broadening, the finite number of readings that can be taken, and the statistical fluctuations in the instrument readings. For a gamma-ray spectrometer, for example, the number of photons per unit energy interval would be the hidden spectrum, the pulse-height distribution recorded would be the observation, and the solution might be the value of "tissue dose," or some approximation (perhaps with part of the instrumental broadening left) to the hidden spectrum. The relation between the hidden spectrum and the observation can be written $Ax = b$, where x is a vector representing the hidden spectrum, b represents the observation, and A is the matrix representation of the instrument-response function. The process whereby functions of the x's are obtained from the b's is called "unfolding." Naturally, the best "solution" is obtained by impressing on the unfolding process all available a priori information. An example of such information is the nonnegative character of x; another, in many cases, is that it is smoothly varying. The basic problem in unfolding, then, is in going directly from the observation to the solution, making use of whatever information is known about x, without actually having to explicitly calculate x. Two IBM-7090 computer codes have been written for unfolding experimental data with the use of a priori information.

The first of these codes, OPTIMO, described in a previous report,[1] is designed to evaluate functions of a nonnegative vector, or the vector itself, with the observations statistically uncertain. The basic equation, which because of this statistical variation must be uncertain, is replaced by the inequality relation $|Ax - b| \leqq \sigma$, where each element of σ is taken typically to be about one standard deviation in the corresponding element of b. A linear programming technique is used to explore the solution in the dual space.

The second, and most recent of these codes, is called SLOP and is described in Sec. 2.2. This code is also designed to evaluate functions of a nonnegative vector x satisfying the uncertain $Ax = b$ relation. It comprises an extension of the conventional least-squares method but also minimizes an extra term arising from a priori nonnegativity requirement. The merit of SLOP lies in its use of a sequence of simple linear transformations and its ability to evaluate several functions of the unknown vector x at once.

Both codes are simplifications of a more general method. A rigorous solution of the general problem would require the solution of two quadratic programming problems for each function of the unknown vector x. Known algorithms for the solution appear to be too time-consuming for consideration, although it is hoped that shortcuts will be found. Consideration is being given to a new code, to be identified as HONEST JOHN, which will combine certain features of OPTIMO and SLOP. The approximation of

[1] W. R. Burrus, *Neutron Phys. Div. Ann. Progr. Rept. Sept. 1, 1961*, ORNL-3193, pp 44–52.

OPTIMO becomes exact in the limiting case where the right-hand side is known exactly and the uncertainty is due to the underdetermined nature of the problem (i.e., more unknowns than knowns, or matrix A singular). SLOP reduces to ordinary least squares when no a priori information is available. The combined code would be correct in both limiting cases.

The OPTIMO code has been continuously modified during the last year, and now most of the options originally planned do work. The last step in completing OPTIMO will be to use evaluations already computed as a starting point for new evaluations. It is expected that this will result in a gain in speed of a factor of 10. The nonnegativity constraint of the original code has been replaced with a more general constraint which allows the specification that the unknown vector x is a positive sum of specified functions. By proper choice of the functions, the condition may be incorporated that the spectrum be monotonically decreasing, or smoothly varying, or so forth, as may be physically justified for a particular problem.

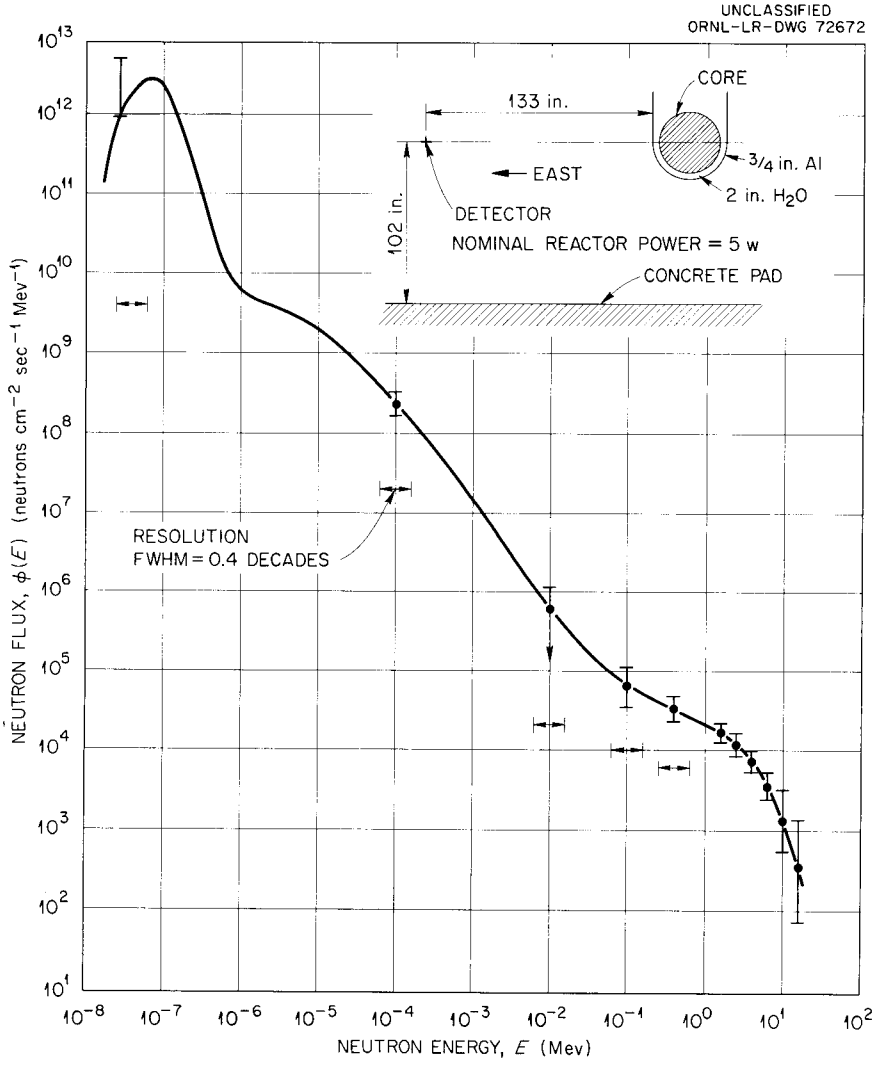

Fig. 2.1.1. Tower Shielding Reactor II Neutron Spectrum Unfolded with OPTIMO Code.

An example of a neutron spectrum which was unfolded with the OPTIMO code, over the range 0.01 ev to 16 Mev, is the Tower Shielding Reactor II spectrum shown in Fig. 2.1.1. The "spectrometer" used was a set of eight Bonner spheres.[2] The a priori information used was the nonnegativity of the spectrum and also the smoothness which would be expected to result from the continuous neutron birth and slowing-down processes. Although the results do not show high accuracy or resolution, competing methods are generally more complex and cover a more restricted energy range. The solution of this problem required about 5 min on the IBM-7090 computer. (The code itself, however, required one year for debugging and initial exploratory solutions.)

An example of the unfolding of a spectrum of gamma rays due to thermal neutron capture by the 27-kev resonance of fluorine is shown in Fig. 2.1.2. The data were obtained with a 9 by 12 in. total absorption NaI(Tl) scintillation spectrometer by R. Bird of the Physics Division. The spectrum was unfolded by the SLOP code using only the nonnegativity a priori condition. The natural instrument resolution of about 10% was not unfolded, but all effects of Compton backscatter, escape, etc., have been removed, making interpretation of the spectrum easier. This problem required about 2 min on the IBM-7090 computer (on the fifth try).

Further details of the performance of these codes and a comparison with competing methods will appear in subsequent annual reports.

---

[2]R. L. Bramblett, R. I. Ewing, and T. W. Bonner, *Nucl. Instr. Methods* **9**, 1–12 (October 1960).

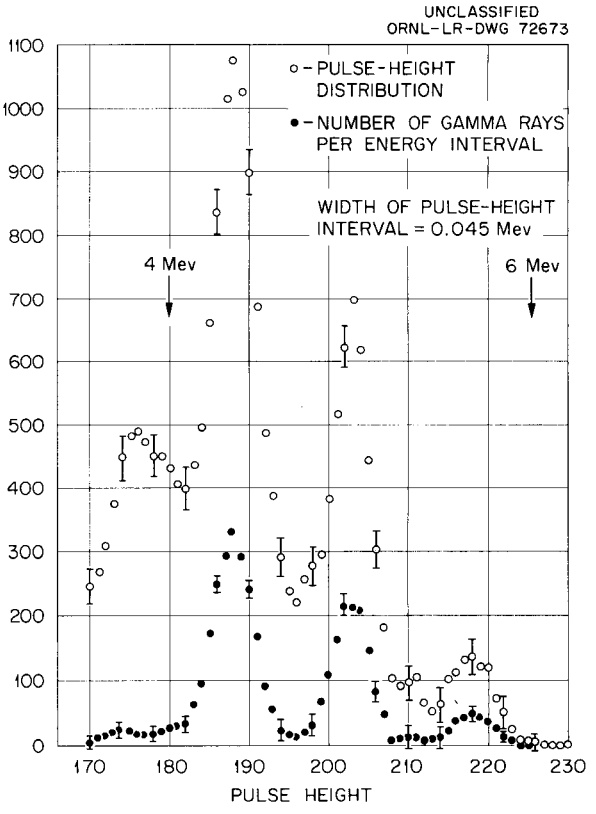

Fig. 2.1.2. Gamma-Ray Spectrum from Neutron Capture in the Resonance of Fluorine, Unfolded with SLOP Code.

2.2. THE SLOP CODE FOR THE UNFOLDING OF INSTRUMENT RESPONSE

V. D. Bogert and W. R. Burrus

The response of an instrument such as a scintillation spectrometer can be expressed in terms of an unknown spectrum by the following matrix equation:

$$Ax = b \ , \tag{1}$$

where

b_i = number of counts (or units of response) in the ith pulse-height bin ($i = 1 , \ldots , m$),

x_j = number of particles in the jth energy bin, which has edges E_j and E_{j+1} ($j = 1 , \ldots , n$),

A_{ij} = probability that a particle in an energy bin j will produce a count in pulse-height bin i, averaged over the jth bin.

An elementary approach to instrument unfolding would be to set up a matrix equation of sufficiently large order to represent the spectral details which can be resolved by the instrument and to solve for x as follows:

$$x = A^{-1}b \ . \tag{2}$$

Unfortunately, this elementary approach will not work on a large system of equations, perhaps of order 100 by 100. One reason for the failure of this approach is that the matrix A is so nearly singular that obtaining its inverse is a formidable computational problem. On machines currently available, multiword precision arithmetic would certainly be required. A second reason is that even if the inverse could be calculated with satisfactory precision, the solution for x would have astronomical errors due to the amplification of the inherent statistical fluctuations in the observed pulse-height distribution.

The SLOP code described in this section avoids the second problem by solving for a broadened version of the solution x. In the case of a properly chosen broadening matrix, the statistical errors of the result may be greatly reduced. This can be explained by assuming that the instrument in question has a certain natural resolution (i.e., full width at half maximum of the peak) and that an attempt to improve this natural instrument resolution width by computational ingenuity can be carried only so far. The best results should be expected when a broadening function approximately the same width as the natural instrument resolution, but never much narrower, is chosen.

The first problem mentioned above may also be avoided by the use of two techniques. First, if we solve for a broadened solution of x, the solution x of Eq. 2 need never be calculated. If we employ the proper strategy, we may go toward the desired solution of the broadened x without the explicit computation of x, which would amount to unfolding all the natural instrument resolution as considered above. Second, the computational problems may be reduced by employing some a priori information about the solution. For example, in the case of a scintillation spectrometer, it is known that $x \geqq 0$. The SLOP code, however, has provisions for incorporating further a priori information about the unknown spectrum. The code will accept a restriction on x which implies that x is the sum of specified functions with positive coefficients such

that

$$x = \sum q_i f_i(E) , \qquad q_i \geq 0 . \tag{3}$$

The proper choice of the functions $f_i(E)$ will restrict the spectrum to be slowly varying, monotonically decreasing, and so forth. In all cases, however, the code imposes these restrictions upon the spectrum x without requiring an explicit solution for x.

It is possible to obtain a value for the x solution vector by choosing a broadening matrix with unit diagonal elements (*the I matrix*), but, as expected, the solutions for x are generally poor for the reasons given above. In certain cases, however, the code can be employed to determine x directly. An example solved previously[1] has also been solved by the SLOP code. The method used previously merely forced a nonnegative solution of x and solved for a point, whereas the SLOP code publishes a confidence region [XUP,XLO] which contains the solution XEST. The results of the two methods, as well as those of a matrix inversion method, are compared in Table 2.2.1.

The mathematical method employed by the SLOP code is a variation[2] of the ordinary method of least squares used for solving an overdetermined system of equations. First we note that when the matrix A has no negative elements, a simple upper bound for x can be found, since

$$x_i \leq \min_j \frac{b_i}{A_{ji}} . \tag{4a}$$

Thus, if we combine this with our knowledge that every x_i is nonnegative, we have established the following constraints on x_i with a trivial calculation:

$$0 \leq x_i \leq \min_j \frac{b_i}{A_{ji}} . \tag{4b}$$

It is interesting to note that for the same example given in Table 2.2.1 this trivial bound already provides a far better solution for x_i than does matrix inversion (see Table 2.2.2).

The ordinary method of least squares seeks a solution x which minimizes the weighted sum squares of the residuals:

$$x^* \text{ minimizes } L^2 = (Ax^* - b)^T V^{-1}(Ax^* - b) . \tag{5}$$

If, however, the matrix A is nearly singular (or underdetermined), then certain combinations of the components can be found such that if they are added to x^*, then they will not appreciably affect the value of L^2. Thus the standard deviation of the resulting components of x^* will be very large or infinite. The modification introduced into the SLOP code consists of adding an additional term to the quantity to be minimized so

---

[1] W. R. Burrus, *Neutron Phys. Div. Ann. Progr. Rept. Sept. 1, 1961*, ORNL-3193, p 44.

[2] First suggested by W. R. Burrus, *The Theory of Corrections for Instrumental Scrambling of Spectra*, p 82, preliminary copy of dissertation, June 1961, to be submitted to the Ohio State University.

Table 2.2.1. Comparison of Solutions by Various Codes of the Equation $Ax = b$

A was a 19 by 19 matrix of the form

$$\begin{bmatrix} \frac{1}{2} & \frac{1}{4} & & & & & & & & & & & & & & & & & \\ \frac{1}{4} & \frac{1}{2} & \frac{1}{4} & & & & & & & & & & & & & & & & \\ & \frac{1}{4} & \frac{1}{2} & \frac{1}{4} & & & & & & & & & & & & & & & \\ & & \cdot & \cdot & \cdot & & & & & & & & & & & & & & \\ & & & \cdot & \cdot & \cdot & & & & & & & & & & & & & \\ & & & & \cdot & \cdot & \cdot & & & & & & & & & & & & \\ & & & & & & & & & & & & & & & \frac{1}{4} & \frac{1}{2} \end{bmatrix}^3$$

Element	x_{true}	b	x from Matrix Inversion	x from 1961 Code[a]	SLOP		
					X	XLO	XUP
1	0	0	−6,680.0	0	0.070	−0.551	0.691
2	0	1,000.0	13,200.0	0	0.054	−0.550	0.658
3	0	6,000.0	−19,403.2	0	0.170	−1.019	1.359
4	0	16,000.0	25,139.2	0.66	1.408	−4.465	7.283
5	64,000.0	26,000.0	33,732.8	63,998.13	63,999	63,974	64,000
6	0	30,000.0	34,659.2	2.34	16.18	−11.80	44.15
7	64,000.0	26,000.0	25,796.8	63,998.56	63,999	63,974	64,000
8	0	16,000.0	40,806.4	0.12	2.626	−4.762	10.02
9	0	6,000.0	−42,398.4	0.33	0.174	−1.559	1.907
10	0	1,000.1[b]	42,934.4	0	0.015	−0.736	0.766
11	0	0	−42,398.4	0	0.005	−0.477	0.488
12	0	0	40,806.4	0	0.014	−0.435	0.463
13	0	0	−38,203.2	0	0.029	−0.434	0.492
14	0	0	34,659.2	0	0.033	−0.433	0.500
15	0	0	−30,267.2	0	0.033	−0.400	0.467
16	0	0	25,139.2	0	0.023	−0.371	0.416
17	0	0	−19,403.2	0.11	0.022	−0.343	0.386
18	0	0	13,200.0	0	0.047	−0.274	0.369
19	0	0	−6,680.0	0	0.097	−0.333	0.526

[a] W. R. Burrus, *Neutron Phys. Div. Ann. Progr. Rept. Sept. 1, 1961*, ORNL-3193, p 44.

[b] An error in the form of 0.1 perturbation introduced here.

that

$$x \text{ minimizes } L^2 = (Ax - b)^T V^{-1}(Ax - b) + \tau(x - d)^T \Delta^{-2}(x - d) , \tag{6}$$

where d = diagonal elements of 0.5 (XMAX + XMIN) and Δ = 0.5 (XMAX − XMIN), where XMAX and XMIN are diagonal matrices with elements x_i^{max} and x_i^{min}, respectively. We note that the values of XMAX and XMIN might be obtained from the inequality $4b$. It is interesting to observe that if the values for XMAX and XMIN are reasonable, then the second term can never be greater than n, the number of components in the solution vector, since the term takes the value 1 at the extremes of XMAX or XMIN for each component. From ordinary least-squares theory we know that the first term is statistically distributed with a mean of $n - r$, where r is the rank of the matrix A. Thus both terms are of the order of unity.

Table 2.2.2. Comparison of Solutions of Equation $Ax = b$ by Matrix Inversion and by Trivial Results of XMAX in the SLOP Code[a]

Element	x_{true}	x from Matrix Inversion	SLOP XMAX
1	0	−6,680.0	0
2	0	13,200.0	0
3	0	−19,403.2	0
4	0	25,139.2	0
5	64,000.0	33,732.8	64,000
6	0	34,659.2	96,000
7	64,000.0	25,796.8	64,000
8	0	40,806.4	0
9	0	−42,398.4	0
10	0	42,934.4	0
11	0	−42,398.4	0
12	0	40,806.4	0
13	0	−38,203.2	0
14	0	34,659.2	0
15	0	−30,267.2	0
16	0	25,139.2	0
17	0	−19,403.2	0
18	0	13,200.0	0
19	0	−6,680.0	0

[a]Same problem as in Table 2.2.1.

Now if we minimize the L^2 in Eq. 6, we find by partial differentiation with respect to x that

$$\frac{\partial L^2}{\partial x} = 2A^T V^{-1}(Ax - b) + 2\tau\Delta^{-2}(x - d) , \tag{7a}$$

and at its minimum

$$A^T V^{-1}(Ax - b) + \tau\Delta^{-2}(x - d) = 0 , \tag{7b}$$

which implies that

$$(A^T V^{-1}A + \tau\Delta^{-2})x = A^T V^{-1}b + \tau\Delta^{-2}d . \tag{7c}$$

Now, solving for x = XEST,

$$\begin{aligned} \text{XEST} &= (A^T V^{-1}A + \tau\Delta^{-2})^{-1} (A^T V^{-1}b + \tau\Delta^{-2}d) \\ &= (A^T V^{-1}A + \tau\Delta^{-2})^{-1} A^T V^{-1}b + (A^T V^{-1}A + \tau\Delta^{-2})^{-1} \tau\Delta^{-2}d . \end{aligned} \tag{8}$$

It is an interesting matrix identity that the second term on the right of the above equation may be written as follows:

$$(A^T V^{-1}A + \tau\Delta^{-2})^{-1} \tau\Delta^{-2}d = -(A^T V^{-1}A + \tau\Delta^{-2})^{-1} A^T V^{-1}Ad + d .$$

Thus we find that

$$\text{XEST} = (A^T V^{-1}A + \tau\Delta^{-2})^{-1} [(A^T V^{-1}(b - Ad)] + d . \tag{9}$$

The variance-covariance matrix of this result can be calculated from the usual rules and expressed in matrix notation as follows:

$$\Sigma = HVH^T ,$$

where $H = (A^T V^{-1}A + \tau\Delta^{-2})^{-1} A^T V^{-1}$. Hence we may compute SX, the standard deviation of XEST, as

$$\text{SX} = \sqrt{\text{diagonal elements } (HVH^T)} .$$

The modification of the least squares results in the introduction of another kind of error. We may assume, for example, that some true x (x_{true}) exists. Then

$$\begin{aligned} x_{true} - \text{XEST} &= x_{true} - \{(A^T V^{-1}A + \tau\Delta^{-2})^{-1} [A^T V^{-1}(b - Ad)] + d\} , \\ &= x_{true} - \{(A^T V^{-1}A + \tau\Delta^{-2})^{-1} [A^T V^{-1}(Ax_{true} - Ad)] + d\} \end{aligned}$$

(inasmuch as the equation we are trying to solve is $Ax_{true} = b$),

$$\begin{aligned} &= x_{true} - [HA(x_{true} - d)] - d \\ &= (I - HA)(x_{true} - d) . \end{aligned}$$

We see that even in the limit of error-free data, the estimates of x may not be correct. This is more easily visualized in the special limiting case where the system of equations is underdetermined and the right-hand side is known exactly. Then the missing degrees of freedom have to be made up by the a priori conditions. Thus each component has a certain amount of freedom commensurate with the requirement that all solution components fall within the a priori constraint set. We note that the a priori requirements on $x_{j\neq i}$ affect the amount of freedom available to x_i. We call this remaining error the BIAS in the estimates of x. The SLOP concept would not be any more than an interesting gimmick if this BIAS error could not be evaluated. The following inequality, making use of the a priori bounds on x, allows us to calculate the BIAS:

$$\text{BIASLO} = (I - HA)^{+}(-\Delta) + (I - HA)^{-}(\Delta) \leqq (I - HA)(x - d)$$
$$\leqq (I - HA)^{+}(\Delta) + (I - HA)^{-}(-\Delta) = \text{BIASUP} ,$$

where $(I - HA)^{+}$ denotes the positive elements of $(I - HA)$, etc. Then the confidence region of x may be expressed as

$$\text{XUP} = \text{XEST} + \text{BIASUP} + \text{SX} ,$$
$$\text{XLO} = \text{XEST} + \text{BIASLO} - \text{SX} .$$

To this point we have only discussed a method of finding the solution vector x, which we earlier asserted that we did not want. We shall now describe the generalizations necessary to compute some function of the solution x, say $p = Wx$, where W is a generalized broadening matrix. Actually, W need not be only a generalized broadening matrix. For example, the first row of W could be the flux-to-dose conversion coefficients, and thus p_1 would be the dose (in suitable units). Other rows of W might be functions with about the same width as the instrument resolution but without any tails. These components of p would correspond to the pulse-height distribution of an ideal analyzer which has only a single peak and no tail. Finally, some elements of W might be unit diagonal so that some elements of p would estimate the components of the unknown spectrum.

W is perfectly general and can be chosen to give as many quantities as are of interest to the experimenter. If some row is unjudiciously chosen, however, the experimenter will be rewarded with a large confidence interval.

In order to calculate p, we form

$$\text{PEST} = W\ \text{XEST}$$

and

$$\text{SP} = \sqrt{\text{diagonal elements } (WHVH^{T}W^{T})} .$$

We must now compute a quantity similar to the BIAS in relation to XEST. This quantity is known as the SLOP. It is calculated in a manner exactly analogous to the calculation of the BIAS:

$$\text{SLOPLO} = [W(I - HA)]^{+}(-\Delta) + [W(I - HA)]^{-}(\Delta) \leqq [W(I - HA)](x - d)$$
$$\leqq [W(I - HA)]^{+}(\Delta) + [W(I - HA)]^{-}(-\Delta) = \text{SLOPUP} .$$

Then the confidence region on p may be expressed as

$$\text{PUP} = \text{PEST} + \text{SLOPUP} + \text{SP} ,$$

$$\text{PLO} = \text{PEST} + \text{SLOPLO} - \text{SP} .$$

Stronger a priori conditions than $x_i \geqq 0$ may be utilized. The problem that we have just solved might be summarized as

$$Ax = b + e ,$$

$$x \geqq 0 ,$$

$$p = Wx ,$$

where e represents the errors on b. With the introduction of a regularization matrix R we may write

$$ARq = b + e ,$$

$$q \geqq 0 ,$$

$$x = Rq ,$$

$$p = WRq = Wx .$$

The computation is the same for either case. The only difference is that on input to the problem in the regularized case, AR replaces A, WR replaces W, and q replaces x. We have now "lost" x. If we want it we must put a unit row in the broadening matrix W.

An example of the usefulness of R is the following. Suppose that we know that the spectrum x is monotonically decreasing. Then a +1 on the diagonal and a −1 on the superdiagonal of R will introduce this additional a priori information.

Two problems remain with the present formulation. First, the matrix $(A^T V^{-1} A + \tau \Delta^{-2})$ must be inverted. This frequently requires more than single-precision accuracy, because if the matrix A is poorly conditioned, then so is $A^T A$. The presence of the diagonal terms helps the situation, but at times their effect is lost on all but the last places of the diagonal elements. The second objection to the above formulation is that constraining conditions of the type $0 \leqq x \leqq \text{XMAX}$ or $0 \leqq q \leqq \text{QMAX}$ are often not general enough.

We can consider, for example, the simple singular 2 by 2 system of equations:

$$\begin{pmatrix} 1 & 1 \\ 1 & 1 \end{pmatrix} \begin{pmatrix} x_1 \\ x_2 \end{pmatrix} = \begin{pmatrix} b_1 \\ b_2 \end{pmatrix} \quad \text{for } b_1 \neq b_2 .$$

Although we cannot solve for x_1 and x_2 separately, we can obtain a solution for $x_1 + x_2$. In fact, there are two solutions for $x_1 + x_2$:

$$x_1 + x_2 = b_1 ,$$

$$x_1 + x_2 = b_2 .$$

The least-squares estimate for $x_1 + x_2$ (with equal errors on b) is

$$x_1 + x_2 = 0.5(b_1 + b_2) .$$

We cannot, however, find any finite estimate of $x_1 - x_2$ from these equations. We may display the confidence region on a graph as in Fig. 2.2.1. The confidence region is open in the direction of $x_1 - x_2$, but it is well-determined in the direction of $x_1 + x_2$. Now if we consider the nonnegativity of x_1 and x_2, the resulting confidence region is a small trapezoid as shown in Fig. 2.2.2, whereas $b_1 = \text{XMAX}_1 = \text{XMAX}_2$ defines a square in our present system. This square is obviously much larger than the true confidence region. Thus a more valuable constraint would be to specify the maximum and minimum values of the components in a rotated coordinate system that is aligned with the axes of the confidence region. The final step in the SLOP process is to rotate the problem to a more natural set of axes. For instruments which are dominated by Gaussian broadening, the natural set of axes to take is the eigenvectors of the Gaussian kernel, or, in matrix notation, the eigenvectors of the matrix A^TA. If A were really symmetric and Gaussian, this rotation would diagonalize it and simplify the problem, as the inverse of a diagonal matrix presents no difficulty. Even if A is not symmetric and Gaussian, it is still plausible to choose the rotation matrix of A^TA for this computational reason.

In order to reduce the number of operations necessary, it is desirable to normalize the problem at the beginning so that the standard errors of b are unity and so that $\Delta = 0.5(\text{XMAX} - \text{XMIN})$ is the unit matrix I. The results are "unnormalized" just before "publication." An additional computational feature is the ability to iterate or repeat the calculation by using the new values of the rotated-regularized spectrum to compute a new XMAX and XMIN and to repeat the problem. Usually, no significant improvement is noticed after two steps.

UNCLASSIFIED
ORNL-LR-DWG 72592

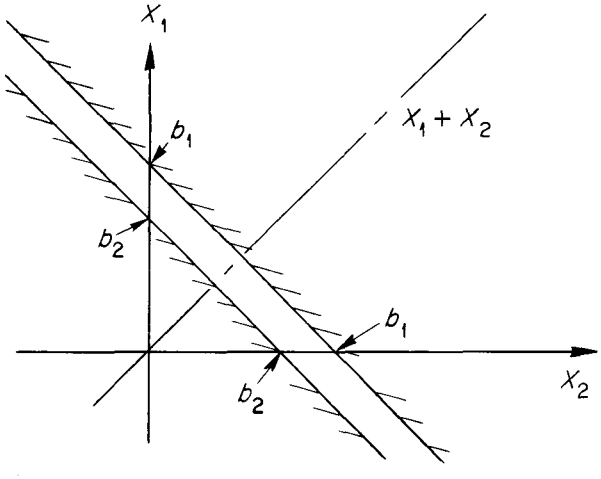

Fig. 2.2.1. Confidence Region for $x_1 + x_2$.

UNCLASSIFIED
ORNL-LR-DWG 72593

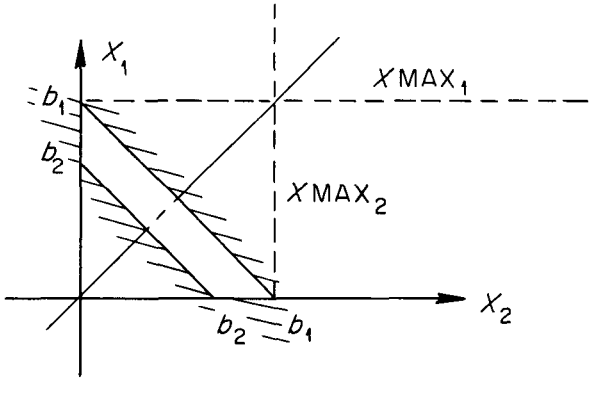

Fig. 2.2.2. Confidence Region for $x_1 + x_2$ Utilizing the Nonnegativity of x_1 and x_2.

A flow diagram of the program is shown in Fig. 2.2.3, and a graphical demonstration is given in Fig. 2.2.4 for the sample problem discussed above:

$$\begin{pmatrix} 1 & 1 \\ 1 & 1 \end{pmatrix} \begin{pmatrix} x_1 \\ x_2 \end{pmatrix} = \begin{pmatrix} b_1 \\ b_2 \end{pmatrix} .$$

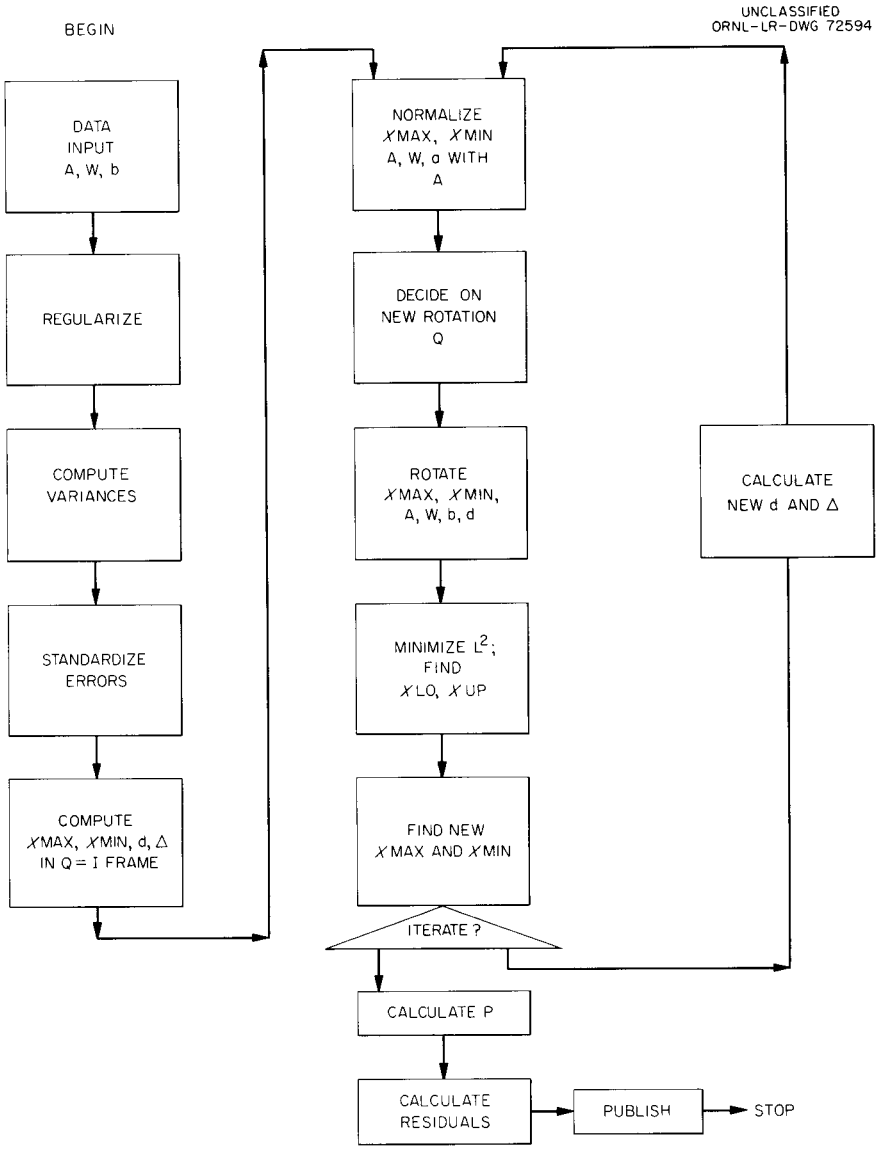

Fig. 2.2.3. Generalized Flow Diagram of SLOP Code.

UNCLASSIFIED
ORNL-LR-DWG 72595

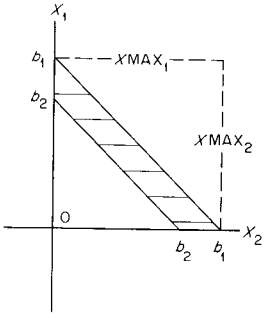

1. PROBLEM AFTER FIRST GUESS AT XMAX AND XMIN HAS BEEN MADE FROM THE APRIORI CONSIDERATIONS.

$$XMAX_1 = XMAX_2 = b_1$$
$$XMIN_1 = XMIN_2 = 0$$
$$\Delta_{ii} = (0.5)(b_1)$$
$$d_i = (0.5)(b_1)$$

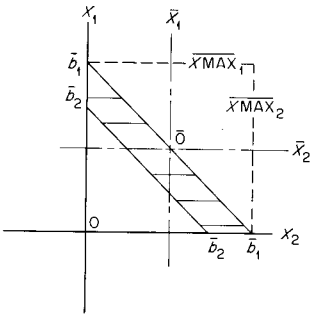

2. PROBLEM AFTER NORMALIZATION.

$$\overline{XMAX}_1 = \overline{XMAX}_2 = 1$$
$$\overline{XMIN}_1 = \overline{XMIN}_2 = -1$$
$$\bar{\Delta}_{ii} = 1$$
$$\bar{d}_i = 0$$

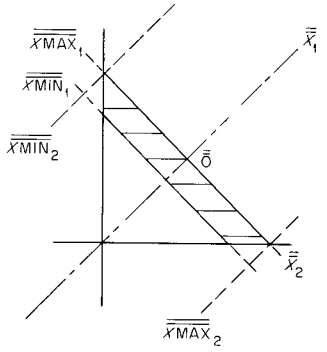

3. PROBLEM AFTER ROTATION OF AXES $\bar{X}_1$ AND $\bar{X}_2$ TO COORDINATES ALONG THE PRINCIPAL AXES OF THE CONSTRAINT REGION AND AFTER NEW GUESS AT ROTATED XMAX$_i$ AND XMIN$_i$ HAS BEEN MADE BY CODE FROM THE MINIMIZATION OF L^2 THESE NEW GUESSES ARE NOTED BY THE DOUBLE SLASH ABOVE THE NAME.

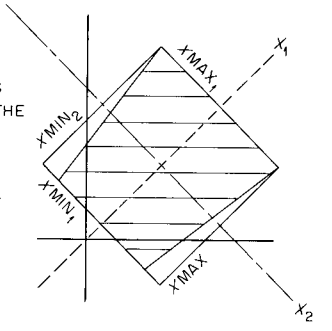

4. PROBLEM AFTER SECOND NORMALIZATION WITH NEW $\Delta = 0.5$ (XMAX-XMIN) COMPUTED IN 3 LEFT. IN GENERAL, FURTHER ITERATIONS WOULD NOW OCCUR AND THE STEPS OF ROTATION AND NORMALIZATION WOULD BE REPEATED. IN THIS PARTICULAR CASE, HOWEVER, INASMUCH AS THE FIRST ROTATION BROUGHT THE AXES PARALLEL WITH THE PRINCIPAL AXES OF THE "UNKNOWN" CONSTRAINT REGION, NO FURTHER IMPROVEMENT WILL BE FOUND.

Fig. 2.2.4. Demonstration of SLOP Code Sample Problem

$$\begin{pmatrix} 1 & 1 \\ 1 & 1 \end{pmatrix} \begin{pmatrix} x_1 \\ x_2 \end{pmatrix} = \begin{pmatrix} b_1 \\ b_2 \end{pmatrix}.$$

3. Critical Experiments

3.1. CRITICAL EXPERIMENTS WITH MIXTURES OF AQUEOUS U^{235}-ENRICHED URANYL NITRATE SOLUTIONS AND BOROSILICATE GLASS RINGS

J. K. Fox and J. T. Thomas

Several critical experiments were performed with large-capacity cylindrical tanks containing fissile material, as aqueous uranyl nitrate solutions, and borosilicate glass Raschig rings. The experiments are part of a series designed to furnish information on the critical parameters of such systems for nuclear safety applications.

The cylindrical vessels are described in Table 3.1.1 and the types of glass rings in Table 3.1.2. The aqueous uranyl nitrate solution was enriched to 92.6% in U^{235}. For most of the experiments the solution had an average uranium concentration of 415 g/liter and a corresponding specific gravity of 1.555 and an $H:U^{235}$ atomic ratio of ~59; however, one experiment was performed with a solution having a uranium concentration of 279 g/liter, a corresponding specific gravity of 1.373, and an $H:U^{235}$ atomic ratio of ~91.

Table 3.1.1. Description of Cylindrical Vessels

Material	Inside Diameter	Dimensions (in.)		
		Wall Thickness	Bottom Thickness	Height
Stainless steel	48	1/8	1/4	60
	20	1/16	1/2	60
Aluminum	30	1/16	1/2	60

Table 3.1.2. Description of Borosilicate Glass Rings

Supplier	Type	Dimensions (in.)			Natural Boron Content (wt %)
		Outside Diameter	Inside Diameter	Length	
Kimble Glass Co.	EN-1	1.56	1.25	1.73	5.7
	KG-33	1.55	1.24	1.76	4.1
	KG-33	0.625	0.43	0.625	3.9
	R-6	1.60	1.28	1.69	0.5
Corning Glass Co.	Pyrex	1.85	1.52	1.89	4.0
	Pyrex	1.55	1.24	1.76	4.0

The critical and noncritical conditions of the various experiments are shown in Table 3.1.3. As can be deduced from the table, all assemblies except those with type R-6 rings were subcritical, with a maximum source neutron multiplication of approximately 2, when the solution and glass ring heights were equal. Most of the subcritical assemblies were made critical by raising the solution above the glass rings so that the resulting critical slab of solution served as a neutron source for measurements of the neutron flux along the axis of each solution-glass mixture. From these exponential experiments the sign of the material buckling of the mixture was obtained. For solutions having a uranium concentration of $\leq$415 g/liter, k_∞ will be less than 1 if the glass rings contain 5.7 wt % natural boron and occupy 24.1 vol % of the mixture. For solutions having a uranium concentration of $\leq$279 g/liter, the corresponding values are 4.0 wt % natural boron and 24.1 vol % glass.

Table 3.1.3. Critical and Noncritical Conditions for Mixtures of Aqueous Uranyl Nitrate Solution and Borosilicate Glass

Diameter of Vessel (in.)	Reflector	Type of Glass	Boron Content of Glass (wt %)	Glass Content of Mixture (vol %)	Glass Height (in.)	Solution Height (in.)	k_{eff} [a]
			Solution Concentration: 415 g of U per liter				
48	Air	EN-1	5.7	24.1	46.5	44.68	<1
	46.0 in. H_2O	EN-1	5.7	24.1	46.5	44.68	<1
	Air	EN-1	5.7	24.1	30.0	34.31	1
	34.0 in. H_2O	EN-1	5.7	24.1	30.0	34.25	1
30	50.0 in. H_2O	Pyrex	4.0	20.9	50.0	50.0	<1
	42.2 in. H_2O	Pyrex	4.0	20.9	35.9	39.49	1
	Air	Pyrex	4.0	20.9	35.9	39.75	1
20	40.2 in. H_2O	EN-1	5.7	24.1	34.6	40.64	1
	Air	EN-1	5.7	24.1	34.6	41.03	1
	38.6 in. H_2O	Pyrex	4.0	20.9	33.8	38.53	1
	Air	Pyrex	4.0	21.0	33.6	38.67	1
	38.4 in. H_2O	Pyrex	4.0	21.0	33.6	38.29	1
	32.4 in. H_2O	KG-33	3.9	30.0	27.2	32.37	1
	Air	KG-33	3.9	30.0	27.2	32.69	1
	Air	R-6	0.5	24.0	21.4	10.86	1
	22.0 in. H_2O	R-6	0.5	24.0	21.4	8.34	1
	Air	KG-33	4.1	24.1	35.6	41.32	1
	41.0 in. H_2O	KG-33	4.1	24.1	35.6	40.84	1
			Solution Concentration: 279 g of U per liter				
20	Air	KG-33	4.1	24.1	35.6	41.48	1
	41.2 in. H_2O	KG-33	4.1	24.1	35.6	41.12	1

[a] k_{eff} = 1 = critical.

3.2. CRITICAL CUBIC ARRAYS OF NEUTRON-INTERACTING UNITS OF AQUEOUS URANYL NITRATE SOLUTION

J. T. Thomas and J. K. Fox

Critical experiments were performed with as many as 125 five-liter units of concentrated aqueous uranyl nitrate solution assembled in cubic arrays. The solution had a uranium concentration of 415 g/liter, a U^{235} enrichment of 92.6%, and a specific gravity of 1.555. Each unit was contained in a right circular cylinder of methacrylate plastic having a height-to-diameter ratio of 0.92 and a 0.635-cm-thick wall. From these experiments the dependence of the number of units required for criticality as a function of their spacing and reflector conditions was determined. The critical number N was found to obey the relation

$$N = N_0 F^{-s} ,$$

where N_0 and s are constants and F is the ratio of the average uranium density in the array to that in a unit. Table 3.2.1 presents values of the constants for the various reflector conditions.

Table 3.2.1. Constants for Various Reflector Conditions of Critical Cubic Arrays of Uranyl Nitrate Solution

Reflector		Constants	
Material	Thickness (cm)	s	N_0
Air		1.928 ±0.028	2.506 ±0.014
Paraffin	1.27	1.831 ±0.118	1.699 ±0.316
	3.81	1.797 ±0.098	0.794 ±0.125
	15.24	1.721 ±0.083	0.606 ±0.084
Plexiglas	1.27	1.804 ±0.116	1.842 ±0.341

3.3. PROMPT-NEUTRON LIFETIME IN HYDROGEN-MODERATED 3% U^{235}-ENRICHED URANIUM CRITICAL ASSEMBLIES

J. T. Mihalczo

Prompt-neutron decay constants in unreflected and reflected delayed-critical parallelepipeds of a homogeneous mixture of UF_4 and paraffin were determined by the pulsed-neutron technique. The fuel mixture had a density of 4.5 g/cc and contained 92 wt % UF_4 in which the U^{235} enrichment of the uranium was 3%. The H:U^{235} atomic ratio was 133. The reflector was a 15-cm thickness of paraffin ($C_{25}H_{52}$) with a density of 0.93 g/cc.

Neutron bursts for these experiments were produced by a 150-kv Cockcroft-Walton accelerator in which deuterons were electrostatically deflected on and off a tritium target. The detectors used were BF_3 counters, proton recoil type scintillators,[1] and NaI scintillators. The decay constant α was determined from 256-channel time analyzer data by a nonlinear least-squares fitting of the equation $y = B_1 + B_2 e^{-\alpha t}$. The results, given in Table 3.3.1, were obtained by counting either neutrons or prompt gamma rays.

The effective delayed-neutron fractions in equivalent reflected and unreflected spheres were calculated by using the S_n transport method of Carlson[2] in the S_4 approximation; the 16-group cross sections of Hansen and Roach;[3] and the experimentally determined values of the buckling (0.006413 cm^{-2}), extrapolation distance (2.5 cm), and reflector savings (5.7 cm). The extrapolation distance was determined from flux distributions and the reflector savings from the difference in critical sizes of reflected and unreflected cubes. The effective delayed-neutron fraction, β_{eff}, was obtained from the difference in the values of k_{eff} calculated first with the fission neutron spectrum and second with the fission neutron spectrum modified by subtracting the delayed neutrons in four energy groups (3 through 6) out of the calculation. This modification, for which the neutron energy distribution of Batchelor and Hyder[4] and the yields of Keepin *et al.*[5] were used, included the delayed neutrons from the fast fission of U^{238}. The results of the calculations are given in Table 3.3.2.

With these values of the prompt-neutron decay constants and the effective delayed-neutron fractions, the prompt-neutron mean lifetime was found to be 2.17×10^{-5} sec and 2.88×10^{-5} sec for the unreflected and reflected critical assemblies, respectively.

---

[1]Nuclear Enterprises crystal No. 102.

[2]B. G. Carlson and G. I. Bell, *Proc. Intern. Conf. Peaceful Uses Atomic Energy, 2nd, Geneva, 1958* **16**, 535–49 (1959).

[3]G. E. Hansen and W. H. Roach, *Six and Sixteen Group Cross Sections for Fast and Intermediate Critical Assemblies*, LAMS-2543 (Dec. 5, 1961).

[4]R. Batchelor and H. R. McK. Hyder, *J. Nuclear Energy* **3**, 7 (1956).

[5]G. R. Keepin *et al.*, *Phys. Rev.* **107**, 1044 (1957).

Table 3.3.1. Prompt-Neutron Decay Constants for a 3% U^{235}-Enriched UF_4-Paraffin Mixture

Reflector	Detector	α, Decay Constant (sec^{-1})
None	BF_6	343 ± 3
	NaI	346 ± 3
	Proton recoil	343 ± 3
Paraffin	Proton recoil	258 ± 2

Table 3.3.2. Calculated Values of k_{eff} and Effective Delayed-Neutron Fraction

Reflector	Equivalent Sphere Radius (cm)	k_{eff}	β_{eff}
None	36.7	0.991	0.00746
Paraffin	31.1	0.999	0.00744

3.4. PROMPT-NEUTRON DECAY CONSTANTS FOR UNMODERATED URANIUM METAL CRITICAL ASSEMBLIES WITH LARGE GAPS

J. T. Mihalczo

A series of critical experiments with enriched-uranium metal assemblies having large gaps at their midplanes has been initiated to provide data on simple critical systems of two interacting components for use in evaluating various methods of calculation. The metal has a density of 18.72 g/cc and a U^{235} content of 93.2 wt %.

The presence of large gaps in these fast unmoderated and unreflected assemblies results in a decrease in the prompt-neutron decay constant and an increase in the amount of uranium metal required for criticality. For a delayed-critical assembly, the prompt-neutron decay constant is inversely proportional to the mean neutron lifetime of the prompt neutrons. The lifetime depends on the gap width since, for these systems, the time required for a neutron to cross the gap is a significant part of its lifetime. It also depends on the probability that a neutron will leak from one-half the assembly and enter the other half. In these experiments critical thicknesses of the slabs as a function of their spacing have been measured, and corresponding prompt-neutron decay constants have been determined.

The prompt-neutron decay constant was obtained by the Rossi-α technique.[1] The lifetime of prompt neutrons is determined from the time distribution of neutrons associated with a common ancestor. A detector that responds to the time distribution of fissions within a chain-reacting system will observe counts which are nonrandom if the fission rate in the critical assembly is sufficiently low for no great overlapping of fission chains to occur.

The detectors used in these experiments were proton recoil type scintillators,[2] lithium iodide crystals, and BF_3 and spiral fission counters. The data were collected in a Technical Measurement Corp. 256-channel time analyzer with a neutron time-of-flight logic unit in which sixty-four 0.25-μsec time channels were used. Both paired and single detectors were used. When two detectors were used, the time distribution of counts from detector B following a count from detector A was observed. When only a single detector was used (always the spiral fission counter), the time distribution of counts after an initial pulse was measured. This initial pulse triggered the time-of-flight analyzer, and the succeeding counts were input signals.

Experiments with two interacting 8 by 10 in. slabs whose large surfaces were separated by various distances were completed, and the results are shown in Figs. 3.4.1 and 3.4.2. Figure 3.4.1 shows the critical thickness of one slab (one-half the total metal thickness of the assembly) as a function of the distance between the two slabs, and Fig. 3.4.2 gives the prompt-neutron decay constant as a function of critical thickness of one slab. A typical decay curve obtained in the Rossi-α measurements is presented in Fig. 3.4.3.

Future experiments will be performed in cylindrical geometry and evaluated by transport theory methods.

---

[1] J. D. Orndoff, *Nucl. Sci. Eng.* **2**, 450 (1957).

[2] Nuclear Enterprises crystal No. 102.

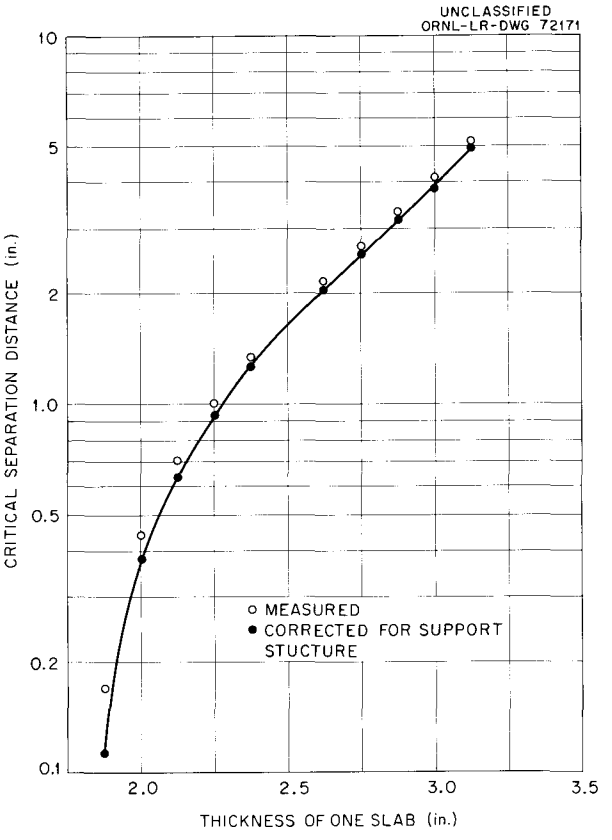

Fig. 3.4.1. Critical Separation Distance of Two Interacting 8 by 10 in. Uranium Metal Slabs as a Function of Slab Thickness.

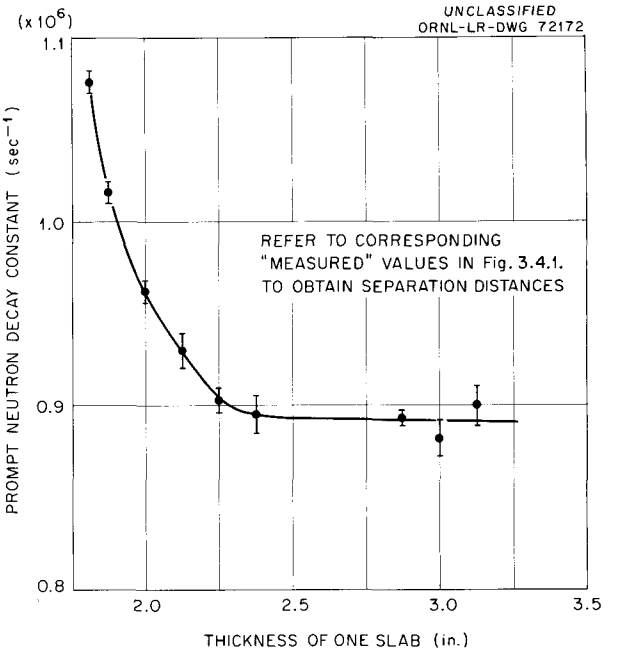

Fig. 3.4.2. Prompt-Neutron Decay Constant for Two Interacting 8 by 10 in. Uranium Metal Slabs as a Function of Slab Thickness.

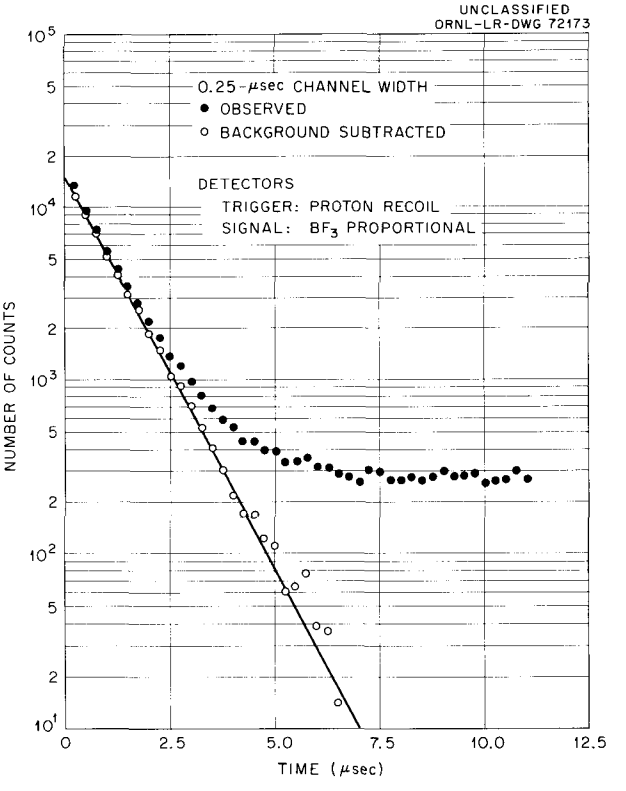

Fig. 3.4.3. Observed Prompt-Neutron Decay for Two Interacting 8 by 10 by $1\frac{7}{8}$ in. Uranium Metal Slabs at a Separation Distance of 0.17 in.

3.5. CRITICAL EXPERIMENTS WITH THE HEALTH PHYSICS RESEARCH REACTOR

J. T. Mihalczo

A series of critical experiments were performed with the Health Physics Research Reactor (HPRR) (previously identified as the Fast Burst Reactor) both at zero power[1] and under superprompt-critical conditions.

The HPRR is basically an unreflected and unmoderated right cylinder of 90 wt % U–10 wt % Mo, with the uranium enriched to 93.2 wt % in U^{235}. By alloying uranium with molybdenum, difficulties with phase changes characteristic of pure uranium during thermal cycling are removed, and the tensile strength and yield strength are increased. These improved physical properties allow the production of neutron bursts of greater than 10^{17} fissions, about an order of magnitude larger than those obtained from Godiva II, and increase the reactor operating lifetime. In addition to its burst capabilities, the HPRR is designed to operate under steady-state conditions at a power level of 1 kw with natural-convection cooling or at 10 kw with forced-air cooling for 10 min.

The HPRR (Fig. 3.5.1) consists of a 20.3-cm-diam by 23-cm-high outer annulus made up of U-Mo disks of several thicknesses held together by nine 1.9-cm-diam U-Mo bolts. Each bolt has a removable axial plug of the same material or of stainless steel. The outer annulus has a 5.1-cm-diam cylindrical steel core which is movable and supported magnetically. To the lower section of this core is attached the safety block, an 8.9-cm-diam fuel annulus containing 9.4 kg of the total 96.6 kg of U^{235} in the reactor. The HPRR contains three movable fuel rods having diameters of 1.59, 1.91, and 2.54 cm, which are used to adjust the reactivity to delayed critical and to provide excess reactivity for burst generation. A vertical, ~23-cm-deep, 0.673-cm-diam "glory hole" is eccentrically positioned for specimen irradiations. Two thermocouples, shown in Fig. 3.5.1, provide temperature measurements.

In the zero-power experiments[1] fission-rate distributions were measured, reactivity calibrations of the various movable parts were made, and the reactivity effects of the presence of neutron-reflecting materials adjacent to the reactor were determined. In addition, the static temperature coefficient of reactivity of the reactor was measured over the range 20 to 135°C and found to be 0.31 ¢/°C, without measurable dependence on temperature. The prompt-neutron lifetime of the reactor was calculated, using perturbation theory,[2] to be 1.04×10^{-8} sec.

The time-dependent behavior of the neutron population in the assembly following the rapid establishment of a superprompt-critical condition[3] was investigated to support the design criterion that the reactor should produce bursts of 10^{17} fissions.[4] The three fuel rods were used to control the reactor

---

[1] J. T. Mihalczo, *Reactivity Calibrations and Fission-Rate Distributions in an Unmoderated, Unreflected Uranium-Molybdenum Alloy Research Reactor*, ORNL TM-189 (May 10, 1962).

[2] W. E. Kinney and J. T. Mihalczo, *Oak Ridge National Laboratory Fast Burst Reactor Critical Experiments and Calculations*, ORNL CF-61-8-71 (August 1961).

[3] J. T. Mihalczo, *Super-Prompt-Critical Behavior of an Unmoderated, Unreflected Uranium-Molybdenum Alloy Assembly*, ORNL TM-230 (May 10, 1962).

[4] T. F. Wimett *et al.*, *Nucl. Sci. Eng.* **8**, 691 (1960).

UNCLASSIFIED
ORNL-LR-DWG.65369

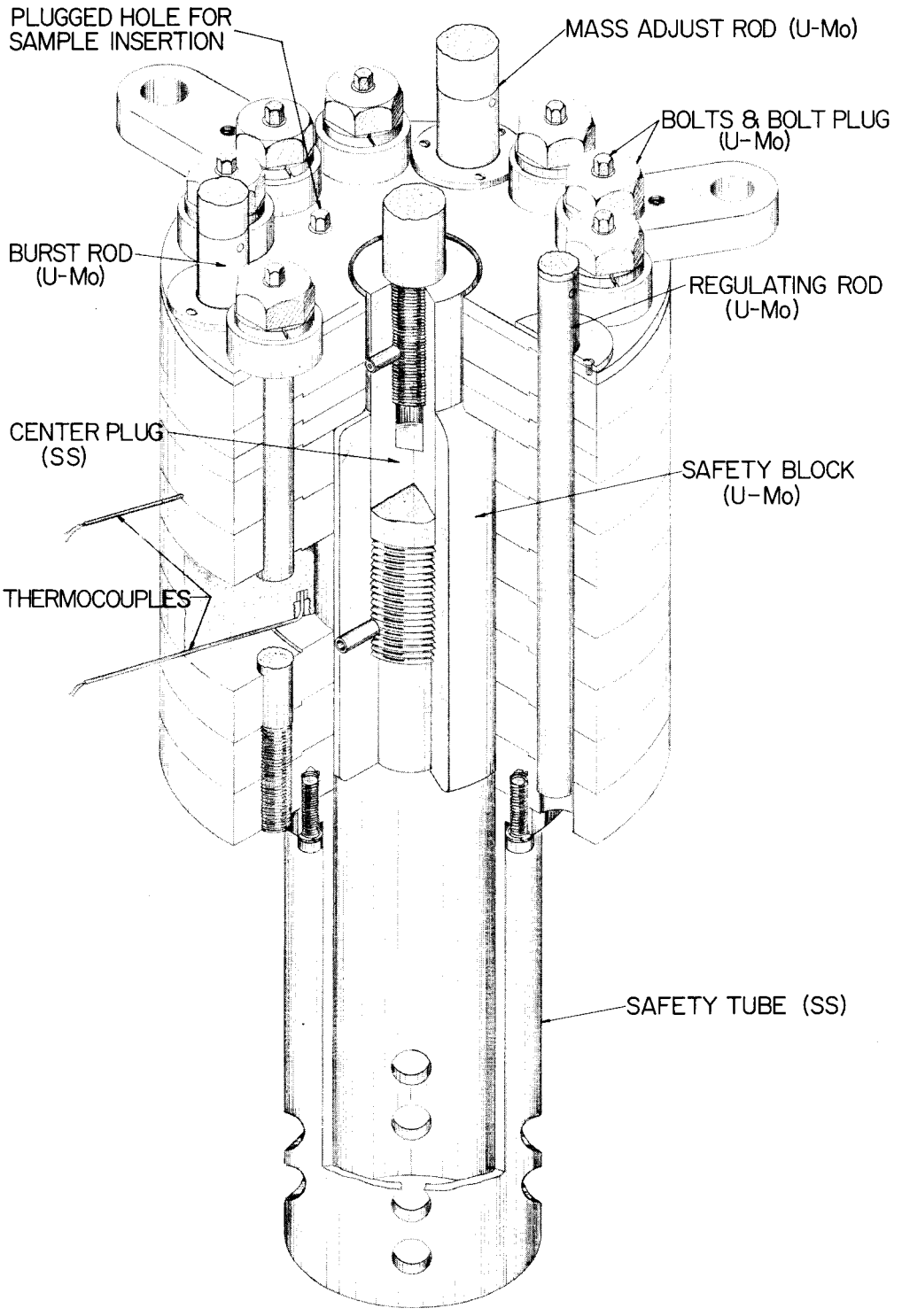

Fig. 3.5.1. Health Physics Research Reactor.

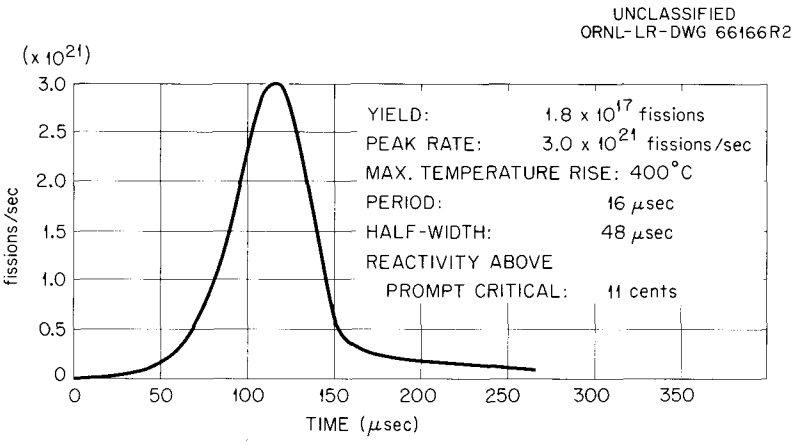

Fig. 3.5.2. Burst Characteristics of the HPRR.

and to provide the excess reactivity required for burst production. Rapid introduction of reactivities up to 11¢ above prompt critical resulted in bursts yielding as many as 1.8×10^{17} fissions with reactor periods as short as 16 μsec and temperature increases as large as 400°C. The characteristics of such a burst are given in Fig. 3.5.2.

The number of fissions required to raise the peak temperature by 1°C obtained from these experiments is 4.6×10^{14}. This is to be compared with the value of 3.8×10^{14} fissions calculated from the specific heat of the U-Mo alloy on the assumption that 178 Mev of heat energy is deposited in the core per average fission.

The 9.4-kg U^{235} safety block of the reactor is attached to the drive shaft of a motor by a magnet. Release of the magnet results in the safety block falling out of the assembly. Pressure waves generated in the safety block by bursts yielding more than 6×10^{16} fissions caused it to disengage from the magnet about 225 μsec after the peak of the burst. Removal of the safety block by this pressure wave terminates the low-amplitude "tail" sustained by delayed neutrons and results in a larger percentage of the fissions occurring in the peak of the burst. This phenomenon enhances the safety of operation of the system in the burst mode, since the reactor will scram itself before the scram instrumentation can cause shutdown.

3.6. CRITICAL EXPERIMENTS WITH ROVER REACTOR FUEL ELEMENTS

E. B. Johnson and J. K. Fox

Experimental bases for the establishment of nuclear safety practices in the fabrication, storage, and transport of Rover Reactor fuel elements were determined in a series of critical and neutron-multiplication experiments. Since the work is classified, it is described in another document.[1]

[1] E. B. Johnson and J. K. Fox, *Critical Mass Studies, Part XII: Rover Reactor Fuel Elements*, ORNL TM-264 (1962).

3.7. HIGH-FLUX ISOTOPE REACTOR CRITICAL EXPERIMENT NO. 2

D. W. Magnuson

The nuclear design of the High-Flux Isotope Reactor (HFIR) has been supported thus far by two series of critical experiments. Preliminary measurements with solutions of uranium and with liquid reflectors were made in the first series and are to be reported by Fox *et al.*[1] The equipment for the second series of experiments, designated as the High-Flux Isotope Reactor Critical Experiment No. 2 (HFIRCE No. 2), and the early results from reactivity coefficient and flux and power distribution measurements were described by Magnuson.[2] More recent experiments have been concerned primarily with evaluations of the proposed reactor control devices and the effect of these devices on the power distribution. The results of these experiments have led to changes in the original design of the controls. Most of the data were, therefore, unique to this reactor design and are not reported here, having served a purpose in guiding the design of a satisfactory control system. The experimental method, however, is described and typical results are given for control plate calibrations.

Method of Reactivity Measurement

The particular geometry of the HFIRCE No. 2 has made it difficult to apply conventional methods for calibration of control rods, such as the rod drop or rod comparison technique. Linear combinations of the individual control plate worths would not give their combined worths because of shadowing or self-shielding effects. Therefore, it was necessary to make measurements on each configuration of interest.

The pulsed-neutron technique was chosen to give a measure of the negative reactivities of the control plates displaced from critical. Briefly, this method measures the prompt-neutron decay period, the exponential factor which describes the time dependence of the neutron flux or density following the introduction of a short burst of neutrons. The decay constant λ is given by

$$\lambda = (1 - \rho)\frac{\beta_{\text{eff}}}{l},$$

where ρ is the reactivity in dollars, β_{eff} is the effective delayed neutron fraction, and l is the neutron lifetime in seconds. At delayed critical, $\rho = 0$ and $\lambda = \lambda_c = \beta_{\text{eff}}/l$. At prompt critical, $\rho = 1$ and $\lambda = 0$, and the chain reaction is sustained on prompt neutrons alone. It is emphasized that the values of β_{eff} and l must be appropriate to the system for which λ is measured. For reactivities near delayed critical, β_{eff} and l will not vary appreciably and

$$\rho = 1 - \lambda\frac{l}{\beta_{\text{eff}}} \approx 1 - \frac{\lambda}{\lambda_c}.$$

---

[1] J. K. Fox, L. W. Gilley, and D. W. Magnuson, *Preliminary Solution Critical Experiments for High-Flux Isotope Reactor Parameter Study* (to be published as ORNL-3359); also J. K. Fox, L. W. Gilley, and D. W. Magnuson, *Neutron Phys. Div. Ann. Progr. Rept. Sept. 1, 1960*, ORNL-3016, p 59.

[2] D. W. Magnuson, *Neutron Phys. Div. Ann. Progr. Rept. Sept. 1, 1961*, ORNL-3193, p 136.

The Critical Experiment Facility has a 150-kv Cockcroft-Walton positive-ion accelerator which produces short bursts of neutrons by electrostatic deflection of accelerated deuterium ions on and off a tritium target.[3] This neutron source was placed at the botton of the radial beam hole, where the beryllium reflector thickness is 3 in. In some experiments the neutron detector was a 1-in.-long and $\frac{3}{16}$-in.-OD BF_3 counter which could be placed at midplane between the fuel annuli of the critical experiment. In other experiments the detector was a plastic scintillator, placed in the water reflector above the fuel. The time analyzer for sorting the counts into successive time channels following the burst could have channel widths from 10 to 2560 μsec, with a 10-μsec dead time between channels.[4]

The first time channel was a background channel whose width could be adjusted from 2 to 256 times the channel width, and at the end of this channel the neutron burst was started. The second time channel could be delayed from 2 to 256 times the channel width, with the remaining channels delayed only 10 μsec each, the dead time between channels. These counting data in each time channel were summed over many neutron bursts to provide adequate statistics. The delayed neutrons contribute an almost constant background to the counts in the time channels which are fitted to the equation $y = B_1 + B_2\, e^{-\lambda t}$ by a nonlinear least-squares curve-fitting code (NLLS) for an IBM-704 or an IBM-7090 computer. Several fittings of the data were made, successive ones omitting some of the input data in the earlier time channels, to determine whether the fundamental mode had truly been established – that is, whether the value of λ had remained constant in the successive calculations.

The decay constant with the assembly at delayed critical was measured. After approximately 200 neutron bursts it was necessary to insert negative reactivity to reduce the neutron density. Then criticality was reestablished and the procedure repeated to provide adequate counting data in the time channels. In these experiments the negative reactivity was introduced by insertion of the safety rod (a cadmium cylinder that moved in the central water-filled target region).

Comparison of Calculated Values of β_{eff}/l with Measured λ_c Values

Calculations of β_{eff} and l have been made for three control plate configurations,[5] the results of which are given in Table 3.7.1 and in Fig. 3.7.1. Two values of the decay constant at critical were measured for comparison with these calculations, one with the control plates inserted and the other with the moderator poisoned with boric acid and the controls withdrawn. There is a general agreement between the calculations and experiments. The calculated values of the decay constant indicate that β_{eff}/l does not change appreciably as the control materials adjacent to the core are changed from nickel to copper-silver.

---

[3] Texas Nuclear Corp. Model 150-IHD neutron generator.

[4] Technical Measurements Corp. 256-channel analyzer CN-110 with Model 212 pulsed neutron logic control.

[5] By R. D. Cheverton, private communication, Sept. 27, 1961.

Table 3.7.1. Calculated and Experimental Neutron Properties for HFIRCE No. 2

Symmetrical Positions of Control Plates (in.)	Calculated[a,b] Neutron Lifetime (μsec)	Calculated[a,b] Effective Delayed Neutron Fraction, β_{eff}	Critical Neutron Decay Constant, $\lambda_c = \beta_{eff}/l$ (sec^{-1})	
			Calculated[b]	Experimental
0.0	35	0.00629	180	
17.4				213[c]
18.7				196[b]
22.0	38	0.00704	185	
44.0	76	0.00714	94	98.5[c,d]

[a] R. D. Cheverton, private communication, Sept. 27, 1961.
[b] Without target assembly installed in central water-filled region.
[c] With target assembly installed.
[d] Moderator contained 1.22 g of natural boron per liter.

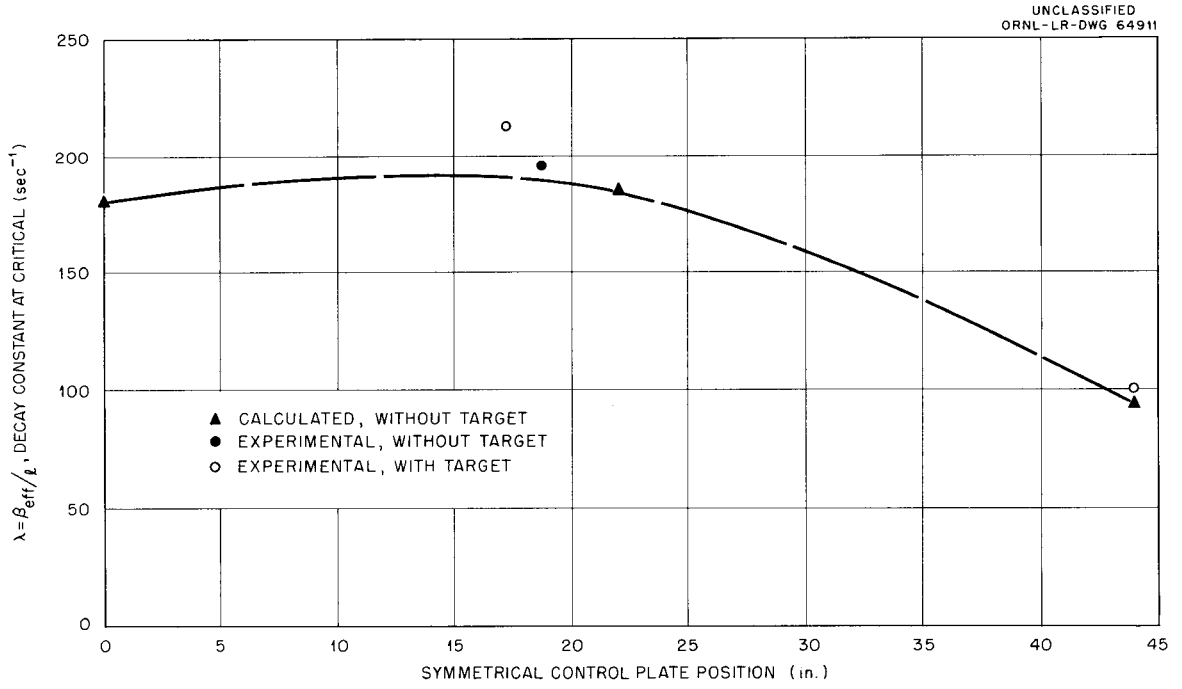

Fig. 3.7.1. Calculated and Experimental Values of the Decay Constant at Critical (HFIRCE No. 2).

Control Plate Reactivities

The experimental results obtained in the control plate studies are typified by the data given in Table 3.7.2 and in Fig. 3.7.2 for the first series of measurements performed to evaluate the shutdown characteristics of the outer control plate. Full insertion of the outer control plate from the critical position introduced −$4.7, which is in agreement with the value of −$4.9 obtained by the summation of control plate sensitivities.

Table 3.7.2. Reactivity Measurements of Outer Control Plate

Outer Control Plate Position[a] (in.)	Decay Constant (sec^{-1})	Reactivity ($)
17.20	213 ± 2[b]	0
16.20	282 ± 3	−0.32
14.20	450 ± 3	−1.11
10.20	841 ± 4	−2.95
6.20	1145 ± 5	−4.38
0.00	1206 ± 5	−4.66
0.00	1219 ± 6	−4.72

[a]The position indicator was set to read 22.0 in. when the nickel section of the control plate was adjacent to the fuel element. A decrease in this reading indicated withdrawal of nickel and insertion of the copper-silver section.

[b]The decay constant was measured for an equivalent critical system when the safety rod was 0.6 in. above the top of fuel.

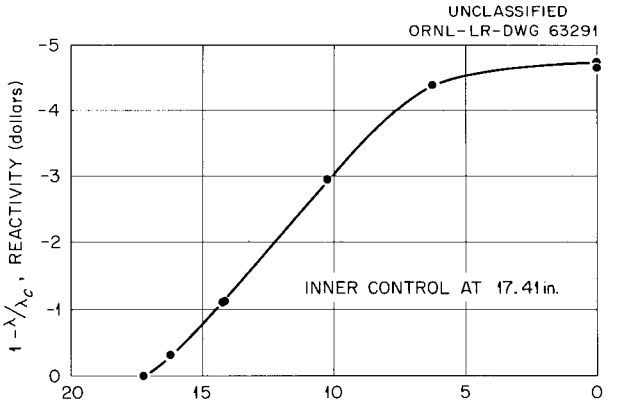

Fig. 3.7.2. Reactivity vs Outer Control Plate Position with Target (HFIRCE No. 2).

To evaluate the effect of thicker control plates, decay constants were measured with a 0.025-in. thickness of cadmium between the control plates when one control plate had the copper-silver section adjacent to the fuel and the other had the nickel section adjacent to the core. The added cadmium increased the worth of the control plates less than $1.5. The same result was obtained when the measurement was repeated with the positions of the two control plates reversed.

The range over which it was possible to calibrate the control plates was increased by adding a neutron absorber, boron, to the moderator. The addition of 1.22 g of natural boron to each liter of moderator allowed almost complete withdrawal of all absorber sections of both control plates before delayed critical was exceeded. Two additional power distributions were measured for the control plate positions that were made possible by adding the natural boron to the moderator.

Measurements were also made after the control cylinders were modified to simulate the condition of one of the four sections, into which the reactor controls will be divided, being inoperative. Holes needed for pressure equalization in the reactor were also drilled in the poison sections.

Additional Safety Devices

A preliminary investigation was made of possible safety devices to augment the control plates in the event of an emergency shutdown. One of these devices was a 0.025-in.-thick cylindrical shell of cadmium inserted stepwise into the annulus between the two sections of the fuel element. The control plates were almost completely withdrawn when this cadmium was inserted 14 in. into the fuel element; thus, it was equivalent to the 1.2 g of natural boron per liter required previously to withdraw the control plates. Insertion of this cadmium shell from 14 in. to 20 in. made the assembly subcritical by $4.2.

Another possible design of a safety device for the reactor might be based on the one with which HFIRCE No. 2 is equipped. It is a cylindrical shell of cadmium, 0.025 in. thick, fitting in the central water column just inside the fuel. The assembly was found to be subcritical by $10.3 when the safety rod was fully inserted.

4. Nuclear and Reactor Physics
Experimental

4.1. THE MEASUREMENT OF α AS A FUNCTION OF ENERGY

G. deSaussure, L. W. Weston, J. D. Kington, R. D. Smiddie,
and W. S. Lyon[1]

The initiation of a program of experiments intended to accurately measure the value of α, the ratio of the capture cross section to the fission cross section, for U^{233}, U^{235}, and Pu^{239} over a wide range of energies was previously reported.[2] Although a part of this program repeats work previously performed elsewhere,[3] the use of a different technique and the recently reemphasized[4] importance of the data justify the repetition. Another part of the program is intended to develop a suitable technique for measuring α for U^{235} at energies from 1 ev to $\sim$20 kev, by using a linear accelerator as a neutron source. The methods reported by Hopkins and Diven[3] cannot be used in this energy range because of large, time-dependent backgrounds produced by scattered neutrons.

At the present time measurements of α for U^{235} at neutron energies of 30 and 64 kev have been completed by two different techniques, and the capture cross section of U^{238} for energies of 30 and 64 kev has been deduced from measurements of the ratio of the U^{238} capture cross section to the U^{235} absorption cross section. Each measurement is discussed below.

Measurement of α for U^{235} at 30 and 64 kev with a Multiplate Fission Chamber

The principle of the measurement of α for U^{235} with a multiplate fission chamber and large liquid scintillator and the equipment developed for the experiment have been described.[2] The electronic arrangement finally adopted differed somewhat from the earlier one,[2] and a revised diagram is shown as Fig. 4.1.1.

Experimental Arrangement. – For the measurements at 30 and 64 kev the ORNL 3.5-Mev Van de Graaff was used to produce monoenergetic, kinematically collimated neutron bursts, a few nanoseconds in width, by p,n reactions on Li^7 and H^3 targets, just above threshold. The accelerator targets were set inside the scintillation tank, about 10 in. from the U^{235} fission chamber. Gamma rays produced in the targets by the proton bursts were separated from the gamma rays accompanying the neutron bursts in the sample by the time-of-flight technique described by Gibbons[5] *et al.*

---

[1]Chemistry Division.

[2]G. deSaussure *et al.*, *Neutron Phys. Div. Ann. Progr. Rept. Sept. 1, 1961*, ORNL-3191, p 177.

[3]J.C. Hopkins and B. C. Diven, *Nucl. Sci. Eng.* **12**, 169 (1962).

[4]*Current Outstanding Reactor Physics Problems*, TID-8210 (May 1961).

[5]J. H. Gibbons *et al.*, *Phys. Rev.* **122**, 182 (1961).

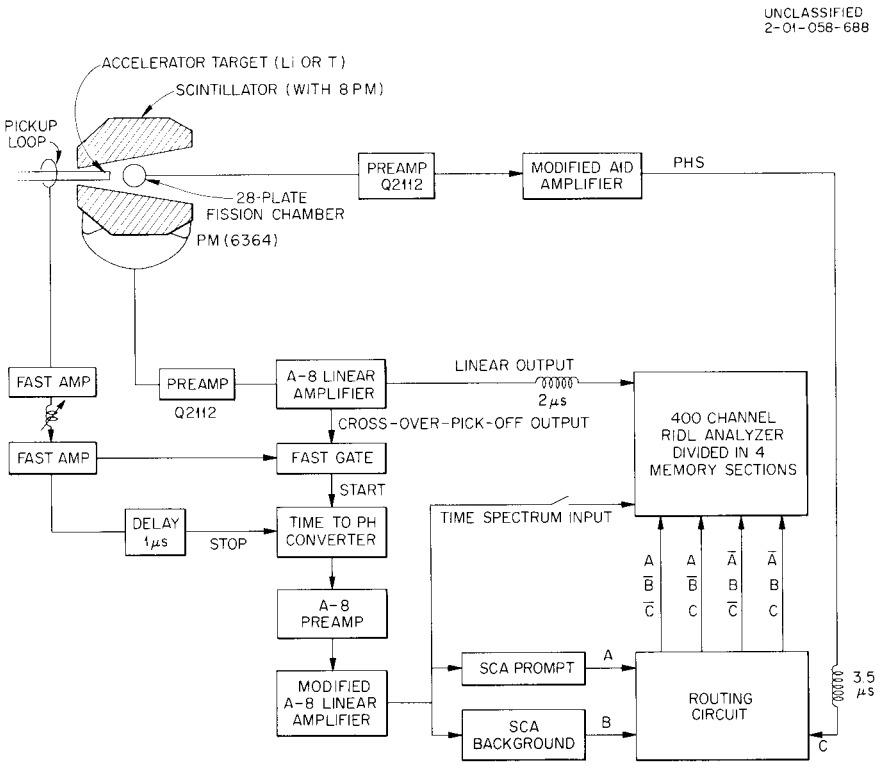

Fig. 4.1.1. Block Diagram of Electronics for Measuring α with a Multiplate Fission Chamber.

The main difficulty in the measurement is associated with the very low signal-to-background ratio. The reaction rate in the sample is low because the absorption cross section of U^{235} at the energies involved is small (~ 3 barns), because the neutron intensity provided by the accelerator is low, and because the sample size is limited by the requirement that the fission fragments be detected in the fission chamber (the total amount of uranium in the chamber is ~ 4 g). The main sources of background in the scintillator are cosmic rays penetrating its 4-in. lead shield, gamma-ray activity of the uranium sample and some of the detector components (traces of K^{40} in the glass of the photomultiplier, etc.), activity due to radioactive trace elements in the walls of the room in which the experiment is being performed, capture gamma rays due to neutrons scattered from the beam, and beam target gamma rays. About half the background was associated with the beam, and it was found that a large increase in signal-to-background ratio could be obtained by reducing[6] the pulse-repetition rate from 1 Mc/sec to 125 kc/sec. The background, except for target gamma rays, was constant during the 8-μsec interval between two successive proton pulses.

Figure 4.1.2 shows a typical time spectrum of the pulses in the scintillator corresponding to energies larger than 2 Mev. Above this bias the signal-to-background ratio is of the order of unity; the ratio decreases rapidly as the bias is lowered. The gamma rays from the uranium sample are barely separated from the target gamma rays, but an increase in the sample-target distance, which would improve this situation, would result in losing the advantage of the kinematic collimation of the neutrons.

---

[6] A beam deflector was designed for this purpose by R. F. King, Instrumentation and Controls Division.

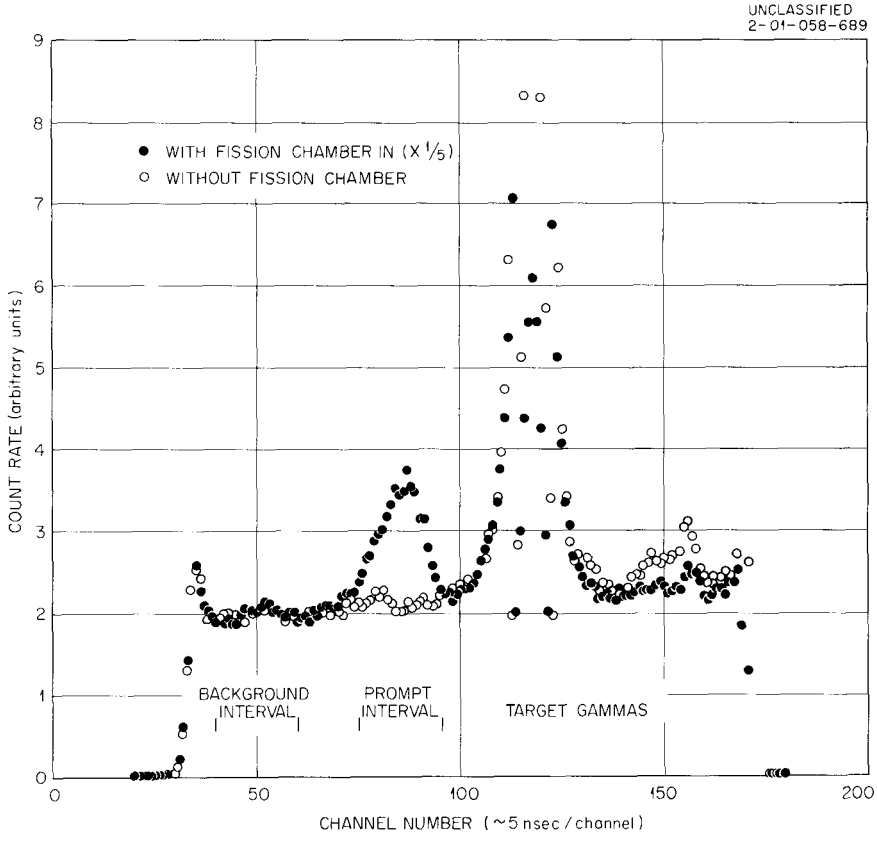

Fig. 4.1.2. Time Spectrum of Scintillator Pulses Having Energies Greater than 2 Mev.

Measurement Procedure. – A measurement at a given energy consists of two sets of four pulse-height spectra each, recorded simultaneously in four memory sections of the pulse-height analyzer. Two of these spectra are time-gated at prompt time; the other two are time-gated at background time. These times are intervals about 100 nsec wide, and correspond, respectively, to the arrival time of the neutron burst on the uranium sample and to a later time when the background is constant. These intervals are shown on Fig. 4.1.2. The spectra corresponding to the two intervals are sorted according to their being in coincidence or in anticoincidence with the pulses from the fission chamber. In order to correct for the gamma rays resulting from neutron captures in the structural material (mostly magnesium) of the fission chamber, a second set of four spectra is taken with a blank chamber, identical with the 28-plate fission chamber except that it contains only one uranium-coated plate. Measurements from the two chambers are normalized to an equal neutron flux by counting the total number of fissions in each chamber and correcting by the relative amounts of uranium.

Figures 4.1.3 and 4.1.4 show typical spectra obtained in coincidence and in anticoincidence with the fission chamber. Figures 4.1.5 and 4.1.6 show net spectra, in which correction has been made for both the background and the effect of the structural materials of the fission chamber.

Fission Chamber Efficiency. – The net coincidence spectrum shown in Fig. 4.1.5 is the spectrum of gamma rays seen by the scintillator in coincidence with fissions detected by the fission chamber (the rate

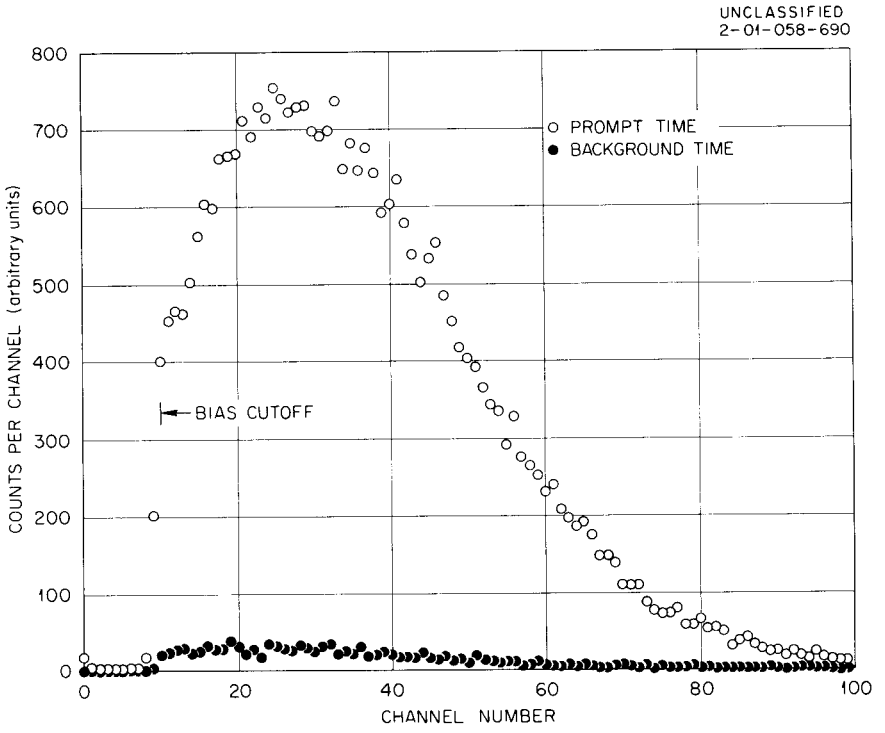

Fig. 4.1.3. Gross Coincidence Spectra for Prompt Time and Background Time.

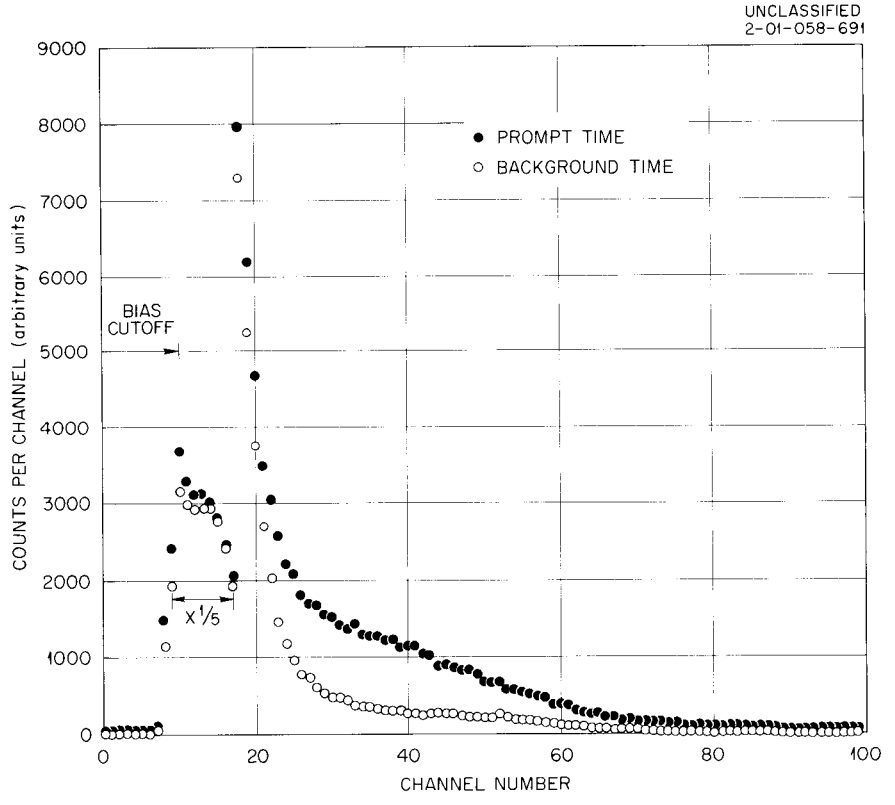

Fig. 4.1.4. Gross Anticoincidence Spectra for Prompt Time and Background Time.

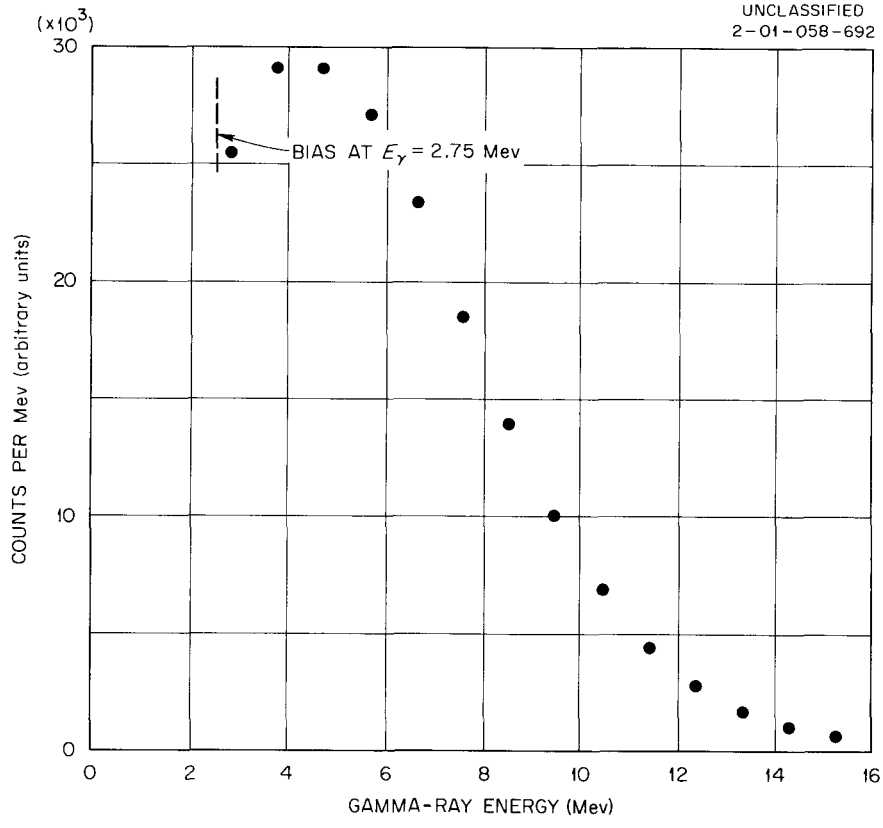

Fig. 4.1.5. Net Coincidence Spectrum.

of accidental coincidences between scintillator pulses and fission chamber pulses due to alpha-particle pulse pile-up is negligible).

Since the fission chamber is only about 70% efficient in detecting fission fragments, the net anticoincidence spectrum of Fig. 4.1.6 must be due not only to uranium-capture gamma rays but also to those fission gamma rays that were not in coincidence with fission chamber pulses because the fission chamber failed to detect the fragments resulting from the fission. To correct for this, an attempt was made to determine the fission chamber detection efficiency by measuring coincidences between fission-fragment pulses in the chamber and prompt-fission neutron pulses detected by a stilbene crystal (the stilbene crystal had been made gamma-ray insensitive by pulse-shape discrimination). It was found, however, that the efficiency of the chamber so measured varied with the position of the fast-neutron detector, probably because of a correlation between the detection efficiency of the chamber, the directions of the fission fragments, and the directions of the fission neutrons. Measured values of the chamber efficiency by the method outlined ranged between 62 and 82%.

Because the fission-fragment detection efficiency of the chamber could not be measured directly with the accuracy desired, the anticoincidence spectrum of Fig. 4.1.6 was corrected for the fissions missed by the fission chamber by subtracting from it a coincidence spectrum normalized at pulse heights corresponding to gamma-ray energies of >10 Mev. Capture of a neutron in U^{235} cannot produce a total gamma-ray

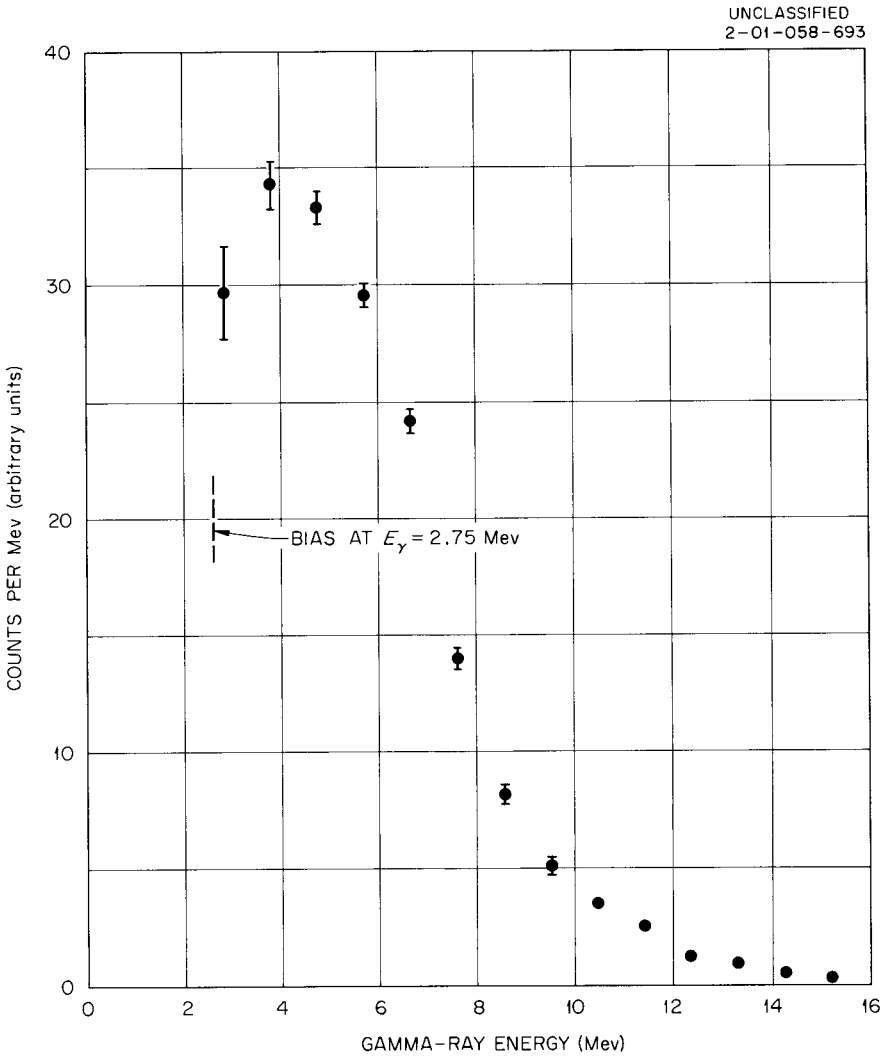

Fig. 4.1.6. Net Anticoincidence Spectrum.

energy greater than the neutron binding energy of 6.3 Mev; thus, allowing for the poor pulse-height resolution of the scintillator, all pulses larger than 10 Mev are caused by fission gamma rays. A similar technique was used by Hopkins and Diven[3] to correct their anticoincidence spectrum for fissions missed by their fission neutron detector.

The net capture gamma-ray spectrum resulting from the above treatment is shown in Fig. 4.1.7.

The fission chamber efficiency, determined by the ratio of the pulse-height spectra above 10 Mev in the coincidence and anticoincidence spectra, was about 70%, the exact value depending on the bias of the chamber amplifier. This result is consistent with the 62 to 82% efficiency determined by the neutron coincidence technique.

The Spectrum-Fraction Correction. – The value of α at a given energy is equal to the ratio of the area of the capture spectrum (Fig. 4.1.7) to that of the fission spectrum (Fig. 4.1.5, corrected for fission anticoincidences). In order to obtain the ratio, these spectra must be extrapolated to zero pulse height. The

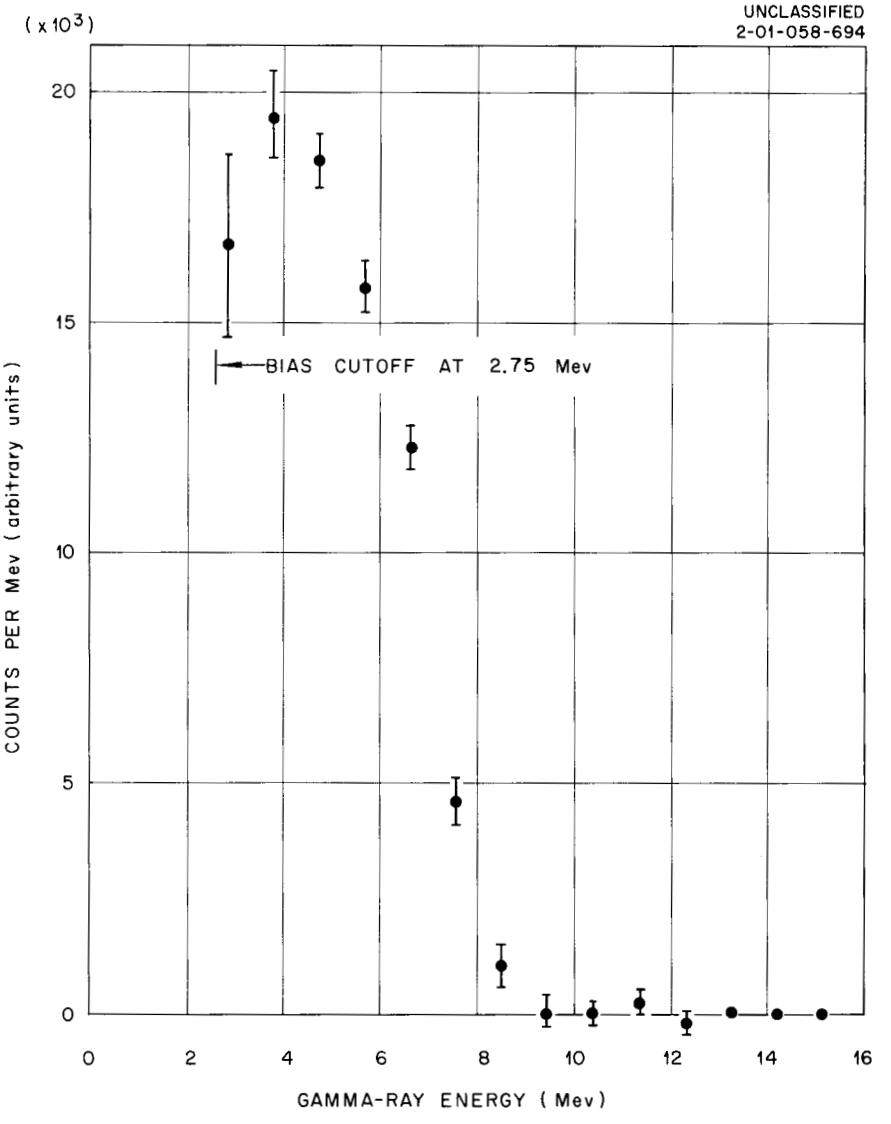

Fig. 4.1.7. Net Capture Spectrum.

fission spectrum may be measured down to zero pulse height by a separate experiment in which the time-of-flight requirement is removed. Figure 4.1.8 shows the fission pulse-height spectrum so obtained. The extrapolation of the capture spectrum, however, introduces the major uncertainty of the measurement.

The quantity which must be determined, the spectrum fraction, is the fraction of the capture pulse-height spectrum above a given bias. In the experiment this bias was set at 2.75 Mev.

Three independent estimates of the spectrum fraction were reviewed in determining a suitable estimate for use in this experiment. Gibbons *et al.*,[7] using the same type of scintillator as is used in this experiment, obtained an empirical relation between the spectrum fraction of capture gamma rays above 2.75 Mev and the neutron binding energy. This relation gives, for U^{235}, a value of 0.68 ±0.04 for the spectrum fraction. The uncertainty quoted is based upon the dispersion of experimental data.

[7] J. H. Gibbons, private communication; see also ref 5.

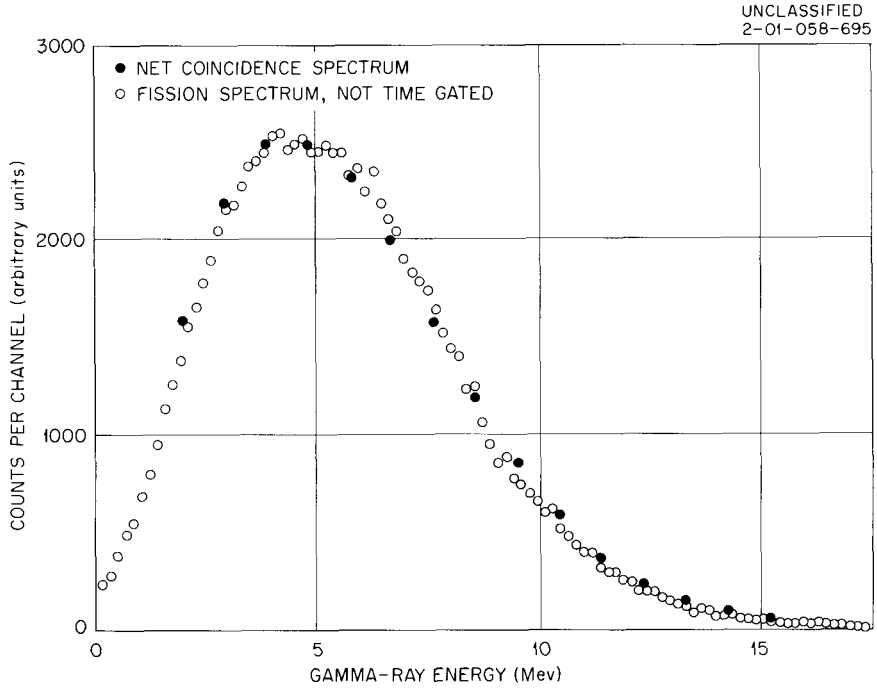

Fig. 4.1.8. Fission Gamma-Ray Spectrum; No Pulse-Height Bias.

A second estimate was obtained by Macklin,[8] who used a Monte Carlo method to compute the gamma-ray pulse-height spectrum resulting from neutron capture in U^{235} for various average multiplicities of the gamma-ray cascade. Computed spectra corresponding to average multiplicities of $4\frac{1}{4}$ and $5\frac{1}{3}$ are compared with an experimental spectrum in Fig. 4.1.9. The experimental spectrum is broader than the computed spectra, probably because in the computation a better pulse-height resolution for the scintillator was assumed than was true at the time of the measurement. The spectrum fraction for the computed spectrum of average multiplicity 5, the most consistent with the experimental spectrum, is 0.72.

The third estimate of the spectrum fraction resulted from an attempt to measure the capture spectrum to as low a pulse height as possible by combining several techniques. Measurement with the fission chamber is impossible below a pulse height corresponding to 2.25 Mev; in fact, the background of smaller pulses is much larger than the capture rate in the 4-g U^{235} sample. Therefore the absorption spectrum of a 200-g sample of U^{235} was measured, and an appropriate amount of fission spectrum subtracted. Even with the large sample, the measurement of the low pulse-height end of the spectrum is difficult, because time-of-flight gating must be used to discriminate against background and because the gamma-ray activity of the sample itself considerably increases the low pulse-height background. The measurement of the absorption spectrum could not be extended below a bias of 1.5 Mev. Below this point the very high background count rate resulted in poor time resolution. This fact is demonstrated by the time spectra for various energy intervals plotted in Fig. 4.1.10.

---

[8] R. L. Macklin, private communication.

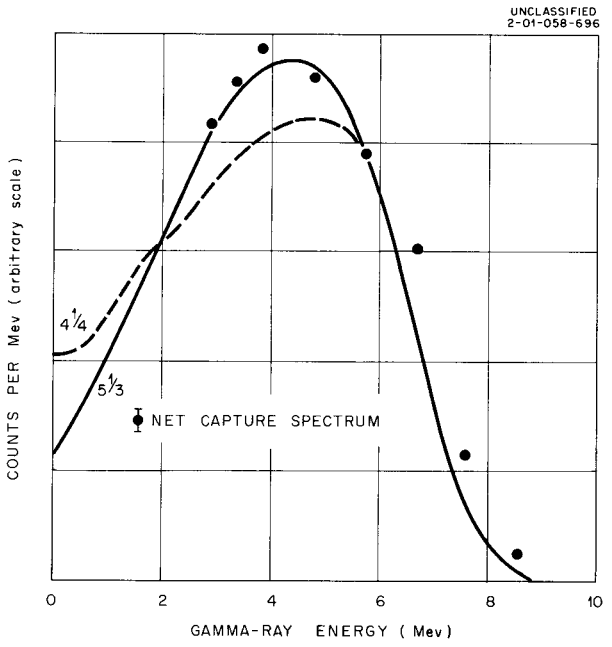

Fig. 4.1.9. Computed Gamma-Ray Pulse-Height Spectra for Cascade Multiplicities of $4\frac{1}{4}$ and $5\frac{1}{3}$.

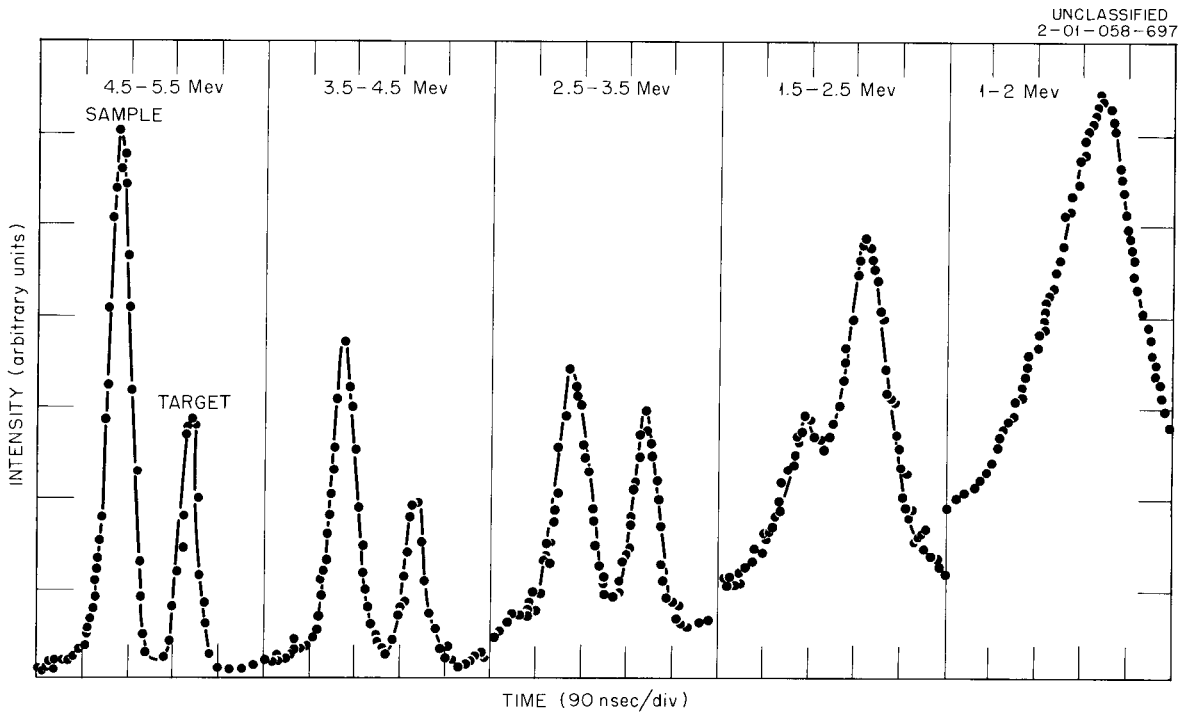

Fig. 4.1.10. Time Spectra of Various Sections of U^{235} Absorption Pulse-Height Spectrum.

The measured absorption spectrum of U^{235} at 30 kev is shown in Fig. 4.1.11. The spectrum was extrapolated from the bias cutoff of 1.5 Mev to zero pulse height, as shown. The hatched area represents the uncertainty in the extrapolation. After the fission portion of the absorption spectrum was subtracted, the value obtained for the spectrum fraction above 2.75 Mev was 0.66 ± 0.08, in which the uncertainty quoted

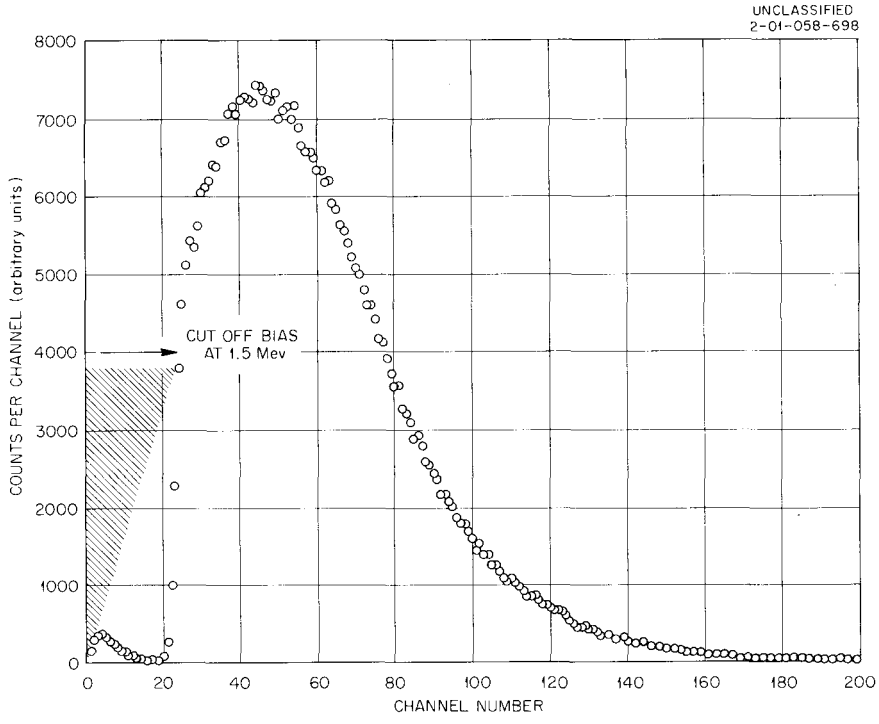

Fig. 4.1.11. Absorption Pulse-Height Spectrum of 200 g of U^{235} and 30-kev Incident Neutrons.

is statistical only. The error does not include the effect of any change in the pulse-height spectrum due to the finite thickness of the sample, which produces some self-absorption and energy degradation of the gamma radiation.

The three estimates of the capture spectrum fraction, 0.68 ± 0.04, 0.72, and 0.66 ± 0.08, are consistent, and the value of 0.68 ± 0.04 was chosen for use in this experiment.

Other Corrections. – Two additional small corrections were applied to the measurement. First, a correction was made because the probability of the radiation escaping the scintillator without interacting differs for capture gamma rays and fission gamma rays. In capture, the total escape probability decreases with increasing multiplicity of the cascade transition. Macklin has calculated[8] a probability of 1.6% for a multiplicity of $5\frac{1}{3}$, and 4.2% for a multiplicity of $4\frac{1}{4}$. Because some theories and the fit of the measured spectrum to the computed spectra (Fig. 4.1.9) indicate a multiplicity of 5 or more, the total escape probability was assumed to be (2 ± 2)% in the present work. The total escape probability for fission was measured by observing coincidences between the scintillator and the fission chamber. The value obtained was (0.15 ± 0.15)%. This low total escape probability is not surprising, since the prompt fission gamma rays are of predominantly low energies.[9]

A second small correction was made to account for the capture of neutrons in the fluorine of the UF_4 deposit in the fission chamber. By using the capture cross sections of fluorine at 30 and 64 kev measured by Gibbons[5,7] and assuming the capture-spectrum fraction of fluorine to be the same as that of U^{235}, the

[9] F. C. Maienschein *et al.*, *Proc. U.N. Intern. Conf. Peaceful Uses Atomic Energy, 2nd, Geneva, 1958* 15, 366 (1959).

correction was computed to be less than 2%. The isotopic purity of the U^{235} of the chamber was >99%; thus no correction was needed for capture in other uranium isotopes.

Results. – Values of α for U^{235} at 30 and 64 kev determined in this experiment are compared in Table 4.1.1 with the earlier results of Hopkins and Diven.[3] The agreement between the two sets of data is good. The technique of the present experiments appears to be suitable for the measurement of α at the lower neutron energies accessible with a linear accelerator.

Table 4.1.1 Values of α for U^{235} at 30 and 64 kev

	α (30 ± 8 kev)	α (64 ± 20 kev)	$\frac{\alpha \text{ (30 kev)}}{\alpha \text{ (64 kev)}}$
This experiment	0.372 ± 0.026	0.315 ± 0.06	1.181 ± 0.26
Hopkins and Diven[a]	0.376 ± 0.036	0.327 ± 0.024	1.115

[a] J. C. Hopkins and B. C. Diven, *Nucl. Sci. Eng.* 12, 169 (1962).

Measurement of α for U^{235} at 30 and 64 kev, Using a Thick U^{235} Sample and Pulse-Height Spectrum Analysis

An attempt was made to measure α for U^{235} at 30 and 64 kev, using a thick sample of U^{235} and discriminating captures from fissions by gamma-ray pulse-height spectrum analysis. The experimental arrangement for this measurement is similar to that used in the measurement with the multiplate fission chamber, except that a thick sample of U^{235} is substituted for the fission chamber. The scintillator pulses associated with the absorption of neutrons in the sample are separated from background pulses by time-of-flight. Since the pulse-height spectra associated with fission and capture have different shapes and the fission pulse-height spectrum can be determined independently with a fission chamber, it should be possible to subtract the fission spectrum from the absorption spectrum and hence to obtain the capture spectrum and the ratio of capture to fission, α.

The fission spectrum to be subtracted from the absorption spectrum must be normalized at high pulse heights corresponding to gamma-ray energies of more than 10 Mev, where no contribution from the capture spectrum is possible.

The advantage of this technique is that it does not require a fission chamber except in an auxiliary experiment to measure the shape of the fission spectrum; hence a thick sample may be used and large count rates obtained.

The method may also be used with the other fissionable isotopes, U^{233} and Pu^{239}, and is suitable for use with a linear accelerator. Its main disadvantage is its poor precision. The quantity directly measured is the ratio of absorption to fission, $1 + \alpha$, but since α in the kev region is small compared with unity, a small-percentage error in $1 + \alpha$ results in a large-percentage error in α. In addition, the precise measurement of the fission pulse-height spectrum and its normalization to the absorption pulse-height spectrum at large pulse heights, where the count rates are very small, are difficult.

Measurement by the thick-sample technique gave a value of 0.5 ± 0.3 for α of U^{235} at 30 kev. The large uncertainty stems from the difficulty in internormalizing the pulse-height spectra due to absorption and to fission. A 2% difference in gain between the two pulse-height spectra results in a 20% error in $1 + \alpha$ and a 50% error in α.

It must be concluded from the results that this method is not very useful in the kev region, where α is small compared with unity. It may be more applicable over some of the low-energy resonances, where α may be of order unity or larger.

Capture Cross Sections of U^{238} at 30 and 64 kev

Since neutron capture in U^{238} is of importance to reactor physics and is interesting from the point of view of nuclear physics,[10] the cross section is being studied. The ratio of the capture cross section in U^{238} to the absorption cross section of U^{235} was measured to be 0.150 ± 0.012 at 30 ± 8 kev and to be 0.126 ± 0.010 at 64 ± 20 kev.

From the above ratios the capture cross section for U^{238} is computed, using the values of α from Table 4.1.1 and the fission cross sections of Hughes and Schwartz,[11] to be 0.531 barn at 30 kev and 0.340 barn at 64 kev. These values are compared with published values[11,12] in Fig. 4.1.12.

---

[10] E. G. Bilpuch, L. W. Weston, and H. W. Newson, *Ann. Phys. (N.Y.)* **10**, 455 (1960).

[11] *Neutron Cross Sections*, compiled by D. J. Hughes and R. Schwartz, BNL-325, 2d ed. (1958).

[12] J. H. Gibbons *et al.*, *Phys. Rev.* **122**, 182 (1961).

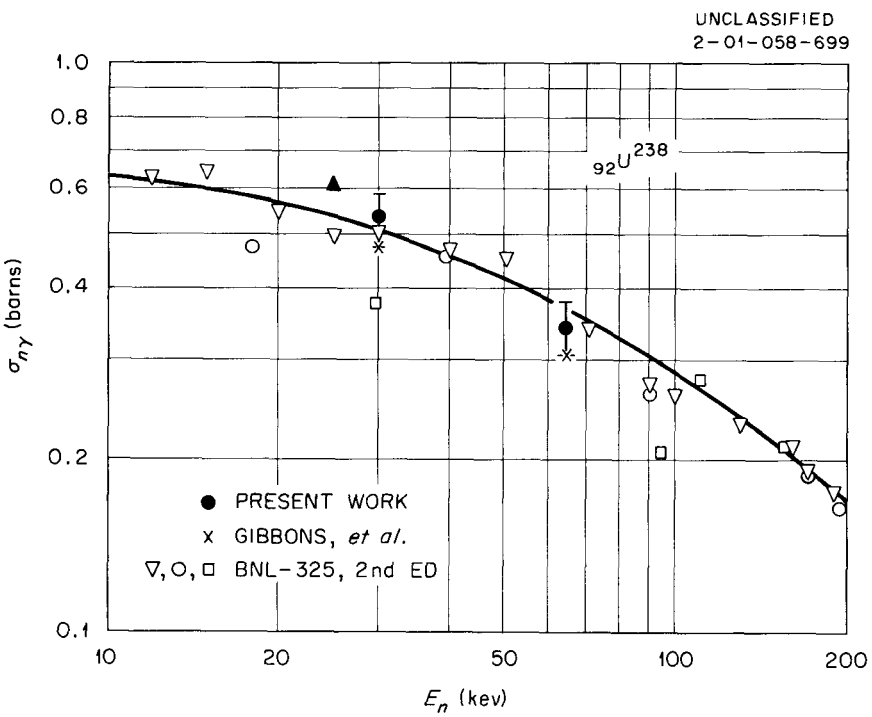

Fig. 4.1.12. Neutron Capture Cross Section of U^{238} Between 10 and 200 kev.

Acknowledgments

We wish to acknowledge the assistance of Instrumentation and Controls Division personnel N. W. Hill and J. H. Todd in electronics design, R. K. Abele, F. E. Gillespie, and M. M. Chiles in design and construction of fission chambers, and R. F. King, A. J. Wyrick, and J. P. Judish in Van de Graaff operation. F. C. VonderLage, of the Director's Division, and L. O. Love, H. R. Gwinn, F. M. Scheitlin, J. T. Barker, R. L. Johnson, and B. J. Massey of the Isotopes Division assisted in the preparation of samples. We are indebted to R. L. Macklin and J. H. Gibbons of the Physics Division for many helpful discussions.

4.2. STATUS OF PULSED-NEUTRON MEASUREMENTS IN LIGHT-WATER ICE

E. G. Silver

It was reported previously[1,2] that low-temperature measurements of the diffusion coefficient in beryllium by the pulsed-neutron method were beset by intrinsic difficulties due to the existence of one or more "trapped" (that is, long-lived) subpopulations of neutrons whose presence makes the attainment of an equilibrium or asymptotic energy spectrum impossible in times short enough to permit measurement of the time decay of the neutron population. The theoretical models on which understanding of this phenomenon is based lead to the conclusion that in H_2O this trapping effect should be absent, or at least of much less importance due to the relatively greater incoherent component of the transport cross section. Therefore an experiment was initiated to investigate the temperature dependence of the diffusion parameters in light-water ice in the range -5 to $-90°C$.

The pulsed-neutron source and refrigeration equipment used for the experiment have been described.[3,4] The ice blocks are cylindrical in shape and are contained in aluminum cans. Each cylinder is used with the ice filled to three different levels in succession in order to obtain three values of buckling with each can.

Initially, D-T neutrons ($\sim$14 Mev) were used as the exciting neutrons; however, the resulting very high background level of neutron counts made measurements impossible. It was shown that the background was due to neutrons arising from the (γ,n) reaction in the deuterium component of ordinary water; the gamma rays came from the decay of 7.4-sec N^{16}, which was produced by the $O^{16}(n,p)N^{16}$ reaction of the 14-Mev neutrons. Accordingly, a 2.4-Mev D-D neutron source was used instead, and the background vanished, as was expected since the (n,p) reaction has a negligible cross section at this neutron energy.

---

[1] E. G. Silver and G. deSaussure, *Neutron Phys. Div. Ann. Progr. Rept. Sept. 1, 1961*, ORNL-3193, pp 215–222.

[2] G. deSaussure, *Neutron Phys. Div. Ann. Progr. Rept. Sept. 1, 1961*, ORNL-3193, pp 223–228.

[3] G. deSaussure and E. G. Silver, *Neutron Phys. Div. Ann. Progr. Rept. Sept. 1, 1958*, ORNL-2609, p 59.

[4] G. deSaussure and E. G. Silver, *Neutron Phys. Div. Ann. Progr. Rept. Sept. 1, 1959*, ORNL-2842, pp 115–117.

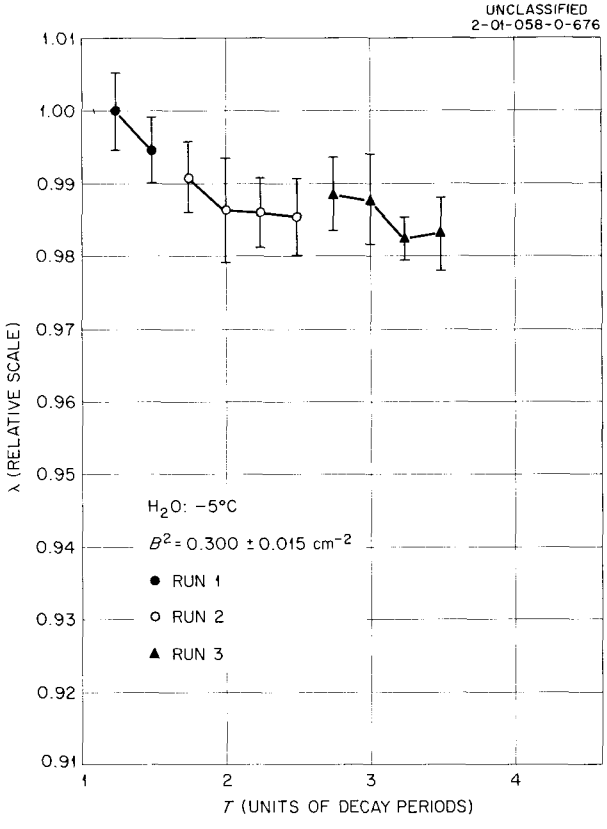

Fig. 4.2.1. Variation of Decay Constant λ as a Function of Waiting Time Between the End of the Neutron Irradiation and Start of Analysis. Cylinder of H_2O ice, $B^2 = 0.300\ cm^{-2}$, temperature of −5°C, time in units of decay period $T(= 1/\lambda)$.

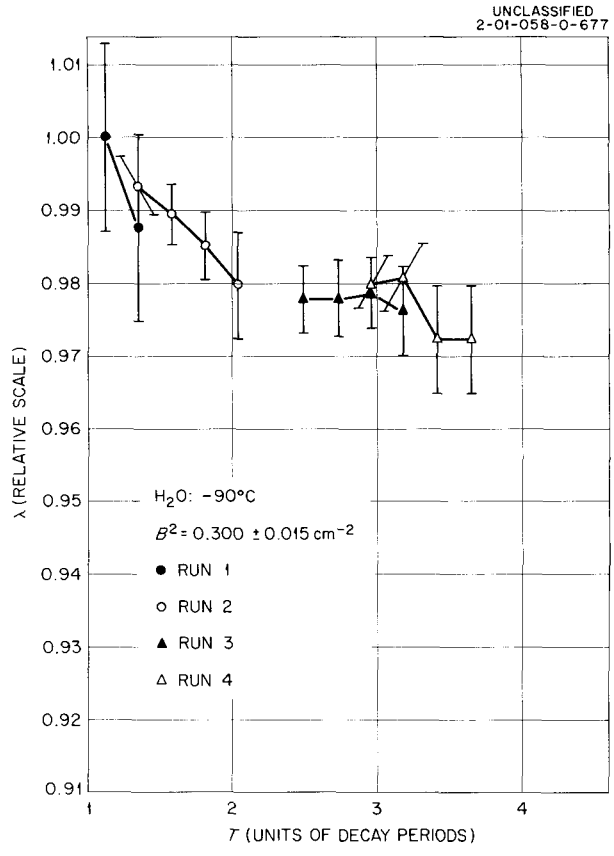

Fig. 4.2.2. Variation of Decay Constant λ as a Function of Waiting Time Between the End of the Neutron Irradiation and Start of Analysis. Cylinder of H_2O ice, $B^2 = 0.300\ cm^{-2}$, temperature of −90°C, time in units of decay period $T(= 1/\lambda)$.

The hypothesis that in H_2O equilibrium spectra should be obtainable at low temperature in finite assemblies was then tested in a single ice cylinder whose buckling was $B^2 = 0.300\ cm^{-2}$. Figures 4.2.1 and 4.2.2 show the change in the decay constant λ as a function of waiting time after the end of the neutron burst for −5 and −90°C, respectively. For comparison Figs. 4.2.3 and 4.2.4 show similar data for a beryllium block ($B^2 = 0.0359\ cm^{-2}$) at 25 and −25°C, respectively. It is apparent that, whereas in beryllium at −25°C there is a large and continuing change in λ with time, at the much lower temperature of −90°C there is no such change in H_2O. Within the limits of accuracy of this experiment, it appears that an asymptotic value of λ is attained soon enough to permit accurate measurement over the entire temperature range of this experiment.

In the attempts to freeze large ice blocks, two problems were encountered. (1) The very small solubility of air in ice, as compared with its solubility in liquid H_2O near the freezing point, caused relatively

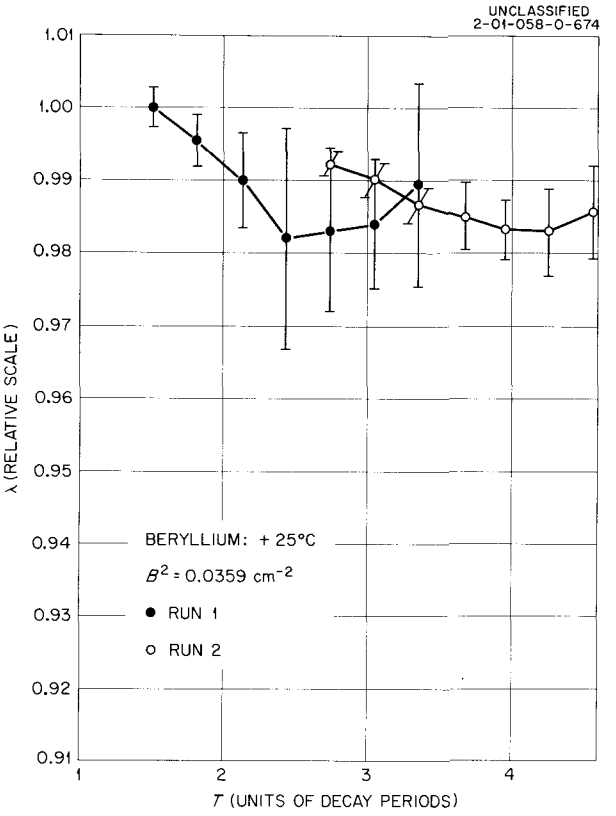

Fig. 4.2.3. Variation of Decay Constant λ as a Function of Waiting Time Between End of Neutron Irradiation and Start of Analysis. Beryllium parallellepiped, B^2 = 0.0359 cm^{-2}, temperature of 25°C, time in units of decay period $T(= 1/\lambda)$.

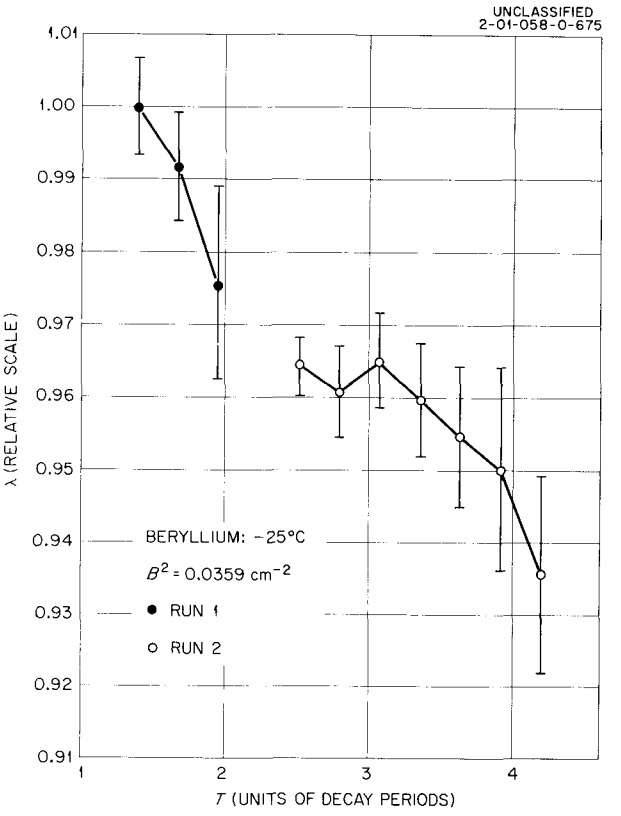

Fig. 4.2.4. Variation of Decay Constant λ as a Function of Waiting Time Between End of Neutron Irradiation and Start of Analysis. Beryllium parallellepiped, B^2 = 0.0359 cm^{-2}, temperature of −25°C, time in units of decay period $T(= 1/\lambda)$.

large volumes of air bubbles to be nonuniformly frozen into the ice. (2) The removal of heat from the water at all surfaces, including the top, caused the interior portion to remain as liquid the longest; upon freezing, this trapped water expanded, thus severely cracking, flaking, and distorting the ice.

With the apparatus shown in Fig. 4.2.5 both problems were finally solved to an acceptable degree. The procedure used is as follows. The cylinder is filled with distilled water to within about 4 in. of the top, and the water is covered with a 2-in. layer of melted pure paraffin and brought to boil. After the water has boiled for about 40 min, which drives out the dissolved gases, the top plug is lowered into the cylinder so that it extends into the paraffin. It is gradually lowered by adjusting the three leveling screws, letting the displaced excess water flow into the overflow volume, and raising the paraffin level around the outside of the plug to the top of the container. The water in the overflow volume is covered with a layer of heavy mineral oil to prevent reabsorption of air as the water cools. As the system cools, the paraffin freezes at about 85°C. Cooling contraction of the water below this temperature and subsequent expansion on

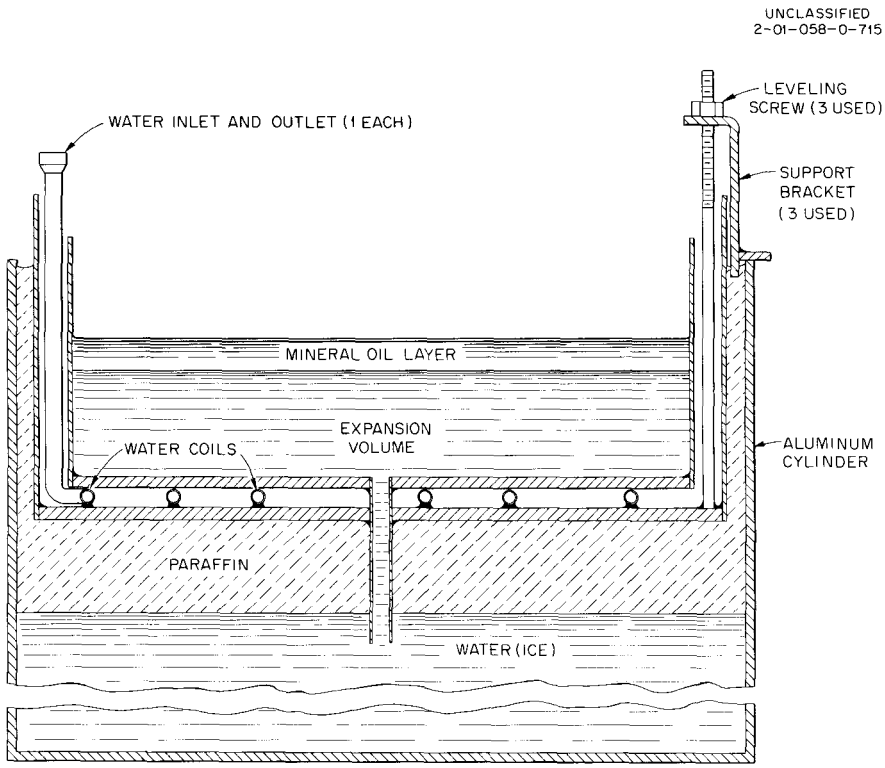

Fig. 4.2.5. Diagram of the Top Plug Used To Freeze Air-Free Ice Cylinders for the Pulsed-Neutron Experiment. Top plug is shown in place in the aluminum cylinder in which the ice is frozen.

freezing are accommodated by the water in the expansion volume of the top plug. Room-temperature water is circulated through the coils in the top plug during freezing to prevent ice formation at the upper surface of the ice block and the cracking associated with it. The thick layer of paraffin between the plug and the water surface is needed to prevent the water density decrease below 4°C from setting up a circulation due to the heat source at the top represented by the water-warmed plug bottom. This circulation, if permitted, prevents freezing altogether, even in a freezer at −20°C. The use of a plain paraffin plug instead of the top plug described here was not feasible, since the shrinkage of paraffin as it freezes causes such a plug to free itself from the container wall and permit air to get at the liquid surface.

With the use of the top plug, air-free ice blocks were produced in the sizes required. After removal of the top plug and paraffin from the ice, several thin layers of water were successively added to the top of the ice to produce a flat final surface. If the water addition is made while the ice is much below 0°C, the thermal shock causes severe cracking of the ice, with air inclusion in the cracks. Even without water addition, some thermal-stress cracking occurs in the ice blocks as they are cooled to −85°C. However, the cracks so formed are exceedingly thin, and no significant volume of air is introduced into the ice in this way. To date, decay data have been taken for eight cylinders ranging from 8 in. in diameter and 6.5 in. in height to 12 in. in diameter and 12 in. in height. Larger cylinders will be made only if analysis of the data shows need for such measurements. In the largest assemblies already measured, the contribution to the neutron decay from absorption is already the dominant term.

In future experiments the data will be extended to small assemblies over the same temperature range (−5 to −90°C). Recent evidence showed that in small H_2O systems there is a shape-dependent factor determining the decay constant, in addition to the buckling and absorption terms.[5] An attempt will be made to observe this effect.

Since, in small assemblies, high source intensity and low beam-caused background are important factors in obtaining good data, a further beam-deflection system will be installed at the accelerator for the purpose of postacceleration cleanup of the residual beam. Work at Brookhaven[6] indicates that in this way the on-off ratio of the beam can be increased from the present value of approximately 10^3 to values as high as 10^6. It may also be possible to make use of the larger neutron yield from the D-T reaction by using deuterium-depleted water to minimize the (γ,n) neutron source described above.

---

[5]K. H. Beckurts, review paper presented at Brookhaven National Laboratory Conference on Neutron Thermalization, April 30–May 2, 1962.

[6]E. Starr and G. A. Price, *Measurement of the Diffusion Parameters of Graphite and Graphite-Bismuth by Pulsed-Neutron Methods*, presented at Brookhaven National Laboratory Conference on Neutron Thermalization, April 30–May 2, 1962.

4.3. MANGANESE BATH MEASUREMENTS OF η OF Pu^{239}[1]

R. L. Macklin,[2] G. deSaussure, J. D. Kington, and W. S. Lyon[3]

A previous report[4] described a measurement of the thermal value of η, the yield of fission neutrons per absorption, for U^{233} and U^{235} by a manganese bath technique. Samples of Pu^{239} were also included in that series of measurements, but because of factors stemming from the appreciable variation of η of Pu^{239} with energy below the cadmium cutoff, the application of appropriate corrections to the experimental value is difficult. The neutron spectrum used for the experiment has not been directly measured, and there is some evidence that the conventional assumption of a Maxwellian plus a $1/E$ portion may not be adequate.[5] However, interest in the value of η of Pu^{239} has continued, and therefore the best values from the experiment are given below.

The result for a black sample in our thermal spectrum, $\bar{\eta}$ corrected except for energy dependence, is 2.058 ± 0.010. This value may be best for solid-fuel reactor calculations. The corrected value of η at 2200 m/sec is $2.143^{+0.010}_{-0.020}$, where the lower uncertainty bound is arbitrarily doubled to allow for spectrum uncertainties.

---

[1]Summarized from *Nucl. Sci. Eng.* **14**, 101 (1962).

[2]Physics Division.

[3]Chemistry Division.

[4]R. L. Macklin *et al.*, *Nucl. Sci. Eng.* **8**, 210 (1960).

[5]R. Ramanna *et al.*, *Proc. U.N. Intern. Conf. Peaceful Uses Atomic Energy, 2nd, Geneva, 1958* **16**, 260–64 (1958).

4.4. THE NEUTRON ASYMPTOTIC DECAY CONSTANT IN A SMALL CRYSTALLINE MODERATOR ASSEMBLY[1]

G. deSaussure

The effect of the narrow peak of the neutron transport cross section of crystalline materials at low energy is being investigated. It is shown that an upper bound can be found for the asymptotic decay constant in a small assembly. This upper bound is lower than the values usually measured by the pulsed-neutron source technique. The apparent discrepancy is discussed.

[1]Abstract of a paper presented at the Brookhaven National Laboratory Conference on Neutron Thermalization, April 30—May 2, 1962.

4.5. AN APPLICATION OF PILE NOISE ANALYSIS TO MEASUREMENTS OF KINETICS PARAMETERS OF A POOL-TYPE REACTOR

M. N. Alam,[1] A. L. Colomb,[2] and K. M. Henry

It was reported previously[3] that instrumentation was being developed with which various reactor kinetics parameters could be measured. This report presents the results of such measurements.

The low-frequency wave analyzer (Fig. 4.5.1) was used to obtain data on three water-moderated reactor configurations between 0.02 and 20 cps. The overall gain necessary to achieve measurements at frequencies larger than 20 cps was so high (approximately 3×10^4) that the analyzer could not be maintained stable. Therefore a commercial wave analyzer was used to scan frequencies larger than 20 cps. The resolution or bandwidth of the analyzer was kept constant for various frequency ranges as shown below:

Frequency Range (cps)	Bandwidth (cps)
0.02 to 0.1	0.0063
0.1 to 1	0.0318
1 to 20	0.318
20 and up	3.5

[1]On loan from Pakistan Atomic Energy Commission.

[2]Operations Division.

[3]M. N. Alam, A. Colomb, and K. M. Henry, *Neutron Phys. Div. Ann. Progr. Rept. Sept. 1, 1961*, ORNL-3193, p 228.

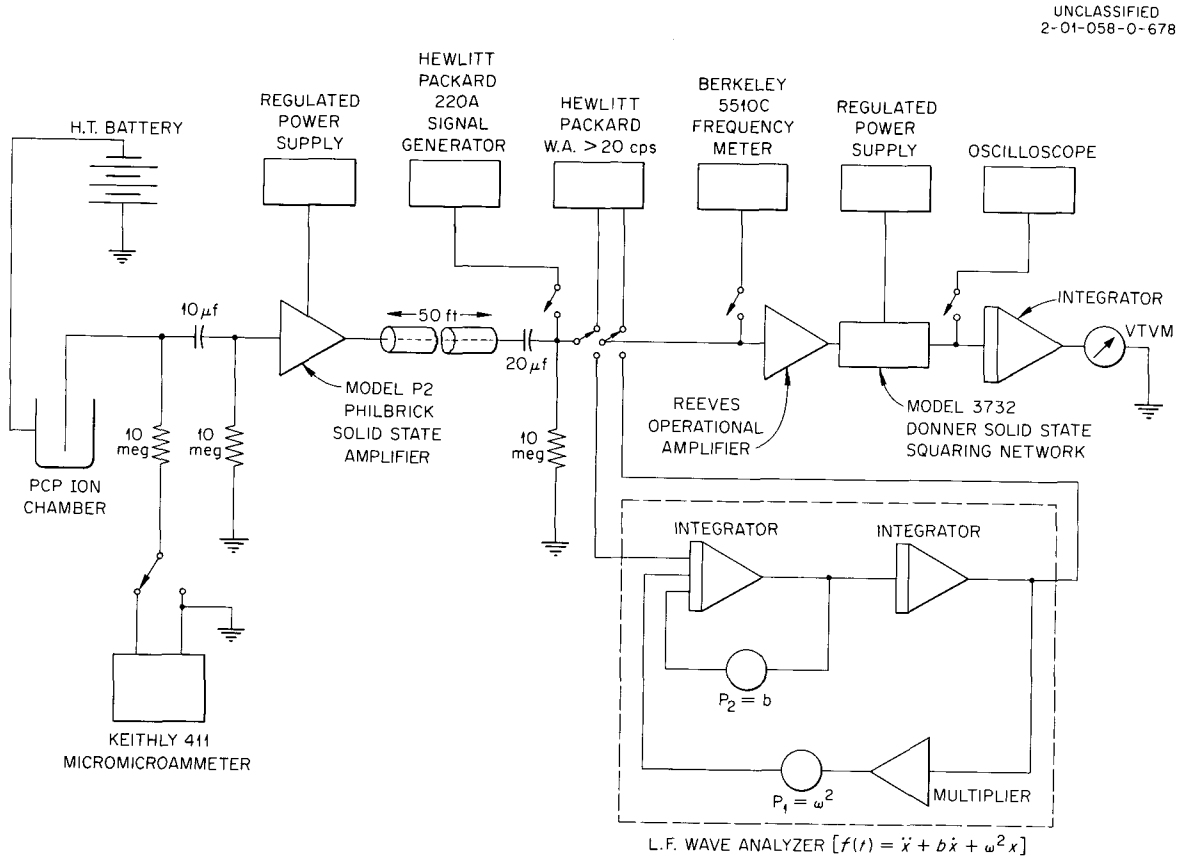

Fig. 4.5.1. Low-Frequency Wave Analyzer.

The instrumentation was calibrated by measuring the spectral density of the fluctuations produced by a Co^{60} gamma-ray source. The spectral density of such a source is constant with respect to frequency, and therefore this measurement will yield the frequency response of the instrumentation. Figure 4.5.2 shows that the frequency response is flat between 0.1 and 50 cps. The amplitude increase at low frequencies is probably due to thermal noise in the load resistor, and the cutoff at high frequencies results from the time constant introduced by the chamber capacity and the load resistor. Reactor spectral densities were corrected for these effects.

The errors drawn in Fig. 4.5.2 are standard deviations and were obtained in the following manner. The amplitude of fluctuations of a decaying radioactive source is normally distributed. The spectral density of these fluctuations is proportional to the square of their amplitudes; therefore the probability distribution function of the spectral density is the product of two normal distribution functions, that is, a chi-square distribution. The variance of a chi-square probability distribution function is equal to two times the number of degrees of freedom of this function. In this case the number of degrees of freedom is proportional to the sampling time, to the filter bandwidth, and to the filter shape factor.

In the case of the reactor spectral density the determination of the standard deviation of the measurement is somewhat more involved. The constant spectral density of the fission, absorption, and scattering process (white noise) is modulated by the reactor frequency response before being analyzed and

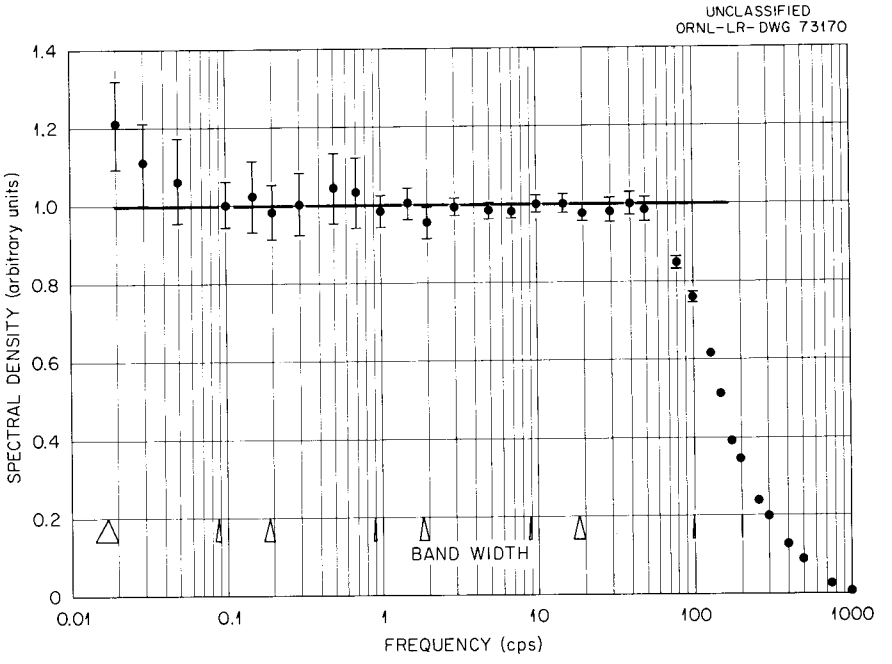

Fig. 4.5.2. Frequency Response of the Instrumentation (Co^{60} Source).

squared. The total standard deviation is the sum of the standard deviation of a white noise analyzed by the above-mentioned method.

The standard deviation of the reactor frequency response was obtained by a method described by Lee,[4] who indicates that the standard deviation σ is

$$\sigma = \sqrt{\int_{-T}^{T} \frac{T - |\tau|}{T^2} \Psi^*(\tau)\, d\tau}\,,$$

where T is the sampling time and $\Psi^*(\tau)$ the normalized autocorrelation function of the system. The autocorrelation is equal to the Fourier transform of the spectral density of the system, implying that the knowledge of σ is dependent on the knowledge of the spectral density.

The spectral densities of three different reactor cores have been measured. Figure 4.5.3 shows the frequency response of the BSR-II stainless-steel-clad core, and Fig. 4.5.4 those of two BSR-I aluminum-clad cores. The measurements shown by the closed circles were made with a 5 × 5 element water-reflected core, and those by the open circles with the same core reflected on four faces with BeO. The latter core was homogeneously poisoned with B_4C so that the control rods were at the same position as in the water-reflected core.

The values of neutron lifetime divided by the delayed neutron effective fraction, l/β_{eff}, obtained from these measurements are given in Table 4.5.1 and show good agreement with measurements made by the pulsed-neutron technique.[5,6]

---

[4] Y. W. Lee, *Statistical Theory of Communication*, pp 278–87, Wiley, New York, 1960.

[5] E. G. Silver *et al.*, *Neutron Phys. Div. Ann. Progr. Rept. Sept. 1, 1959*, ORNL-2842, p 35.

[6] R-Perez-Belles *et al.*, *Neutron Phys. Div. Ann. Progr. Rept. Sept. 1, 1960*, ORNL-3016, p 12.

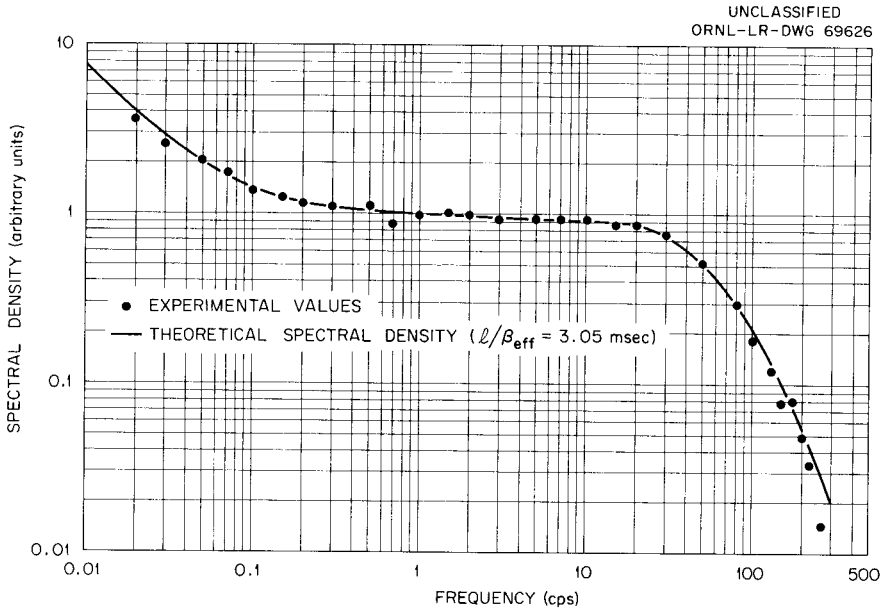

Fig. 4.5.3. Frequency Response of BSR-II Stainless-Steel-Clad Core.

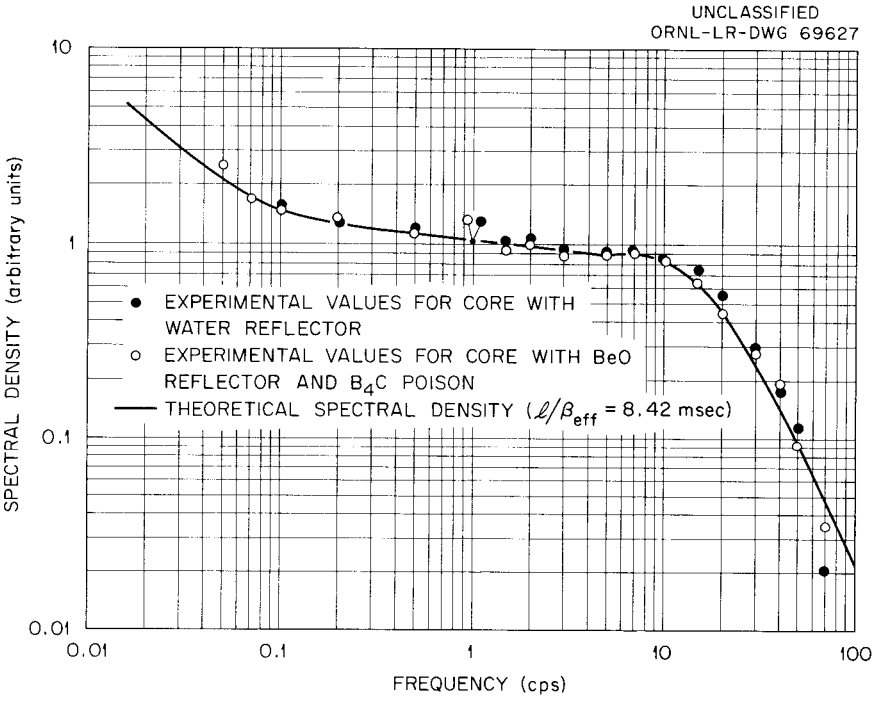

Fig. 4.5.4. Frequency Responses of Two BSR-I Aluminum-Clad Cores.

The standard deviations attributed to these measurements are too large to allow any conclusions to be drawn from the difference between the measurements on the water-reflected core and those on the BeO-reflected core. Nevertheless, this work indicates that the measurement of reactor spectral densities is

an adequate method for providing knowledge of some reactor kinetic parameters. It also shows that the instrumentation used to perform the measurements is simple and reliable and can be operated without difficulty at frequencies as low as 0.02 cps.

Table 4.5.1. Measurements of l/β_{eff} for Various Reactor Cores

Reactor	l/β_{eff} (msec)	
	This Experiment	Pulsed-Neutron Experiment
BSR-II	3.05 ± 0.10	3.2 ± 0.2[a]
BSR-I, 5 × 5, H_2O-reflected	7.93 ± 0.27	8.5 ± 0.3[b]
BSR-I, 5 × 5, BeO-reflected, B_4C-poisoned	8.42 ± 0.25	

[a] E. G. Silver *et al., Neutron Phys. Div. Ann. Progr. Rept. Sept. 1, 1959,* ORNL-2842, p 35.

[b] R. Perez-Belles *et al., Neutron Phys. Div. Ann. Progr. Rept. Sept. 1, 1960,* ORNL-3016, p 12.

5. Nuclear and Reactor Physics
Theoretical

5.1. ISOPERIMETRIC AND OTHER INEQUALITIES IN THE THEORY OF NEUTRON TRANSPORT, II[1]

Lawrence Dresner

In a previous paper[2] the author stated and proved 14 theorems concerning five quantities of interest that arise in the one-velocity theory of neutron transport. These quantities are all set-functions referring to bare, homogeneous, convex solids with *isotropic scattering*. The purpose of the present paper is to lift the restriction of isotropic scattering; accordingly the case of *linear anisotropy* is considered here.

Of the five quantities previously considered[2] only the first-collision probability P of neutrons from the persisting distribution, and the nonescape (absorption) probability P_a of neutrons from a uniform, isotropic source in the solid need be considered here. The other three, the first-collision probability P_c from a uniform, isotropic source, the buckling B^2, and P_{ad}, the diffusion-theoretic value of P_a, need not be considered here at all. This is true for the diffusion-theoretic quantities B^2 and P_{ad} because the *form* of diffusion theory does not change with a changing angular distribution of scattering, although the constants involved in the theory do. Thus, the theorems regarding B^2 and P_{ad} hold, with at most some alterations in the constants. That P_c is entirely independent of any anisotropy follows from the fact that the angular distribution of scattering cannot make itself felt until after the first scattering has occurred; the theorems of ref 2 regarding it hold without any changes at all.

The theorems proved[2] about P and P_a are of five distinct types: (1) the inclusion theorem, which compares values of P and P_a in two solids, one of which can be entirely inscribed in the other; (2) the *symmetrization theorem*, which compares values of P and P_a in two solids related by some process of symmetrization;[3] from this theorem isoperimetric theorems can easily be derived;[3] (3) the theorem related to the so-called "second fundamental theorem of reactor physics"[4] and arising from the convexity[5] of the Fourier transform of the infinite-medium transport kernel; (4) the factorization theorem, which compares, for example, the values of P for a considered solid with the product of the respective values for certain other solids whose orthogonal intersection is the considered solid; and (5) the theorem relating the values of P, P_a, and P_c for a given solid.

---

[1]Abstracted from ORNL-3229 (Feb. 9, 1962).

[2]L. Dresner, *J. Math. Phys.* **2**, 829 (1961).

[3]G. Pólya and G. Szegö, *Isoperimetric Inequalities in Mathematical Physics*, Princeton University Press, Princeton, 1951.

[4]A. M. Weinberg and E. P. Wigner, *The Physical Theory of Neutron Chain Reactors*, pp 397–406, University of Chicago Press, Chicago, 1958.

[5]G. H. Hardy, J. E. Littlewood, and G. Pólya, *Inequalities*, p 70 ff, Cambridge University Press, Cambridge, 1934.

All these theorems are proved[2] by using variational representations for P and P_a. These representations are of the maximum type, that is, the functional whose stationary value is P or P_a is always $\leq P$ or P_a, respectively. This latter property is ultimately a consequence of the isotropy of scattering assumed;[2] the most important direct effect of this assumption is to allow the ordinarily non-self-adjoint transport equation to be reduced to a self-adjoint form. This self-adjointness, combined with some other properties, is enough to prove the maximum property of the variational principles used.[2] The maximum property fails when the restriction of isotropy is lifted, and since it is a central feature in all the proofs,[2] its failure prevents the direct transcription of these proofs.

In this paper[1] two devices are used to circumvent the loss of the maximum property. The first of these depends on the extremum property of the variational principle against small variations in the trial functions and is essentially a form of perturbation theory. It runs as follows: When a physical property of the solid (volume, shape, degree of anisotropy of the scattering) changes by a small amount, the change induced in either P or P_a is independent to first order of the induced changes in the flux. This fact allows the derivation of formulas for the derivatives of P and P_a with respect to the physical parameters of the solid that do not involve the variation of the flux although they involve the flux itself. Frequently, it can be shown from these formulas that the derivatives of P and P_a with respect to certain properties of the solid have only one sign; from this fact an inequality can be immediately constructed. The second device involves the construction of an auxiliary problem that is self-adjoint and in which a quantity P' exists that is always $< P$ and that can be represented by a variational principle of the maximum type.

Using these two devices, it has been possible to prove some but not all of the types of theorems proved in ref 2. An inclusion theorem has been proved for P and P_a identical with that of ref 2. No symmetrization theorems have been proved nor has it been possible to prove an isoperimetric theorem (although it seems certain that both are true); all that has been shown is that P and P_a are stationary against small, volume-preserving deformations of a sphere. A theorem of the third type mentioned above (that related to the second fundamental theorem) which is analogous to that of ref 2 has been proved. No factorization theorem has been proved. None of the three relations given in ref 2 between P, P_a, and P_c have been proved; but one new type of theorem has been proved: one that compares the values of P (or P_a) corresponding to different degrees of anisotropy.

The theorems that were proved represent on the whole a less satisfying body of knowledge than their analogues in ref 2. Presently, the proof of the inequality related to the second fundamental theorem of reactor physics is marred by two restrictive but apparently superfluous conditions.

5.2. A REMARK ON THE SECOND FUNDAMENTAL THEOREM IN ONE-VELOCITY TRANSPORT THEORY

Lawrence Dresner

In the approximate calculation of the criticality of bare, homogeneous reactors the finite reactor is sometimes replaced by an infinite one of the same composition and the requirements are added that the angular flux satisfy the wave equation and the scalar flux vanish on the extrapolated boundary of the finite reactor. The resulting criticality problem can then be solved, and the criticality equation obtained

from it can be interpreted to mean that the nonescape probability P from the associated finite reactor is the Fourier transform of the *infinite-medium fission-to-absorption* kernel evaluated at the buckling of the infinite-medium flux.[1] This statement is the so-called "second fundamental theorem of reactor theory."[2]

Strictly speaking, the criticality equation obtained in this procedure is correct only in an infinite medium. The connection with the original finite reactor is made by noticing that the replacement of the finite reactor by an infinite reactor ought not to affect the flux deep in the interior significantly if the finite reactor is large enough and the infinite-medium solution is suitably chosen.

The accuracy of this method has been carefully analyzed in the past. Using bucklings deduced from the extrapolation distance obtained by solving the Milne problem, Inönü[3] and Dresner[4] were able to show that in one-velocity transport theory the second fundamental theorem yields results of surprising accuracy even for reactors with dimensions comparable to one mean free path.

In spite of this high accuracy, however, the use of the second fundamental theorem to estimate the criticality of finite reactors is equivocal because of the ambiguity present in the choice of buckling. Searching for a rigorous connection between the finite- and the infinite-medium problems in one-velocity transport theory with isotropic scattering, the author[5] was able to prove that if the buckling corresponded to zero extrapolation distance, then the second fundamental theorem *always* gave a lower limit, P_∞, to the nonescape probability.

The author's original proof of this fact was based on the integral equation formulation of transport theory. An attempt to generalize this proof to the case of linearly anisotropic scattering[6] met with only partial success, the desired result being proved essentially only for positive $\bar{\mu}$, the mean cosine of the scattering angle.[7] The present paper[8] supplies a complete proof of this inequality in the case of linearly anisotropic scattering for slabs, spheres, and infinite cylinders.

By a combination of techniques the author has shown that $P > P_\infty$ in the following cases: (1) for all convex shapes for isotropic scattering,[5] (2) for all convex shapes for linearly anisotropic scattering,[6] but with a restriction of $\bar{\mu}$ to certain positive values, and (3) for slabs, spheres, and infinite cylinders for linearly anisotropic scattering for all $\bar{\mu}$. It seems very reasonable on this basis to conjecture that $P > P_\infty$ for all convex solids and all orders of anisotropy.

---

[1] Subject to the assumption that the spatial neutron distributions before and after any process in an infinite medium (e.g., slowing down, thermal diffusion, etc.) are proportional and satisfy the wave equation, the Fourier transform of the infinite-medium kernel for this process represents the probability of nondisappearance of neutrons in this process. Since the interest in this paper is in the nonescape probability in critical one-velocity systems, the relevant process is survival from one generation to the next and the relevant kernel is the single-collision kernel (see ref 3). In many ways it is best to consider the procedure of this paper simply as the development of a rigorous connection between the solutions of finite-medium criticality problems and certain related infinite-medium ones and thus to avoid the sometimes confusing references to the second fundamental theorem.

[2] A. M. Weinberg and E. P. Wigner, *The Physical Theory of Neutron Chain Reactors*, pp 397–400, University of Chicago Press, Chicago, 1958.

[3] E. I. Inönü, *Nucl. Sci. Eng.* **5**, 248 (1959).

[4] L. Dresner, *Nucl. Sci. Eng.* **7**, 419 (1960).

[5] L. Dresner, *Nucl. Sci. Eng.* **9**, 151 (1961); *J. Math. Phys.* **2**, 829 (1961).

[6] L. Dresner, *Isoperimetric and Other Inequalities in the Theory of Neutron Transport, II*, ORNL-3229 (1962).

[7] In the case of anisotropy the infinite-medium kernel may be a matrix whose order depends on the order of anisotropy. In this case, P_∞ is the largest root of the secular determinant of its spatial Fourier transform.

[8] Soon to be published as ORNL-3330.

5.3. RESONANCE SELF-SHIELDING IN THE MEASUREMENT OF RADIATIVE CAPTURE CROSS SECTIONS[1]

Lawrence Dresner

A number of workers[2] have recently made measurements of average neutron capture cross sections in the kilovolt range of energies. These cross sections are local averages over high, sharp resonances. Because the samples used in the measurements are not always thin at the centers of the resonances, the measured average cross sections must be corrected for the effects of resonance self-shielding. The calculation of the resonance self-shielding correction for these experiments is very similar to the calculation of the resonance self-shielding factor in the problem of resonance absorption of neutrons in reactors. However, the two calculations differ in one important respect: in a reactor, the absorbing sample (e.g., a fuel rod) is assumed to be immersed in a uniform, isotropic flux of neutrons with a $1/E$ spectrum, whereas in the cross-section experiments the absorbing sample (e.g., a foil) is known to be exposed to a well-collimated, monoenergetic beam of neutrons. However, by only slightly altering the procedure in customary use for the reactor calculation, one can calculate self-shielding factors applicable to the cross-section experiments.

The conceptual arrangement considered is this: a foil of material of mass number A whose off-resonance transmission is of the order of 95% is exposed to a well-collimated beam of neutrons with a fairly well-defined energy E. The neutron interaction cross section of the material consists of two parts, an energy independent potential scattering cross section of the order of 10 barns and a series of high, sharp Breit-Wigner resonances in the scattering and absorption cross sections. The average spacing of these resonances in energy is D. The energy spread, Δ, of the incident beam is $\ll E$ but $\gg D$; E lies in the range 5 to 50 kev.

The goal of the calculation is C, the self-shielding correction, which is defined as the ratio of the average absorption per atom in the foil to the average absorption per atom in an infinitely thin foil exposed to the same flux. C can be written as the sum of two parts, $C^{(1)}$ and $C^{(2)}$, where $C^{(1)}$ refers to the absorption of uncollided neutrons and can be written as below, and $C^{(2)}$ refers to the absorption of already collided neutrons:

$$C^{(1)}(\alpha,\beta,\theta)=\frac{2}{\pi\alpha}\int_0^\infty \frac{\Psi(\theta,x)}{\Psi(\theta,x)+\beta}\left(1-\exp\{-\alpha[\Psi(\theta,x)+\beta]\}\right), \tag{1}$$

where

$\alpha = 2aN\sigma_0$,

$2a$ = foil thickness,

N = atomic density of absorbing atoms,

---

[1] The paper on which this summary is based has been accepted for publication in *Nuclear Instruments and Methods*.

[2] An extensive bibliography may be found in the paper of J. H. Gibbons *et al.*, *Phys. Rev.* **122**, 182 (1961); see also J. L. Fowler and J. B. Marion (eds.), *Fast-Neutron Physics*, Vol. II, Chap. 5, Interscience, New York (in press).

$\beta = \sigma_p/\sigma_0$,

σ_0 = peak total cross section at exact resonance,

σ_p = energy-independent potential scattering cross section per absorbing atom,

$\theta = \Gamma/(4E_0\, kT/A)^{1/2}$,

Γ = natural width of the resonance,

E_0 = resonance energy,

k = Boltzmann's constant,

T = absolute temperature,

$$\Psi \equiv \Psi(\theta,x) = \frac{\theta}{2\sqrt{\pi}} \int_{-\infty}^{+\infty} \frac{\exp\left[-\frac{\theta^2}{4}(x-y)^2\right]}{1+y^2}\, dy\,. \tag{2}$$

In the case of no Doppler broadening, that is, $\theta = \infty$ and $\Psi = (1 + x^2)^{-1}$, $C^{(1)}$ can be calculated either from an asymptotic expression (for large α) or from a power series (for small α). When $\theta \neq \infty$, explicit evaluation of $C^{(1)}$ is difficult. In the presence of Doppler broadening explicit evaluation of $C^{(1)}$ is difficult, but several functions, in terms of which it may be estimated, are known. These functions are

1. $J(\theta,\beta) = \int_0^\infty \Psi(\theta,x)\,[\Psi(\theta,x) + \beta\,]^{-1}\, dx$, which has been studied and tabulated by Dresner[3] and by Nather and Nordheim,[4]
2. $C^{(1)}(\alpha, 0, \theta)$, which has been given in graphical form by Melkonian *et al.*,[5]
3. $\Psi_n(\theta) = \int_{-\infty}^{+\infty} \Psi^n(\theta,x)\, dx$, which have been mentioned by Gurevich and Pomeranchouk[6] and discussed and tabulated by Cook and Elliott[7] and by Keane and McKay,[8]
4. $C^{(1)}(\alpha, \beta, \infty)$, which can be explicitly calculated as mentioned above.

In the paper on which this summary is based a variety of inequalities relating $C^{(1)}$ to these functions have been derived. In Fig. 5.3.1 estimates of $C^{(1)}(\alpha,\beta,\infty)$ based on these inequalities are shown for cases in which $\alpha\beta = 0.05$ (corresponding to about 95% off-resonance transmission). The true value must always lie in the cross-hatched area, which is bounded at each abscissa by the lowest of the upper limits and the highest of the lower limits. In Fig. 5.3.2 corresponding estimates of $C^{(1)}(\alpha,\beta, 0.1)$ for $\alpha\beta = 0.05$ are

---

[3] L. Dresner, *Resonance Absorption in Nuclear Reactors*, pp 37–44, Pergamon, New York, 1960.

[4] V. W. Nather and L. W. Nordheim, *Extended Tables for the Computation of the Volume Term of the Resonance Integral*, GA-2460 (Aug. 30, 1961).

[5] E. Melkonian, W. W. Havens, Jr., and L. W. Rainwater, *Phys. Rev.* **92**, 702 (1953).

[6] I. I. Gurevich and I. Y. Pomeranchouk, *Proc. Intern. Conf. Peaceful Uses Atomic Energy, Geneva, 1955* **5**, 466 (1956).

[7] J. L. Cook and D. Elliott, *Australian J. Appl. Sci.* **11**, 16 (1960).

[8] A. Keane and M. H. McKay, *Australian J. Appl. Sci.* **11**, 321 (1960).

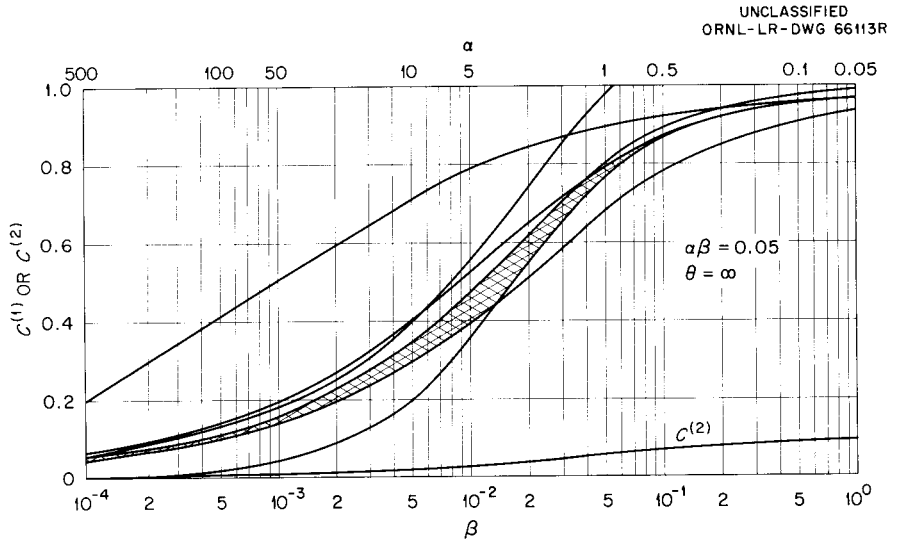

Fig. 5.3.1. Resonance Self-Shielding Corrections for Uncollided $[C^{(1)}]$ and Collided $[C^{(2)}]$ Neutrons as a Function of α or β for $\theta = \infty$.

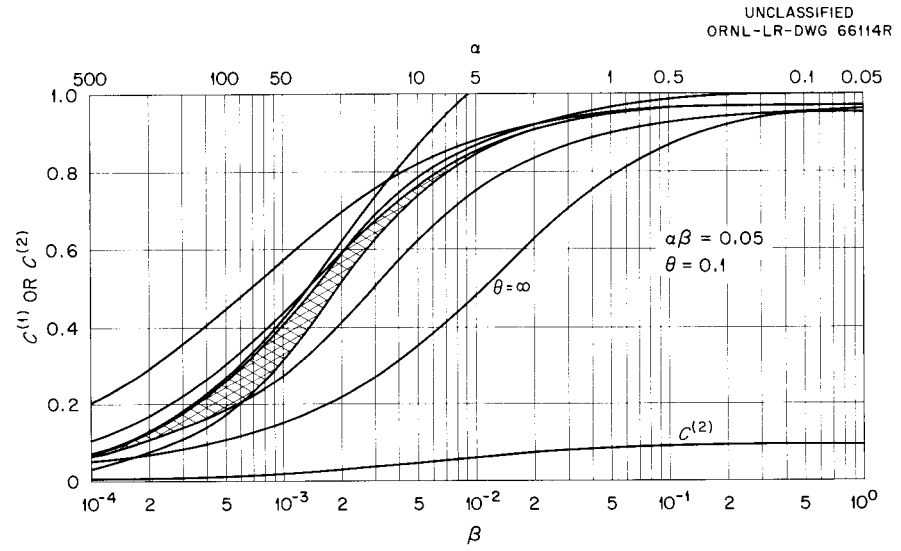

Fig. 5.3.2. Resonance Self-Shielding Corrections for Uncollided $[C^{(1)}]$ and Collided $[C^{(2)}]$ Neutrons as a Function of α or β for $\theta = 0.1$.

shown. Also shown in Fig. 5.3.2 for comparison is the curve of $C^{(1)}(\alpha,\beta,\infty)$. It lies well under the band in which $C^{(1)}(\alpha,\beta,0.1)$ must be, showing that the Doppler effect can produce a large effect on the resonance self-shielding correction.

Values of $C^{(2)}$ calculated by a variational technique are included in both figures. In both cases $C^{(2)}$ is about 10% for the largest β and much smaller for smaller β. In both cases the ratio of $C^{(2)}$ to $C^{(1)}$ is always in the neighborhood of 10%.

In the original paper[1] the effect of fluctuations in the neutron widths is also considered.

5.4. AN EXTENSION OF O5R MONTE CARLO CALCULATIONS TO THE THERMAL-NEUTRON RANGE

G. R. Dalton[1] and R. R. Coveyou

The O5R code[2] has been extended to include a more elaborate treatment of the thermal-neutron range than afforded by the simple one-speed treatment currently available. The new thermal part of the O5R code takes into account the thermal motion of the struck nuclei, the anisotropic angular distribution of scattered neutrons after scatter, the variation of the temperature of the medium from region to region, and the dependence of reaction rates and collision probabilities on the magnitude of the neutron (vector) velocity minus the nucleus (vector) velocity.

A separate computer code was written for converting the raw zero-temperature cross-section data to the cross sections at the temperatures and densities needed by the problem. The code then prepares a set of probability tables, which give the probability of scatter, of fission, etc., over a wide range of neutron speeds for each of the isotopes in the various regions needed by the problem. This probability table is then available to the O5R code on magnetic tape for use in processing thermal neutrons.

The O5R code processes neutrons in much the same manner as before. It follows each step in the history of a neutron as it slows down from the source energy. The neutron speed, direction of travel, location of last collision, etc., are written on magnetic tape as usual. However, with the new addition to O5R, whenever neutrons pass a specifiable cutoff energy (say, 32 times kT), the target nuclei are not assumed to be at rest but rather are assumed to have velocities of a Maxwell-Boltzmann distribution. The Maxwell-Boltzmann distribution used will depend on the type of nuclei struck and the temperature of the medium in which the collision occurs. After a neutron has once crossed the boundary into the thermal range, it may scatter up or down, depending on the nuclei it strikes. If the neutron crosses this thermal cutoff going back up the energy scale, it is still considered a thermal neutron and is given the full thermal treatment for the remainder of its history.

The code has the limitations that it cannot treat nonisotropic media such as large crystals, nor can it take into account rotational or vibrational states of a nucleus bound in a molecule or in a crystal lattice.

The code is being used to calculate some infinite media spectra and some spatial distributions from point thermal sources in order to check the numerical procedures used.

---

[1]Research participant, University of Florida, Gainesville.

[2]R. R. Coveyou, J. G. Sullivan, and H. P. Carter, *Neutron Phys. Div. Ann. Progr. Rept. Sept. 1, 1958*, ORNL-2609, p 87.

5.5. EXCITATION OF TWO PHONON STATES BY INELASTIC α-PARTICLE SCATTERING

B. Buck

The Blair phase rule[1,2] for the inelastic scattering of strongly absorbed particles states that the angular distributions corresponding to even values of the angular-momentum transfer L are out of phase with those corresponding to odd-L transfer. Furthermore, the elastic scattering angular distributions should be in phase with the odd-L transfer angular distributions. The conditions for the validity of the phase rule should be adequately fulfilled by 40-Mev (α,α') reactions exciting low-lying collective levels of even-even nuclei. The rule has been extensively verified for the excitation of the lowest 2^+ and 3^- collective states.

Recent experiments[3,4] have shown that the rule is not obeyed by the inelastic angular distributions of 43-Mev α-particles exciting known 4^+ states of nuclei in the nickel region. The experimental distributions for the 4^+ levels are found to be almost exactly out of phase with the 2^+ distributions.

Calculations have been performed which indicate that the anomaly arises as an interference effect between two possible mechanisms for exciting the first 4^+ state, i.e., a direct transition and a multiple transition. This conclusion is contrary to previous interpretations based on plane-wave-perturbation calculations. The calculations are discussed elsewhere.[5]

---

[1] J. S. Blair, *Phys. Rev.* 115, 928 (1959).

[2] E. Rost and N. Austern, *Phys. Rev.* 120, 1375 (1960).

[3] H. Broek, J. L. Yntema, and B. Zeidman, to be published.

[4] R. Beurtey, *Comp. Rend.* 252, 1756 (1961).

[5] Abstracted from paper submitted for publication in *Physical Review.*

5.6 EFFECT OF NUCLEAR COLLECTIVE MOTIONS ON S- AND P-WAVE STRENGTH FUNCTIONS[1]

B. Buck and F. Perey

In recent years much experimental effort has been devoted to the measurement of the S- and P-wave strength functions. These functions can be related to average transmission coefficients derived from the nuclear optical model. However, some details of the experimental data were not completely explained by the theoretical mechanisms previously proposed.

In the present calculation, we have noted that many even-even nuclei, while not permanently deformed, are easily set into quadrupole vibration. Since the strong permanent distortions of the rare-earth nuclei

---

[1] Summarized from *Phys. Rev. Letters* 8 (11), 444 (1962).

have satisfactorily been used to explain certain effects observed in the experimental data, it is not unreasonable to expect that dynamical distortions may have effects similar to those of the permanent distortions.

We have employed essentially the methods of Chase, Wilets, and Edmonds[2] to calculate the S– and P–wave strength functions for a large number of even-even nuclei. The axially symmetric rotator model of Bohr was used for the permanently deformed nuclei, and the pure quadrupole vibration model of Bohr for the dynamically deformable nuclei. The interaction of a neutron with a diffuse-edged collective nucleus was described by an expansion of the neutron-neutron optical potential in powers of the collective coordinates. Terms to first order only were retained. Calculations were performed for an incident neutron energy of 40 kev.

The agreement between the calculation results and experiment is markedly improved over the predictions of the spherical optical model with normal spin-orbit coupling. A discrepancy still exists, however, in the S–wave results in the neighborhood of $A \approx 100$. A similar discrepancy appears in the P–wave results between the $3p$ and $4p$ resonances. This may indicate that S– and P–wave neutrons different optical absorption potentials in some mass regions.

---

[2]D. M. Chase, L. Wilets, and A. R. Edmonds, *Phys. Rev.* **110**, 1080 (1958).

5.7. THE CALCULATION OF ELASTIC AND INELASTIC PROTON SCATTERING WITH A GENERALIZED OPTICAL MODEL[1]

B. Buck

The optical model for the elastic scattering of neutrons by complex nuclei has proved very successful in the last few years. As more and better experimental data have become available, it has been possible to find good average parameters which enable the accurate calculation of the expected elastic scattering for a wide range of nuclei. A generalization of the optical model has now been developed which makes possible the simultaneous calculation of the elastic scattering of nucleons and the inelastic scattering to low-lying excited states of the target nucleus.

The methods used in the calculation are, in principle, very similar to those of Chase *et al.*,[2] but the formalism is extended to include the consideration of charged incident particles, spin-orbit effects, and easy specialization to rotational, vibrational, or single-particle excitation models. The basis for the development is the Schroedinger equation for the system consisting of an incident nucleon and a target nucleus, and the calculation is carried out in the center-of-mass coordinate system, so that only reduced masses and relative energies and momenta appear in the equations.

---

[1]This is an extremely brief summary of a paper to be submitted to *Phys. Rev.*

[2]D. M. Chase, L. Wilets, and A. R. Edmonds, *Phys. Rev.* **110**, 1080 (1958).

The entire calculation was coded for the IBM-7090. For incident protons the code gives the total absorption cross section, the total inelastic 2^+ cross section, the elastic and inelastic differential cross sections, and the corresponding polarizations. For incident neutrons the total nuclear and total elastic cross sections are also given.

In the complete report from which this brief summary is taken, a large number of comparisons between the results of the calculation and experimental data appear in graphical form. In general, the elastic angular distributions are fitted remarkably well. The inelastic differential cross sections are fitted reasonably well in all cases, and sometimes very well.

The results of the calculations can be used to justify the validity of the simple collective model treatment. The values of the nuclear distortion parameters obtained in this work are, in general, consistent with those obtained by electromagnetic methods, that is, by Coulomb excitation and lifetime measurements.

It has been noted that great care must be exercised in the interpretation of experimental data and theoretical results for cases where the incident proton energy is less than about 5 Mev above the nuclear (p,n) threshold energy. In such a case, if a compound nucleus is formed, one of the main channels for compound nuclear decay (that is, neutron emission) is greatly inhibited, and compound elastic and inelastic proton reactions cannot be ignored. This situation has been fairly well demonstrated in comparisons of theory with experiment for Cr, Ni, and Zn at $E \approx 10$ Mev.

Further progress in extending the calculation and in clearing up various ambiguities existing in it rests upon the availability of additional proton experimental data. It may be concluded, however, that the generalized optical model appears to be a useful way of correlating experimental data and studying nuclear collective states.

5.8. OPTICAL MODEL ANALYSIS OF PROTON ELASTIC SCATTERING IN THE RANGE OF 9 TO 22 Mev

F. G. Perey

An analysis of 35 proton elastic scattering angular distributions in the range of 9 to 22 Mev covering elements from aluminum to gold has been made to find an optical potential which would exhibit only smooth variations as a function of mass number and incident proton energy. The real well is of the Saxon type and the imaginary well of the surface type (derivative of a Saxon form).

In order to limit the number of variables, the geometrical parameters of the wells were kept fixed at the same value for all elements and at all energies, and only the well depths were allowed to vary to obtain a best fit to the data.

The spin-orbit potential of the Thomas form is found to decrease slightly in going from 9 to 22 Mev. The real well depth at a given incident proton energy increases as a function of mass number. This

variation is attributed to a coulomb energy effect (the well depth increases because, as the coulomb energy increases, the momentum inside the well decreases) and a symmetry energy effect (the potential depth is isotopic spin dependent and therefore increases as a function of neutron excess in the nucleus).

The real well depth is found to decrease smoothly as a function of energy for each element, and fluctuations in the energy variation from element to element are correlated to the strength of the excitation of the collective states in the different nuclei. If only a surface imaginary well is used, the well depth is found to increase as a function of mass number, with fluctuations correlated to the strength of the excitation of the collective state (as measured by coulomb excitation), and for a given element decrease as a function of energy. At 17 and 22 Mev the fits to the data are improved at angles greater than 140° if a small amount of volume imaginary potential is added. More volume imaginary potential is required at 22 Mev than at 17 Mev. The elastic scattering polarizations and the total reaction cross sections obtained are in general agreement with the experimental data.

5.9. OPTICAL MODEL ANALYSIS OF DEUTERON SCATTERING IN THE RANGE OF 10 TO 27 Mev

C. M. Perey[1] and F. G. Perey

An analysis of 30 deuteron elastic scattering angular distributions in the range of 10 to 27 Mev covering elements from magnesium to gold has been made to find an optical potential which would exhibit only smooth variations as a function of mass number and incident deuteron energy. The optical model considered has a real well of the Saxon form and a surface peaked imaginary potential; no spin-orbit coupling is included. It is found that such a potential can be found for a large domain of real well radii, but that the diffuseness of the real well remains constant for all the different radii. The radius of the imaginary well is found to be well determined. It is also found that for each set of geometrical parameters two real well depths in the ratio of about 1.6 will give equally good fits to the data.

[1]Consultant.

5.10. CORRESPONDENCE BETWEEN NONLOCAL AND LOCAL OPTICAL POTENTIALS

F. G. Perey

A study has been made of the relationship between the nonlocal potential[1] and the equivalent local potential (i.e., giving on a particular element at a given energy the same asymptotic wave function). It was found that for neutrons below 25 Mev it is always possible to reproduce the nonlocal scattering matrix

[1]F. Perey and B. Buck, *Nuclear Phys.* **32**, 353 (1962).

by an energy-dependent local potential. (No "specifically nonlocal" effects were found in the value or the distribution of the scattering matrix elements.) Although the wave functions for the nonlocal and the local equivalent potentials are asymptotically the same, owing to a property of the integral operator in the nonlocal potential the wave functions for the nonlocal case are reduced by about 15% in the region of the potential. An understanding has been achieved of the reason for the validity of the local W.K.B. approximation to the nonlocal potential.

6. Reactor Shielding

6.1. THE RADIATION LEAKAGE SURVEY OF THE SHIELD OF THE NUCLEAR SHIP "SAVANNAH"[1]

E. P. Blizard, T. V. Blosser, and R. M. Freestone, Jr.

A detailed survey of the radiation from the NS "Savannah" shield was made during the period May 20 through May 25, 1962. The study was accomplished with the reactor at its full power of 69 Mw during a cruise of 2821 miles in the Atlantic Ocean, out of Yorktown, Virginia. The data were obtained with the ORNL Mobile Radiation Shielding Laboratory No. 1, which was designed and built especially for this survey.

The results of the detailed shield survey show that the design dose rate of 0.5 rem/yr for passenger spaces is not exceeded in any region to which passengers have access. In the areas restricted to crew access, the design dose rate of 5.0 rem/yr is not exceeded except in a small region on "D" deck, in a room to which entry can readily be controlled. Specifications for cargo-hold dose rates, 0.5 rem/yr at one-fifth full power, are satisfactorily met.

Additional data obtained include measurements of special points for comparison with dose rates predicted in design calculations and an experiment examining the result of loss of water from the ship's subreactor shield tank. Predicted dose rates were conservatively higher than the dose rates measured, and the result of the water-loss experiment showed that even when the tanks are totally empty, a safe condition exists only a few feet from the shield.

[1]Abstracted from ORNL-3336 (Aug. 15, 1962).

6.2. A STUDY OF THE SHIELD OF THE UNIVERSITY OF ILLINOIS TRIGA MARK II RESEARCH REACTOR[1]

T. V. Blosser, R. M. Freestone, Jr., and J. M. Miller

Detailed measurements have been made of the fast-neutron and gamma-ray dose rates and the thermal-neutron fluxes existing at the surfaces of the biological shield of the University of Illinois TRIGA Mark II Research Reactor. Dose rates and fluxes were found to be extremely low. A comparison was made by

[1]Abstracted from ORNL-TM-178 (Apr. 23, 1962).

means of threshold foil techniques between the fast-neutron flux in a beam hole of the reactor during steady-state operation at 1 kw and during a nominal 250-Mw, 30-msec pulse produced by rapid insertion of ~$2 of excess reactivity. The flux over the duration of the pulse was approximately four times that for steady-state operation for 1 hr at 1 kw. Fast-neutron dose rates and thermal-neutron fluxes were measured at each of the four beam ports of the reactor at operating powers of 0, 1, and 5 w. Some gamma-ray dose-rate data were also obtained at 0 and 1 w. An appendix in the report briefly describes the threshold foil technique used.

6.3. A STUDY OF THE SHIELD OF THE VIRGINIA POLYTECHNIC INSTITUTE UTR-10 REACTOR[1]

T. V. Blosser and R. M. Freestone, Jr.

A study of the radiation leakage from the shield of the Virginia Polytechnic Institute UTR-10 nuclear reactor was completed in February 1962. Fast-neutron, thermal-neutron, and gamma-ray dosimeters of high sensitivity were employed to obtain a detailed network of data over all surfaces of the shield. In supplementary experiments the gamma-ray dose rates in a corridor and in a classroom adjoining the reactor room were evaluated and a rough value of argon dispersal through the reactor room ventilating system was determined.

The results of the detailed survey showed generally satisfactory performance of the shield for fast- and thermal-neutron radiations, but a number of regions were identified in which the gamma-ray dose rate was higher than that predicted by the shield design.

[1]Abstracted from ORNL-TM-290 (in press).

6.4. A RADIATION STUDY OF THE WESTINGHOUSE TESTING REACTOR[1]

T. V. Blosser and R. M. Freestone, Jr.

Gamma-ray, fast-neutron, and thermal-neutron dose-rate measurements were made, with instruments of high sensitivity, over a major portion of the biological shield of the Westinghouse Testing Reactor (WTR) at Waltz Mill, Pennsylvania. Observed rates were well below the 1 mr/hr predicted for the shield for a reactor power of 60 Mw. Selected regions of the area within the WTR security fence were examined to determine radiation levels due to gamma-ray shine from the elevated primary coolant tank. Dose rates ranging from 0.08 to 10 mr/hr were observed. The existence of a considerable fast-neutron flux in the reactor coolant exit stream at distances as great as ~245 ft from the core was established, but the source for these neutrons was not definitely determined.

[1]Abstracted from ORNL-TM-332 (1962).

6.5. A SYSTEM FOR GENERATING GAMMA-RAY CROSS-SECTION DATA FOR USE WITH THE IBM-7090 COMPUTER

S. K. Penny, M. B. Emmett,[1] and D. K. Trubey

A system for generating detailed tables of gamma-ray cross-section data for any mixture of elements, as well as providing a means of rapid access to these data, has been devised for use on the IBM-7090 computer. The system, which was primarily designed for use in various Monte Carlo codes but can be easily used with other codes, consists of a master magnetic tape containing a limited amount of cross-section data, a code to update and edit the master tape, and a package of subroutines to generate detailed tables by using the data on the master tape.

The detailed table that is constructed may contain several media (several mixtures). Within each medium table there are subtables corresponding to total cross sections, the ratios of the scattering cross section to the total cross section, and, optionally, the ratios of the pair-production cross section to the total cross section. Each subtable is constructed on the basis of the gamma-ray energy being in electron rest mass units. The subtables contain energy groups that are bounded by energies which are exactly powers of two. Within each of these groups the energy is evenly spaced and the number of intervals is also exactly a power of two. This construction of the tables is to provide for the more rapid variation of the cross sections at lower energies as well as to provide a means of rapid access to any number in the table, given a gamma-ray energy.

The master tape contains photoelectric and pair-production cross sections which are listed in standard compilations.[2-4] It also contains the atomic number and the atomic density (atoms/g $\times 10^{-24}$) for each element. The photoelectric-absorption edges are handled by listing two energies which are quite closely spaced.

The detailed table is constructed by using the absorption data from the master tape and a subroutine which computes the Compton scattering cross section. For each element a table of the total cross section corresponding to energies on the master tape is formed. For each energy in the detailed table, a total cross section and/or a pair-production cross section is obtained by log-log interpolation (or extrapolation only when necessary) in the data tables from the master tape. These cross sections, as well as scattering cross sections, are then accumulated element by element in the detailed table.

The use of the system is described elsewhere.[5]

---

[1]Mathematics Panel.

[2]G. W. Grodstein, *X-Ray Attenuation Coefficients from 10 kev to 100 kev,* NBS Circular 583 (1957).

[3]R. I. McGinnies, *X-Ray Attenuation Coefficients from 10 kev to 100 kev,* Supplement to NBS Circular 583 (1959).

[4]Ellery Storm *et al., Gamma Ray Absorption Coefficients for Elements 1 through 100 Derived from the Theoretical Values of the National Bureau of Standards,* LA-2237 (1958).

[5]S. K. Penny, M. B. Emmett, and D. K. Trubey, *A System for Generating Gamma-Ray Cross-Section Data for Use with the IBM-7090 Computer,* ORNL TM-234 (1962).

6.6. OGRE – A MONTE CARLO SYSTEM FOR THE CALCULATION OF GAMMA-RAY TRANSPORT

S. K. Penny, D. K. Trubey, and M. B. Emmett[1]

OGRE is a Monte Carlo code system for the IBM-7090 computer which is used for calculations of gamma-ray transport. The system is a skeleton program consisting of a number of subroutines that provide the basic framework or structure repeated in every Monte Carlo code dealing with gamma-ray transport. The advantage of such a program is that most types of gamma-ray codes can be "manufactured" by writing a few special subroutines, such as routines describing the source and the geometry.

The system provides a cross-section generation package (see Sec. 6.5), which eliminates large quantities of input data, and packages for generating photon collisions in a straight analog fashion; however, it is not restricted to the use of these particular subroutine packages. For instance, one could write a collision generation package in a straight-forward manner which incorporates an importance sampling scheme. Other modifications can be similarly incorporated.

Adaptations of the system to the calculation of gamma-ray dose rates and heating are given in Secs. 6.7–6.9 below.

[1]Mathematics Panel.

6.7. OGRE-P1 – A MONTE CARLO PROGRAM FOR COMPUTING GAMMA-RAY TRANSMISSION THROUGH LAMINATED SLABS (MONOENERGETIC SOURCE)

D. K. Trubey, S. K. Penny, and M. B. Emmett[1]

A Monte Carlo program, OGRE-P1, has been written within the framework of the OGRE system (see Sec. 6.5) for the IBM-7090 computer to solve the problem of the transmission of monoenergetic gamma rays through laminated slabs of various materials. Special routines used by OGRE-P1 to solve the plane problem include a source routine, a geometry routine, a routine for computing the estimator, and input and output routines.

The source is an infinite plane of monoenergetic gamma rays located on the face of the laminated slab. It may be either monodirectional, isotropic in the half sphere, or cosine distributed about the normal. The number of homogeneous slabs (regions) is limited to 50. Descriptions of the media are given on input cards listing the densities of each element in each medium, the region thicknesses, and medium numbers.

A list of flux-to-dose conversion factors, used to generate a statistical estimation dose rate at the "rear" of the slab, is also required. The standard deviation of the mean "collided" dose rate is computed. For the monodirectional case, the uncollided dose rate is computed analytically by using $\exp(-T/\gamma)$, where T

---

[1]Mathematics Panel.

is the thickness in mean free paths and γ is the cosine of the angle (measured from the normal), multiplied by the flux-to-dose conversion factor at the incident gamma-ray energy. For the isotropic and cosine cases, $E_1(T)$ and $E_2(T)$ are multiplied by the conversion factor. Thus the dose rate is normalized per unit incident photon current.

The basic cross-section data for each element in the problem must be available on a tape (see Sec. 6.5). A routine in OGRE-P1 reads this tape and generates the detailed cross sections needed (total and ratio of scattering to total) for each medium covering the range of energy required. The energy limits are input numbers and must overlap or coincide with the range bounded by the initial energy and cutoff energy. This detailed cross-section table will be written on another tape. For subsequent runs of the same media-array and energy range, only the latter tape need be used.

The histories are reduced in weight at each collision to account for absorption. They are terminated either by leakage or by failing the energy cutoff or weight cutoff tests. In the case of the weight cutoff, a game of Russian Roulette is played. The number of photons which were terminated by each mechanism is printed out.

A summary of the input to the OGRE-P1 program is given elsewhere.[2]

---

[2]D. K. Trubey, S. K. Penny, and M. B. Emmett, *OGRE-P1, A Monte Carlo Program for Computing Gamma-Ray Transmission Through Laminated Slabs,* ORNL TM-167 (Revised) (1962).

6.8. OGRE-P2 – A MONTE CARLO PROGRAM FOR COMPUTING GAMMA-RAY LEAKAGE FROM LAMINATED SLABS CONTAINING DISTRIBUTED SOURCES

D. K. Trubey, S. K. Penny, and M. B. Emmett[1]

A Monte Carlo program, OGRE-P2, has been written within the framework of the OGRE system (see Sec. 6.6) for the IBM-7090 computer to solve the problem of gamma-ray leakage from a slab of laminated regions of various materials containing distributed sources. The program is essentially the same as the code OGRE-P1 (see Sec. 6.7) except for slightly different input, a new source routine (with slave subroutines), a special routine for computing the uncollided dose rate semianalytically, and a special program for preparing data for the source routine.

The source is distributed in energy between a minimum, E_{min}, and a maximum, E_{max}. In addition to a continuous energy spectrum, an array of monoenergetic sources may also be included. The source is isotropic in direction of emission and is distributed in space throughout the slab in an arbitrary fashion. Thus a source distribution, $S(z, E)$, must be supplied, giving the magnitude of the source at the energy E and at the distance z from a given slab face. The dose rate is computed at the opposite slab face.

The procedure for choosing from the source energy and spatial distributions is as follows. The source data for a continuous energy spectrum and/or a group of delta functions in energy may be supplied to the

---

[1]Mathematics Panel.

preparation program on either cards or tape. The problem is simplified in that, over arbitrary spatial intervals, the source will be assumed to be constant. In these intervals, the energies will be picked from a cumulative energy distribution averaged over the interval. To conserve storage space, only one of these distributions will be in memory at one time.

To provide these and other data to the main OGRE-P2 code, the preparation code proceeds as follows: It first reads in the source data, $S(z, E)$, photons $\text{sec}^{-1}\ \text{cm}^{-3}\ \text{Mev}^{-1}$, and $S_j(z)$, photons $\text{sec}^{-1}\ \text{cm}^{-3}$; the monoenergetic sources of energy E_j; and the boundaries of the intervals in which the spatial distribution will be taken to be constant. The final z value read in determines the spatial extent of the source, regardless of the z values associated with $S(z, E)$. The values of interval thicknesses and of E_j are written on tape followed by the values of

$$SV_i(E) = \int_{z_i}^{z_{i+1}} S(z, E)\, dz\ ,$$

where the z_i's are interval boundaries for use by the subroutine ATTEN to be described below. The cumulative distribution function for each interval and the total source are then produced:

$$C_i(E') = \frac{\int_{E_{\min}}^{E'} \int_{z_i}^{z_{i+1}} S(z, E)\, dz\, dE}{\int_{E_{\min}}^{E_{\max}} \int_{z_i}^{z_{i+1}} S(z, E)\, dz\, dE}\ ;$$

$$\text{TOTAL} = \int_{E_{\min}}^{E_{\max}} \int_0^{z_{\max}} S(z, E)\, dz\, dE + \sum_j \int_0^{z_{\max}} S_j(z)\, dz\ .$$

The fractions

$$\text{FRACØN}(i) = \frac{\int_{E_{\min}}^{E_{\max}} \int_{z_i}^{z_{i+1}} S(z, E)\, dz\, dE}{\text{TOTAL}}$$

and

$$\text{FRADEL}(i, j) = \frac{\int_{z_i}^{z_{i+1}} S_j(z)\, dz}{\text{TOTAL}}$$

and a table of $C_i(E')$ and E' values are then written on tape for each interval for use by the source routine. The above integrals are performed by using Simpson's rule with an arbitrary number of points and either linear or exponential interpolation between values of $S(z, E)$.

The source routine uses the above fractions and table to determine how many histories to initiate in each interval and to choose the initial energy for each history. If the energy for a history is to be picked from

the continuous distribution, a value of E' is then taken at random from a table of 1000 values uniformly spaced in $C(E')$. The initial space points are picked uniformly in the interval.

In order to select a direction, a method of importance sampling is used since photons started in a backward direction have a small probability of escaping in the forward direction. This is especially true if the distance to the face of the slab, where the dose rate is computed, is large. Consequently, the direction cosine, γ, is picked from the sum of isotropic and $\cos^n$ distributions. This distribution is

$$f(\gamma) = \frac{A}{2} + (1 - A)(n + 1)\gamma^n H(\gamma) ,$$

where

$H(\gamma) = 1$ for $\gamma > 0$,

$H(\gamma) = 0$ for $\gamma \leqq 0$,

A = fraction of histories in isotropic distribution.

To take into account distance from the "detector," the value of A is set equal to $\exp(-\alpha x)$, where x is the distance in mean free paths and α is an input parameter. The value of A is used to pick randomly from either distribution. The weight of the photon is

$$W = \frac{1/2}{(A/2) + (1 - A)(n + 1)\gamma^n H(\gamma)} .$$

The procedure for choosing from the $\cos^n$ distribution is to select the largest of $n + 1$ random numbers. The value of n is an input number and may be 0.

The uncollided dose rate is computed in the subroutine ATTEN. The uncollided flux from the continuous spectrum may be written

$$\phi_c = \int_{E_{min}}^{E_{max}} \int_0^{z_{max}} S(z, E) \frac{E_1[x(E)]}{2} dz\, dE ,$$

where

$x(E) = \mu(E)(T - z)$,

T = thickness of slab,

$\mu(E)$ = total linear absorption coefficient;

or since the source is assumed constant over an interval,

$$\phi_c = \int_{E_{min}}^{E_{max}} dE \sum_i \frac{SV_i(E)}{2(z_{i+1} - z_i)} \int_{z_i}^{z_{i+1}} E_1(x)\, dz$$

$$= \int_{E_{min}}^{E_{max}} \frac{dE}{\mu(E)} \sum_i \frac{SV_i(E)}{2(z_{i+1} - z_i)} \left[E_2(x) \Big|_{z_{i+1}} - E_2(x) \Big|_{z_i} \right] .$$

In like manner, the flux from the monoenergetic sources may be written

$$\phi_d = \text{TOTAL} \sum_i \sum_j \frac{\text{FRADEL}(i,j)}{2\mu(E_j)(z_{i+1} - z_i)} \left[E_2(x)\big|_{z_{i+1}} - E_2(x)\big|_{z_i} \right] ,$$

where x is a function of energy E_j.

Since dose rate, and not flux, is desired, a flux-to-dose conversion factor is included in the integrand and divided by TOTAL to yield the uncollided dose rate independent of the number of histories. Thus, the Monte Carlo result must be multiplied by TOTAL to yield the dose rate (in rads/hr) with the given sources $S(z, E)$ and $S_j(z)$. If the units of source are integrated over time, the result must be divided by 3600 to yield the dose in rads.

6.9. MONTE CARLO CODE FOR CALCULATION OF ENERGY DEPOSITION BY GAMMA RAYS IN A LAMINATED INFINITE SLAB

S. K. Penny, D. K. Trubey, and M. B. Emmett[1]

A Monte Carlo code has been written in the OGRE system (see Sec. 6.6) for the IBM-7090 computer to compute energy deposition by gamma rays in an infinite slab geometry. The slab may consist of 50 laminations, which in turn may consist of as many as 13 distinct homogeneous mixtures of elements.

The gamma-ray source is a current incident upon one face of the slab and monoenergetic. This incident current may be monodirectional or it may be distributed according to an isotropic or cosine angular distribution about the slab normal. Each lamination is divided evenly into many spatial intervals. The energy deposition is computed by means of statistical estimation at the boundaries of each of the intervals, as well as by straight analog estimates of the flux to obtain average heating values within each interval. The emergent energy and angular distribution and dose rate of photons which penetrate the slab are also computed by means of statistical estimation.

This code has a small amount of input since it makes use of a cross-section generation package described in Sec. 6.5 to obtain the cross sections for mixtures of many elements.

[1]Mathematics Panel.

6.10. USE OF RENUPAK AND NIOBE NEUTRON TRANSPORT CODES

D. K. Trubey and S. K. Penny

The IBM-7090 neutron transport codes RENUPAK[1] and NIOBE[2] have been obtained from United Nuclear Corporation of America (NDA) and are in use on the Oak Ridge IBM-7090 machine. The actual operation of the codes is carried out by personnel at the Oak Ridge Gaseous Diffusion Plant. Cross sections

[1]J. Certaine *et al.*, *Nucl. Sci. Eng.* **12**, 446 (1962); see also J. Certaine *et al.*, *RENUPAK, An IBM-704 Program for Neutron Moment Calculations*, NDA-2120-3 (December 1959).

[2]Stanley Preiser, *Nucl. Sci. Eng.* **12**, 447 (1962); see also S. Preiser *et al.*, *A Program for the Numerical Integration of the Boltzmann Transport Equation – NIOBE*, ARL-TR-60-314 (December 1960).

for the following nuclides are available: H, Li, Be, B^{10}, B^{11}, C, N, O, Na, Al, Si, S, Ca, Mn, Fe, Zr, Cd, Pb, U^{235}, and U^{238}.

Considerably more experience has been obtained with RENUPAK than with NIOBE. The RENUPAK code uses the moments method to solve the neutron slowing-down problem in an infinite homogeneous medium for a point isotropic source. The source energy distribution may be specified at energy points, or a fission spectrum may be used. The moments of the distributions are written on a tape that can be processed later to yield the neutron flux (or current) energy-spatial distribution. These data are written on another tape, as well as printed in the output. The flux is constructed from the moments by fitting a sum of either exponential or Gaussian terms. The exponential fit appears to be the better, but under certain conditions the code fails to make the fit, or the resulting flux is negative.

The NIOBE code solves the Boltzmann equation numerically for a spherically symmetric finite medium. The source must be specified in space and have an energy distribution like that described above.

In order to use these codes effectively, an input data form for RENUPAK has been prepared and is now available, and certain auxiliary codes have been written. The form, consisting of two sheets, allows the user to specify the required input ready for keypunching.

The auxiliary codes, written at ORNL, are described below:

Response Function Code.[3] – This code will generate and punch response function cards for either RENUPAK or NIOBE. Typical response functions are flux-to-dose conversion factors or heating cross sections. The input cards are the FORTRAN type, which list any number of response function values at convenient energies. The code will interpolate (log-log) to compute values at the points required by the NIOBE or RENUPAK codes.

RENUPAK Tape Edit.[3] – This code will read one or more flux tapes and print (via output tape) an edit of the spatial-energy distribution on $8\frac{1}{2} \times 11$ paper. This edit is extremely compact compared with the usual RENUPAK output. In addition, the code will compute and print the dose rate as a function of distance. A FORTRAN subroutine, called REDREN,[3] is used by the tape edit and may be used in other codes. This routine will automatically read one or more flux tapes and deliver the distance, energy, and flux values to memory.

The RENUPAK code results for a fission source in water, air, and BeO have been obtained in the edited form for publication. Data for other media will be obtained in the future. Some difficulties have been experienced. For example, media with iron result in failure at most energies. Data points close to the source often result in negative fluxes for the exponential fit. However, at these distances, moments-method results are not expected to be accurate. The Gaussian fit almost never fails but the spatial variation of the slope of the flux sometimes varies much too drastically to be reasonable.

---

[3]D. K. Trubey, *Two Auxiliary Codes for Use with RENUPAK*, ORNL TM-307 (to be published).

6.11. TRANSFUSION – A NUMERICAL METHOD FOR COMPUTING LOW-ENERGY NEUTRON SPATIAL DISTRIBUTIONS

D. K. Trubey and S. K. Penny

With the development of large, fast computers, many numerical techniques and codes have been developed to solve the neutron slowing-down problem in shields. These generally have been either transport theory codes or multigroup diffusion codes. The best available transport codes are designed to solve the problem by incorporating a physical model as nearly exact as possible and by using the best cross sections available. The results at high energy are good and can be obtained with a small amount of machine time; at low energy, however, they are usually less accurate and require a large amount of computer time.

The diffusion codes are not well suited to the deep-penetration problems. Neutrons which arrive deep in a shield are generally either unscattered or have suffered only a few small-angle scatterings. Thus they are at high energies and the flux is anisotropic. This picture is not in accord with the assumptions of diffusion theory; however, as the neutrons are reduced to low energies, the flux becomes more isotropic and so do the cross sections. The diffusion theory then is more applicable.

A technique has been developed that is a combination of the transport and diffusion theories and thus has been designated as the Transfusion method. In this method transport theory is used for the neutrons at high energy, and diffusion theory for those at low energy.

Blizard[1] discussed a possible combination of the two theories and suggested that Gaussian slowing down from the first collision might be assumed, which would predict the thermal-neutron flux from the fast-neutron current. Another technique was developed and applied in the United Kingdom to predict the thermal-neutron flux in concrete shields and in other types of shielding.[2] In that technique, the high-energy neutron transport is handled by using removal theory. The removal flux is calculated by means of an energy-dependent removal cross section, and neutrons are then fed into a multigroup slowing-down process from the removal flux.

Examples of transport theory codes that can be used in the Transfusion method are RENUPAK[3] (moments method), NIOBE[4] (numerical integration of the Boltzmann equation), and Monte Carlo codes. For the example reported here, the RENUPAK code was used to generate the spatial-energy flux distribution from a point fission source in water. These data were used to generate the "source" distribution of neutrons appearing at various energies below 1 kev at various space points from scatterings above 1 kev. This distribution then was used as the source distribution by MODRIC,[5] an Oak Ridge one-dimensional multigroup diffusion code.

---

[1]E. P. Blizard, p 7–89 in *Nuclear Engineering Handbook* (H. Etherington, editor), McGraw-Hill, New York, 1958.

[2]A. F. Avery *et al., Methods of Calculation for Use in the Design of Shields for Power Reactors,* AERE-R-3216 (1960).

[3]J. Certaine *et al., Nucl. Sci. Eng.* **12,** 446 (1962).

[4]Stanley Preiser, *Nucl. Sci. Eng.* **12,** 447 (1962).

[5]J. Replogle, *MODRIC: A One-Dimensional Neutron Diffusion Code for the IBM-7090,* K-1520 (1962).

The case of a point source in water was selected as a first test case since experimental results of the thermal-neutron flux are available from ORNL Lid Tank Shielding Facility data.[6] Since the LTSF source is a 28-in.-diam disk, the data had to be transformed to that of a point source.[7]

Thermal-neutron fluxes from the preliminary transfusion results[8] for a point fission source in water are shown in Figs. 6.11.1 and 6.11.2, along with diffusion theory results. The transfusion predictions are much better than the diffusion theory results at large distances. A difficulty in this calculation, especially for short distances, is in the fitting of the moments to construct a fast-neutron flux by the RENUPAK code. Two types of fluxes are obtained by RENUPAK (Gaussian or exponential) and they sometimes disagree by a factor of 2.

---

[6]A. D. MacKellar, *Prediction of Thermal-Neutron Fluxes in the Bulk Shielding Facility from Lid Tank Shielding Facility Data,* ORNL CF-59-1-24 (Jan. 12, 1959).

[7]E. P. Blizard, *loc. cit.*

[8]The assistance of W. E. Kinney, V. E. Anderson, and H. E. Murchison in successfully completing the calculation is gratefully acknowledged.

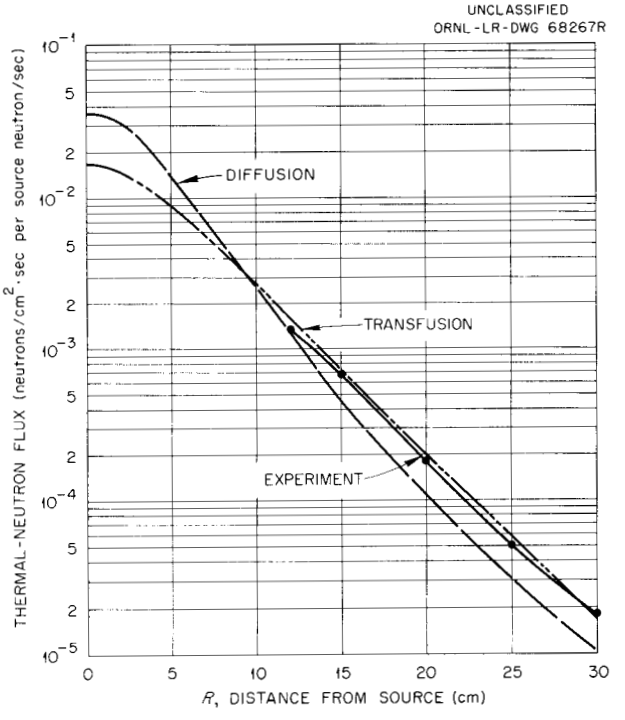

Fig. 6.11.1. Thermal-Neutron Flux in Water Close to the Source.

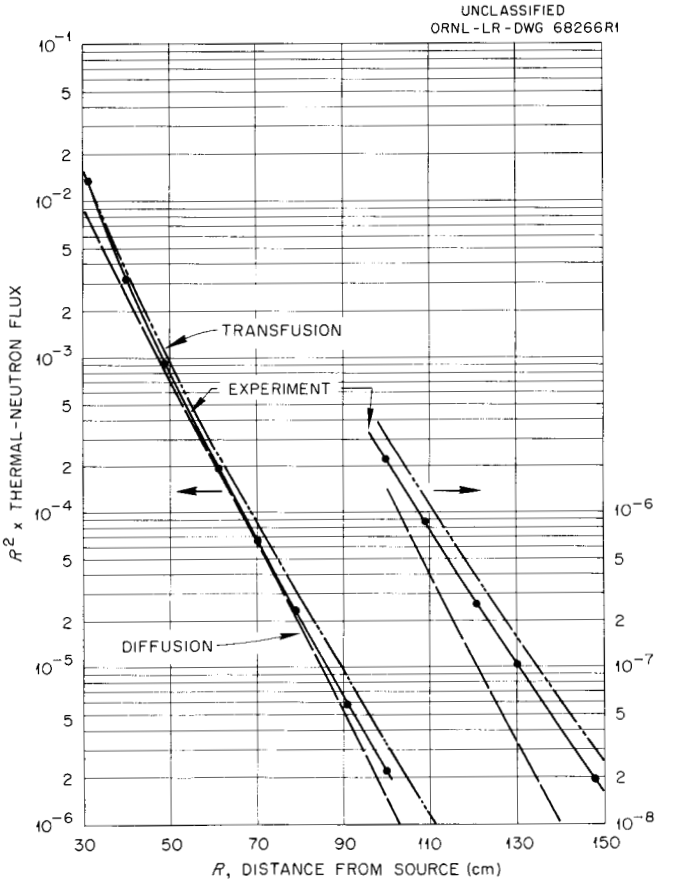

Fig. 6.11.2. Thermal-Neutron Flux in Water Beyond a Distance of 30 cm from the Source.

6.12. IBM-7090 GAUSSIAN INTEGRATION PACKAGE WITH OPTIONAL POINT QUADRATURE[1]

S. K. Penny

A Gaussian integration package consisting of four FAP subroutines, GAUSS1, GAUSS2, GAUSS3, and GAUSS4, has been written for the IBM-7090 computer. The scheme used in these routines is similar to Gaussian integration routines reported previously[2,3] but has been generalized and made more efficient, more flexible, and simpler to use.

The generalization is the inclusion of the subroutine GAUSS4 and the option in all four routines for the use of a 2-, 4-, 8-, or 16-point Gaussian quadrature. GAUSS4 allows for the possibility of a fourfold integral.

The flexibility is effected by requiring the user to write a simple FAP pseudosubroutine for the required storage area. Thus the user has complete control over the number of simultaneous integrals to be computed without touching the Gaussian package itself. The subroutines which the user must write merely use a simplified call statement to the appropriate Gaussian integration routine and then evaluate the appropriate partial integrand with no multiplication.

It is assumed that the problem is to evaluate, in general, n fourfold integrals over the same four volumes of the form

$$\int_{L1}^{U1} F_i(x)\,dx \int_{L2}^{U2} G_i(x,y)\,dy \int_{L3}^{U3} H_i(x,y,z)\,dz \int_{L4}^{U4} J_i(x,y,z,v)\,dv\ ,$$

where $i = 1, 2, \ldots, n$.

[1] Abstracted from ORNL-3263 (Mar. 16, 1962).

[2] M. P. Lietzke, *IBM-704 Gaussian Integration Routines*, ORNL CF-60-3-48 (Mar. 14, 1960), and addendum.

[3] M. B. Emmett and S. K. Penny, *IBM-7090 Gaussian Integration Routines*, ORNL CF-61-5-65, Revised (Dec. 6, 1961).

6.13. A FORTRAN SUBROUTINE FOR TABLE GENERATION BY DATA INTERPOLATION[1]

S. K. Penny

A Fortran subroutine TERPØL has been written which generates a table of values by interpolation (or extrapolation) in another table of data. There are four options for the interpolation scheme desired. The values in the generated table correspond to values of the independent variable which are evenly spaced either in the variable itself or in its logarithm.

The computing cost of a "table look-up" by this method is usually much smaller than that of direct computation. Therefore in certain types of codes where computational time is at a premium, while storage area is not, this type of table generation is highly desirable and useful.

[1] Abstracted from ORNL-3255 (Feb. 21, 1962).

The user must have data arrays in storage corresponding to functional values which have a one-to-one correspondence with values of the independent variable arranged in monotonically increasing order. The user must determine whether the data supplied are adequate to obtain the accuracy desired in the generated table.

6.14. ENØFX – AN IBM-7090 ROUTINE FOR COMPUTING THE EXPONENTIAL INTEGRALS $E_n(x)$

D. K. Trubey

An IBM-7090 subroutine has been written in FAP language to compute the exponential integrals

$$E_n(x) = x^{n-1} \int_x^\infty \frac{e^{-y}\, dy}{y^n} = \int_1^\infty e^{-xu}\, u^{-n}\, du$$

$$= \int_0^1 \mu^{n-2}\, e^{-x/\mu}\, d\mu$$

$$= \sum_{\substack{m=0 \\ m \neq n-1}}^{\infty} \frac{(-x)^m}{m!\,(n-1-m)} + (-1)^n \frac{x^{n-1}}{(n-1)!} (\log x - A_n + \gamma),$$

where $\gamma = 0.57721566$, $A_1 = 0$, and $A_n = \sum_{m=1}^{n-1} 1/m$ for $n > 1$.

The user may call the routine, which has been written to be compatible with Fortran and the Oak Ridge Gaseous Diffusion Plant IBM-7090 monitor system, with the Fortran statement

CALL ENØFX(N,X,F),

where N is the highest value of n desired for any number of exponential integrals, X is the argument, and F is a dimensioned array (unless $N = 1$) in which the values are stored. The result for $E_1(x)$ will be stored in $F(1)$, $E_2(x)$ in $F(2)$, etc. Note that F must be dimensioned as large or larger than N. The variable N is a Fortran integer and X and F are floating point variables.

The routine ENØFX uses the routine EXPI, which was written originally by J. M. Cooley[1] (SHARE distribution 753) for computing

$$E_i(x) = -\int_{-x}^\infty \frac{e^{-t}}{t}\, dt$$

---

[1]New York University, Institute of Mathematical Sciences, AEC Computing and Applied Mathematics Center.

and modified by E. B. Carter, Jr.,[2] for the Oak Ridge IBM-7090 monitor system. Then the relations

$$E_1(x) = -E_i(-x)$$

and

$$E_n(x) = \frac{1}{n-1}\left[e^{-x} - xE_{n-1}(x)\right]$$

are used to generate all exponential integrals from 1 to N. The value of $X \gtrsim 80$ will return a zero for $F(1)$. Testing showed that values of X as small as 10^{-35} will give accurate answers. Decks or listings may be obtained from the author.

[2]Oak Ridge Gaseous Diffusion Plant.

6.15. AN IBM-7090 ROUTINE FOR READING 05R TAPES

D. K. Trubey

A subroutine called REDØ5R has been written to aid the programmer who uses the 05R neutron Monte Carlo code.[1] The routine, which is compatible with Fortran and the Oak Ridge IBM-7090 computer monitor system, has a buffered input so that the machine may process the neutron histories and read tape simultaneously.

The 05R code generates neutron histories by Monte Carlo methods and writes the details of each collision on magnetic tape. The user, having formulated a Monte Carlo tallying procedure, must write a program to process these collisions. If the standard Fortran statements are used entirely, time will be wasted since the central processing unit will be idle while tape is being read. Consequently, REDØ5R was written to take advantage of the machine's ability to compute in the central processing unit while reading tape.

In the explanation which follows, a knowledge of the 05R tape format, Fortran, and the monitor will be assumed. Any processing routine will consist of a main routine and probably some special-purpose subroutines. The first things to be done, of course, are the initialization and reading of input data. The program then calls REDØ5R with the statement

$$\text{CALL REDØ5R } (I,J,K,L,M,N)\ ,$$

where

I = number of parameters per collision listed on the Ø5R tape,

J = number of collisions per record,

[1]R. R. Coveyou, J. G. Sullivan, and H. P. Carter, *Neutron Phys. Div. Ann. Progr. Rept. Sept. 1, 1958*, ORNL-2609, p 87.

K = number of cells in CØMMØN *above* the block where collision parameters are to be stored by REDØ5R,

L = second data word in a record which is used as a signal by REDØ5R to terminate processing if necessary.

The number L may be used by the calling program to decide whether more batches are to be processed. The value of $L = 1$ indicates an end of batch and $L = 3$ indicates the end of information. If the routine REDØ5R encounters $L = 2$ (end of tape), the tape is rewound and the next tape is read (see below). If $L = 4$, there has been an error detected (see below). When control returns to the calling program, either an end of batch, the end of information, or an error has been detected, and if subsequent batches are to be processed, the routine REDØ5R must be called again.

The value of M is the number of tapes to be processed. The value of N is the output tape number for use in the error routine (see below). The value of N and the input tape number *must* be greater than M. All the parameters I–N are Fortran integers and, with the exception of L, are supplied by the user.

A slave of REDØ5R is the routine CØMPUT which must be coded by the user. All information fed to or from CØMPUT is through CØMMØN. The routine REDØ5R places the collision parameters for each record in CØMMØN according to I, J, and K defined above. The values of the first parameter of all collisions on the record are stored downward (Fortran style), starting in cell $77461_0 - K$. The values of the second parameter are then stored and so on. This makes it convenient for processing since each parameter may be named (either integer or floating point as the case may be) and indexed by record collision number. It should be noted that CØMPUT must recognize special collisions such as source collisions. No input or output should be done in CØMPUT. When control returns to the calling program, either more batches will be processed or the normalization and writing of the output will be done, terminating the problem. Figure 6.15.1 shows a simplified flow chart.

The tapes to be processed must be numbered logically from 1 upward in the order in which they were written by the Ø5R code. The tapes may be placed on any channel or drive on the machine. The routine REDØ5R will pick up its needed information from the monitor IØU table. Normally, only one or two tapes will be used.

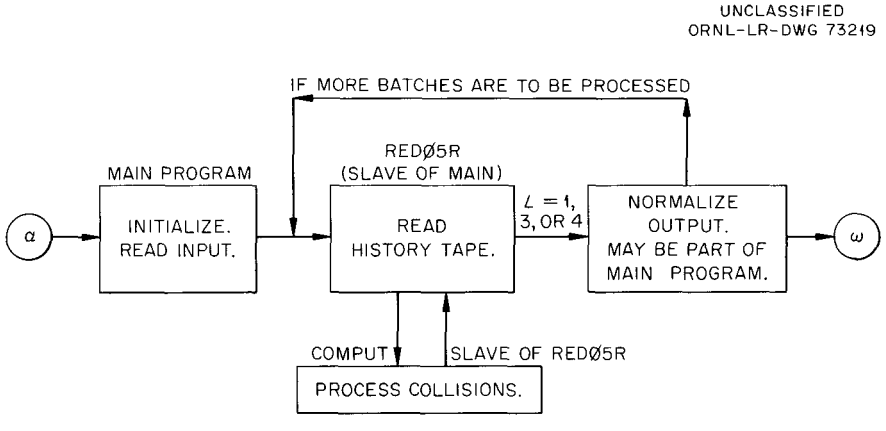

Fig. 6.15.1. Flowsheet of a Fortran O5R Processing Program.

There is a slave to REDØ5R which writes on the specified output tape in case of certain tape reading errors, such as

1. the current record number not being 1 greater than the previous record number,
2. the value of L read from tape not being equal to 0, 1, 2, or 3,
3. the routine having attempted to read the current record 10 times with a redundancy check each time,
4. the tape number having been advanced beyond M and no endof information signal having been encountered.

The type of error, record number, and tape number will be printed out and the tape will be backspaced once so that a dump of the offending record may be taken. Control will return to the calling routine with $L = 4$ (set by REDØ5R). If many histories have been processed, the problem can be terminated successfully but with fewer histories than were expected. Thus the computing time will not have been wasted.

A copy of the FAP list or card decks may be obtained from the author.

6.16. SHIELDING RESEARCH FOR NUCLEAR SPACE POWER PLANTS

C. E. Clifford

Shielding research in direct support of the Space Nuclear Auxiliary Power (SNAP) Program wherein reactors are utilized as the power source for space vehicles has been initiated in the Neutron Physics Division. A major effort has been directed toward the measurement and calculation of the details of neutron transmission through lithium hydride (see Secs. 6.17 and 6.18). This work is a continuation of a study of low-energy neutron penetration originally motivated by the needs of the Aircraft Nuclear Propulsion Program; it now has been reoriented toward high-energy neutrons, the angular and energy distributions of which are of most interest to space shield design.

Neutron shield penetration is, of course, of major importance in the design of a shadow shield; however, in a practical application where the reactor and shadow shield are placed in a system, structural scattering of radiation bypassing the shadow shield is also of importance. This scattering of radiation, primarily neutrons, results from the unfortunate necessity for placing structure in the form of radiators, reactor controls, and vehicle parts in such a relationship to the reactor that the shadow shielding of these components would require an excessive weight. It therefore becomes necessary to develop and utilize a calculational technique to determine the scattered contribution accurately.

A simplified technique is sufficient for systems in the early stages of design where many changes will be made as the design progresses, but a more accurate calculation is required to predict doses in systems with existing flight hardware. A calculational program has recently been initiated which should develop both techniques. The simplified one will be a single-scattering calculation in which reactor codes are used to obtain the source energy distribution and perhaps the angular distribution. The more

accurate calculation will be performed by Monte Carlo techniques, and will include the determination of detailed angular and energy distributions of neutrons penetrating the reactor reflector and parts of the shadow shield. The probability for these neutrons to be scattered into the body of the vehicle, taking into account multiple collisions, will subsequently be calculated.

Some preliminary experiments have been completed at the Tower Shielding Facility (TSF) in which neutrons scattered from a beryllium block were measured. The geometry of the experiment was relatively clean in that the neutrons incident on the slab were fairly well collimated and the detector was far enough from the slab to give good angular resolution of the neutrons emerging from the slab. Only one angle of scattering (90°) was measured, but this was done for a multiplicity of thicknesses and for two sizes of slabs. Also, the angular orientation of the slabs was varied in 45° increments with respect to the axis perpendicular to the plane of the scattering angle. Analysis of these data by a single-scattering theory indicated that the number of neutrons scattered was quite sensitive to the energy spectrum of the incident beam of neutrons. This sensitivity requires, then, an accurate determination of the neutron spectrum emitted by the reactor. Given this spectrum, the results of a single-scattering calculation can then be compared with the experimental results in order to deduce the range of thicknesses of beryllium over which multiple scattering becomes important.

An experimental mockup of a beryllium control drum was also tested for neutron scattering at the TSF. A hinged beryllium block was mounted on the side of the bare reactor. The free end of the block could be moved laterally so that it extended beyond the edge of a thick water-filled conical shadow shield mounted beneath the reactor. Fast-neutron detectors were placed in a collimator 15 ft below the center of the reactor. The solid angle seen by the collimated detector was approximately that subtended by the beryllium block. Measurements of the intensity (dose) of the neutrons scattered by this block into the particular solid angle subtended by the detector were made. The data are being analyzed by Atomics International; however, the experiment did demonstrate that such scattering experiments could yield meaningful results in the sense that the flux due to neutrons scattered by the block was significantly larger (as much as a factor of 4) than the background due to air scattering and other structure scattering. It was possible also to detect the increase in scattered neutrons from a cylinder of nickel (2-in. outside diameter and 3-in. length). The direction of the collimator in this case was such that the detector could also see the tank structure above the reactor, which increased the background considerably over that to be expected from air scattering alone.

It becomes apparent from a detailed consideration of the SNAP reactor design, where the geometry of both the reflector and the control components is quite intricate, that meaningful information on the dose from neutrons scattered into the payload by these components can only be obtained from experiments with a prototype reactor and shield. Experiments with a simplified geometry test only a portion of the calculational technique and, when the TSR-II is used, test this with a neutron spectrum different both in energy and in angular distribution.

In the high-powered SNAP systems, a correct design of the shadow shield becomes very important simply because the weight of these shadow shields is of the order of several thousand pounds. Therefore, even a 10% decrease in shield weight would allow the payload to be increased several hundred

pounds. Good design, particularly in the shaping of these shields, should lead to an appreciable weight savings. The shield shaping problem is a difficult one in that it requires both experiments and calculations of deep penetration of radiations through material where the leakage out of the boundaries of the material influences the total radiation being transmitted. Shaping of the thermal and/or gamma-ray shield, which will be required for the higher-power levels, should also result in a significant weight savings. These shaping problems in a shadow shield geometry have not been worked on in previous shielding programs, and therefore basic techniques will have to be developed for solving them. Deep-penetration Monte Carlo calculations appear to offer the only straightforward method for handling a calculation of the dose transmitted through shaped shields; however, this type of work consumes a great amount of machine time and might become prohibitively expensive if it becomes necessary to examine a large number of configurations. The technique to be developed then is one which will reduce the number of configurations to a minimum and still give an optimized shield design with respect to minimum weight.

The calculational program must be concurrently supported by an experimental program which must determine the transmission and angular distribution of both neutrons and gamma rays through a shaped shadow shield. When compared with the results of calculations, the experimental data will determine whether the fundamental information used in the Monte Carlo calculation is correct.

6.17. TRANSPORT OF FAST NEUTRONS THROUGH LITHIUM HYDRIDE. PART I: NEUTRON SPECTRA[1]

V. V. Verbinski, T. A. Love, R. D. Smiddie,
H. A. Todd, and T. Fuse[2]

This work is part of a basic shielding program initiated about $2\frac{1}{2}$ years ago for the purpose of evaluating calculations of the type that provide the spatial and spectral details of neutron flux at every point in a shield (see Sec. 6.18).

In recent experiments two measurements have been made of the spectra of neutrons penetrating slabs of lithium hydride: one of neutrons emerging normally from a 20-cm-thick slab and one of neutrons emerging 30° to the normal of the slab. The energy range of the measurements is about 0.5 to 10 Mev, and the accuracy of the calibrations for this set of measurements is expected to be about as good as the statistical spread of the data above 2 Mev. The spectrum of the neutron source was also measured and used as input to NIOBE code[3] calculations of neutron transport, the outputs of which were compared with the experimental results. The following discussion represents an interim report, the measurements having since been repeated for a greater range of energy and lithium hydride thickness.

Experimental Arrangement

The electron linear accelerator (LINAC) of General Atomic was used to provide short bursts of 28- to 30-Mev electrons which when incident on a large lead target (6 × 6 in. in cross section and 7 in. thick), Fig. 6.17.1, produced a near-fission spectrum of neutrons. The neutrons penetrated the 20-cm-thick lithium

[1]Summary of ORNL TM-375 (to be published).

[2]Affiliated with the Transportation Technical Research Institute, Japan; formerly on loan to ORNL.

[3]S. Preiser *et al., A Program for the Numerical Integration of the Boltzmann Transport Equation,* ARL Technical Report 60-314, U. S. Department of Commerce, Washington 25, D. C. (December 1960).

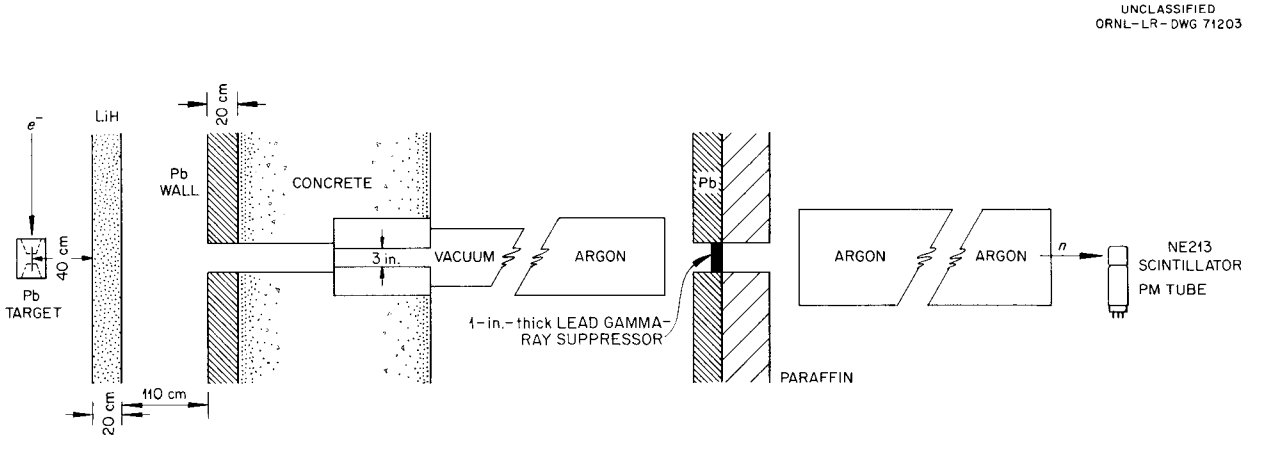

Fig. 6.17.1. Experimental Arrangement for Measurements of the Spectra of Neutrons from Lithium Hydride.

hydride slab, passed down a 50.6-m flight path, and were sampled by a liquid scintillator (2 in. in diameter and 2 in. high). A 1-in.-thick lead slab was placed in the beam about halfway down the flight path to reduce the effect of bremsstrahlung radiation emitted from the lead target. The spectrum of neutrons emergent from the lithium hydride at 30° was measured by rotating the source-slab configuration about the point where the neutron drift-tube axis intersected the "emergent" face of the slab.[4]

A block diagram of the electronic circuitry used to obtain time-of-flight spectra is shown in Fig. 6.17.2. A gamma-ray flash detector located near the accelerator target is used to start a time-to-pulse-height converter and to turn on the neutron detector at about 0.7 μsec after the bremsstrahlung radiation has irradiated the NE 213 organic scintillator and before a 15-Mev neutron has arrived. Any neutron that deposits greater than about 0.3 Mev of energy in the scintillator by an elastic collision with a hydrogen atom will initiate a pulse in each of the two amplifier-discriminator blocks shown. (Carbon collisions give a much smaller pulse height in organic scintillators because of the high ionization density of carbon nuclei.) The coincidence circuit following these two discriminators then sends a STOP pulse to the time-to-pulse-height converter. The height of this pulse, as measured by a pulse-height analyzer, then gives a measure of the neutron's time of flight, or equivalently, its energy. Further details of the electronics, the correction for neutron attenuation along the flight path, and the ultimate conversion of time-of-flight spectra to energy spectra are given elsewhere.[1]

The efficiency of the organic scintillator for neutron detection as a function of neutron energy was calculated by hand. The cylindrical detector was assumed to consist of a set of 18 slabs with the efficiency of each slab being equal to $1 - e^{\Sigma_s(H)} \times L$, where L is defined in Fig. 6.17.3. This hand calculation has recently been followed by a calculation with a Monte Carlo code (O5R)[5] that gave the same energy dependence within about ±5%, although the absolute efficiency was lower by about 10%. Calibration with monoenergetic neutrons from the 5-Mev ORNL Van de Graaff generator supplied shapes of pulse-height spectra from which corrections could be made for a nonzero bias setting of the linear and Forté amplifiers shown in Fig. 6.17.2.

Results

The spectrum of neutrons produced in a small lead target ($1\frac{1}{4} \times 1\frac{1}{4}$ in. in cross section and 1 in. thick) is shown in Fig. 6.17.4. Superposed on this is a fission spectrum.[6] If the results below 2 Mev are ignored, the spectrum from the target is the same as a fission spectrum with the exception of a slight hardening above 5 Mev that can be explained by some direct emissions of neutrons by the bremsstrahlung radiation; that is, *direct* (γ,n) interactions. Below 2 Mev, the apparent rise above the fission spectrum is probably due to three sources: neutrons from (γ,pn), $(\gamma,2n)$, or other multiple emissions, in cases where the last neutron is emitted by a nucleus whose excitation is only slightly higher than the

[4]E. Haddad, R. B. Walton, W. M. Lopez and others of the General Atomic LINAC staff contributed much in the form of suggestions and circuit modifications during the early planning stages, and William Bertozzi of the MIT LINAC staff gave valuable suggestions for the fast gating of photomultiplier tubes.

[5]R. R. Coveyou, J. G. Sullivan, and H. P. Carter, *Neutron Phys. Div. Ann. Progr. Rept. Sept. 1, 1958*, ORNL-2609, p 87.

[6]L. Cranberg *et al.*, *Phys. Rev.* **103**, 662 (1956).

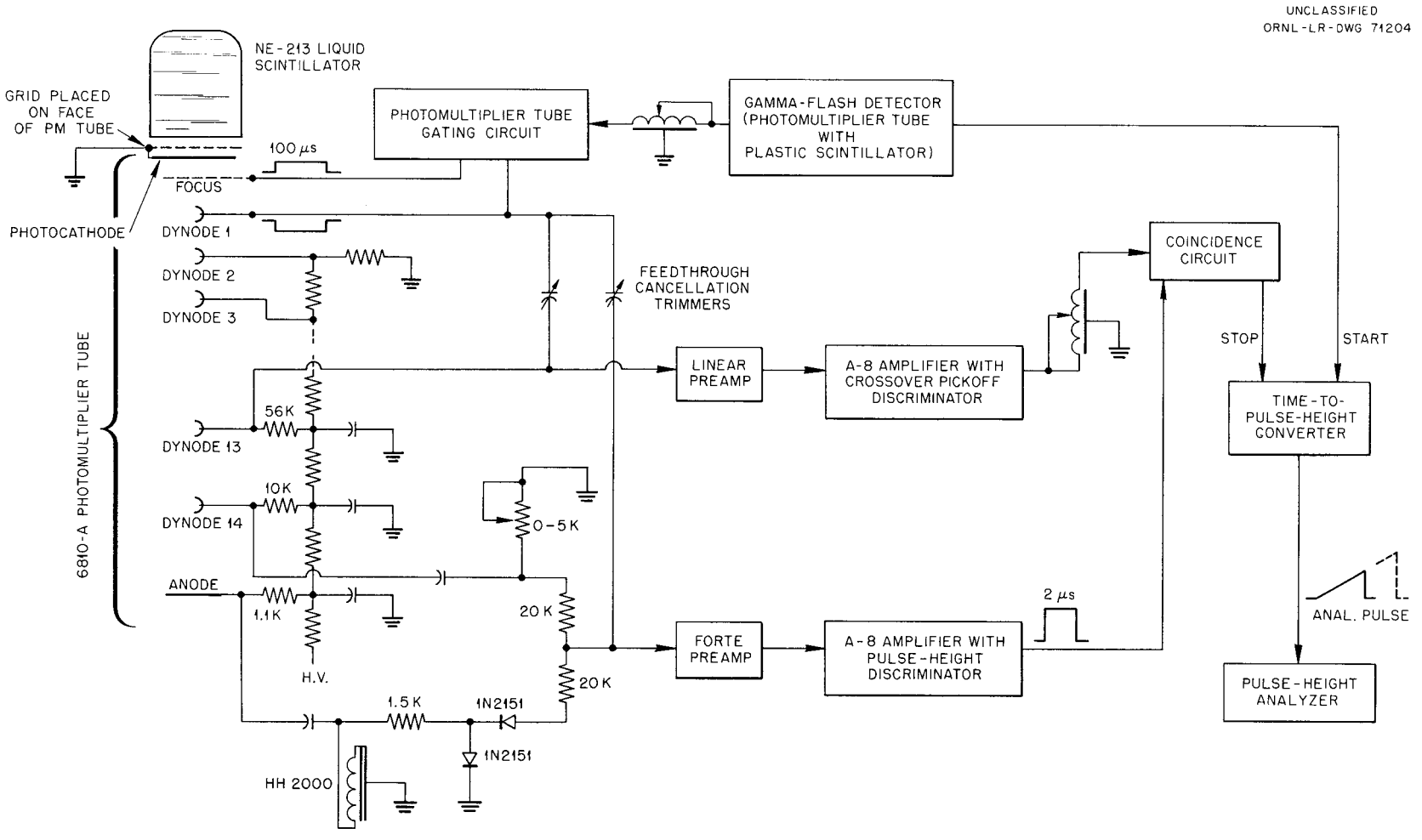

Fig. 6.17.2. Block Diagram of Electronics to Obtain Time-of-Flight Neutron Spectra.

UNCLASSIFIED
ORNL-LR-DWG 71202R1

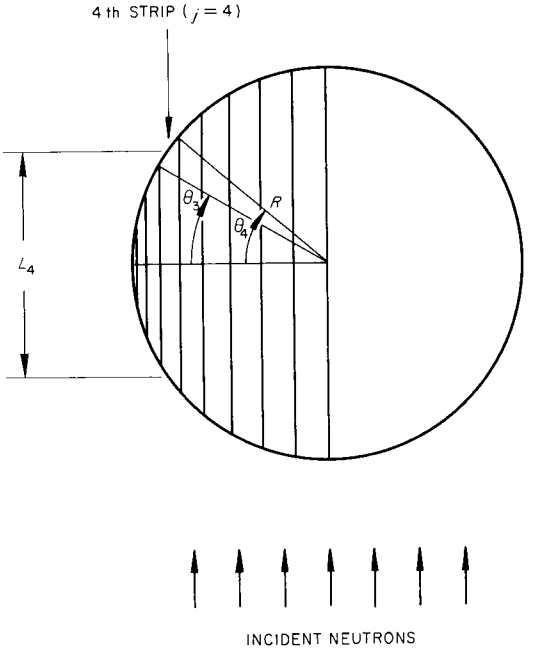

Fig. 6.17.3. Calculation of Detector Efficiency. The cylindrical detector is divided into 18 parallel strips for computation of the average first-scattering probability by a hydrogen atom.

UNCLASSIFIED
ORNL-LR-DWG 71201

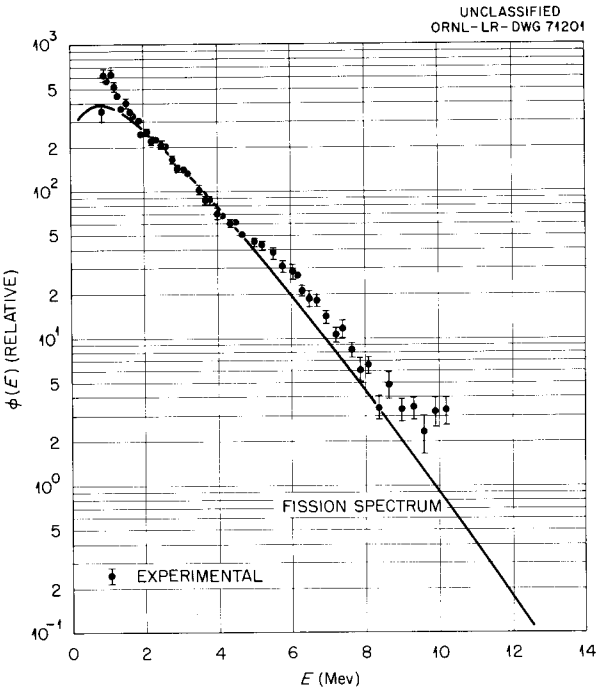

Fig. 6.17.4. Spectrum of Neutrons from Small ($1\frac{1}{4} \times 1\frac{1}{4} \times 1$ in.) Lead Target.

binding energy of the emitted neutron; slowing down of fast neutrons in the lead target by inelastic scattering; and inaccurate initial calibration of the detector. The initial calibration was the least accurate below 2 Mev. The final calibration, which is still incomplete, should be reasonably accurate down to 0.5 Mev.

For measurements with the lithium hydride, the larger lead target was used to suppress the amount of bremsstrahlung radiation reaching the neutron detector. The spectrum of neutrons from this large target is shown in Fig. 6.14.5. Since it was 7 in. thick, the neutrons, all produced near the center of the target, had to penetrate ~4 in. of lead, on the average, before reaching the face of the lithium hydride slab; consequently, because of inelastic scattering in lead, the source is a softened fission spectrum above 5 Mev.

In Fig. 6.17.6 is presented the spectrum of neutrons from the large target as modified by the 20-cm-thick lithium hydride slab. The neutrons are normally emergent from the slab. The results are compared to a NIOBE calculated spectrum for *fission* neutrons incident on a 200-cm-diam by 20-cm-thick lithium hydride shell. The agreement is not good; however, when the measured source spectrum of Fig. 6.17.5 was used as an input to the NIOBE calculation, much better agreement with experimental results was obtained, as shown in Fig. 6.17.7. A coarse-mesh O5R calculation,[5] using a fission source as input, is also shown in Fig. 6.17.7. It is in qualitative agreement with the measurements.

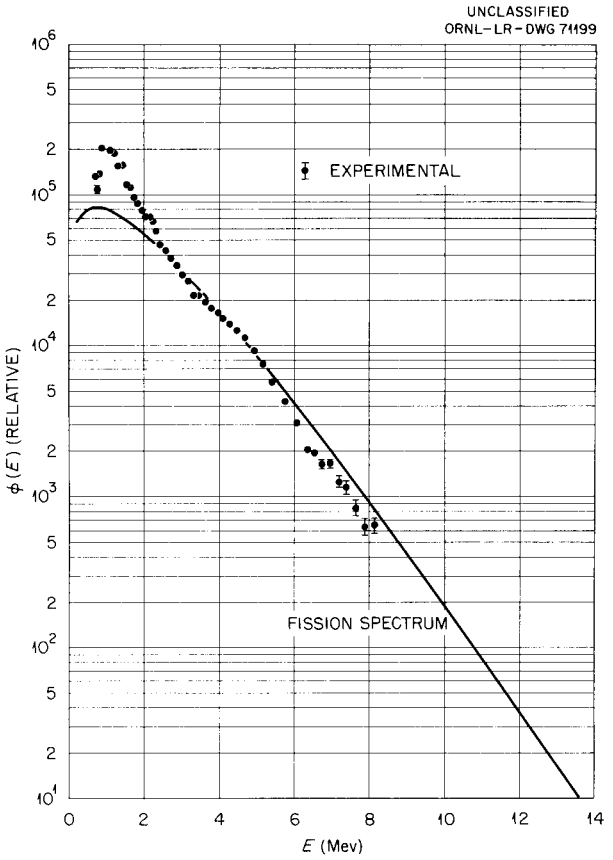

Fig. 6.17.5. Source Spectrum from Large (6 × 6 × 7 in.) Lead Target.

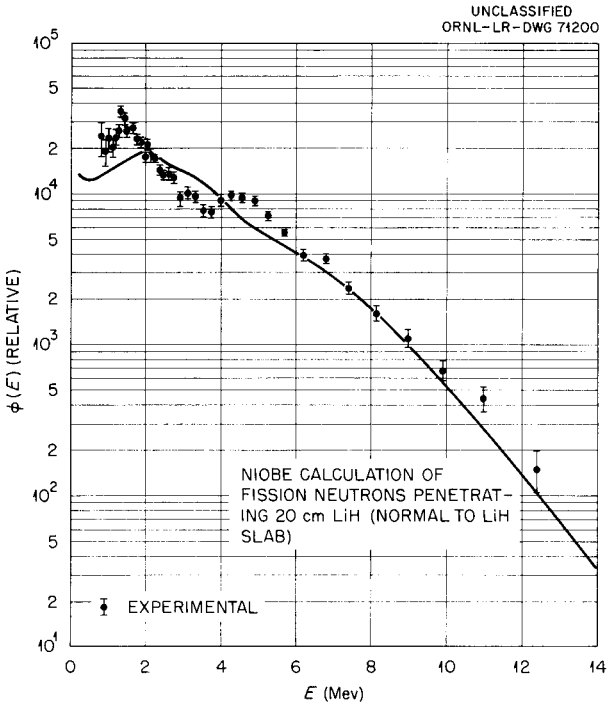

Fig. 6.17.6. Comparison of Measured Spectrum of Neutrons Leaking Normally from Lithium Hydride Slab with NIOBE Calculations.

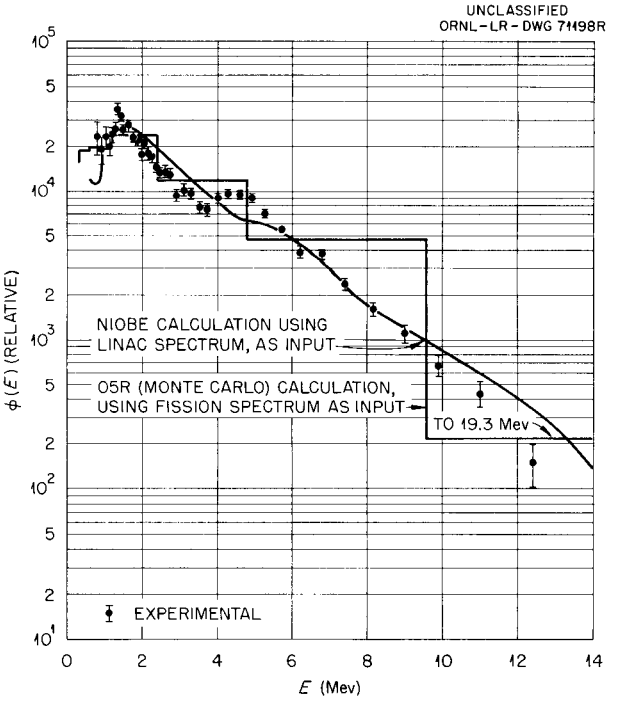

Fig. 6.17.7. Comparison of Measured Spectrum of Neutrons Leaking Normally from Lithium Hydride Slab with NIOBE and 05R Monte Carlo Calculations.

From the comparison of the NIOBE and experimental results of Fig. 6.17.7, it seems likely that the assumed cross sections for lithium hydride used in NIOBE are probably the source of disagreement in the shapes of the curves between 2 and 6 Mev. The unprocessed time-of-flight data recently obtained for a 27.5-cm penetration of lithium hydride give a peak (at 4.5 Mev) to valley (at 3.5 Mev) ratio that is greater than that given in Fig. 6.17.7.

To obtain the spectrum of neutrons emergent at 30° to the normal of the slab, both slab and neutron source were rotated bodily by 30° about the central point on the "emergent face" of the slab, as viewed by the neutron detector. This is almost equivalent to rotating the drift tube and neutron detector about this point on the slab. The resulting neutron spectrum is shown in Fig. 6.17.8. Also shown are the results from a NIOBE calculation in which the experimental spectrum of Fig. 6.17.5 was used as input and the results from an O5R calculation in which a fission source was used as input. The agreement of all three spectra is quite good above 1½ Mev. These neutrons are all large-angle-scattered neutrons and their spectral shapes are less sensitive to cross-section assumptions than that of the 0° spectrum.

Other NIOBE calculations for penetrations in lithium hydride up to 105 cm show little structure for this diffuse component of penetrating neutrons, while the collimated component (the near-forward neutrons) of the neutron flux has a high-energy bump in the spectral shape, a bump that increases with depth of penetration in lithium hydride. This bump is a hardening of the spectrum that arises from the drop in total cross section of lithium hydride above a few Mev.

Conclusions

An electron linear accelerator is a useful tool for neutron transport measurements through moderate thicknesses of shielding materials, penetrations of 40 to 50 cm being attainable. The measurements

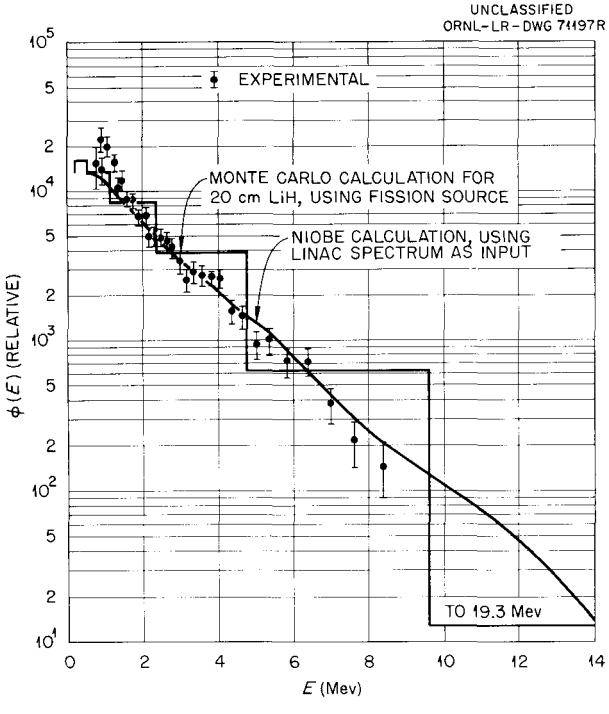

Fig. 6.17.8. Comparison of Measured Spectrum of Neutrons Leaking 30° from Normal to Lithium Hydride Slab with NIOBE and O5R Monte Carlo Calculations.

can provide the spectral details of neutron flux required for a careful evaluation of neutron transport calculations for shields.

The difference between NIOBE calculations and experimental results indicates that NIOBE needs modification, probably in the direction of better input cross sections for lithium hydride. However, it would be best first to compare a NIOBE calculation and a finer-mesh O5R calculation in which the NIOBE cross sections are used. This should provide valuable insight as to whether the calculational method or the assumed cross sections are inaccurate. Better yet, a careful measurement on liquid hydrogen, whose differential cross sections are very well known, should provide a useful standard for comparison for almost any calculational method. A measurement with a water slab might suffice. Although the cross sections for oxygen are not known as well as those for hydrogen, the two hydrogen atoms per oxygen reduce the effects of inaccuracies in oxygen cross sections.

Finally, a rerun of the measurements with a greater range of lithium hydride penetration, higher resolution, and better time calibration and an improved calculation of the energy-dependent sensitivity of the detector are required before any firm appraisal of the shielding calculations can be made. This rerun has been made and the data are being processed. The results are to be submitted for publication in *Nuclear Science and Engineering.*

6.18. TRANSPORT OF FAST NEUTRONS THROUGH LITHIUM HYDRIDE. PART II: ANGULAR DISTRIBUTIONS

V. V. Verbinski, T. Fuse,[1] J. D. Kington, and K. M. Henry

The advent of portable reactor power plants requiring high-performance, light-weight shields has placed great emphasis on neutron transport calculations that provide complete spatial and spectral details of neutron fluxes. Some of the most important shielding problems at the time the program discussed here and in Sec. 6.17 was initiated were the calculation of gamma-ray production within the lamina of an aircraft nuclear propulsion shield and the calculation of neutron-capture gamma radiation in the air surrounding the shield. Therefore, the details of low-energy neutron spectra within a shield and the spectral and angular details of neutrons leaking from it were needed. The first phase of this program, which has been reported previously,[2] was aimed at providing such data for the high-performance shielding material lithium hydride. Calculations were performed by Monte Carlo,[3] moments-method,[4] and NIOBE[5] techniques and the results compared with experimental data.

---

[1] Affiliated with the Transportation Technical Research Institute, Japan; formerly on loan to ORNL.

[2] V. V. Verbinski, *Neutron Physics Div. Ann. Progr. Rept. Sept. 1, 1961,* ORNL-3193, pp 265, 278.

[3] R. R. Coveyou, J. G. Sullivan, and H. P. Carter, *Neutron Phys. Div. Ann. Progr. Rept. Sept. 1, 1958,* ORNL-2609, p 87.

[4] Obtained from H. Goldstein, United Nuclear Corporation, White Plains, N.Y.

[5] S. Preiser *et al., A Program for the Numerical Integration of the Boltzmann Transport Equation,* A.R.L. Technical Report 60-314, U.S. Department of Commerce, Washington, D.C. (December 1960).

Recently, the problem has shifted to that for a spacecraft carrying a reactor power plant on one end, an electronic payload on the other, and a lithium hydride shadow shield between the two. Here the fast-neutron bombardment of semiconductor devices will be the important effect of reactor radiations[6] because of the sensitivity of these materials to dislocations produced in the crystal lattice. Thus a complete knowledge of the angular and energy distributions of the high-energy neutron leakage fluxes is required for the design of an optimum light-weight shield. The energy distribution at each location in the payload is needed to estimate the radiation damage, and the angular distribution at the shield edge determines the optimum shaping of the shield. In an effort to evaluate the accuracy of transport calculations for these special shields, experiments are being carried out to measure pertinent spectra and angular distributions.

In the discussion which follows, neutron angular distribution predictions from NIOBE calculations performed by the United Nuclear Corporation (NDA) are compared with measurements for lithium hydride thicknesses of 20 and 45 cm. Five different threshold detectors, including three fission foils, were used for the measurements with the 20-cm thickness, but for those with the 45-cm thickness, the three fission-foil detectors were not usable because photofission predominates at leakage angles where the foils are in direct view of the reactor gamma-ray flux. The spectral shape given by threshold detectors, but not the absolute magnitude of the flux, is compared to that of the NIOBE prediction.

Experimental Arrangement

The most complicated geometry employed in this investigation is represented in Fig. 6.18.1. It shows the standard configuration of the Bulk Shielding Reactor I employed in all the measurements; a $\frac{3}{8}$-cm-thick layer of water that always abutted the flat face of the reactor; a 1-m precollimator used for two of the runs; a 45-cm thickness (two slabs) of lithium hydride; an additional 30° wedge of lithium hydride used for one of the runs; a hemispherical void 3 ft in radius; six postcollimators, each 6 ft in length and each terminated with a 15-in.-long beam-catcher (and foil-holder) cap; and one short postcollimator (monitor tube) that always contained a monitor pellet of sulfur. The center of the apparatus was ~18 ft below the surface of the Bulk Shielding Facility pool.

The 3.8-cm-thick water gap abutting the reactor was required to reduce the change in reactivity to a safe level in the event that the lithium hydride slab (or in one case, the void) was accidentally displaced from the reactor during an exposure. The 1-m precollimator was used to mock up the geometry of two of the transport calculations. The 30° wedge was used in one run to determine what effect inclining the lithium hydride surface might have on the emergent angular distribution of fast neutrons. The hemispherical void with a 3-ft radius was selected to reduce back-scattering effects to 3 to 4% as determined by some albedo calculations[7] and by NIOBE calculations[8] of spectral and angular distributions, both within

---

[6]D. S. Billington and J. H. Crawford, *Radiation Damage in Solids*, p 312, Princeton University Press, 1961.

[7]D. K. Trubey, *Neutron Physics Div. Ann. Progr. Rept. Sept. 1, 1961*, ORNL-3193, p 288.

[8]H. Goldstein, United Nuclear Corporation.

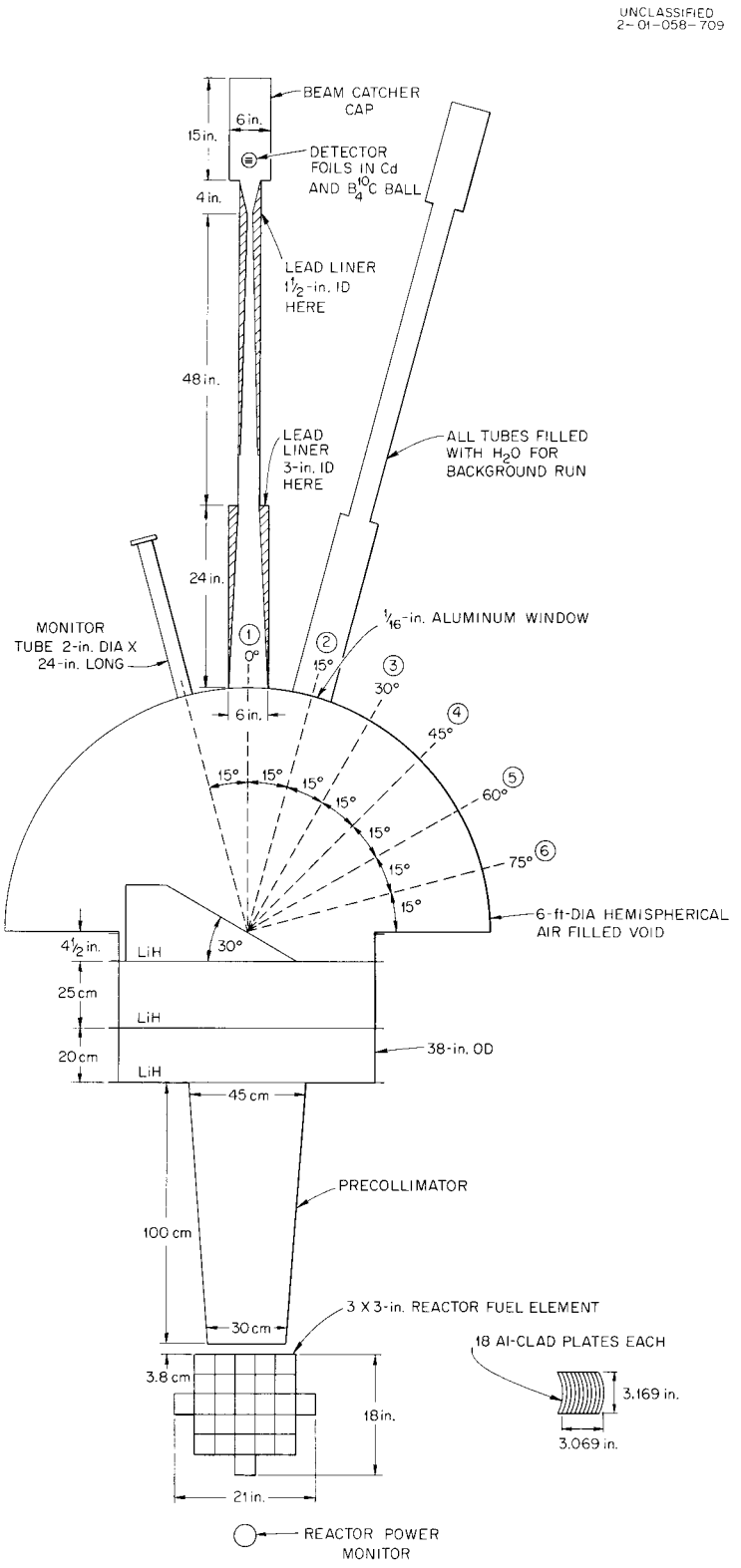

Fig. 6.18.1. Experimental Arrangement for Neutron Angular Distribution Measurements.

a shell of lithium hydride and at the surface of the shell. This back-scattering raises the flux at 1 Mev approximately 0.5% more than it does at 5 Mev. The postcollimators were lead-lined to reduce energy degradation of scattered neutrons. These postcollimators were overdesigned in that wall-scattering effects were calculated[9] to be less than one part in 10^3, whereas air scattering in the void was much more important, approaching a 1% effect. The beam-catcher caps at the end of the postcollimator tubes were designed to give less than 1% back-scattering from the water. Reactor neutrons and neutrons leaking from the lithium hydride face and penetrating the 6-ft depth of water (postcollimator length) were reduced to a small fraction of 1%, as compared to the leakage neutrons passing unhindered through the postcollimators. For safety, the lithium hydride slabs were doubly contained at the surfaces exposed to water, first in a coolant of xylene pumped through the inner container, and next in a static film of oil, $\frac{1}{4}$ in. thick, on the face of the 20-cm-thick slab that was next to the reactor.

Five threshold-detector foils were employed: Pu^{240}, Np^{237}, U^{238}, sulfur, and aluminum. The three fission foils were about 2 cm in diameter and had average weights of 2.98 g (Pu^{240}), 0.401 g (N^{237}), and 4.96 g (U^{238}). The sulfur pellets were 2.3 cm in diameter and 0.95 cm thick; the aluminum slugs were 2.3 cm in diameter and 1 cm thick.

Each geometric configuration that was used required a series of three 6-hr exposures. In one exposure a set of the three fission foils was placed in each of six $B_4^{10}C$ balls having wall thicknesses of 1.25 g/cm^2. The Pu^{240} foil was nearest the reactor, the Np^{237} foil in the center, and the U^{238} foil the farthest from the reactor. The other two exposures were made with the sulfur pellets and the aluminum slugs placed successively in the six balls. During each exposure a fresh sulfur pellet was placed in the short postcollimator tube, and its activity was used as a check against the fission monitor located near one side of the reactor. This fission-chamber monitor always showed about 5% or better agreement with the sulfur-pellet monitor. Still, the fission monitor linearity is not known; therefore, the attenuation measurements discussed below are for two runs at the same nominal reactor power level (1 Mw).

Foil Calibration and Counting Techniques

An NaI(Tl) scintillator crystal (3 in. in length and 3 in. in diameter) was used for detecting postfission gamma-ray activity from the three fission foils. The background radiation due to the residual long-lived activity of these foils and to the nonfission neutron-capture gamma radioactivity was reduced in the counting process by three precautions normally employed by T. V. Blosser of ORNL: background counting of the foils before a run, biasing the photomultiplier-preamplifier-amplifier string at 1.27 Mev, and placing a $\frac{1}{2}$-in.-thick lead shield atop the NaI(Tl) crystal. A plot of counting rate versus time after exposure was obtained for each type of fission foil after a 6-hr exposure to reactor neutrons.

The decay curves so obtained were used to obtain $\sigma\phi$, the foil activation per atom, defined below, by cross calibration against the sulfur pellets and aluminum slugs when all five detectors were exposed to 14-Mev, 3-Mev, and reactor neutrons. In addition, $\sigma\phi$ was calculated for each detector by using the

[9] By Kevin Rooney, Atomics International.

reactor spectrum as measured earlier by other workers.[10-12] Here $\sigma\phi$ represents the integral

$$\sigma\phi = \int_{E_{thr}}^{E_{max}} \sigma(E)\,\phi(E)\,dE\ , \tag{1}$$

where $\sigma(E)$ is the energy-dependent cross section of a threshold detector, $\phi(E)$ is the flux at the detector (in neutrons cm^{-2} sec^{-1} Mev^{-1} Mw^{-1}), E_{thr} is the threshold energy of the detector (taken as about 1% of the maximum cross-section value), and E_{max} is about 14 Mev.

The aluminum activation was also counted with the NaI(Tl) scintillator. A $\frac{1}{4}$-in.-thick plate of aluminum was placed atop the crystal to intercept beta radiation during the measurements of aluminum slug activation. After an exposure of aluminum to the reactor spectrum, the resultant Na^{24} activation was counted at bias levels of 0.67, 1.38, and 2.10 Mev. Since all biases gave a half life of 15 hr, the lowest bias setting was used for all subsequent runs. The aluminum slugs were counted after about a 5-hr waiting period to let spurious activities decay. The aluminum purity was quoted as 99.999% by the manufacturer.[13]

The sulfur pellets, both burned and unburned, were counted for P^{32} activation with a $\frac{1}{4}$-in.-thick plastic scintillator. These pellets were cast and machined after distillation of the sulfur at ORNL. The half life of the sulfur was measured to be about 14 days, indicating that the other possible activations were unimportant. The sulfur was always counted after a waiting period of at least 10 hr.

Results

The NIOBE calculations performed by NDA employed the geometry shown in Fig. 6.18.2. Here, the fission source, which was presumed not to scatter, was uniformly distributed through a sphere 30 cm in diameter. The lithium hydride shell was concentric with the source and had an inner diameter of 200 cm. Calculations were made for shell thicknesses of 20 and 45 cm.

The first experimental run was made without the precollimator or lithium hydride slabs in position. That is, the reactor was separated from the void only by 3.8 cm of water and 0.6 cm of aluminum. The results for this exposure are shown in Fig. 6.18.3, where $\mu = \cos\theta$ (θ is the angle of neutron emergence) and $\sigma\phi$ (see Eq. 1) is the probability per second ($\times 10^{24}$) of exciting one atom by the neutron flux incident on the detector foil. Its units are barns $\times$ neutrons cm^{-2} sec^{-1} Mw^{-1}. The flux $\phi(E)$ in Eq. 1 is that incident on the detector foil and not that leaving the face of the lithium hydride slab. The NIOBE and measured points at $\mu = 1$ in Fig. 6.18.3 give the values of $\sigma\phi$ that would be expected if the 3.8-cm layer

---

[10] J. B. Trice, F. J. Muckenthaler, F. W. Smith, and E. B. Johnson, *Two Neutron Energy Measurements in the Bulk Shielding Facility Using Radioactivants*, ORNL CF-53-5-139 (1953).

[11] R. G. Cochran and K. M. Henry, *Fast Neutron Spectra of the Bulk Shielding Facility Reactor*, ORNL CF-53-5-105 (1953).

[12] F. C. Maienschein, *Influence of Energy Spectra on Radiation Effects*, presented at the Third Semiannual Radiation Effects Symposium at Lockheed Aircraft Corp., Marietta, Georgia, October 28–30, 1958.

[13] AIAG Metals, Inc., New York 20, N.Y.

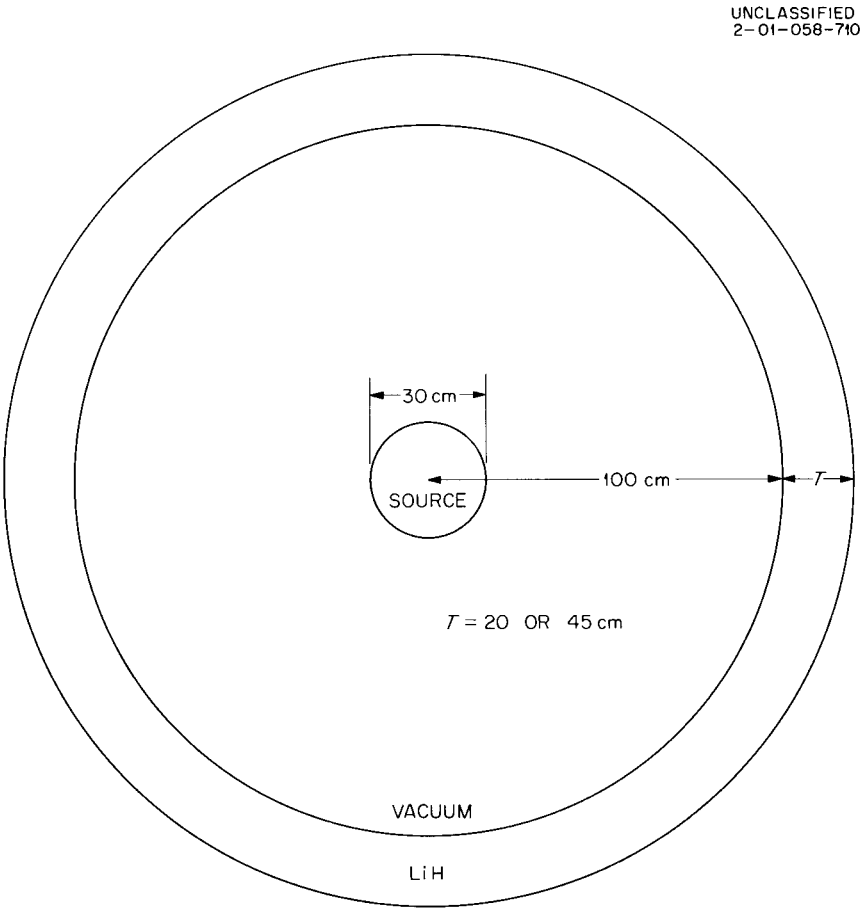

Fig. 6.18.2. Geometry for NIOBE Calculations of Neutron Transport Through a Spherical Shell.

of water were removed. The measured values were obtained from spectral measurements of neutron flux emergent from the reactor face,[10-12] and the NIOBE points from a calculation (fission source) of the spectrum at R = 100 cm (see Fig. 6.18.2), which is at the inside of the lithium hydride shell. Arbitrary normalization is employed.

In the second run, a 1-m precollimator was placed between the reactor and a 20-cm-thick slab of lithium hydride, which mocked up the geometry of one of the NIOBE calculations mentioned above. The experimental and calculated results are compared in Fig. 6.18.4, where the NIOBE results are normalized to the sulfur pellet exposure. The predicted angular distributions are in very good agreement with experimental distributions except for the fission foil activation values at 0°. On the order of 20% of the 0° yield for the fission foils can arise from photofission. Therefore, at 0° the spectral and angular predictions of these foils cannot be taken too seriously. The photofission yields were estimated from cross-section measurements of Katz *et al.*[14] and ORNL determinations[15] of gamma-ray flux.

---

[14]L. Katz *et al., Proc. U.N. Intern. Conf. Peaceful Uses Atomic Energy, 2nd, Geneva, 1958* **15**, 188 (1959).

[15]G. T. Chapman, *Neutron Phys. Div. Ann. Progr. Rept. Sept. 1, 1961*, ORNL-3193, p 304.

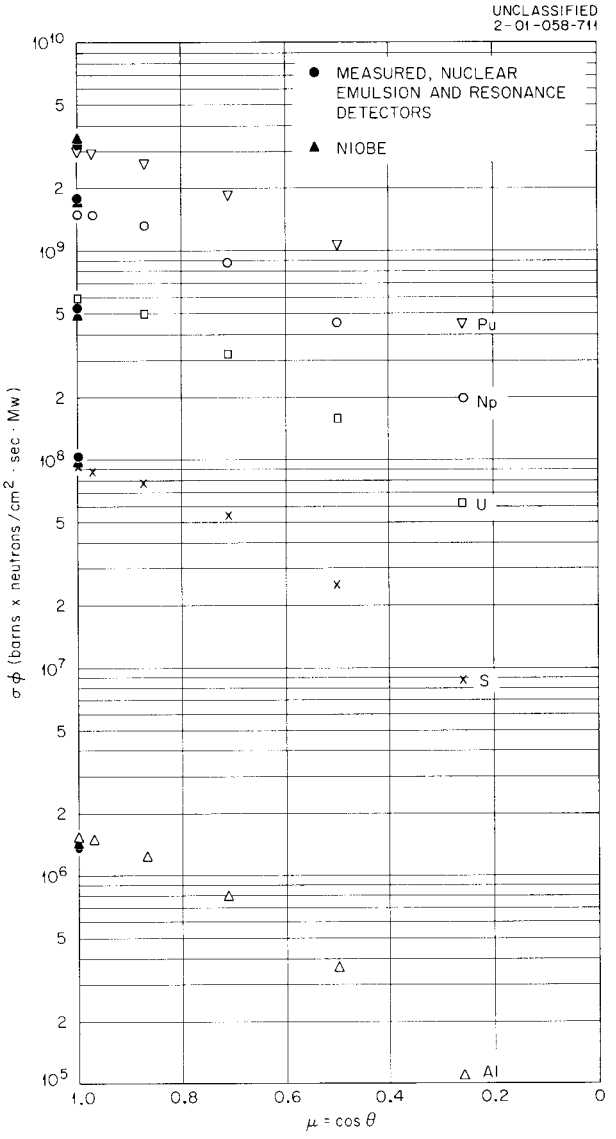

Fig. 6.18.3. $\sigma\phi$ as a Function of μ for No Lithium Hydride and No Precollimator.

At angles greater than 0°, the relative heights of the $\sigma\phi(\mu)$ curves contain spectral information. The measured curves for the Pu^{240} and Np^{237} foils lie below the NIOBE curves, and the measured aluminum activation is higher. The measured spectrum, therefore, appears to be somewhat harder than the NIOBE spectrum.

In the next run, a 45-cm-thick lithium hydride slab and the 1-m precollimator were used. The NIOBE results for sulfur activation were again normalized to the experimental value, as shown in Fig. 6.18.5, and the difference in attenuations of the 45-cm slab and that of the 20-cm slab was measured to be a factor of 1.26 greater than predicted by NIOBE, after corrections were made for attenuation by the xylene coolant and its aluminum container. Some of this difference is probably associated with reactor power monitoring. The measured and calculated angular distributions for the aluminum and sulfur foils are almost identical. No statistically significant results were obtained with the fission foils for the 45-cm

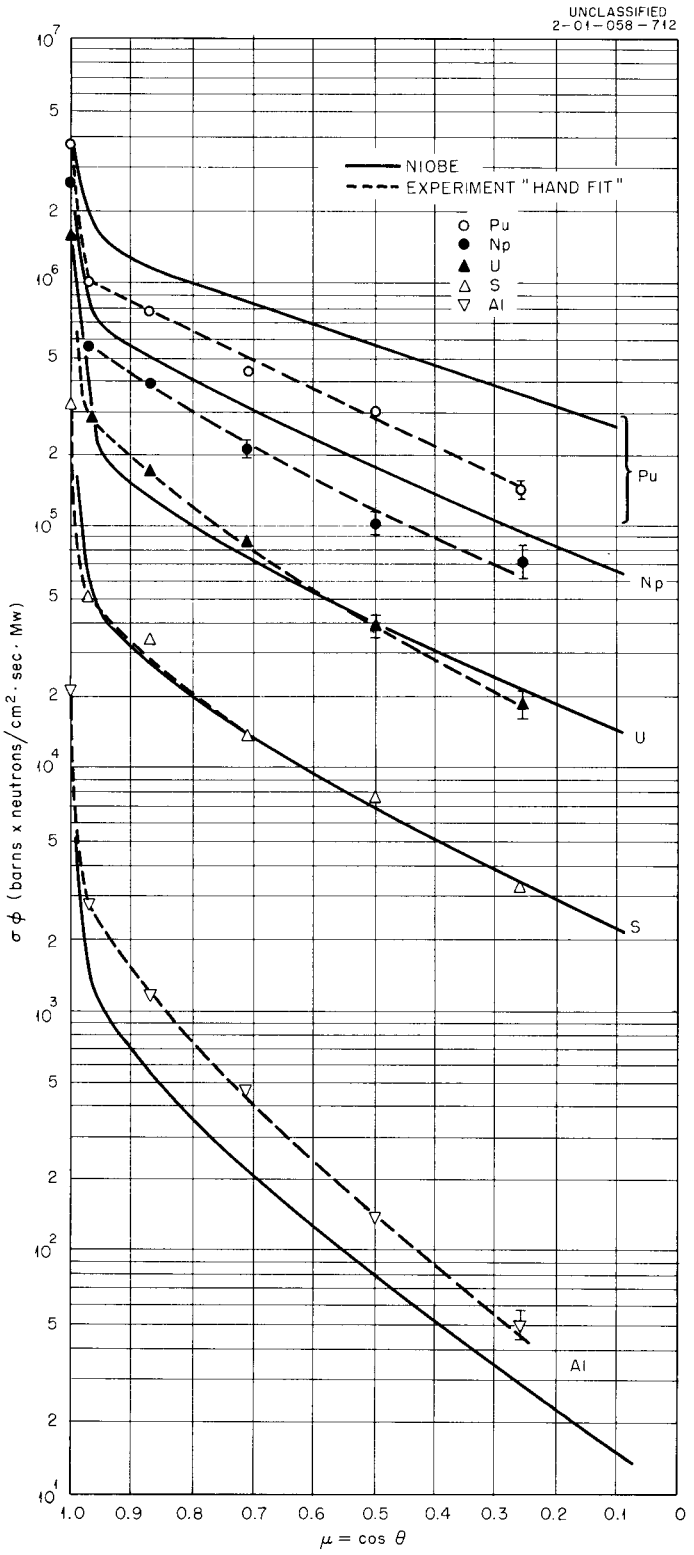

Fig. 6.18.4. $\sigma\phi$ as a Function of μ for 20-cm-Thick Lithium Hydride Slab with Precollimator.

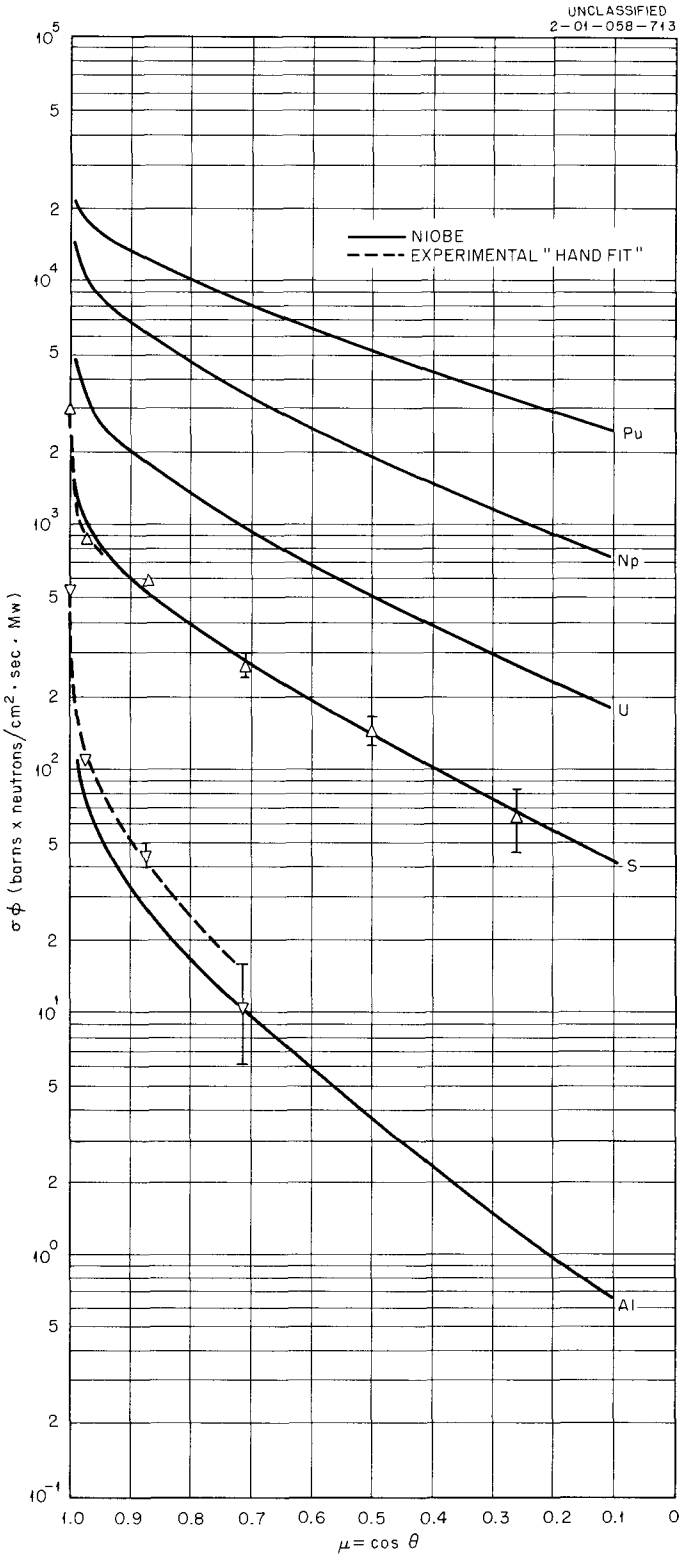

Fig. 6.18.5. $\sigma\phi$ as a Function of μ for 45-cm-Thick Lithium Hydride Slab with Precollimator.

lithium hydride slab and the 1-m precollimator because of the small mass of each of these foils. The height of the measured aluminum points, relative to the sulfur points, again is indicative of a spectrum slightly harder than that given by NIOBE.

It is interesting to note in Figs. 6.18.4 and 6.18.5 that NIOBE predicts an angular distribution from $\mu = 0.946$ to 0.095 that is invariant with depth of penetration in the lithium hydride. Only the $\mu = 0.989$ results differ. (NIOBE gives no value for $\mu = 0$ because of computational difficulties.) Thus, at angles far from those where the relatively small source is viewed, the angular distribution is invariant with depth of penetration. The experimental results, which are of a finer mesh in $\mu = 1$, give an angular distribution that is invariant with penetration depth for angles from 15 to 75° ($\mu = 0.97$ to 0.26). This is in agreement with the two-component theory of neutron penetration of Moteff;[16] the forward component, called the collimated component, has a strong forward peaking while the diffuse component is given as $\phi(\mu) \sim (1 + 5.5\mu^2)$. This function fits the Pu^{240} foil activation data fairly well, but the Np^{237} and U^{238} foil data are better fitted by a $(1 + 10\mu^2)$ angular distribution. For sulfur and aluminum, the $(1 + k\mu^2)$ function gives a much poorer fit for any value of k. For all angular distributions, a much better fit would be obtained with a $(1 + k_1\mu + k_2\mu^2)$ function and, better yet, with an expression of the form $(k_1 e^{\mu} + k_2 e^{2\mu})$.

Finally, a run was made with a 30° wedge placed atop the 45-cm-thick lithium hydride slab with no precollimator in position. The wedge had the orientation shown in Fig. 6.18.1. The experimental points obtained with sulfur and aluminum detectors are plotted, along with those obtained without the 30° wedge, in Fig. 6.18.6. The two runs are normalized at $\mu = 1$ for the sulfur detector. There is evidence of a flattening of the angular distribution, but it is small. If the experimental points are moved bodily to the right, from $\mu = 1$ to 0.866 (30°), and renormalized, the data at larger angles fit the curve for the no-wedge case slightly better. But the $\phi(\mu)$ curve is rather straight at these angles. Furthermore, the error bars are large here. Therefore, it can only be concluded that there is no disagreement with the expectation that the "tilt" of the wedge shifts the angular distribution of the diffuse component by 30°.

Conclusions

Fission-foil threshold detectors must be used with caution in conjunction with low-Z neutron shields, because the photofission can predominate at deep penetrations (35 to 40 cm). The experiments employing the geometry wherein a collimator mocks up a rather "good geometry" NIOBE calculation show remarkably good agreement with the calculations. The attenuations are also in fair agreement. In these readily calculable experiments, there is evidence of a harder spectrum than that given by the NIOBE code.

The angular distribution of emergent neutrons exhibits a distinct dichotomy: a collimated component appears at angles that "view" the source, and a diffuse component appears at larger angles. The angular distribution of this diffuse component, $\phi(\mu, E_0)$, is invariant with penetration depth after a few decimeters of penetration and is of the form $\phi(\mu, E_0) = (k_1 e^{\mu} + k_2 e^{2\mu})$, where k_1 and k_2 begin increasing rapidly with E_0 above about 4 Mev but vary slowly below this energy.

[16] John Moteff, Nuclear Materials and Propulsion Operations, General Electric, Cincinnati 15, Ohio, private communication.

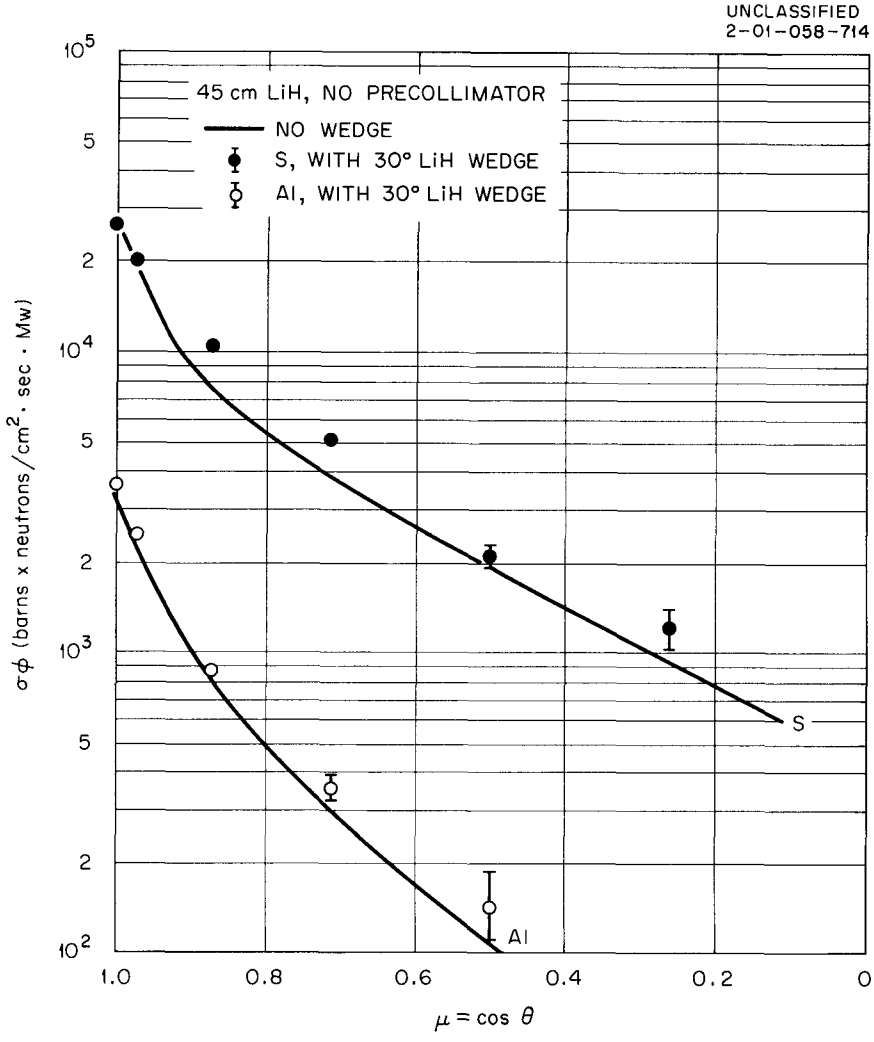

Fig. 6.18.6. $\sigma\phi$ as a Function of μ for 45-cm-Thick Lithium Hydride Slab with No Precollimator (With and Without Wedge).

6.19. SHIELDING AGAINST PROMPT WEAPONS RADIATION

L. B. Holland, V. R. Cain, R. E. Maerker, H. E. Stern,
F. H. Clark, J. L. Hull, J. J. Manning, and D. R. Ward

Experiments and parallel calculations relating to the penetration of prompt weapons radiation into shielded and open underground configurations have been carried out. The source of radiation was the approximately spherically symmetrical Tower Shielding Reactor II (TSR-II) operated in air at various positions. In order to make the reactor radiation leakage similar to that from a weapon, a thin modifying shield, identified as COOL-I and shown in Fig. 6.19.1, was used. The underground installations for which radiation levels were to be studied were simulated by vertical concrete-lined cylindrical holes, 4 ft in diameter and 20 ft in depth, dug in the ground at distances of 53, 161, and 435 ft from the reactor pool, as shown in Fig. 6.19.2. The uppermost 3 ft of each hole was recessed to a square cross section, 6×6 ft, to accommodate square slabs. The covering shield for the hole was simulated by one or more slabs of shielding material (iron or concrete) which were placed in the recessed region. In order to make the top of the shield flush with the ground, an appropriate thickness of concrete spacer slabs with centered 4-ft-diam circular holes was first inserted in the recessed area. These items are shown in Fig. 6.19.3.

A vertical traversing mechanism was constructed to move a detector along a vertical line in the hole, either on the axis or on any of several selected vertical lines parallel to the axis. Neutrons were measured by means of a Hurst recoil-proton proportional-counter dosimeter. Gamma-ray dose rates were measured with an anthracene scintillation detector.

The configurations studied are summarized in Table 6.19.1, and the terminology describing the geometry of the various measurements is given in Fig. 6.19.4. It will be noted that most of the shields studied were concrete but that some configurations included iron as well. Where no shield is indicated, measurements were made in the open hole with the spacer slabs extending up to the ground level.

The measurements in Hole No. 1 were all made with the reactor at a distance ρ of 100 ft from the top center of the cylindrical hole. This was accomplished by moving the reactor in the vertical plane which includes its two hoisting sheaves. For the measurements in Hole Nos. 2 and 3, the reactor was raised in a vertical line over its storage pool.

Measurements with Hole No. 1 were the most revealing as regards the effect of the angle of elevation of the radiation source. This was, of course, the only hole for which the direct overhead position was available. Typical of the data for the open hole are those given in Fig. 6.19.5, which shows the gamma-ray dose rate versus reactor angle of elevation at various distances down along the axis of the hole. These distances are given in terms of diameters (that is, $l/D = 3$ means that the measurement was taken at $3 \times 4 = 12$ ft from the ground level). It is interesting to note that the gamma-ray intensities in this figure can be understood, for those cases in which the reactor is not directly visible from the detector location, on the basis that the radiation observed is capture gamma rays produced in the walls of the hole. Allowance must of course be made for the variation with reactor elevation angle of the spatial distribution of capture gamma-ray production in the hole wall.

In Fig. 6.19.6 similar data are shown for the case in which Hole No. 1 is covered by a 6-in.-thick concrete shield. Here the capture gamma-ray source is of course in the covering shield itself, and it will be noted that the attenuation with depth is accordingly somewhat different.

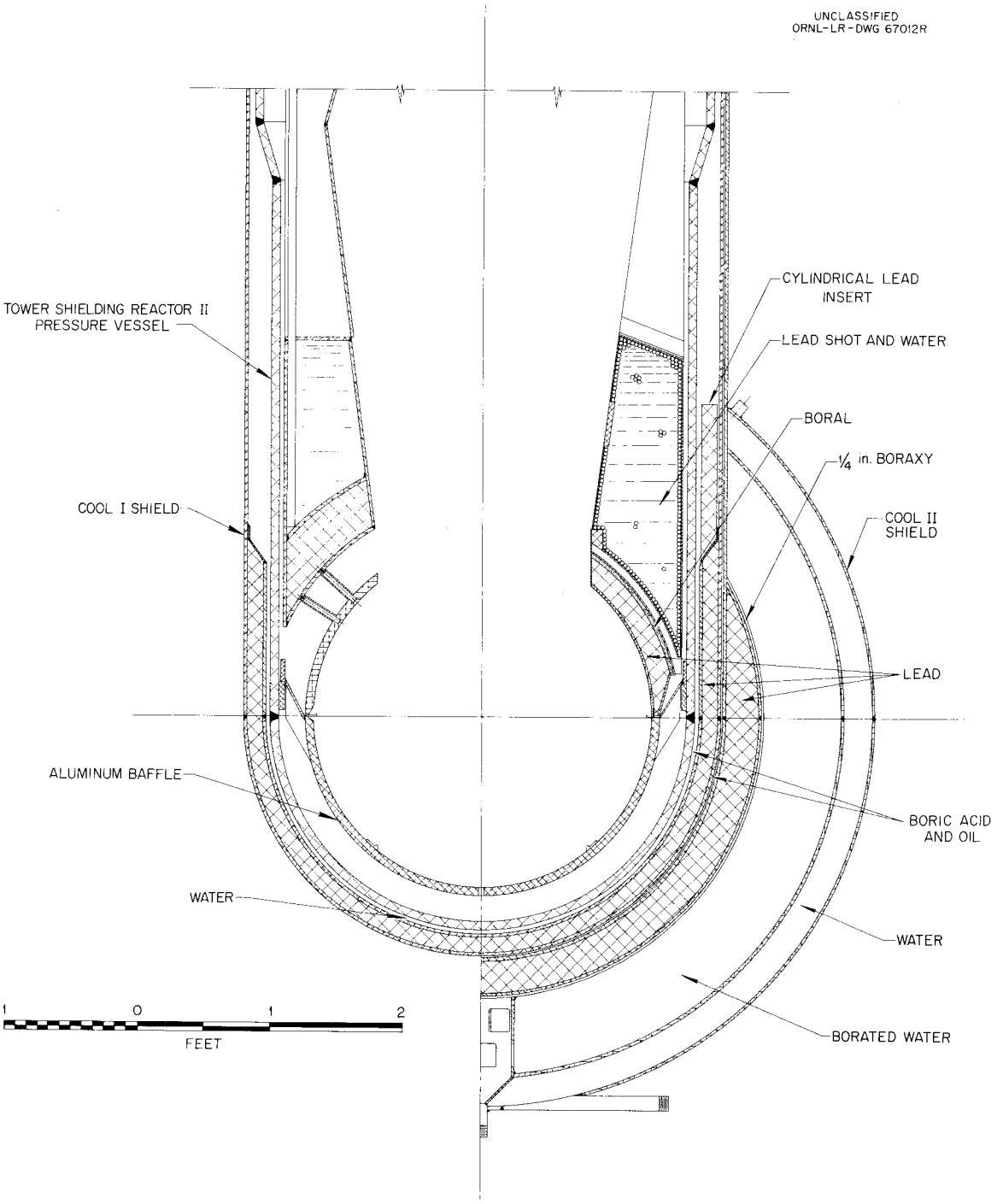

Fig. 6.19.1. COOL-I Shield for Tower Shielding Reactor II.

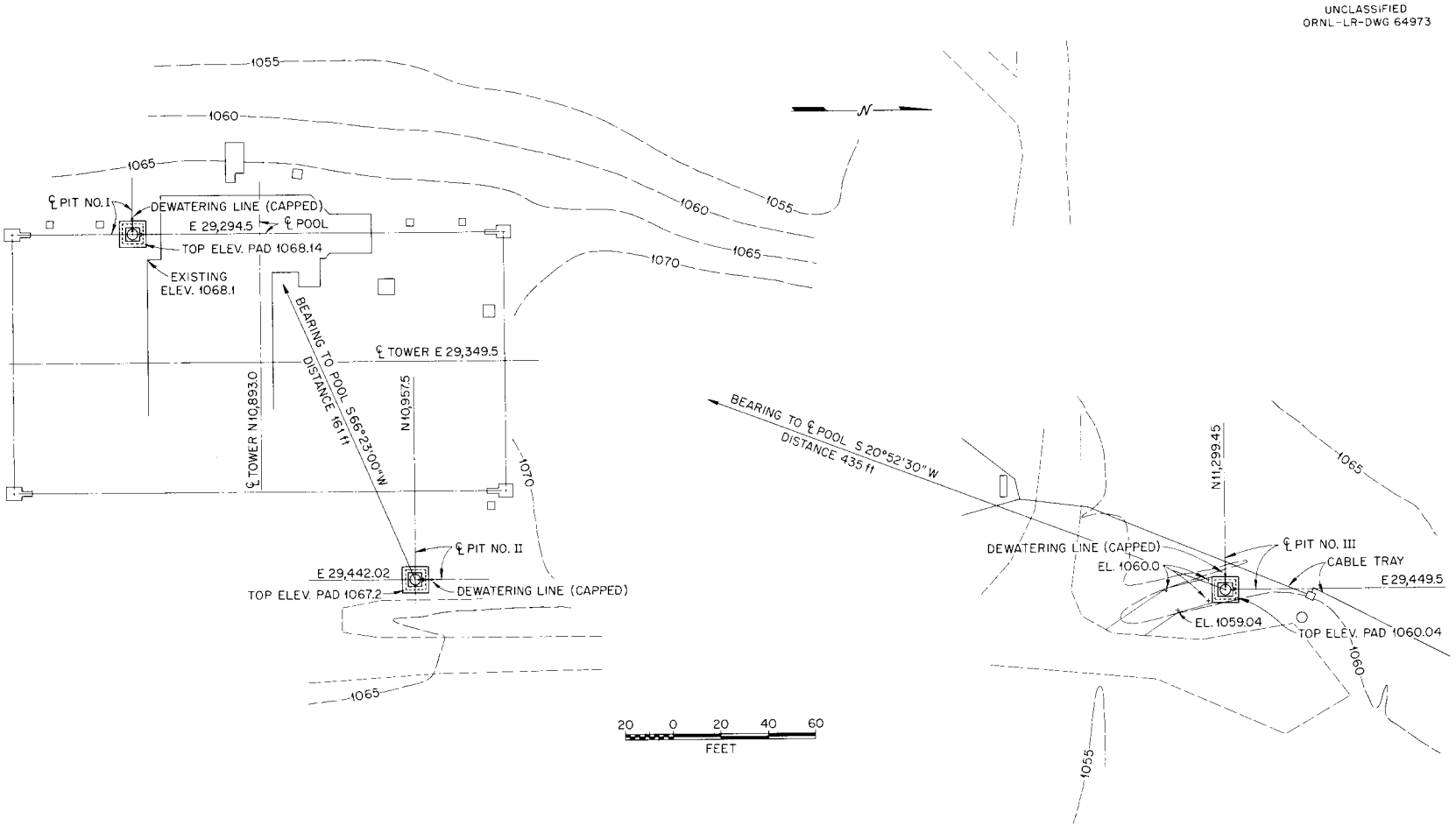

Fig. 6.19.2. Relative Positions of Cylindrical Holes (Pits) at TSF Site.

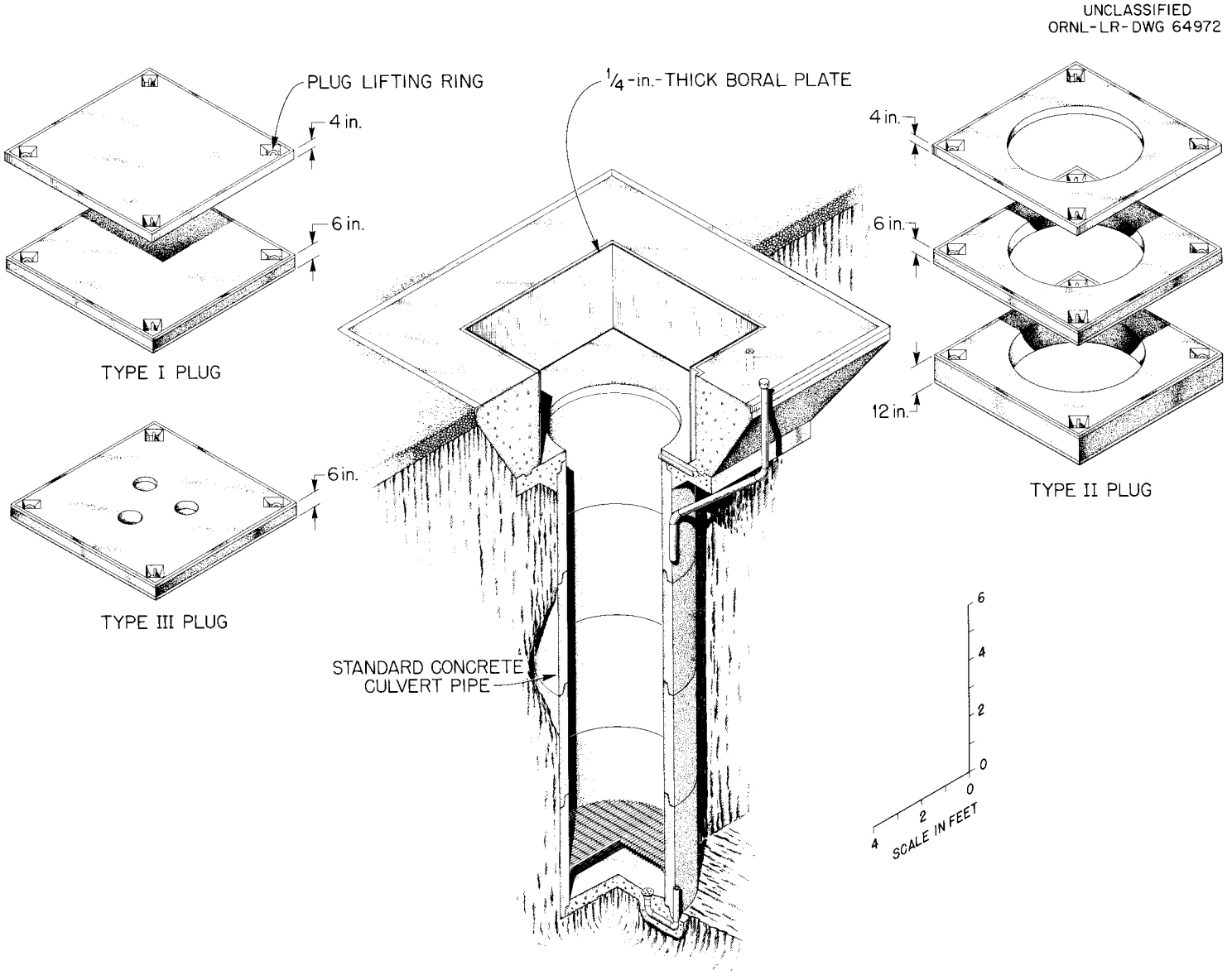

Fig. 6.19.3. Concrete-Lined Cylindrical Holes and Covers.

Table 6.19.1. Configurations Measured

Shield			γ (deg)	r (ft)	η (deg)
Upper Fe (in.)	Concrete (in.)	Lower Fe (in.)			
			Hole No. 1		
0	0	0	15,[a] 30, 45,[b] 60,[b] 90[b]	0	
	3	0	15, 30, 45, 60[b]	0	
	6	0	15, 30, 45, 60, 90	0	
			15	1	0
					90
					180
				1½	0
					90
					180
	12	0	15, 45,[a] 60, 90	0	
	18	0	15, 30, 45, 60	0	
	24	0	15, 45	0	
	30	0	60, 90	0	
3.5	0	0	15, 45	0	
	6	0	15, 45	0	
	12	0	15, 45	0	
	6	1.5	15, 45	0	
	15	1.5	15, 45	0	
	6	3.5	15, 45	0	
	15	3.5	15, 45	0	
	3	1.5	15, 45	0	
	9	1.5	15, 45	0	
	3	3.5	15, 45	0	
	9	3.5	15, 45	0	
0	0	0	15	1	0
				1.5	0
1.5	0	0	5	0	
3.5	12	1.5	15, 45	0	
		3.5	15, 45	0	
	3	0	15, 45	0	
0	36	0	15, 45	0	
			Hole No. 2		
0	6	0	45	0	
	18	0	45	0	
3.5	15	1.5	45	0	
0	0	0	45	1	0
				1.5	0
					180
	3	0	45	0	

Table 6.19.1 (continued)

Shield			γ	r	η
Upper Fe (in.)	Concrete (in.)	Lower Fe (in.)	(deg)	(ft)	(deg)
		Hole No. 2 (continued)			
0	30	0	45	0	
	15	3.5	45	0	
	0	0	45	0	
	12	0	45	0	
	24	0	45	0	
1.5	0	0	45	0	
5	0	0	45	0	
7	0	0	45	0	
		Hole No. 3			
0	0	0	15	0	
	6	0	15	0	
	12	0	15	0	
3.5	6	1.5	15	0	
		3.5	15	0	
	15	3.5	15	0	
0	3	0	15	0	
3.5	0	0	15	0	
	15	3.5	15	0	
7	0	0	15	0	
5	0	0	15	0	
1.5	0	0	15	0	

[a] Gamma-ray data not available.
[b] Neutron data not available.

Of considerable interest in studying the protection afforded by structures against weapons radiation is an estimate of the angular distribution of radiation leaving the inside shield surface. It is possible to study this angular distribution in terms of the variation of the dose with depth in the hole on the assumption that scattering from the walls of the hole is not a significant effect. In Fig. 6.19.7 the variation of the gamma-ray dose rate with depth is shown for a variety of concrete shield thicknesses. It will be seen that in general the gamma rays are more isotropic for the thicker shields for the case in which the source is directly overhead. Figure 6.19.8 shows the data for the case in which the source is at an elevation angle of 45°, so that the detector cannot see the source below an l/D of about 1. For this case the gamma rays enter the hole nearly isotropically whether it is shielded or not. Except for the case of near normal incidence, the radiation varies more or less as the square of the cosine of the exiting polar angle for concrete shields up to 9 in. thick, as the cube for thicknesses between 9 and 30 in., and as the fourth power for thicknesses between 30 and 42 in. For the laminated iron and concrete shields the angular distribution is somewhat more peaked toward the normal.

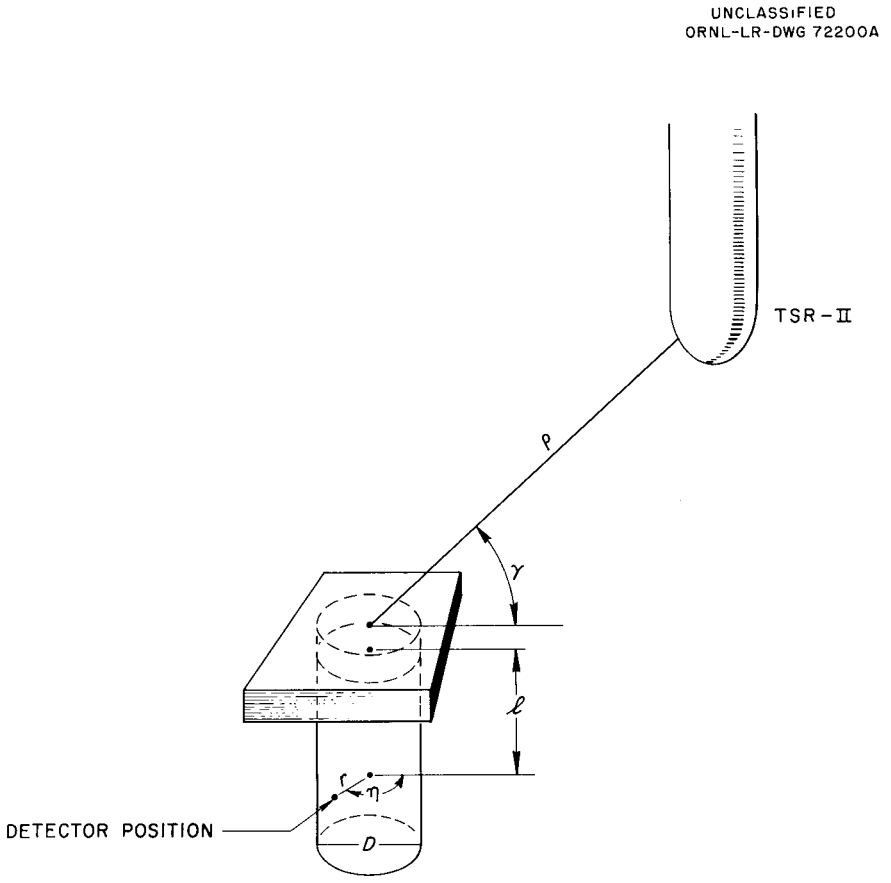

Fig. 6.19.4. Geometrical Parameters for TSF Measurements.

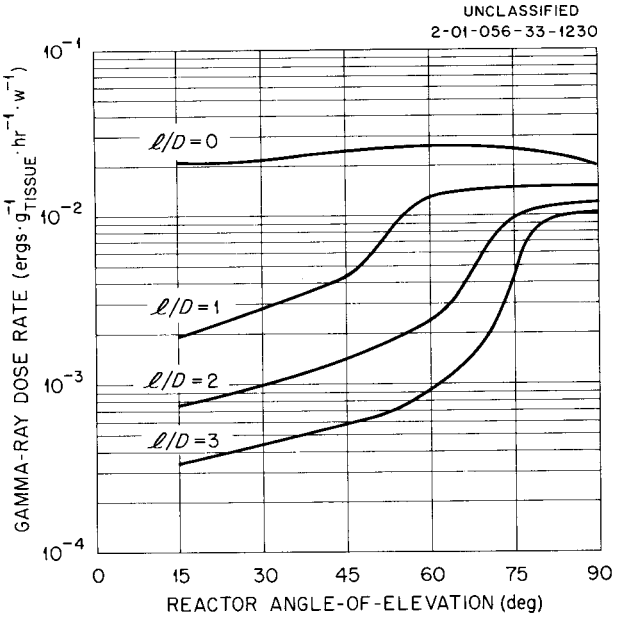

Fig. 6.19.5. Gamma-Ray Dose Rate in Hole No. 1 as a Function of Reactor Angle of Elevation: Open Hole.

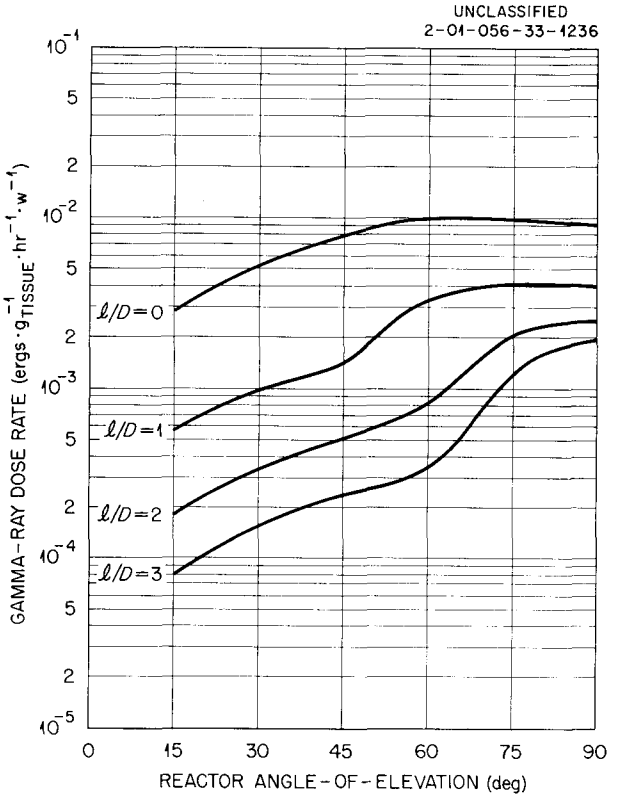

Fig. 6.19.6. Gamma-Ray Dose Rate in Hole No. 1 as a Function of Reactor Angle of Elevation: 6-in. Concrete Shield.

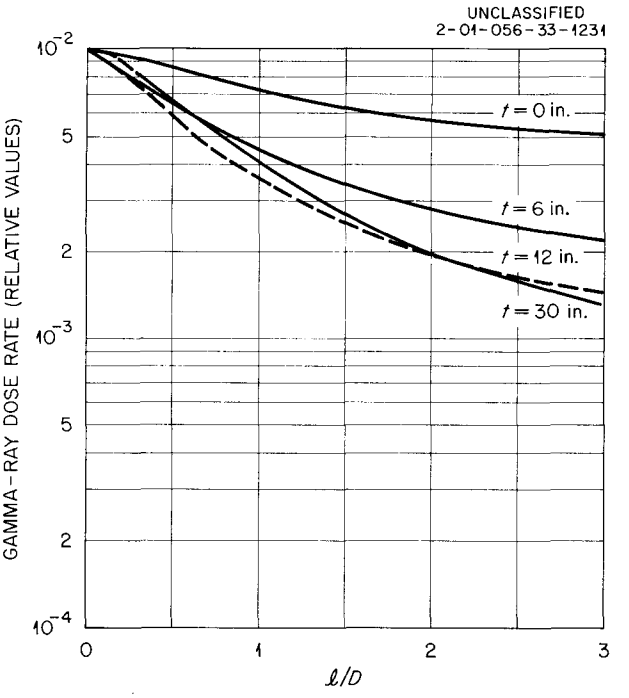

Fig. 6.19.7. Gamma-Ray Dose Rate in Hole No. 1 as a Function of l/D for Various Concrete Shield Thicknesses: $\gamma = 90°$.

Figure 6.19.9 shows the gamma-ray attenuation in concrete for several angles of elevation. Several interesting conclusions can be drawn from this figure. In the first place the variation with concrete thickness is very nearly the same for all angles of elevation, which indicates that the real source being observed is capture gamma rays produced in the first layers of concrete. Second, the intensity varies somewhat more strongly than the sine of the angle of elevation. This can be explained in part from the lower radiation leakage from the upper hemisphere of the reactor and in part from the fact that for slant incidence the capture gamma rays are produced nearer the top shield surface.

Figure 6.19.10 shows neutron dose-rate attenuation in concrete at Hole No. 1 for several angles of elevation of the reactor. Again the attenuation is nearly the same for all angles of incidence, indicating the importance of scattered neutrons in penetration. The slightly steeper slope of the 15° curve can be explained on the basis of increased energy reduction (and hence greater subsequent attenuation) on scattering through large angles. Here again the relative intensities vary more than proportionally with the sine of the elevation angle and this may again be attributable to the reduced leakage from the reactor upper hemisphere.

Since all the concrete attenuations measured show nearly an exponential form, it is possible to derive a relaxation length (e-folding length) for all cases. These approximate values are shown in

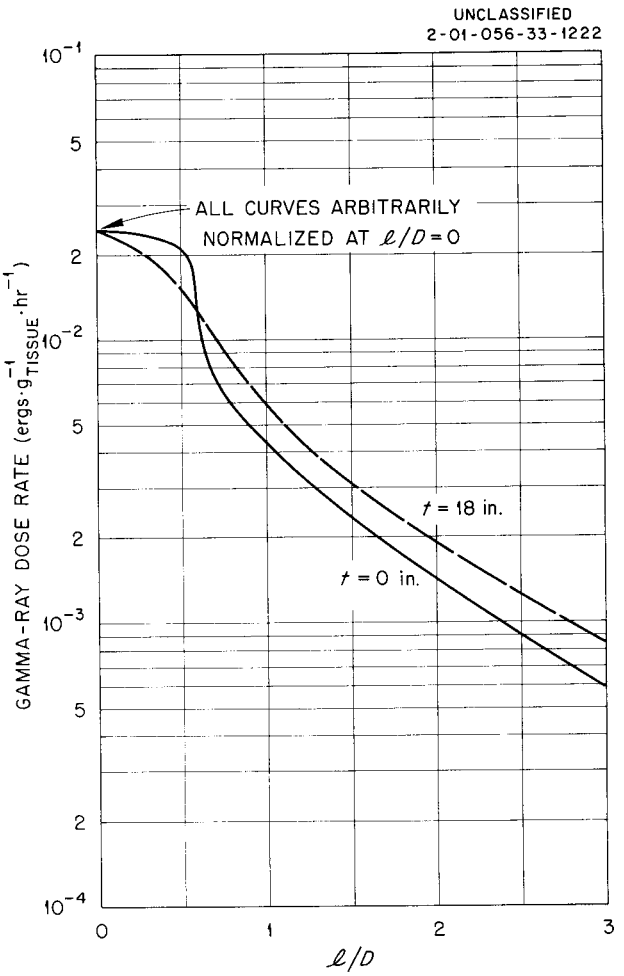

Fig. 6.19.8. Gamma-Ray Dose Rate in Hole No. 1 as a Function of l/D for No Concrete and for 18 in. of Concrete: $\gamma = 45^{\circ}$.

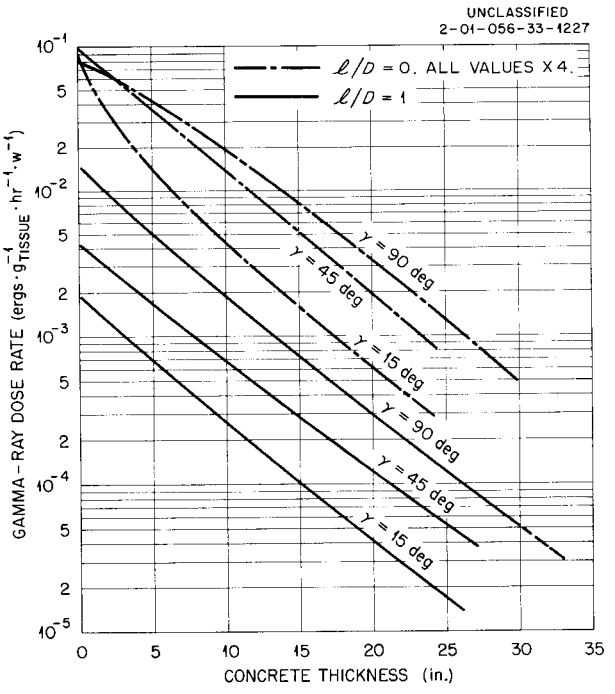

Fig. 6.19.9. Gamma-Ray Dose Rate in Hole No. 1 as a Function of Concrete Thickness for Various Reactor Angles of Elevation.

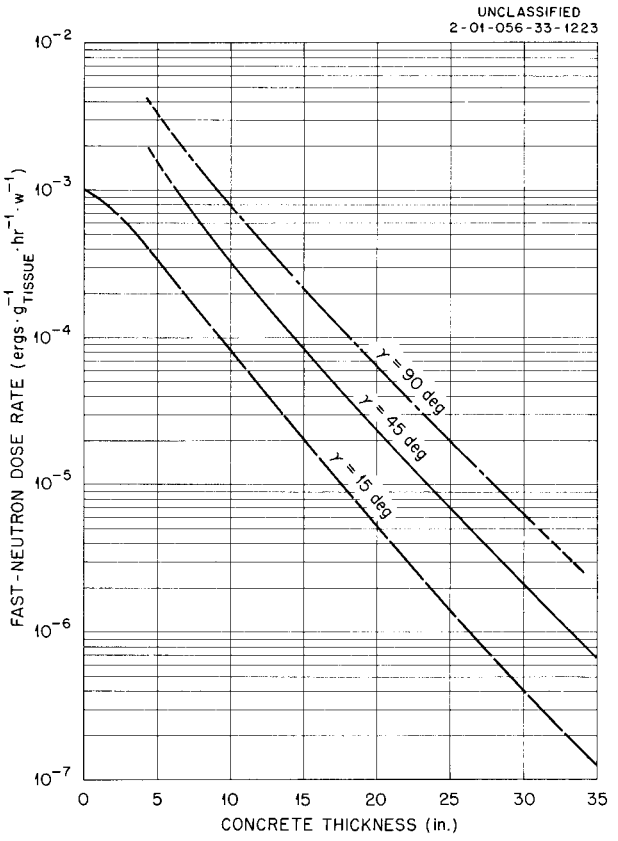

Fig. 6.19.10. Fast-Neutron Dose Rate in Hole No. 1 as a Function of Concrete Thickness for Various Reactor Angles of Elevation: $l/D = 1$.

Table 6.19.2. The neutron data agree very well with those obtained from removal cross-section calculations,[1] namely, 10.5 cm, and the gamma-ray dose is not inconsistent with the gamma-ray relaxation length for 6 Mev (that is, 15 cm).[1]

In an extension of these experiments, a horizontal tunnel, rectangular in cross section, was dug so that it was connected to Hole No. 1 with its top 10 ft below the ground level. It was 20 ft long and perpendicular to the vertical plane that included the reactor and the cylindrical hole axis. Measurements were made in this tunnel, mostly with no shield on top of the cylindrical hole, but in some cases with a thin shield in that location. These studies were intended to give information on the effect of a turn in a shelter entryway.

The calculations[2] which were performed for this investigation drew on certain results of the experiments, such as the variation of dose rate with depth in the hole, but in the main were intended to be independent of the experiment. They were, however, compared to them and adjusted before application to actual weapon burst cases.

---

[1]E. P. Blizard, in *Nuclear Engineering Handbook*, H. E. Etherington, Editor, p 7-112, McGraw-Hill Book Company, Inc., New York, 1958.

[2]E. P. Blizard, V. R. Cain, F. H. Clark, L. B. Holland, R. E. Maerker, and H. E. Stern, ORNL TM-253 (Aug. 30, 1962) (Classified).

Table 6.19.2. Relaxation Lengths for Concrete Shields

Elevation Angle (deg)	λ, Relaxation Length (cm)		
	Hole No. 1, ρ = 100 ft	Hole No. 2, ρ = 250 ft	Hole No. 3, ρ = 450 ft
	Neutrons		
90	11.0		
45	10.5	9.9	
15	9.6		9.3
	Gamma Rays		
90	13.8		
45	14.6	13.9	
15	14.0		13.5

The calculations comprised a synthesis of different methods. Penetration of the neutrons through the air in the presence of the ground interface was done by a Monte Carlo method. Angular distributions of neutrons so determined were used to obtain first collisions in the shield, and these first-collision points comprised the sources for moments-method calculations of further penetration. The dose at the lower face was obtained by integration over the first-collision point sources so attenuated. Since the moments method applies strictly only to infinite homogeneous media, corrections were needed for the finite geometry to which it was applied. To evaluate the effect of the lower boundary, O5R code[3] Monte Carlo calculations were made for finite and infinite concrete shields. A comparison of these results yields an estimation of the boundary effect. Other uncertainties, such as the effect of anisotropy of the first-collision sources, were more difficult to remove, and hence the calculations were performed for the TSF experiment geometry and compared with the experimental results. The calculated transmission factors for concrete were consistently higher, in one case by as much as a factor of 3.

Computations of the photon dose below the shield were divided into two classes: those treating photons which originate outside the shield and those treating shield secondary photons. The photons born outside the shield were dealt with by adapting and modifying calculations already available. General Dynamics/Fort Worth Monte Carlo calculations[4] were used both for computing the transmission of photons through air from a point source and for computing the transmission through air of secondary photons formed in air by neutrons from a point source; and NBS calculations[5] were used to determine the dose from the slant penetration of gamma rays through concrete. These methods permitted calculations

[3]R. R. Coveyou, J. G. Sullivan, and H. P. Carter, *Neutron Phys. Div. Ann. Progr. Rept. Sept. 1, 1958*, ORNL-2609, p 87.

[4]M. B. Wells, FZK 134-1 and FZK 134-2 (Dec. 1961) (Classified).

[5]L. V. Spencer and J. V. Lamkin, *Slant Penetration of Gamma Rays in Concrete*, NBS-6591 (Nov. 10, 1959).

of dose from gamma rays originating at the source point and from those stemming from neutron capture or neutron inelastic scattering in air.

The shield secondary photons were computed by assuming an exponential distribution of secondary events in the shield, a ray-tracing model of photon attenuation, and a two-exponential representation of the buildup factor. Secondary doses so computed were, in magnitude, consistent with TSF measurements and corresponded with measurements very well in shape of the dose versus depth curve as shown in Fig. 6.19.11.

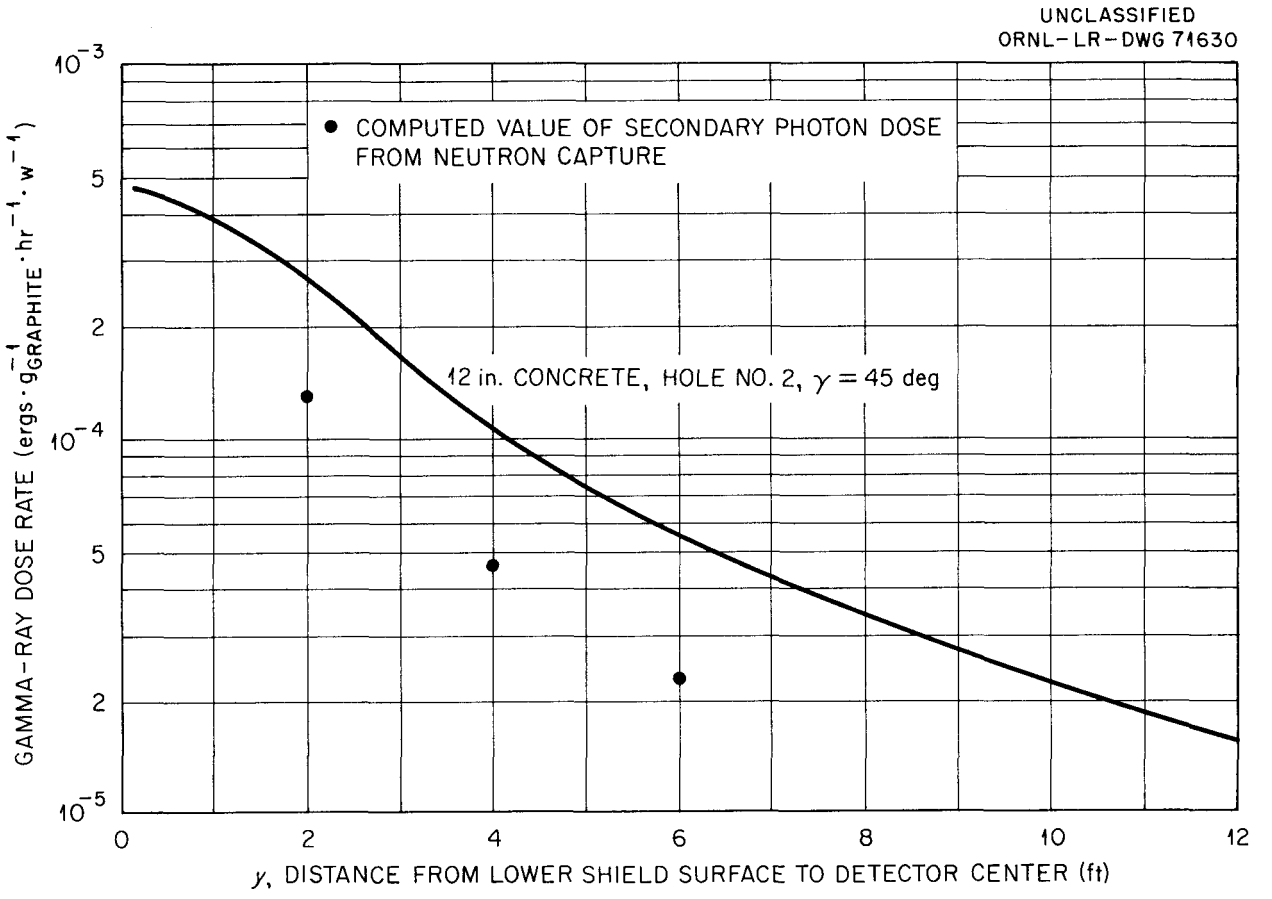

Fig. 6.19.11. Comparison of Computed TSF Shield Capture Gamma-Ray Dose Rate with Measured Total Dose Rate.

7. Shielding Against High-Energy Radiations

7.1. MONTE CARLO CALCULATIONS ON INTRANUCLEAR CASCADES FOR INCIDENT-PARTICLE ENERGIES FROM ABOUT 50 TO 350 Mev

H. W. Bertini

A code to calculate the reactions of high-energy particles with complex nuclei was described previously.[1,2] The code, which has been written for the IBM-7090 computer and treats incident nucleons and pions on any nucleus greater than helium, is now complete and is being used to obtain a large volume of data which will be illustrated in Sec. 7.2. This section consists of a brief review of the code and compares some of the calculated results with experimental data.

Nuclear Model and Cross-Section Data

In the nuclear model it is assumed that for incident-particle energies of the order of 50 Mev or higher, the reactions with complex nuclei can be described in terms of particle-particle events that take place inside the nucleus. Each event gives rise to other high-energy particles, which in turn make other collisions, and in this way a cascade develops inside the nucleus. These events can be calculated and the history of each particle involved can be traced by using free-particle empirical data and statistical sampling techniques.

The density distribution of nucleons inside the nucleus was made to approximate the continuously varying charge distribution obtained by Hofstadter.[3] This was done by taking three concentric spheres, one nested inside the other, with individual uniform densities such that the proton density in each sphere or region corresponded to the average value of the continuous charge distribution over the same region. The region boundaries applied to neutrons as well, and the ratio of the neutron to proton density in each region was taken to be the same as the ratio of the total number of neutrons in the nucleus to the total number of protons. A few calculations were made with a constant nucleon density distribution used throughout the nucleus to determine its effect. These considerations are illustrated in Fig. 7.1.1.

In each region the nucleons were assumed to have a zero-temperature Fermi energy distribution. The binding energy of the loosest nucleon was assumed to be constant, 7 Mev, for all regions and all nucleons. The potential for nucleons inside the nucleus was taken to be 7 Mev plus the zero-temperature Fermi energy in each region. This is illustrated in Fig. 7.1.2 for a typical case.

---

[1] H. W. Bertini and C. D. Zerby, *Neutron Phys. Div. Ann. Progr. Rept. Sept. 1, 1960*, ORNL-3016, p 235.

[2] H. W. Bertini, *Neutron Phys. Div. Ann. Progr. Rept. Sept. 1, 1961*, ORNL-3193, p 323.

[3] R. Hofstadter, *Rev. Mod. Phys.* **28**, 214 (1956).

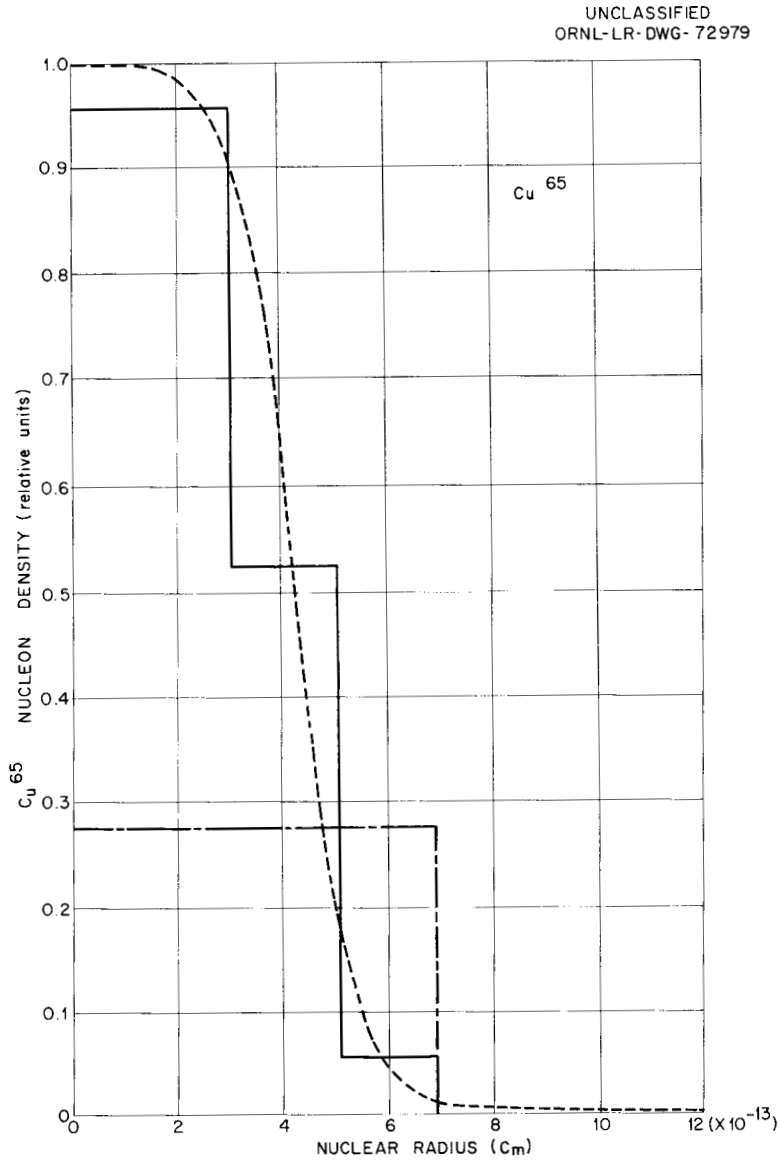

Fig. 7.1.1. Nucleon Density Distributions Within the Nucleus When the Nuclear Radius Is Assumed To Be Small. Solid lines: nonuniform distribution; dot-dashed lines: uniform distribution; dotted lines: Hofstadter's curve [*Rev. Mod. Phys.* **28**, 214 (1956)].

The total free-particle cross sections that were used are illustrated in Figs. 7.1.3–7.1.5. The differential cross sections for nucleon-nucleon collisions were taken from the work of Hess,[4] Beretta *et al.*,[5] and Hughes and Schwartz.[6] The differential cross sections for pion-nucleon collisions were calculated by using the phase shifts of Orear.[7] From the results of these calculations the exchange scattering cross sections and

[4]W. N. Hess, *Rev. Mod. Phys.* **30**, 368 (1958).

[5]L. Beretta, C. Villi, and F. Ferrari, *Nuovo Cimento* **12**, S-499 (1954).

[6]D. J. Hughes and R. B. Schwartz, *Neutron Cross Sections*, BNL-325 (1958).

[7]J. Orear, *Phys. Rev.* **100**, 288 (1955).

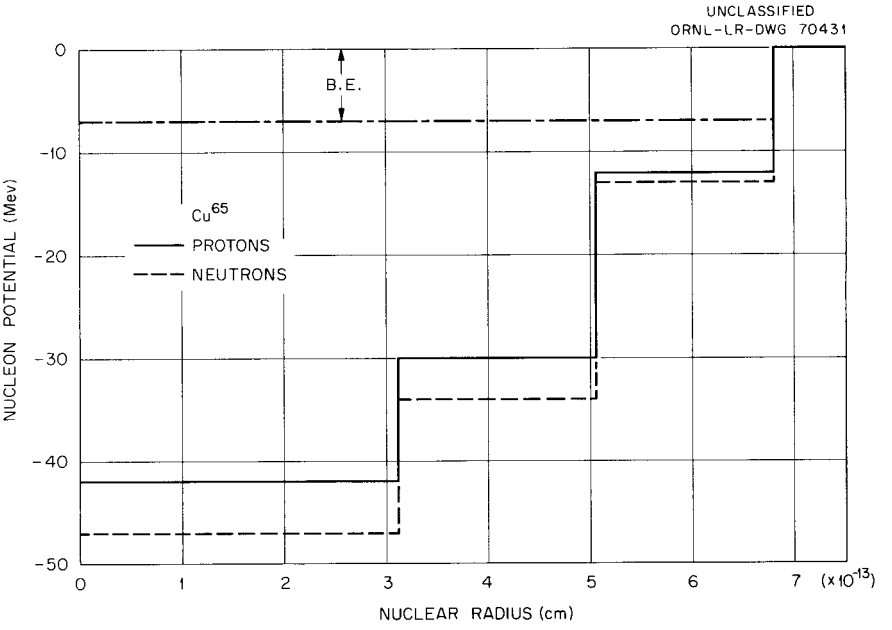

Fig. 7.1.2. Nucleon Potential vs Nuclear Radius for a Typical Nucleus. "B. E." is the fixed binding energy of the most loosely bound nucleon.

the π^0 cross sections could be deduced with the results given in Fig. 7.1.6. The numerical work of Metropolis *et al.*[8] was used for the pion-absorption cross section. This reaction was assumed to take place with two-particle nucleon clusters inside the nucleus. All the cross-section data were tabulated at every 20-Mev interval.

The basic sampling technique for determining the point of collision, type of collision, and momentum of the struck particle was that described by Zerby *et al.*[9]

Comparison with Experiment: Incident Nucleons

Table 7.1.1 contains comparisons of calculated total nonelastic cross sections with experimental data, and Table 7.1.2 comparisons of the average excitation energy of the residual nucleus with calculations based on experiment. In both cases the agreement is quite good.

Figures 7.1.7 and 7.1.8 illustrate the cascade particle spectra in the forward direction for low-energy incident protons. The comparison for carbon, Fig. 7.1.7, shows one of the apparent deficiencies of the model. At higher energies this serious discrepancy in the shape of the spectrum in the forward direction is no longer manifest, as is shown in Figs. 7.1.9 and 7.1.10.

In Figs. 7.1.11–7.1.13 some comparisons at other angles are illustrated. The high-energy peaks in the experimental spectrum are due to elastic scattering, and the comparisons should be made at the energies below the peaks. Other comparisons, illustrated in Figs. 7.1.14–7.1.21, indicate low-energy peaks in

---

[8]N. Metropolis *et al.*, *Phys. Rev.* **110**, 204 (1958).

[9]C. D. Zerby, R. B. Curtis, and H. W. Bertini, *The Relativistic Doppler Problem*, ORNL CF-61-7-20 (July 12, 1961).

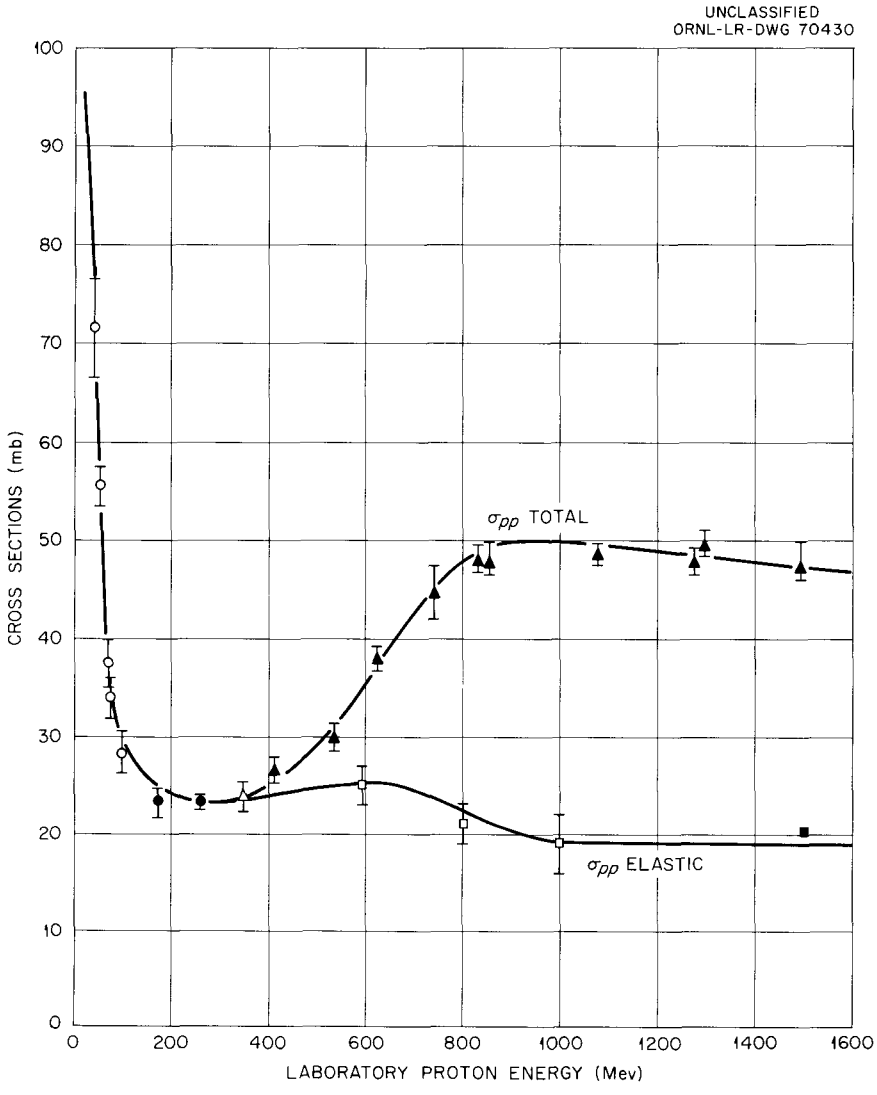

Fig. 7.1.3. Proton-Proton Total and Elastic Cross Sections vs Energy.

○ U. E. Kruse, J. M. Teem, and N. F. Ramsey, *Phys. Rev.* **101**, 1079 (1956).
● O. Chamberlain and J. D. Garrison, *Phys. Rev.* **95**, 1349 (L) (1954).
△ O. Chamberlain, E. Segrè, and C. Wiegand, *Phys. Rev.* **83**, 923 (1951).
▲ F. F. Chen, C. P. Leavitt, and A. M. Shapiro, *Phys. Rev.* **103**, 211 (1956).
□ L. W. Smith, A. W. McReynolds, and G. Snow, *Phys. Rev.* **97**, 1186 (1955).
■ W. B. Fowler *et al.*, *Phys. Rev.* **103**, 1479 (1956).

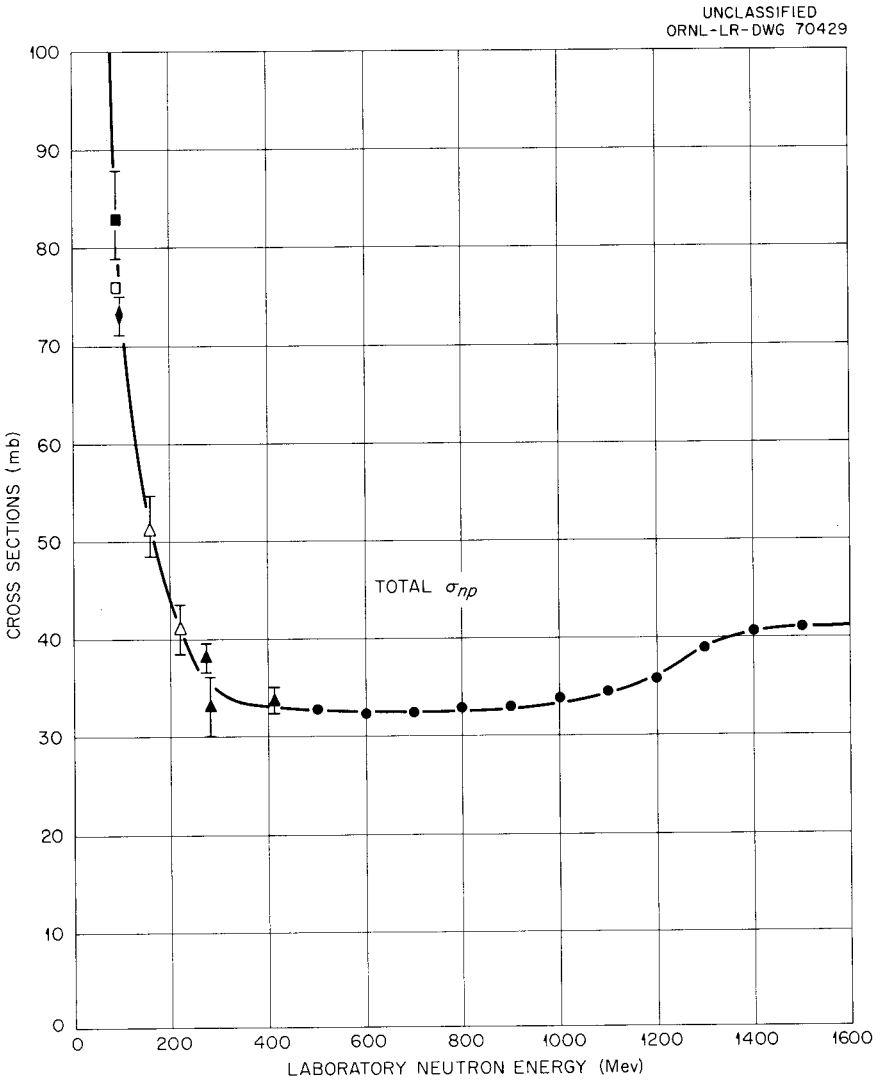

Fig. 7.1.4. Neutron-Proton Total Cross Sections vs Energy.

■ L. J. Cook *et al.*, *Phys. Rev.* 75, 7 (1949).
□ J. Hadley *et al.*, *Phys. Rev.* 75, 351 (1949).
⧫ J. DeJuren and N. Knable, *Phys. Rev.* 77, 606 (1950).
△ J. DeJuren and B. J. Moyer, *Phys. Rev.* 81, 919 (1951).
▲ A. V. Nedzel, *Phys. Rev.* 94, 174 (1954).
● F. F. Chen, C. P. Leavitt, and A. M. Shapiro, *Phys. Rev.* 103, 211 (1956).

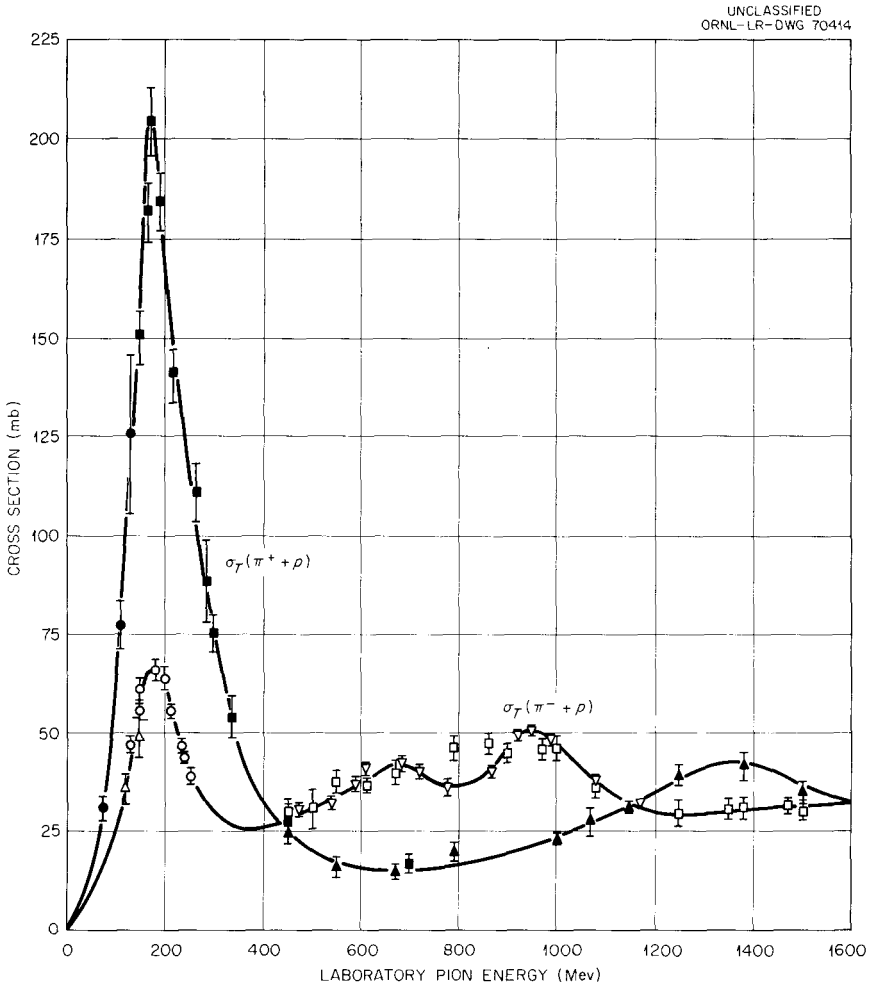

Fig. 7.1.5. π^+-Proton and π^--Proton Total Cross Sections vs Energy.

●,△ H. L. Anderson *et al.*, *Phys. Rev.* **91**, 155 (1953).
■ S. J. Lindenbaum and L. C. L. Yuan, *Phys. Rev.* **100**, 306 (1955).
▲,□ R. Cool, O. Piccioni, and D. Clark, *Phys. Rev.* **103**, 1082 (1956).
○ J. Ashkin *et al.*, *Phys. Rev* **96**, 1104 (1954).
▽ H. C. Burrowes *et al.*, *Phys. Rev. Letters* **2**, 119 (1959).

some of the experimental results. These peaks are caused by nuclear evaporation, and the comparisons should be made at energies greater than about 15 Mev since evaporation is not included in the calculation. Comparisons with some of the data on emulsions are given in Figs. 7.1.22–7.1.25. Except for incident nucleon energies below 100 Mev on light- to medium-weight nuclei for particles emitted forward, the calculations indicate excellent agreement with experiment for emitted cascade particles. The angular distributions for a few reactions are given in Figs. 7.1.26–7.1.28.

The calculations are compared with some experimental data on cascade particle multiplicities in Table 7.1.3. Although the agreement is not bad, the calculation does not predict the symmetry that was observed in the experiments for neutron-induced and proton-induced reactions.

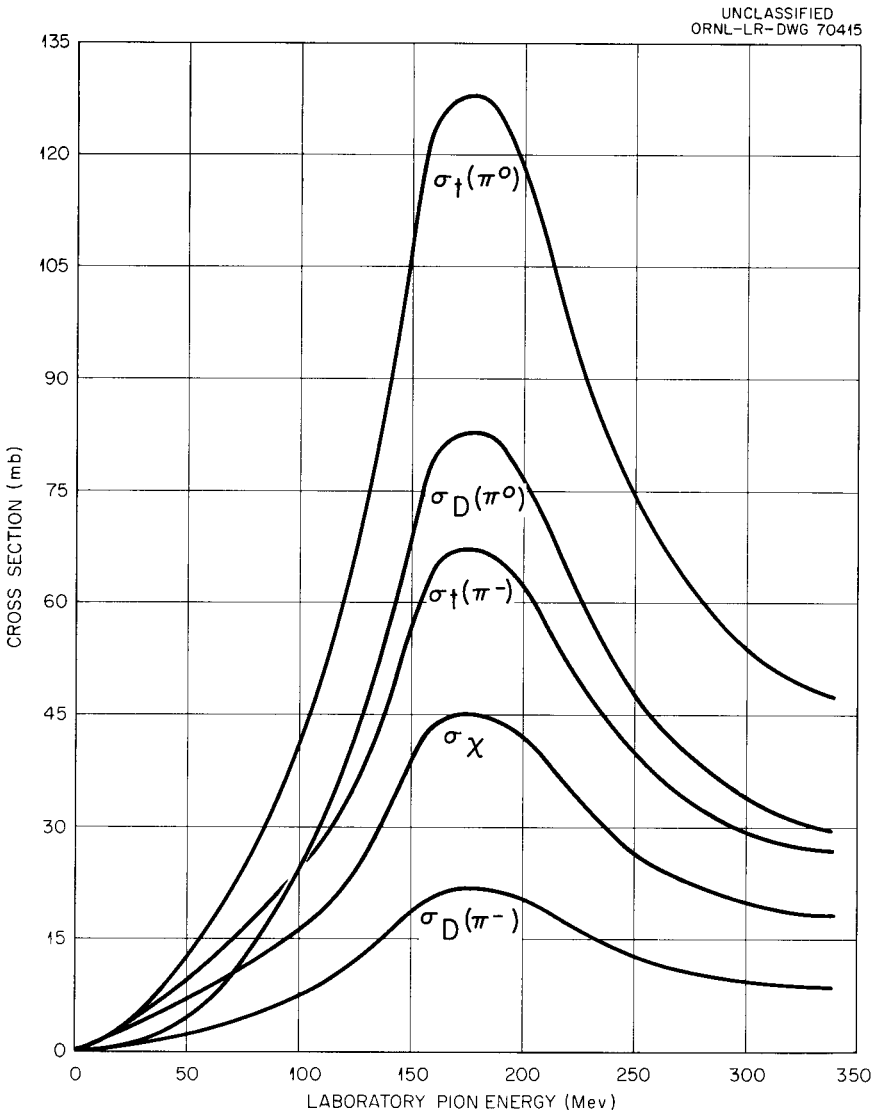

Fig. 7.1.6. Calculated Pion-Proton Cross Sections vs Pion Energy.

$\sigma_t(\pi^0)$ Total cross section for $\pi^0 + p$ scattering.
$\sigma_D(\pi^0)$ Cross section for $\pi^0 + p$ direct scattering.
$\sigma_t(\pi^-)$ Experimental $\pi^- + p$ total cross section included for comparison purposes.
σ_x Cross section for $\pi^- + p$, $\pi^+ + n$, $\pi^0 + p$, and $\pi^0 + n$ exchange scattering.
$\sigma_D(\pi^-)$ Cross section for $\pi^- + p$ direct scattering.

Comparison with Experiment: Incident Pions

The comparison of calculated nonelastic cross sections for incident pions with experimental data is given in Table 7.1.4. The agreement is not quite so good as that for incident nucleons.

The energy spectra of nonelastically scattered pions into various angular intervals are shown in Figs. 7.1.29–7.1.33. The agreement is not bad although all the comparisons for these data are on a relative basis.

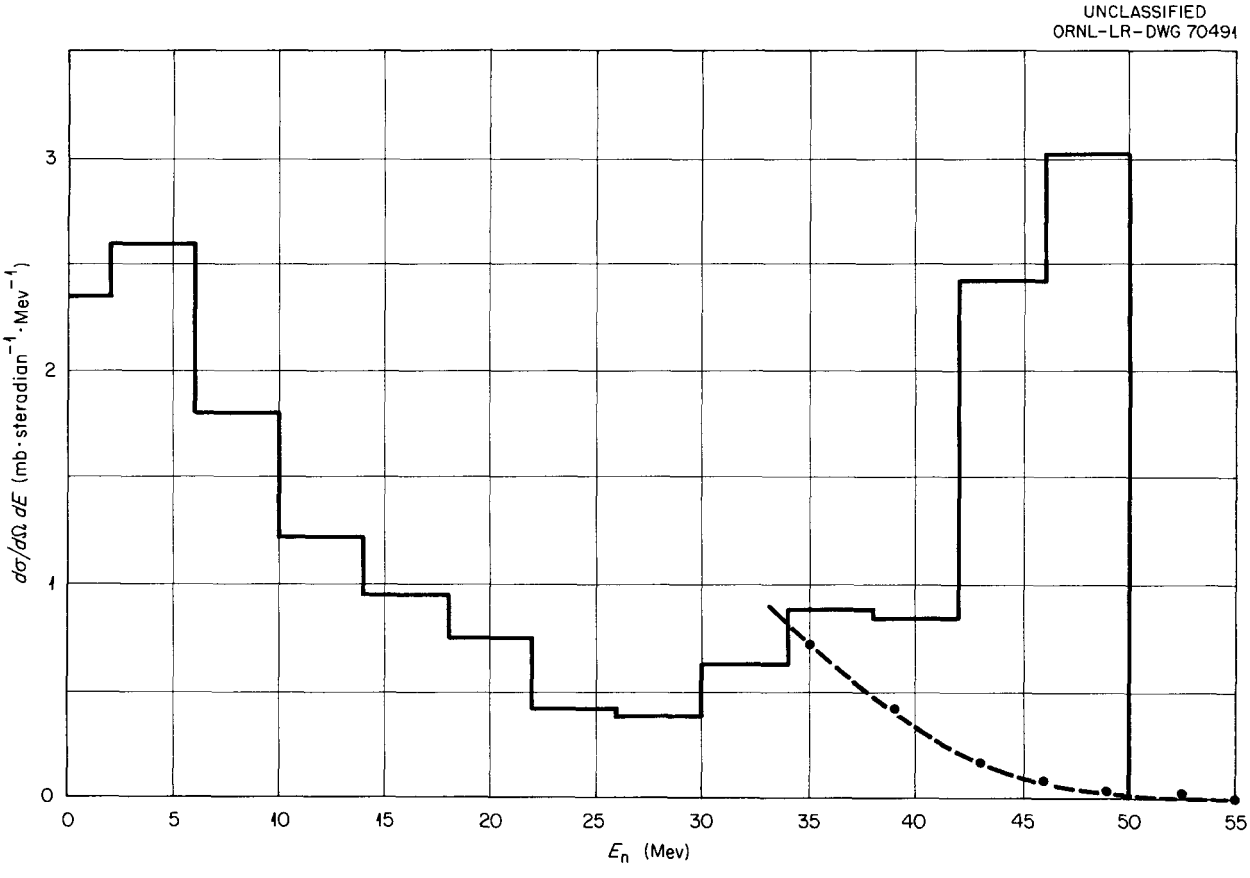

Fig. 7.1.7. Neutron Spectra at 0° from 50-Mev Protons on Carbon. Dotted curve: Hofmann's experimental results (*Neutrons Ejected from Nuclei by 50 Mev Protons*, Ph. D. Thesis submitted to the Faculty of Arts and Sciences of Harvard University, Cambridge, August 1952); solid lines: calculated spectrum for neutrons emitted in the angular interval 0 to 11°.

A discrepancy between the calculated data and experiments exists for nonelastic scattering at right angles and in the backward direction, as is illustrated in Figs. 7.1.34 and 7.1.35 for two different nuclear configurations. This discrepancy was observed when previous calculations of this type[8] were compared with the data obtained from use of a smaller radius nuclear model with a constant nucleon density.

The data from emulsion work are compared in Figs. 7.1.36 and 7.1.37; reasonable agreement is indicated. Other angular distributions are illustrated in Figs. 7.1.38–7.1.41. Here the calculation indicates the trends properly, but the agreement is not very good on an absolute basis.

The spectra from slow π^- absorption are compared with experimental results in Fig. 7.1.42 for a nucleus with a standard configuration and for one with a constant nucleon density distribution and a smaller nuclear radius ($r = 1.3 \times 10^{-13} A^{1/3}$). The agreement is fair and independent of nuclear configuration.

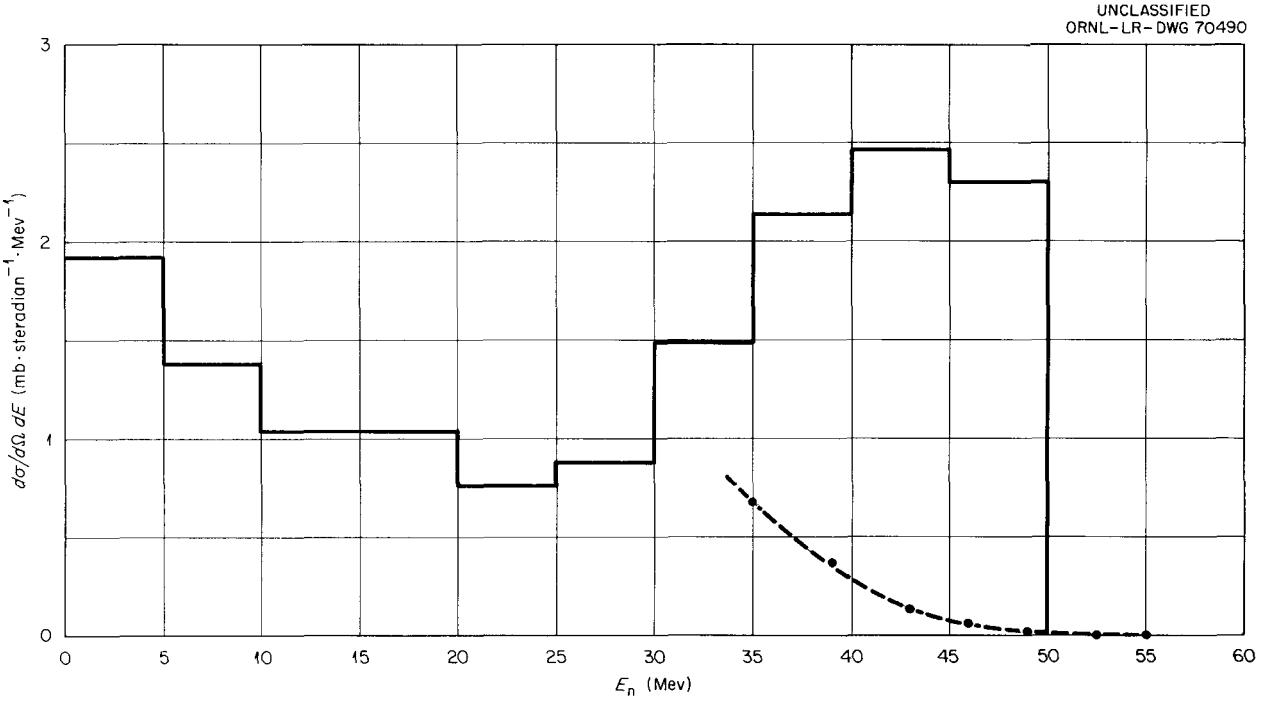

Fig. 7.1.8. Neutron Spectra at 16° from 50-Mev Protons on Carbon. Dotted curve: Hofmann's experimental results (*Neutrons Ejected from Nuclei by 50 Mev Protons*, Ph. D. Thesis submitted to the Faculty of Arts and Sciences of Harvard University, Cambridge, August 1952); solid lines: calculated spectrum for neutrons emitted in the angular interval 5 to 25°.

Calculated pion absorption and charge-exchange cross sections are compared with experimental values in Tables 7.1.5 and 7.1.6, respectively.

The agreement is reasonable for the absorption cross section but not very good for the charge-exchange cross section. This seems to be persistent and difficult to explain since the experiments imply a smaller cross section than the calculated values. However, the free-particle charge-exchange cross section is quite large.

In Table 7.1.7 the calculated and experimental charge-exchange plus absorption cross-section data are compared, and except for the last two entries the agreement is quite good.

Conclusions

This calculation seems to reproduce most of the experimental data for incident nucleons very well. The largest discrepancy is in the spectra of cascade particles emitted in the forward direction for small incident nucleon energies on light- to medium-weight nuclei.

The data for incident pions appear to represent the gross features of the experimental data, but they can not be used to predict detailed experimental data as well as the results for incident nucleons can be.

Table 7.1.1. Calculated and Experimental Nonelastic Cross Sections for Protons and Neutrons Incident on Various Nuclei

Incident Particle	Target	Energy (Mev)	Nonelastic Cross Section (mb)	
			Calculated[a]	Experimental[b]
Proton	Be	185	187 ± 7	172 ± 17
		305	176 ± 7	151 ± 15
	Al	185	417 ± 9	408 ± 41
		305	394 ± 11	334 ± 33
	Cu	170	795 ± 23	
		185		746 ± 75
		240	747 ± 23	667 ± 67
	U	185	1825 ± 38	1900 ± 190
		305	1754 ± 28	1600 ± 160
Neutron	Be	95	217 ± 7	210 ± 8[c]
	Al	84	502 ± 16	500 ± 50[d]
		300	383 ± 11	390 ± 23
	Cu	84	825 ± 23	910 ± 50[d]
		300	725 ± 16	755 ± 33
	Pb	84	1654 ± 26	1850 ± 180[d]
		300	1552 ± 27	1720 ± 80

[a] Errors shown are the limits for the standard 68% confidence interval.

[b] Unless otherwise noted, all the data come from G. P. Millburn *et al.*, *Phys. Rev.* **95**, 1268 (1954).

[c] P. E. Hodgson, *Nuclear Phys.* **21**, 21 (1960).

[d] Upper limit.

Table 7.1.2. Calculated and Experimental Average Excitation Energies for 190-Mev Incident Protons on Various Nuclei

Target	Excitation Energy (Mev)	
	Calculated	Experimental[a]
C	22	27 ± 5
Al	36	50 ± 8
Ni	59	57 ± 9
Ag	72	69 ± 12
Au	92	83 ± 17
U	95	88 ± 18

[a] E. Gross, *The Absolute Yield of Low Energy Neutrons from 190-Mev Protons on Gold, Silver, Nickel, Aluminum, and Carbon*, UCRL-3330 (Feb. 29, 1956); *Absolute Neutron Spectra from 190-Mev Protons on Uranium*, UCRL-3337 (Mar. 8, 1956).

Table 7.1.3. Calculated and Experimental Fast Prong Distributions for Heavy-Emulsion Nuclei[a]

Number of Fast Prongs	Percentage of Stars Induced			
	By 300-Mev Neutrons		By 375-Mev Protons	
	Calculated	Experimental[b]	Calculated	Experimental[b]
0	54	30 ± 4	14	29 ± 3
1	42	63 ± 5	76	60 ± 4
2	4	7 ± 2	10	9 ± 2
3	0.4	0	0.5	2 ± 1

[a] Fast prongs indicate protons with energies greater than 30 Mev.

[b] G. Bernardini, E. T. Booth, and S. J. Lindenbaum, *Phys. Rev.* **85**, 826 (1952).

Table 7.1.4. Calculated and Experimental Total Nonelastic Cross Sections for Pions Incident on Various Nuclei

Pion	Target	Energy (Mev)	Nonelastic Cross Section (mb)	
			Calculated[a]	Experimental
π^+	Li	195	324 ± 10	226 ± 18[b]
	C	185	455 ± 11	325 ± 26[b]
		270	358 ± 10	$296 + 35^{c}_{-28}$
	Pb	50	1563 ± 26	1620[d]
π^-	C	125	458 ± 11	308 ± 43[e]
		150	478 ± 11	430 ± 42[f]
		225	423 ± 11	346 ± 21[g]
	Al	225	653 ± 14	596 ± 30[g]
	Cu	225	1038 ± 19	1058 ± 45[g]
	Sn	225	1471 ± 20	1550 ± 70[g]
	Pb	125	2062 ± 29	2477 ± 385[e]
		150	2145 ± 29	2490 ± 160[f]
		225	1993 ± 29	2290 ± 90[g]

[a] Errors indicated apply for a confidence coefficient of 68%.

[b] N. I. Petrov, U. G. Ivanov, and U. A. Rusakov, *Soviet Phys. JETP (English Transl.)* **10**, 682 (1960).

[c] W. Kan Chang *et al.*, *Soviet Phys. JETP (English Transl.)* **8**, 625 (1959).

[d] Calculated from the mean free path in nuclear matter given by G. Saphir, *Phys. Rev.* **104**, 535 (1956).

[e] J. O. Kessler and L. M. Lederman, *Phys. Rev.* **94**, 689 (1954).

[f] R. H. Miller, *Nuovo Cimento* **6**, 882 (1957).

[g] V. G. Ivanov *et al.*, *Soviet Phys. JETP (English Transl.)* **4**, 922 (1957).

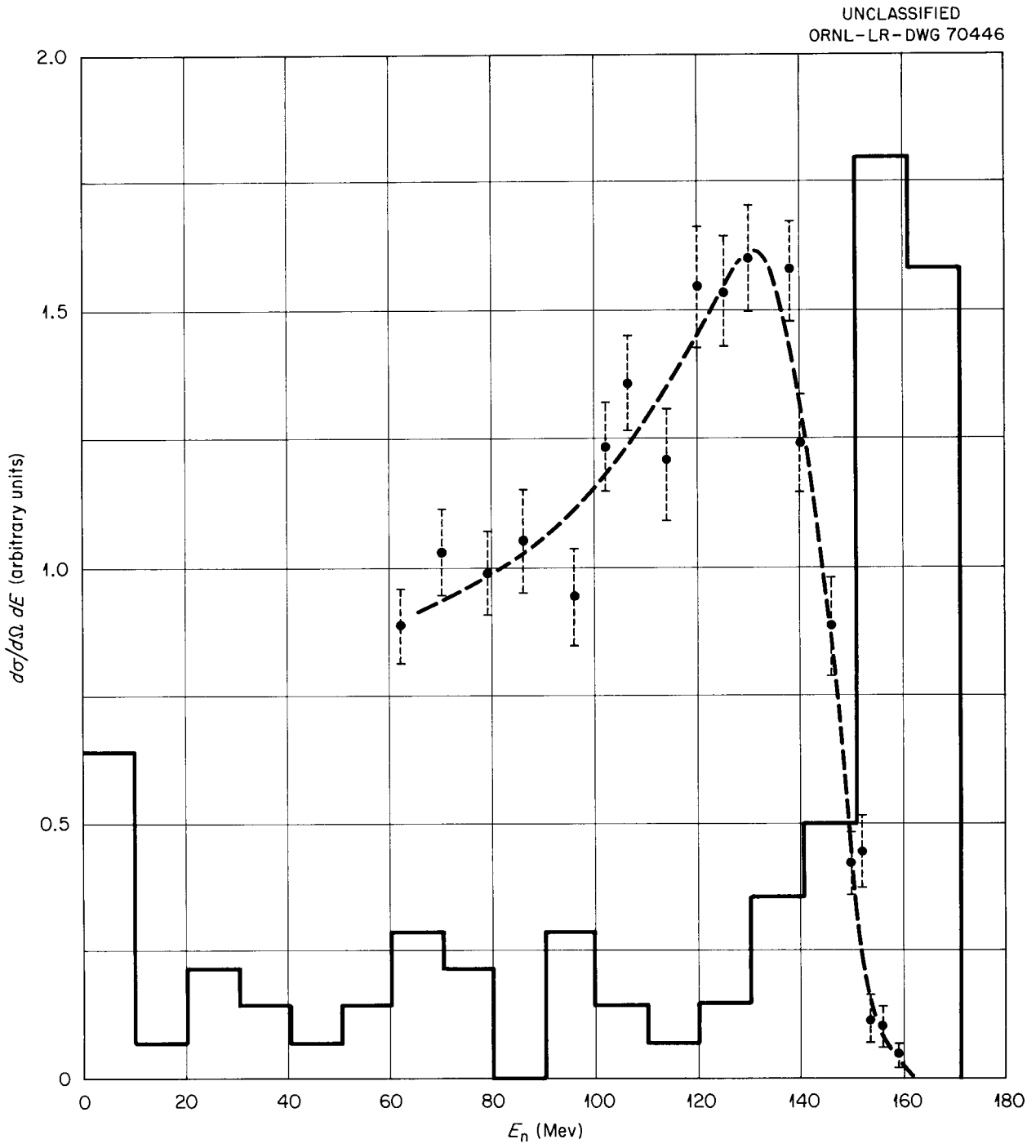

Fig. 7.1.9. Neutron Spectra at 2.5° from 171-Mev Protons on Carbon. Dotted curve: experimental results of Cassels *et al.* [*Phil. Mag.* **42**, 215 (1951)]; solid lines: calculated spectrum of neutrons emitted in the angular interval 0 to 15°; ordinate units are arbitrary.

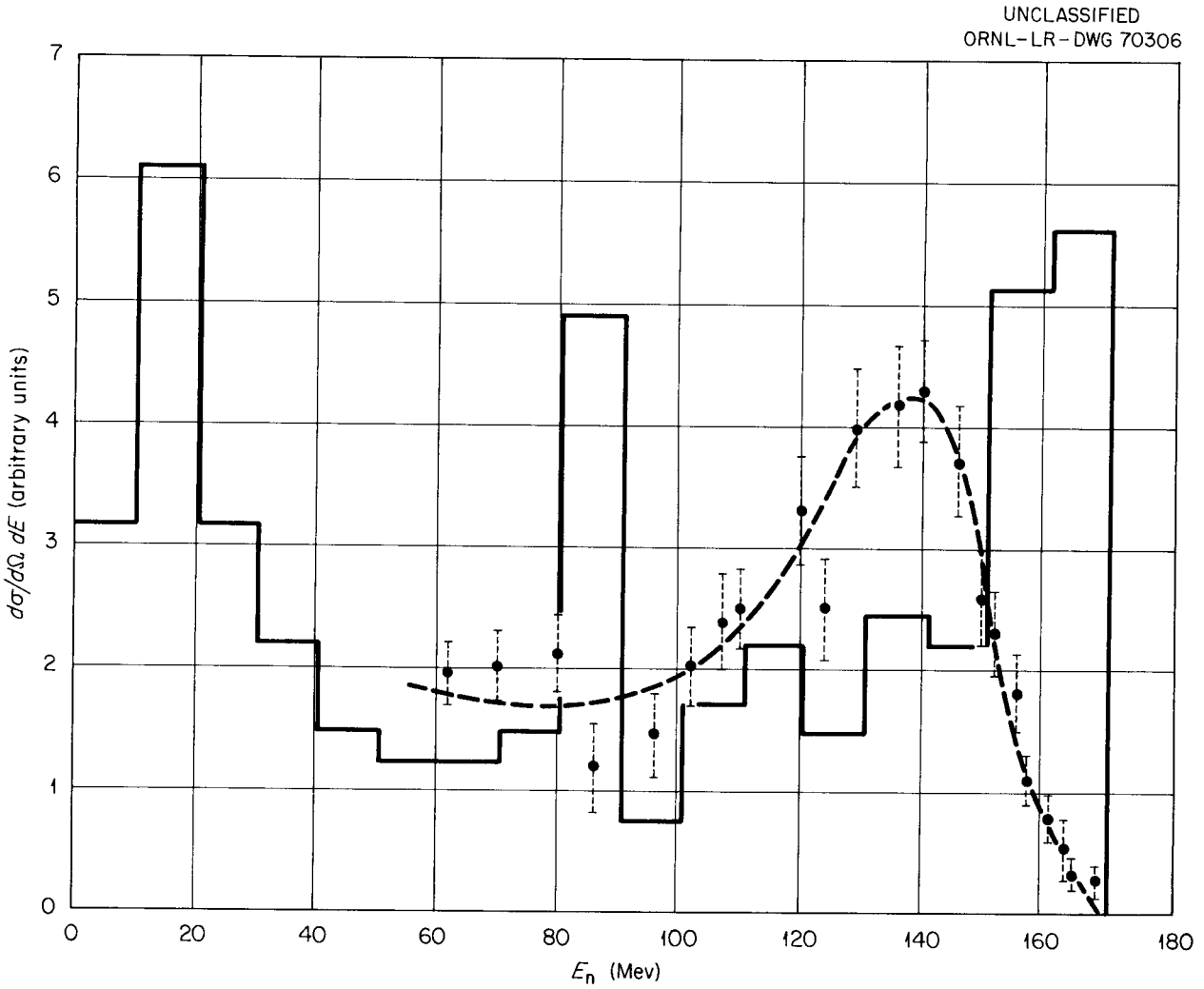

Fig. 7.1.10. Neutron Spectra at 2.5° from 171-Mev Protons on Uranium. Dotted curve: experimental results of Cassels *et al.* [*Phil. Mag.* **42**, 215 (1951)]; solid lines: calculated spectrum of neutrons emitted in the angular interval 0 to 15°; ordinate units are arbitrary.

Table 7.1.5. Calculated and Experimental Absorption Cross Sections for Pions Incident on Beryllium

Pion	Energy (Mev)	Cross Section (mb)	
		Calculated	Experimental[a]
π^+	20	58	56 ± 9
π^+	30	63	74 ± 13
π^+	40	67	96 ± 20

[a] F. H. Tenney and J. Tinlot, *Phys. Rev.* **92**, 974 (1953).

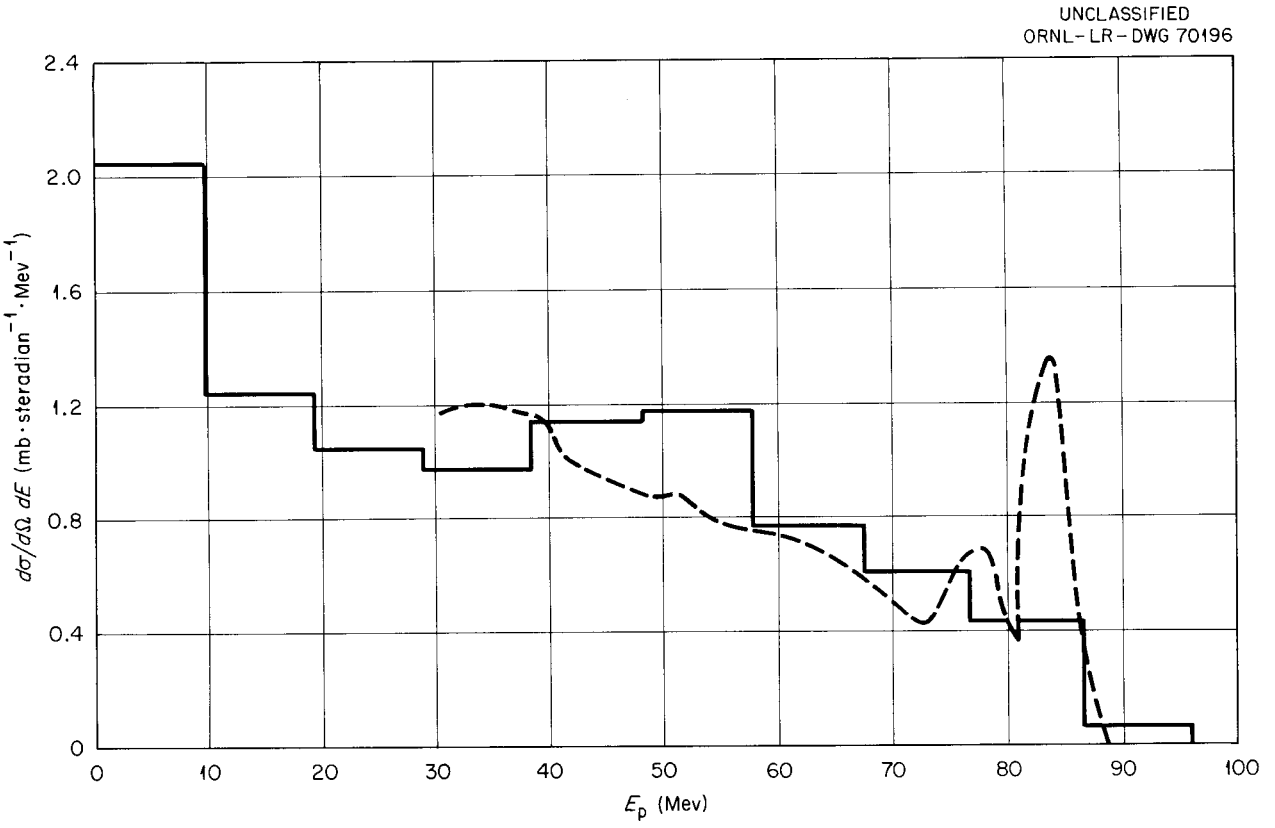

Fig. 7.1.11. Proton Spectra at 40° from 96-Mev Protons on Fluorine. Dotted curve: experimental results of Strauch and Titus [*Phys. Rev.* **104**, 191 (1956)]; solid lines: calculated spectrum of protons emitted in the angular interval 30 to 50°.

Table 7.1.6. Calculated and Experimental Charge-Exchange Cross Sections for Pions Incident on Lead and Carbon

Pion	Target	Energy (Mev)	Cross Section (mb)	
			Calculated	Experimental
π^+	Pb	50	206	27 ± 19^a
π^-	C	125	61	$20 + 20^b$ $- 10$
π^-	Pb	125	215	$100 + 80^b$ $- 40$

[a] G. Saphir, *Phys. Rev.* **104**, 535 (1956).
[b] J. O. Kessler and L. M. Lederman, *Phys. Rev.* **94**, 689 (1954).

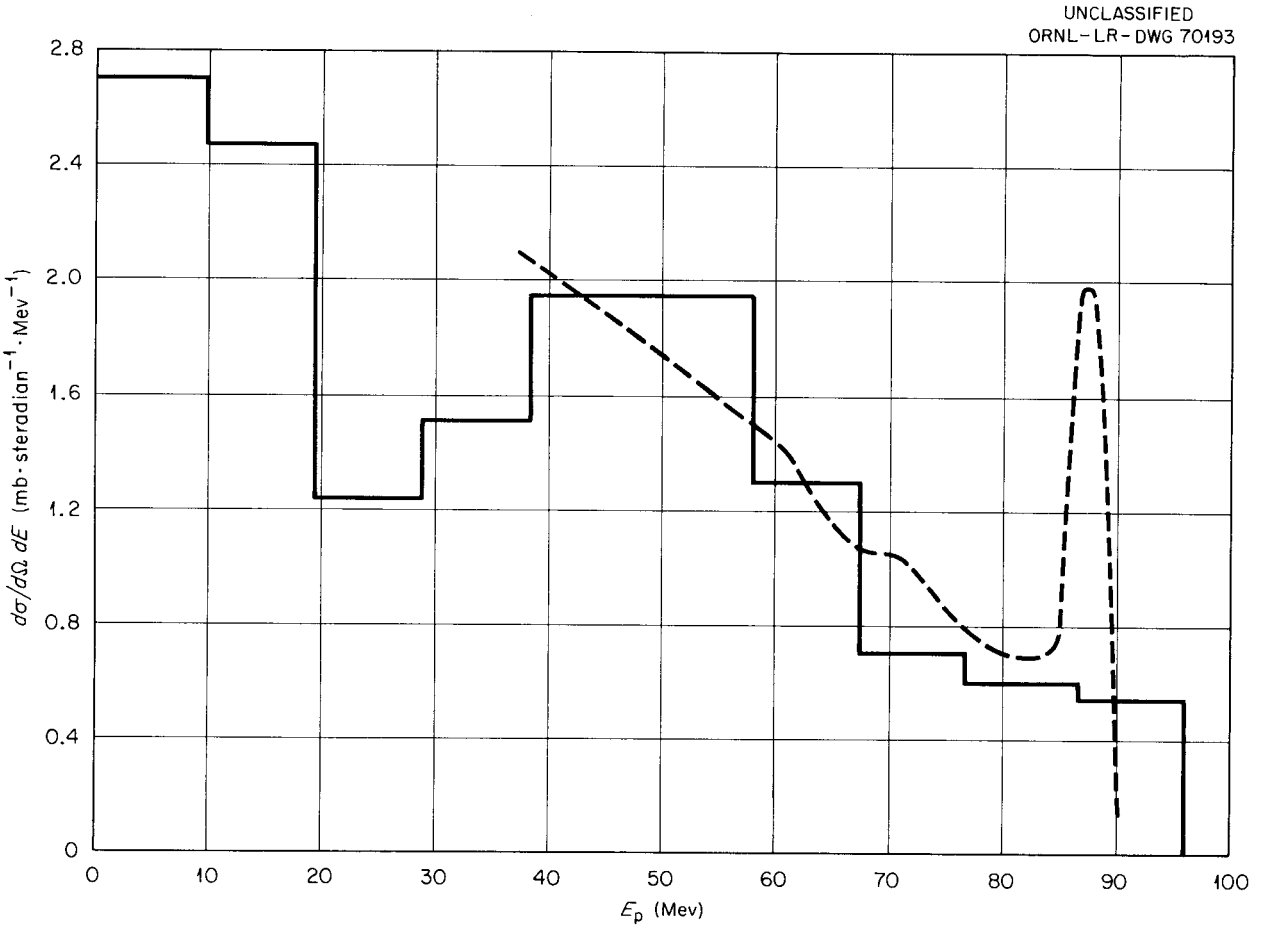

Fig. 7.1.12. Proton Spectra at 40° from 96-Mev Protons on Copper. Dotted curve: experimental results of Strauch and Titus [*Phys. Rev.* **104**, 191 (1956)]; solid lines: calculated spectrum of protons emitted in the angular interval 30 to 50°.

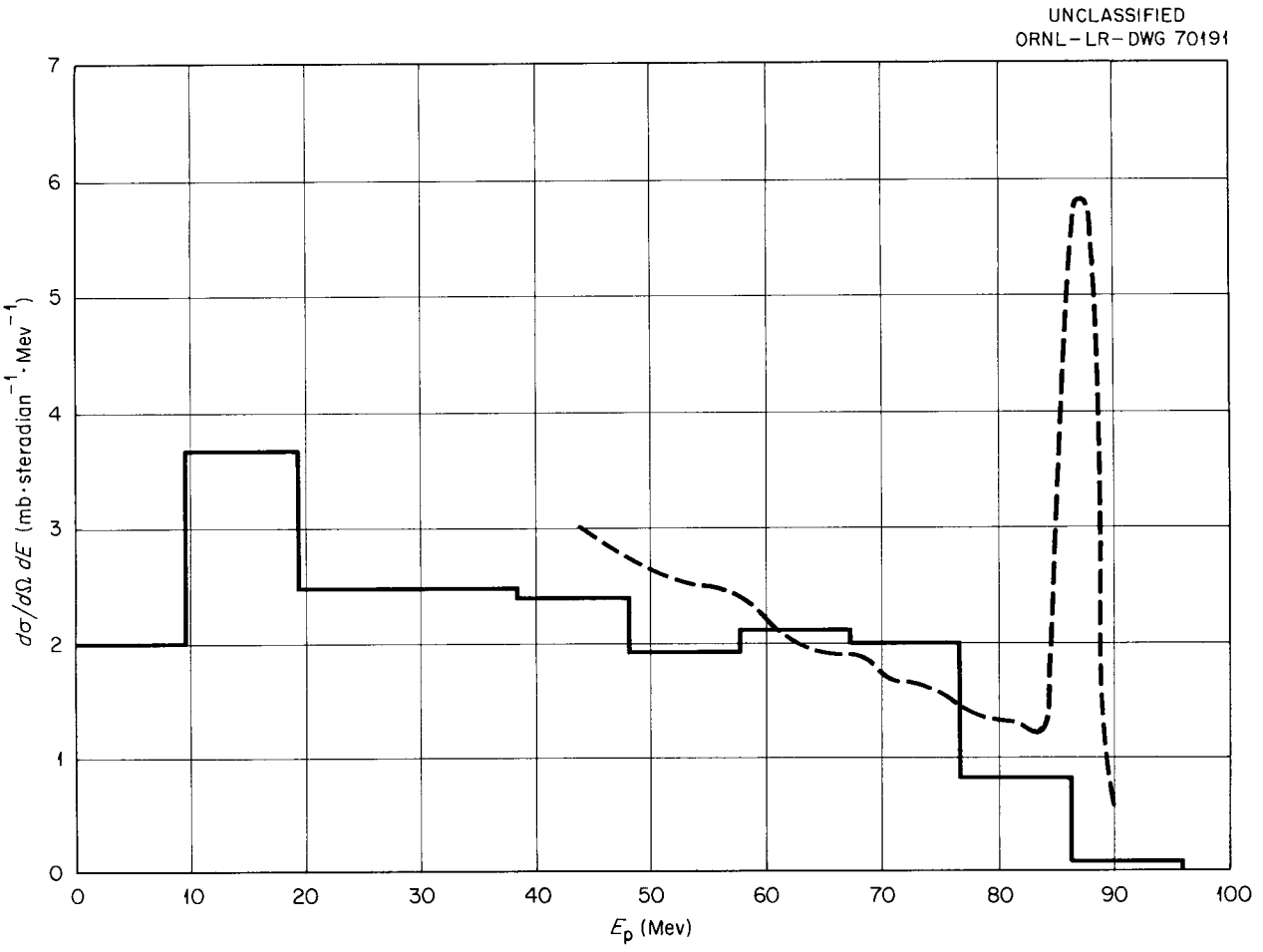

Fig. 7.1.13. Proton Spectra at 40° from 96-Mev Protons on Bismuth. Dotted curve: experimental results of Strauch and Titus [*Phys. Rev.* 104, 191 (1956)]; solid lines: calculated spectrum of protons emitted in the angular interval 30 to 50°.

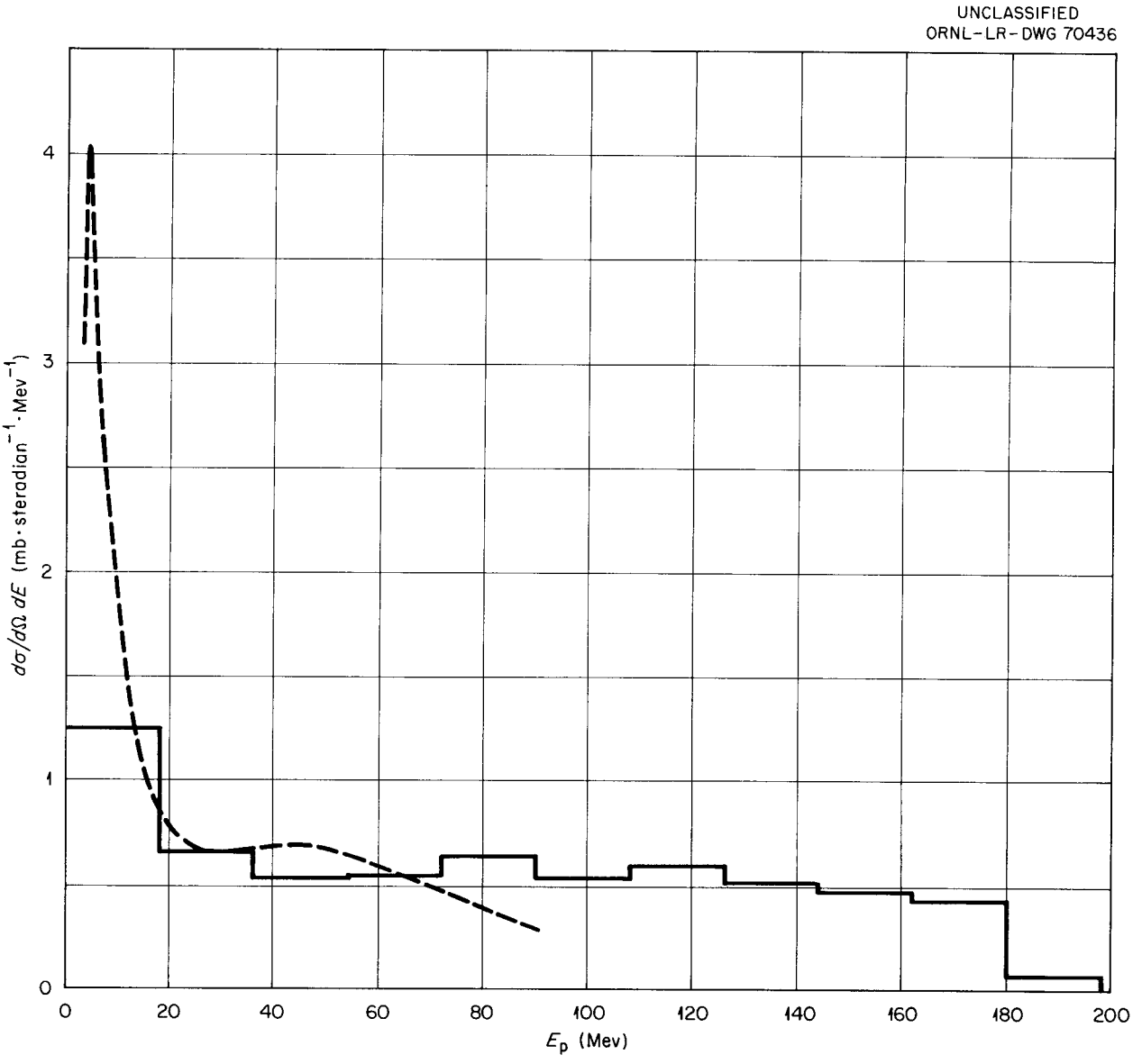

Fig. 7.1.14. Proton Spectra from 0 to 65° for 190-Mev Protons on Aluminum. Dashed curve: Bailey's experimental results [*Angle and Energy Distributions of Charged Particles from the High Energy Nuclear Bombardment of Various Elements*, UCRL-3334 (Mar. 1, 1956)]; solid lines: calculated spectrum.

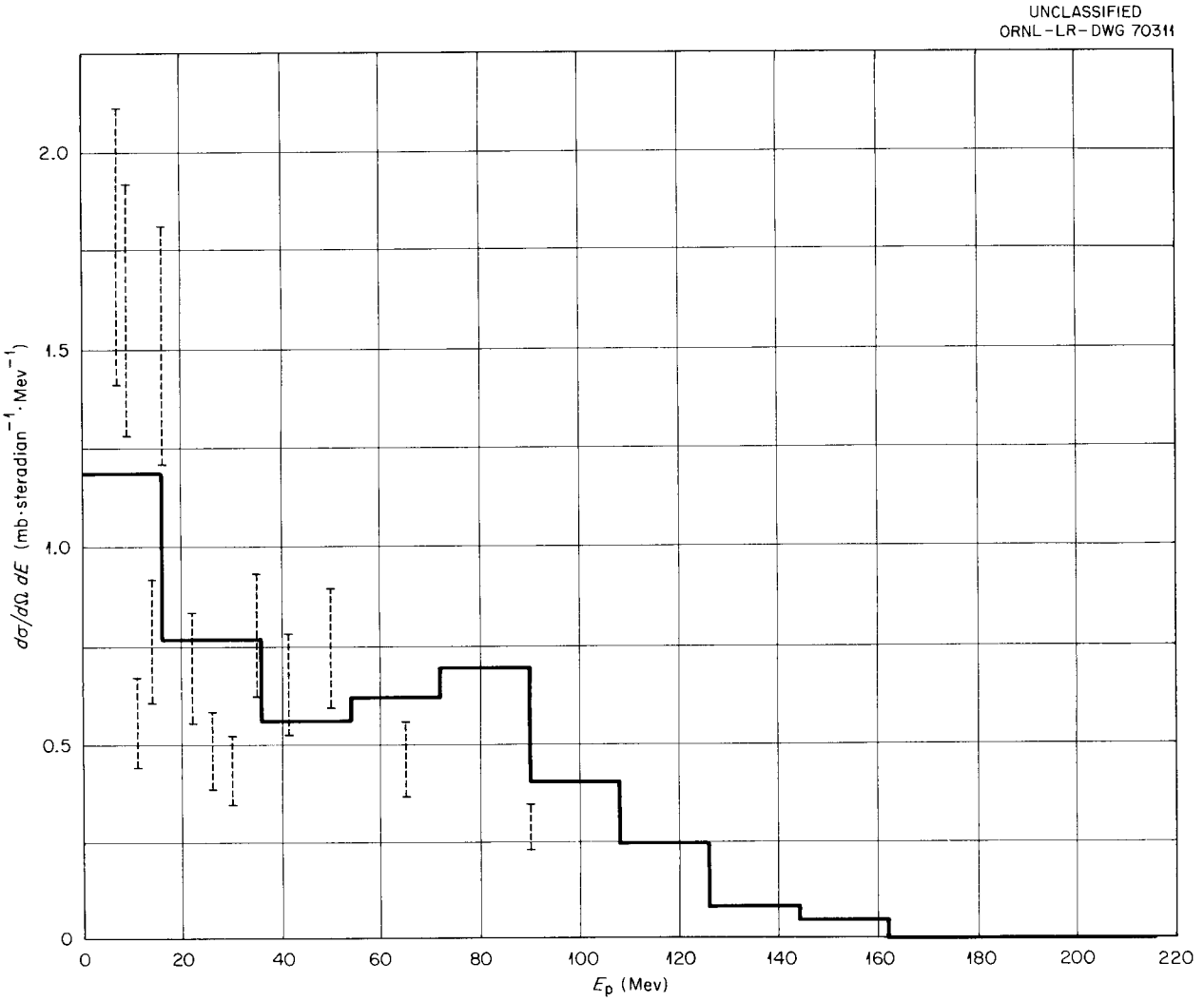

Fig. 7.1.15. Proton Spectra from 46 to 65° for 190-Mev Protons on Aluminum. Dotted lines: Bailey's experimental results (UCRL-3334); solid lines: calculated spectrum.

Table 7.1.7. Calculated and Experimental Charge-Exchange Plus Absorption Cross Sections for Pions Incident on Various Nuclei

Pion	Target	Energy (Mev)	Cross Section (mb)	
			Calculated	Experimental
π^+	Li	195	142	164 ± 16[a]
π^+	C	78	174	195 ± 20[b]
		195	205	203 ± 22[a]
		270	146	$165 + 34 - 22$[c]
π^+	Pb	50	930	880 ± 73[d]
π^-	C	125	206	220 ± 40[e]
		150	209	192 ± 34[f]
	Pb	125	923	1840 ± 350[e]
		150	957	380 ± 310[f]

[a] N. I. Petrov, V. G. Ivanov, and V. A. Rusakov, *Soviet Phys. JETP (English Transl.)* **10**, 682 (1960).

[b] R. G. Sulukvadze and D. Neagu, *Soviet Phys. JETP (English Transl.)* **14**, 59 (1962).

[c] W. Kan Chang *et al.*, *Soviet Phys. JETP (English Transl.)* **8**, 625 (1959).

[d] G. Saphir, *Phys. Rev.* **104**, 535 (1956).

[e] J. O. Kessler and L. M. Lederman, *Phys. Rev.* **94**, 689 (1954).

[f] R. H. Miller, *Nuovo Cimento* **6**, 882 (1957).

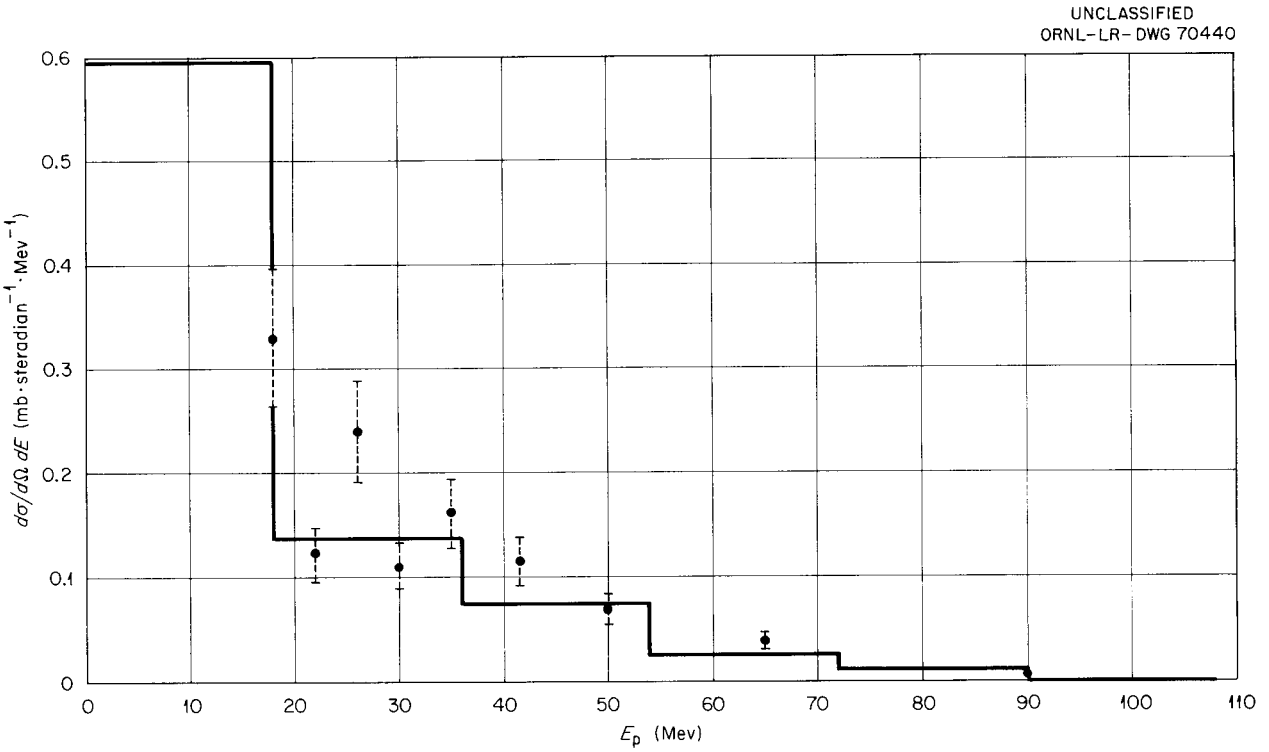

Fig. 7.1.16. Proton Spectra from 102 to 117° for 190-Mev Protons on Aluminum. Dotted lines: Bailey's experimental results (UCRL-3334); solid lines: calculated spectrum.

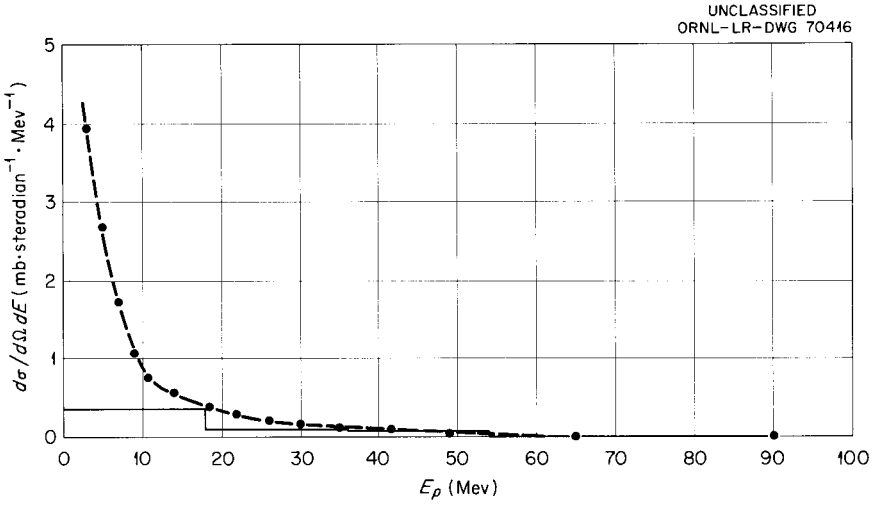

Fig. 7.1.17. Proton Spectra from 100 to 180° for 190-Mev Protons on Aluminum. Dotted curve: Bailey's experimental results (UCRL-3334); solid lines: calculated spectrum.

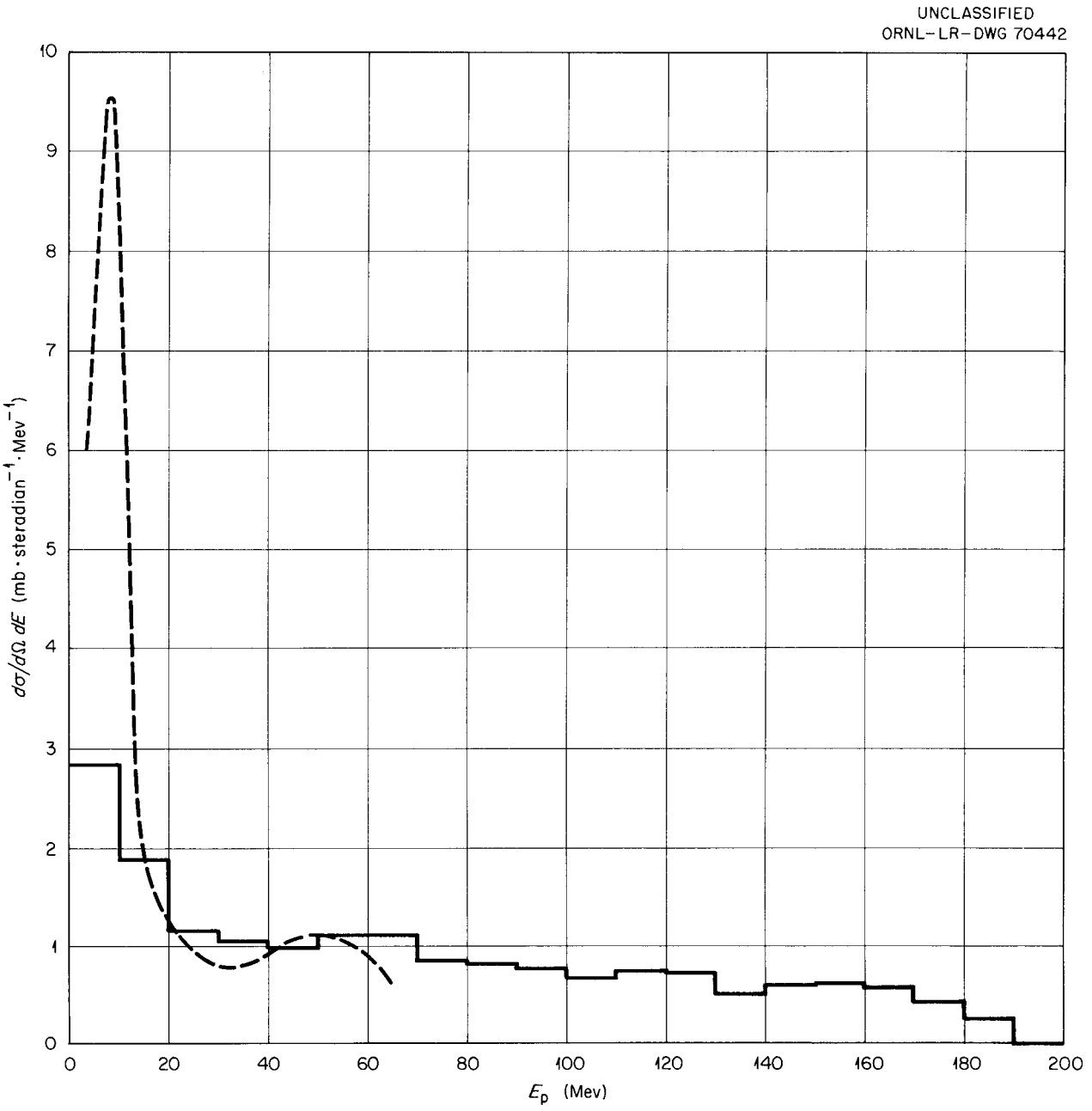

Fig. 7.1.18. Proton Spectra from 0 to 65° for 190-Mev Protons on Nickel. Dotted curve: Bailey's experimental results (UCRL-3334); solid lines: calculated spectrum.

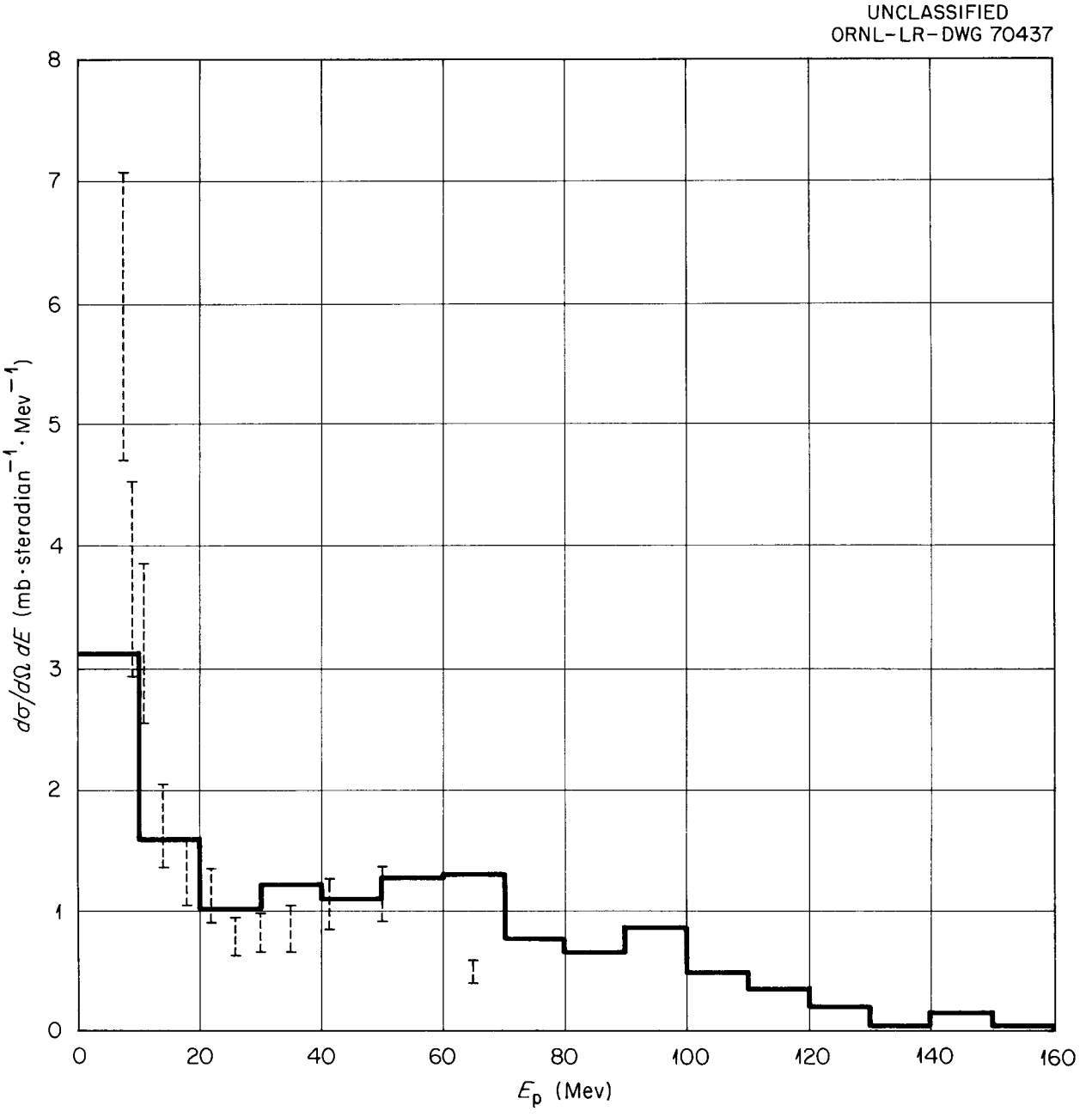

Fig. 7.1.19. Proton Spectra from 46 to 65° for 190-Mev Protons on Nickel. Dotted lines: Bailey's experimental results (UCRL-3334); solid lines: calculated spectrum.

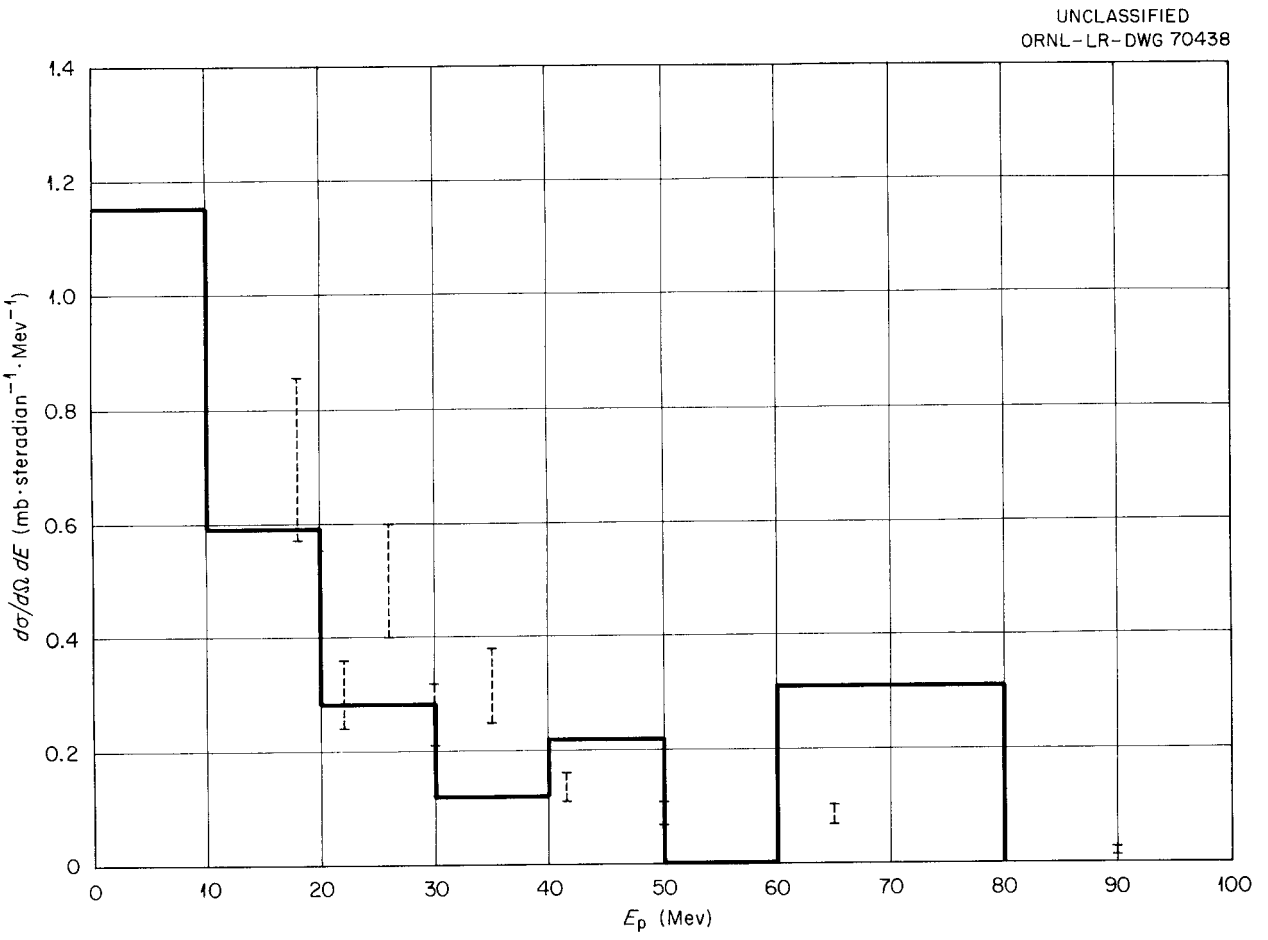

Fig. 7.1.20. Proton Spectra from 102 to 117° for 190-Mev Protons on Nickel. Dotted lines: Bailey's experimental results (UCRL-3334); solid lines: calculated spectrum.

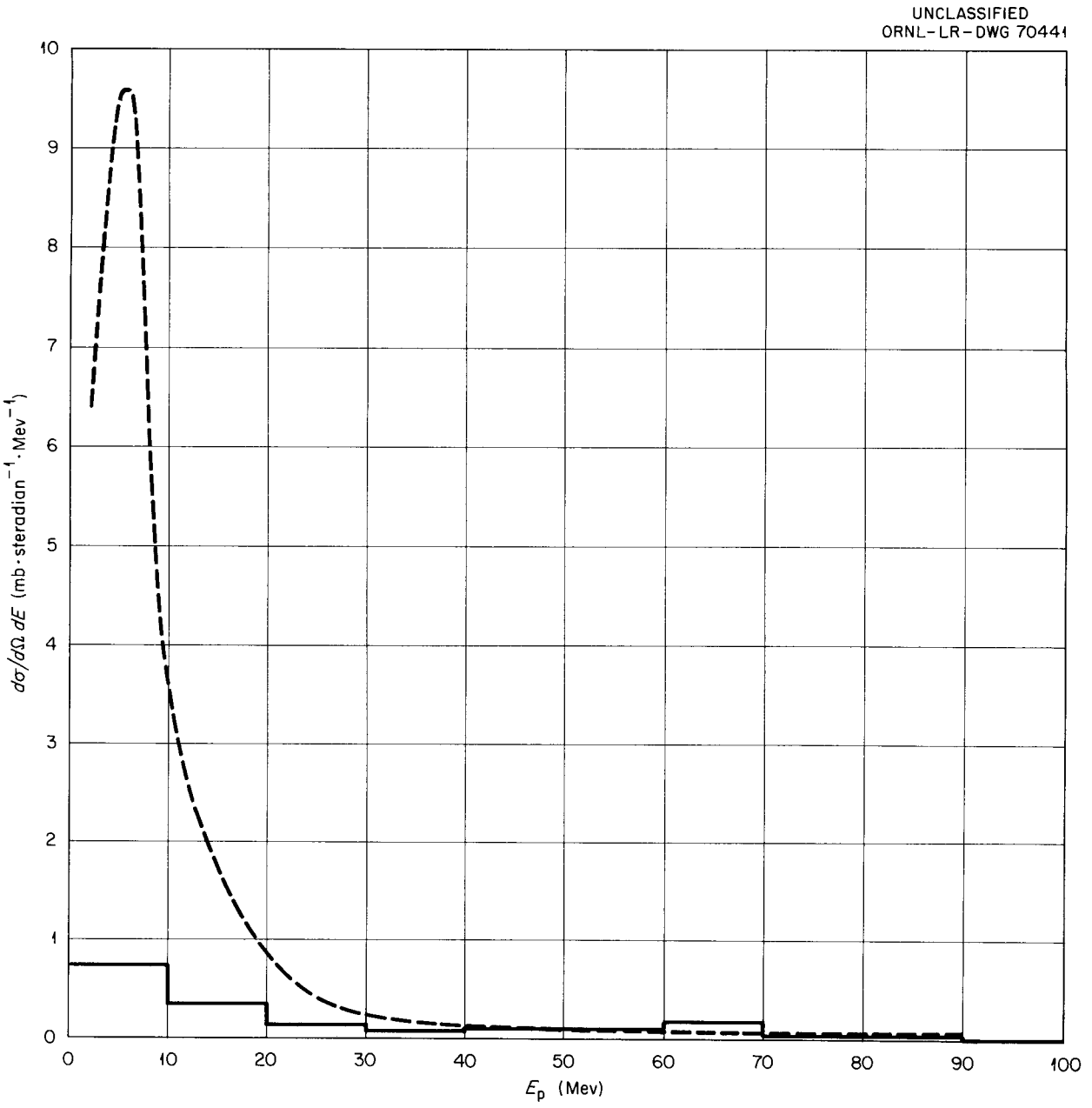

Fig. 7.1.21. Proton Spectra from 100 to 180° for 190-Mev Protons on Nickel. Dotted curve: Bailey's experimental results (UCRL-3334); solid lines: calculated spectrum.

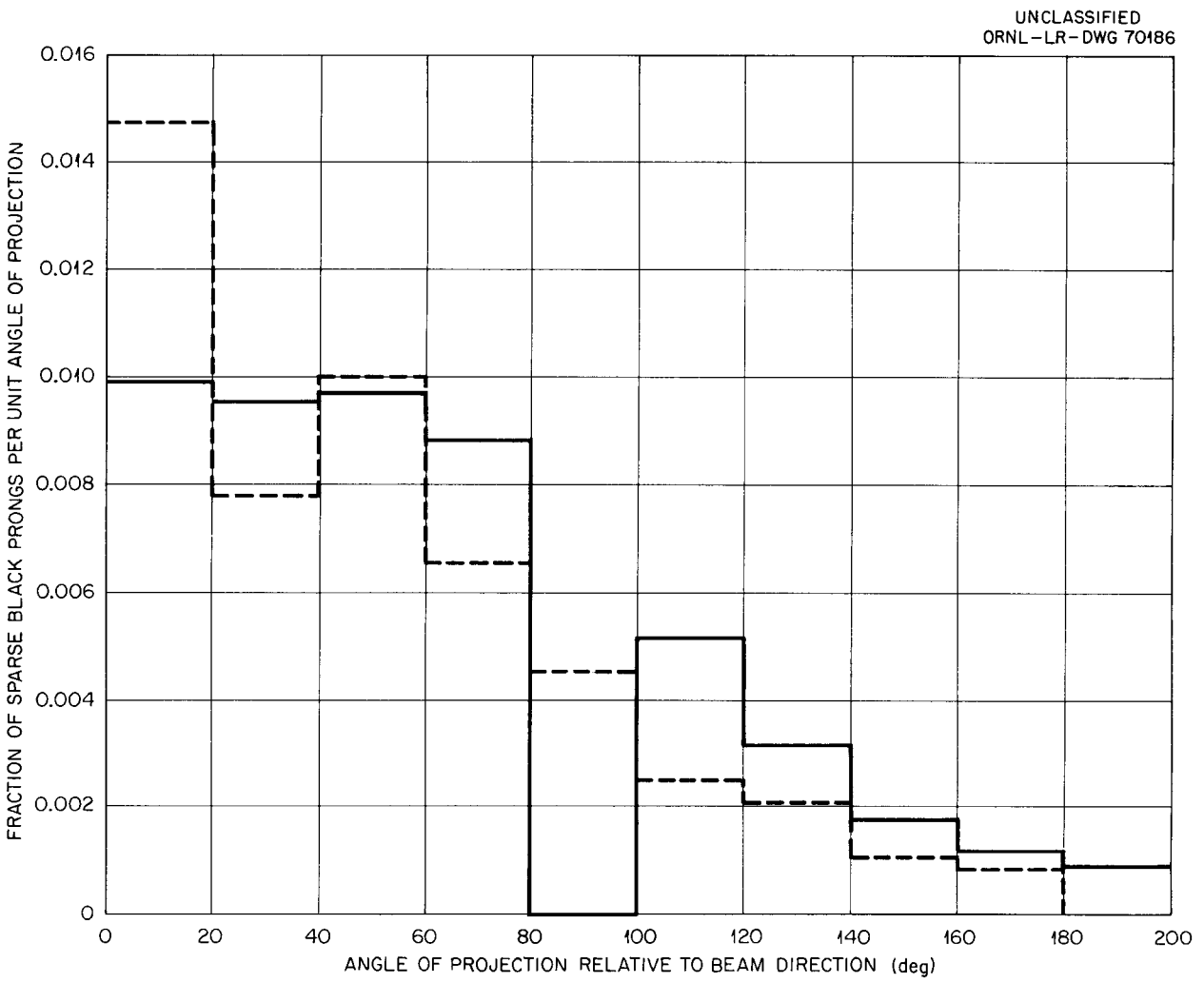

Fig. 7.1.22. Angular Distribution of Sparse Black Prongs from 375-Mev Protons on Heavy-Emulsion Nuclei. Dotted lines: experimental results of Bernardini *et al.* [*Phys. Rev.* 85, 826 (1952)]; solid lines: calculated distribution for protons emitted with energies from 30 to 100 Mev for 376-Mev protons on Ru^{100}.

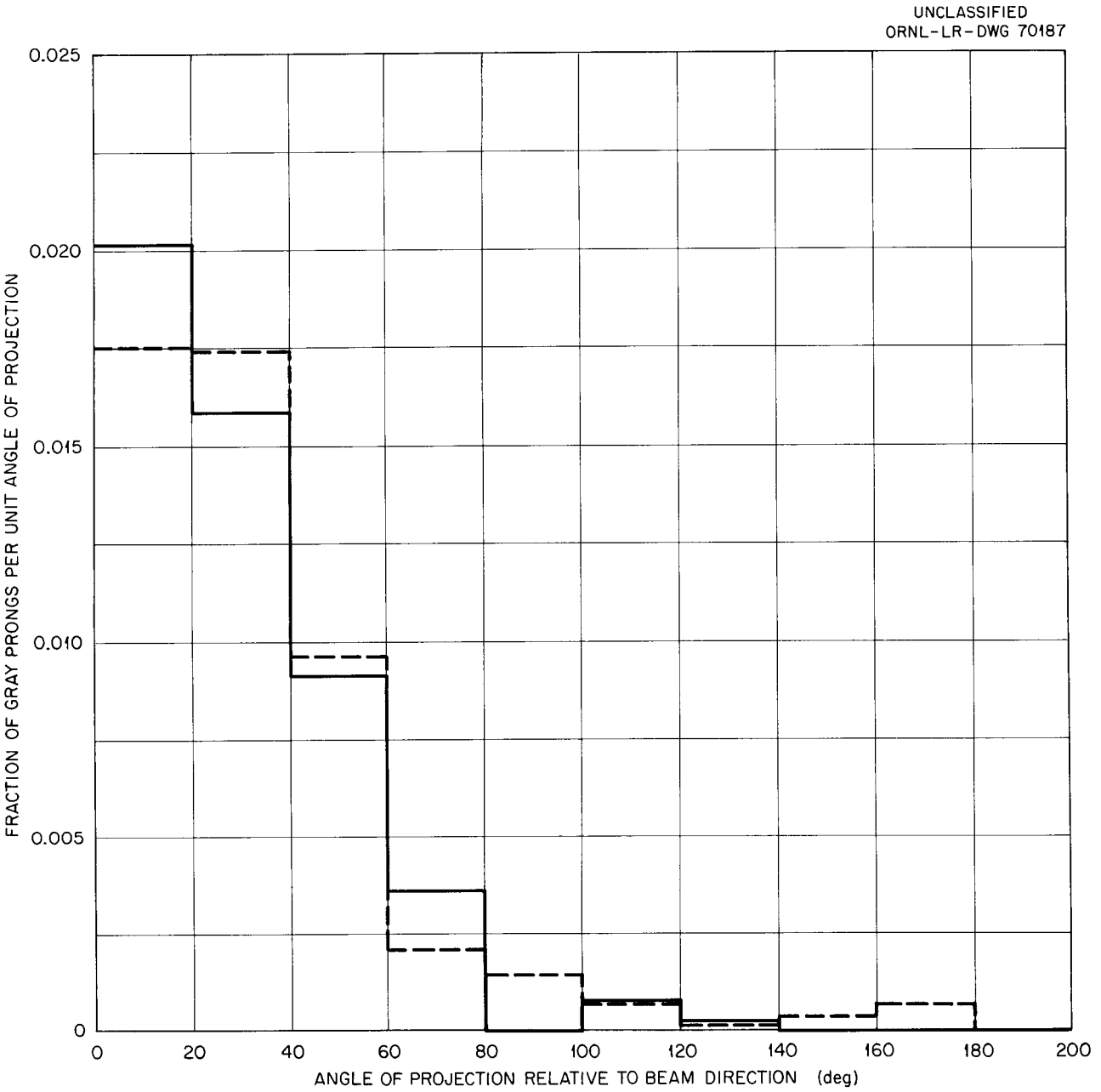

Fig. 7.1.23. Angular Distribution of Gray Prongs from 375-Mev Protons on Heavy-Emulsion Nuclei. Dotted lines: experimental results of Bernardini *et al.* [*Phys. Rev.* 85, 826 (1952)]; solid lines: calculated distribution for protons emitted with energies from 100 to 375 Mev for 375-Mev protons on Ru^{100}.

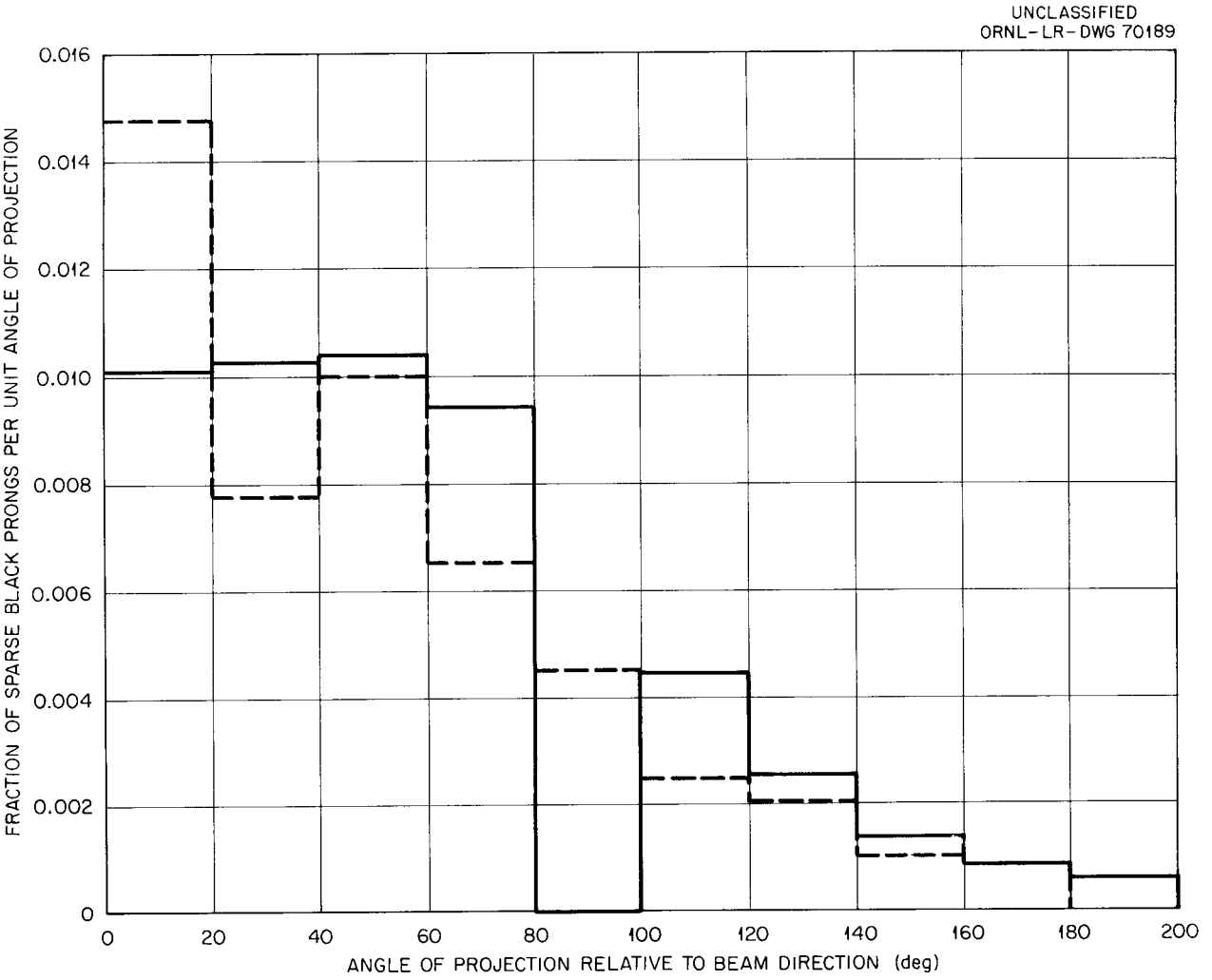

Fig. 7.1.24. Angular Distribution of Sparse Black Prongs from 300-Mev Neutrons on Heavy-Emulsion Nuclei. Dotted lines: experimental results of Bernardini *et al.* [*Phys. Rev.* 85, 826 (1952)]; solid lines: calculated distribution for protons emitted with energies from 30 to 100 Mev for 300-Mev neutrons on Ru^{100}.

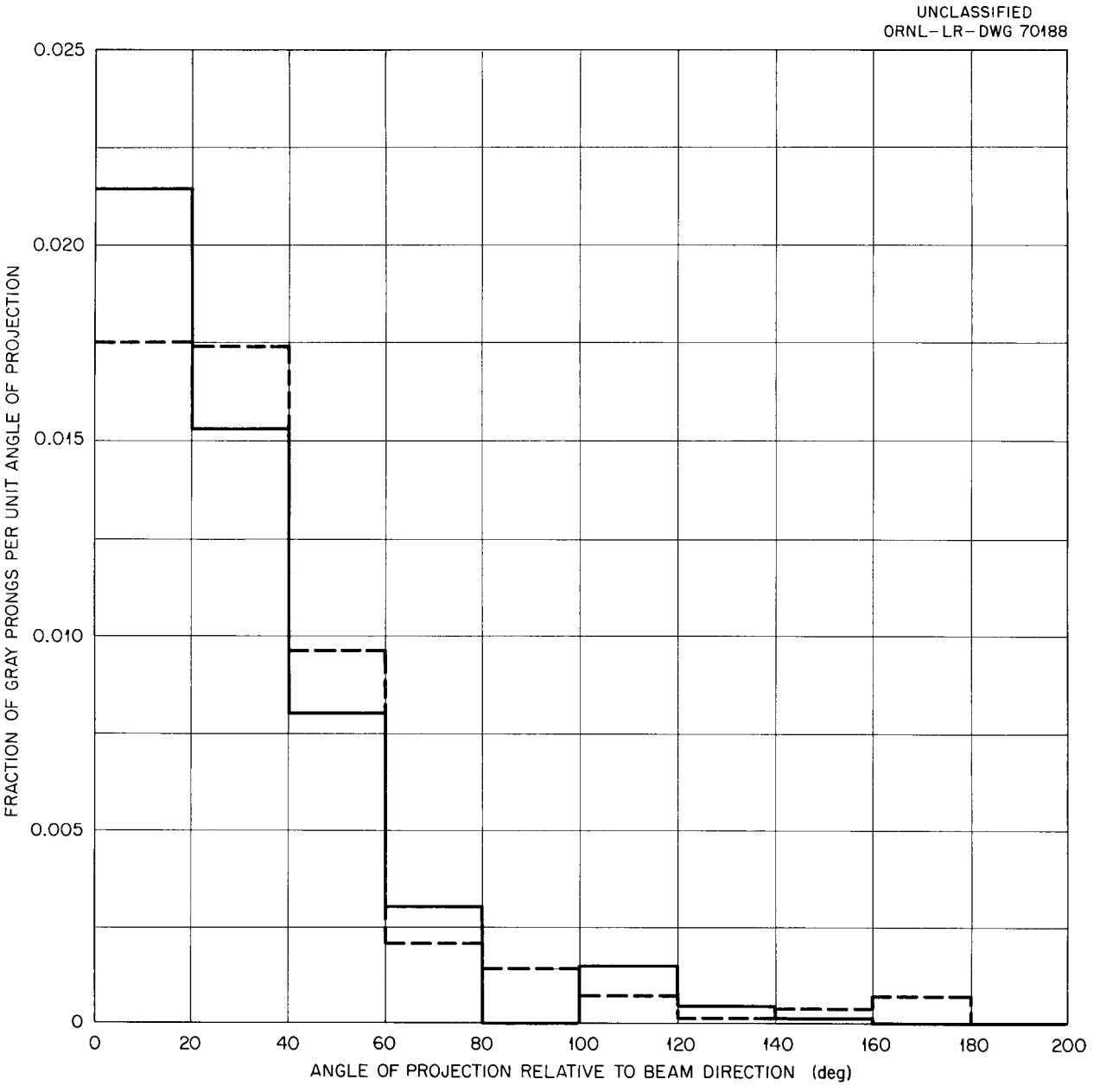

Fig. 7.1.25. Angular Distribution of Gray Prongs from 300-Mev Neutrons on Heavy-Emulsion Nuclei. Dotted lines: experimental results of Bernardini *et al.* [*Phys. Rev.* 85, 826 (1952)]; solid lines: calculated distribution for protons emitted with energies from 100 to 300 Mev for 300-Mev neutrons on Ru^{100}.

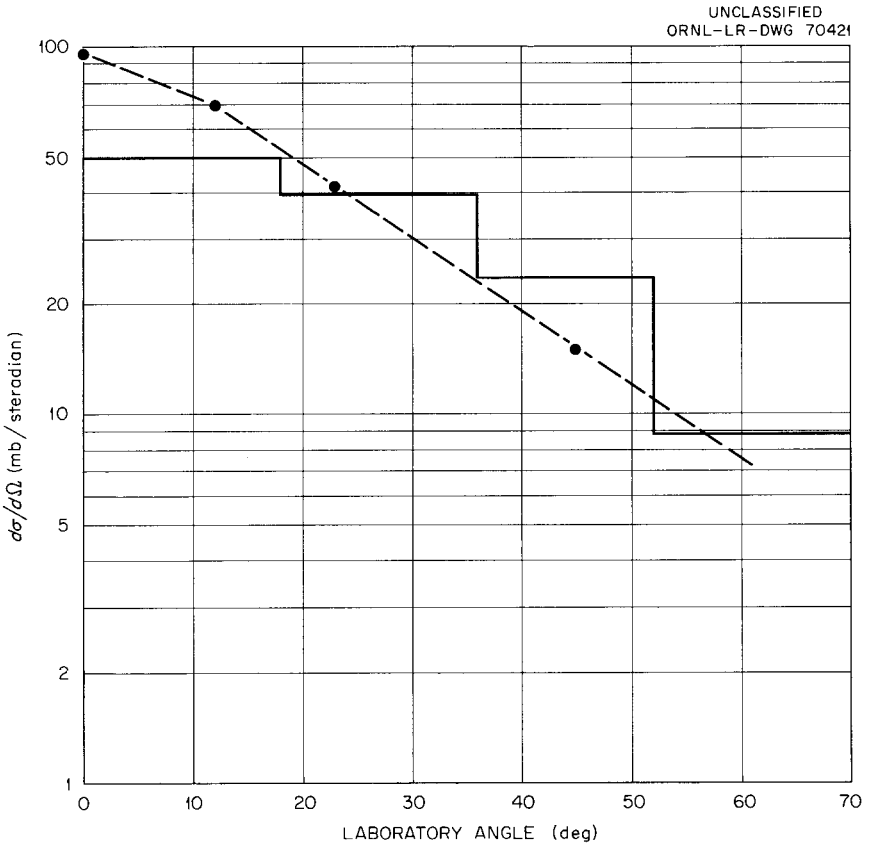

Fig. 7.1.26. Angular Distribution of Protons with Energies Greater Than 20 Mev from 90-Mev Neutrons on Carbon. Dotted lines: experimental results of Hadley and York [*Phys. Rev.* 80, 345 (1950)]; solid lines: calculated distribution.

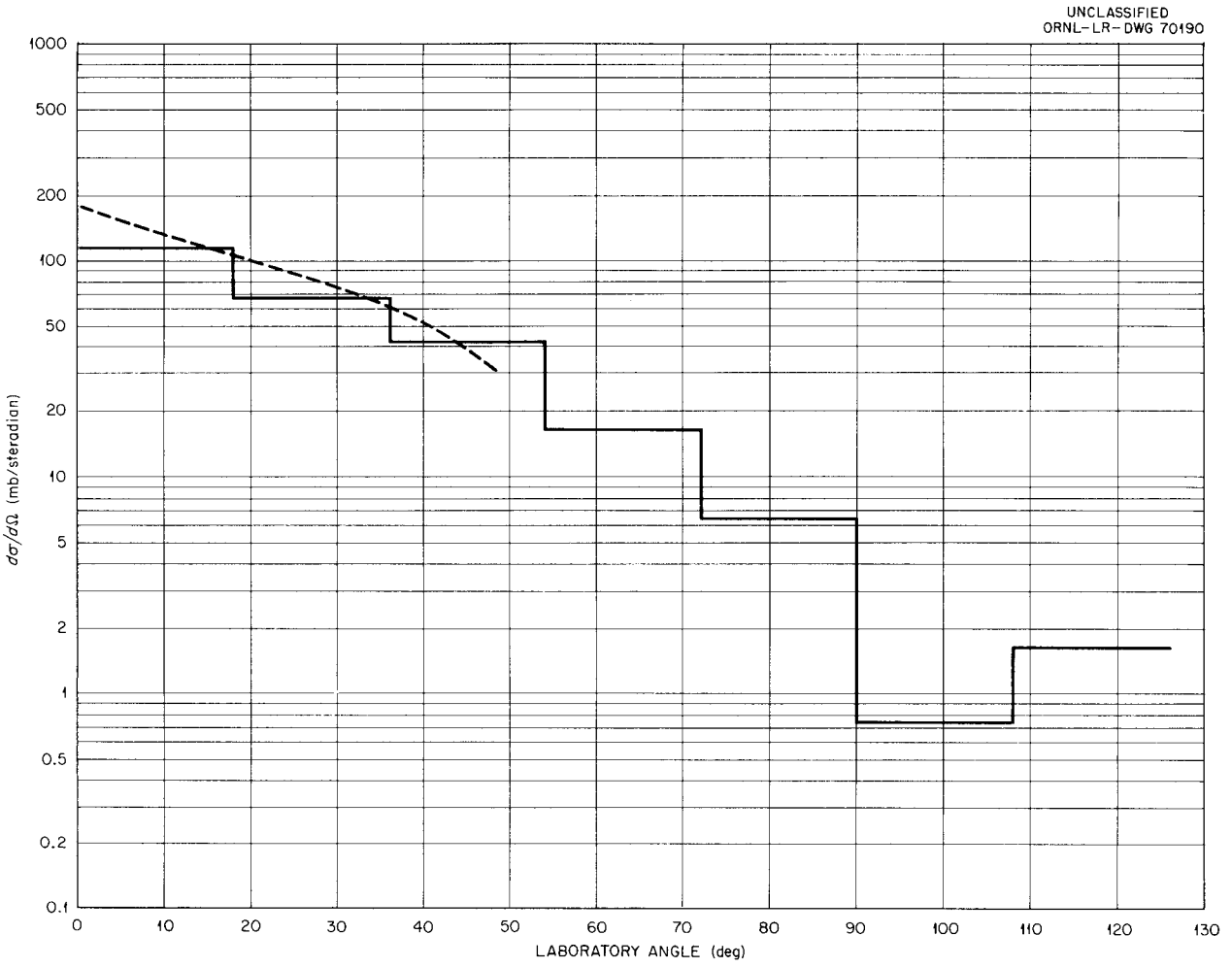

Fig. 7.1.27. Angular Distribution of Protons with Energies Greater Than 20 Mev from 90-Mev Neutrons on Copper. Dotted lines: experimental results of Hadley and York [*Phys. Rev.* **80**, 345 (1950)]; solid lines: calculated distribution.

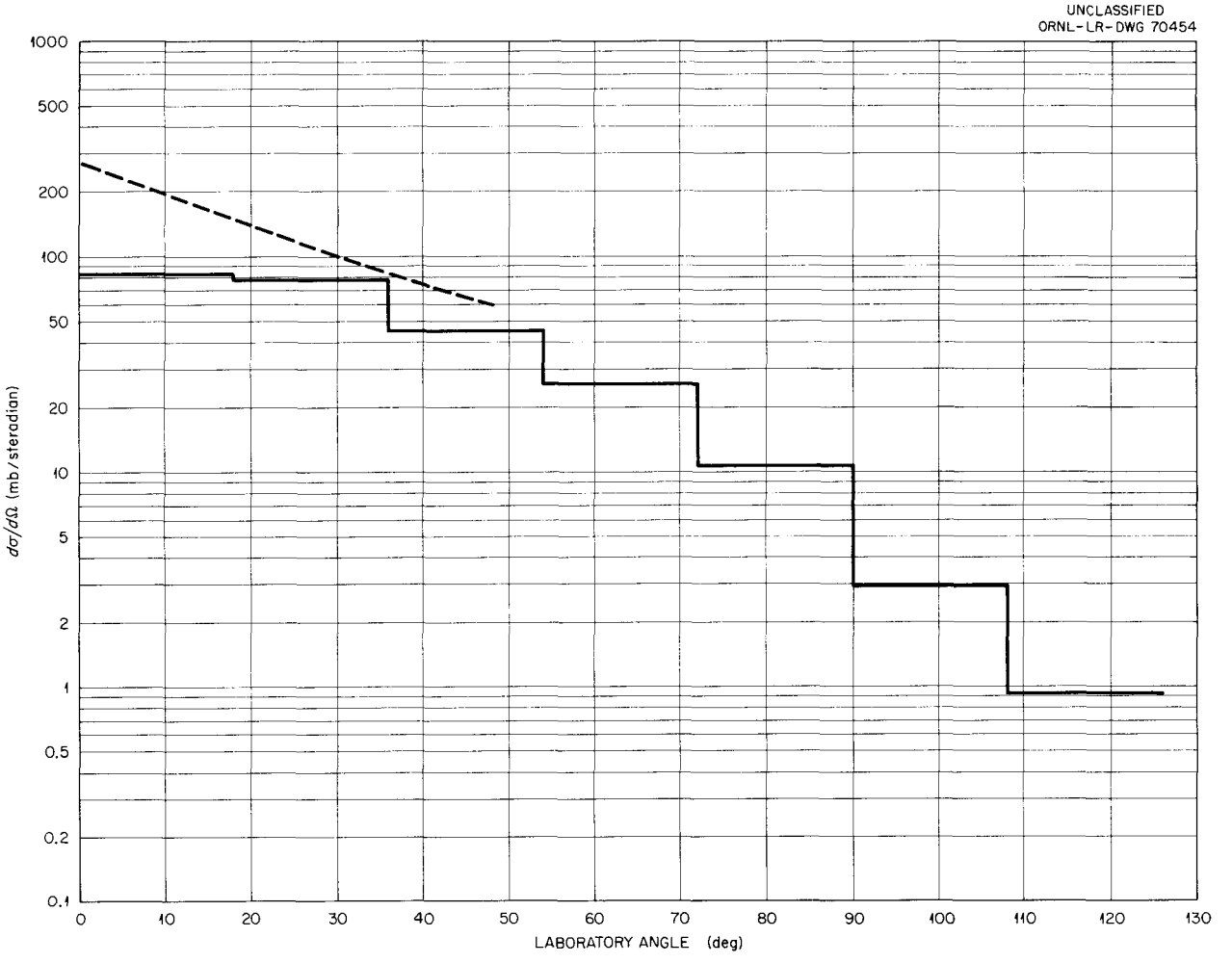

Fig. 7.1.28. Angular Distribution of Protons with Energies Greater Than 20 Mev from 90-Mev Neutrons on Lead. *Dotted lines: experimental results of Hadley and York [Phys. Rev. 80, 345 (1950)]; solid lines: calculated distribution.*

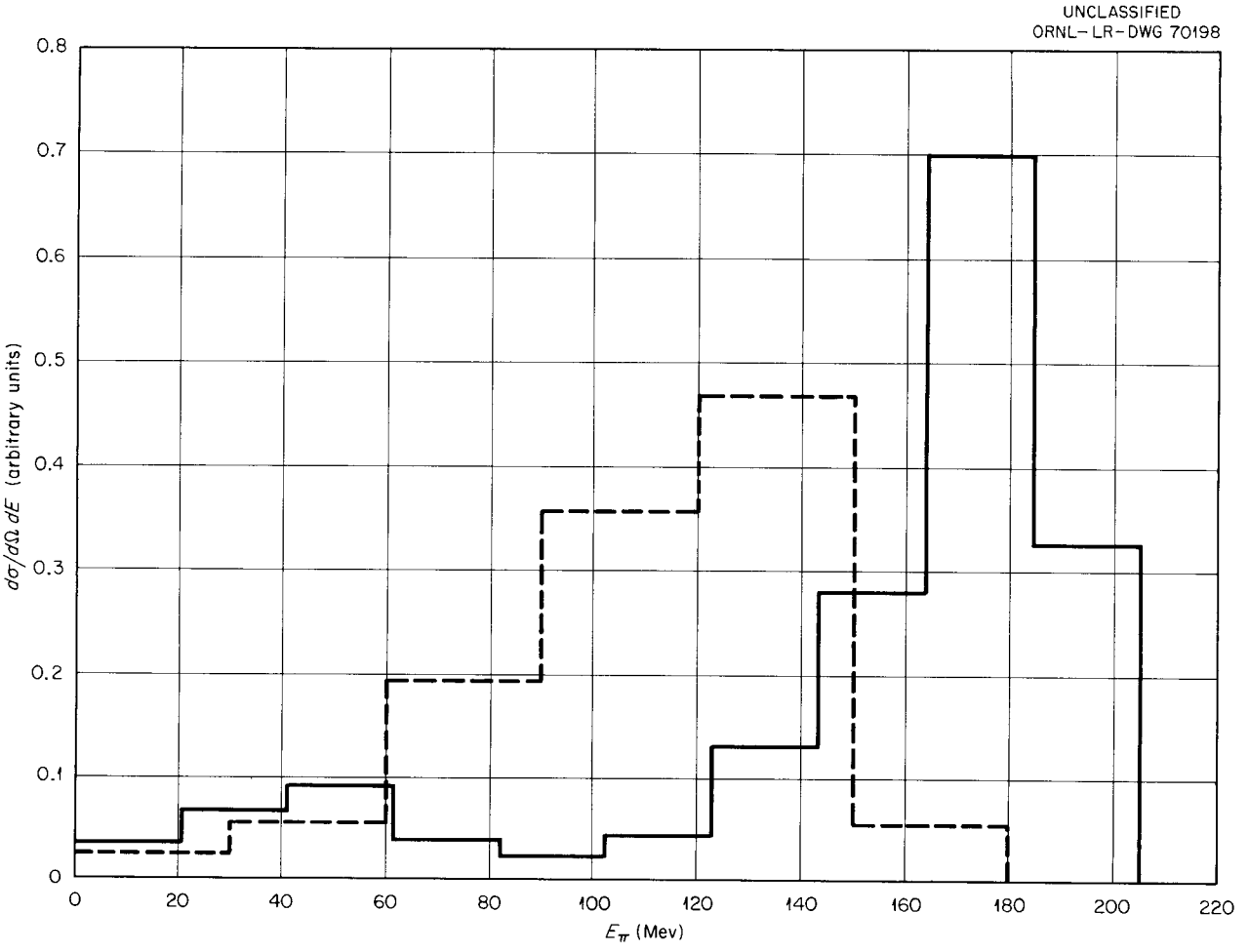

Fig. 7.1.29. Energy Spectra of Nonelastic π^+ Emitted in the Angular Interval 0 to 60° from 195-Mev π^+ on Lithium and Carbon. Dotted lines: experimental results of Petrov *et al.* [*Soviet Phys.-JETP (English Transl.)* 10, 682 (1960)]; solid lines: calculated spectrum; ordinate units are arbitrary.

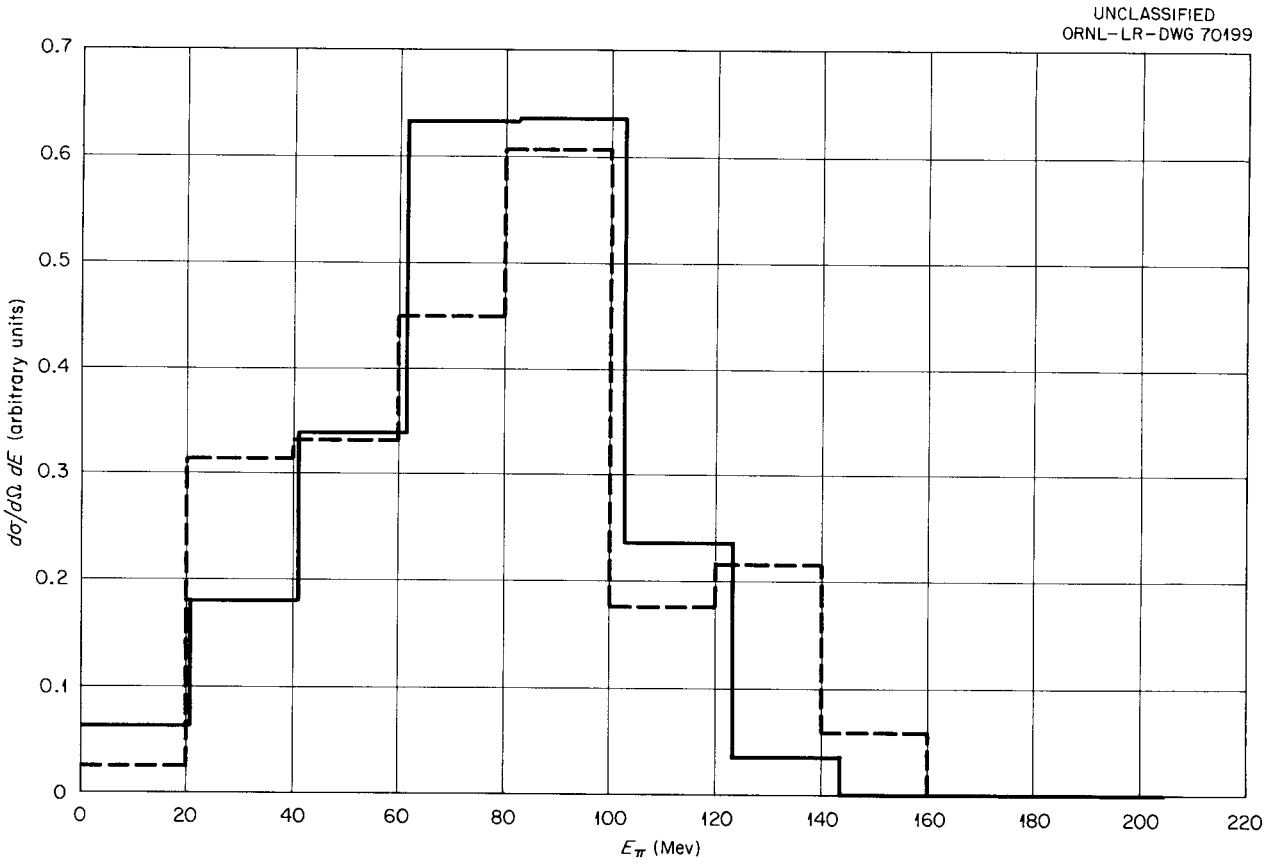

Fig. 7.1.30. Energy Spectra of Nonelastic π^+ Emitted in the Angular Interval 120 to 180° from 195-Mev π^+ on Lithium and Carbon. Dotted lines: experimental results of Petrov *et al.* [*Soviet Phys.-JETP (English Transl.)* 10, 682 (1960)]; solid lines: calculated spectrum; ordinate units are arbitrary.

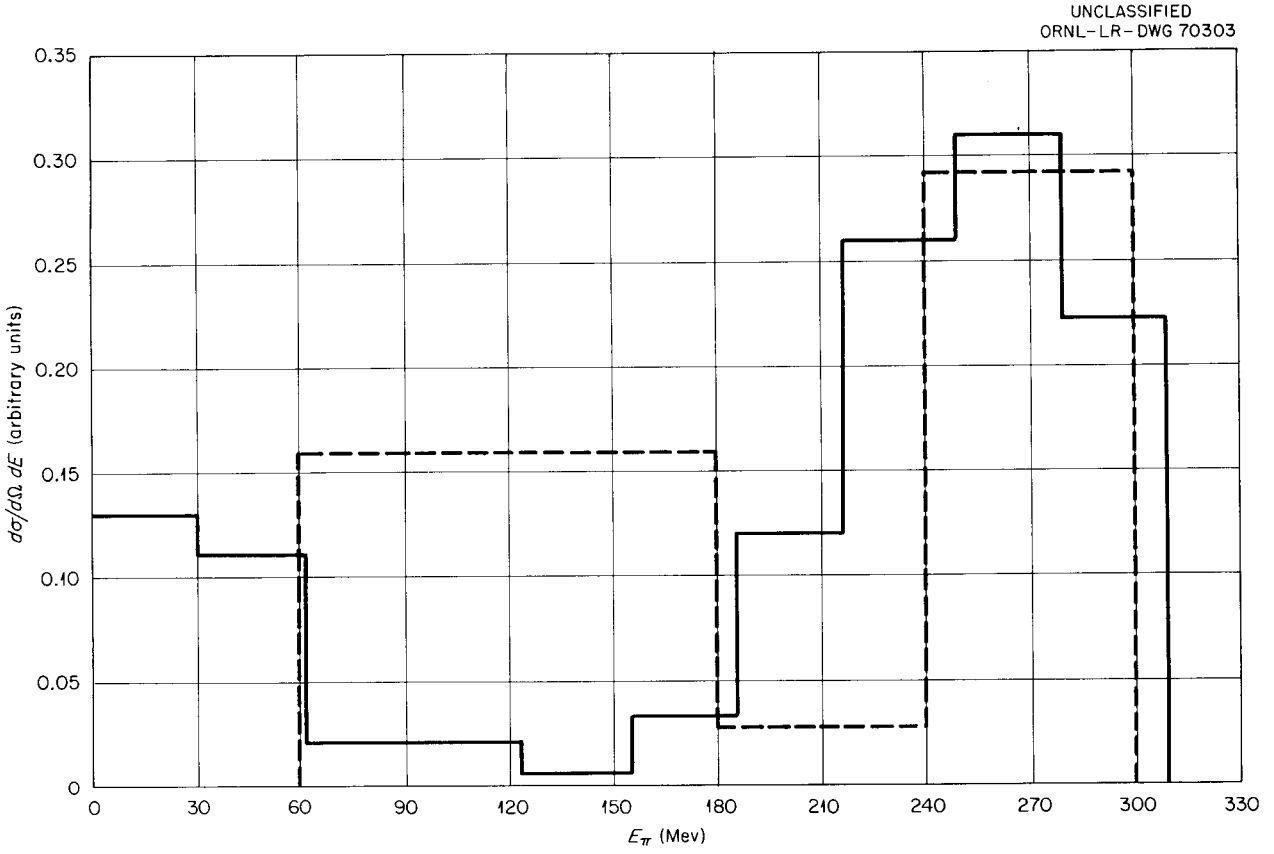

Fig. 7.1.31. Energy Spectra of Nonelastic π^- Emitted in the Angular Interval 0 to 60° from 300-Mev π^- on Heavy-Emulsion Nuclei. Dotted lines: experimental values of Willot-Chemel [*Ann. Phys. (Paris)* 6, 703 (1961)]; solid lines: calculated values for 300-Mev π^- on Ru^{100}.

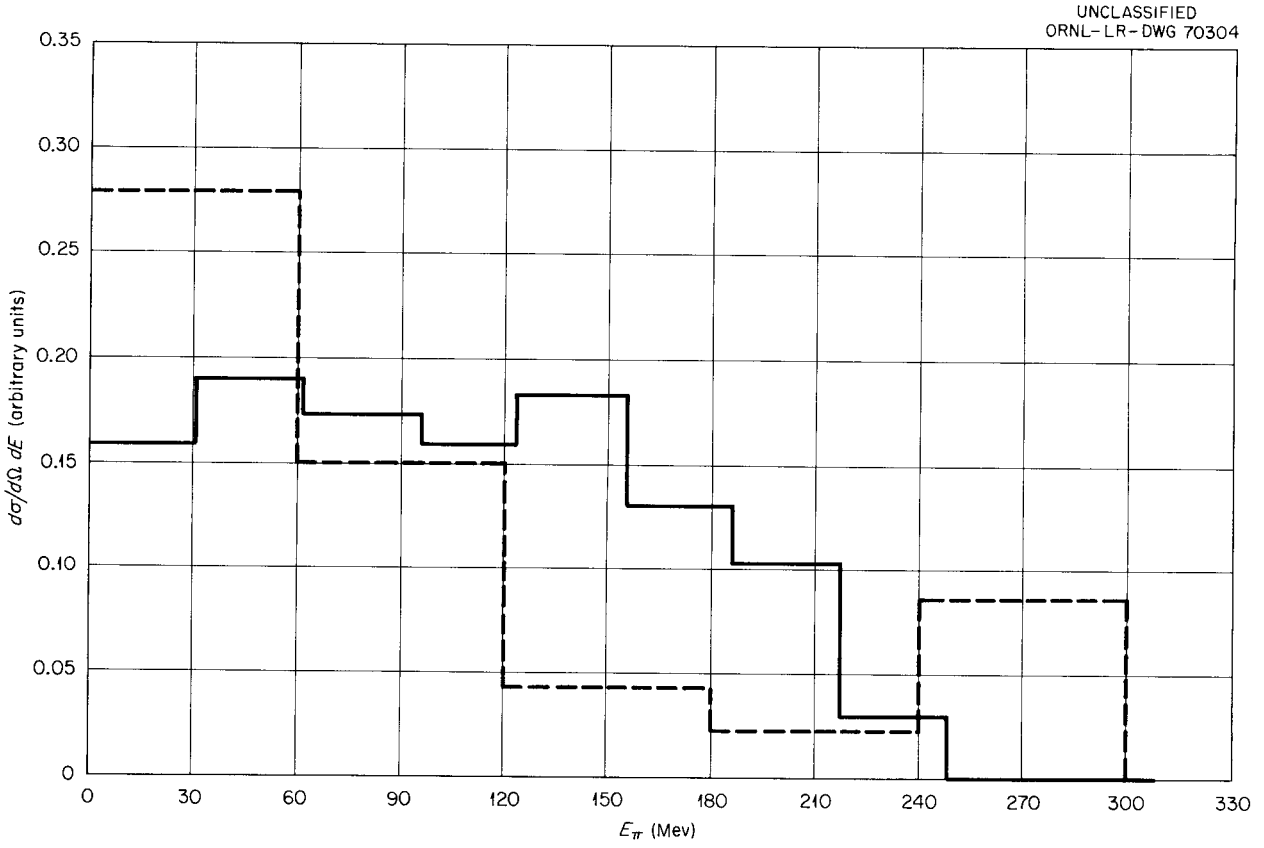

Fig. 7.1.32. Energy Spectra of Nonelastic π^- Emitted in the Angular Interval 60 to 120° from 300-Mev π^- on Heavy-Emulsion Nuclei. Dotted lines: experimental values of Willot-Chemel [*Ann. Phys. (Paris)* 6, 703 (1961)]; solid lines: calculated values for 300-Mev π^- on Ru^{100}.

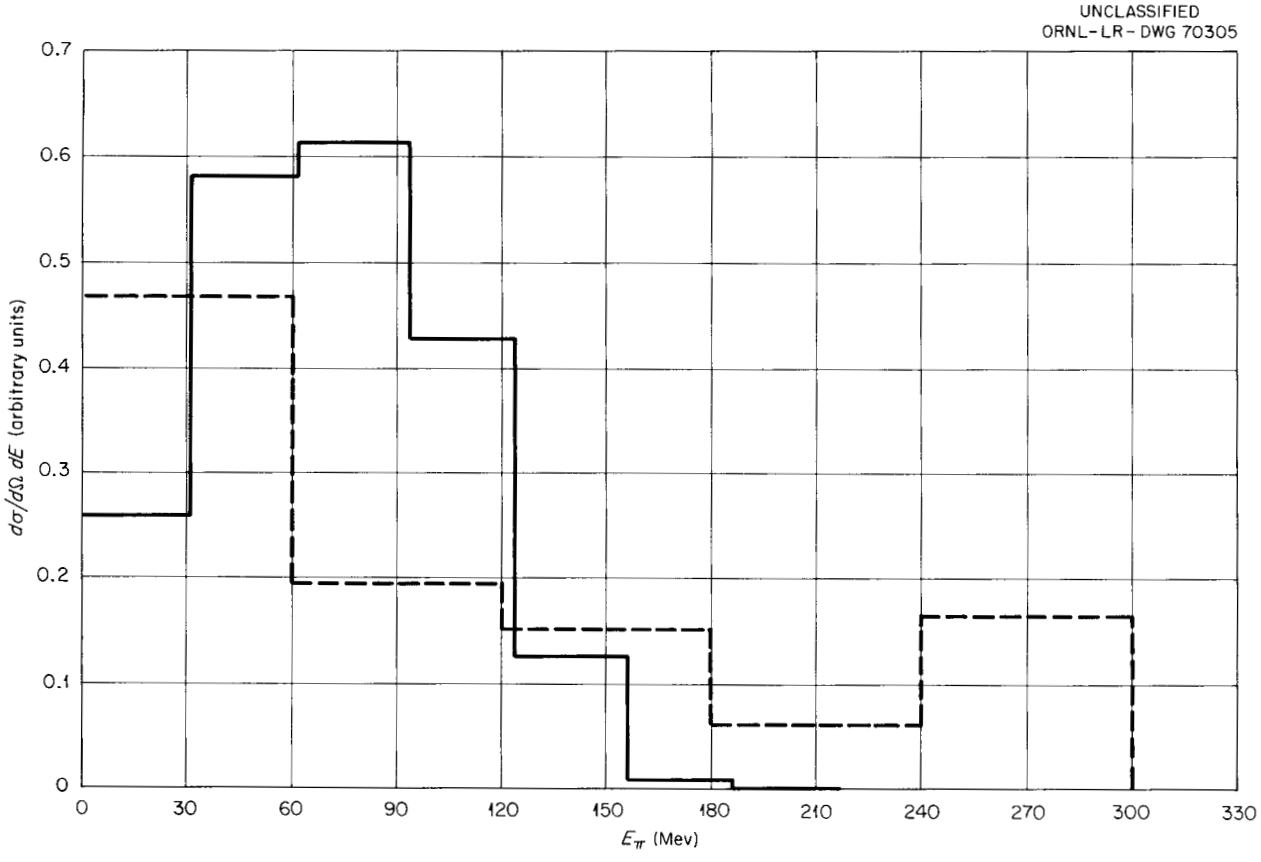

Fig. 7.1.33. Energy Spectra of Nonelastic π^- Emitted in the Angular Interval 120 to 180° from 300-Mev π^- on Heavy-Emulsion Nuclei. Dotted lines: experimental values of Willot-Chemel [*Ann. Phys. (Paris)* 6, 703(1961)]; solid lines: calculated values for 300-Mev π^- on Ru^{100}.

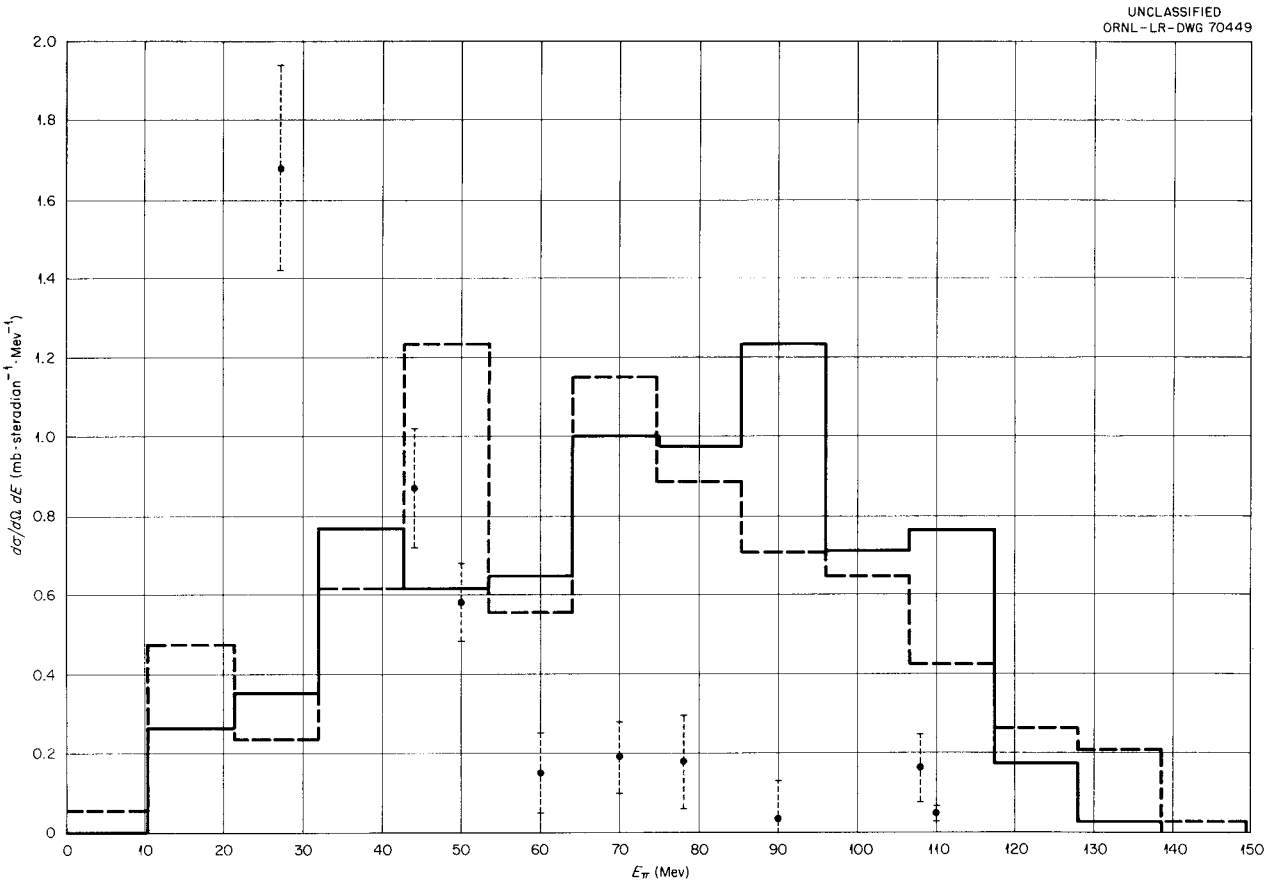

Fig. 7.1.34. Nonelastic π^- Spectra at 90° from 150-Mev π^- on Lead. Calculated spectra for π^- in the interval 78 to 102° for nucleus with medium radius. Solid lines: nonuniform nucleon density distribution within the nucleus; dotted lines: uniform density distribution; circles: Miller's experimental values [*Nuovo Cimento* 6, 882 (1957)].

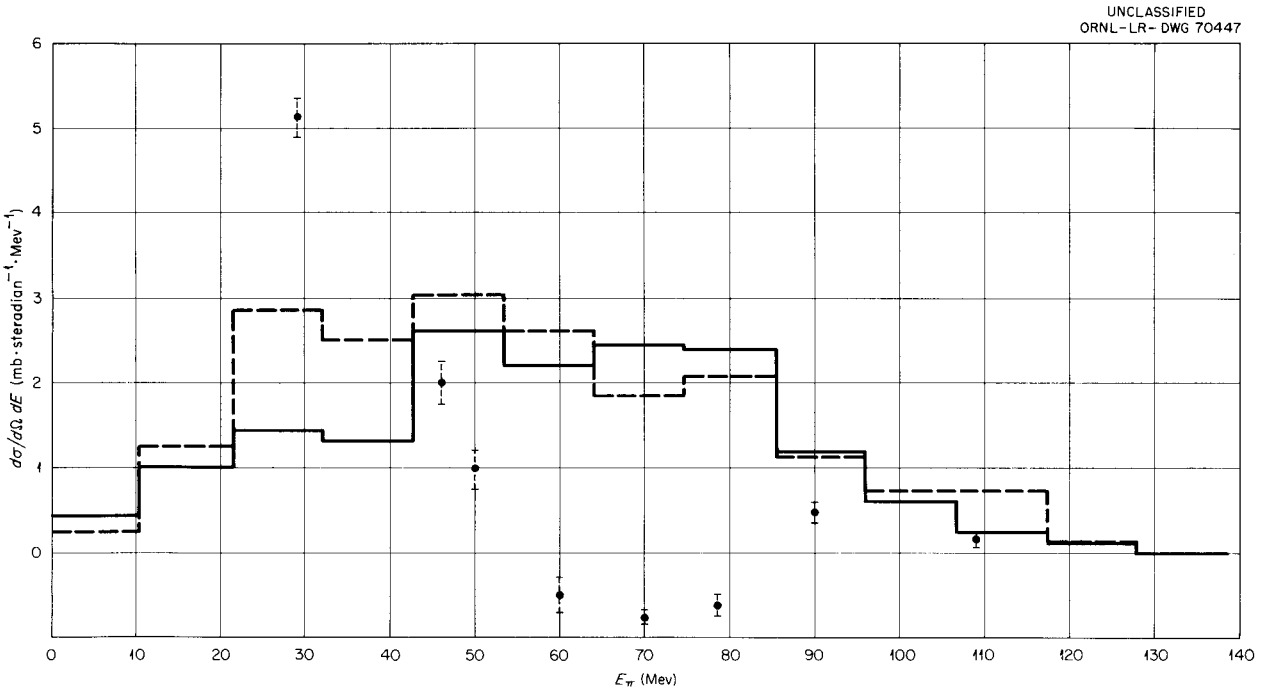

Fig. 7.1.35. Nonelastic π^- Spectra at 138° from 150-Mev π^- on Lead. Calculated spectra for π^- in the interval 130 to 148° for nucleus with medium radius. Solid lines: nonuniform nucleon density distribution within the nucleus; dotted lines: uniform density distribution; circles: Miller's experimental values [*Nuovo Cimento* 6, 882 (1957)].

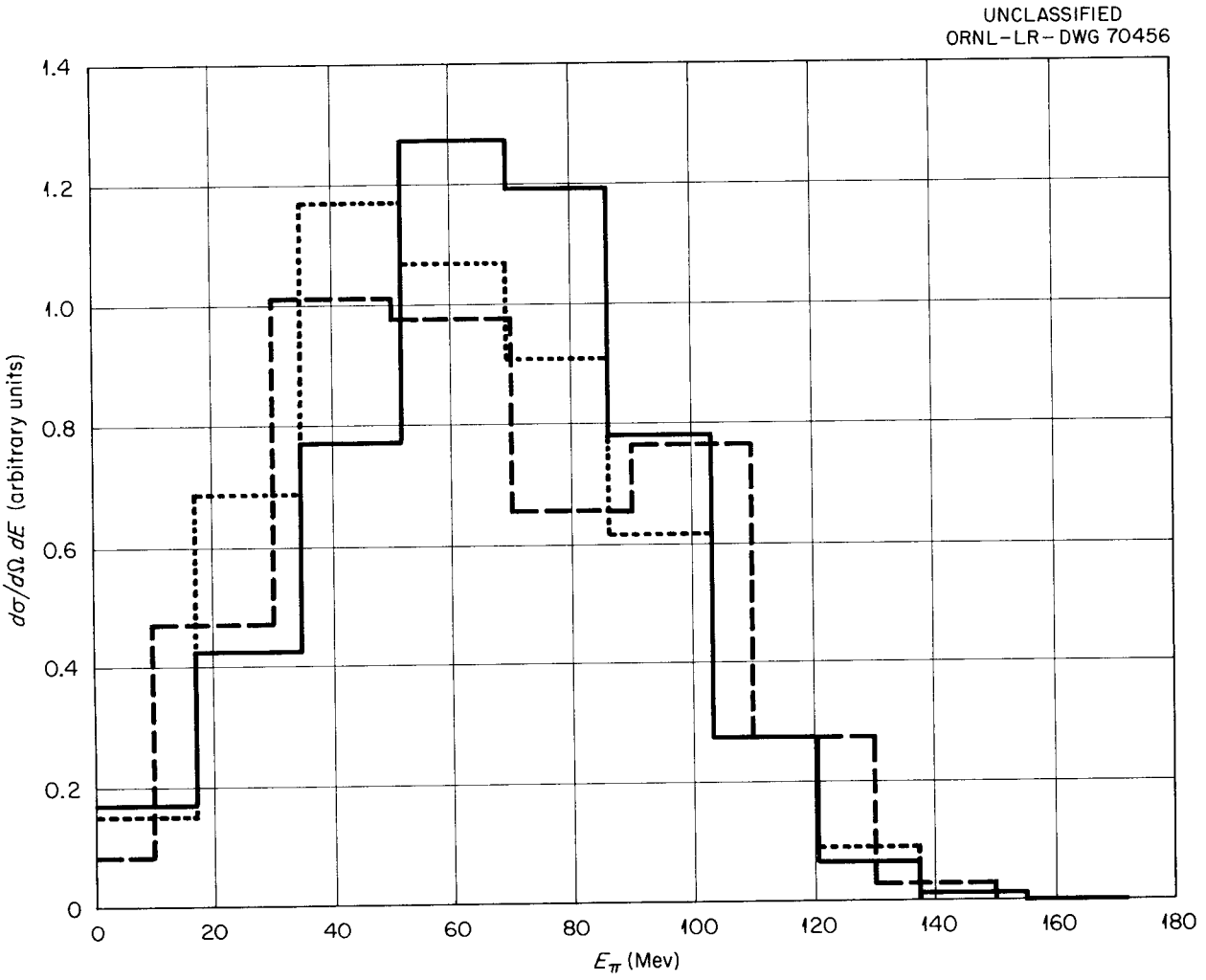

Fig. 7.1.36. Nonelastic Spectrum for π^- Emitted into the Backward Hemisphere from 162-Mev π^- on Heavy-Emulsion Nuclei. Calculated values are for 162-Mev π^- on Ru^{100} with a medium nuclear radius. Solid lines: nonuniform nucleon density distribution within the nucleus; dashed lines: uniform nucleon density distribution; dotted lines: experimental results of Nikolskii *et al.* [*Soviet Phys.-JETP (English Transl.)* 5, 93 (1957)]; ordinate units are arbitrary.

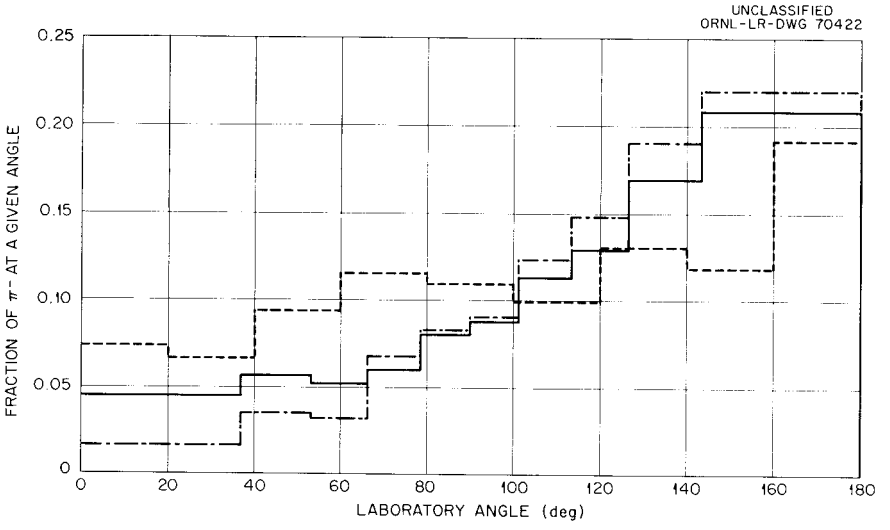

Fig. 7.1.37. Angular Distribution of Nonelastic π^- from 162-Mev π^- on Heavy-Emulsion Nuclei. Calculated distribution for nucleus with medium radius. Dotted lines: experimental values of Nikolskii *et al.* [*Soviet Phys.-JETP (English Transl.)* 5, 93 (1957)]; solid lines: calculated spectra for nonuniform nucleon density distribution within the nucleus; dash-dot lines: uniform nucleon density distribution.

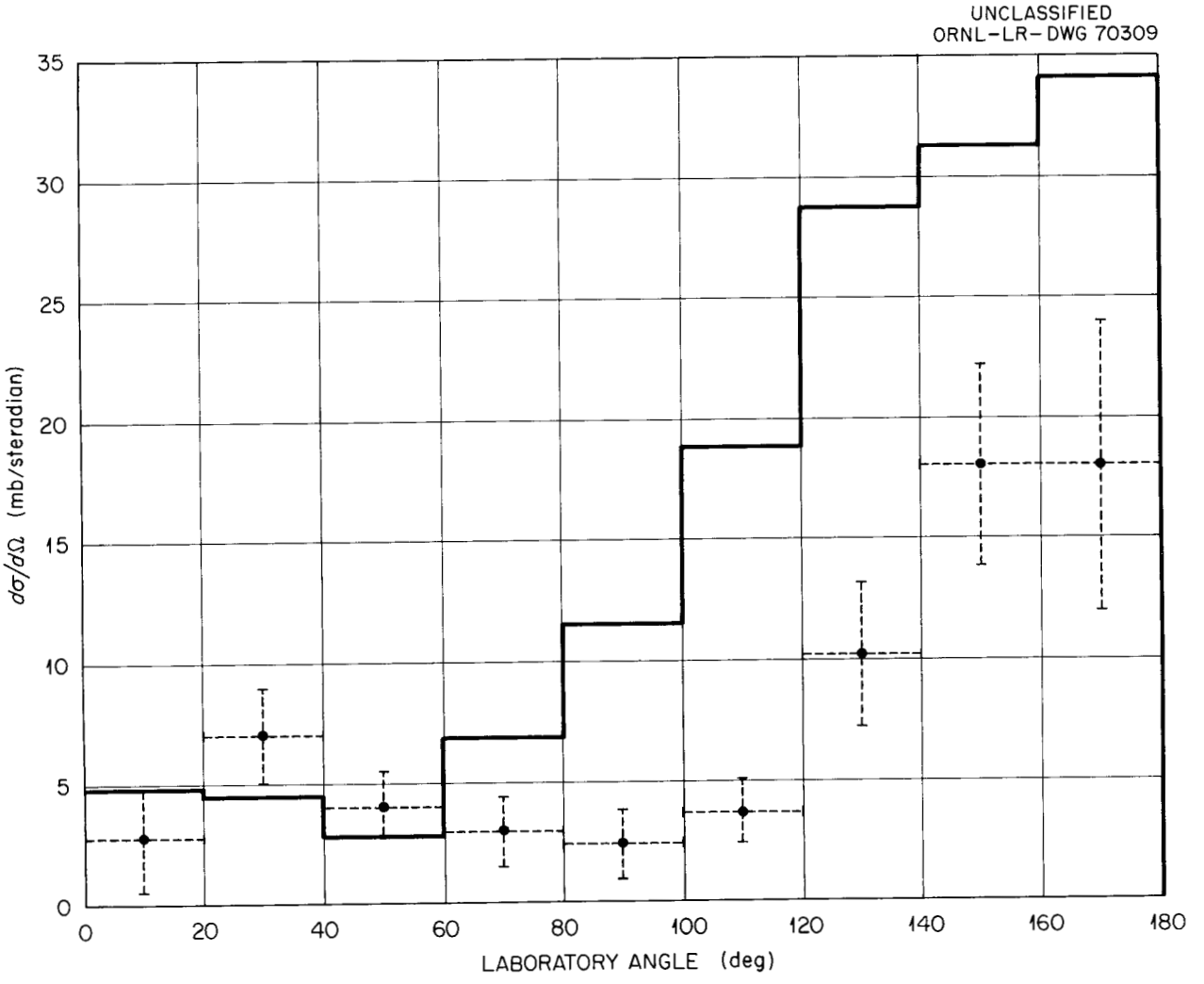

Fig. 7.1.38. Angular Distribution of Nonelastic π^- Scattered with Energy Loss Greater Than 40 Mev for 125-Mev π^- on Carbon. Circles: experimental values of Kessler and Lederman [*Phys. Rev.* 94, 689 (1954)]; solid lines: calculated distribution.

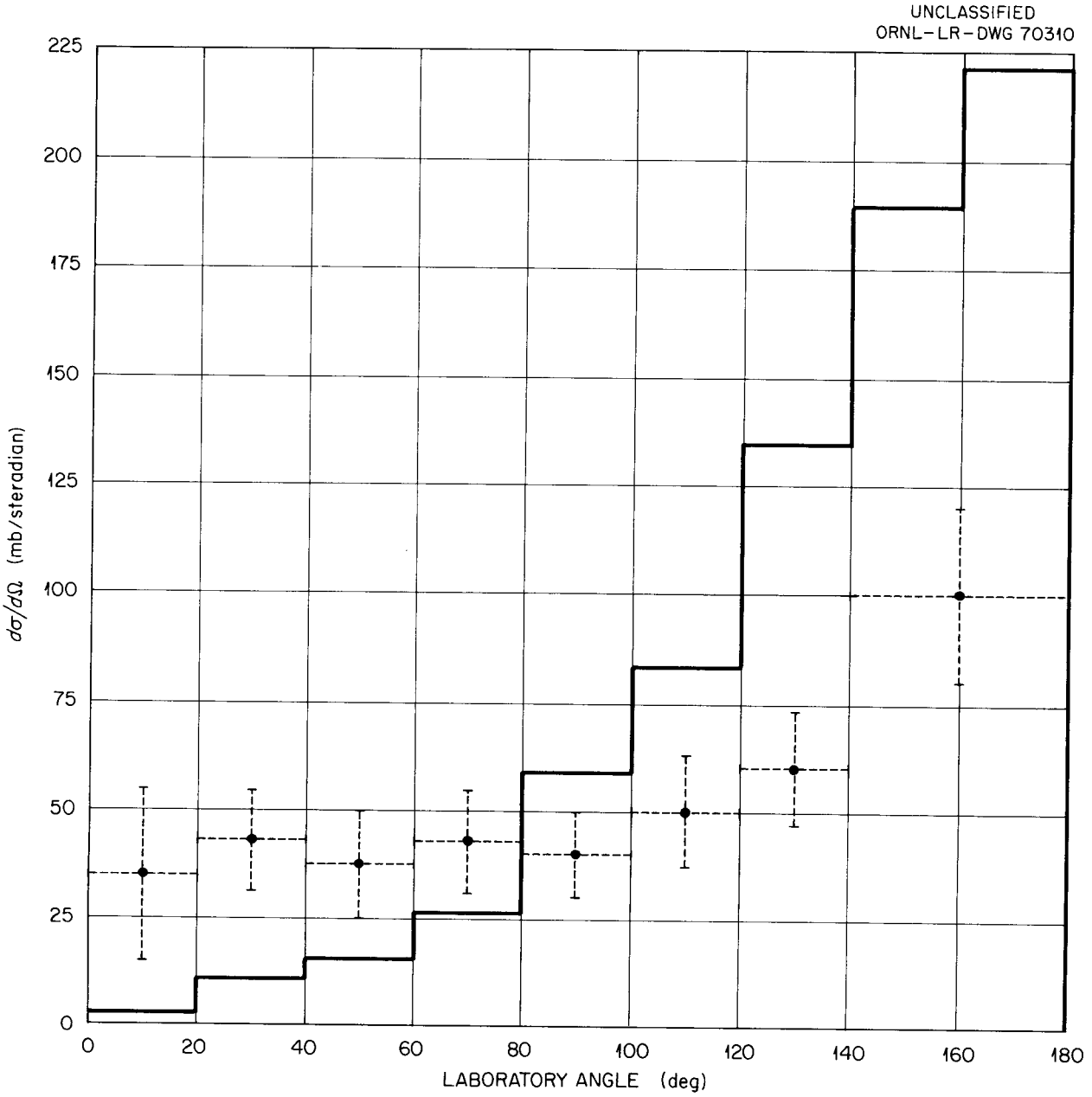

Fig. 7.1.39. Angular Distribution of Nonelastic π^- Scattered with Energy Loss Greater Than 40 Mev for 125-Mev π^- on Lead. Circles: experimental values of Kessler and Lederman [*Phys. Rev.* 94, 689 (1954)]; solid lines: calculated distribution.

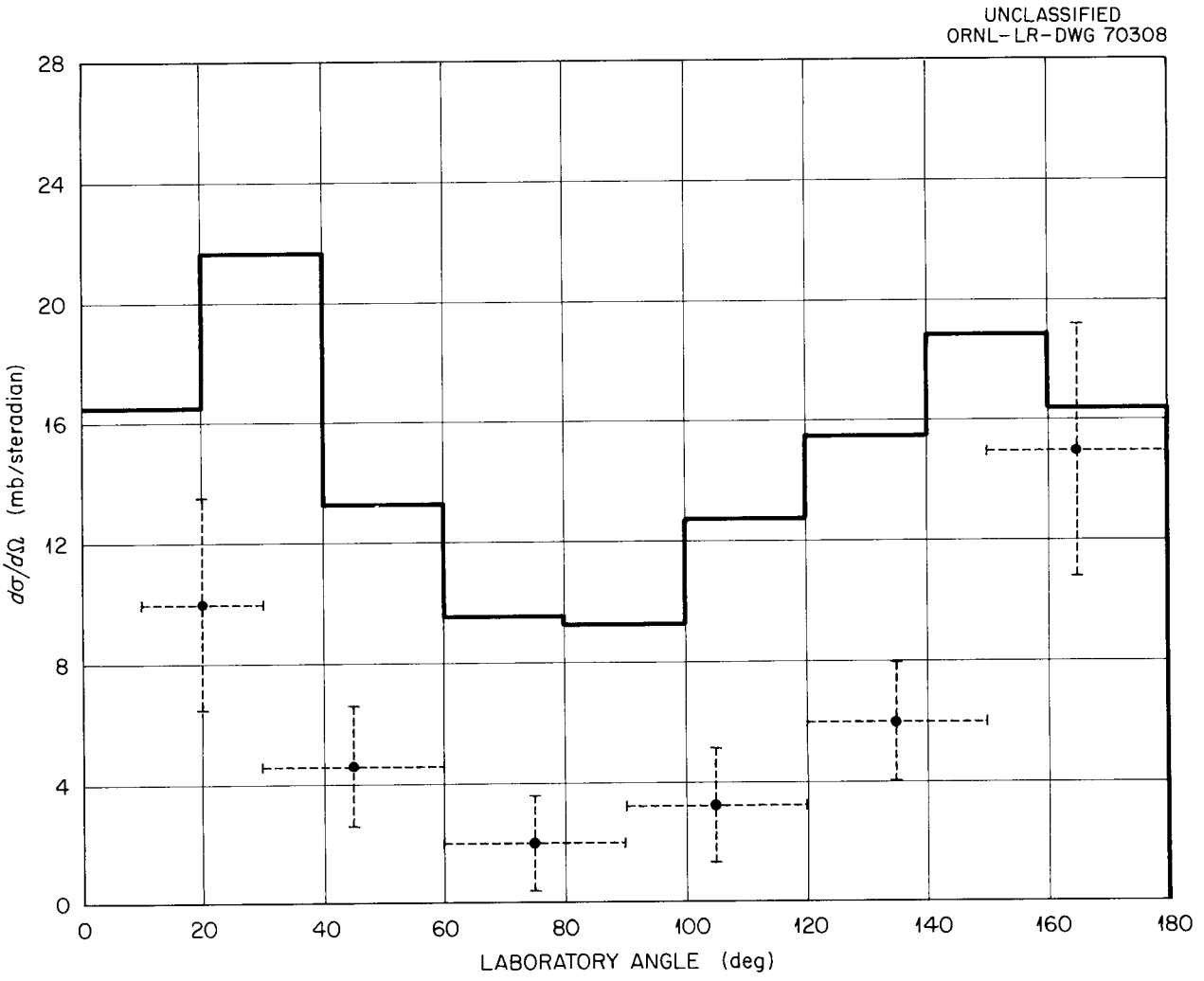

Fig. 7.1.40. Angular Distribution of Nonelastic π^+ from 195-Mev π^+ on Lithium. Circles: experimental values of Petrov *et al.* [*Soviet Phys.-JETP (English Transl.)* **10**, 682 (1960)]; solid lines: calculated π^+ spectrum reduced by the ratio of the experimental to the calculated total nonelastic cross section.

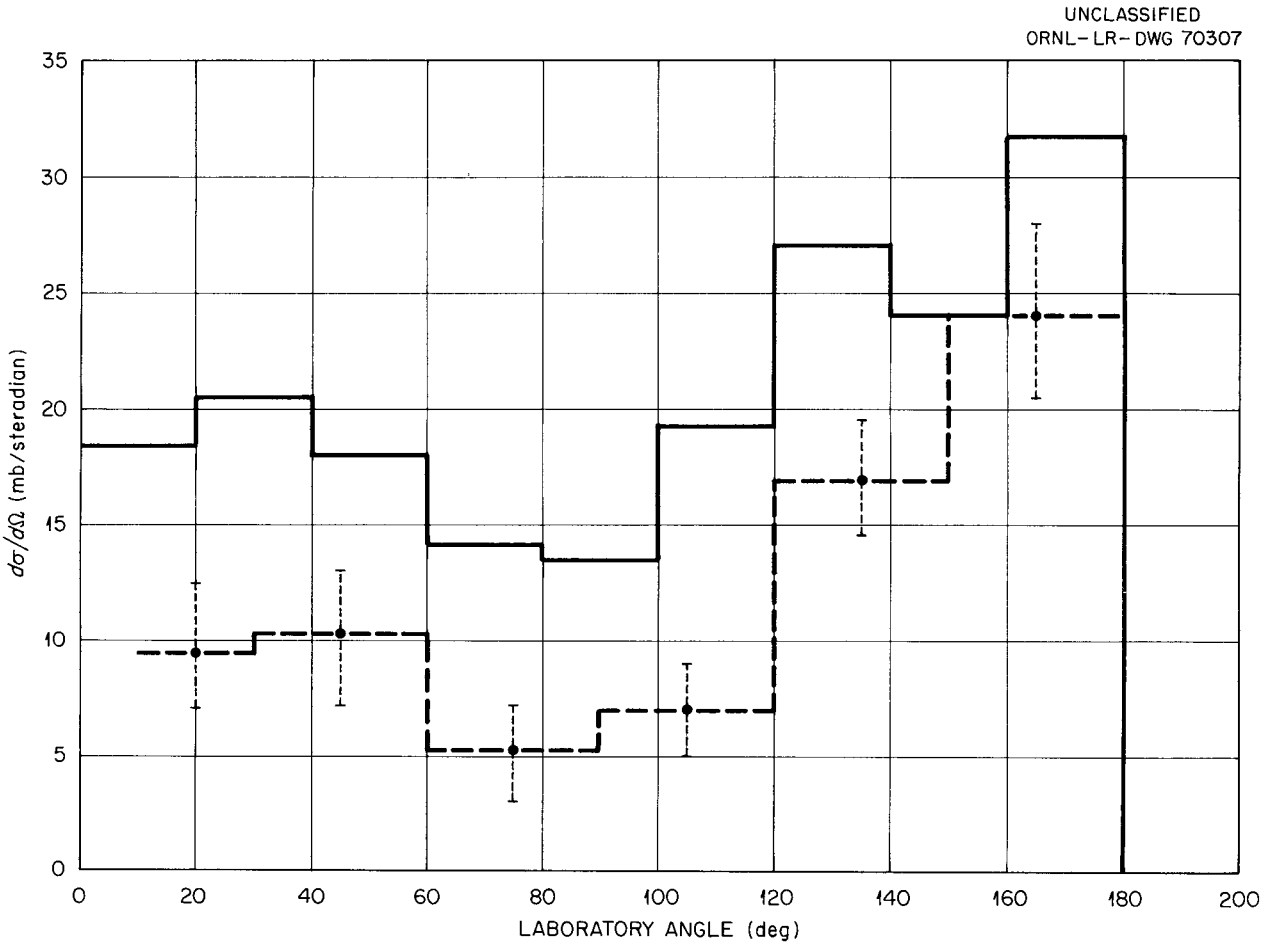

Fig. 7.1.41. Angular Distribution of Nonelastic π^+ from 195-Mev π^+ on Carbon. Circles: experimental values of Petrov *et al.* [*Soviet Phys.-JETP (English Transl.)* 10, 682 (1960)]; solid lines: calculated spectrum.

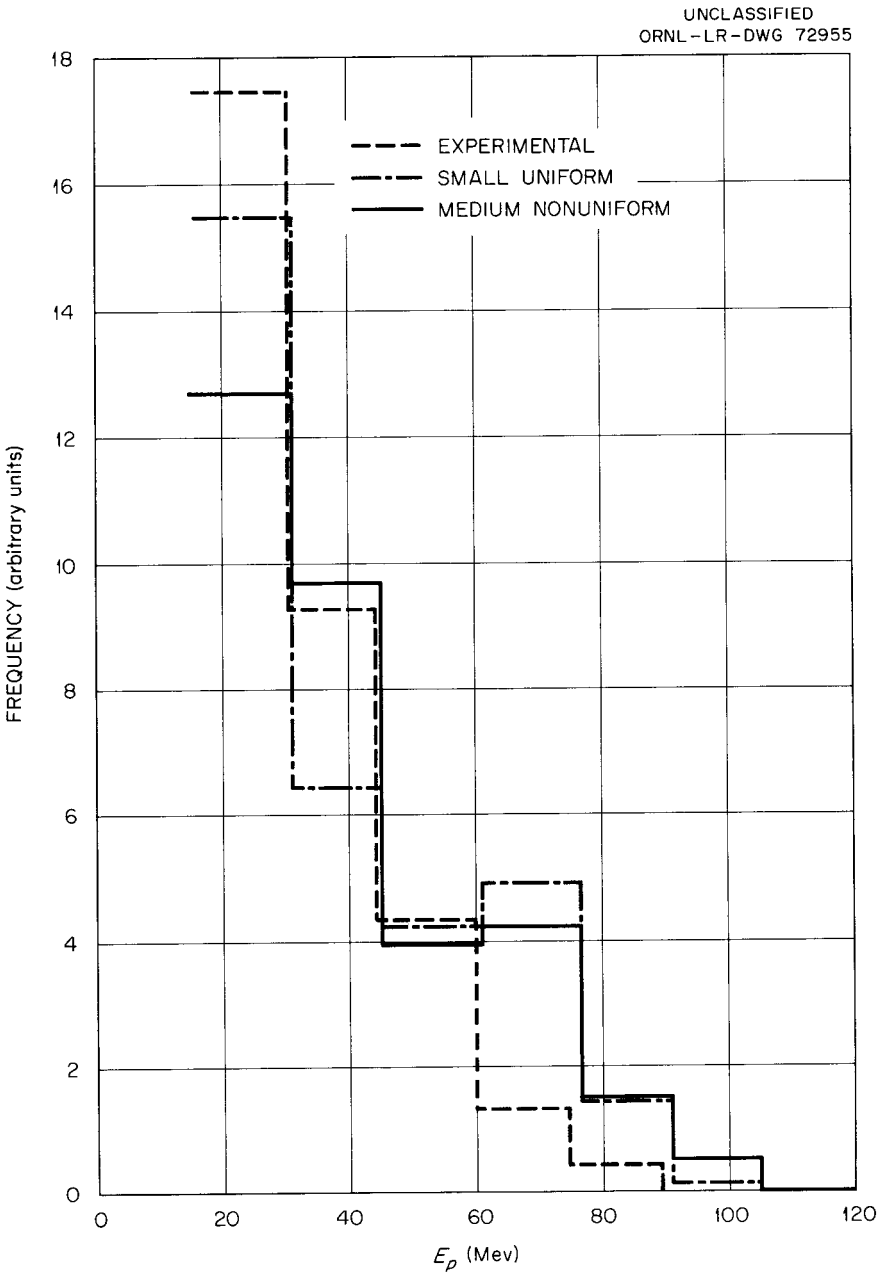

Fig. 7.1.42. Energy Spectra of Protons with Energies Greater Than 15 Mev for Slow π^- Absorption of Heavy-Emulsion Nuclei. Calculated values are for 1-Mev π^- on Ru^{100}. Solid lines: calculated spectrum for medium nonuniform nuclear configuration; dash-dot lines: calculated spectrum for small uniform configuration; dotted lines: experimental results of Azimov *et al.* [*Soviet Phys.-JETP (English Transl.)* 4, 632 (1957)]; ordinate units are arbitrary.

7.2. COMPILATION OF REACTIONS CALCULATED FOR PARTICLES WITH ENERGIES FROM ABOUT 50 TO 350 Mev

H. W. Bertini and L. Dresner

The completion of the intranuclear cascade code (Sec. 7.1) makes it possible to calculate a vast quantity of data on nuclear reactions. These data are expected to be of value for all problems involving radiation from nucleons or pions in the energy range from about 50 to 350 Mev. A compilation of the data is under way and should be completed within the next three or four months.

The cases to be calculated are as follows: incident neutrons and protons with energies at 25, 50, 100, 150, ... 400 Mev on C^{12}, O^{16}, Al^{27}, Cr^{52}, Cu^{65}, Ru^{100}, Ce^{140}, W^{184}, Pb^{207}, and U^{238}; and incident π^+ and π^- on the same elements with energies at the same intervals but extending only to 300 Mev. The calculation is valid at higher energies for incident nucleons than it is for pions because pion production for incident nucleons, which is ignored in the calculation, takes place at higher energies. The end points in the energy ranges to be used are probably beyond the limits of validity of the calculation but are included for purposes of extrapolation.

The compilation will consist mainly of tables and graphs of data from representative cases. The data for the remaining cases will be available on request. The work will include results from the cascade process alone, from the evaporation process alone,[1] and from the combined processes.

As a reminder, the cascade calculation is based on the assumption that high-energy nuclear reactions can be treated as though the interactions occur on a particle-particle basis within the nucleus. When the particle energy becomes small ($\lambda \rightarrow$ large), this assumption is no longer valid, and the reaction is assumed to be represented by the de-excitation of a highly excited nucleus, which occurs by the evaporation or "boil-off" of nucleons. In the calculations this transition is abrupt and occurs at a somewhat arbitrary energy – the cutoff energy of the cascade calculation. However, neither the total nucleon multiplicities nor the combined cascade and evaporation spectra are very sensitive to this cutoff energy, as is illustrated in Figs. 7.2.1–7.2.7. The cutoff energies used in the calculations are 1.6 Mev for Al^{27}, 4.2 Mev for Ru^{100}, and 6.7 Mev for Pb^{208}. The lower limit of the proton spectra for lead, Fig. 7.2.7, is determined by the cascade cutoff energy because there is very little proton evaporation. The correct spectra would drop rapidly for energies smaller than the coulomb barrier; so some care must be exercised in using the data for similar cases. The combined neutron spectrum is illustrated in Fig. 7.2.4 for Ru^{100} only, since it is very similar to those for Al^{27} and Pb^{208}.

A list of the data that will be available on request is as follows:

I. Cascade process
   A. For the cascade residual nucleus
      1. Parallel and perpendicular momentum distributions and average value of each
      2. Momentum distribution and average value
      3. Excitation energy distribution and average value

[1] L. Dresner, *EVAP – A Fortran Program for Calculating the Evaporation of Various Particles from Excited Compound Nuclei*, ORNL CF-61-12-30 (Dec. 19, 1961).

4. Angular distribution
5. Average residual mass

B. For the emission of combinations of cascade particles
1. Cross section for each combination
2. All the distributions above for several specific combinations

C. For each type of emitted cascade particle (proton, neutron, π^+, π°, π^-)
1. Average number emitted
2. Average energy
3. Energy spectra for all angles
4. $\frac{d\sigma}{d\Omega E}(E)$ for four angular intervals
5. Differential cross section for scattering into these intervals
6. Average energy of emission into these intervals
7. Angular distribution for all energies
8. $\frac{d\sigma}{d\Omega}(\theta)$ for three energy intervals
9. Cross section for the emission of η particles into three energy intervals ($\eta = 1, 2, \ldots 15$)
10. $\frac{d\sigma}{d\Omega}(x)$ for the emission of two protons, where x is the angle between them

D. For incident pions
1. Pion absorption cross section
2. Pion charge-exchange cross section

E. Total nonelastic cross section for the incident particles

II. Evaporation process
A. Cross sections for the various residual nuclei following evaporation
B. For the evaporation particles (protons, neutrons, deuterons, tritons, He^3, alphas)
1. Average number
2. First, second, and third moments of the energy distribution
3. Energy distribution

III. Combined cascade and evaporation process
A. For emitted neutrons and protons
1. Average number emitted
2. Energy spectra

Figures 7.2.8–7.2.29 exemplify the type of data to be contained in the compilation. The curves drawn through the points of some of the data illustrate the general trends. The deviations of the points from the curves can be quite large in cases where the statistics are poor (Fig. 7.2.26).

Some of the data will suffer because of poor statistics, but prohibitive machine time would be involved in providing good statistics for all the data. A reasonable compromise in this respect was attempted.

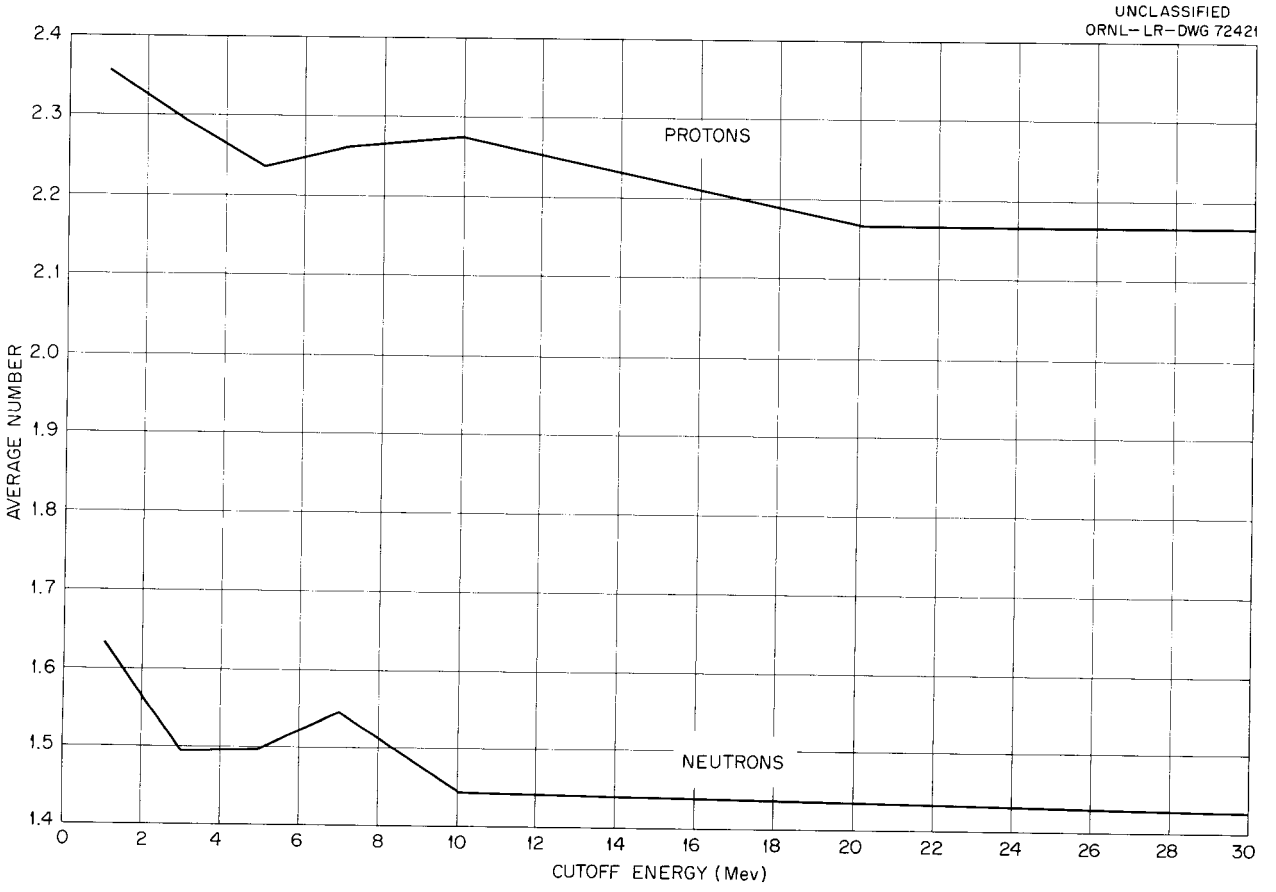

Fig. 7.2.1. Average Number of Cascade and Evaporation Protons and Neutrons vs Cutoff Energy for 150-Mev Protons on $_{13}Al^{27}$.

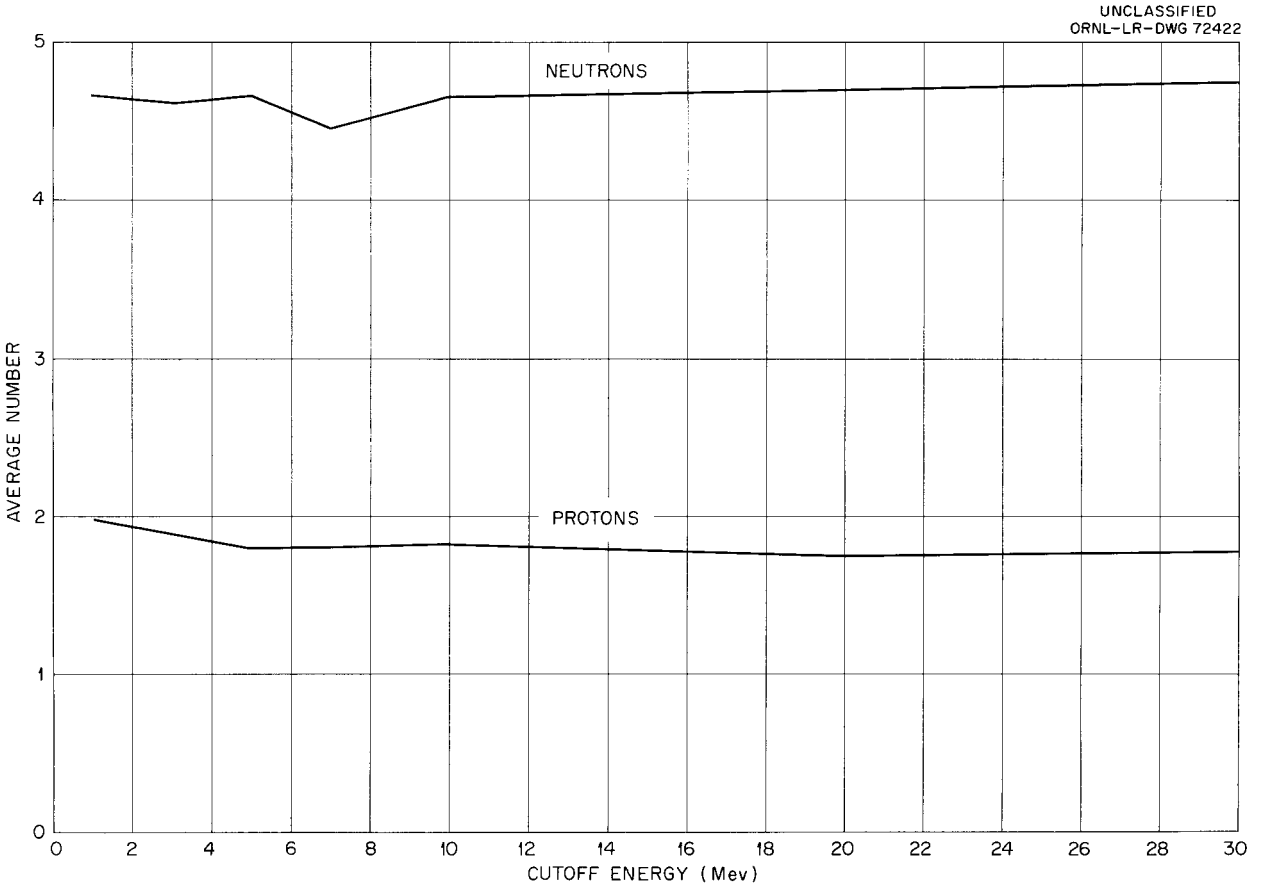

Fig. 7.2.2. Average Number of Cascade and Evaporation Protons and Neutrons vs Cutoff Energy for 150-Mev Protons on $_{44}Ru^{100}$.

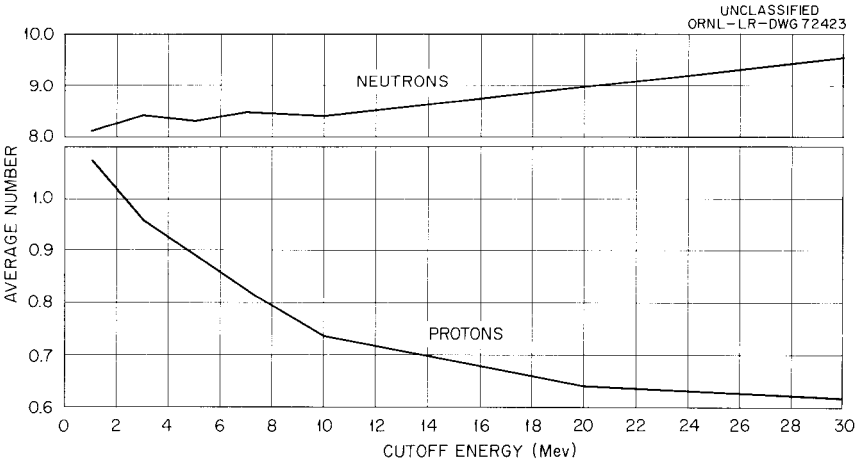

Fig. 7.2.3. Average Number of Cascade and Evaporation Protons and Neutrons vs Cutoff Energy for 150-Mev Protons on $_{82}Pb^{208}$.

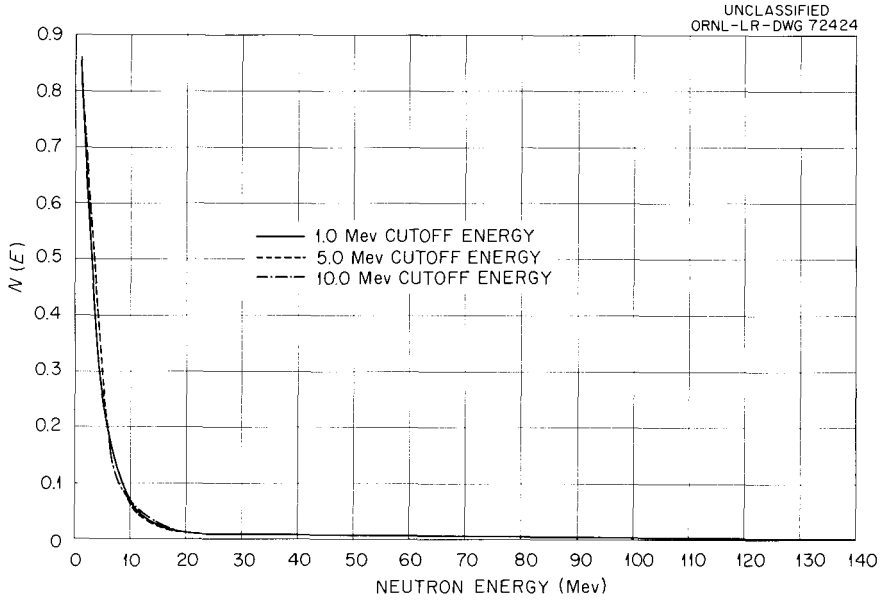

Fig. 7.2.4. Cascade and Evaporation Neutron Spectra for 150-Mev Protons on $_{44}Ru^{100}$.

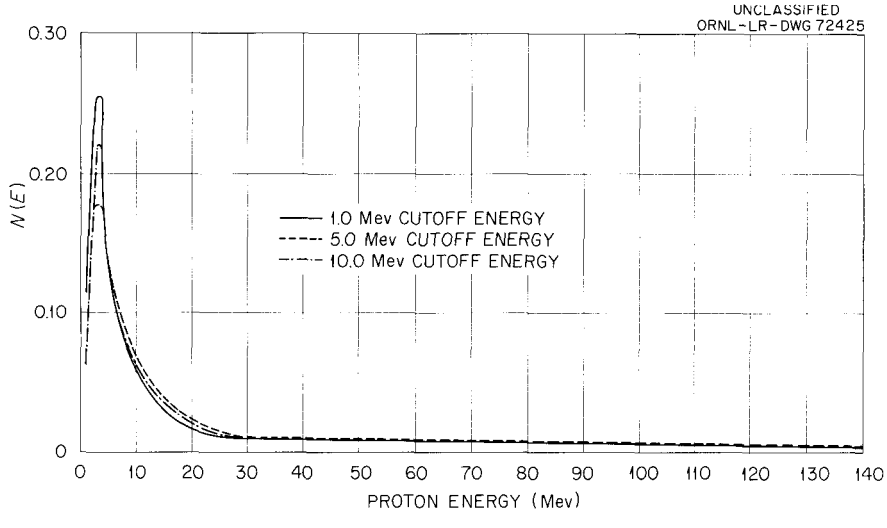

Fig. 7.2.5. Cascade and Evaporation Proton Spectra for 150-Mev Protons on $_{13}Al^{27}$.

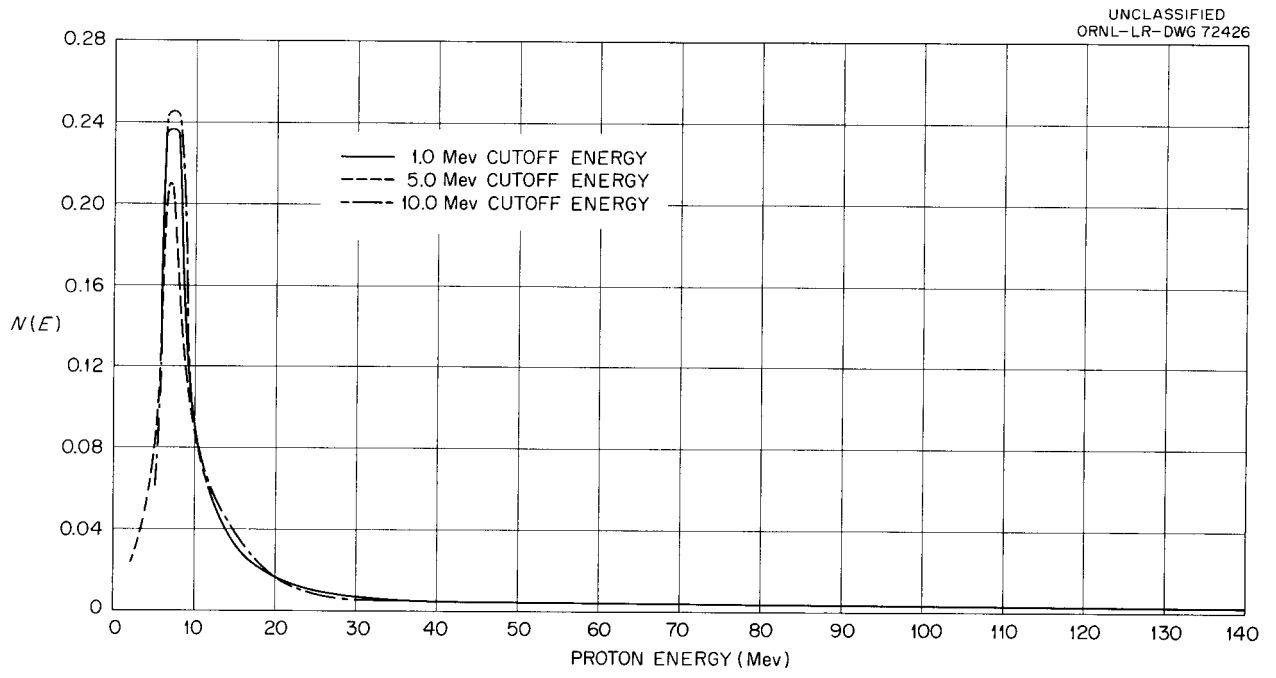

Fig. 7.2.6. Cascade and Evaporation Proton Spectra for 150-Mev Protons on $_{44}Ru^{100}$.

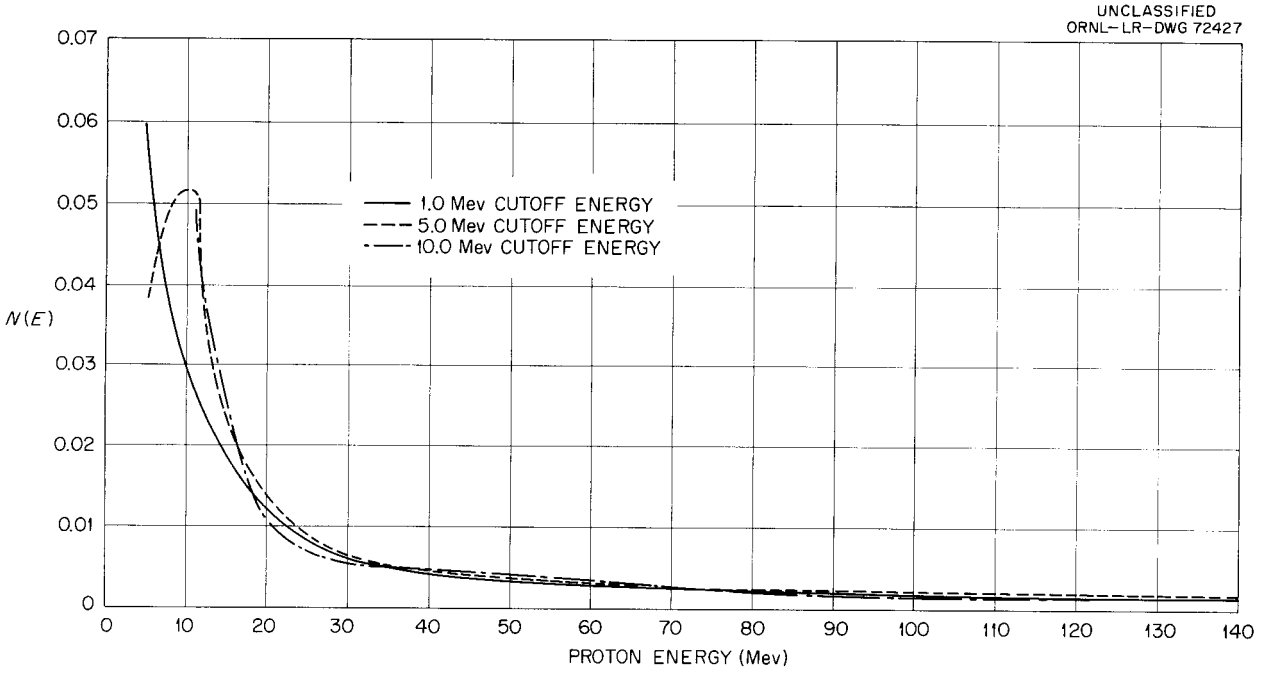

Fig. 7.2.7. Cascade and Evaporation Proton Spectra for 150-Mev Protons on $_{82}Pb^{208}$.

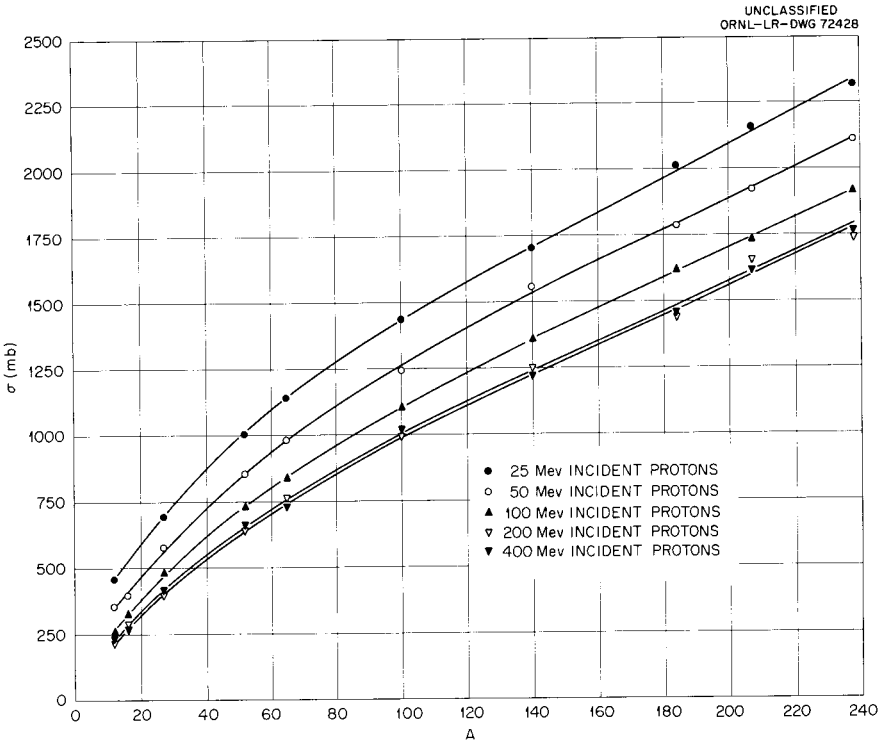

Fig. 7.2.8. Total Nonelastic Cross Section vs Atomic Number A for Incident Protons.

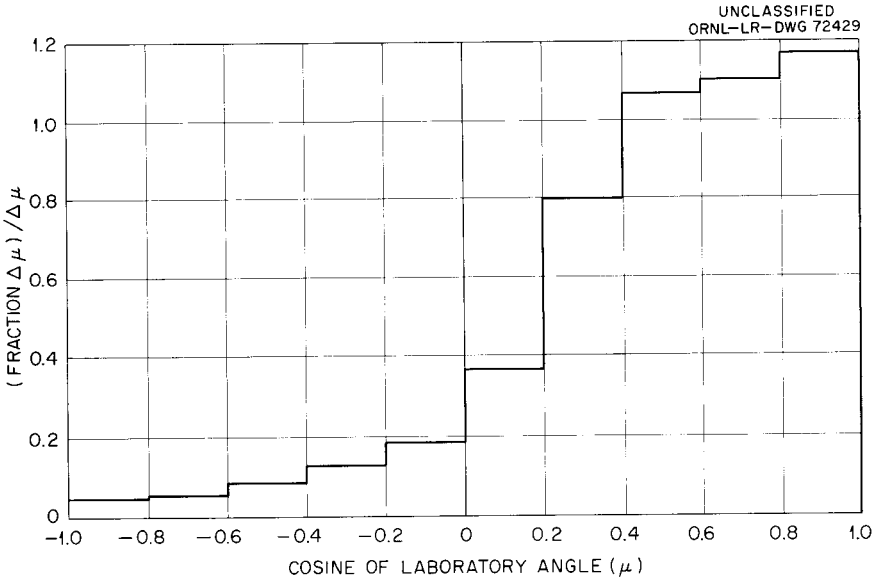

Fig. 7.2.9. Angular Distribution of the Cascade Residual Nucleus for 200-Mev Protons on $_{13}Al^{27}$.

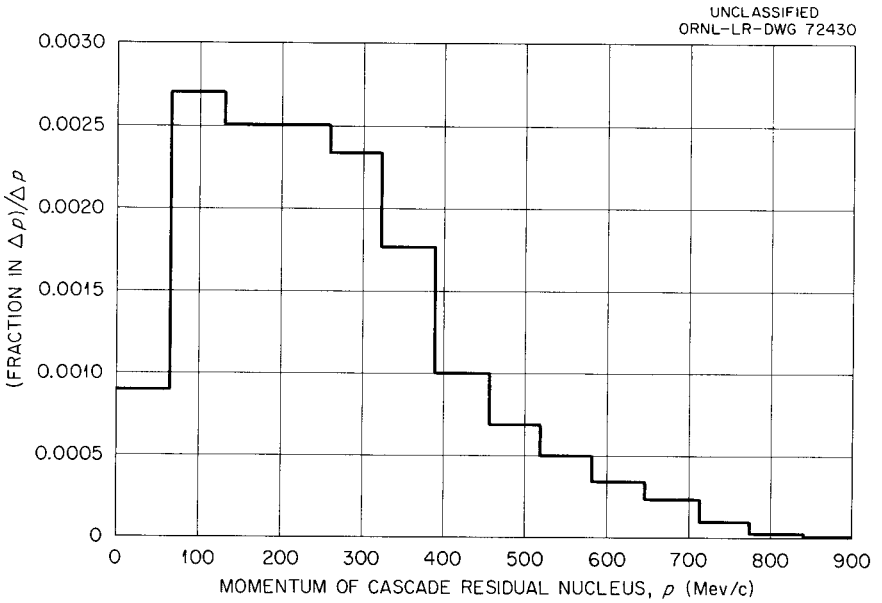

Fig. 7.2.10. Momentum Distribution of the Cascade Residual Nucleus for 200-Mev Protons on $_{13}Al^{27}$.

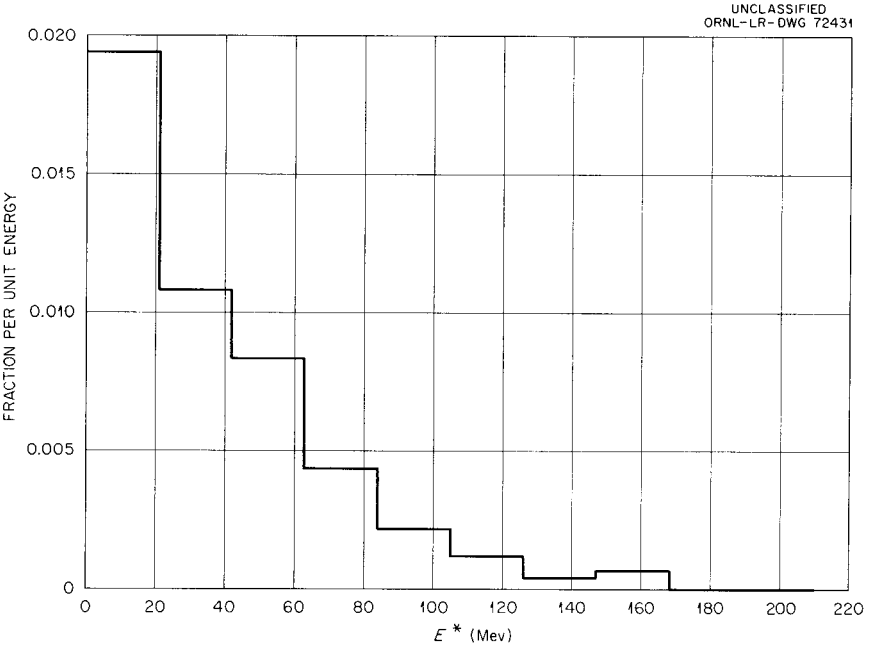

Fig. 7.2.11. Excitation Energy Distribution of the Cascade Residual Nucleus for 200-Mev Protons on $_{13}Al^{27}$.

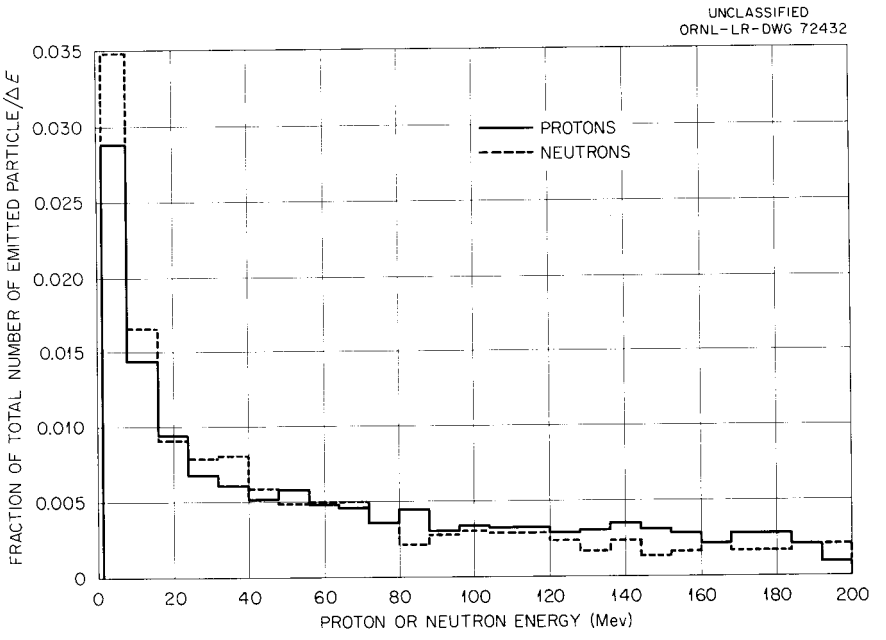

Fig. 7.2.12. Energy Spectrum of Emitted Cascade Protons and Neutrons for 200-Mev Protons on $_{13}Al^{27}$.

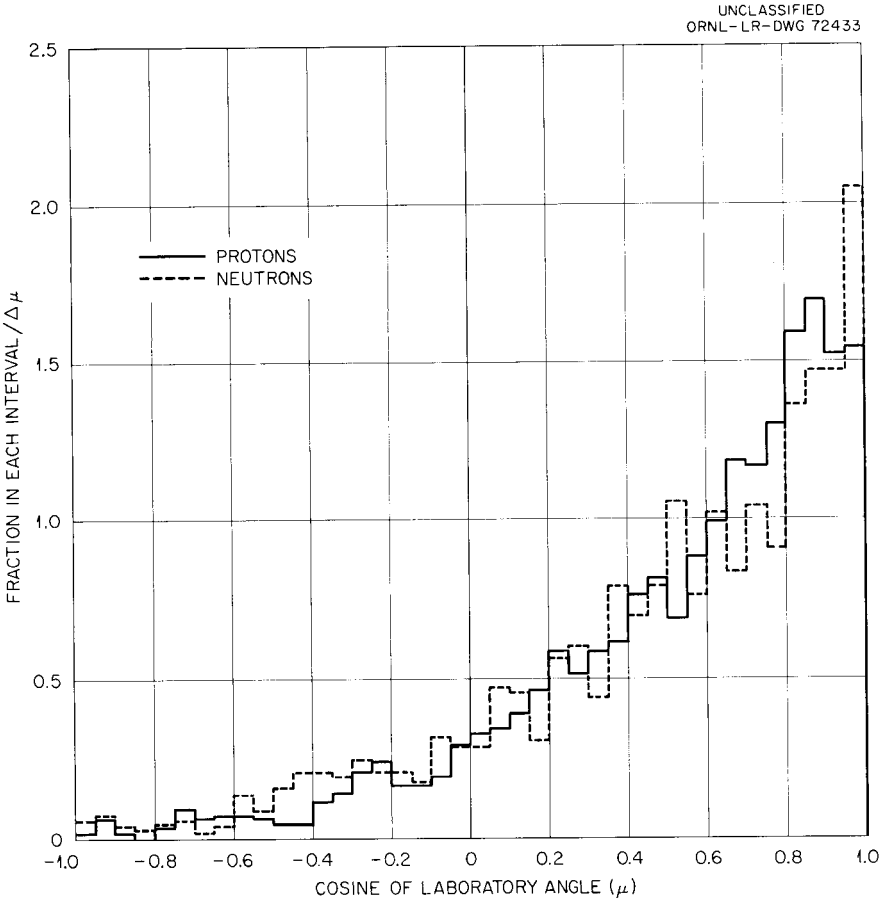

Fig. 7.2.13. Angular Distribution of Emitted Cascade Protons and Neutrons for 200-Mev Protons on $_{13}Al^{27}$.

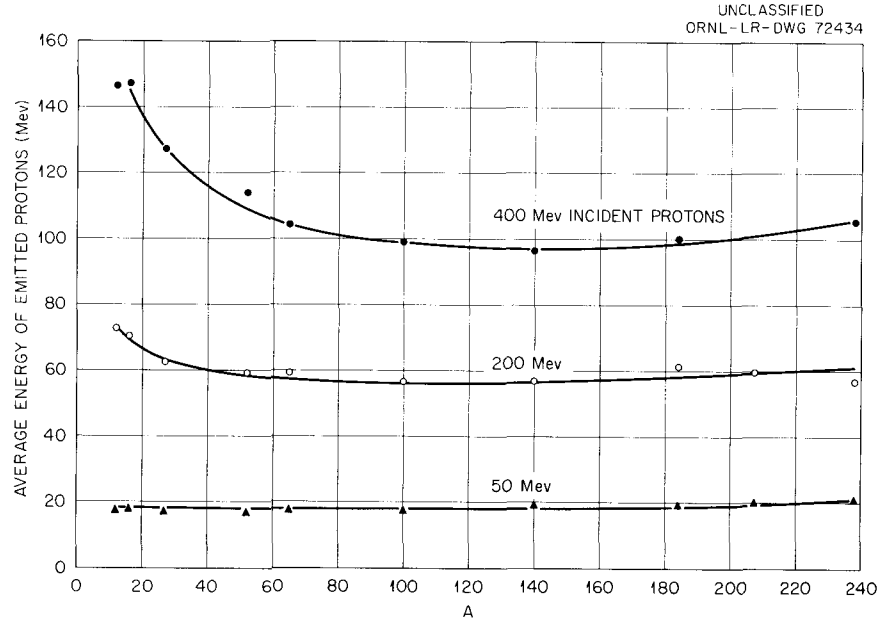

Fig. 7.2.14. Average Energy of Emitted Cascade Protons vs Atomic Number A for Incident Protons.

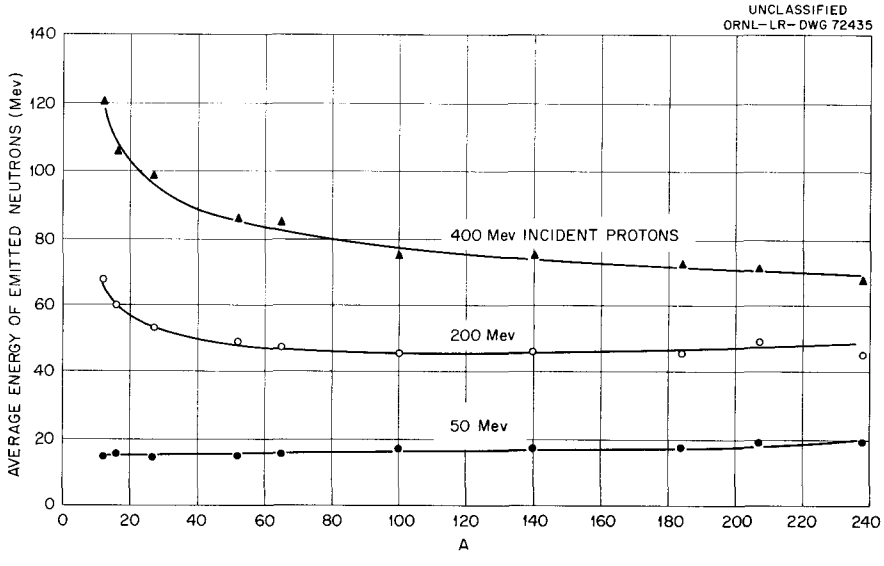

Fig. 7.2.15. Average Energy of Emitted Cascade Neutrons vs Atomic Number A for Incident Protons.

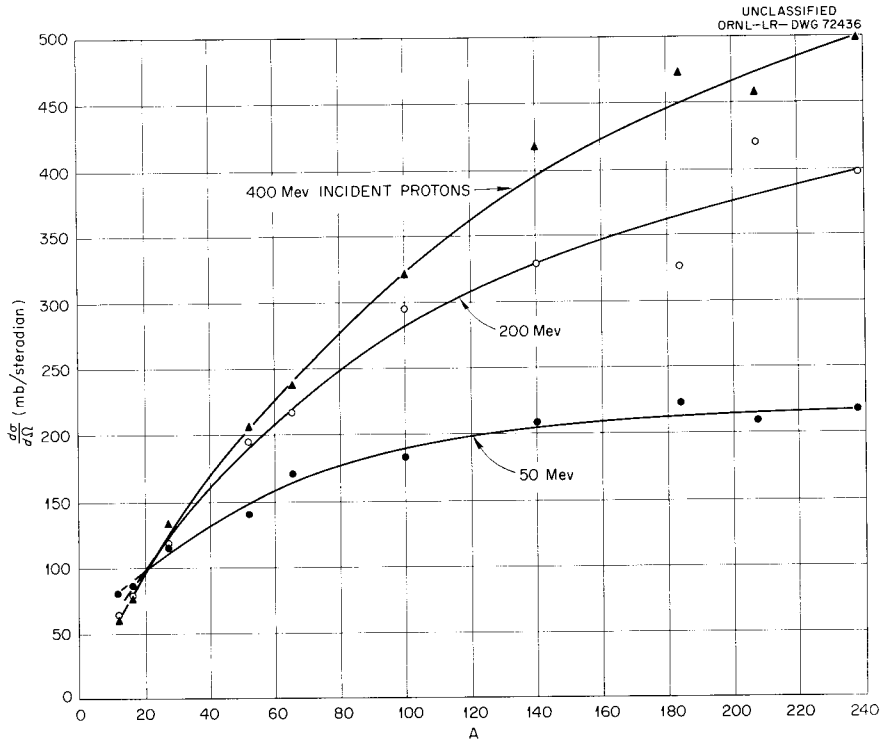

Fig. 7.2.16. Differential Cross Section vs Atomic Number A for Emission of Cascade Neutrons into the Laboratory Angular Interval 0 to 30° for Incident Protons.

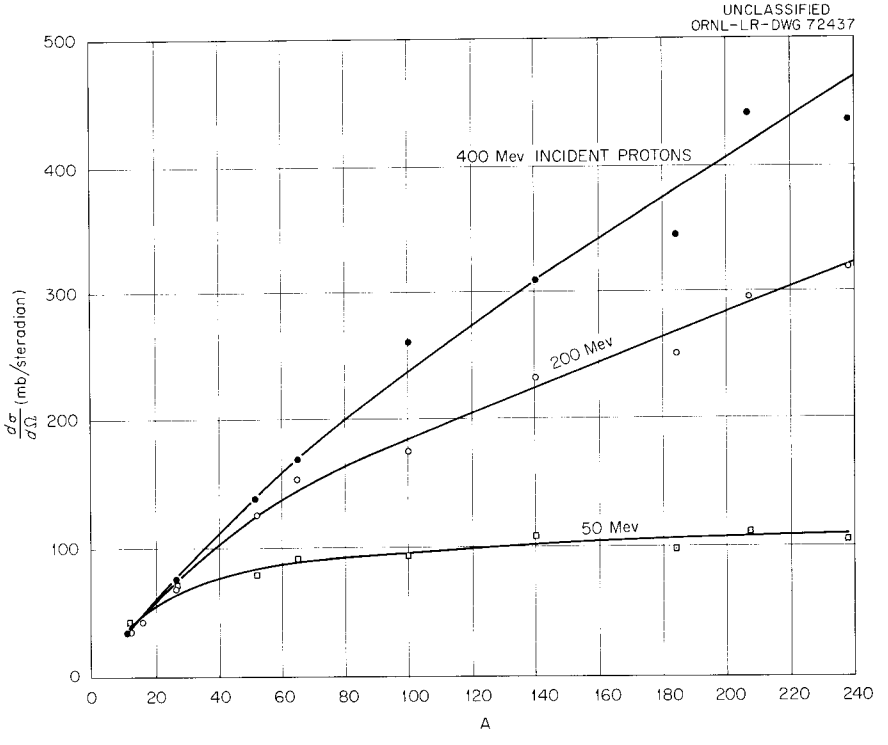

Fig. 7.2.17. Differential Cross Section vs Atomic Number A for Emission of Cascade Neutrons into the Laboratory Angular Interval 30 to 60° for Incident Protons.

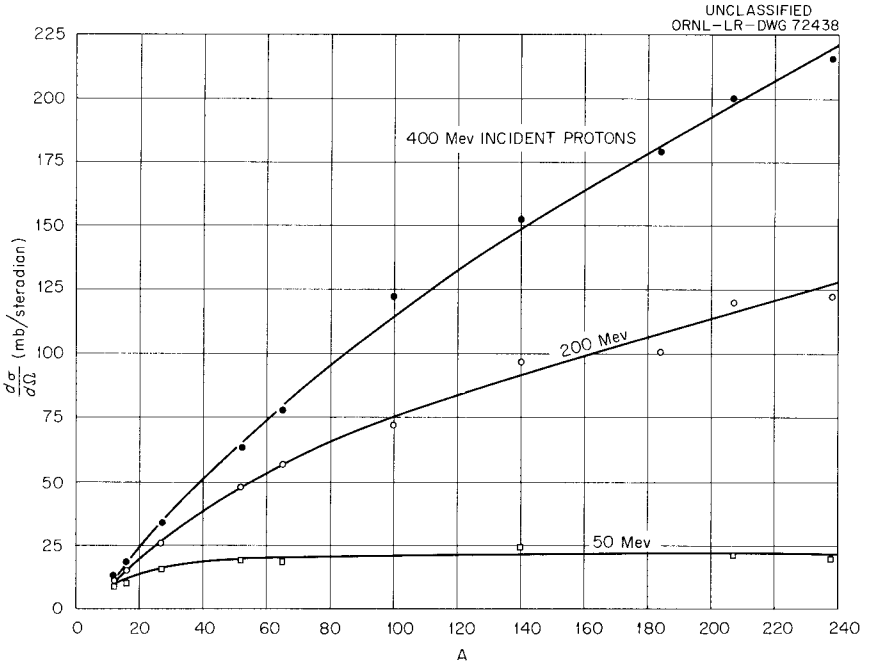

Fig. 7.2.18. Differential Cross Section vs Atomic Number A for Emission of Cascade Neutrons into the Laboratory Angular Interval 60 to 120° for Incident Protons.

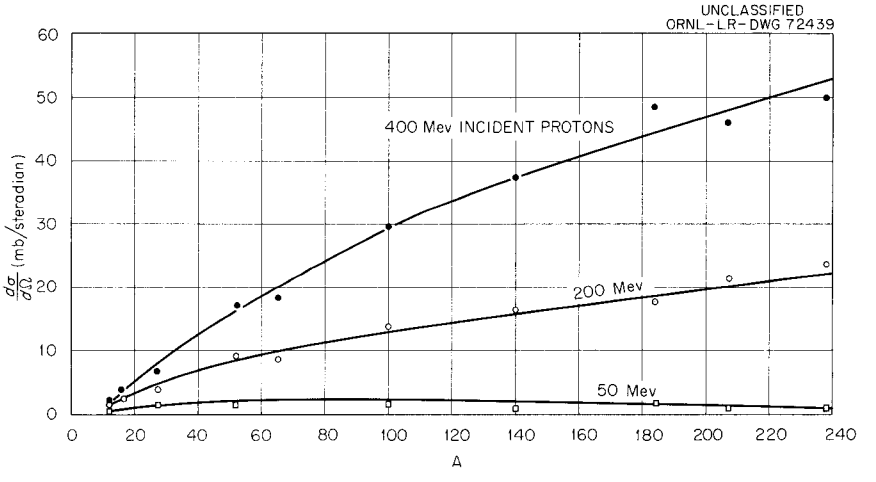

Fig. 7.2.19. Differential Cross Section vs Atomic Number A for Emission of Cascade Neutrons into the Laboratory Angular Interval 120 to 180° for Incident Protons.

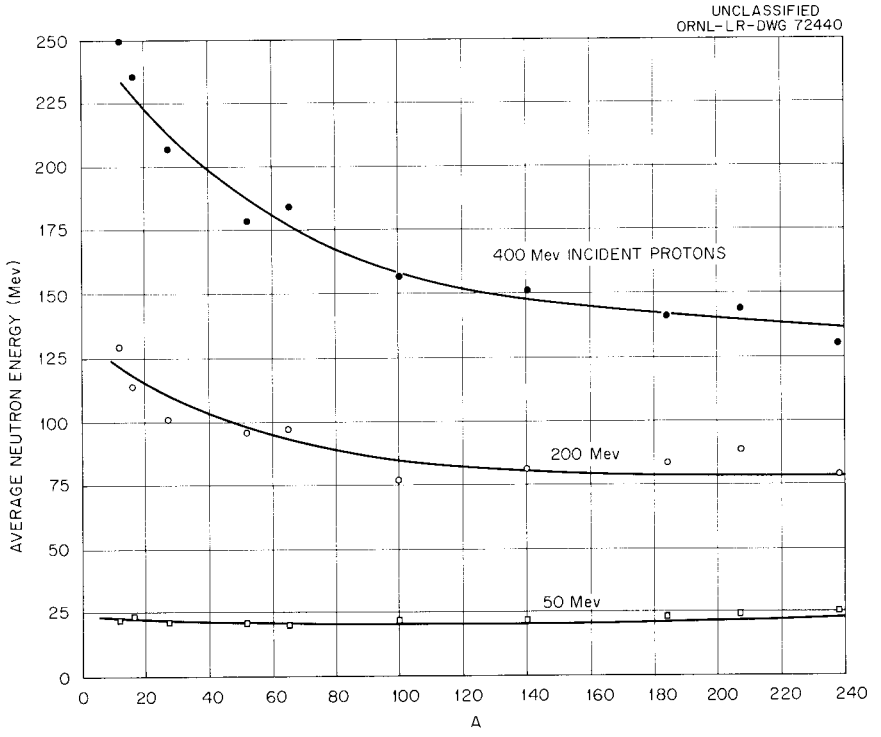

Fig. 7.2.20. Average Energy of Cascade Neutrons Emitted into the Laboratory Angular Interval 0 to 30° vs Atomic Number A for Incident Protons.

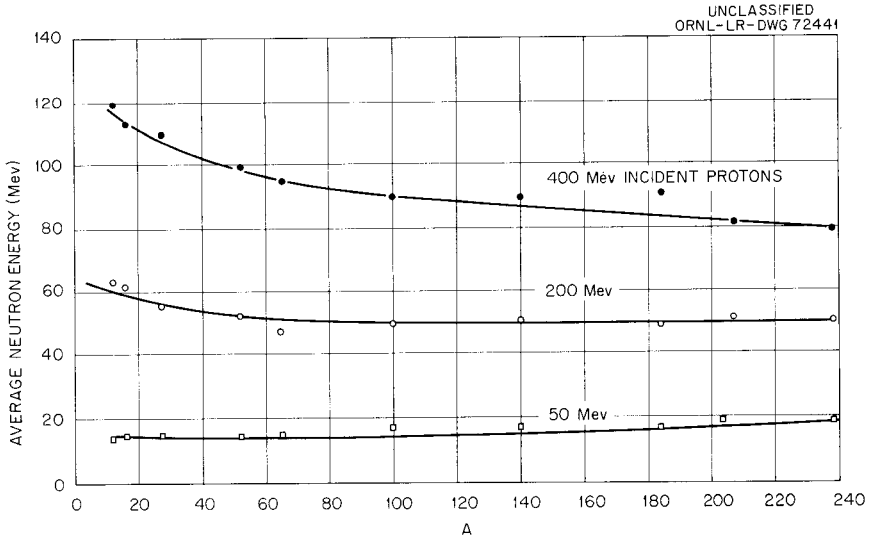

Fig. 7.2.21. Average Energy of Cascade Neutrons Emitted into the Laboratory Angular Interval 30 to 60° vs Atomic Number A for Incident Protons.

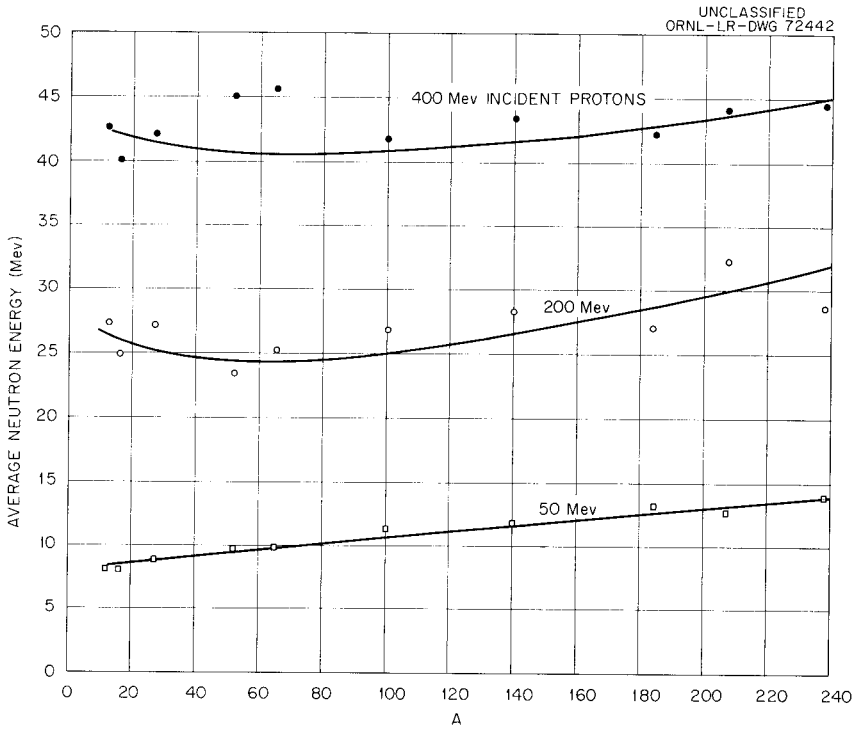

Fig. 7.2.22. Average Energy of Cascade Neutrons Emitted into the Laboratory Angular Interval 60 to 120° vs Atomic Number A for Incident Protons.

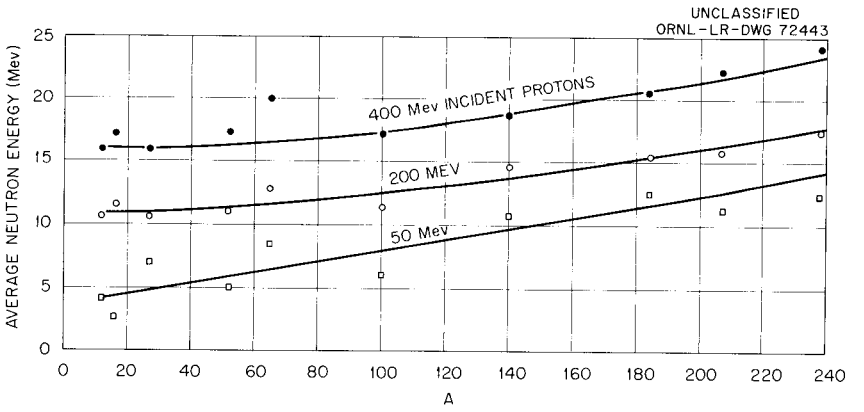

Fig. 7.2.23. Average Energy of Cascade Neutrons Emitted into the Laboratory Angular Interval 120 to 180° vs Atomic Number A for Incident Protons.

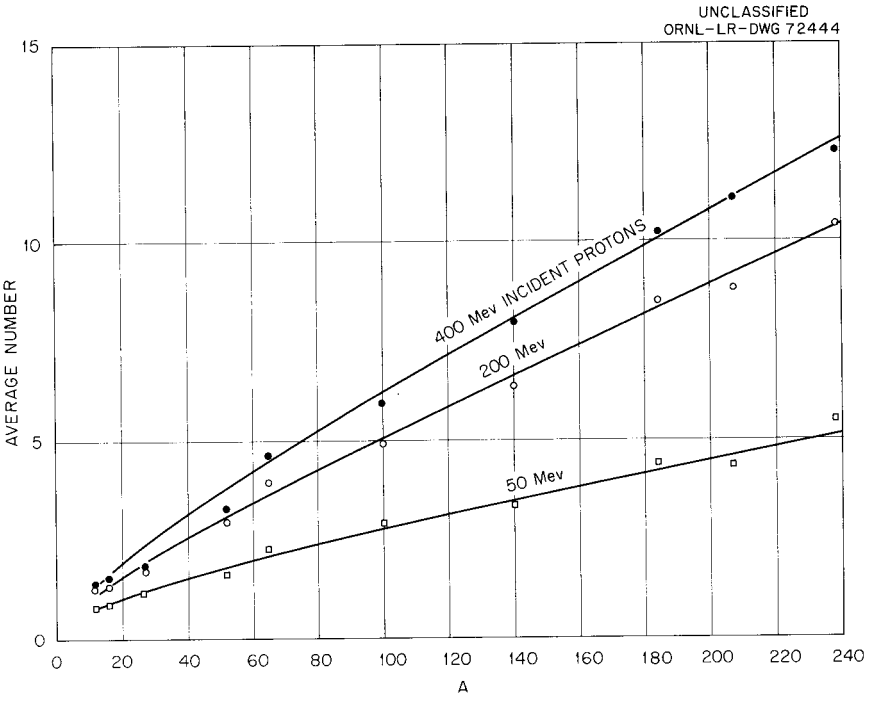

Fig. 7.2.24. Average Number of Cascade and Evaporation Neutrons vs Atomic Number A for Incident Protons.

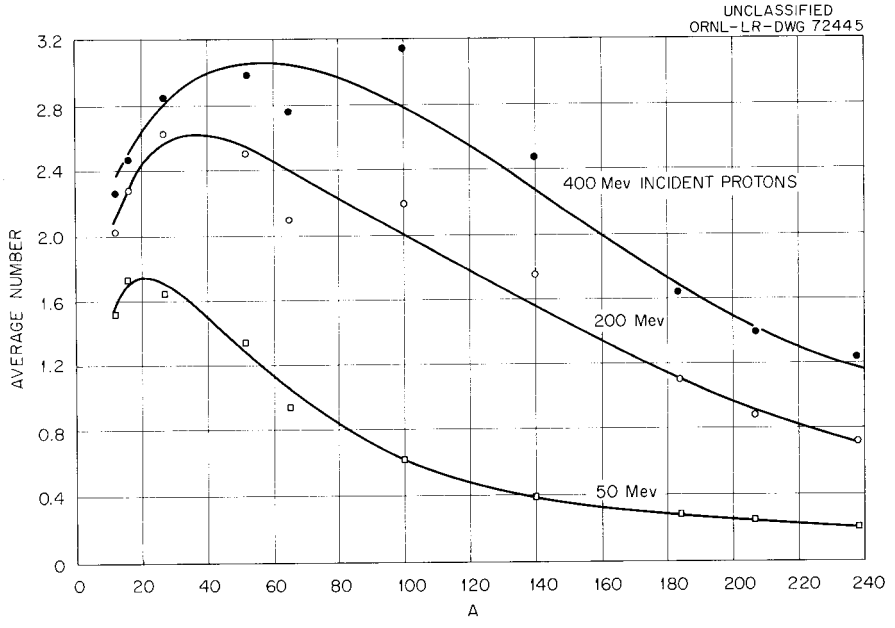

Fig. 7.2.25. Average Number of Cascade and Evaporation Protons vs Atomic Number A for Incident Protons.

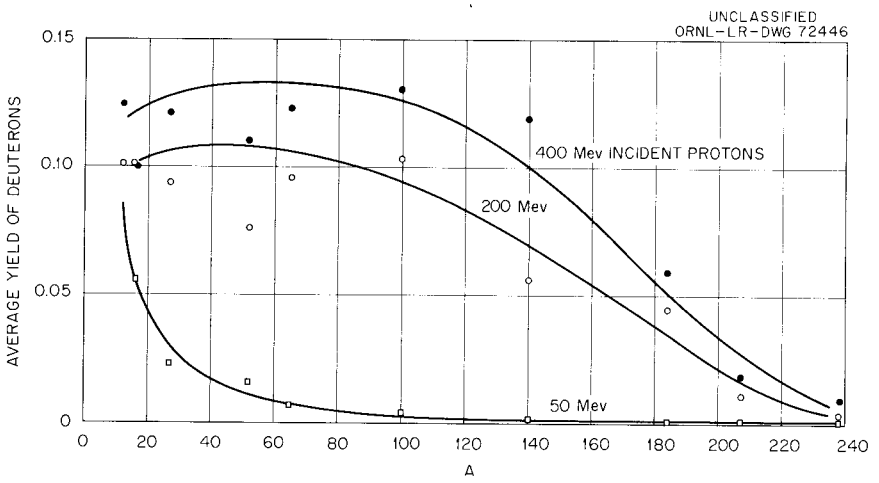

Fig. 7.2.26. Average Yield of Evaporation Deuterons per Inelastic Event vs Atomic Number A for Incident Protons.

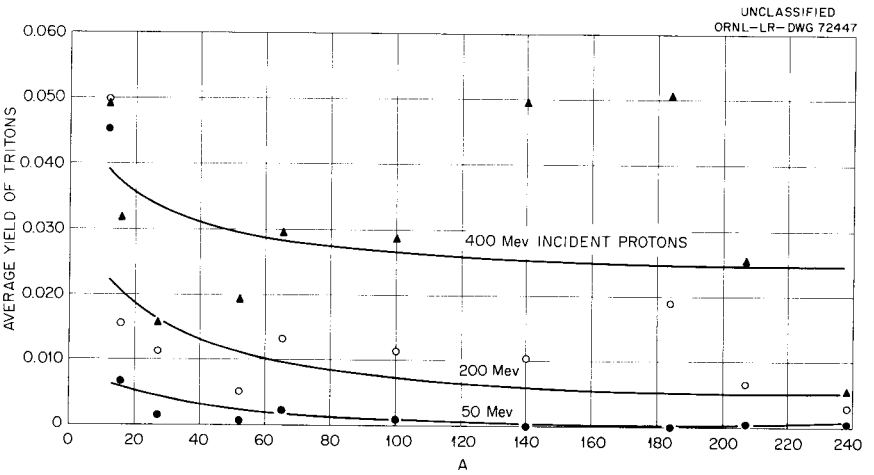

Fig. 7.2.27. Average Yield of Evaporation Tritons per Inelastic Event vs Atomic Number A for Incident Protons.

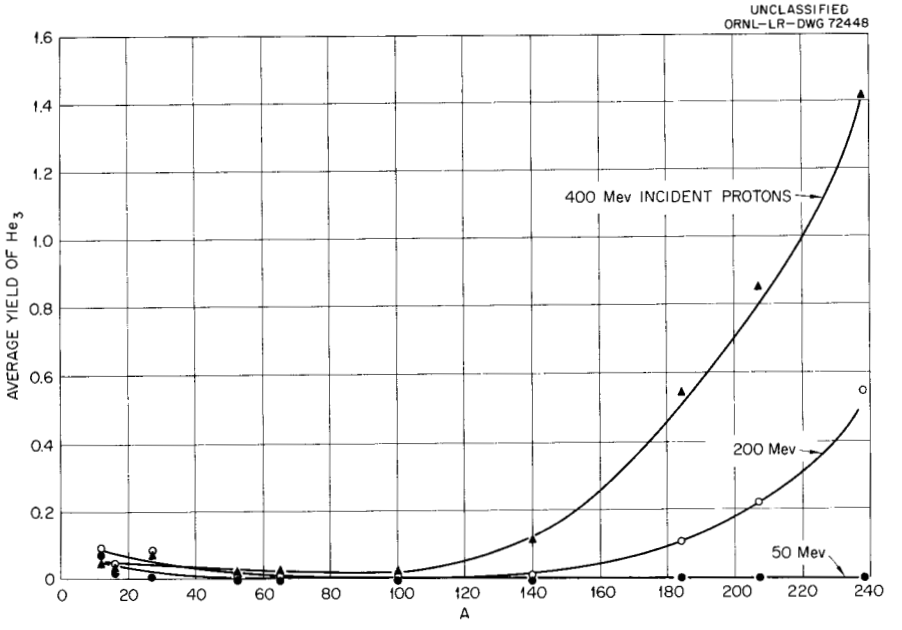

Fig. 7.2.28. Average Yield of Evaporation He_3 per Inelastic Event vs Atomic Number A for Incident Protons.

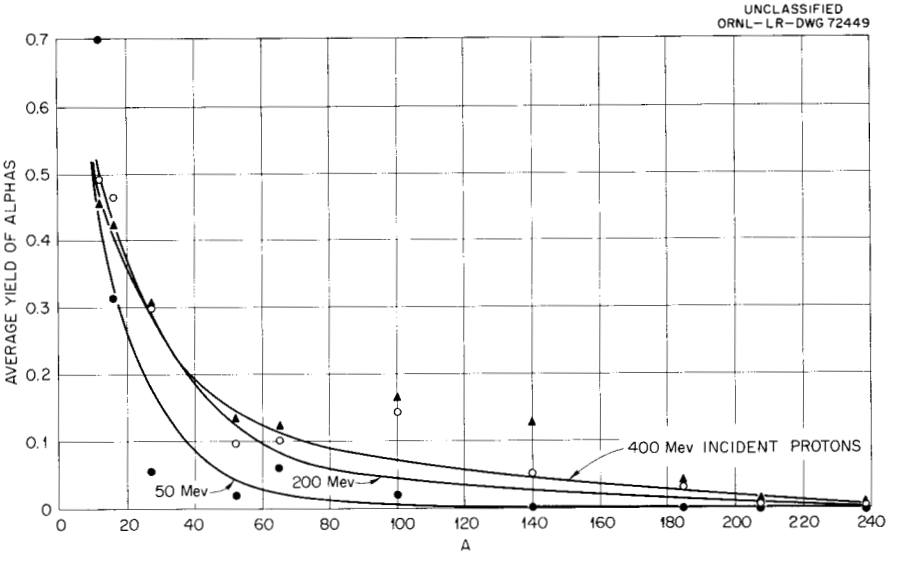

Fig. 7.2.29. Average Yield of Evaporation Alphas per Inelastic Event vs Atomic Number A for Incident Protons.

7.3. MONTE CARLO CALCULATIONS ON INTRANUCLEAR CASCADES FOR INCIDENT-PARTICLE ENERGIES FROM ABOUT 50 Mev TO 2 Gev

H. W. Bertini

The intranuclear cascade calculation for the energy range of incident particles from about 50 to 350 Mev (Sec. 7.1) is being extended to higher energies. When completed, the calculation will be able to treat nuclear reactions for incident nucleons up to about 2.5 Gev and incident pions up to about 1.5 Gev.

The nuclear model will remain unchanged, but the particle-particle collisions that occur inside the nucleus will include inelastic collisions, which result in the creation of pions. Only single pion production will be considered for pion-nucleon collisions, and single or double pion production for nucleon-nucleon collisions. The 2.5- and 1.5-Gev energies are higher than the thresholds for the production of pions of greater multiplicity than will be treated in the calculation. Therefore the energy limits of validity of the calculations are nearer to 2 and 1 Gev, respectively, but the production processes which are ignored at the higher energies would constitute only about 15% of all the reactions.

The isobar model will be used for determining the type of reaction products and their angular distribution in the inelastic particle-particle collisions.[1] This model assumes that a $T = \frac{3}{2}$, $J = \frac{3}{2}$ isobar (excited nucleon state) occurs as a collision product which subsequently decays into a pion and a nucleon; T is the isotopic spin quantum number and J is the total angular-momentum quantum number. In nucleon-nucleon collisions two such isobars can be formed, leading to the decay of two pions and two nucleons. If sufficient energy is available, the model allows for the formation of a $T = \frac{1}{2}$ isobar, which can decay into one pion and one nucleon or into two pions and one nucleon. A considerable amount of experimental data (not yet available) would have been required to fix the contribution of the $T = \frac{1}{2}$ isobar, and hence this reaction mode was not considered. The data for the description of the production processes decided upon were scarce enough in certain areas, and rather drastic assumptions had to be made in those cases.

Pion Production in Nucleon-Nucleon Reactions

The type of production event, single or double production, in nucleon-nucleon collisions within the nucleus is determined by the free-particle cross section for that event. The data for p-p single production were taken from the paper by Fickinger *et al.*[2] and are illustrated in Fig. 7.3.1. The n-p single-production cross section was assumed to be one-half the p-p cross section for the following reasons: The isotopic spin part of the n-p wave function can be written as a combination of $T = 0$ and $T = 1$ isotopic spin states, each comprising one-half the total state. If single pion production occurs through the formation of a $T = \frac{3}{2}$ isobar only, the $T = 0$ state cannot contribute. Therefore only one-half the total n-p state contributes to pion production via the composite $T = 1$ state, while all of the total p-p state (a pure $T = 1$ state) contributes.

---

[1] R. M. Sternheimer and S. J. Lindenbaum, *Phys. Rev.* **123**, 333 (1961); *Phys. Rev.* **109**, 1723 (1958); *Phys. Rev.* **105**, 1874 (1957).

[2] W. J. Fickinger *et al.*, *Phys. Rev.* **125**, 2082 (1962).

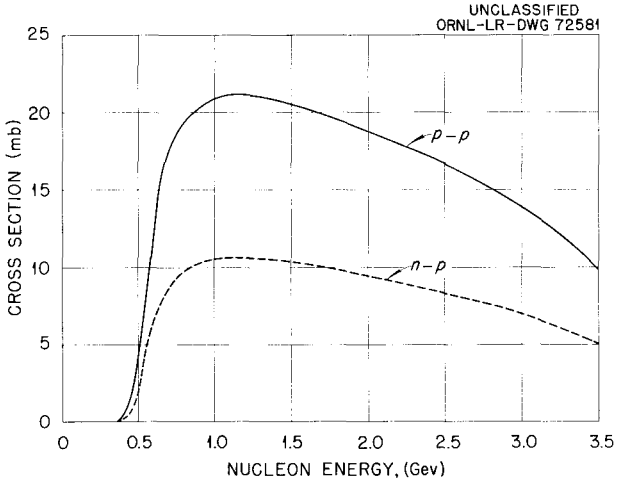

Fig. 7.3.1. Single Pion Production Cross Sections for *p-p* and *n-p* Collisions [from W. J. Fickinger *et al.*, *Phys. Rev.* 125, 2082 (1962)].

The *p-p* double-production cross section[3] is illustrated in Fig. 7.3.2. Since double production is assumed to occur via the formation of two $T = \frac{3}{2}$ isobars, the $T = 0$ part of the *n-p* isotopic spin state does contribute. The cross section for the formation of two isobars through the $T = 0$ state must be known in order to determine the isobaric states being formed. The cross section for formation of two isobars through the $T = 1$ state is known (i.e., the *p-p* double-production cross section). From the expression $\sigma_{T=0} = 2\sigma_{p-n} - \sigma_{p-p}$, the ratio of the total cross sections for *n-p* scattering in the $T = 0$ and $T = 1$ states can be calculated:

$$R = \frac{\sigma_{T=0}}{\sigma_{T=1}} = \frac{2\sigma_{n-p}}{\sigma_{p-p}} - 1 .$$

This ratio was assumed to be the same for the formation of two $T = \frac{3}{2}$ isobars. The *n-p* double-production cross section (illustrated in Fig. 7.3.2) can then be calculated.

---

[3] W. O. Lock *et al.*, *Phil. Mag.* **2**, Ser. 8, 215 (1957); W. B. Fowler *et al.*, *Phys. Rev.* **103**, 1479 (1956); F. F. Chen, C. P. Leavitt, and A. M. Shapiro, *Phys. Rev.* **103**, 211 (1956).

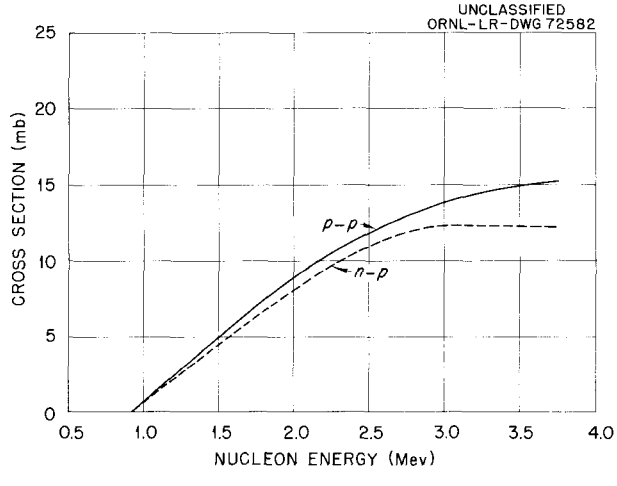

Fig. 7.3.2. Proton-Proton [from W. O. Lock *et al.*, *Phil. Mag.* 2, Ser. 8, 215 (1957); W. B. Fowler *et al.*, *Phys. Rev.* 103, 1479 (1956); F. F. Chen, C. P. Leavitt, and A. M. Shapiro, *Phys. Rev.* 103, 211 (1956)] and Neutron-Proton Double-Production Cross Section.

After the type of event is determined, it is necessary to calculate the mass, m, of the isobar. For single pion production this is done by using the following expression, which is assumed to give the probability for formation of an isobar of mass m when the relative kinetic energy of the colliding particles is T_r:

$$P(m,T_r) = k\sigma_{3/2}\, F(m,T_r) ,$$

where $\sigma_{3/2}$ is the pure $T = \frac{3}{2}$ cross section ($\pi^+ + p$ cross section), F is the phase space available to the isobar decay products, and k is a normalizing constant. This expression is a slight modification of the one given by Sternheimer and Lindenbaum.[1] For double pion production the expression

$$P(m_1 , m_2 , T_r) = k\sigma_{3/2}(m_1)\, \sigma_{3/2}(m_2)\, F(m_1 , m_2 , T_r)$$

is used, where m_1 and m_2 are the masses of the two isobars.

When the isobar masses are known, the recoil angles of the isobars must be determined. The code is presently set up with any one of three options in this respect: Isobars are produced in either a forward or backward direction in the center-of-mass (C) system, isotropically in the C system, or in each of them 50% of the time. At present the latter alternative seems best,[4] but the others are included to determine their effects. Relativistic kinematics are used to determine the final momenta of the isobars, and they are allowed to decay isotropically in their own rest mass system to give the produced pions and decay or recoil nucleons.

The Clebsch-Gordon coefficients, in the framework of the isotopic spin formalism, are used to determine the final products.

Pion Production in Pion-Nucleon Reactions

The calculation of the production of pions in pion-nucleon collisions is carried out in exactly the same way as that for nucleon-nucleon collisions. Most of the data needed for these reactions are contained in an excellent article by Falk-Vairant and Vallados.[5] The inelastic cross sections that they give for $\pi^+ + p$ and $\pi^- + p$ reactions were assumed to be all single-production cross sections. These are given in Figs. 7.3.3 and 7.3.4.

The composite isotopic spin states involved in pion-nucleon collisions are generally the pure $T = \frac{3}{2}$ and $T = \frac{1}{2}$ state. Each of these can in turn be written in terms of the isotopic spin states of a recoil pion and a $T = \frac{3}{2}$ isobar. Here both the composite $T = \frac{3}{2}$ and $T = \frac{1}{2}$ states contribute to the production process. The phase angle, ϕ, between the matrix elements of the states and the ratio of the cross sections for production through each of these states must be known, as well as the single-production cross section, in order to determine the mode of formation of the isobar. By using the isotopic spin formalism, the single-production $\pi^- + p$ cross section can be written:

$$\sigma_{s.p.} = \frac{2}{3}\sigma_{11}(1 + \rho_1) ,$$

---

[4] A. C. Mellissinos, Rochester University, private communication.

[5] P. Falk-Variant and G. Vallados, *Rev. Mod. Phys.* **33**, 362 (1961).

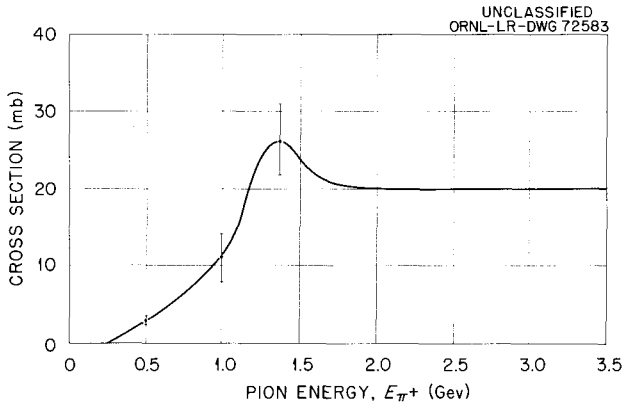

Fig. 7.3.3. $\pi^+ + p$ **Inelastic Cross Section** [**from P. Falk-Vairant and G. Vallados,** *Rev. Mod. Phys.* **33, 362 (1961)**].

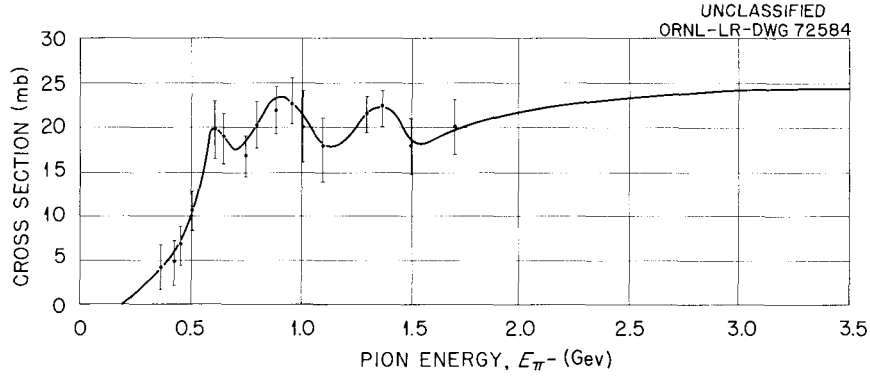

Fig. 7.3.4. $\pi^- + p$ **Inelastic Cross Section** [**from P. Falk-Vairant and G. Vallados,** *Rev. Mod. Phys.* **33, 362 (1961)**].

where $\rho_1 = \sigma_{31}/2\sigma_{11}$, and σ_{31} and σ_{11} are the single-production cross sections for the pure $T = 3/2$ and $T = 1/2$ states, respectively. The $T = 1/2$ nonelastic cross section is given elsewhere.[5] This cross section was assumed to be all single production, and hence ρ_1 could be determined. By again making use of the isotopic spin formalism, the cross section for the reaction $\pi^- + p \rightarrow n + \pi^+ + \pi^-$ can be written

$$\sigma = \frac{2}{3}\sigma_{11}\left(\frac{5}{9} + \frac{26}{45}\rho_1 + \frac{7}{9}a\right) ,$$

where $a = 2\sqrt{\rho_1/5}\cos\phi$, and ϕ is the phase angle mentioned before. The cross section is given by Perkins *et al.*[6] and by Walker,[7] and therefore a can be calculated. These quantities are sufficient for determining all the formation and decay modes of the $T = 3/2$ isobar for any pion-nucleon reactions.

---

[6]W. A. Perkins *et al.*, *Phys. Rev.* **118**, 1364 (1960).

[7]W. I. Walker, *Proceedings of the Sixth Annual Rochester Conference for 1956*, p IV-16, Interscience, New York.

Status

The coding for the extended intranuclear cascade calculation is nearing completion. Extensive checks must be made and the code debugged; then the code must be run so that comparisons with experiment can be made. The estimated completion time for this portion of the work is about six months.

7.4. A MONTE CARLO CALCULATION OF SCATTERED NEUTRON FLUXES AT AN AIR-GROUND INTERFACE DUE TO POINT ISOTROPIC SOURCES ON THE INTERFACE

W. E. Kinney

When the beam of a high-energy accelerator strikes a target or machine structure, it produces high-energy particles which, in turn, interact with surrounding material to produce secondary particles of lower energy. Of these, the charged particles are readily stopped, but some of the neutrons, mostly low-energy neutrons, leak from the shield and present a potential radiation hazard. In order to determine whether the neutron dose levels at various distances from a given accelerator shield are below specified limits, it is necessary to know the total neutron flux arising from the leakage neutrons as a function of distance from the shield. Since the doses near the ground level are of primary interest, that being the location of the operating personnel and surrounding population, the problem basically consists of the determination of the neutron flux at the air-ground interface.

The calculation of the uncollided flux is straightforward, but the presence of the ground creates a two-media problem for the scattered flux for which no satisfactory calculational method has been available. As a result, estimates of the effect of the ground on scattered fluxes have been crude modifications of calculations for an infinite medium of air.

A calculational method that offers a solution to the treatment of the ground is the Monte Carlo method, which simulates a counting experiment with perfect counters on a system that approximates the real system but has properties that are completely known. This is the method that was chosen for calculations of scattered neutron fluxes at an air-ground interface due to point isotropic sources located on the interface. The O5R code,[1] a 7090 general-purpose Monte Carlo code for treating neutrons, was used to trace the paths in phase space of sample neutrons emitted from several monoenergetic sources with energies (1 to 19 Mev) sufficient to cover the low-energy leakage spectrum. Simple analysis codes then looked at the paths, counted the neutrons, and computed the flux as a function of space and energy. The calculations covered distances out to 4×10^5 cm from the source.

Although the Monte Carlo method has the advantage of being as readily applied to two media as to one medium, it has the disadvantage of introducing counting uncertainties inherent in all neutron counting experiments. Thus, the "experimental" data should be compared with theoretical results. The moments

---

[1] R. R. Coveyou, J. G. Sullivan, and H. P. Carter, *Neutron Phys. Div. Ann. Progr. Rept. Sept. 1, 1958*, ORNL-2609, p 87.

method, which cannot be applied to more than one medium but which is highly reliable, was used as a basis for comparison. The moments method calculations were those of Holland and Richards,[2] who computed the spatial and energy variation of the flux from several point isotropic monoenergetic neutron sources in an infinite medium of air, and two more recent calculations[3] with the Renupak moments method code[4] for 2- and 14-Mev sources in an infinite air medium.

Throughout the calculations air was assumed to be 79% N_2 and 21% O_2 with a density of 0.0012 g/cm^3. Ground was approximated by SiO_2 with a density of 1.8 g/cm^3. The limiting case of neutron fluxes at the interface of black ground and air was also calculated.

It was concluded that the Monte Carlo method with a simple statistical estimation method of analysis yields neutron fluxes from point isotropic monoenergetic sources in an infinite air medium that are in good agreement with moments method fluxes out to approximately 8 source mean free paths using, effectively, 2000 histories. Treating inelastic scattering as isotropic elastic scattering in the Monte Carlo calculations overestimates the high-energy flux and underestimates the low-energy flux; allowing only P_1 anisotropic elastic scattering overestimates the high-energy flux near the source and underestimates it far from the source. The fluxes, then, for the air-ground problem should be reliable estimates for distances out to 10^5 cm from the source for the 1- and 2-Mev source energies. They are somewhat less reliable for a source energy of 5 Mev because of the assumptions used for anisotropic elastic scattering. At higher source energies they must be regarded as crude but useful estimates.

The results of the calculations are reported elsewhere.[5]

---

[2]S. S. Holland, Jr., and P. I. Richards, *J. Appl. Phys.* **27**, 1042 (1956).

[3]S. K. Penny, Oak Ridge National Laboratory, private communication.

[4]J. Certaine, E. DeDufour, and G. Robonowitz, *Renupak, An IBM-704 Program for Neutron Moment Calculations*, NDA-2120-3 (Dec. 1, 1959).

[5]W. E. Kinney, *A Monte Carlo Calculation of Scattered Neutron Fluxes at an Air-Ground Interface Due to Point Isotropic Sources on the Interface*, ORNL-3287 (1962).

7.5. A CODE GROUP APPLYING THE MONTE CARLO METHOD TO THE COMPUTATION OF THE TRANSPORT OF NUCLEONS OF ENERGY LESS THAN 400 Mev

W. E. Kinney, R. R. Coveyou, and C. D. Zerby

The interaction of a high-energy proton with the material of a radiation shield initiates a complex avalanche of lower-energy secondary particles, which then proceed through the shield, snowballing in number and decreasing in energy. The designer of the shield for a space vehicle or a high-energy particle accelerator must know the behavior of the cascade as a function of energy and distance into the shield to determine the effectiveness of his design.

A calculational method that can include as much detail of the cascade as desired is the Monte Carlo method. It, in essence, performs an idealized experiment on a system whose properties are completely

known, with counters of known resolution and 100% efficiency. Like any counting experiment, however, the method is subject to counting uncertainties, so that a balance must be struck between acceptable counting statistics and the cost of calculation.

The Monte Carlo method has been employed in 05R,[1] a code for the IBM-7090 computer, to treat neutron transport at fission energy and below. In going to particle energies higher than fission two circumstances prevent a high-energy nucleon transport code from being a simple extension of 05R. First, there are the nuclear cascades wherein a nucleon disappears, giving rise to several lower-energy secondaries, whereas in the 05R a neutron is never absorbed in a collision but continues with its statistical weight changed. Secondly, protons are present, and their ionization energy loss in traversing matter must be considered. A simplifying feature of the high-energy region, however, is the much-improved "behavior" of the nucleon cross sections at high energies over that of neutron cross sections at lower energies.

It is thus logical to calculate high-energy nucleon transport in two stages: transport of nucleons of energy > 50 Mev, the approximate threshold for high-energy effects, and, using the 05R, transport of only neutrons of energy <50 Mev. Protons, since they have only small ranges at energies <50 Mev, may be transported straight ahead with only small error. Since nearly all the particles evaporated from an excited nucleus after a nonelastic collision have energies <50 Mev, 50 Mev forms a convenient boundary.

In this report the manner of performing the two-stage calculation by means of a code group is first discussed in general terms. The high-energy transport code is then described in detail, together with the coupling code to 05R. Typical results are given, and plans for extension of the code to higher energies and more complex geometries are laid out.

Code Group Organization

A flow chart of the two-stage, high-energy nucleon transport code group is shown in Fig. 7.5.1. The first portion, the High-Energy Transport Code, computes the transport of nucleons of energies between 50

[1] R. R. Coveyou, J. G. Sullivan, and H. P. Carter, *The 05R Code: A General Purpose Monte Carlo Reactor Code for the IBM-704 Computer*, a paper presented at the Symposium on Codes for Reactor Computations, Vienna, Austria, 1961; see also R. R. Coveyou, J. G. Sullivan, and H. P. Carter, *Neutron Phys. Div. Ann. Progr. Rept., Sept. 1, 1958*, ORNL-2609, p 87.

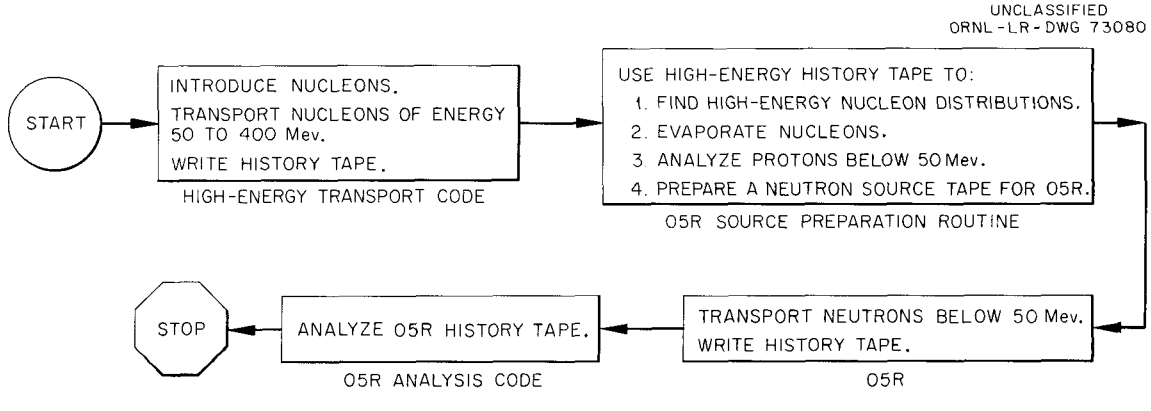

Fig. 7.5.1. A Flow Sheet for the Two-Stage High-Energy Nucleon Transport Code.

and 400 Mev through a maximum of ten adjoining infinite slabs, each composed of one of four materials. Each material may contain as many as ten isotopes. In the operation of the code a specified number of source neutrons is introduced arbitrarily into the system and transported through the composite slab, where they undergo nuclear interactions. Whenever a nucleon suffers a collision or crosses either a spatial or an energy boundary, the details of the event are recorded on magnetic tape for later analysis. Separation of history generation from analysis was first devised by Coveyou and Sullivan for 05R and allows the user of the code to analyze the results in any way he chooses. It also permits a set of histories to be saved for a possible future reanalysis for additional information.

The second portion of the group, the 05R Source Preparation Routine, does four things: (1) It analyzes the high-energy nucleon histories for spatial, energy, or angular distributions as desired by the user; (2) it calculates the evaporation of particles from the excited residual nuclei resulting from each nuclear interaction and computes the spatial distribution of final residual nucleus energy and heavy charged-particle kinetic energy; (3) it analyzes the protons having energies below 50 Mev in any fashion desired; (4) as its main job, it prepares a neutron source tape for 05R.

The third part of the group, the 05R, then calculates the transport of neutrons having energies below 50 Mev, and may follow their histories to thermal energies if desired. Nonelastic events may be treated by an 05R subroutine, essentially a short version of Dresner's evaporation code,[2] which records the details of each nonelastic event on tape. The main code produces a tape containing the parameters of all other neutron events. Both these tapes may be analyzed at the pleasure of the user in the 05R Analysis Code.

High-Energy Transport Code

An abbreviated flow chart of the High-Energy Transport Code is given in Fig. 7.5.2. The calculation is begun by reading in the parameters of the problem. These include the upper and lower energy limits, the number of major energy groups, the number of materials, the number of regions, and the number of source particles to be treated. The charge and mass numbers, the nuclear densities, and the ionization potentials of each isotope in each mixture must be given, as well as the neutron and proton cross sections at the major-group energy limits. The boundaries and material-identifying numbers for each region must also be supplied. Finally, a set of weight standards is supplied to help direct particles into regions of interest.

The energy region is first broken into i (≤ 10) major energy groups of equal width. The nuclear reaction cross sections are assumed to vary linearly over each group. The i major groups are then subdivided into 10 minor groups. The proton range to the bottom of a major group is assumed to vary linearly over each minor group. The values of the ranges at the minor-group limits are put into a table. A table of inverse range, that is, the energy corresponding to a given range, is also constructed by dividing the range from the top to the bottom of the group into 10 subranges, over which the energy associated with that range

[2] L. Dresner, *Numerical Calculation of the Evaporation of Particles from Excited Compound Nuclei*, ORNL-3193, p 262 (Oct. 31, 1961).

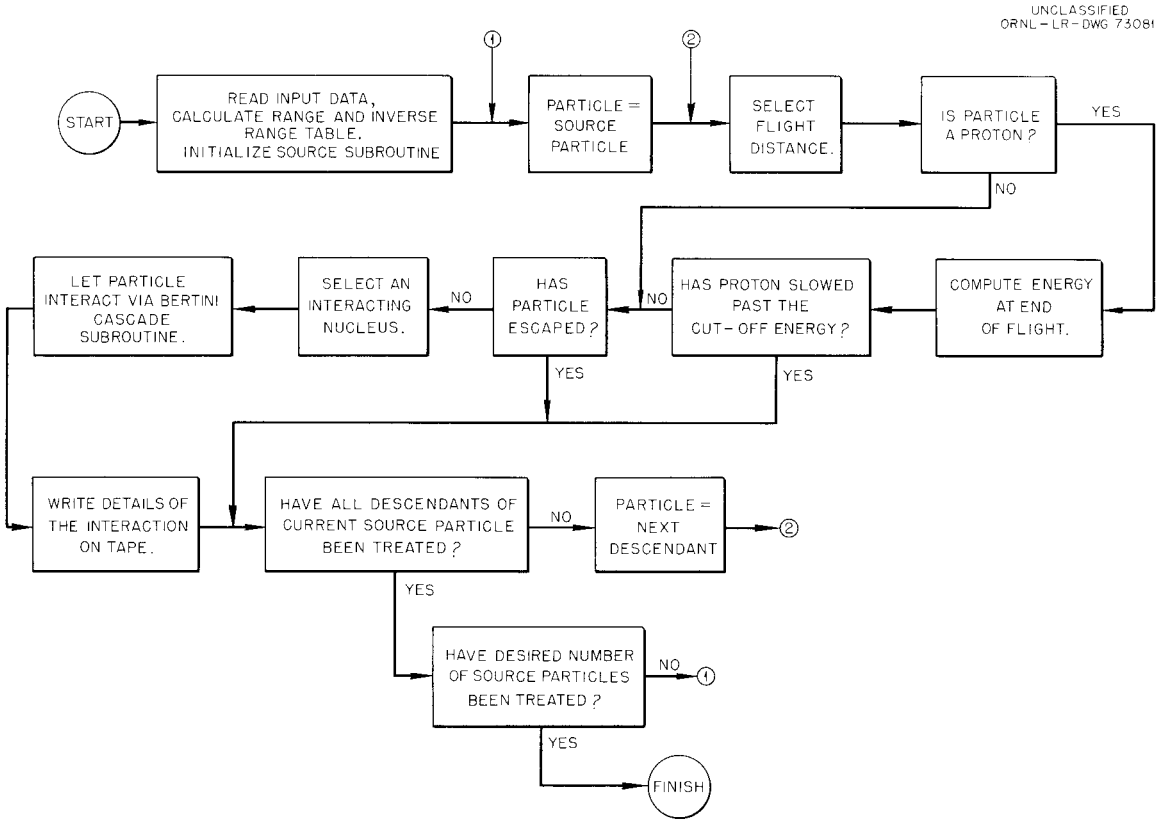

Fig. 7.5.2. A Flow Chart of the High-Energy Transport Code.

is assumed to vary linearly. The stopping-power formula for ionization collision derived by Bethe[3] is used to compute ranges. An example of a range and inverse range table for a mixture of elements approximating the composition of tissue is given in Table 7.5.1.

The weight standards noted above are established by dividing each major region into j subregions, where j may differ for each region. High and low weight limits for both neutrons and protons are supplied for each of the i major energy groups and j subregions. Each particle then is assigned a statistical weight, equal to 1 if the particle is a source particle and equal to the parent's weight if the particle is a cascade product. Whenever a particle's weight exceeds the high limit for the group or region into which the particle falls, the particle is split into two particles, each having half the original weight.

If the particle weight falls below the lower weight limit, the particle, with equal probability, is either removed from further consideration or continues with double its original weight.

The random selection of a particle path to a nuclear interaction, inherent in the Monte Carlo method, offers no difficulty when the particle is a neutron since the neutron energy does not change in flight. A proton, however, continually loses energy during flight by ionization. A rejection technique is used to select a proton path to interaction. Suppose a proton finds itself in the ith major energy group. The larger of the group limit cross sections, Σ_{max}, is found and a path is chosen from the distribution $\Sigma_{max} e^{-\Sigma_{max} r}$.

[3]H. A. Bethe, *Z Physik* **76**, 293 (1938).

Table 7.5.1. Range and Inverse Range Tables for a Tissue-Like Material[a] and a Major Energy Group Extending from 365 to 400 Mev

Range Table (ΔE = 3.5 Mev)		Inverse Range Table (ΔR = 1.1227 cm)	
Energy (Mev)	Range to 365 Mev (cm)	Range to 365 Mev (cm)	Inverse Range (Mev)
400.0	11.227	11.227	400.00
396.5	10.082	10.104	396.57
393.0	8.942	8.982	393.12
389.5	7.806	7.859	389.66
386.0	6.676	6.736	386.19
382.5	5.550	5.614	382.70
379.0	4.430	4.491	379.19
375.5	3.315	3.368	375.67
372.0	2.204	2.245	372.13
368.5	1.100	1.123	368.57
365.0	0	0	365.00

[a]Nuclear densities: N(H) = 6.265×10^{22}; N(C) = 9.3975×10^{21}; N(O) = 2.5508×10^{22}; N(N) = 1.3425×10^{21}.

If the distance r is greater than the range to the bottom of the ith group, then the proton drops from the ith group, its energy is set equal to the lower energy limit of the ith group, and it is not considered until particles in group $i + 1$ are considered. If, however, the selected distance is less than the range to the bottom of the group and the proton has not left the region, the energy corresponding to distance r, E_r, is computed and the ratio $\Sigma(E_r)/\Sigma_{max}$ is tested against a random number. (A random number is defined here as a random variable drawn from a distribution uniform on the interval 0 to 1.) If the random number is less than the ratio, an interaction is considered at the distance r. If the random number is greater than the ratio, the proton continues from the point at distance r, and another choice from $\Sigma_{max}e^{-\Sigma_{max}r}$ is made, the process being continued until an acceptable point of interaction is found.

After all input data have been read into the computer, the code proceeds to calculate the entries in the range and inverse range tables. The last step in the "initialization" of the calculation is the reading-in of the source specification as defined by the source subroutine. (We define initialization as the completion of all of the preparatory steps of the calculation, just preceding the actual insertion of an "experimental" particle.) The practice of specifying the source by means of a subroutine allows complete generality in the choice of a source. The source subroutine used in investigations to date introduces monoenergetic neutrons or protons normally at the origin of coordinates.

The code starts the "experiment" by calling on the source subroutine to provide a source particle. A flight distance for the particle is selected from the exponential distributed as described above. A test is then made to see whether the particle will escape from the system, cross a region boundary, or cross a

major-energy-group boundary in going the selected distance. If any one of these things happens, the position of the event and the energy of the particle at the time of the event are written on magnetic tape. If the event consists of escape from the system or slowing down below the cutoff energy, the particle is obviously removed from further consideration and another source particle is called for. If, however, the particle has crossed an internal boundary or one of the upper-energy-group boundaries, it is treated as a new particle, born at the site of the event.

If the test shows that none of the above events occur, the particle is permitted to undergo a nuclear interaction. A nucleus with which it is to interact is chosen by selecting a random number and comparing it with the relative interaction probabilities for the nuclei in the medium. The interaction then takes place according to a cascade subroutine due to Bertini.[4]

Given the type and energy of the incident particle and the charge and mass numbers of the target nucleus, the subroutine gives the kinds and energies of the cascade products, as well as the direction cosines of their velocity vectors.

The data describing the results of the interaction are recorded on magnetic tape. Data include the position, energy, and velocity of the incident particle at birth, the location of the interaction, and the interaction energy of the incident particle. Also recorded are the charge and mass numbers and the excitation and recoil energies of the residual nucleus. The cascade particles having energies above the low-energy cutoff are put into the list of descendants of the current source particle and are processed in turn, just as the source particle was treated. Descendants with energies below cutoff energy are merely recorded on magnetic tape for consideration in the 05R Source Preparation Code. The calculation continues tracing particle paths until the specified number of source particles has been introduced and all progeny have been followed to cutoff energy.

05R Source Preparation Routine

The 05R Source Preparation Routine has as its main function the preparation of a magnetic tape containing the positions, velocities, and statistical weights of the neutrons, all with energies below 50 Mev, resulting from the processes of the High-Energy Transport Code. The tape then can be used as a neutron source input for 05R in carrying out the second part of the two-stage calculation. A flow chart of the routine is shown as Fig. 7.5.3. Neutrons below 50 Mev either result directly from the cascade process previously noted or are evaporated from the highly excited nuclei residual to the nuclear interactions. This evaporation or boil-off process is calculated by a subroutine due to Dresner.[2] The assumption is made that all the evaporated particles have energies below the high-energy transport cutoff energy. This assumption is valid for the cutoff energy of 50 Mev which was assigned. The neutrons from this process are put on the 05R source tape with velocities isotropic in the laboratory system.

It is economical to analyze the high-energy transport history tape for whatever other information the user desires while it is being examined to find 05R source neutrons. Provision is therefore made to treat the particles above the transport code cutoff energy arbitrarily by subroutine Analysis I. This must be a

---

[4]H. Bertini, *Intranuclear Cascade Calculation*, ORNL-3193, p 323 (Oct. 31, 1961).

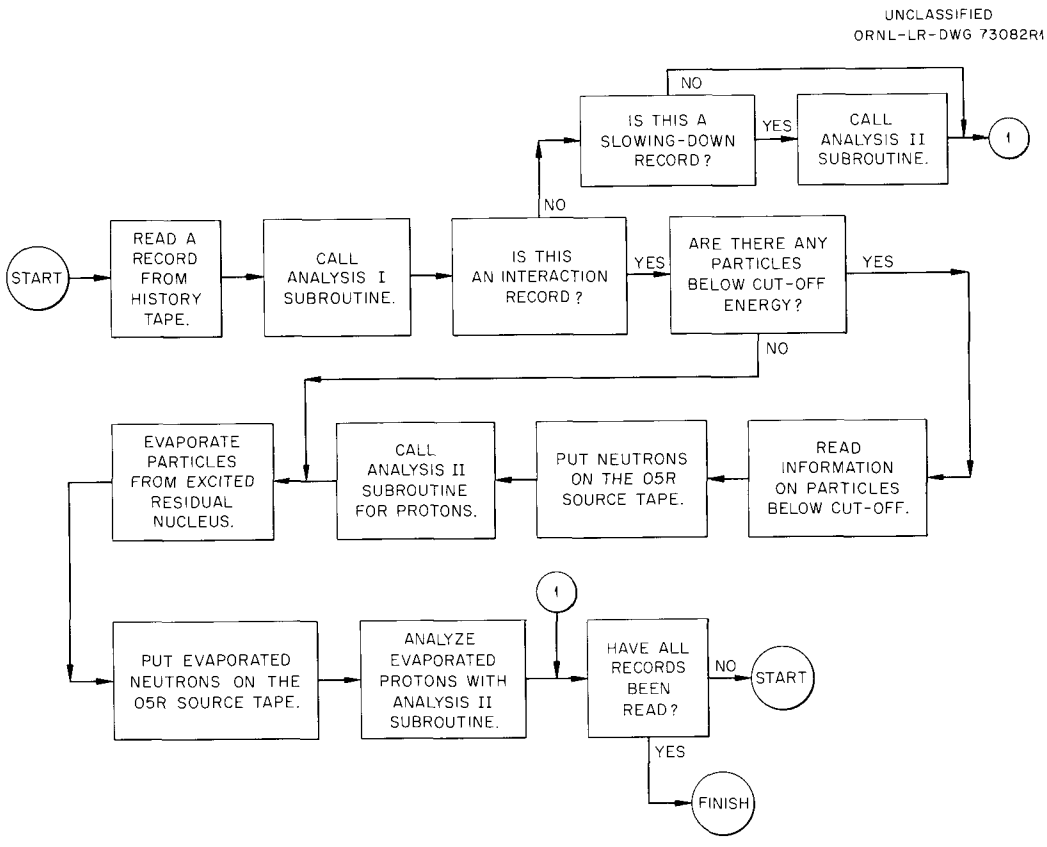

Fig. 7.5.3. A Flow Chart of the 05R Source Preparation Routine.

self-contained subroutine which selects whatever input is necessary and writes its own output. It could, for example, compute the neutron and proton fluxes in specified spatial and energy intervals.

A second subroutine, Analysis II, analyzes protons with energies below cutoff, whether they are high-energy protons slowing down below cutoff, are born below cutoff, result from a nuclear interaction, or are evaporated from an excited nucleus.

The main routine, while computing the evaporation of particles, also calculates the spatial distribution of evaporated heavy-charged-particle energy and residual nucleus energy.

05R Code and Analysis

The 05R code for calculating neutron transport has been described elsewhere.[1] In applying it to the present problem the ability to treat nonelastic scattering by means of a simplified version of the evaporation subroutine noted above has been added. The treatment assumes that only neutrons, protons, and alpha particles can be emitted. Details of the nonelastic scattering event are recorded on magnetic tape for subsequent analysis.

It should be pointed out that only an approximate calculation of the elastic-scattering angular distribution is presently possible. If the average cosine of the scattering angle in the center-of-mass system, f_1, is greater than $\frac{1}{3}$, the center-of-mass cosine of the scattering angle, μ, is chosen from the distribution

$(1 + \mu)/2$, with probability $(3 - 3f_1)/2$, and from $\delta(1 - \mu)^2$, with probability $(3f_1 - 1)/2$. This is a good approximation over the range ~15 to 50 Mev, where the scattering is highly peaked in the forward direction. If f_1 is less than $\frac{1}{3}$, μ is chosen from $(1 + 3f_1\mu)/2$.

The results of the 05R computation are recorded on magnetic tape, and it is a small matter to construct an appropriate code to analyze them.

Results

Representative results from the code group solution of a typical problem are shown in Fig. 7.5.4. The calculation considers a beam of 400-Mev protons, infinite in extent, normally incident upon a 65-cm-thick slab of aluminum. Partial dose rates due to primary protons, secondary protons above and below 50 Mev, and secondary neutrons above 50 Mev are plotted as a function of depth in the slab. The flux-to-dose conversion factors employed in obtaining these results are those given by Alsmiller,[5] and are plotted in Fig. 7.5.5.

For the results discussed above, a total of 1940 incident source protons was employed. The running time for the High-Energy Transport Code was ~35 min, and that for the 05R source preparation, ~15 min.

Future Plans

The series of codes discussed above is somewhat awkward to use at present and, more importantly, wasteful of time because each must be run separately. It is planned to link them together into a continous code chain in the near future so that a single run on the IBM-7090 will yield results from the high-energy transport code and 05R, plus a standard analysis output.

[5] R. G. Alsmiller, Jr., F. S. Alsmiller, and J. E. Murphy, *Nucleon-Meson Cascade Calculations: Transverse Shielding for a 45-Gev Electron Accelerator, Part I*, ORNL-3289 (1962).

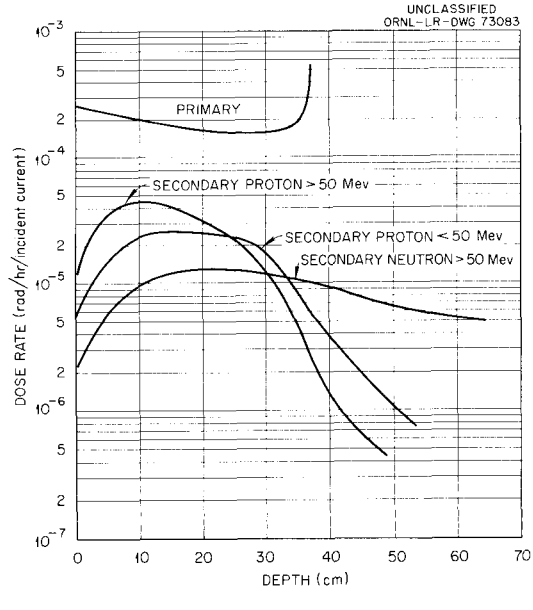

Fig. 7.5.4. Partial Dose Rates as a Function of Depth in 65-cm-Thick Aluminum Slab from Normally Incident 400-Mev Protons.

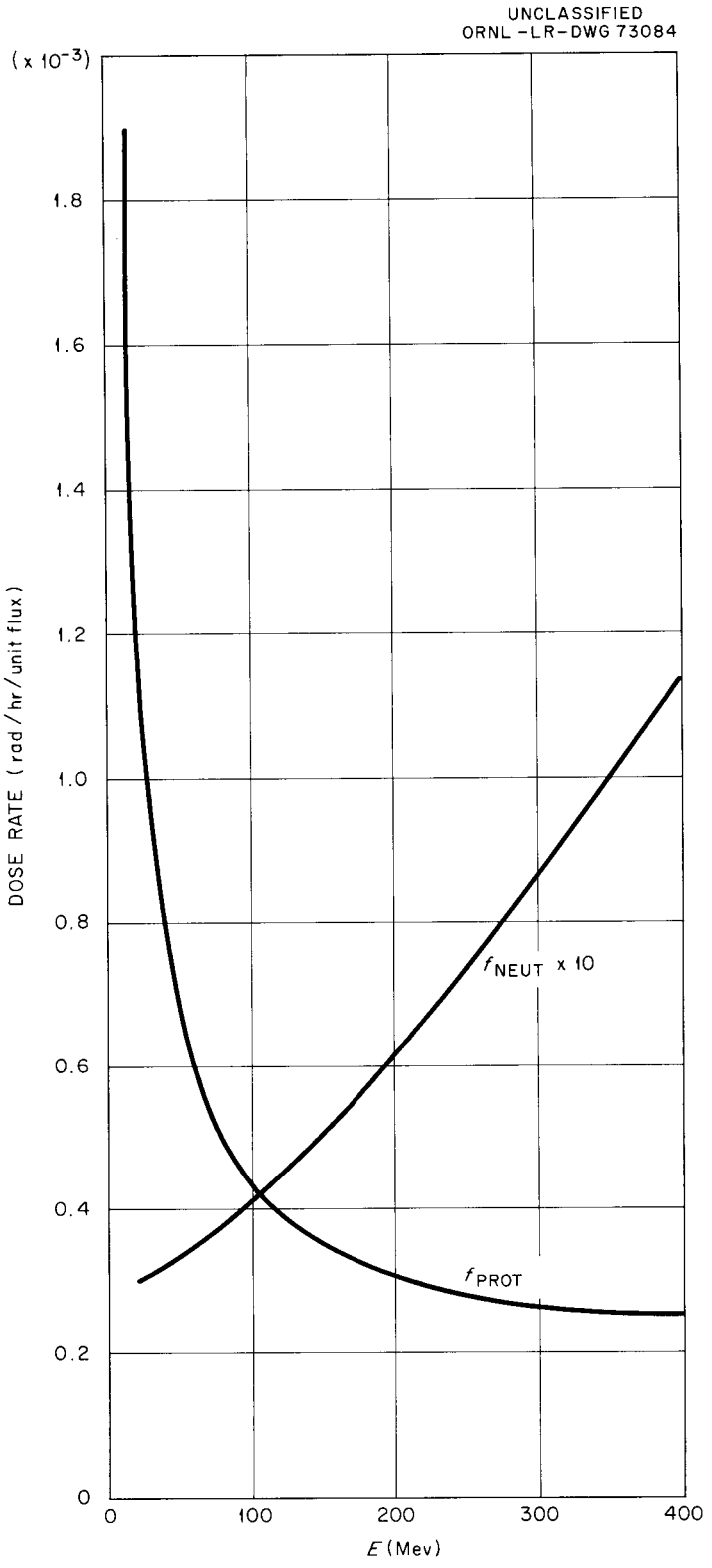

Fig. 7.5.5. Neutron and Proton Flux-to-Dose Conversion Factors vs Energy.

The present code will also be extended to include consideration of complex configurations by incorporating a general geometry routine (see Sec. 7.11). Given the beginning and end points of a path, this routine determines whether or not a boundary has been crossed and, if so, the coordinates of the crossing point.

The code will also be extended upward in energy to 1.5 Bev by using an extended cascade subroutine and providing for charged pion transport.

7.6. ENERGY DEPOSITION BY HIGH-ENERGY NUCLEONS AS A FUNCTION OF DEPTH IN TISSUE

W. E. Kinney, C. D. Zerby, and R. P. Leinius[1]

To properly evaluate the hazard to an astronaut created by the radiations encountered in space, it is necessary to have some measure of the biological damage caused by these radiations. Calculations and experiments to determine the composition and energy spectra of penetrating radiations that reach the astronaut are useless unless they are translated into terms which indicate the resulting biological damage. This rather old problem has been studied extensively in connection with low-energy radiation associated with radioactivity and fission. On the other hand, very little is known about the biological effects of higher energy radiation such as will be encountered in space.

Although the mechanism by which radiation damages tissue and causes observable physiological changes is now known, it is felt that these changes can be, to a first approximation, associated and correlated with the energy deposited by the radiation. For this reason the physiological effects are almost always correlated with tissue dose measurements which indicate the energy deposited by the incident radiation. There is much speculation about next-order approximations which correlate the effects of various kinds of radiation through their respective linear energy transfers (stopping power for ionization collisions) in tissue.

The present calculation was constructed for two purposes: to study the energy deposited in tissue by high-energy incident radiation as a function of depth and to separate out various contributions to the energy deposited to determine which are the most important. The first purpose also serves to provide badly needed conversion factors that can be used to translate information about incident radiation into units which, to a first approximation, indicate the biological damage.

The Nucleon Transport Code Group, described in Sec. 7.5, has been used to calculate the transport of normally incident high-energy protons or neutrons through 30- and 50-cm-thick slabs of infinite extent which are composed of a tissue-equivalent material. An elemental composition of $C_{21}H_{140}O_{57}N_3$ was chosen for the material,[2] and the density was taken to be 1 g/cm^3.

---

[1]Mathematics Panel.

[2]*Recommendations of the International Commission on Radiological Protection and of the International Commission on Radiological Units 1950*, NBS Handbook 47, 1950, p 16.

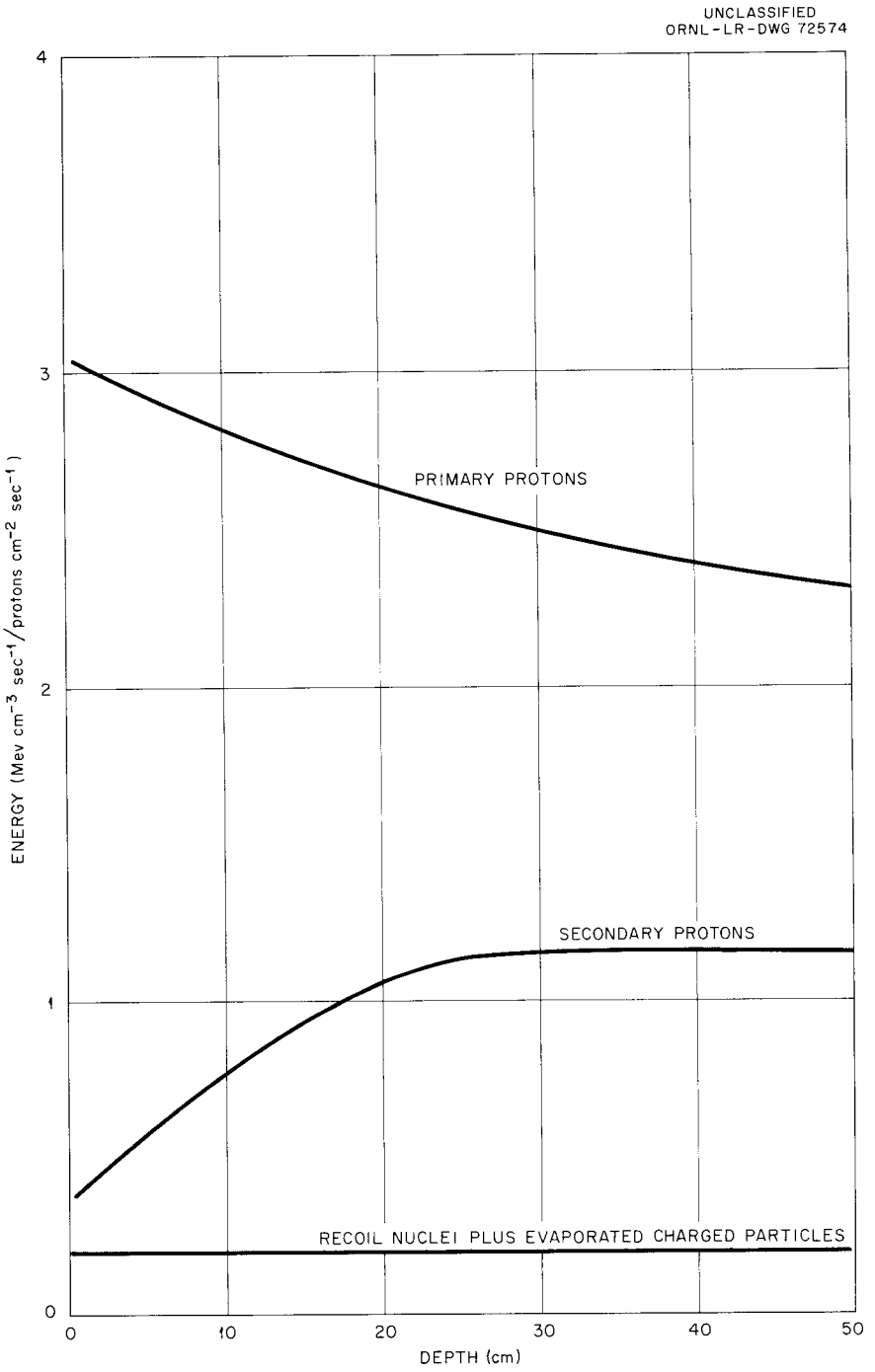

Fig. 7.6.1. Energy Deposition Resulting from 400-Mev Protons Normally Incident on a 50-cm-Thick Infinite Slab of Tissue as a Function of Depth of Penetration.

The analysis codes have been written for this calculation to obtain the contribution to the energy deposition as a function of depth in tissue by primary incident protons (if protons are the source particles), secondary cascade protons, evaporation protons, heavy evaporation particles (d, t, He^3, α), and residual nuclei that recoil after a nonelastic interaction. The energy deposited by neutrons in elastic scattering events with nuclei is also calculated. Finally, the energy available for gamma-ray production through the decay of excited nuclei is obtained, along with an estimate of the capture gamma-ray production.

Calculations have been performed for incident protons with energies from 100 to 400 Mev in 50-Mev steps. Two thousand protons were used in each case. Complete analyses of the results have not yet been made. Preliminary results are shown in Fig. 7.6.1 for 400-Mev protons incident normally on a 50-cm-thick slab of tissue.

7.7. AN IMPROVED CODE FOR THE NUMERICAL ANALYSIS OF A NUCLEON-MESON CASCADE

R. G. Alsmiller, Jr., F. S. Alsmiller, and J. E. Murphy[1]

In a series of recent reports[2-4] nucleon-meson cascade calculations have been presented. Primarily because there is a lack of data concerning high-energy interactions, the IBM-7090 code written to solve the cascade equations included several approximations. Before long theoretical results for high-energy interactions will become available and make the use of these approximations unnecessary; hence, a new code is being written which does not impose them.[5] At the same time several new features are being included so that the new code will be not only more accurate but also more efficient and more versatile.

The major improvements in the code are listed below:

1. Each of the secondary energy distributions, $F_{jk}(E', E)$, that is, the number of particles per unit energy of type j produced with energy E when a particle of type k and energy E' induces a nuclear reaction, may be an arbitrary function of E and E'. (The subscripts j and k take values N, P, and π corresponding to neutrons, protons, and pions.)

2. Monoenergetic sources, in addition to sources with a continuous energy distribution, may be considered.

3. The density of the medium in which the cascade takes place may be an arbitrary function of depth. (This allowance for density variation was introduced so that the propagation of cosmic rays in the atmosphere could be considered.)

---

[1]Central Data Processing Facility of the Oak Ridge Gaseous Diffusion Plant.

[2]R. G. Alsmiller, Jr., F. S. Alsmiller, and J. E. Murphy, *Nucleon-Meson Cascade Calculations: Transverse Shielding for a 45-Gev Electron Accelerator (Part I)*, ORNL-3289 (1962).

[3]*Ibid.*, Part II, ORNL-3365 (to be published).

[4]R. G. Alsmiller, Jr., and J. E. Murphy, *Space Vehicle Shielding Studies: Calculations of the Attenuation of a Model Solar Flare and Monoenergetic Proton Beams by Aluminum Shields*, ORNL-3317 (1962).

[5]The coding is being done by D. S. Marion of the Central Data Processing Facility of the Oak Ridge Gaseous Diffusion Plant.

4. The production of muons from the decay of pions is treated more rigorously.

5. A provision has been made for including neutron-proton elastic scattering in hydrogenous media. The slowing-down effect of this elastic scattering on the cascade neutrons is included, as is the introduction of the recoil protons into the cascade, but the method used is very approximate.

The basic approximation, the one-dimensional cascade treatment, is retained in the new code. The cascade components considered are neutrons, protons, charged pions, and charged muons; no distinction is made between positive and negative pions or positive and negative muons.

For numerical convenience all calculations will be done in terms of a lethargy variable U defined by

$$U = \ln \frac{E_0}{E} ,$$

where E is the particle kinetic energy and E_0 is an arbitrary energy which defines the zero of lethargy. However, the code will be written in such a way that all inputs (e.g., initial flux, secondary energy distribution, etc.) must be specified as a function of energy, and all outputs be given in energy.

The primary particle fluxes may be given analytically, and thus in the numerical calculation it will be convenient to separate the primary, $\phi_{ij}(E, r)$, and secondary, $\phi_{sj}(E, r)$, components.

The equations for the primary fluxes, to which we give the solutions, are the same as the equations for the secondary fluxes with the right-hand side set equal to zero. Although the equations will be coded in terms of lethargy, for clarity they are written here in terms of energy. The neutron, proton, and pion equations are:

$$\phi_{ij}(E,r) = \phi_j(E, 0)\,(1 - C_j)\,e^{-Q_j(E)r} + \phi_j(E_j, 0)\,C_j \frac{S_j(E_j)}{S_j(E)} \times \exp\left[- \int_E^{E_j} \frac{Q_j(E') + \delta_{\pi j} Q_{\pi D}(E', r')}{S_j(E')}\, dE' \right] , \quad j = N, P, \pi , \quad (1)$$

where

$$C_N = 0 \text{ or } 1,$$

$$C_P = 1,$$

$$C_\pi = 1,$$

$$\int_E^{E_j} \frac{dE'}{S_j(E')} = r; \text{ that is, } E_j = E_j(E, r),$$

$$\int_{E'}^{E_j} \frac{dE''}{S_j(E'')} = r'; \text{ that is, } r' = r'(E_j, E'),$$

$$\delta_{\pi j} = 1 \text{ if } j = \pi$$

$$= 0 \text{ if } j \neq \pi ,$$

$$Q_{\pi D}(E, r) = \frac{C_\rho \lambda_0}{\rho \Lambda_\pi(E)} + \frac{(1 - C_\rho)\lambda_0}{\rho_c(r)\Lambda_\pi(E)} ,$$

in which

$$\frac{1}{\Lambda_\pi(E)} = \frac{m_\pi}{\tau_\pi}\left[\frac{1}{E(E+2m_\pi)}\right]^{1/2},$$

$C_\rho = 0$ or 1;

and

$$\frac{\partial}{\partial r}\phi_{sj}(E,r) + [Q_j(E) + \delta_{\pi j} Q_{\pi D}(E,r)]\phi_{sj}(E,r) - C_j \frac{\partial}{\partial E}[S_j(E)\phi_{sj}(E,r)]$$

$$= \sum_k \int_E^{E_{max}} F_{jk}(E',E) Q_k(E') [\phi_{ik}(E',r) + \phi_{sk}(E',r)]\, dE'$$

$$+ \delta_{Pj} H_R(E,r) + H_j(E,r), \qquad j,k = N,P,\pi, \quad (2)$$

where

$\phi_{iN}(E,r) = N_i(E,r)$

= primary neutron flux per unit energy from a neutron source at $r = 0$ with a continuous energy spectrum;

$\phi_{sN}(E,r) = N_s(E,r)$

= secondary neutron flux per unit energy;

$\phi_N(E,r) = N_i(E,r) + N_s(E,r)$

= total neutron flux per unit energy when there are no monoenergetic sources present; since $N_s(E,0) = 0$, then $\phi_N(E,0) = N_i(E,0)$ is one of the initial values which must be specified;

ϕ_{iP}, $\phi_{i\pi}$, etc., have similar definitions. Furthermore,

r = dimensionless distance variable defined by the relation $r = (\rho/\lambda_0)R$ if the density of the medium, ρ, is a constant, and by $r = [x(t) - x_0]/\lambda_0 \cos\theta$, where $x(t) \int_0^t \rho_c(t')\,dt'$, if the density of the medium, ρ_c, is a function of position;

θ = angle of the flux with respect to the vertical; this angle is introduced so that the propagation of the cascade can be considered in a direction other than the vertical;

ρ = density of the medium, g/cm^3, if this density is constant;

R = distance in the direction θ, cm;

λ_0 = an arbitrary constant with dimensions g/cm^2 which determines the units in which the dimensionless variable r is measured;

x_0 = pressure, g/cm^2, at the point from which r is measured;

$\rho_c(t)$ = density of the medium, g/cm^3, as a function of position;

t = depth, cm;

C_j = constant which takes the value 0 or 1; the quantities C_P and C_π are always unity, but C_N may be 0 or 1; if $C_N = 1$, neutron slowing down (e.g., by elastic scattering from protons) is included; when $C_N = 0$, neutron slowing down is omitted;

$$Q_j(E) = \frac{\lambda_0 N_0}{A}\sigma_j(E);$$

$\sigma_j(E)$ = nonelastic cross section for particles of type j in the medium being considered;

N_0 = Avogadro's number;

A = atomic weight of the nuclei in the medium;

$S_j(E) = \dfrac{\lambda_0 N_0}{A}\,\epsilon_j(E)$;

$\epsilon_j(E)$ = atomic stopping cross section for particles of type j in the medium;

C_ρ = constant which takes value 0 or 1; when a medium of constant density is considered, $C_\rho = 1$; when a medium of variable density is considered, $C_\rho = 0$;

m_π = rest mass of the charged pion, Mev;

τ_π = mean life of the charged pion, sec, multiplied by the velocity of light, cm/sec;

$F_{jk}(E', E)dE$ = the number of secondary particles of type j in the energy interval E to $E + dE$ produced by the nonelastic collision of a particle of type k of energy E'.

Still to be discussed are the source terms H_R and H_j. The equations without H_j are satisfactory if only sources with continuous energy distributions are to be considered; however, monoenergetic sources are most conveniently handled by introducing H_j. By utilizing the fact that the primary flux from a monoenergetic source may be calculated analytically, the number of secondary particles per unit energy range per unit volume, H_j, produced per second by the primary flux may be written

$$H_j = \sum_k F_{jk}(E'_k, E)\,Q_k(E'_k)\,\phi_{k\delta}(r)\,\Theta(E'_k - E)\,, \qquad j,k = N, P, \pi \tag{3}$$

where

$$E'_k = E_{0k}(1 - C_k) + E_{Rk}C_k\,,$$

$$\phi_{k\delta} = \phi_{k\delta 0}(1 - C_k)e^{-Q_k(E_{0k})r} + \phi_{k\delta 0}C_k \exp\left\{-\int_{E_{Rk}}^{E_{0k}}\left[\frac{Q_k(E') + \delta_{k\pi}Q_{\pi D}(E', r')}{S_k(E')}\right]dE'\right\}\,,$$

$$\int_{E_{Rk}}^{E_{0k}} \frac{dE'}{S_k(E')} = r\,,$$

$$\int_{E'}^{E_{0k}} \frac{dE''}{S_k(E'')} = r'\,,$$

$\Theta(E_k - E) = 1$ if $E_k - E \geqq 0$

$= 0$ if $E_k - E < 0$,

$\phi_{N\delta}(r) = N_\delta(r)$

= flux strength of source neutrons which reach position r when a flux of $N_{\delta 0}\delta(E - E_{0N})$ source neutrons start at the origin with energy E_{0N},

$N_{\delta 0}$ = strength of neutron monoenergetic source,

E_{0N} = energy of monoenergetic neutron source,

E_{RN} = energy of monoenergetic source neutrons when they reach position r.

The other quantities, $\phi_{P\delta}$, $P_{\delta 0}$, etc., have similar definitions.

The Θ functions are introduced into H_j to indicate that a particle of energy E' cannot produce secondary particles of energy greater than E'. The physically correct functions F_{jk} have the property

$$F_{jk}(E', E) = 0 , \qquad E \geq E' ,$$

so that the Θ functions are superfluous when these functions are used. In some cases, however, we use approximations to the F_{jk}'s which do not have this property,[6] and then it is necessary to introduce this property through the Θ functions.

The three terms in H_j correspond to the production of secondary particles of type j by the three kinds of monoenergetic sources allowed – neutrons, protons, and pions. The code will be written so that monoenergetic and continuous sources for all three types of particles may be considered simultaneously.

The term $H_R \delta_{jP}$ is introduced for the purpose of including recoil protons from neutron-proton elastic scattering in hydrogenous media. Assuming that when a neutron-proton collision takes place the neutron transfers, on the average, a given portion of its energy to the proton, then

$$H_R = C_s \frac{S_N(KE)}{E} [N_i(E, r) + N_\delta(E, r)]$$

$$+ C_s \frac{KS_N[E_{RN} C_N + E_{0N}(1 - C_N)]}{E_{RN} C_N + E_{0N}(1 - C_N)} G[E_{RN} C_N + E_{0N}(1 - C_N), E]$$

$$\times N_\delta(r) \Theta[E_{RN} C_N + E_{0N}(1 - C_N) - E] , \quad (4)$$

where

C_s = 0 or 1 and is introduced so that the recoil proton terms may be omitted; note that since C_s and C_N are specified separately it is possible to include the recoil protons and at the same time neglect the effects of elastic scattering on the neutrons;

$1/K$ = fraction of the neutron's energy which on the average is given to the proton when a neutron-proton elastic scattering occurs;

$G(E', E)$ = energy distribution of the recoil proton when a neutron of energy E' is scattered by a proton; to be consistent with the first term in H_R we should have $G(E', E) = \frac{1}{K} \delta(E' - KE)$, but because of the difficulties associated with introducing a delta function into the equation we shall use an analytic function which approximates the delta function.

In writing Eq. 4 we assumed that $S_N(E)$ is given by

$$S_N(E) = n_P \sigma_E(E) \frac{E}{K} ,$$

where n_P = number density of protons in the medium, and σ_E = elastic scattering cross section.

The muon equations are similar to those for the other cascade particles, but differ in one important way: since the small muon nuclear interactions are neglected, the muons do not produce neutrons, protons, or pions and thus do not take an active part in the cascade.

---

[6] See Sec. 3 of ref 2.

The muon equations are[7]

$$\mu_i(E,r) = \mu_i(E_\mu,0)\frac{S_\mu(E_\mu)}{S_\mu(E)}\exp\left[-\int_E^{E_\mu}\frac{Q_{\mu D}(E',r')}{S_\mu(E')}\,dE'\right] , \tag{5}$$

where

$$\int_E^{E_\mu}\frac{dE'}{S_\mu(E')} = r ,$$

$$\int_{E'}^{E_\mu}\frac{dE''}{S_\mu(E'')} = r' ,$$

$$Q_{\mu D}(E,r) = \frac{C_\rho\lambda_0}{\rho\Lambda_\mu(E)} + \frac{(1-C_\rho)\lambda_0}{\rho_c(R)\Lambda_\mu(E)} ,$$

$$\frac{1}{\Lambda_\mu(E)} = \frac{m_\mu}{\tau_\mu}\left[\frac{1}{E(E+2m_\mu)}\right]^{1/2} ;$$

and

$$\frac{\partial}{\partial r}\mu_s(E,r) + Q_{\mu D}(E,r)\mu_s(E,r) - \frac{\partial}{\partial E}[S_\mu(E)\mu_s(E,r)] = \int_{E_{\mu 1}}^{E_{\mu 2}} dE'\,F(E')Q_{\pi D}(E',r)[\pi_i(E',r)+\pi_s(E',r)]$$

$$+ \begin{cases} \pi_\delta(r)\,F(E_{R\pi})Q_{\pi D}(E_{R\pi},r) , & E_{\mu 1} \leqq E_{R\pi} \leqq E_{\mu 2} , \\ 0 , & E_{\mu 2} < E_{R\pi} < E_{\mu 1} , \end{cases} \tag{6}$$

where

$$F(E') = \frac{(m_\pi/m_\mu)E'}{2U_2[E'(E'+2m_\pi)]^{1/2}} ,$$

$$E_{\mu 1} = \frac{m_\pi}{m_\mu}\{U_1(E+m_\mu) - U_2[E(E+2m_\mu]^{1/2}\} - m_\pi ,$$

$$E_{\mu 2} = \frac{m_\pi}{m_\mu}\{U_1(E+m_\mu) + U_2[E(E+2m_\mu)]^{1/2}\} - m_\pi .$$

---

[7]The form of the muon source term from pion decay is discussed in detail in Appendix 3 of ref 2. The secondary muon equation may be solved in quadrature, but in the present code the differential equation was found to be more convenient to use than the solution.

7.8. TWO CATEGORIES OF SOLUBLE NUCLEON-MESON CASCADE EQUATIONS

F. S. Alsmiller and R. G. Alsmiller, Jr.

We consider nucleon-meson cascade equations simplified to the point where the only physical processes included are absorption and production of secondary particles. Charged-particle slowing down and pion decay are specifically omitted. The nonelastic collision cross section is assumed to be the same for all particles and independent of energy. Finally, the energy distributions, $F_{jk}(E', E)$, of the secondary particles of the jth kind, formed in a collision between an incident particle of the kth kind with a nucleus of the cascade medium, are assumed to be separable functions of the energies, E' and E, of the incident and secondary particles.

With these restrictions, the equations can be solved analytically for two forms of the distribution functions:

Case A:

$$F_{jk}(E', E) = f_j(E) g_k(E') ,$$

Case B:

$$F_{jk}(E', E) = f(E) g(E') [\alpha_j \gamma_k + \beta\, h(E') \delta_{jk}] ,$$

where $\delta_{jk} = 1$ if $j = k$ but $= 0$ if $j \neq k$, *and* α_j, γ_k, and β are constants. An example, under Case A, is the function

$$F_{jk}(E', E) = \alpha_j \frac{E'^l}{E^n} \theta(E' - \eta_k) ,$$

where $\theta(x) = 0$ if $x < 0$ but $= 1$ if $x > 0$, for which the solution was carried out by Passow.[1] The use of the step function is an attempt to account very roughly for charged-particle energy losses by ionization; η_k is an energy limit for the kth kind of particle above which the energy loss is assumed to be zero and below which it is infinite, so that no further production of secondaries takes place.

Note that the functions in Case A are far from being the most general kernels separable in the energies, because they are separable in the indices j and k as well.

In Case B, the added term in $\beta\, h(E')\delta_{jk}$ gives a larger multiplicity for emergent secondaries of the same kind as the incident particle. That this is necessary, at least at low energies, is indicated by recent results of Bertini[2] for incident protons at 400 Mev. The limitation is that a solution could be obtained only

---

[1] C. Passow, Deutsches Elektronen-Synchrotron, Hamburg, Germany, *Phänomenologische Theorie zur Berechnung einer Kaskade aus schweren Teilchen (Nukleonkaskade) in der Materie*, Desy-Notiz A 2.85 (February 1962).

[2] H. Bertini, ORNL, private communication; see also Sec. 7.2.

if $f(E)$, $g(E')$, and $b(E')$ are the same functions for all particles. This means, for one thing, that the secondary pion energy distributions must be assumed to have the same shape in E as those of the nucleons.

We will use the same notations and definitions as in Sec. 7.7 in writing the set of equations satisfied by the secondary flux components, $\phi_{sj}(E,r)$:

$$\frac{\partial}{\partial r}\phi_{sj} + Q\,\phi_{sj} = Q\sum_k \int_E^{E_0} dE'\,F_{jk}(E',E)[\phi_{ik}(E',r) + \phi_{sk}(E',r)] + S_j(E,r)\,, \tag{1}$$

where we have added an arbitrary source term, $S_j(E,r)$. We assume $S_j(E_0,r) = \phi_{sj}(E_0,r) = 0$, for all r.

In the absence of slowing-down terms, the primary flux components, $\phi_{ij}(E,r)$, are simply the initial spectra, $\phi_j(E,0)$, multiplied by an attenuation factor; i.e.,

$$\phi_{ij}(E,r) = \phi_j(E,0)e^{-Qr}\,. \tag{2}$$

The present work was motivated by the recognition that Passow's results could be generalized, since they depend essentially on the possibility of finding a single uncoupled equation for a suitable linear combination of the ϕ_{sj}.

Case A. – Use $F_{jk}(E',E)$ of Case A and define

$$\chi_{sj}(E,r) = \frac{\phi_{sj}(E,r)e^{Qr}}{f_j(E)}\,, \tag{3}$$

$$G_j(E,r) = \frac{S_j(E,r)e^{Qr}}{f_j(E)}\,, \tag{4}$$

$$\phi_0(E) = Q\sum_j g_j(E)\phi_j(E,0)\,, \tag{5}$$

$$\alpha(E) = Q\sum_j f_j(E)g_j(E) = Q\sum_j F_{jj}(E',E)\,, \tag{6}$$

$$\chi_s(E,r) = \frac{Q\sum_j f_j(E)g_j(E)\chi_{sj}(E,r)}{\alpha(E)}\,, \tag{7}$$

$$G(E,r) = \frac{Q\sum_j f_j(E)g_j(E)G_j(E)}{\alpha(E)}\,. \tag{8}$$

Equation 1 may then be transformed to

$$\frac{\partial\chi_{sj}}{\partial r} = \int_E^{E_0} dE'[\phi_0(E') + \alpha(E')\chi_s(E',r)] + G_j(E,r)\,. \tag{9}$$

Multiply by $Q f_j(E) g_j(E)/\alpha(E)$ and add equations to obtain an uncoupled equation for χ_s:

$$\frac{\partial \chi_s}{\partial r} = \int_E^{E_0} dE' [\phi_0(E') + \alpha(E') \chi_s(E', r)] + G(E, r) . \tag{10}$$

Differentiate with respect to E, and then apply the method of Laplace transforms to obtain the solution of Eq. 10 in terms of integrals over hyperbolic Bessel functions:

$$\chi_s(E, r) = \int_E^{E_0} dE' \phi_0(E') \sqrt{\frac{r}{B(E', E)}} I_1(2\sqrt{B(E', E) r})$$

$$+ \int_0^r dr' G(E, r') + \int_0^{E_0} dE' \int_0^r dr' \alpha(E') G(E', r - r') \sqrt{\frac{r'}{B(E', E)}} I_1(2\sqrt{B(E', E) r'}) , \tag{11}$$

where

$$B(E', E) = \int_E^{E'} dE'' \alpha(E'') .$$

The solutions for the individual cascade components may be obtained by a somewhat laborious integration of Eq. 9, using Eq. 11:

$$\chi_{sj}(E, r) = \int_E^{E_0} dE' \phi_0(E') \sqrt{\frac{r}{B(E', E)}} I_1(2\sqrt{B(E', E) r})$$

$$+ \int_E^{E_0} dE' \int_0^r dr' G(E', r - r') \alpha(E') \sqrt{\frac{r'}{B(E', E)}} I_1(2\sqrt{B(E', E) r'}) + \int_0^r dr' G_j(E, r') . \tag{12}$$

Case B. – The method of solution is similar to that for Case A; only the results for the individual cascade components are given here. We define the following quantities:

$$\chi_{sj}(E, r) = \frac{\phi_{sj}(E, r) e^{Qr}}{\alpha_j f(E)} , \tag{13}$$

$$G_j(E, r) = \frac{S_j(E, r) e^{Qr}}{\alpha_j f(E)} , \tag{14}$$

$$\phi_0(E) = Q g(E) \sum_j \gamma_j \phi_j(E, 0) , \tag{15}$$

$$\gamma = \sum_j \alpha_j \gamma_j , \tag{16}$$

$$\alpha(E) = \gamma Q g(E) f(E) , \tag{17}$$

$$G(E,r) = \sum_j \frac{\alpha_j \gamma_j G_j(E,r)}{\gamma}, \tag{18}$$

$$C(E',E) = \int_E^{E'} \alpha(E'') \left[1 + \frac{\beta b(E'')}{\gamma} \right] dE'' , \tag{19}$$

$$D(E',E) = \int_E^{E'} \alpha(E'') \frac{\beta b(E'')}{\gamma} dE'' . \tag{20}$$

The solutions for $\chi_{sj}(E,r)$ are

$$\chi_{sj}(E,r) = \int_E^{E_0} dE' \left\{ \phi_0(E') \left[1 + \frac{\beta b(E'')}{\gamma} \right] \sqrt{\frac{r}{C(E',E)}}\, I_1(2\sqrt{C(E',E)\, r}) \right.$$
$$\left. - \left[\phi_0(E') - \frac{\gamma}{\alpha_j} \phi_j(E',0)\, Q\, g(E')\right] \frac{\beta b(E')}{\gamma} \sqrt{\frac{r}{D(E',E)}}\, I_1(2\sqrt{D(E',E)\, r}) \right\}$$
$$+ \int_E^{E_0} dE' \int_0^r dr' \alpha(E') \left\{ G(E',r-r') \left[1 + \frac{\beta b(E')}{\gamma} \right] \sqrt{\frac{r}{C(E',E)}}\, I_1(2\sqrt{C(E',E)\, r'}) \right.$$
$$\left. - \left[G(E',r-r') - G_j(E',r-r')\right] \frac{\beta b(E')}{\gamma} \sqrt{\frac{r'}{D(E',E)}}\, I_1(2\sqrt{D(E',E)\, r'}) \right\} + \int_0^r dr'\, G_j(E,r') . \tag{21}$$

7.9. SPACE VEHICLE SHIELDING STUDIES: CALCULATIONS OF THE ATTENUATION OF A MODEL SOLAR FLARE AND MONOENERGETIC PROTON BEAMS BY ALUMINUM SHIELDS[1]

R. G. Alsmiller, Jr., and J. E. Murphy[2]

In the design of shielding experiments for manned space vehicles, such as those being conducted at ORNL, it is necessary to know which energy region is most important in the shielding problem. Calculations have been carried out to give a preliminary answer to this question.

Using the equations and method of computation discussed in a previous report,[3] nucleon-meson cascade calculations were performed for both continuous and monoenergetic proton beams incident on aluminum slab shields. Because many of the approximations used, particularly the straight-ahead approximation, are invalid at low energies, the calculations were carried out only for energies greater than 30.4 Mev.

---

[1] R. G. Alsmiller, Jr., and J. E. Murphy, *Calculations of the Attenuation of a Model Solar Flare and Monoenergetic Proton Beams by Aluminum Shields*, ORNL-3317 (1962).

[2] Central Data Processing Facility of the Oak Ridge Gaseous Diffusion Plant.

[3] R. G. Alsmiller, Jr., F. S. Alsmiller, and J. E. Murphy, *Nucleon-Meson Cascade Calculations: Transverse Shielding for a 45-Gev Electron Accelerator (Part I)*, ORNL-3289 (1962). (The part of this report which is relevant is also reproduced as an appendix in ref 1).

The various particle fluxes were converted to dose by a method similar to that introduced by Gibson.[4] Since the fluxes are calculated only at the higher energies (>30.4 Mev) we can, strictly speaking, calculate the dose only from these high-energy particles. However, there will be particles at the lower energies, and it is desirable to estimate their contribution to the dose. Such an estimate has been obtained by a crude extrapolation procedure and is included.

On the basis of the calculations a few tentative conclusions can be drawn. The tentative nature of these conclusions must be emphasized since the calculations are very approximate (straight-ahead approximation), are for only one element, and yield essentially no information below 30.4 Mev.

In shielding against solar flares of the general form of the May 10, 1959, flare[5] it seems that secondary nucleons will not be a problem unless thick shields (>50 g/cm^2) are considered.

In experiments in which monoenergetic beams are used to obtain direct information for shielding against the May 10 flare, there is no single energy of the most interest. Rather, an experimental shield thickness and a proton energy should be used such that the proton range at this energy is slightly greater than the shield thickness. This ensures that the measurements will be made under conditions giving the largest dose; however, since most of the dose will be from the primary beam (and can thus readily be calculated), such measurements will be relatively uninteresting.

In experiments in which monoenergetic beams are used to obtain information for checking shielding calculations, the secondary fluxes are necessarily of the most interest. Then – always with the May 10 flare in mind – all energies greater than 200 Mev are of roughly the same interest, and the shield thickness used must be such that the primary beam is stopped in the shield.

[4]W. A. Gibson, *Energy Removal from Primary Proton and Neutron Beams by Tissue*, ORNL-3260 (1962).

[5]W. L. Gill, *Statement on the Approach to the Radiation Problem for Apollo*, submitted to National Academy of Sciences, Space Science Board, Working Group on Radiation Problems in Space Flight, Jan. 12–13, 1962, NASA Manned Spacecraft Center, Life Systems Division.

7.10. COMPARISON OF PRIMARY PROTON DOSE WITH THE DOSE FROM GAMMA RAYS PRODUCED BY INELASTIC SCATTERING OF SOLAR FLARE PROTONS

F. S. Alsmiller, R. G. Alsmiller, Jr., and D. K. Trubey

Most of the radiation dose behind thin shields exposed to solar flare protons can be attributed to the primary protons. However, the possible importance of secondary gamma rays produced in proton nonelastic collisions has been pointed out recently by Madey *et al.* [1] They computed the gamma dose rate at the center of an aluminum spherical shell, as a function of shield thickness, and found it comparable to the primary proton dose for a thickness of about 12 cm. These results are based on the use of experimental values of

[1]R. Madey, A. G. Duneer, Jr., and T. J. Krieger, *Gamma Dose from Solar Flare Protons Incident on an Aluminum Shield*, presented at the Annual Meeting of the American Nuclear Society, June 18–21, 1962, Boston, Mass.

the gamma spectrum and yield for 14-Mev protons[2] which were assumed to be the same for all proton energies above the Coulomb barrier up to 30 Mev.[3] Also, the flare spectrum used is one which emphasizes the low-energy protons to a greater extent than does the May 10, 1959, flare spectrum.[4]

Since many questions remain, we have performed several further calculations for both spherical shell and infinite slab aluminum shields. The gamma spectrum is constructed from theoretical gamma production cross sections[5] which are available for *inelastic* (n,n') *neutron* scattering in aluminum, for neutron energies from 0.9 to 18 Mev. We assume the gamma production cross sections for proton inelastic scattering can be approximated with sufficient accuracy by the relation

$$\begin{aligned} \sigma_{pp'\gamma}(E,E_\gamma) &= \sigma_{nn'\gamma}(E - V_c, E_\gamma) && (V_c \leqq E \leqq 22.3 \text{ Mev}) \\ &= \sigma_{nn'\gamma}(22.3 - V_c, E_\gamma) && (22.3 \text{ Mev} \leqq E \leqq E_{c_{max}}) , \end{aligned} \quad (1)$$

where V_c is the Coulomb potential barrier, E the incident proton energy, and E_γ the photon energy; $E_{c_{max}}$ is an upper limit on the proton energy, taken variously as 22.3, 30, and 50 Mev.

In Fig. 7.10.1, we compare our curve of the gamma dose rate, d_γ, versus spherical shell thickness, with the results of Madey *et al.* for an isotropically incident differential proton flux,

$$\begin{aligned} P(E,0) &= 3.1 \times 10^9 \, E^{-4.6} && (85 \text{ Mev} \leqq E \leqq 45 \times 10^3 \text{ Mev}) \\ &= 1.0 \times 10^6 \, E^{-2.8} && (5 \times 10^{-2} \text{ Mev} \leqq E \leqq 85 \text{ Mev}) , \end{aligned} \quad (2)$$

where $P(E,0)$ has the units of protons cm^{-2} sec^{-1} steradian^{-1} Mev^{-1}. The primary proton flux is calculated as a function of distance through the shield in the usual manner, described in Sec. 7.7; the proton stopping power in aluminum was computed from Sternheimer's[6] formula for $E > 2$ Mev, and from tables[7] based on experimental values for $E < 2$ Mev. The proton total nonelastic collision cross section was taken mostly from the Monte Carlo calculation of Bertini above 30 Mev (see Secs. 7.1 and 7.2) and from Howerton's[8] compilation of neutron nonelastic cross sections for neutron energies below 15 Mev, using the same approximation as in Eq. 1; i. e.,

$$\sigma_{p,\text{nonel}}(E') = \sigma_{n,\text{nonel}}(E' - V_c) . \quad (3)$$

In the calculations for spherical shell shields, the photons are assumed to be produced by primary protons only, to have the same direction as the incident proton, and to be attenuated[9] exponentially through the shield. Photon flux-to-dose conversion factors for tissue were taken from ref 10.

---

[2]T. Wakatsuki *et al.*, *J. Phys. Soc. Japan* **15**, 1141 (1960).

[3]T. J. Krieger, private communication.

[4]W. L. Gill, *Statement on the Approach to the Radiation Problems for Apollo,* submitted to the National Academy of Sciences, Space Science Board, Working Group on Radiation Problems in Space Flight, Jan. 12–13, 1962, NASA Manned Spacecraft Center, Life Systems Division.

[5]E. S. Troubetzkoy, *Fast Neutron Cross Sections of Iron, Silicon, Aluminum, and Oxygen,* NDA-2111-3, Vol. C, pp 38,39.

[6]R. M. Sternheimer, *Phys. Rev.* **115**, 137 (1959).

[7]*American Institute of Physics Handbook,* McGraw-Hill Book Co., Inc., 1957.

[8]R. J. Howerton, *Semi-Empirical Neutron Cross Sections,* UCRL-5351 (1958).

[9]G. W. Grodstein, *X-ray Attenuation Coefficients from 10 Kev to 100 Mev,* NBS Circular 583 (1957).

[10]B. J. Henderson, *Conversion of Neutron or Gamma-Ray Flux to Absorbed Dose Rate,* XDC-59-8-179 (1959).

The numerical differences in the two estimates of the gamma dose rate shown in Fig. 7.10.1 are consistent with the differences in the assumed gamma spectrum. Figure 7.10.1 also shows a comparison of the primary proton dose rate, $d_{P,dE/dx}$, calculated considering only the proton ionization and elastic scattering energy losses in tissue,[11] with the results of Madey *et al.* A crossing point between the gamma and proton curves in our calculations does not occur in a thickness of 150 g/cm^2 (44.4 cm). The gamma dose rate is only about 10% of the proton dose at a thickness of 25 g/cm^2 (9.3 cm), but the ratio increases rapidly with increasing shield thickness.

The spherical shell calculations were repeated for the time-integrated May 10 solar flare spectrum,[4]

$$\begin{aligned} P(E,0) &= 0 && (0 \leqq E < 5 \text{ Mev}) \\ &= 2.5 \times 10^{11} E^{-2.07} && (5 \text{ Mev} \leqq E \leqq 60 \text{ Mev}) \\ &= 5.486 \times 10^{14} E^{-3.95} && (60 \text{ Mev} \leqq E \leqq 10^3 \text{ Mev}) \end{aligned} \quad (4)$$

[11] W. S. Snyder and J. Neufeld, *Radiation Research* **6**, 67 (1957).

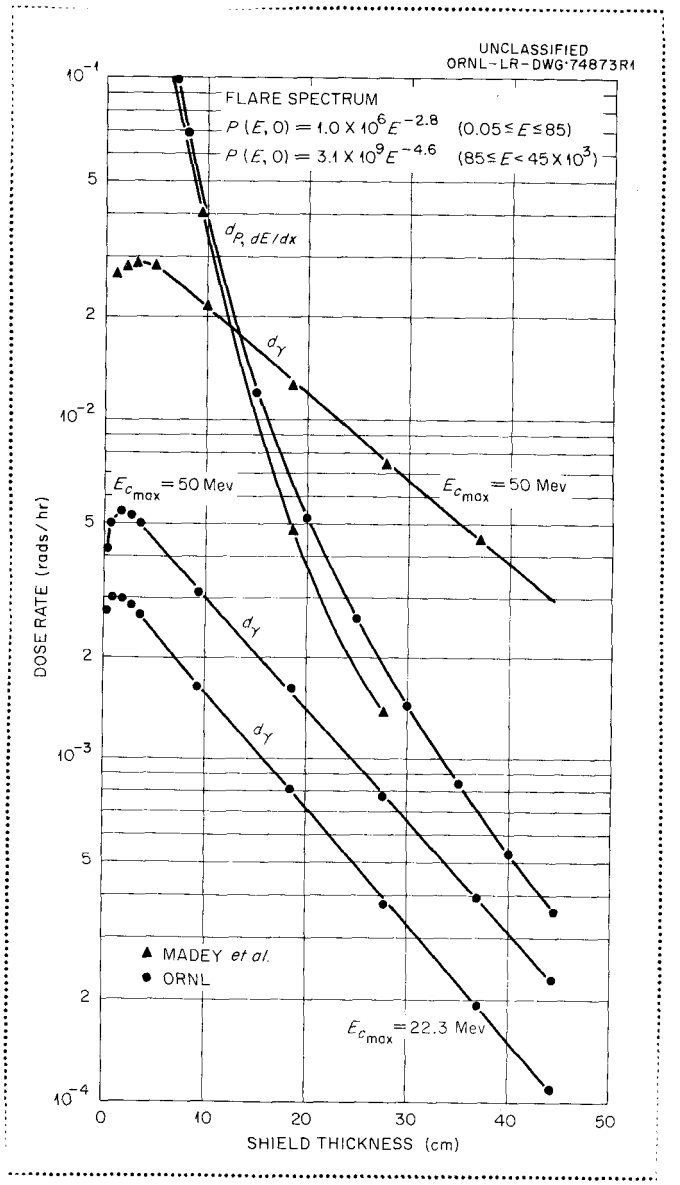

Fig. 7.10.1. Gamma and Primary Proton Dose Rates at the Center of a Spherical Aluminum Shell from Solar Flare Protons.

(units are protons cm^{-2} steradian^{-1} Mev^{-1}), and are shown in Fig. 7.10.2. The curve labeled d_P is a total proton dose, in which the additional energy deposition by proton absorption in tissue is roughly accounted for by a method similar to that used by Gibson.[12]

The effect of varying the upper limit, $E_{c_{max}}$, on the energy of protons assumed capable of producing gamma rays, from 22.3 Mev to 50 Mev, is about a factor of two. At 25 g/cm^2, the gamma dose is less than 7% of the proton dose.

These factors are changed very little in Fig. 7.10.3, in which we plot the dose results for the May 10 flare incident isotropically on an infinite slab shield. This is true even though three changes were made in the calculation. First, the photons were more realistically assumed to be emitted isotropically, rather than in the direction of the incident proton. Second, photon transport through the shield was calculated by means of the OGRE-P2 Monte Carlo code (see Sec. 6.8), which takes buildup of the photon flux into

[12]W. A. Gibson, *Energy Removal from Primary Proton and Neutron Beams by Tissue*, ORNL-3260 (1962).

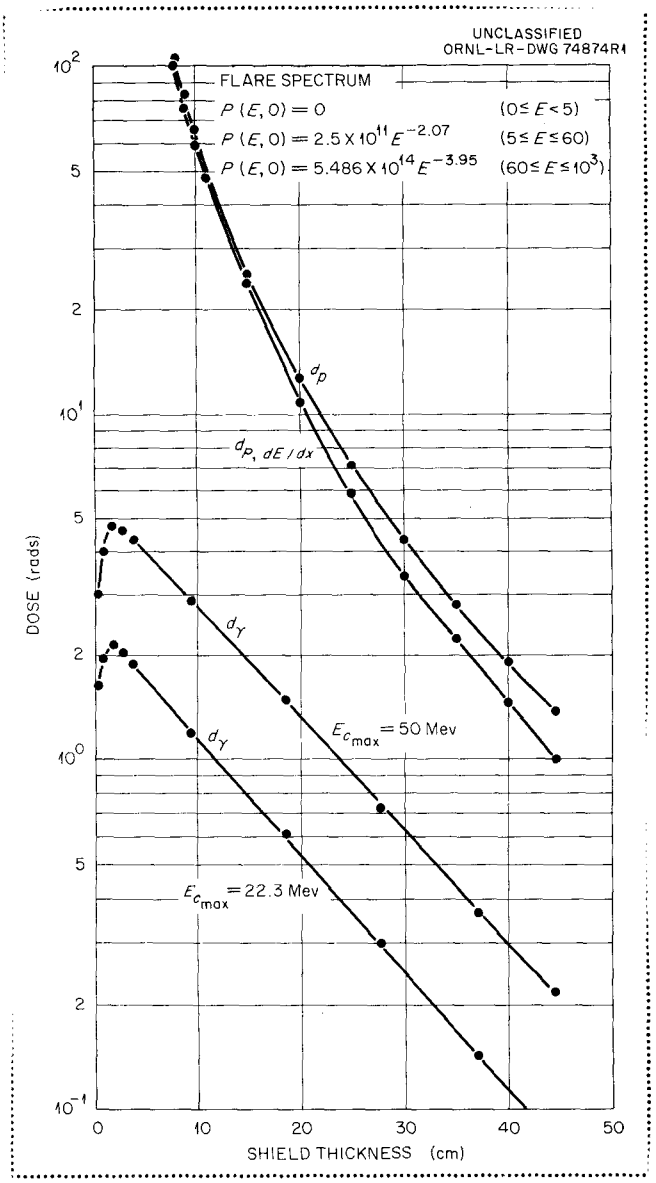

Fig. 7.10.2. Gamma and Primary Proton Doses at Center of Spherical Aluminum Shell from Solar Flare (May 10, 1959) Protons.

account. A major part of the gamma dose at the larger shielding distances is due to the "collided" photon flux, as opposed to the "uncollided" flux; only the latter was considered in the spherical shell cases.

Third, the primary proton flux is calculated as a function of position by taking into account the variation of path length with angle of incidence, and integrating over all angles; i.e., a Gross transformation is carried out. It is worth noting that the geometry effect is rather important, since the change from a spherical shell to a slab decreases the primary proton dose by almost a factor of 10.

On the basis of so few calculations, only very tentative conclusions can be drawn. In general, we find that with our cross sections the gamma dose is not so important as the calculations of Madey *et al.* would indicate. By comparing Figs. 7.10.1 and 7.10.2, it is clear that the ratio of the gamma dose to the primary proton dose at larger shield thicknesses is very dependent on the shape of the incident flare spectrum.

Finally, comparing the results of this paper with calculations of secondary neutron and proton dose (see Sec. 7.9), it seems that in general the gamma rays are neither more nor less important than secondary nucleons.

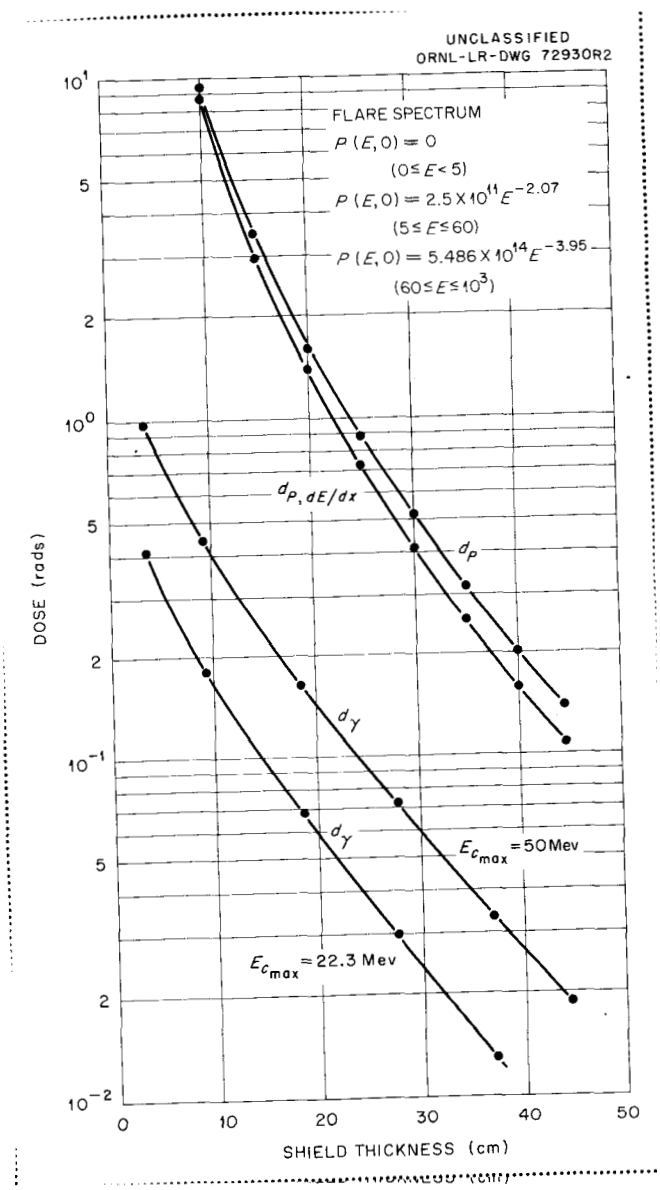

Fig. 7.10.3. Gamma and Primary Proton Doses from Solar Flare (May 10, 1959) Protons Incident on Aluminum Slab Shield.

7.11. COMPUTER ROUTINE FOR TREATING COMPLEX GEOMETRIES IN MONTE CARLO AND OTHER TYPES OF CALCULATIONS

D. Irving

A general-purpose geometry (GEOM) routine has been written for the IBM-7090 for use in Monte Carlo and other calculations. With this routine it is possible to systematically specify complex geometrical configurations such as a structure containing many media that might be under study in a radiation transport problem. The purpose of the routine is simply to take any straight-line path through the configuration and determine the media through which it passes and the length of the path segment in each medium.

The path may be specified either by the coordinates of the starting point and the end point of the path or by the coordinates of the starting point and the direction cosines of the path. In the latter case the path will extend along the given direction from its starting point to the boundary of the system being considered.

The output from the subroutine will consist of the coordinates of the points where the path passes from one medium to another (includes the starting and ending points of the path), the medium in which each segment of the path lies, and the length of each segment of the path.

The types of geometrical configurations that can be specified by GEOM are indicated by the method of specification described below.

The entire system of interest should be enclosed in a parallelepiped whose faces are parallel to the coordinate planes. The system is then divided into one or more smaller parallelepipeds, called "zones," by planes parallel to the coordinate planes. Planes used as zone boundaries must extend as a boundary completely across the system. In a similar manner each zone is divided into one or more smaller parallelepipeds, called "blocks." The block system used in any one zone need bear no relationship to that used in any other zone.

The purpose of the zone arrangement is to allow parts of the system to be broken up into smaller blocks than is necessary for other parts of the system. If the whole system is relatively simple or requires a similar description throughout, the system should be composed of one zone divided into many blocks rather than of many zones of one block each.

The planes used as block (or zone) boundaries need not also be boundaries between different media. However, where a boundary between two media is a plane parallel to a coordinate plane, it is advantageous to make it a block (or zone) boundary also.

Boundaries between media which are not block boundaries may be any quadric surface. A quadric surface is defined by the zeros of a quadratic function, and divides all space into two regions. In one region the function defining the surface will be positive, while in the other region it will be negative. The positive side of a quadric surface is not necessarily its exterior. Determination of just which region is positive must be done by inspection, and depends on how the function is written. For example, if a sphere is described by $r^2 - x^2 - y^2 - z^2$, then the interior of the sphere is the positive region.

Each block may contain up to 18 quadric surfaces used as material boundaries. The surfaces will divide the block into regions. A region is defined as being positive with respect to one set of quadric surfaces and negative with respect to another set, while the rest of the surfaces in the block are irrelevant. Each region must contain only one medium but different regions may contain the same medium.

For example, in considering the description of a block containing a hemisphere of medium 1 surrounded by medium 2 (shown in Fig. 7.11.1 in two dimensions), there would be two quadric surfaces in the block: the sphere and the plane forming the base of the hemisphere. (It can be assumed that the interior of the hemisphere is negative to both surfaces.) Then the block would have to be divided into at least three regions: a region that would be the hemisphere, defined as negative to both surfaces and containing medium 1; a region that would contain medium 2, defined as positive to the sphere but negative to the plane, labeled $2a$ in the figure; and a region that would also contain medium 2, defined as positive to the plane with the sphere irrelevant to its definition. The third region could have been divided into two regions, one inside and one outside the sphere, labeled $2b$ and $2c$, respectively, but since they contain the same medium such a division is unnecessary. The second and third regions cannot be combined, although they contain the same medium, because a complete definition of the combined region cannot be given in the form stated above. Medium 2 could have been divided into regions in an alternate but equivalent manner. One region would be defined as outside the sphere with the plane irrelevant, thus containing areas $2a$ and $2c$, and the other region, $2b$, defined as negative to the sphere but positive to the plane.

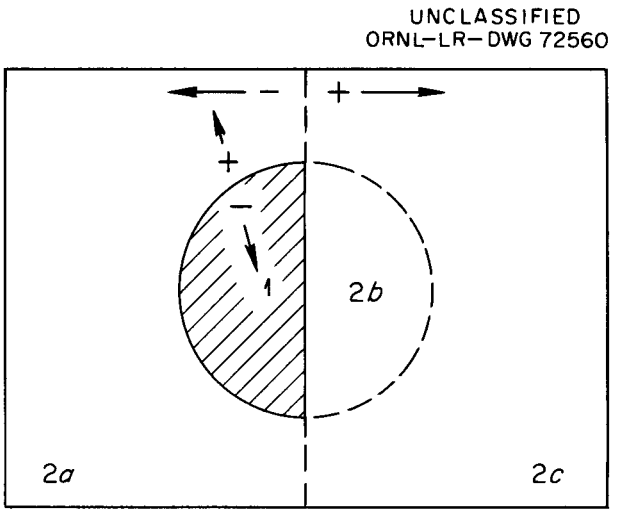

Fig. 7.11.1. Illustration of Geometry Which Can Be Used with GEOM Routine.

7.12. TISSUE DOSE RATE FROM BREMSSTRAHLUNG RADIATION BEHIND AN IDEALIZED APOLLO VEHICLE WALL EXPOSED TO ELECTRONS IN THE EARTH'S OUTER RADIATION BELT

C. D. Zerby, H. S. Moran, S. K. Penny, and D. K. Trubey

One of the radiation hazards that will be encountered by vehicles orbiting the earth at high altitudes or venturing out into space is that associated with the electrons in the earth's outer radiation belt. Although these particles can be readily stopped in the outer surface of the vehicle, a hazard arises because they generate bremsstrahlung radiation that can penetrate to the interior of the vehicle.

The purpose of the present calculation was to obtain a reasonably accurate estimate of the tissue dose rate due to the bremsstrahlung radiation penetrating an idealized Apollo vehicle wall. For purposes of normalization the electron flux chosen is that at the heart of the earth's outer radiation belt.

Recently O'Brien *et al.*[1] reported the measurements obtained on Explorer XII of the omnidirectional flux of electrons in the heart of the radiation belt. Their results have been used to produce the spectral data presented in Fig. 7.12.1. The estimate by O'Brien *et al.* of the highest intensity in the outer belt is considered to be the most accurate estimate available, although it is three orders of magnitude lower than that previously reported.[2] The difference is attributed entirely to a misinterpretation of what the instruments recorded in the previous experiments.

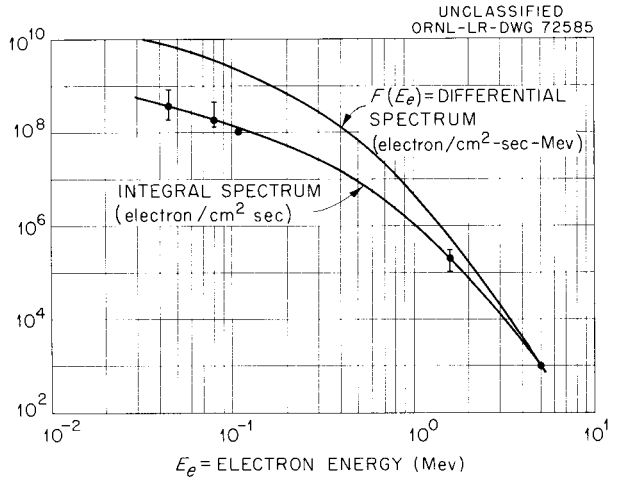

Fig. 7.12.1. Omnidirectional Flux of Electrons in the Heart of the Outer Radiation Belt. Based on the experiment of B. J. O'Brien *et al.* [*J. Geophys. Research* **67**, 397 (1962)].

The wall of the Apollo vehicle used in the calculation reported here was idealized to be a stratified slab of infinite extent and taken to have a total thickness of 2.75 g/cm^2. The composition and arrangement of the stratifications are presented in Table 7.12.1. This information represents a configuration that resulted from early design studies of the Apollo vehicle.[3] A minimum thickness for the charring ablator in the first layer was chosen to give a conservative tissue dose rate. The composition of this layer is only approximate. However, a study with an alternate composition of $C_{12}H_{22}O_2N$ with the same density did not affect the results reported here.

It was assumed that the electrons in the outer radiation belt have an isotropic angular distribution. Hence, if the energy flux of electrons (summed over all directions) is $F(E_e)$, as shown in Fig. 7.12.1, then one-fourth of the electrons will be incident per square centimeter of the surface of the wall (stratification 1). It is assumed that once the electrons hit the surface they stop entirely in the charring ablator (C_2H_4O) near the surface. Since they enter the surface isotropically and also have a devious path in the process of losing energy by ionization and radiative collisions, the bremsstrahlung radiation given off is assumed to be released isotropically.

---

[1] B. J. O'Brien *et al.*, *J. Geophys. Research* **67**, 397 (1962).

[2] J. A. Van Allan and L. A. Frank, *Nature* (*London*) **184**, 219 (1959).

[3] W. L. Gill, Manned Spacecraft Center of NASA, private communication.

Table 7.12.1. Typical Apollo Vehicle Wall Specifications[a]

Stratification	Material	Element	Weight Percent	Thickness (cm)	Density (g/cm^3)
1	C_2H_4O	C	54.5	0.9652	0.7512
		H	9.2		
		O	36.3		
2	PH 15-7 steel	Fe	73.25	0.0508	7.854
		Cr	16.00		
		Ni	7.75		
		Mo	3.00		
3	PH 15-7 steel	Fe	73.25	1.102	0.0481
		Cr	16.00		
		Ni	7.75		
		Mo	3.00		
4	PH 15-7 steel	Fe	73.25	0.0508	7.854
		Cr	16.00		
		Ni	7.75		
		Mo	3.00		
5	SiO_2	Si	46.7	3.20	0.0561
		O	53.3		
6	Al-2014-T6	Al	95.0	0.3556	2.7966
		Cu	5.0		

[a]Total wall thickness, 2.75 g/cm^2.

The amount of bremsstrahlung radiation released by an electron slowing down in the charring ablator was calculated with a computing machine code constructed by Zerby and Moran.[4] This calculation treats the radiation collisions as a perturbation (which is valid only for low electron energies such as those considered here) and uses the Bethe-Heitler cross section with corrections for the screening effects. The results of the calculations are shown in Fig. 7.12.2, where E_e is the initial electron kinetic energy, E_γ is the photon energy, and $\alpha = E_\gamma/E_e$. The quantity $B(E_e, \alpha)\, d\alpha$ is the number of bremsstrahlung photons produced in interval $d\alpha$ by an electron with initial kinetic energy E_e that is stopped in the charring ablator.

The attenuation of the bremsstrahlung photons through the stratified slab was determined by means of an existing Monte Carlo calculation.[5] The penetrating flux was converted to tissue dose rate by using the flux-to-dose conversion factors calculated by Henderson[6] and shown in Table 7.12.2. In these calculations the photon source was considered to be on the surface of the charring ablator and to be isotropic and monoenergetic. A series of cases at different energies were calculated in which 50,000 histories for each source energy were considered. In these runs statistical estimation was employed to improve the accuracy of the

[4]C. D. Zerby and H. S. Moran, *Bremsstrahlung Spectra in NaI and Air*, ORNL-2454 (1958).

[5]D. K. Trubey, S. K. Penny, and M. B. Emmett, *A Monte Carlo Program for Computing Gamma-Ray Transmission Through Laminated Slabs*, ORNL TM-167 (rev.) (1962).

[6]B. J. Henderson, *Conversion of Neutron or Gamma-Ray Flux to Absorbed Dose Rate*, XDC-59-8-179 (1959).

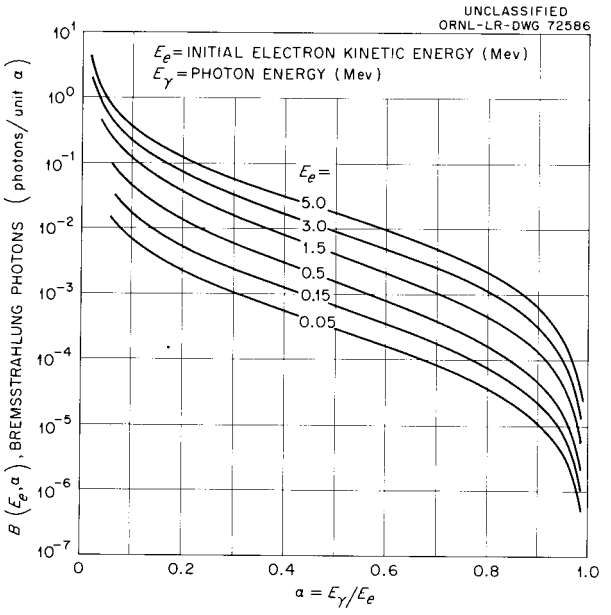

Fig. 7.12.2. Bremsstrahlung Radiation Produced in the Charring Ablator of an Apollo Vehicle.

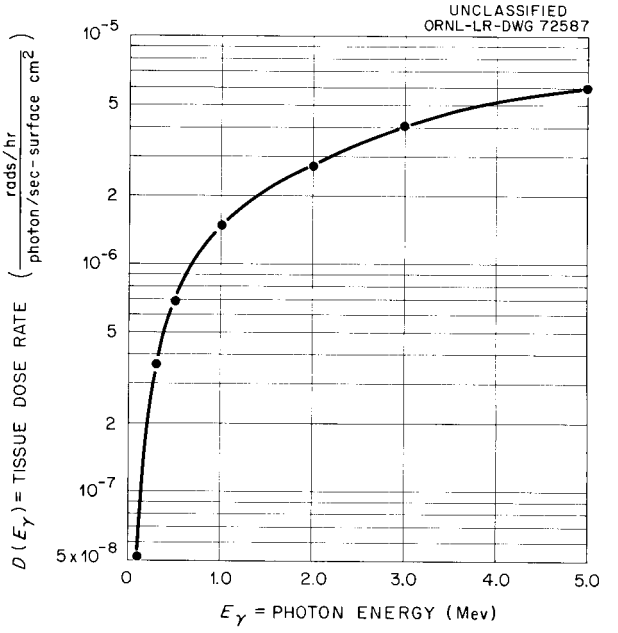

Fig. 7.12.3. Tissue Dose Rate Behind an Apollo Vehicle Wall Resulting from an Isotropic Surface Source of Monoenergetic Photons.

Table 7.12.2. Gamma-Ray Flux to Tissue Dose Rate Conversion Factors[a]

Photon Energy (Mev)	Conversion Factor (rad hr^{-1}/photon sec^{-1} cm^{-2})
0.01	3.38×10^{-6}
0.02	7.75×10^{-7}
0.04	1.92×10^{-7}
0.06	1.23×10^{-7}
0.08	1.53×10^{-7}
0.10	1.49×10^{-7}
0.2	3.38×10^{-7}
0.4	7.39×10^{-7}
0.6	1.10×10^{-6}
0.8	1.44×10^{-6}
1.0	1.76×10^{-6}
2.0	2.76×10^{-6}
3.0	3.93×10^{-6}
4.0	4.79×10^{-6}
5.0	5.57×10^{-6}

[a]B. J. Henderson, *Conversion of Neutron or Gamma-Ray Flux to Absorbed Dose Rate*, XDC 59-8-179 (1959).

estimates. The results of these calculations are shown in Fig. 7.12.3, where $D(E_\gamma)$ is the tissue dose rate from a monoenergetic photon source at energy E_γ.

The penetrating tissue dose rate, $D(E_e)$, for incident electrons with energy E_e is obtained from the data presented in Figs. 7.12.2 and 7.12.3 by finding the integral

$$D(E_e) = \int_0^{E_e} D(E_\gamma)\, B\left(E_e, \frac{E_\gamma}{E_e}\right) \frac{dE_\gamma}{E_e} .$$

The results of a series of these calculations are shown in Fig. 7.12.4. The total tissue dose rate is finally obtained from

$$D = \int_0^{\infty} D(E_e) \frac{F(E_e)}{4}\, dE_e . \qquad (1)$$

The integrand of Eq. 1 is presented in Fig. 7.12.5 since it serves as an importance function, indicating which electron energy range caused the greatest contribution to the dose rate by penetrating bremsstrahlung radiation. Surprisingly enough, it is around 0.15 Mev.

The total dose rate was calculated to be 8.58×10^{-3} rad/hr.

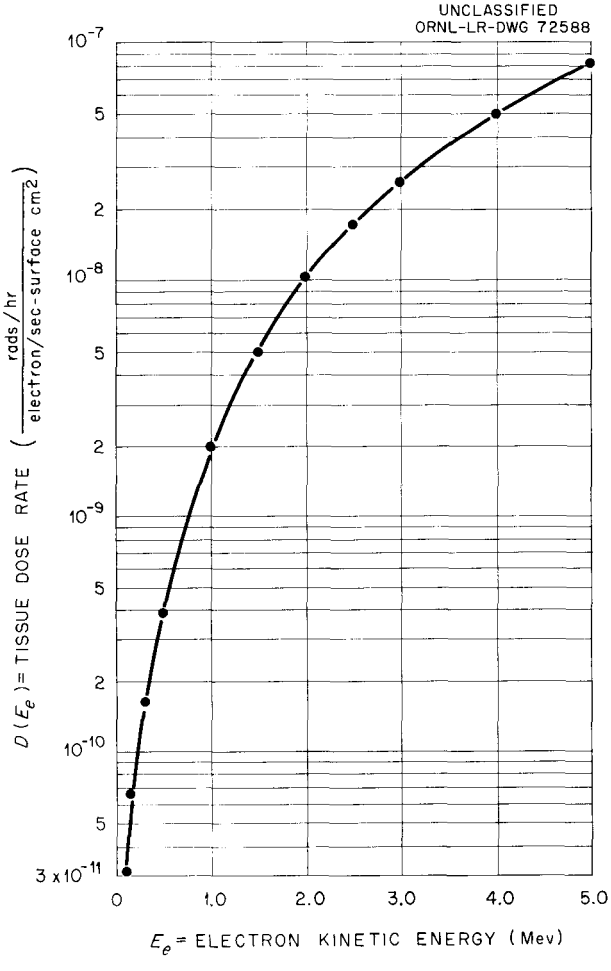

Fig. 7.12.4. Tissue Dose Rate from Bremsstrahlung Radiation Behind an Apollo Vehicle Wall Resulting from an Incident Beam of Monoenergetic Electrons.

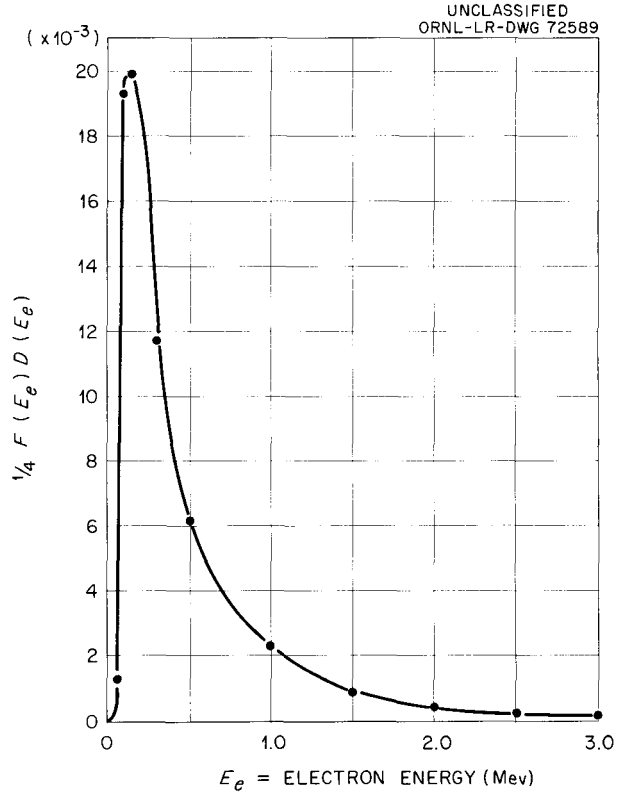

Fig. 7.12.5. Integrand of the Total Tissue Dose Rate Integral.

7.13. TISSUE DOSE RATE FROM BREMSSTRAHLUNG RADIATION BEHIND AN IDEALIZED APOLLO VEHICLE WALL EXPOSED TO ELECTRONS IN THE ARTIFICIAL RADIATION BELT

C. D. Zerby and H. S. Moran

The artificial electron radiation belt which has been created recently by a high-altitude nuclear bomb blast appears to be of high enough intensity to constitute a radiation hazard. The maximum omnidirectional flux of electrons in this belt is estimated to be 10^9 electrons cm^{-2} sec^{-1} (ref 1) and to have the same energy spectrum as the electrons released in nuclear fission.[2] This spectrum is much flatter than the spectrum of electrons in the outer radiation belt.[3] Hence, there is a radiation problem from the penetrating electrons as well as from the penetrating bremsstrahlung radiation.

The purpose of the present calculation was to obtain a reasonably accurate estimate of the tissue dose rate due to bremsstrahlung radiation penetrating an idealized Apollo vehicle wall. Most of the data used in this calculation were taken from a previous report on the penetration of bremsstrahlung radiation created by electrons in the outer radiation belt (see Sec. 7.12 and ref 4). For purposes of normalization, the maximum electron flux in the artificial belt was chosen to be incident on the wall.

The energy spectrum in the artificial belt is shown in Fig. 7.13.1. These data were obtained from the formula[2]

$$F(E_e) = 7.0995 \times 10^8 \exp(-0.575E - 0.055E^2) ,$$

where $F(E_e)$ is the omnidirectional flux in particles cm^{-2} sec^{-1} Mev^{-1}, E is the electron kinetic energy in Mev, and the normalization constant was chosen to give a total flux of 10^9 particles cm^{-2} sec^{-1}.

In this calculation the Apollo vehicle wall was the same as that considered in Sec. 7.12 and the calculation was performed in the same manner as described there. The only difference between the two calculations is in the shape of the electron spectrum used. In the present case the data shown in Fig. 7.13.1 were used for the spectrum.

The total tissue dose rate was obtained from

$$D = \int_0^\infty D(E_e) \frac{F(E_e)}{4} dE_e . \qquad (1)$$

The integrand of Eq. 1 is presented in Fig. 7.13.2 since, as is indicated in Sec. 7.12, it serves as an importance function. Although the data for the function $D(E_e)$ shown in Fig. 7.12.4 do not extend above 5 Mev, the shape of the integrand in Fig. 7.13.2 was extrapolated to higher energies. An error is introduced by this procedure, but it is expected to be relatively small. It should be observed that the maximum

---

[1] W. N. Hess, Goddard Spaceflight Center (private communication).

[2] C. E. Carter, F. Reines, J. J. Wagner, and M. E. Wyman, *Phys. Rev.* **113**, 280 (1959).

[3] B. J. O'Brien *et al.*, *J. Geophys. Res.* **67**, 397 (1962).

[4] C. D. Zerby *et al.*, *A Study of the Penetration of a Typical Apollo Capsule Wall by Bremsstrahlung Radiation Created in the Ablator Material by Electrons in the Outer Radiation Belt*, ORNL-3360 (to be published).

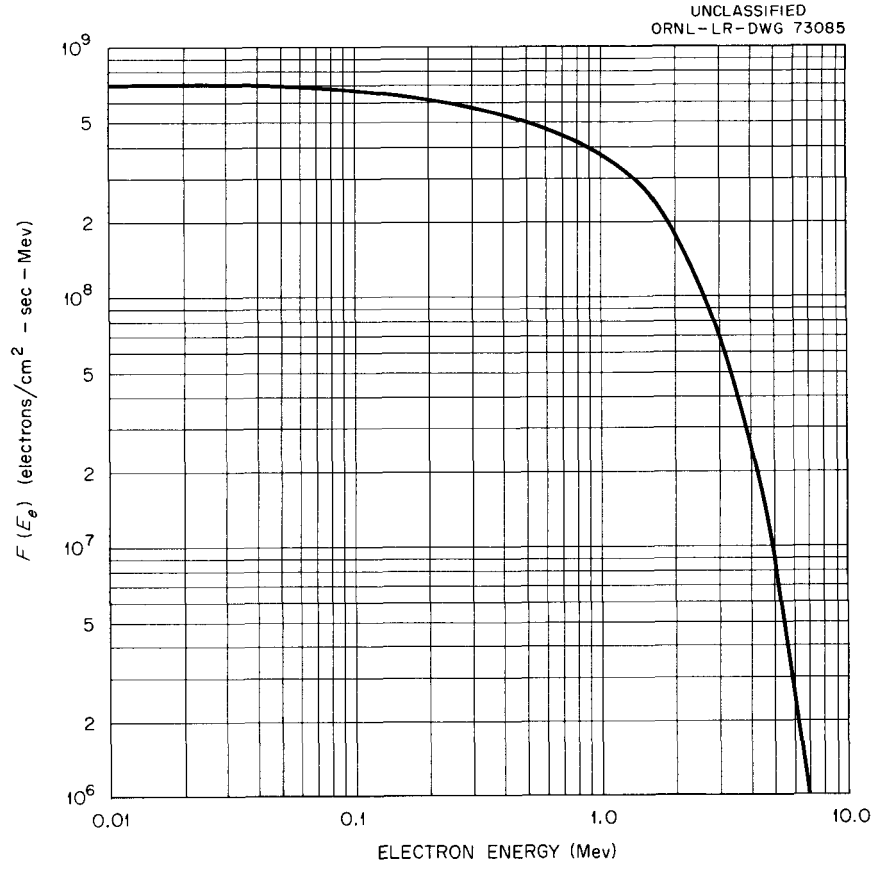

Fig. 7.13.1. Maximum Omnidirectional Flux of Electrons in the Artificial Radiation Belt of the Earth.

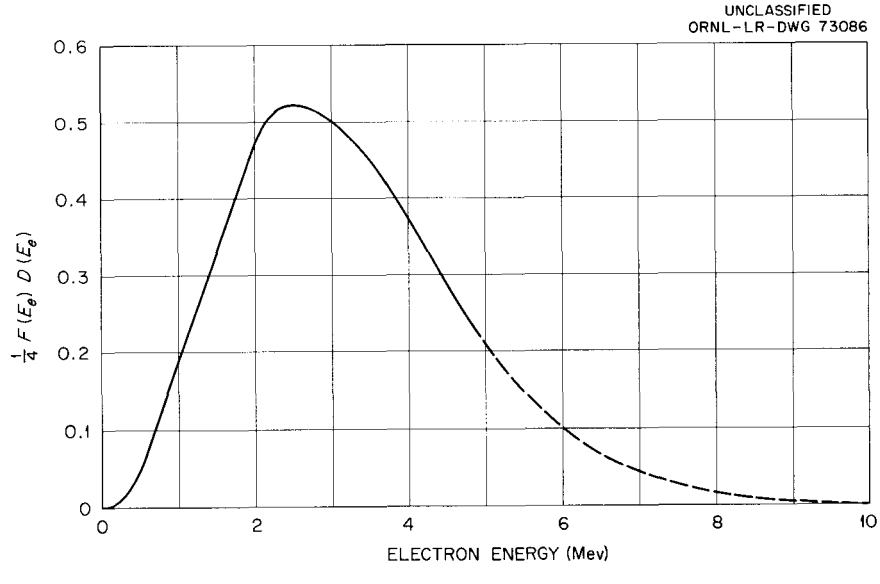

Fig. 7.13.2. Integrand of the Total Tissue Dose-Rate Integral.

contribution to the bremsstrahlung dose rate behind the wall comes from incident electrons with energies about $2\frac{1}{2}$ Mev.

The total dose rate, which is the area under the curve shown in Fig. 7.13.2, is calculated to be 1.91 rads/hr.

7.14. NUCLEON-MESON CASCADE CALCULATIONS: TRANSVERSE SHIELDING FOR A 45-Gev ELECTRON ACCELERATOR[1]

R. G. Alsmiller, Jr., F. S. Alsmiller, and J. E. Murphy[2]

In the Stanford University 45-Gev electron accelerator it is expected that some electrons will strike the walls of the accelerator tube and give rise to penetrating photonucleons and photopions. The accelerator tube will be surrounded by an earth shield; estimates of the shielding thickness required have been obtained by the Stanford group.[3,4] To check these estimates, nucleon-meson cascade calculations have been carried out for several cases of interest.

With the straight-ahead approximation (that is, the assumption that a particle and all of the secondaries, tertiaries, etc., produced by the particle travel in the same straight line), a set of coupled integrodifferential transport equations are obtained which give the neutron, proton, charged pion, and muon fluxes as functions of energy and distance. Because there is very little experimental information about high-energy interactions, these equations include many quantities (cross sections, multiplicities, etc.) that are known only very approximately. In obtaining the necessary information we have relied insofar as possible on cosmic-ray data,[5] but even so, many extrapolations, interpolations, and *ad hoc* assumptions are required.

For the calculations reported in Part I of ref 1 the photonucleon and photopion yields that result when a high-energy electron strikes a copper target were taken from the calculations of Dedrick,[6-8] while for the calculations described in Part II the more recent results of DeStaebler[9] were used. The major difference between their results is that DeStaebler finds a significant number of pions at angles as large as

---

[1]The details of these calculations are given in two reports: R. G. Alsmiller, Jr., F. S. Alsmiller, and J. E. Murphy, *Nucleon-Meson Cascade Calculations: Transverse Shielding for a 45-Gev Electron Accelerator, Part I,* ORNL-3289 (1962); and *Part II,* ORNL-3365 (to be published).

[2]Central Data Processing Facility of the Oak Ridge Gaseous Diffusion Plant.

[3]*Proposal for a Two-Mile Linear Electron Accelerator,* Stanford University, Stanford, Calif. (April 1957).

[4]H. C. DeStaebler, Jr., *A Review of Transverse Shielding Requirements for the Stanford Two-Mile Accelerator,* W. W. Hansen Laboratories of Physics, M-262 (1961).

[5]U. Camerini, N. O. Lock, and D. H. Perkins, Chap 1 in *Progress in Cosmic Ray Physics,* vol 1, North Holland Publishing Co., Amsterdam, 1952.

[6]K. G. Dedrick, *Deuteron Model Calculations of Photonucleon Yields,* W. W. Hansen Laboratories of Physics, M-227 (1960).

[7]K. G. Dedrick, *Calculation of Pion Photoproduction from Electron Accelerators According to the Statistical Model,* W. W. Hansen Laboratories of Physics, M-228 (1960).

[8]K. G. Dedrick, *More Calculations of Photopion Yields,* W. W. Hansen Laboratories of Physics, M-229 (1960).

[9]H. DeStaebler, W. W. Hansen Laboratories of Physics, Stanford, Calif., private communication.

90° (with respect to the incident electron direction), whereas Dedrick found no pions at angles greater than 40°.

The equations have been solved numerically by using an IBM-7090 code that was written for this purpose.[10] Because of the approximations involved the equations are valid only at reasonably high energies and the particle fluxes are calculated only above 30 Mev. The results are converted to dose (in rads) by a method similar to that introduced by Gibson.[11] Since only the flux above 30 Mev is calculated, the dose can be calculated only from these high-energy particles. However, since the low-energy neutron dose is important, an estimate is included of the dose obtained by normalizing the measured cosmic-ray neutron spectrum[12] to our computed neutron flux.

---

[10]The coding and numerical computations were carried out by R. G. Mashburn, D. S. Marion, J. R. Parsley, and C. S. Hodge of the Central Data Processing Facility of the Oak Ridge Gaseous Diffusion Plant.

[11]W. A. Gibson, *Energy Removal from Primary Proton and Neutron Beams by Tissue,* ORNL-3260 (1962).

[12]W. N. Hess *et al., Phys. Rev.* **116**, 2 (1959).

7.15. NUCLEON-MESON CASCADE CALCULATIONS: SHIELDING AGAINST AN 800-Mev PROTON BEAM

R. G. Alsmiller, Jr., and J. E. Murphy[1]

Nucleon-meson cascade calculations have been carried out for an 800-Mev proton beam incident on a shield. The equations and method of calculation are the same as those described previously (see Sec. 7.14 and ref 2). The physical data used to represent the shielding material are also the same as those described previously, except that the density of the shielding material was changed to 2.3 g/cm^2.[2,3] This density is a rough average of the density of shielding materials usually used – earth, heavy concrete, etc. Of course, the other physical properties of the medium are only a rough approximation to the properties of any particular medium.

The various particle fluxes are converted to dose by the same method used before.[2] In particular, an estimate of the dose from low-energy neutrons (<109 Mev) obtained from the measured cosmic-ray neutron spectrum is included, but no estimate of the dose from low-energy charged particles is included. The total dose as a function of depth in the shield is shown in Table 7.15.1. This dose exhibits an early exponential decay with depth over the depths shown in the table.

---

[1]Central Data Processing Facility of the Oak Ridge Gaseous Diffusion Plant.

[2]R. G. Alsmiller, Jr., F. S. Alsmiller, and J. E. Murphy, *Nucleon-Meson Cascade Calculations: Transverse Shielding for a 45-Gev Electron Accelerator, Part I,* ORNL-3289 (1962).

[3]*Ibid., Part II,* ORNL-3365 (to be published).

Table 7.15.1. Total Dose Versus Depth in Shield

Depth in Shield (ft)	Dose [(rad/hr)/(proton/cm^2-sec)]
13.3	6.32×10^{-7}
16.0	1.53×10^{-7}
18.7	3.65×10^{-8}
21.4	8.61×10^{-9}
24.1	2.01×10^{-9}
26.8	4.53×10^{-10}

7.16. NUCLEON-MESON CASCADE CALCULATIONS: THE STAR DENSITY PRODUCED BY A 24-Gev PROTON BEAM IN HEAVY CONCRETE

R. G. Alsmiller, Jr., and J. E. Murphy[1]

Nucleon-meson cascade calculations have been carried out for a 24-Gev proton beam incident on heavy concrete. The equations and method of calculation are the same as described previously (see Sec. 7.14 and Ref. 2). The physical data used are also the same as described previously, except that the density and interaction mean free path of the shielding material were changed to correspond to heavy concrete (density = 3.6 g/cm^3, mean free path = 38 cm).[2-4] These data were to some extent derived from measurements on cosmic rays in emulsions; the remainder was chosen so as to be appropriate for aluminum. Thus, while some of the properties of heavy concrete are being used, many of the properties of the shielding medium are only very approximately those of heavy concrete.

In passing through matter, the cascade particles – protons, neutrons, and pions – produce nuclear stars, and it is convenient to characterize the cascade by the density of nuclear stars produced. By defining a nuclear star to be any nuclear reaction produced by a cascade particle of energy greater than Γ, the star density from the cascade has been calculated. Since the value of Γ is somewhat arbitrary, star densities were obtained for various values of Γ.

[1]Central Data Processing Facility of the Oak Ridge Gaseous Diffusion Plant.

[2]R. G. Alsmiller, Jr., F. S. Alsmiller, and J. E. Murphy, *Nucleon-Meson Cascade Calculations: Transverse Shielding for a 45-Gev Electron Accelerator, Part I*, ORNL-3289 (1962).

[3]*Ibid., Part II*, ORNL-3365 (to be published).

[4]A. Citron, L. Hoffman, and C. Passow, *Nucl. Instr. Methods* **14**, 97 (1961).

The star-density results are compared with the experimental measurements made at CERN.[4] However, since the CERN measurements include only those stars formed "on the axis," while the results of a one-dimensional cascade calculation imply an integration over the plane transverse to the beam axis, the calculated and experimental values are not comparable. The calculated star-density attenuation length is larger than the measured value (as it should be, since the calculated results include stars that are not included in the measured results), but no firm conclusions can be drawn.

7.17. PRELIMINARY RESULTS FROM EMULSIONS EMBEDDED IN A CONCRETE SHIELD EXPOSED TO A NARROW 9-Gev/*c* INCIDENT PROTON BEAM

R. L. Childers[1]

The nuclear cascade, or shower, plays an important part in the attenuation of radiation in a thick material, such as the shielding wall of a large accelerator. The primary particle, by its interaction with a nucleus of the material, gives rise to a number of secondary particles, which in turn give rise to tertiary particles, and so on. If the primary energy is sufficiently high, the initial attenuation of the shower is less than its buildup, and the number of interactions per unit volume, usually called the "star density," will be increased along the beam direction. However, after some distance, because of the decrease in the average energy of the shower particles, the star density begins to fall off. This decrease in average energy comes about both because of an increased number of daughter particles to share the total energy and because of a decrease in the total energy by ionizing collisions of the shower particles. Many of the daughter particles then do not have sufficient energy to eject energetic secondaries in nonelastic nuclear events. At sufficiently great distances, the star density is fairly well approximated by an exponential drop-off as a function of depth. The parameters associated with such showers are of interest from both the purely scientific and the economic points of view. Since a large fraction of the total cost of a high-energy accelerator goes into the cost of shielding walls, it is important that the shielding, while providing adequate protection, be no thicker than necessary.

A series of investigations of showers in various materials is being done with the CERN proton synchrotron. Many laboratories, including DESY (Hamburg), Hanover, Stanford, Harwell, and Oak Ridge, have exhibited an interest in these experiments, and several are making measurements on sets of nuclear emulsions exposed under identical conditions. This is a report of the initial scanning at Oak Ridge of one of two sets of nuclear emulsions used to determine some of the parameters of the nuclear cascade in barytes concrete.

---

[1]Consultant, Physics Department, University of Tennessee.

The other set is being scanned at Harwell.[2] For this experiment the incident particles were 9-Gev/c protons (where c is the velocity of light). Previous exposures[3] have also been made in concrete and earth at 24 Gev/c and in concrete at 20 Gev/c. Future exposures are planned in steel at 20 and 9 Gev/c and in graphite, aluminum, and lead at 20 Gev/c.

Exposure

Figure 7.17.1 shows a schematic sketch of the experimental setup. The incident beam was the C4 scattered proton beam of the CERN PS machine. The concrete has a density of 3.65 g/cm^3. Ten 6 × 2 cm Ilford G5 emulsions, which are capable of recording the tracks of highly relativistic particles, were placed at the points indicated by A_0 through J_0. Plate A_0 was on the front face of the concrete shield, and plate

[2]We would like to thank Dr. R. H. Thomas of the Rutherford High Energy Laboratory at Harwell for providing us with the exposed and developed set of plates used in this scanning program. He has also provided us with the details of the exposure and with the preliminary results obtained for the duplicate set of plates at Harwell.

[3]A. Citron, L. Hoffman, and C. Passow, *Nucl. Instr. Methods* **14**, 97 (1961).

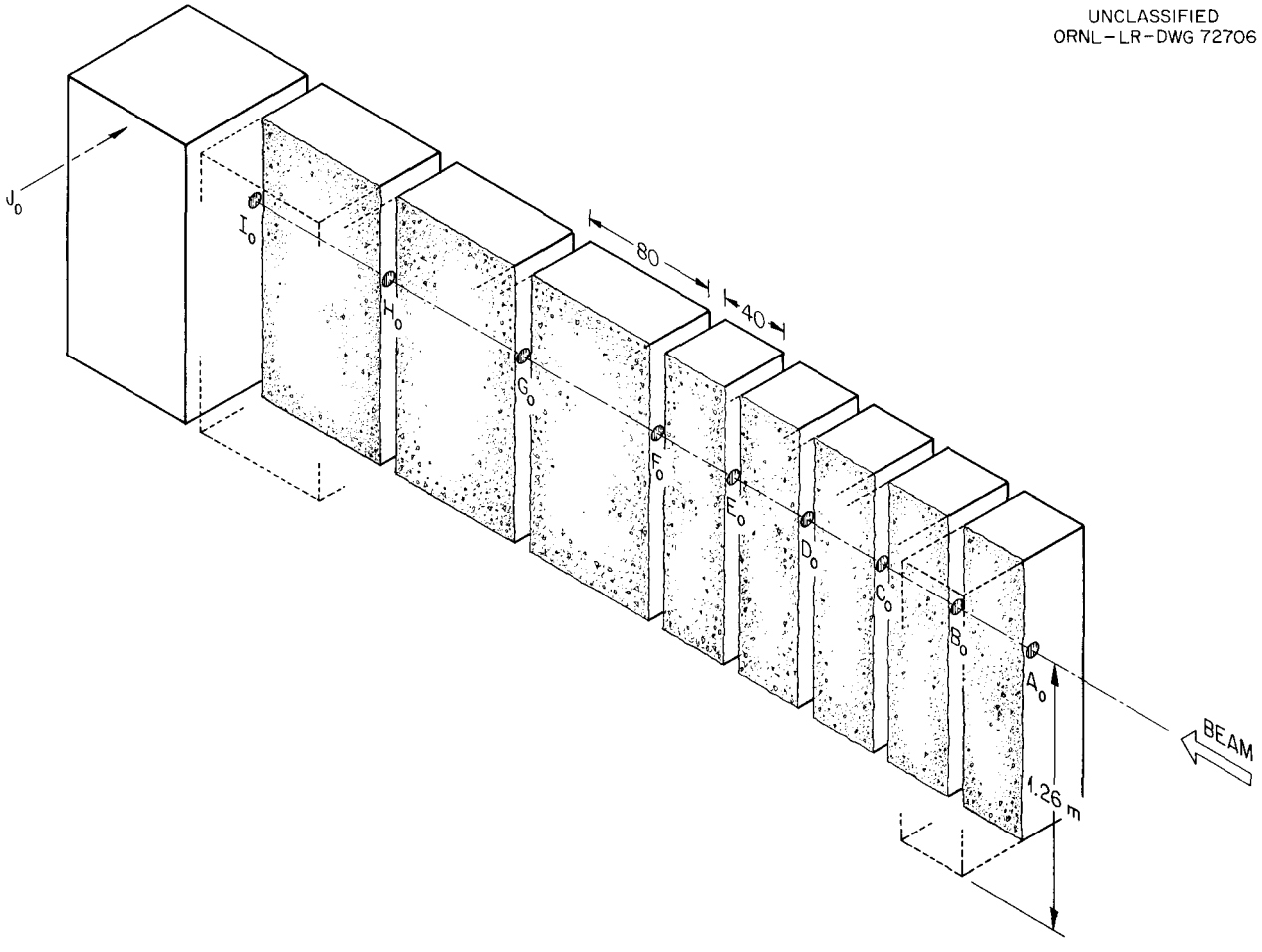

Fig. 7.17.1. Arrangement of Barytes Concrete Blocks and Emulsions.

J_0 was on the near face. Plates A_0 and J_0 were separated by 520 cm of concrete. Since the star density falls off quite sharply after the maximum is reached, all the emulsions were not exposed for the same length of time. However, the exposures were monitored by a 1×1 cm scintillation counter on the beam line in front of the concrete. Thus the observed star densities could be adjusted to correspond to equal exposure times. The experimental parameters for the Oak Ridge set of plates (placed along the center line of the beam) are given in Table 7.17.1. Other plates were also exposed slightly off the beam line in order to investigate the lateral spread in the shower, but none of these plates are included in the Oak Ridge set.

Table 7.17.1. Experimental Parameters of the Emulsion Exposure

Plate	Depth in Concrete (cm)	Original Thickness (μ)	Exposure at Front Face (particles/cm^2)
A_0	0	200	6.78×10^5
B_0	40	200	6.78×10^5
C_0	80	200	3.66×10^6
D_0	120	200	7.62×10^6
E_0	160	600	1.21×10^7
F_0	200	600	1.21×10^7
G_0	280	600	1.21×10^7
H_0	360	600	1.21×10^7
I_0	440	600	1.21×10^7
J_0	520	600	1.21×10^7

Scanning and Classification

The emulsions were scanned on a Bausch and Lomb Dyna Zoom microscope with 10X oculars and a 21X dry objective. By turning a knob the effective power of the objective could be smoothly varied from its normal value to twice that value. The emulsion could then be scanned for stars under low power, and the stars examined under a higher power. In most plates 200 events were found and classified, and the volume occupied by the stars was recorded. For those plates which did not have a total of 200 stars in them (plates H_0, I_0, and J_0), the stars in only about 80% of each plate were counted. A thin strip around the edge was never used, since the development usually introduced severe distortion in this region.

The scanning field in the microscope was restricted to 0.5×0.5 mm. This was done by employing a glass eyepiece disk that was ruled with a square of proper dimensions. Since the depth of field of the microscope is quite small in comparison with the thickness of the emulsion, each field of view was scanned twice in depth, sweeping out an effective volume of 0.5×0.5 mm $\times$ the original thickness of the emulsion.

Since the emulsion shrinks by a factor of about 2 during processing, it is necessary to use the original thickness rather than the postdevelopment thickness in calculating star densities. The process was continued in a regular manner across the plate until the required number of stars was found. Numbered coordinate grids were pasted to the underside of the glass plates, which made it easy to ensure that no volume was unknowingly scanned twice.

The track density was determined for each plate by counting the number of light tracks that crossed the unit area normal to the beam direction. Only those tracks that were within $\pm 10^\circ$ of the beam direction were accepted. Experience showed that almost all the light tracks were within $\pm 5^\circ$ of the beam direction. Two hundred or more tracks were counted in each plate whenever possible. If there were less than 200 tracks in the plate, then as many as crossed the leading edge were counted. As before, the original thickness of the plates was used.

Classification of Stars

It is of interest to know not only the total star density but also the densities of various kinds of stars; for example, whether the incident particle was charged or neutral. Since an estimate of the incident energy can be made by considering the outgoing tracks, a rough classification of outgoing tracks was made.

As the shower proceeds deeper into the stack, there is some ambiguity as to whether a star is caused by a neutral particle or a charged particle. This ambiguity arises because the secondary particles do not necessarily travel parallel to the beam direction; consequently, an incident particle at an angle to the beam can be mistaken for a fast secondary particle ejected in the backward hemisphere. For this reason angular limits were set for classification of tracks as incident or secondary. The projection of the polar angle of the particle with the beam direction on the plane of the emulsion was designated as the angle θ, and if a light track was within $\pm\theta$ of the beam direction, the star was considered to be caused by a charged particle. If not, it was classified as a neutral-induced star. Reasonable but arbitrary values of $\theta = 5^\circ$ for plates A_0 through D_0 and $\theta = 10^\circ$ for E_0 through J_0 were used. The angles were determined by lines ruled on the same eyepiece disk that delineated the scanning field. The fact that the emulsion is a thin slab makes the use of the projected angle rather than the polar angle a satisfactory approximation for setting an upper limit to the acceptable deviation from the center line.

Since the grain density of the track of a particular particle is determined by its energy, the charged incident tracks were classified as light tracks and dark or gray tracks. Dark or gray tracks correspond to kinetic energies below a value slightly less than the particle's rest mass (for singly charged particles). Light tracks correspond to higher kinetic energies.

The stars were classified according to their secondary products by whether there was or was not a light track emergent. This again is a rough indication of energy. Since this experiment was preliminary in nature, no attempt was made to classify the stars according to the number of light, gray, or black secondary tracks. The scanning speed was considerably greater than if such a detailed (and perhaps unnecessary) approach had been made.

Experimental Results

As was pointed out, the results obtained hold only for star densities and track densities as measured along the center line of the shower. Although the stars were separated into six classes, it is not particularly informative to consider each of the classes separately, especially in view of the relatively small size of some of the samples.

Figure 7.17.2 shows the total star density as function of depth. The data have been normalized to unity at the front face of the concrete. This corresponds to an actual star density of 11×10^{-3} star cm^{-3}/proton cm^{-2} as measured by the scintillation counter and is a factor of about $\frac{1}{2}$ below the absolute star density measured at Harwell (19×10^{-3} star cm^{-3}/particle cm^{-2}). In view of the good agreement between the normalized data from both the Oak Ridge and Harwell sets of plates, the difference is not believed to be physically significant. If, for the Harwell plates, the postdevelopment thickness rather than the original thickness was used, then the difference would be explained.

The error bars in Fig. 7.17.2 represent the statistical errors only. Since plate J_0 was on the outside of the concrete and had an extremely low star density (the total number, including background, was nine stars), a correction was made for background in that plate. No star which had all its charged particles entirely to

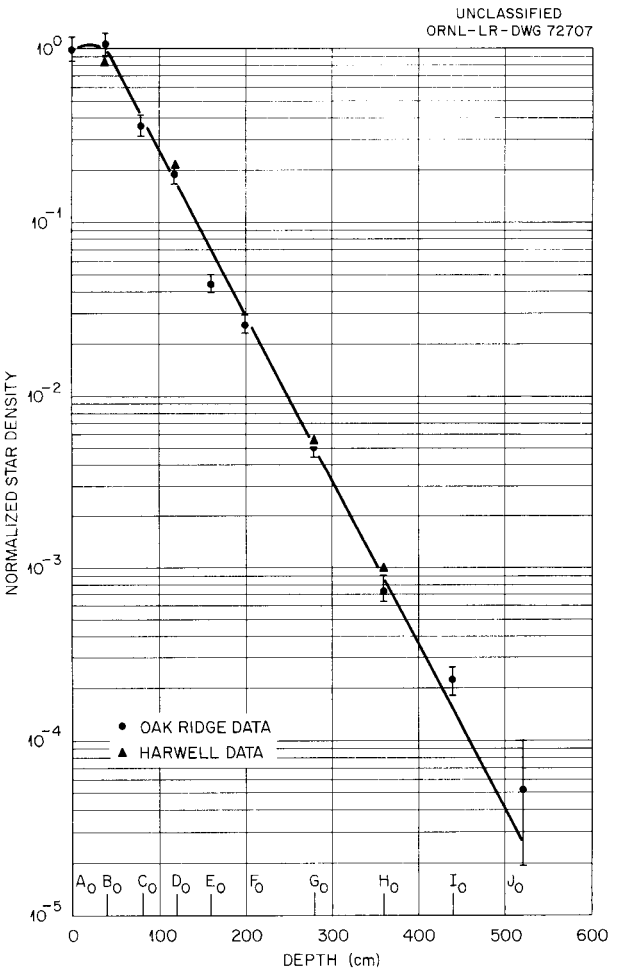

Fig. 7.17.2. Normalized Star Density as a Function of Depth in Concrete.

one side of the beam direction was kept in the sample of shower events, since it is unlikely that the momentum is divided among the charged and neutral secondaries in such a way that all the charged particles lie on one side of the beam direction.

There is a slight initial rise in the total star density, followed by an exponential drop off. It decreases to its original value in a distance of about 50 cm (180 g/cm^2). The exponential decrease shows an attenuation length of 45 ± 5 cm (164 ± 18 g/cm^2). For purposes of comparison, the results of scanning done on the Harwell plates are also shown in Fig. 7.17.2. The difference for the plates at 40 cm may be due to statistical fluctuations. The attenuation length for this 9-Gev/c exposure is approximately the same as the value of 140 g/cm^2 obtained in barytes concrete with 20-Gev/c protons. A value of 145 g/cm^2 was obtained at Harwell in the same material for 24-Gev/c protons.

Figure 7.17.3 shows the ratio of the number of stars induced by neutral particles to the total number of stars for various depths into the concrete. The value of 0.11 at the front of the stack indicates that the beam was not a pure proton beam but contained some neutral particles, probably neutrons. If it is assumed that the interaction cross section for high-energy protons and neutrons is the same and that background radiation is of little importance, it can be said that the incident beam consists of 11% neutral particles.

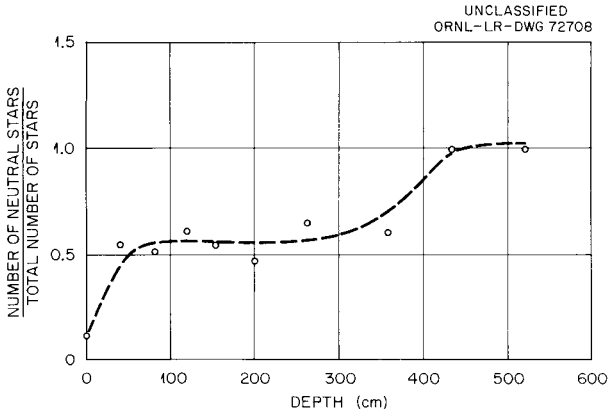

Fig. 7.17.3. Fraction of Neutral Stars at Various Depths in Concrete.

An equilibrium value of approximately ½ is reached for the neutral-induced/total ratio at a depth of about ½ m. This value is maintained for some 3 m before the ratio rises to unity. The rise to unity can be explained by taking into account that charged particles lose energy by ionization loss while neutral particles do not. It should be noted that, even though the fraction of neutral stars is higher in the exponential decay region than at the beginning of the cascade, the actual number of neutral-induced stars per unit volume is a decreasing function of depth in the concrete.

Figure 7.17.4 gives the track densities as a function of depth. The densities are normalized to correspond to one track in A_0 per particle counted by the scintillation counter. The actual observed density is 0.615 track/count, which is in good agreement with the value of 0.645 track/count determined for the duplicate set of plates at Harwell. The Harwell data are plotted for comparison. We do not observe an initial rise in the track density, such as was observed by the Harwell group. As in the case of the star densities,

the most probable explanation is just that of statistical fluctuation. The attenuation length is approximately 45 ± 5 cm (164 ± 18 g/cm^2). This is in reasonable agreement with a value of 140 g/cm^2 obtained at Harwell. The displacement of one curve from the other has not been explained at this point. It is especially curious in view of both laboratories having measured the attenuation length and the absolute track density in A_0 to be essentially the same. A careful check and remeasurement of the track densities in plates H_0, I_0, and J_0 are in progress.

The high values (compared with an exponential decrease) for the last few plates indicate the presence of charged μ-mesons. Since their interaction length is quite large, they would be expected to be present after most of the other particles were no longer in evidence.

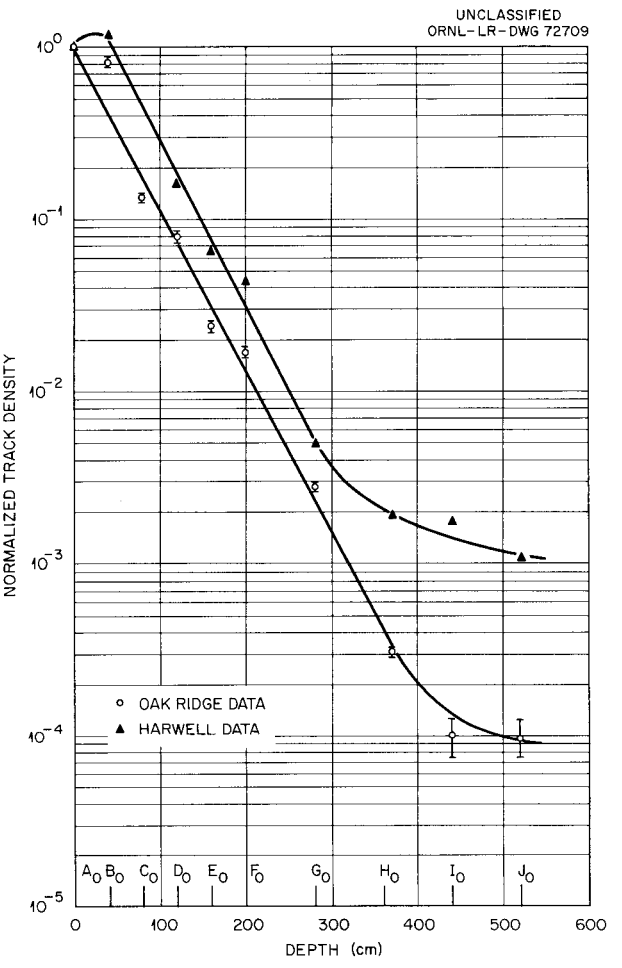

Fig. 7.17.4. Normalized Track Density as a Function of Depth in Concrete.

Discussion

It is worthwhile to mention again that the results of this experiment apply only to that part of the shower which is along the original direction of the incident beam. It is not necessarily valid to assume that the buildup region and attenuation length for the shower as a whole are the same as for the central part.

Even though this is a preliminary survey it is possible to note the interesting fact that the attenuation length in concrete does not vary much in the momentum range 9 to 24 Gev/c. However, at the higher momenta the initial rise is more pronounced and extends over greater distances than the corresponding rise at lower momenta. Therefore, even though the attenuation length is approximately constant, a greater thickness of material is needed to bring the star density down by a given factor for the higher energy incident particles.

In this particular exposure the various classes of stars have not separately yielded a great deal of information up to the present. Two things can be done to better this situation. More data can be taken to increase the confidence that small effects are real effects, and, somewhat more usefully, other methods of classification can be picked for subsequent experiments which will investigate particular points. For instance, some classification of stars according to the angles of the secondaries should prove of value.

As mentioned before, further exposures are planned. In these exposures the complete lateral spread of the showers will be investigated.

7.18. A MONTE CARLO CALCULATION OF THE THREE-DIMENSIONAL DEVELOPMENT OF HIGH-ENERGY ELECTRON-PHOTON CASCADE SHOWERS

C. D. Zerby

In the past few decades considerable interest has been generated in the theory of high-energy electron-photon cascade showers because of its use in analyzing cosmic-ray showers in air and emulsions. The advent of the high-energy electron accelerator has placed additional emphasis on the theory since it has applications in the design of accelerator equipment and experimental apparatus.

Many applications of the theory require extensive information about the three-dimensional development of the shower. Until recently, however, the analytic work on the theory dealt only with the longitudinal development of the shower. This work has been summarized by Rossi.[1] Previous Monte Carlo studies have also been limited to the one-dimensional development for simplicity. References to these calculations are given in a report by Zerby and Moran.[2]

Kamata and Nishimura[3] reported equations that could be solved numerically to obtain the lateral and angular distribution of a shower as a function of depth in an infinite medium. These equations resulted from extensive analytic work in which several approximations were made. Most of them introduce inaccuracies in the low-energy components of the shower.

---

[1] B. Rossi, *High-Energy Particles*, Prentice-Hall, Englewood Cliffs, N. J., 1952.

[2] C. D. Zerby and H. S. Moran, *Studies of the Longitudinal Development of High-Energy Electron-Photon Cascade Showers in Copper*, ORNL-3329 (1962).

[3] K. Kamata and J. Nishimura, *Progr. Theoret. Phys. (Kyoto)* **6**, 93 (1958).

The present calculation solves the three-dimensional shower problem by using the Monte Carlo method of computation. It was designed to have as few approximations as possible so that it would be applicable to relatively low energies (a few Mev). In addition, it was designed to consider any transporting medium with any elemental mixture in various geometrical configurations such as slabs, cylinders, and cylindrical shells. To increase its versatility, positrons and electrons are treated separately in the calculation.

Approximating the Physical Processes

The most significant of the basic approximations[1-4] introduced in high-energy shower theory is that only a few of the physical processes possible need be included in the calculation to obtain accurate information about the shower. The energy degradation and transport of the photons are accurately treated if only pair production and Compton events are allowed. For the electrons and positrons, only radiative collisions and Coulomb collisions with the bound atomic electrons and the nucleus are required for accuracy. The remaining interactions can be neglected because the cross sections for their occurrence are small compared with those for the processes retained in the calculation.

Compton scattering is the only mechanism retained in the calculation by which the photon changes direction and contributes to the lateral and angular spread of the shower. The charged particles change directions by Coulomb scattering from the nucleus and the bound atomic electron and by radiative collisions. As pointed out by Rossi and Greisen,[4] however, the ratio of the root-mean-square angle of deflection of charged particles by nuclear Coulomb scattering in one radiation length to the average angle of emission in radiative collisions is approximately 40 to 1. Hence, no significant error is introduced if the angular deflections in radiative collisions are neglected. A parallel argument applies for neglecting the angular spread of the pairs produced in a pair production by photons.

Cross Sections. – The differential and total cross sections for pair production, Compton scattering, and bremsstrahlung were treated in this calculation as described by Zerby and Moran.[2] In all cases the correct energy dependence of the cross sections was used, in contrast to the asymptotic forms used in the analytic studies. In addition, screening effects were included in the expressions for pair production and bremsstrahlung. The Bethe-Heitler cross section for pair production, using the Born approximation, was modified further to correct for distortion of the electron wave functions in the electrostatic field of the nucleus. This correction is most important for the heavy elements at high energies, where the Bethe-Heitler expression underestimates the true cross section by as much as 10%.

The cross sections for each interaction were introduced into the calculation as equations or tables in such a way that the cross section for any elemental composition of the transporting medium could be obtained with a minimum of computation.

Small-Angle Scattering of the Charged Particles. – It is not practical to treat the Coulomb scattering from the nucleus and the bound atomic electrons by the charged particles in the shower entirely as individual events in the Monte Carlo calculation. The charged particles experience far too many of these interactions as they travel from one point to another. The method adopted for handling this problem was to

---

[4] B. Rossi and K. Greisen, *Rev. Mod. Phys.* **13**, 240 (1941).

separate the large-angle Coulomb scattering from the small-angle Coulomb scattering and to treat them independently. Analytic results for the lateral and angular deflection of a charged particle caused by multiple small-angle deflections were used to account for the small-angle Coulomb scattering, while large-angle scattering was treated as individual events. One advantage of this approach is that proper account can be taken of those bound atomic electrons given enough energy in a collision to become part of the shower.

The angle that separates the small-angle Coulomb scattering from the large-angle Coulomb scattering was dictated to a certain extent by the analytic solution used for small-angle multiple scattering. The demonstration of this dependence first requires a consideration of the equation used to represent the Coulomb scattering at small angles.

The cross section for positron or electron scattering from the nucleus in the limit $E >> mc^2$ and for small angles without screening is given by

$$d\sigma = 8\pi NZ^2 r_e^2 \left(\frac{mc^2}{E}\right)^2 \frac{d\theta}{\theta^3}, \tag{1}$$

where N is the nuclear density, r_e is the classical electron radius, and θ is the polar angle of scattering. This equation must be modified to include small-angle scattering from the atomic electrons and screening effects. The scattering from the atomic electrons can be accounted for approximately by replacing the factor Z^2 by $Z(Z + 1)$ in Eq. 1, and the screening effects can be accounted for approximately by using $V = Ze^2r^{-1} \exp(-r/a)$, where $a = \hbar r^2 Z^{-1/3}/mc^2$, for the electrostatic field of the atom in the modification of the derivation of Eq. 1 as described by Goudsmit and Saunderson.[5] The result of both these modifications is the expression

$$d\sigma = 8\pi NZ(Z + 1)r_e^2 \left(\frac{mc^2}{E}\right)^2 \frac{\theta d\theta}{(\theta^2 + \theta_1^2)^2}, \tag{2}$$

where $\theta_1 = Z^{1/3}\alpha(mc^2/E)$ and $\alpha = 1/137$. Equation 2 applies only for small angles of scattering, say, $0 \leqq \theta \leqq \theta_m$.

The root-mean-square angle of scattering from Eq. 2 in the range $0 \leqq \theta \leqq \theta_m$, which will be useful later, is given by

$$\langle\theta^2\rangle = 4\pi NZ(Z + 1)r_e^2 \left(\frac{mc^2}{E}\right)^2 \left\{ \ln\left[\left(\frac{\theta_m}{\theta_1}\right)^2 + 1\right] - 1 + \frac{\theta_1^2}{(\theta_1^2 + \theta_m)^2} \right\}. \tag{3}$$

The analytic solution to the multiple small-angle scattering problem used in the calculation was the one obtained by Eyges[6] as a modification of the derivation by Fermi.[1,4] Fermi first obtained a solution to

[5] S. A. Goudsmit and J. L. Saunderson, *Phys. Rev.* **57**, 24 (1940) and *Phys. Rev.* **58**, 36 (1940).

[6] L. Eyges, *Phys. Rev.* **74**, 1534 (1948).

an approximate charged-particle transport equation that is applicable for small-angle multiple scattering and gives the joint distribution function for the lateral and angular spread of a charged particle beam as a function of depth. The basic approximations in the formulation of the transport equation were that only small angular deviations from the initial direction of the beam occurred, no energy loss need be considered, and only scattering interactions took place. In addition, however, the Landau approximation[3] was made in the scattering term of the transport equation. The modification made by Eyges was to obtain the first-order solution to the same equation with a constant energy loss by ionization collisions included. The joint-distribution function derived by Eyges is

$$f(z, x, \theta)\, dx\, d\theta_x = \frac{dx\, d\theta_x}{4\pi B} \exp\left(\frac{-A_2\theta_x^2 + 2A_1 x\theta_x - A_0 x^2}{4B}\right) , \tag{4}$$

where

$$A_n(z) = \int_0^z \frac{(z - z')^n dz'}{W^2(z')} \quad \text{for } n = 0, 1, 2 , \tag{4a}$$

$$W^2(z) = 4/\left\langle \theta^2 \right\rangle , \tag{4b}$$

$$B(z) = A_0(z)A_2(z) - A_1^2(z) . \tag{4c}$$

In Eq. 4 the distance along the z axis, which coincides with the original direction of the beam, is given by z, and θ_x is the projection on the x axis of a unit vector along the direction of angular deflection under the assumption that the polar angle of deflection is small. The quantity $\left\langle \theta^2 \right\rangle$ in Eq. 4*b* is the root-mean-square polar angle of scattering. The independent distribution function $f(z, y, \theta_y)$ is obtained from Eq. 4 by replacing x with y. The lateral displacement is given by $r = (x^2 + y^2)^{1/2}$, and the polar angle by $\theta = (\theta_x^2 + \theta_y^2)^{1/2}$.

There are difficulties with Eyges' solution, however, because of the use of the Landau approximation in the transport equation. The distribution function for θ_x, which is obtained from Eq. 4 by integrating over all values of x, actually falls below the single-scattering estimate at thickness z for large values of θ_x. This is clearly impossible. Use of the Landau approximation would become more valid, however, if the scattering cross section did not have a large-angle contribution. This suggests the criteria for separating the large-angle scattering from small-angle scattering that was referred to previously.

Letting θ_m be a small angle forming a boundary between small-angle and large-angle scattering and also the maximum angle of small-angle scattering considered in Eyges' derivation, then we expect Eq. 4 to be accurate for angles in the distribution function less than θ_m. For angles greater than θ_m the distribution function is supplemented by the large-angle single-scattering events. For an average distance traveled of length z at least one large-angle single scattering is required to contribute to the distribution function to assure accuracy. Hence,

$$1 \lesssim z \int_{\theta_m}^{\infty} \frac{d\sigma}{d\theta} d\theta , \tag{5}$$

where $d\sigma/d\theta$ is the differential cross section for large-angle scattering. By using Eq. 1 for the large-angle scattering in Eq. 5,

$$\theta_m \leqq \left(\frac{zQ}{2}\right)^{1/2}, \tag{6}$$

where $Q = 8\pi NZ^2 r_e^2 (mc^2/E)^2$. The average distance traveled, z, in this process is approximately the mean free path for bremsstrahlung events, which can be determined from the asymptotic form of the bremsstrahlung cross section. When that distance is used, an acceptable value for θ_m is $2.8(mc^2/E)$; with the aid of this expression, Eq. 3 now becomes

$$\langle\theta^2\rangle = \frac{4P}{E^2}, \tag{7}$$

where the condition $\theta_1/\theta_m \ll 1$ was used to simplify the equation, and $P = 2\pi NZ(Z+1)r_e^2 (mc^2)^2 [\ln(2.8 \times 137) - \frac{1}{2} - \frac{1}{3}\ln Z]$.

The root-mean-square angle of scattering is made a function of z by introduction of the stopping power for ionization collisions, ν, which is assumed to be constant over short distances involved, so that

$$\langle\theta^2\rangle = \frac{4P}{(E-\nu z)^2}. \tag{7a}$$

Equation 7*a* was substituted into Eq. 4*a* to obtain

$$A_0(z) = \frac{Pz}{E(E-\nu z)}, \tag{8a}$$

$$A_1(z) = \frac{P}{\nu^2}\left[\ln\left(\frac{E}{E-\nu z}\right) - \frac{\nu z}{E}\right], \tag{8b}$$

$$A_2(z) = \frac{P}{\nu^2}\left[2z - \frac{\nu z^2}{E} - \frac{2(E-\nu z)}{\nu}\ln\left(\frac{E}{E-\nu z}\right)\right], \tag{8c}$$

which completely specify the functions needed in the distribution function given in Eq. 4.

The stopping power for ionization collisions required in the above derivation is not the usual one, because the large-angle scattering is treated as individual events in this calculation and therefore should not make a contribution to the continuous energy degradation characterized by the stopping power ν. This is discussed below.

Large-Angle Scattering of the Charged Particles. – It was most convenient to use Eq. 1 for large-angle Coulomb scattering from the nucleus. The minimum angle to which this equation applies is $\theta_m = 2.8(mc^2/E)$. At larger angles Eq. 1 must be modified because the structure of the nucleus affects the scattering, tending to reduce it appreciably as θ becomes larger than $\theta_2 = 280A^{-1/3}(mc^2/E)$. Along with Williams,[7] we make the approximation that the cross section is zero for $\theta > \theta_2$. If $\theta_2 > \pi$, then the cross section is set equal to zero for $\theta > \pi$.

[7] E. J. Williams, *Proc. Roy. Soc.* **A169**, 531 (1939).

For large-angle charged-particle collisions with the atomic electrons the free electron-electron cross section derived by Møller[8] and the free positron-electron cross section derived by Bhabha[9] are used. These cross sections are given by

$$\frac{d\sigma}{dx} = 2\pi N Z r_e^2 \frac{(\epsilon+1)^2}{\epsilon^2(\epsilon+2)}\left[\frac{1}{x^2} - \frac{(2\epsilon+1)}{x(1-x)(\epsilon+1)^2} + \frac{1}{(1-x)^2} + \frac{\epsilon^2}{(\epsilon+1)^2}\right], \quad x_m \leqq x \leqq \tfrac{1}{2}, \tag{9}$$

for electrons and

$$\frac{d\sigma}{dx} = 2\pi N Z r_e^2 \frac{(\epsilon+1)}{x^2\epsilon^2}\left\{\frac{1}{(\epsilon+2)(\epsilon+1)}\left[(\epsilon+1)^2 - \frac{(2\epsilon^2+8\epsilon+5)\epsilon x}{\epsilon+2} + \frac{(3\epsilon^2+12\epsilon+13)(\epsilon x)^2}{(\epsilon+2)^2} + \frac{2(\epsilon+1)(\epsilon x)^3}{(\epsilon+2)^2} + \frac{(\epsilon x)^4}{(\epsilon+2)^2}\right]\right\}, \quad x_m \leqq x \leqq 1, \tag{10}$$

for positrons. In these equations ϵ is the kinetic energy of the incident particle, in mc^2 units, and x is the fraction of the incident kinetic energy transmitted to the target particle. The cosines of the polar angles of ejection in these processes are given by

$$\mu_1 = \left[\frac{x(\epsilon+2)}{\epsilon x+2}\right]^{1/2}, \tag{11a}$$

and

$$\mu_2 = \left[\frac{(1-x)(\epsilon+2)}{\epsilon(1-x)+2}\right]^{1/2}, \tag{11b}$$

where μ_1 refers to the electron and μ_2 to the positron in positron-electron scattering. They both refer to the electrons in electron-electron scattering.

The smallest value of x_m allowed in Eqs. 9 and 10 is determined from Eq. 11*b* by using θ_m as the smallest polar angle of scattering. This results in $x_m = (2.8)^2/2\epsilon$, when $\theta_m \ll 1$ and $\epsilon \gg 2.8$ are employed to simplify the equation. This means that all atomic electrons given an energy greater than ~2 Mev in electron-electron or positron-electron collisions are added to the cascade.

Stopping Power for Ionization Collisions. – As pointed out previously, since the large-angle electron-electron scattering and positron-electron scattering are treated as individual events, the energy degradation attributed to them must be subtracted from the usual form of the stopping-power expression for ionization collisions.[10] When this is done and $x_m \ll 1$ is used, then

$$\nu \equiv -\frac{dE}{dx} = 2\pi N Z r_e^2 mc^2 \left\{\ln\left[\frac{E^2(2.8)^2}{I^2}\right] - 1\right\} \tag{13}$$

for both positrons and electrons, where E is the total energy of the particle and I is the average ionization potential.[10]

---

[8] C. Møller, *Ann. Physik* **14**, 531 (1932).

[9] H. J. Bhabha, *Proc. Roy. Soc.* **A154**, 195 (1936).

[10] E. A. Uehling, *Ann. Rev. Nucl. Sci.* **4**, 315 (1956).

The Monte Carlo Procedure

The Monte Carlo procedure for treating the photons was straightforward. For each photon that appeared in the cascade the total macroscopic cross section, Σ_γ, which was the sum of the pair production and Compton cross sections, was calculated for the medium being studied. The distance to the next collision point, x, was selected from the exponential distribution, $\Sigma_\gamma \exp(-\Sigma_\gamma x)$. At the point of interaction the choice between a pair-production event and a Compton event was made in the standard way.

If a pair-production event occurred at the point of collision, then the partition of energy between the positron and the electron was determined by a random selection technique, and both members were added to the cascade. These particles were directed along the incident direction of the photon. If a Compton event took place, the degraded energy of the photon was selected from the Klein-Nishina distribution function and the new direction of the degraded photon determined. The Compton-ejected electron was also added to the cascade, with energy and direction determined from the kinematics of the collision.

For each charged particle that appeared in the cascade the total macroscopic cross section, Σ_c, which was the sum of the cross sections for bremsstrahlung, large-angle nuclear Coulomb scattering, and large-angle Coulomb scattering from the atomic electrons, was calculated from tables or equations for the medium under study. The distance to the next collision point, z, was then selected in an appropriate manner, using that cross section. If the cross sections were constant, then the selection would be from out of an exponential distribution as in the case of photons; however, Σ_c changes with distance as the charged particle loses energy by ionization collisions, and a special technique had to be devised to treat this problem.

Having selected the distance traveled, z, the lateral and angular deviation of the charged particle by small-angle Coulomb collisions was selected from the joint distribution functions $f(z, x, \theta_x)$ and $f(z, y, \theta_y)$ described in Eq. 4, and the new particle energy was determined by using the stopping-power formula for the medium. The collision point of the particle was then shifted by the distance $r = (x^2 + y^2)^{1/2}$, and the direction of the particle was rotated through the polar angle $\theta = (\theta_x^2 + \theta_y^2)^2$.

At the point of interaction the type of interaction was selected in a standard manner. For a bremsstrahlung event the partition of the energy between the photon and the charged particle was selected with the appropriate probability and the two were added to the cascade. The angular deflection for large-angle Coulomb scattering from the nucleus was determined from a selection technique based on Eq. 1. The selection techniques for large-angle scattering from the atomic electrons were based on Eqs. 9 and 10. In these processes the incident particle was allowed to change direction and lose energy. The direction and energy of the atomic electron were also calculated from the kinematics of the collision and added to the cascade.

The Computer Program

The present version of the computer program, which was written for the IBM-7090, will develop cascades in a homogeneous material with mixtures of up to 20 elements. The composition is specified by input to the program, and the cross sections are set up automatically. The geometrical configuration of the medium can be a slab, cylinder, or cylindrical shell, as specified by input to the program. The cascades can be initiated by normally incident positrons, electrons, or photons at any incident energy up to 50 Gev.

One feature of the program is the variable nature of the energy bounds for spectral data. It is possible to arbitrarily select up to 15 such bounds other than the source energy, thus dividing the spectral data into the corresponding number of intervals. In addition, eight radial bounds can be specified which divide the scattering medium into cylindrical shells. The depth in the medium is automatically divided into half-radiation-length-thick layers out to 10 radiation lengths.

The results of the calculation include data on the track length[2] for charged particles and for photons in each energy interval, radial interval, and depth interval. Fluxes of charged particles and of photons are also given in each energy interval at each radiation length of depth out to a depth of 10 radiation lengths. The calculation also provides the energy deposited in each depth interval and radial interval and provides the energy spectra and angular distribution of the radiation penetrating the scattering medium if the medium has a finite thickness.

A Study Calculation

One calculation performed with this new program was for comparison with some previously reported analytic results. The analytic results selected were those reported by Snyder and Scott[11] and discussed by Rossi.[1] Snyder and Scott obtained a solution to the electron transport equation without using the Landau approximation; however, they did not include the generation or transport of the photons in their derivation

[11] H. S. Snyder and W. T. Scott, *Phys. Rev.* **75**, 220 (1949).

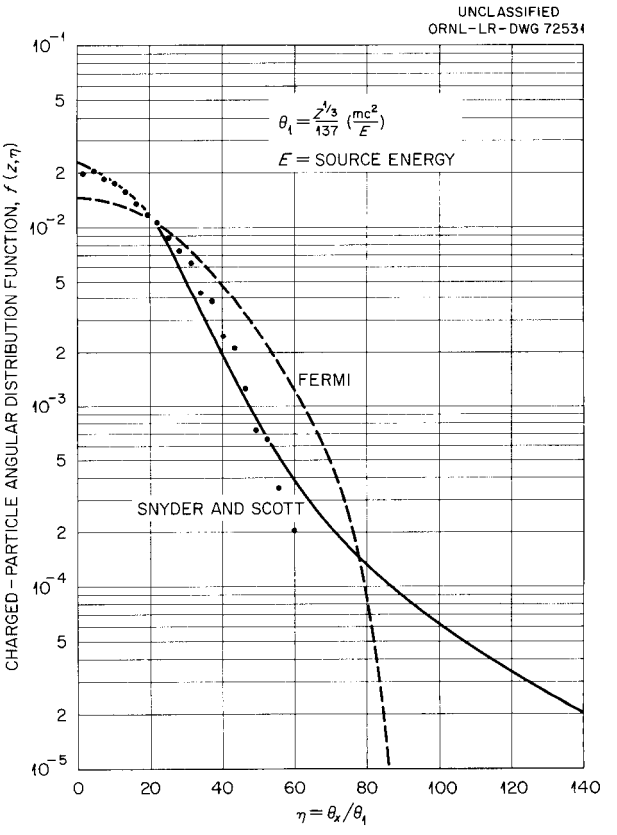

Fig. 7.18.1. The Angular Distribution of Charged Particles in a Cascade Shower Initiated by 100-Mev Electrons at a Depth of 0.00088 Radiation Length (0.00045 cm) in Lead. The solid curve is from Snyder and Scott (ref 11), and the dashed line is Fermi's result (ref 1). The data points are from the present calculation.

nor the energy degradation of the radiation. Hence their solution should be reliable only to small depths in the scattering medium.

Figure 7.18.1 presents a comparison of the results of the present calculation for a 100-Mev electron beam incident on lead with those of Snyder and Scott.[11] In this figure the distribution function is presented as a function of $\eta = \theta_x/\theta_1$, where $\theta_1 = Z^{1/3}\, mc^2/137E$ (E is the source energy). To obtain this distribution function in the present work the problem was calculated in three dimensions, and the unit vector along the direction of each charged particle at the exit surface of the slab was projected on to the x axis to obtain θ_x.

For the small depth in the scattering medium shown in Fig. 7.18.1 the comparison between the two calculations is very good. Further studies with this program are in progress.

7.19. COLLIMATOR STUDIES FOR HIGH-ENERGY ELECTRON BEAMS

C. D. Zerby and H. S. Moran

In high-energy linear electron accelerators the electrons are focused into a narrow beam as they are accelerated down the length of the accelerator tube. The confinement is not absolute, however, and some of the electrons stray out of the beam and are stopped by the tube. This presents a shielding problem over the length of the machine, because the stopped electrons initiate electron-photon cascades, which in turn produce a number of penetrating photo-ejected particles. In addition, the stopped electrons could generate enough heat to require the accelerator tube to be cooled during operation.

At Stanford it has been proposed that constrictions or collimators be placed periodically along the tube of their linear accelerator to strip off the electrons in the outer part of the beam that might otherwise be deposited in the tube. By this procedure it is hoped that the shielding and cooling problems would be restricted to the rather localized regions containing the collimators. With this design there should be some savings in construction costs.

A collimator cannot be constructed to totally absorb the primary and secondary radiations that strike it or are produced in it; hence a certain amount of the radiation is expected to enter the accelerator tube from the body of the collimator and at such an angle as to be sure of hitting the tube downstream. A study is being made at ORNL to determine how radiation behaves in a collimator such as required for the Stanford machine and, in particular, how much radiation is likely to leak back into the accelerator tube from the collimator to be deposited downstream. The three-dimensional electron-photon cascade calculation described in Sec. 7.18 was used to consider the collimator problem.

Geometry

The collimator geometry that could be considered in the calculation is shown in Fig. 7.19.1. The parameters L_i, $i = 1,2 \ldots , 20$, separate the accelerator tube into downstream length intervals for the purpose of recording where radiation strikes the tube. The collimator length is specified as T, and its

inside and outside radius as r_1 and r_3, respectively. The inside radius of the accelerator tube is specified by r_4. The radiation that strikes the collimator was assumed to be normally incident at a point a distance r from the center line. All these parameters are specified by the input to the computer program.

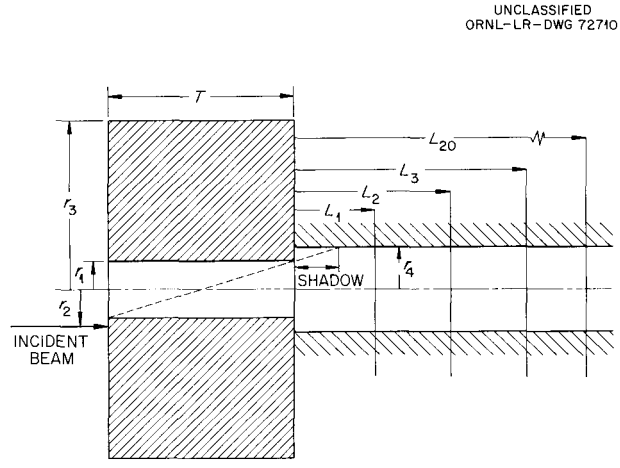

Fig. 7.19.1. Geometry of the Collimator Showing the Parameters That Describe It.

Calculation of Boundary Effects

There is no particular problem in the calculation with treating photons that cross boundaries, since they travel in a straight line and remain monoenergetic. Thus when a photon leaves the collimator and travels down the accelerator tube, there is no particular problem with determining its energy and position at the point where it hits the tube. This is not the case for the charged particles.

As pointed out in Sec. 7.18, there is actually a sequence of mathematical operations required in moving a charged particle from one point to another. First, the distance z along the initial path of the charged particle is selected, and then the lateral and angular deflections. The particle is moved to the new position determined by z and the lateral deflection, and then given the new direction determined by the angular deflection. This new position locates the next interaction, and the new direction determines the direction of incidence of the charged particle on the target.

With the geometry shown in Fig. 7.19.1 it is obvious that cases can arise where the initial position of the particle is inside the body of the collimator but the final position is, for example, in the vacuum of the hole. This means that the point where the particle enters the hole and the direction it has at that point must be determined in order to determine where it will travel. (Similar problems arise in the cases of reflection, penetration, lateral escape, and of the path passing through the hole but with its initial and final positions in the body of the collimator.) The techniques used to select the angular and lateral deflections, necessary to the procedure used in the determination, are described below.

As was pointed out in Sec. 7.18, the joint distribution for the lateral and angular deflections is given by

$$f(z,x,\theta_x)dx\,d\theta_x = \frac{dx\,d\theta_x}{4\pi B}\exp\left[\frac{-A_2\theta_x^2 + 2A_1 x\theta_x - A_0 x^2}{4B}\right], \qquad (1)$$

where z is the distance along the z axis, which coincides with the original direction of the particle; θ is the projection on the x axis of a unit vector along the direction of angular deflection under the assumption that the polar angle of deflection is small; x is the lateral deflection along the x axis; and A_0, A_1, A_2, and B are functions of z only. The independent joint-distribution function $f(z,y,\theta_y)$ is obtained from Eq. 1 by replacing x and θ_x with y and θ_y, respectively.

The distribution function for x is obtained from Eq. 1 as

$$g(z,x) = \int_{-\infty}^{+\infty} f(z,x,\theta_x)d\theta_x = (4\pi A_2)^{-1/2} \exp\left(\frac{-x^2}{4A_2}\right) . \tag{2}$$

The conditional distribution function for θ_x is given by

$$h(z,\theta_x|x) = \frac{f(z,x,\theta_x)}{g(z,x)} . \tag{3}$$

The procedure for selecting a random distance X from the distribution function given in Eq. 2 was to select a random variable U_1 from the distribution $v(u) = (2\pi)^{-1/2} \exp(-u^2/2)$, for $-\infty \leq u \leq +\infty$, using standard technique and letting

$$X = [2A_2(z)]^{1/2} U_1 . \tag{4}$$

After selecting X the random variable Θ_x can be obtained from the distribution given by Eq. 3 by first selecting U_2 from $v(u)$ and letting

$$\Theta_x = [2B(z)/A_2(z)]^{1/2} U_2 + A_1(z)[2/A_2(z)]^{1/2} U_1 . \tag{5}$$

Equations similar to Eqs. 4 and 5 arise in connection with random selection of Y and Θ_y. For the present discussion, however, it is assumed that Y and Θ_y are both zero and that the problem of crossing a boundary is two-dimensional, as indicated in Fig. 7.19.2. It is also assumed that a charged particle

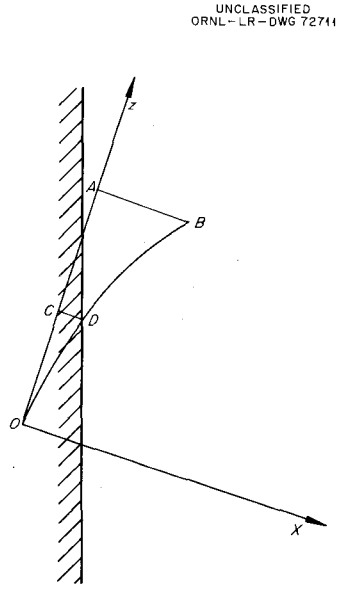

Fig. 7.19.2. Schematic Sketch of Boundary Problem.

starts from point O and is directed toward A. The distance z along this direction is represented by OA. From Eq. 4 is obtained the value of X that corresponds to the distance AB and therefore places the next collision of the particle at B. As constructed in Fig. 7.19.2, the point B is outside the body of the collimator and the point where the particle left the surface must be calculated. The procedure developed to accomplish this was to proceed along the curve OB specified by Eq. 4, using an iterative technique until the point D is reached; the new distance z corresponding to OC was then calculated and used in Eq. 5 to select the angle of deflection at the surface.

Results

Calculations have been performed for the case of 5-Gev electrons incident on two different aluminum collimators. In each case the inside radius of the accelerator tube was taken to be $r_4 = 1.1303$ cm. The radius to the outside of each of the collimators was $r_3 = 50.8$ cm, and their thickness was $T = 132.78$ cm. The difference between the collimators was the inside radius. In one case it was $r_1 = 0.3175$ cm and in the other $r_1 = 0.7239$ cm.

A series of cases were calculated for each collimator in which the radius to the point of incidence, r, was varied from r_1 to r_4. Some of the results are shown in Figs. 7.19.3–7.19.5.

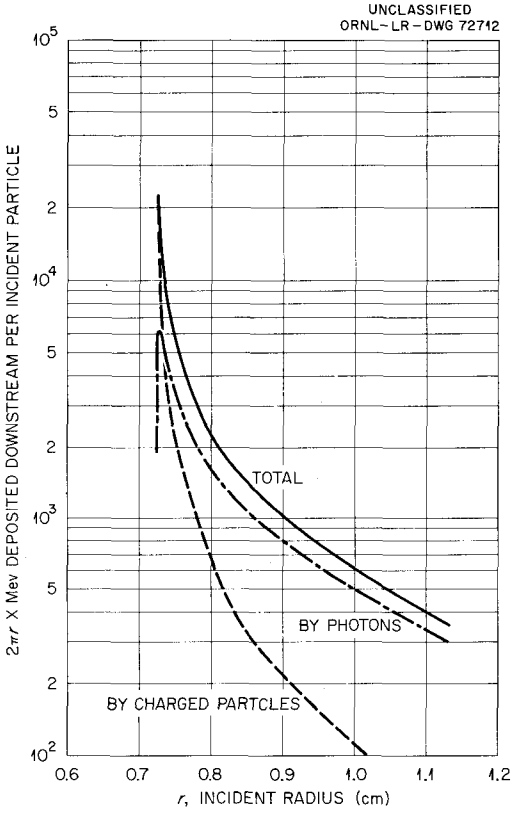

Fig. 7.19.3. Energy Deposited in Accelerator Tube by Radiation Escaping from an Aluminum Collimator with a 0.7239-cm Inside Radius. 5-Gev electrons incident on the collimator.

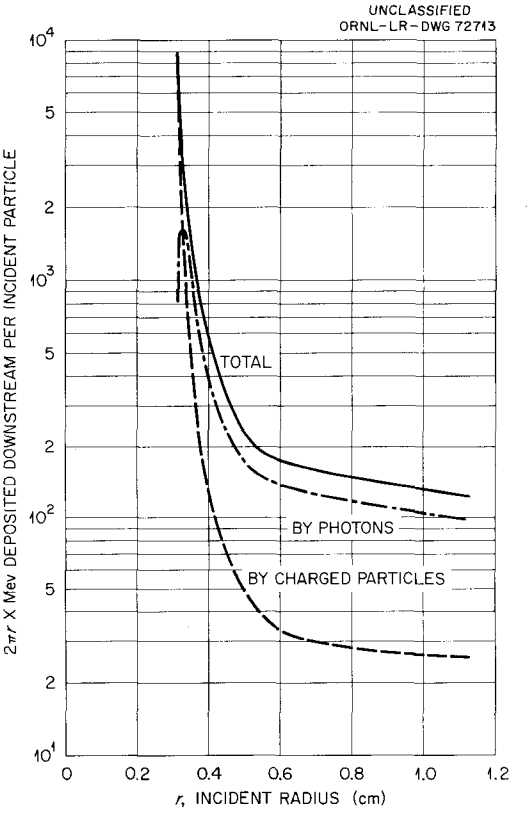

Fig. 7.19.4. Energy Deposited in Accelerator Tube by Radiation Escaping from an Aluminum Collimator with a 0.3175-cm Inside Radius. 5-Gev electrons incident on the collimator.

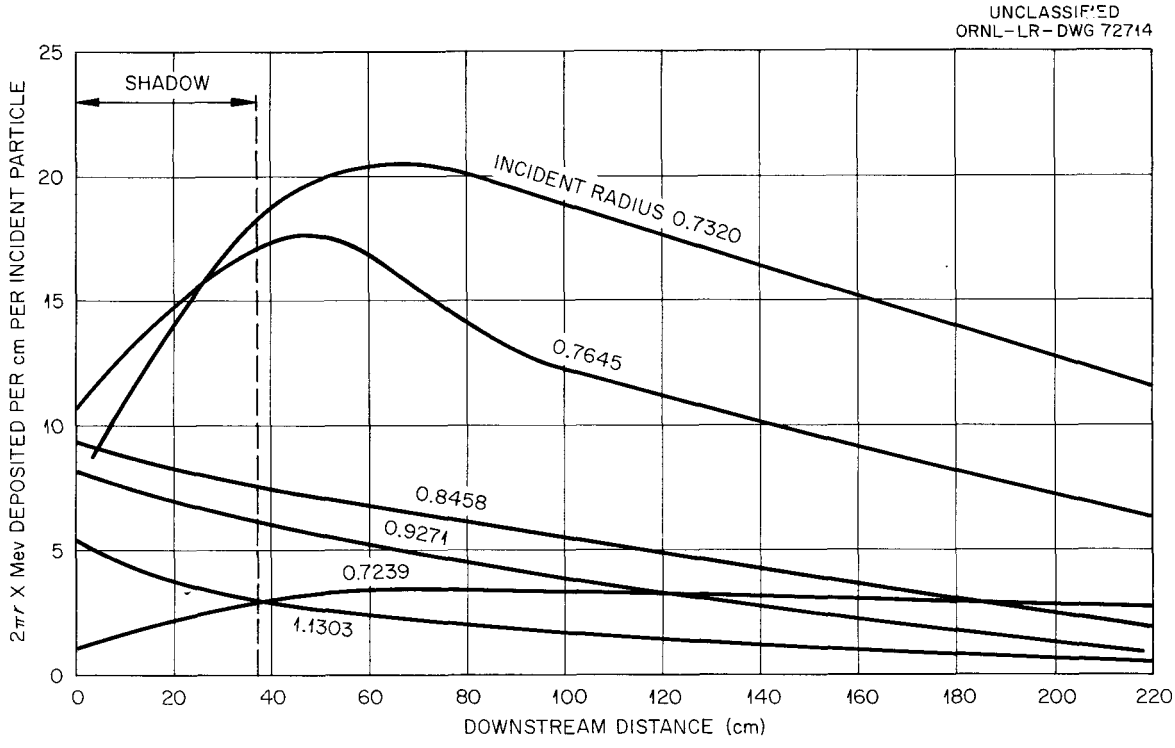

Fig. 7.19.5. Distribution of Energy Deposited in Accelerator Tube by Radiation Escaping from an Aluminum Collimator with a 0.7239-cm Inside Radius. 5-Gev electrons incident on the collimator.

In Figs. 7.19.3 and 7.19.4 the energy that escapes from the collimator and is deposited in the accelerator tube is presented for each collimator studied. It is interesting to note that for radii of incidence only slightly greater than the inside radius of the collimator the largest fraction of the energy is carried downstream by photons. For r very close to r_1, however, the electrons contribute most to the energy deposited downstream since they make relatively few Coulomb collisions before being deflected into the hole and therefore do not have a chance to produce bremsstrahlung radiation.

Assuming a uniformly distributed beam over the opening in the accelerator tube and normalizing to one 5-Gev electron in the beam, then the collimator with $r_1 = 0.3175$ cm removes 4605 Mev from the beam. Of this amount, 44.7 and 42.7 Mev are deposited downstream by photons and charged particles, respectively. For the case of the collimator with $r_1 = 0.7239$ cm, 2950-Mev energy is removed from the beam and of this amount 112.8 and 72.0 Mev are deposited downstream by photons and charged particles, respectively.

Figure 7.19.5 presents the energy deposited in the accelerator tube as a function of distance downstream for the case of the collimator with $r_1 = 0.7239$ cm. The various curves represent the results for different incident radii. Of particular interest is the shadow effect of the collimator that is indicated by the dashed line in Fig. 7.19.1. For the smaller incident radii the shadow effect on the energy deposition downstream is quite evident.

7.20. POSITRON SOURCE STUDIES FOR A HIGH-ENERGY POSITRON ACCELERATOR

C. D. Zerby and H. S. Moran

High-energy linear electron accelerators can be easily converted to produce positron beams by putting an internal target at some point in the accelerator tube and reversing the polarity of the accelerating field on the downstream side. In this case the electrons which are accelerated in the first part of the tube strike the target and produce a cascade shower of electrons, positrons, and photons. The positrons in the shower which penetrate to the downstream side are picked up by the reversed field and are accelerated down the remainder of the tube, producing a high-energy positron beam.

A few of the questions associated with conversion of an accelerator in this manner are how far downstream should the target be, what material should the target be made of, and how thick should the target be. All these questions bear on the efficiency of converting the electrons to positrons and on the energy spectrum of the positrons that are accelerated.

Studies of the target problem for the Stanford University linear accelerator have been initiated with the calculational method reported in Sec. 7.18 used for calculating the electron-photon cascade. Results from the first of these studies, in which a target of gold was used, are shown in Figs. 7.20.1 and 7.20.2. The incident energies for these cases were 300, 1000, and 5000 Mev, which correspond to the various distances downstream.

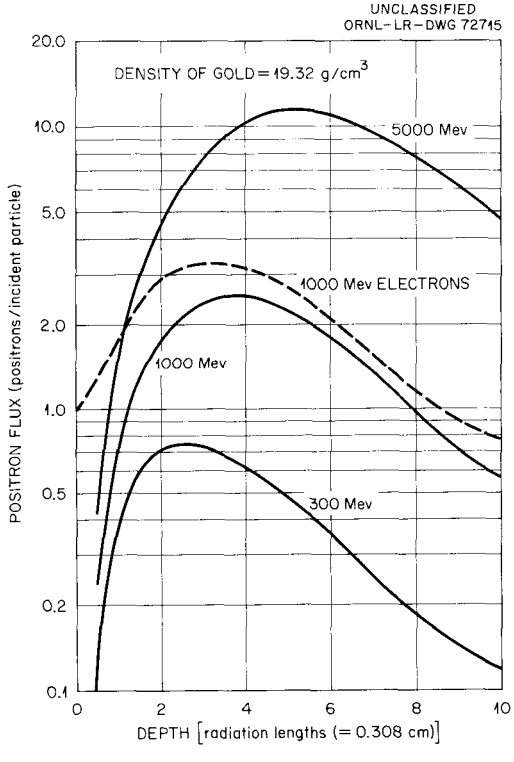

Fig. 7.20.1. Positron Flux Integrated Over the Entire Plane at Each Depth and Integrated Over the Energy Above 6 Mev. Cascades initiated by 300-, 1000-, and 5000-Mev electrons in gold; electron flux for 1000-Mev incident energy shown as dashed line for comparison.

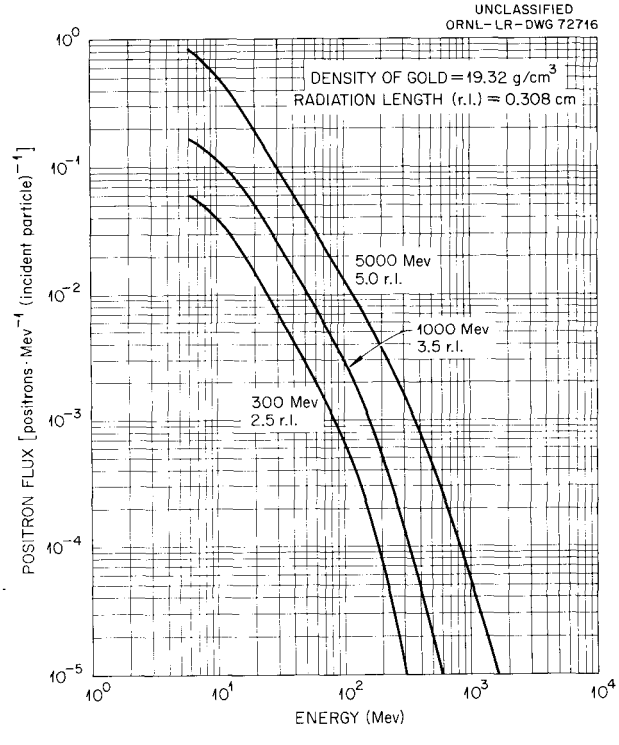

Fig. 7.20.2. Positron Flux Integrated Over the Entire Plane at the Peak of the Transition Curve for 300-, 1000-, and 5000-Mev Electron-Initiated Cascade Showers in Gold.

The calculations were carried out for a narrow beam of electrons incident on a target 10 radiation lengths thick. The positron flux integrated over the entire plane and over all energies above 6 Mev is shown in Fig. 7.20.1 as a function of depth in the target. These transition curves very closely approximate the number of positrons above 6 Mev crossing a plane at each depth because the radiation is concentrated in a forward direction. For the same reason the data presented also approximate the number of positrons penetrating a slab with a thickness corresponding to the indicated depth. For comparison purposes the electron transition curve is shown for the 1000-Mev case.

It is interesting to note that the number of positrons above 6 Mev at the peak of the transition curves varies almost linearly with the source energy, that is, 0.75, 2.55, and 11.5 positrons per incident particle at 300, 1000, and 5000 Mev, respectively.

The energy spectra of the positrons near the peak of the transition curves are shown in Fig. 7.20.2.

7.21. A COMPILATION OF DATA CONCERNING SECONDARY PARTICLES RESULTING FROM PARTICLE-PARTICLE INTERACTIONS AT HIGH ENERGIES[1]

J. A. Elder[2]

A comprehensive search of the recent literature concerning secondary particles resulting from particle-particle interactions at high (cosmic or high-energy accelerator) energies has resulted in a compendium of data representing the results of over 40 theoreticians and experimentalists. The work abstracted can be broadly divided into two categories, the first having to do with the variation in the average number of secondary particles with incident particle energy and including limited data on the production of "strange" particles, and the second concerned with the characteristics of the transverse momentum of secondary particles.

Average Number of Secondary Particles vs Incident Particle Energy

Two types of data were available for this part of the investigation. The first type gives the average number of a particular secondary particle resulting from an interaction as a function of incident particle energy. The reactions considered are p,p; p,n; p,nucleon; pion,p; and pion,nucleon. A second type of data is that in which particle tracks in nuclear emulsions are classified according to density. From the observed density, the type of particle causing the track and its energy can be generally determined. All the data are presented in graphical form in the original paper.[1]

The literature examined seems to show general agreement that the data describing the average number of secondaries produced as a function of incident particle energy can be well fitted, at least for incident protons, by an expression of the form $N = aE_0^{1/4}$, in which N is the number of secondaries, E_0 the incident proton energy in the laboratory system, and a a constant of the order of 2.7 to 2.9.

---

[1]Summarized from a paper to be published as ORNL TM-374.

[2]Summer Student Trainee, Oak Ridge Institute of Nuclear Studies. Present address: Berry College, Mt. Berry, Ga.

The compilation also includes a tabulation of calculated average values of the number of strange particles (pions, antinucleons, K and $\overline{K}$ particles, hyperons and antihyperons) produced in p,p and p,n collisions, as well as published observations concerning strange-particle production for a number of interactions at various energies.

Transverse Momentum Characteristics of Secondary Particles

The available data concerning the transverse momentum, P_T, of secondary particles appear to show agreement upon three points: first, that the average P_T is a constant; second, that the shape of the P_T distribution curve is an invariant which may be represented by the Boltzmann-like expression

$$f(P_T)\,dP_T = \frac{P_T}{P_{10}^2}\,\exp\left(-\frac{P_T}{P_{10}}\right)dP_T\,,$$

in which $P_{10} = 0.17$ Gev/c; and third, that P_T has no correlation with the angle of emission of the particle. The original paper[1] presents several tabulations of data supporting these conclusions, as well as some graphical comparisons.

8. Experimental Techniques for the Measurement of Secondary Nuclear Particles from the Interactions of High-Energy Protons

8.0. INTRODUCTION

F. C. Maienschein

As is pointed out in Sec. 7, considerable calculational effort has been spent in the Neutron Physics Division to provide data pertinent to the shielding of space vehicles. The important sources of radiation which must be considered arise from protons trapped in the Van Allen belt(s) and from solar flares. The Van Allen protons will be most troublesome for vehicles with a slow rate of vertical ascent, such as those powered with ion-propulsion engines, while the solar-flare protons will be dangerous for occupants of any extraterrestrial spacecraft. The danger of solar flares is not accurately predictable, however, since their occurrence is statistical, the average rate varying periodically with time. Further, the calculations available, which take into account the production of secondary particles by the interactions of the protons, do not give consistent results for the dose which results from a single flare.[1-3] Therefore, at present it is not possible to conclude whether the shields required for the approximately seven-day Apollo mission to the moon will be of sufficient thickness to make secondary nuclear interactions of importance. But it is clear that manned interplanetary flights will require shields of such thicknesses that the production of secondary particles must be accurately predicted, and the great cost of extra-terrestrial transport emphasizes the need for accurate and not overly conservative calculations.

The calculations necessary for spacecraft shielding are of two basic types: those of cross sections and the spectra of secondary particles for intranuclear cascades and those of the transport of secondary particles through shields. Energy losses by ionization are included in the transport calculation and are considered to be well understood, but serious uncertainties arise in other parts of the calculations which make experimental checks highly desirable. Thus preparations are under way for a series of experiments to provide such checks. The present status of the preparations is described in the following papers; however, it must be understood that these experiments are at an early stage and that modifications in the equipment and plans may be necessary.

As an aid in determining which measurements would be most pertinent for spacecraft shielding, Alsmiller and Murphy[2] have performed preliminary calculations of the dose resulting from incident monoenergetic protons of various energies. Although these calculations contain many approximations, they represent the best information presently available and several conclusions may be drawn: for example, for shields thinner than the range of the incident protons the dose from the primary protons is dominant; the dose due to secondary protons decreases rapidly with increasing shield thickness, while the dose due to secondary neutrons drops slowly and becomes dominant for thicknesses greater than the incident proton range; and the dose due to secondary mesons is only a few percent of the total dose for any shield thickness appropriate for spacecraft. The dose due to secondary gamma rays was not considered by

---

[1] R. I. Allen *et al.*, *Shielding Problems in Manned Space Vehicles*, NR-140 (September 1961).

[2] R. G. Alsmiller, Jr., and J. E. Murphy, *Space Vehicle Shielding Studies: Calculations of the Attenuation of a Model Solar Flare and Monoenergetic Proton Beams by Aluminum Slab Shields*, ORNL-3317 (in press); see also Sec. 7.9, this report.

[3] R. K. Wilson *et al.*, *A Study of Space Radiation Shielding Problems for Manned Vehicles*, FZK-144 (June 8, 1962).

Alsmiller and Murphy,[2] but Alsmiller *et al.* (see Sec. 7.10, this report) and Madey,[4] who estimated the production of inelastic scattering gamma rays, indicate that there will be a significant dose due to secondary gamma rays. In summary, then, it appears that the measurements most needed are for secondary neutrons, protons, and gamma rays. The energy spectra and angular distribution of these particles must be determined in order to provide definitive tests of the theory. (It is assumed that the spectra of the incident primary particles in space will be available from other sources.)

To determine the energies of the incident protons that are the most important, Alsmiller and Murphy[5] calculated two "importance functions." The second of these gives the total secondary dose as a function of incident proton energy and shield thickness for the flare spectrum occurring on May 10, 1959. The importance function for an aluminum shield of 0.5 collision length (~ 42 g/cm^2) appears to peak at about 300 Mev and to decrease by a factor of $\sim$10 at 1 Bev. It would be desirable to know the importance function for lower energies, but, unfortunately, the lowest energy point given is at 200 Mev. For thicker shields the importance function is roughly constant from 200 to 600 Mev, with a small decrease at still higher energies. The production of gamma rays is expected to be most important at lower energies, where the proton intensities are highest. Thus the incident-particle energy range of most interest for space shielding lies below about 600 Mev, with a lower limit of perhaps 20 to 50 Mev (lower when secondary gamma rays from nuclear excitation are considered).

Finally, consideration must be given to the choice of target thickness. For checking the intranuclear cascade calculations, experiments are needed with a few "thin" targets with widely varying Z values. For checking the transport calculations, spectra at various angles must be obtained with one or more "thick" targets. Actually, the targets will not be thick with respect to a mean free path for nuclear interactions, but their thickness will be greater than the range of the incident protons.

Previous Research

A number of spectral measurements have been made with synchrocyclotrons, the type of accelerator that covers most of the energy range of interest. Table 8.0.1 summarizes the pertinent characteristics of some of these measurements, all of which cover a limited energy range for the outgoing particles, suffer from poor energy resolution, or are otherwise seriously limited. In general, the proton spectra and the neutron spectra with the best resolution show effects of nuclear level structure. Perhaps the most surprising feature of the data is the apparent absence of an exchange peak in the neutron spectra observed at Harvard ($\leqq 100$ Mev) for elements heavier than beryllium. At other laboratories exchange peaks were observed for all Z with energies as low as 143 Mev.

The one set of spectra listed for deuterons and tritons indicates that cascade particles with $Z > 1$ are unlikely to give an effect of more than a few percent. The gamma-ray data, however, when considered together with one lower energy measurement,[6] are of quite limited value. None of the previous studies were made with a target "thick" from the transport point of view.

---

[4] R. Madey *et al.*, *Trans. Am. Nucl. Soc.* **5**(1), 213 (1962).

[5] ORNL-3317, *op. cit.*, p 20.

[6] T. Wakatsuki *et al.*, *J. Phys. Soc. Japan* **15**, 1141 (1960).

Table 8.0.1. References to Measurements of Spectra of Secondary Particles from High-Energy Proton Interactions

Observed Particle	Accelerator	Incident Proton Energy (Mev)	Spread of Incident Proton Energy (Mev)	Target Thickness	Materials	Observed Energy Range (Mev)	Observed Angles (deg)	Type of Spectrometer	Energy Resolution	Comments	References
Protons	Harvard	96		~8 Mev	C		3–90	Range telescope	~3 + (*a*)	Observed level structure in C	Strauch and Titus, *Phys. Rev.* 103, 200 (1956)
Protons	Harvard	96			17 elements from Li to Bi	30–90	40	Range telescope	3–17 Mev including target thickness	Level structure for lower Z	Strauch and Titus, *Phys. Rev.* 104, 191 (1956)
Protons	Harvard	160			Zn, Sn, Ta, Pb	5–23	60, 90, 120	Range telescope and magnetic deflection	Good	Peaks slightly below Coulomb barriers	Fox and Ramsey, *Phys. Rev.* 125, 1609 (1962)
Protons	LRL	190		Thin	C, Al, Ni, Ag, Au	~3–90	0–65, 100–180	Nuclear emulsions and magnetic deflection	Very large angular acceptance	Also measured *d* and α spectra	Bailey, UCRL-3334 (1956)
Protons	Rochester	240	±8	7 Mev	C	60–190	90	Nuclear emulsions	Poor		Temmer, *Phys. Rev.* 83, 1067L (1951)
Protons	LRL	340	11	4 Mev	H, D, C, O	100–350	30, 40	Magnetic deflection	(*a*)	Nucleon momentum distributions are deduced	Cladis, Hess, and Moyer, *Phys. Rev.* 87, 425 (1952)
Neutrons	Harvard	50	Large		Li, Be, C, Pb	35–70	0, 5, 10, 16	Telescope	(*a*)	Li and Be indicate exchange reactions; C and Pb do not	Hoffman, Harvard thesis, 1952
Neutrons	Harvard	100	Large	0.125 in.	Be, C	40–110	0	Telescope	(*a*)	Li and Be indicate exchange reactions; C and Pb do not	Bodansky and Ramsey, *Phys. Rev.* 82, 831 (1951)
Neutrons	Harvard	95	~20		D, Li, Be, C, Al, Cu, Pb	50–110	0, 5, 10, 16, 28	Telescope	8–10 Mev and (*a*)	Li and Be indicate exchange reactions; C and Pb do not	Hoffman and Strauch, *Phys. Rev.* 90, 449 (1953)
Neutrons	Harwell	143	3	2.5–7.0 Mev	D, Li, Be, C, Al, Cu, Pb, U	15–140	~0	Time-of-flight	$0.07 \leqq (\Delta E/E)_n \leqq 0.14$	Measurements all relative; high-energy peak for all Z	Bowen *et al.*, *Nuclear Phys.* 30, 475 (1962)
Neutrons	Harwell	171		1–2 g/cm^2	Be, C, Al, U	50–200	2.5	Range telescope	(*a*)	High-energy peak for all Z	Cassels *et al.*, *Phil. Mag.* 44, 425 (1953)
Neutrons	Rochester	244		~0.3–1.0 in.	Be, C, Pb	120–240	0, 15	Telescope	$0.10 \leqq (\Delta E/E)_n \leqq 0.15$	High-energy peak for all Z	Nelson *et al.*, *Phys. Rev.* 88, 1 (1952)
Neutrons	LRL	190	±15	4.7–14.6 Mev	C, Al, Ni, Ag, Au, U	0.5–12	45, 90, 135	Nuclear emulsions	(*a*)	Primarily evaporation neutrons	Gross, UCRL-3330 and UCRL-3337 (1956)
$Z \geqq 1$	ORSAY	154			Au^{197}	>30	15, 30, 60	$(dE/dx - E)$ telescope	±20%	$d/p \approx 1/10$, $t/p \approx 1/20$	Genin *et al.*, *J. Phys. Radium* 22, 615 (1961)
Gamma rays	Harvard	35	Large		LiH, Be, B, C, Mg, Al, Si, Cu, Au	~3–~20	90	NaI scintillation		Pulse-height spectra only; serious neutron-induced backgrounds	Culler, Harvard thesis, 1956
Gamma rays	Harvard	24, 56, 90	Large		C, Al	~3–~20	90	NaI scintillation		Pulse-height spectra only; serious neutron-induced backgrounds	Culler, Harvard thesis, 1956
Gamma rays	Harwell	150		20–40 Mev	Li, Be, B, C, N	<15	90	NaI scintillation		Large neutron-induced backgrounds	Clegg *et al.*, *Proc. Phys. Soc.* 78, 681 (1961)
Gamma rays	Harwell	150		20 Mev	O, F	<15	90	NaI scintillation		Large neutron-induced backgrounds	Foley *et al.*, *Nuclear Phys.* 31, 53 (1962)
Gamma rays	LRL	30–340			C	8–22	90	180° pair spectrometer		Studied C^{12} level at 15.2 Mev	Cohen *et al.*, *Phys. Rev.* 96, 714 (1954)

(*a*) Energy resolution limited by energy spread of incident beam.

Planned Experiments

As described in a previous report of this series,[7] experiments are planned with the primary goal of determining energy spectra at selected angles for secondary neutrons, protons, and gamma rays. Preliminary or feasibility studies were made at the Harvard University synchrocyclotron (156-Mev protons) in May and August 1962. The object of these studies was not to produce spectral data but to determine the necessary beam intensities, to measure backgrounds, and to check the operation of the spectrometers. Substantial modifications to the equipment were required after each test. The test results have not been analyzed in detail, and the comments presented in this series are all tentative. Further measurements are planned at Harvard for October 1962.

The arrangement of the targets and spectrometers at the Harvard accelerator is described in Sec. 8.1. Also discussed are the measurements of the proton-beam average intensity and spatial extent, as well as the necessary studies of the complex time behavior of the beam. The use of targets thicker than the range of the primary protons simplifies many experimental problems, especially for measurements near the forward direction. However, both thin and thick targets will be studied (as feasible) in order to check the two types of calculations (cross sections and transport). Targets will be chosen from Be, C, Al, Co, Bi, and H_2O. Copper and lead were used in the preliminary studies. The change to cobalt and bismuth will provide single isotopes, a potential advantage in interpreting nuclear level effects.

The choice of spectrometers was dictated by the need to move the equipment to several accelerators and the stringent time schedule imposed by the need for shielding information for the Apollo mission to the moon. Thus for neutron spectroscopy, magnetic deflection of proton recoils was not seriously considered, but three other approaches have been followed with extensive development. Proton-recoil telescopes of two types have been studied, with current emphasis centering on a dE/dx scintillation spectrometer for the energy range above 50 Mev. Neutron time of flight over a short path is being utilized to cover the energy range from a few Mev to $\sim$50 Mev with reasonable resolution, and, finally, a set of Bonner spheres is used for the energy range below 10 Mev. These three systems are described in Secs. 8.2, 8.3, and 8.4.

In connection with the interpretation of the Bonner sphere data (Sec. 8.4) and their extension to higher energy, several threshold detectors were tried. These depended upon fission reactions or $C^{12}(n,2n)C^{11*}$ activation. It was decided not to use these detectors, basically because of their inability to differentiate between neutron- and proton-induced reactions.

In a cooperative effort with the Fort Worth Division of General Dynamics, nuclear emulsions of varying thickness and sensitivity were exposed in the feasibility studies.[8] It has been determined that appropriate exposures were achieved for many of the plates, but they have not yet been subjected to detailed scanning. The separation of proton tracks from the neutron-induced proton-recoil tracks is quite difficult at the energies considered here, and the efficacy of the approach remains to be demonstrated. If successfully used, the emulsions should give useful data up to about 25 Mev.

---

[7] W. A. Gibson, W. R. Burrus, and T. A. Love, *Neutron Phys. Div. Ann. Progr. Rept. Sept. 1, 1961*, ORNL-3193, p 325.

[8] Sponsored by the U.S. Air Force, Wright Air Development Division.

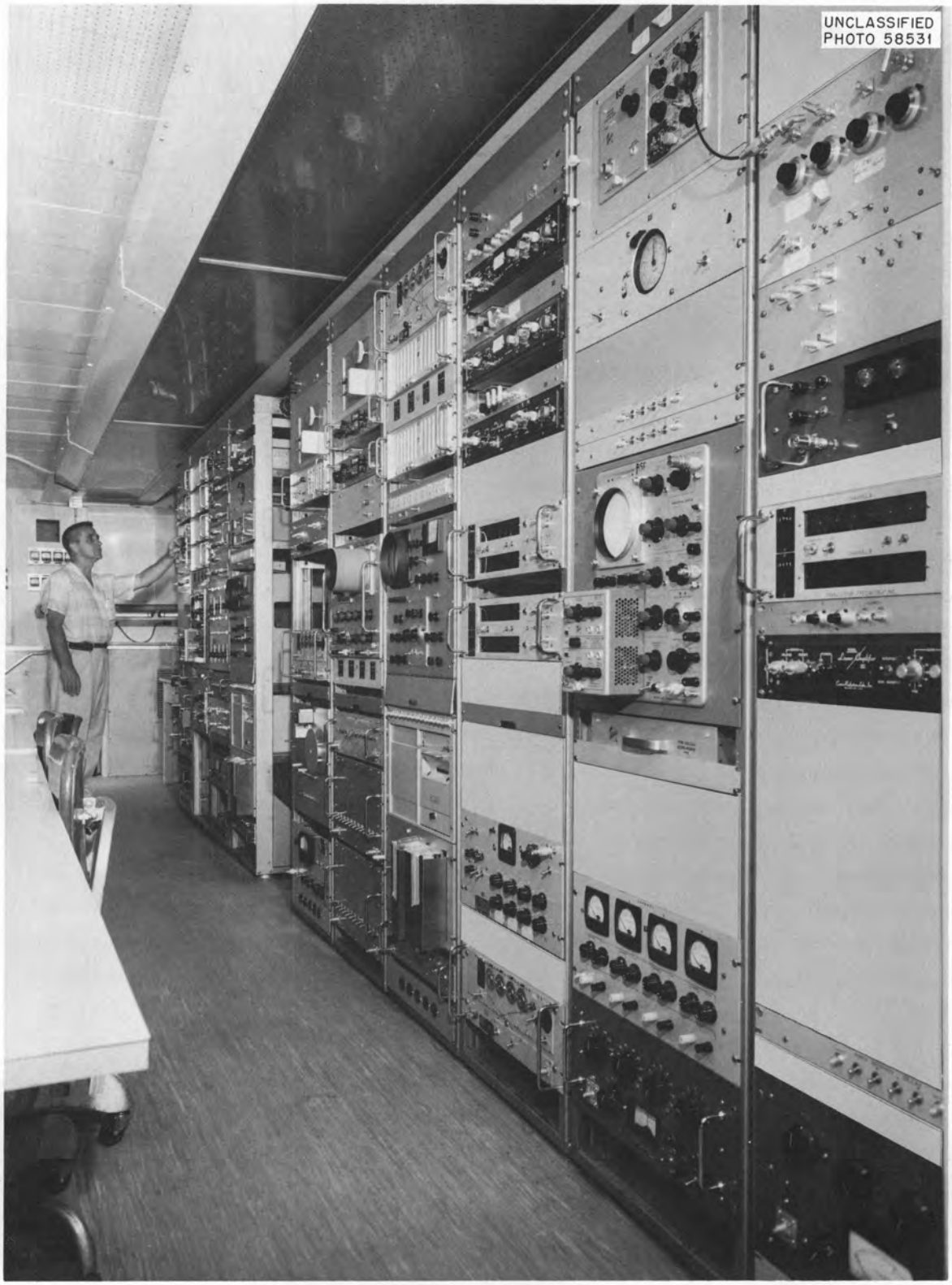

Fig. 8.0.1. Inside View of Mobile Shielding Laboratory II.

For proton spectroscopy the telescopes may be used by removing the hydrogenous radiator. The time-of-flight equipment may also be used for protons, although the energy resolution from flight-time measurements becomes inferior to that available from energy absorption in a dE/dx scintillator above about 30 Mev. Flight time can be used to relieve the ambiguity between total absorption and dE/dx. For low-energy protons (less than ~10 Mev) no spectrometer, other than the nuclear emulsions, is available; nor is this energy region considered to be of particular importance.

Because of their complexity and size, Compton-recoil or pair magnetic deflection spectrometers were not considered for gamma rays. A NaI(Tl) scintillation spectrometer has an efficiency for neutrons comparable to that for gamma rays in the Mev region, and the resulting neutron-induced background was considered to be overwhelming. Thus a three-crystal (NaI) pair spectrometer with a high inherent neutron rejection was chosen and is described in Sec. 8.5.

As stated previously, the major goal for the experiments is to provide accurate spectral data for comparison with calculations. A further check may be provided by determining the distribution in depth of the dose resulting in a spherical phantom from the interaction of all secondary particles. Fractionation of the dose with respect to the type of radiation would require dosimeters which are not available. The "integral" dose measurement described in Sec. 8.6 will, if successful, test whether the interactions of secondary particles in water (or tissue) and the integrations over angle required by the complex geometry can be handled by the calculation.

The electronics for the various spectrometer systems is located in two mobile laboratories so that it may be transported to the accelerators of interest. Connecting cables ~200 ft long permit operation of the experiment from the mobile laboratories. Figure 8.0.1 shows part of the 17 relay racks of equipment, which is largely transistorized. Use of the electronic components is described in Secs. 8.1–8.6. Detailed descriptions of individual components designed for this experiment but of general interest will be prepared for publication elsewhere.

The design, purchase, fabrication, test, and assembly of the apparatus were possible in the short time available only through the extraordinary efforts of the electronic design, counter, and mechanical design groups of the Instrumentation and Controls Division of ORNL. The tests at Harvard were greatly facilitated by the cooperation afforded by the synchrocyclotron group, particularly A. M. Koehler.

8.1. PROTON INTENSITY MEASUREMENTS

R. T. Santoro, R. W. Peelle, W. A. Gibson, W. R. Burrus, and R. J. Scroggs[1]

The preceding paper (Sec. 8.0) has outlined the series of experiments currently in progress at the Harvard University synchrocyclotron.[2] For a meaningful interpretation of the experimental data, the detector position as a function of angle and distance from the experimental target must be accurately known. In

[1]Instrumentation and Controls Division.

[2]F. T. Howard, *Cyclotrons and High-Energy Accelerators*, ORNL-2644 (January 1959).

addition, the spatial and time distributions of protons incident upon the target, as well as the absolute intensity of the proton beam, must be known. Solutions to these problems are individually discussed below.

Experimental Arrangement

The general experimental arrangement is shown in Fig. 8.1.1. The Harvard University 95-in. synchrocyclotron is a frequency-modulated machine capable of producing unpolarized protons at an energy of 156 Mev, with an energy spread of 2 Mev, and fluxes up to 5×10^{10} protons/sec. Its frequency range is from 23 to 30 Mc/sec, modulated by a rotating condenser. The nominal beam area is $\leqq 7$ cm^2. The permanent shield of the machine consists of from 3 to 8 ft of ordinary concrete.

The proton beam emerging from the machine passes through a vertical slit, which was introduced late in the experiments to reduce the effects of backgrounds observed in dosimetry measurements. It is then deflected by the steering magnet and focused by the quadrupole magnet, after which it continues through the beam tube and impinges onto the target. The lead bricks shown were added to further reduce backgrounds.

The target and detector-holding device is shown in Fig. 8.1.2. The apparatus is first centered on the proton beam by adjustment of the alignment posts at either end. Polaroid film is used as the beam-locating

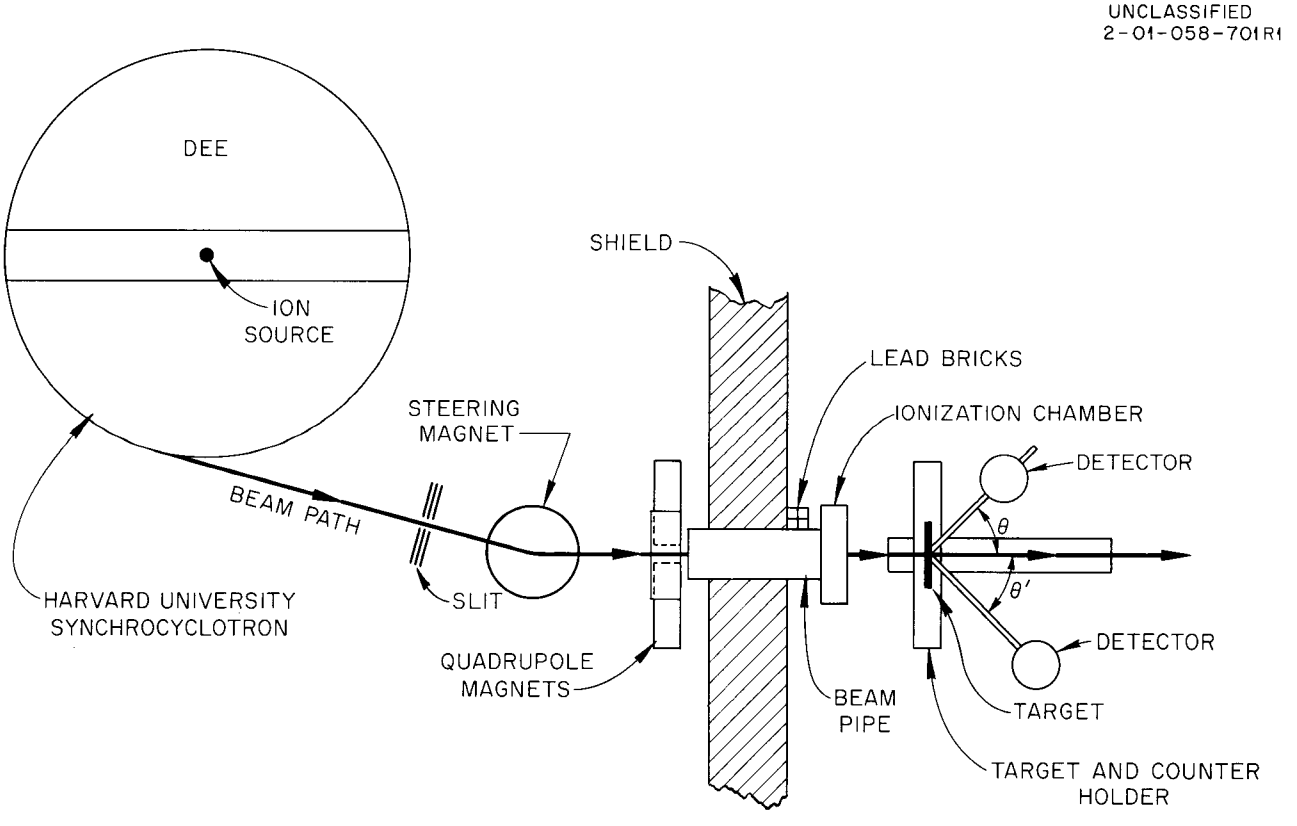

Fig. 8.1.1. Experimental Arrangement at Harvard University Synchrocyclotron.

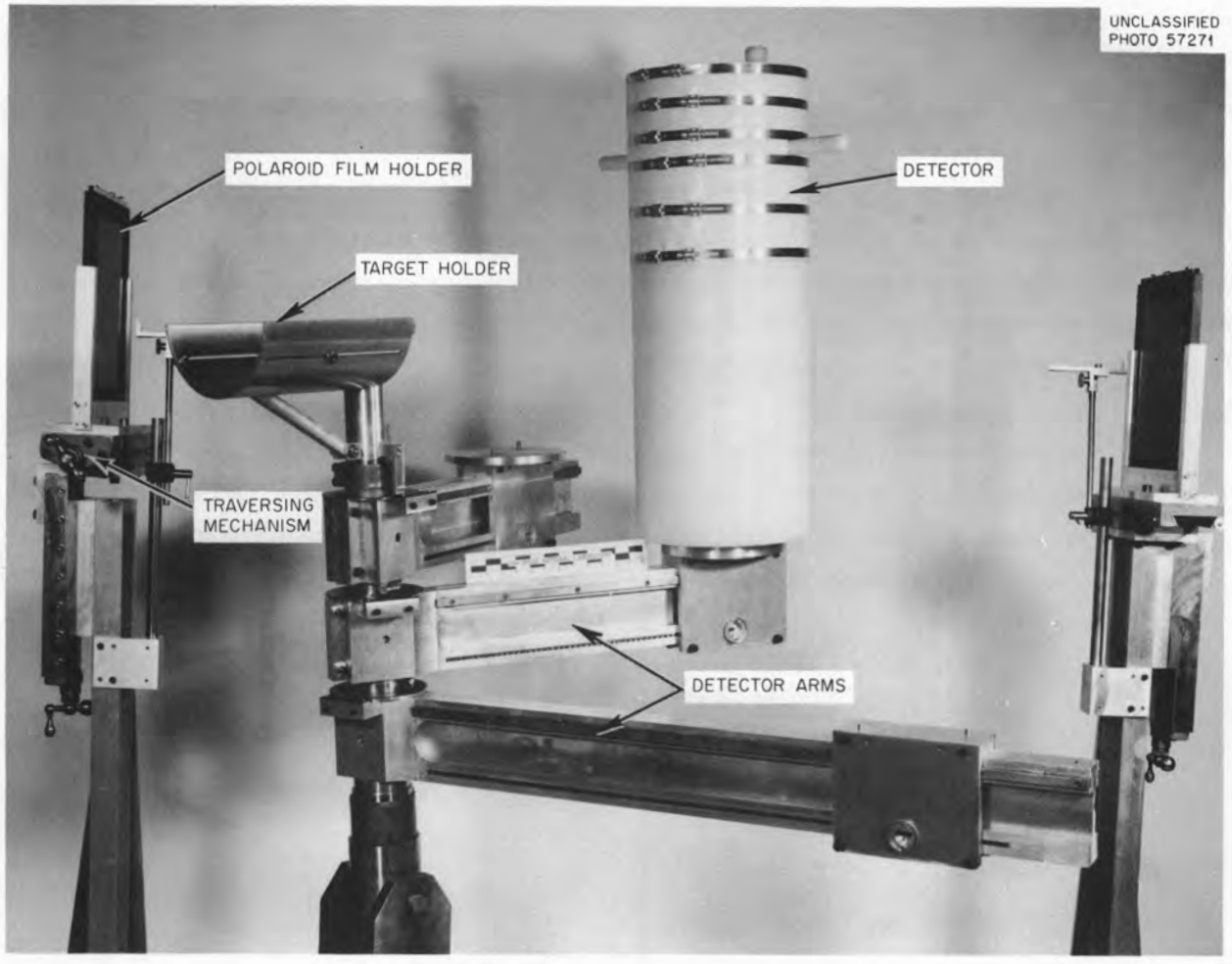

Fig. 8.1.2. Target and Detector Holder.

sensor. The target holder and detector arms are then positioned by using an alignment bar extending between the alignment posts. The detectors are rotatable through large angles about the target axis and can be varied in distance from the target up to 100 cm, depending upon which arm is used. All three arms can be used independently, permitting three simultaneous experiments to progress at three different angles and distances.

Proton Distribution Over the Beam

Film Studies. – The intensity distribution in a plane perpendicular to the beam, called the beam profile, was determined from Polaroid film exposures in the beam at several distances from the beam pipe. The shape of the image was indicative of the condition of focus. Because of the shape of the slit, the ideal cross section should have been a vertically elongated rectangle. In practice, however, the image attained was an oval, with its major axis horizontal. The contradiction is believed to be due to difficulties in adjustment of the quadrupole focusing magnet.

An attempt was made to determine a correlation between the density of Polaroid film negatives exposed in the beam and the number of protons per unit area causing the exposure. A nitrogen-filled ionization chamber at the beam pipe monitored the beam protons while the films were exposed approximately 1 m from the end of the pipe. Densitometer readings of the developed images showed a linear relationship between density and proton flux over the range from 5×10^8 to 1.6×10^{10} protons. Figure 8.1.3 plots the percent light transmission of the film negatives as a function of distance from the center of the image for various ionization chamber integrated currents. This figure and Fig. 8.1.4, a graph of relative beam intensity as a function of image width, contain useful data but lack sufficient information to accurately determine a density vs proton intensity relationship.

Profile Telescope. – The need for a more accurate device with which to analyze the distribution of protons in the beam led to the construction of a profile telescope. The profile telescope, diagrammed in Fig. 8.1.5, consists of two small cylindrical crystals, with their z axes coincident and parallel to the axis of the proton beam. The signals from the crystals are in coincidence, so that it is possible to count only those protons which pass through both crystals and to minimize the effects of noise, gamma-ray background, and neutron-induced counts present in the individual counters.

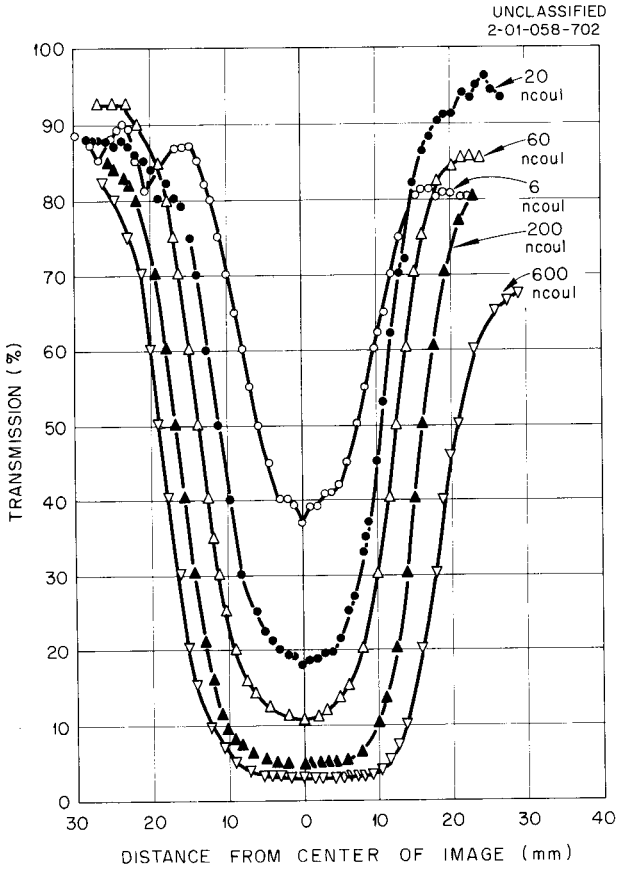

Fig. 8.1.3. Light Transmission of Polaroid Negative as a Function of Distance from the Center of the Image.

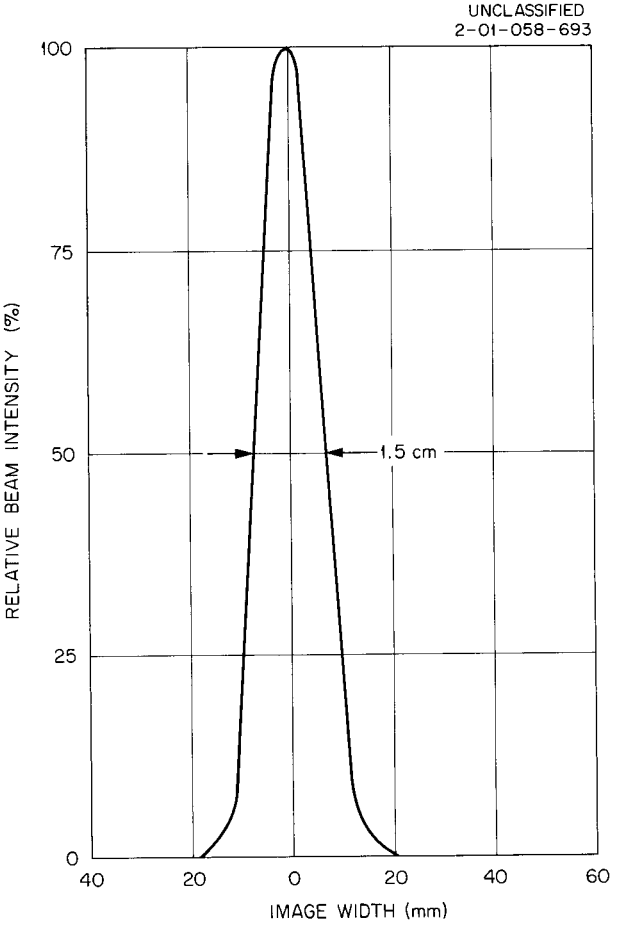

Fig. 8.1.4. Relative Beam Intensity as a Function of Image Width.

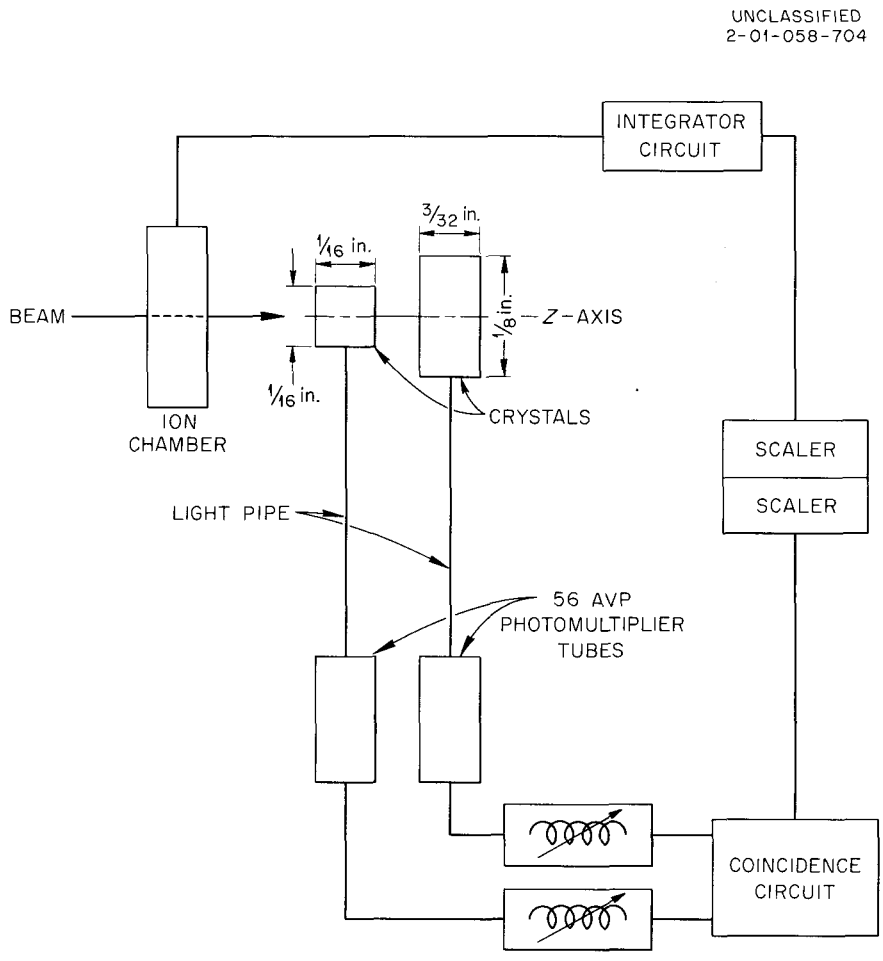

Fig. 8.1.5. Schematic of Profile Telescope.

The telescope is used to scan the beam horizontally and vertically, counting the number of protons across the beam profile. When it is used in conjunction with the film exposures described above, the number of protons causing a particular exposure can be determined. Additionally, by using the telescope to scan the back face of a target, the intensity distribution of neutrons or protons emerging from the target can be measured.

Beam Monitoring

During preliminary studies, the proton beam was monitored both by a Faraday cup and by ionization chambers. The Faraday cup, provided by the Harvard staff, was initially used to provide a calibration point for calibration of the ionization chambers. The device consists of a brass cup mounted in an evacuated housing. No provision was made for the suppression of secondary electrons, other than the fact that it was used in the magnetic field of the cyclotron (about 10 gauss outside the shield). From known criteria for Faraday cup design, an error no larger than 10% was assumed. A new Faraday cup that provides magnets and grids for suppression of secondary electrons has been built for future use.

Three ionization chambers were tested: an air-filled chamber, a nitrogen-filled chamber, and a helium-filled chamber. The sensitivity of the air-filled chamber was satisfactory at low beam currents ($\sim 10^7$ protons/sec), but the effects of columnar recombination made the chamber unacceptable for higher beam levels ($> 2 \times 10^8$ protons/sec). Although the nitrogen-filled chamber was operable in the 10^8-protons/sec region, it also suffered from the effects of recombination. The most useful chamber at high beam current levels (up to $\sim 10^{10}$ protons/sec) was the helium-filled chamber. Its sensitivity was low because of the low gas density, but no recombination effects were observed. Its performance is compared with those of the air-filled and nitrogen-filled chambers in Fig. 8.1.6. A new helium-filled chamber, containing twice the number of plates of the original and therefore even less subject to recombination effects, has been constructed for future work. A more sensitive current integrator has also been obtained to extend the operating range of the ionization chambers.

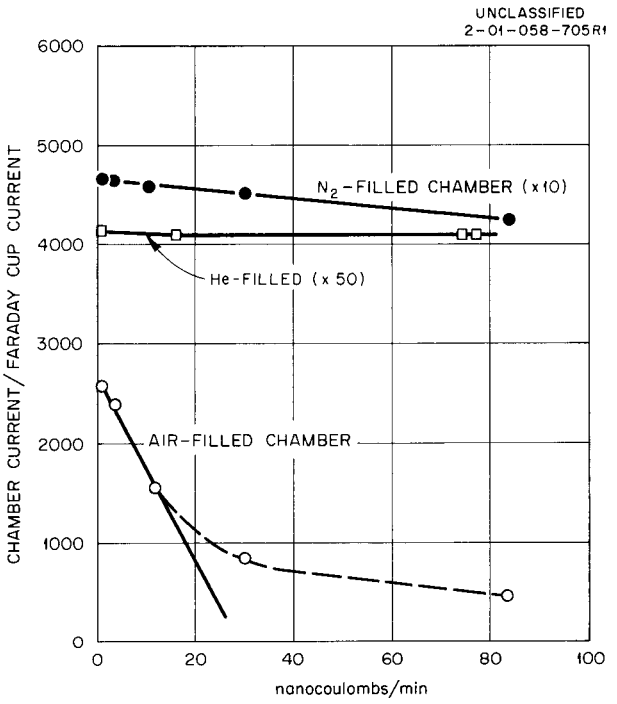

Fig. 8.1.6. Comparison of Ion Chamber Performances. The ordinates of the points plotted for the N_2-filled chamber have been multiplied by 10; those for the He-filled chamber have been multiplied by 50.

Time Dependence of the Proton Beam

Protons can be extracted from a synchrocyclotron only when the frequency of the accelerating voltage lies within narrow limits, that is, at the extraction frequency. To minimize the corrections required for random counts in experimental data, it is desirable to extract the beam for as long a period as possible (a continuous beam would be ideal). It is therefore important to understand how the duration of the beam is affected by the adjustment of cyclotron parameters and also to have a knowledge of the shape of the individual bursts.

Frequency modulation in the Harvard machine is accomplished with a 16-tooth rotating condenser, which rotates at about 20 rps. There is one proton burst per tooth per revolution, or 320 bursts/sec. The

320-burst/sec modulation is defined as the macrostructure. There is an additional modulation which takes place at the accelerating voltage frequency due to bunching of protons in phase with the accelerating field.

Because of the limited time available in the preliminary studies, the examination of the macroburst was restricted to a feasibility study.

A study of the structure was made for one synchrocyclotron setting. The circuit employed is shown in Fig. 8.1.7. The detector, an organic scintillator, was positioned so as to obtain a count rate of somewhat

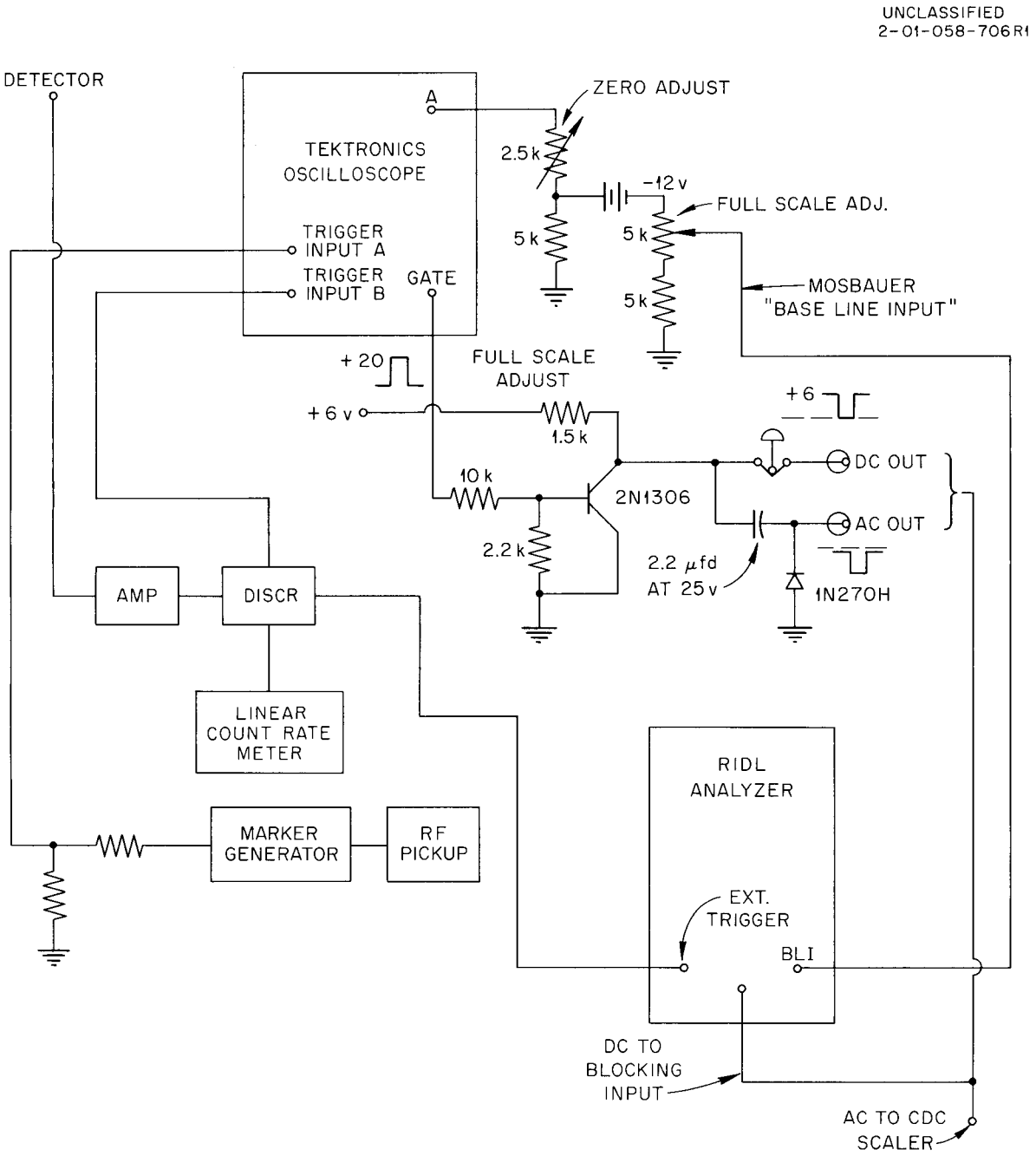

Fig. 8.1.7. Circuit Used in Macroburst Studies.

less than one count per macroburst. A marker pulse was obtained on the downswing of the frequency modulation cycle just before proton extraction. The elapsed time between the marker pulse and a proton signal from the scintillator was then analyzed and stored. Since there is a variation from tooth to tooth of the condenser (due to fabrication differences, eccentric alignment, wobble in the mechanical support, etc.), a gate was used which permitted analysis of only the pulse from each sixteenth tooth. The tooth with the widest frequency swing was arbitrarily designated tooth No. 7. As shown in Fig. 8.1.7, it was possible to implement all of the necessary gating by using a dual-sweep oscilloscope. The main sweep was set for 500 μsec; the delayed sweep was synchronized to the condenser rotation.

Figure 8.1.8 shows intensity vs time profiles for teeth 1 and 9. It is evident that the burst shape varies with individual teeth.

In future investigations, the effects of changes in rf voltage, injection conditions, and other cyclotron parameters will be studied.

A closer analysis of the macroburst shows that it is composed of a series of finer bursts, the microstructure. The fine structure of the beam was analyzed by observing the pulses from an organic scintil-

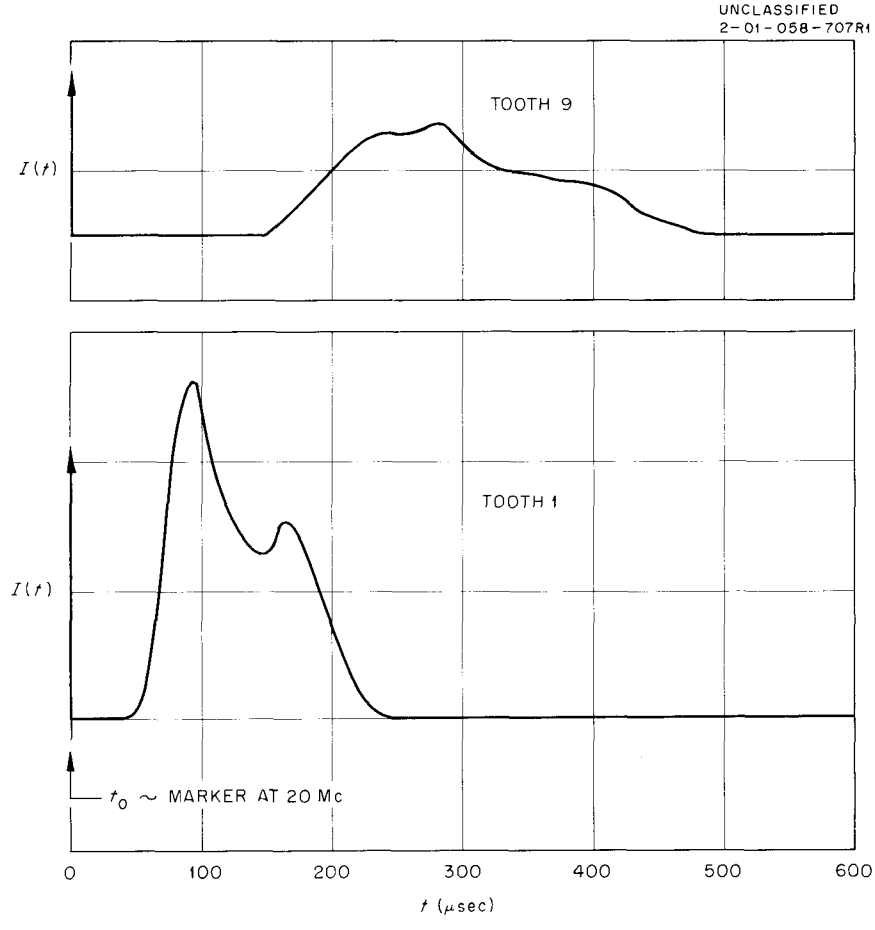

Fig. 8.1.8. Intensity as a Function of Time for Teeth 1 and 9.

lator with an oscilloscope. The detector pulse was used to simultaneously trigger the oscilloscope and furnish the vertical input. The counting rate was adjusted by positioning the crystal so that two pulses could sometimes be observed during one sweep, the sweep rate being about 20 nsec/cm. Photographic time exposures of multiple oscilloscope traces show that the microburst has a width of 4 to 7 nsec and a frequency of 22.7 Mc/sec. The microburst structure is shown in Fig. 8.1.9, drawn from an oscilloscope trace.

A fuller knowledge of the microstructure is required, both for proper analysis of gamma-ray spectral data and for establishing criteria for coincidence circuits. A more detailed study will be attempted in future work, using other circuits[3] as well as time-to-pulse-height converter techniques.

[3]N. E. Booth and G. W. Hutchinson, *Nuclear Instr.* **1**, 80 (1957).

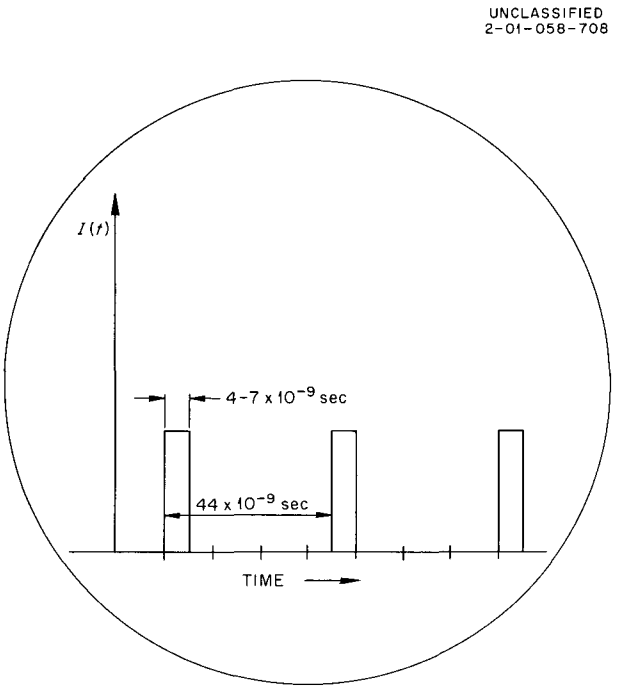

Fig. 8.1.9. Microburst Structure.

8.2. PROTON-RECOIL TELESCOPES FOR SPECTRAL MEASUREMENTS OF NEUTRONS AND PROTONS WITH ENERGIES > 10 Mev

W. A. Gibson, W. R. Burrus, and C. F. Johnson[1]

A brief description of the proton-recoil telescopes proposed for measurements of the energy spectra of neutrons with energies from ~8 Mev to several hundred Mev was given previously,[2] and the efficiency for neutron detection was calculated for neutron energies between 8 and 50 Mev. These instruments have now been constructed and tested in the preliminary experiments at Harvard (see Sec. 8.0) in the spectra of neutrons arising from the bombardment of a thick copper slab by 156-Mev protons. The results of these tests and the suggested constructional changes are discussed below.

Spectral Measurements of 8- to 50-Mev Neutrons

The telescope used for the ~8- to 50-Mev neutron range consists of a polyethylene radiator followed by two proportional counters and an NaI crystal. All three counters are placed in coincidence, and a recoil proton originating from the radiator produces pulses in coincidence which gate on a multichannel

[1]On assignment from General Dynamics/Fort Worth.

[2]W. A. Gibson, W. R. Burrus, and T. A. Love, *Neutron Phys. Div. Ann. Progr. Rept. Sept. 1, 1961*, ORNL-3193, p 325.

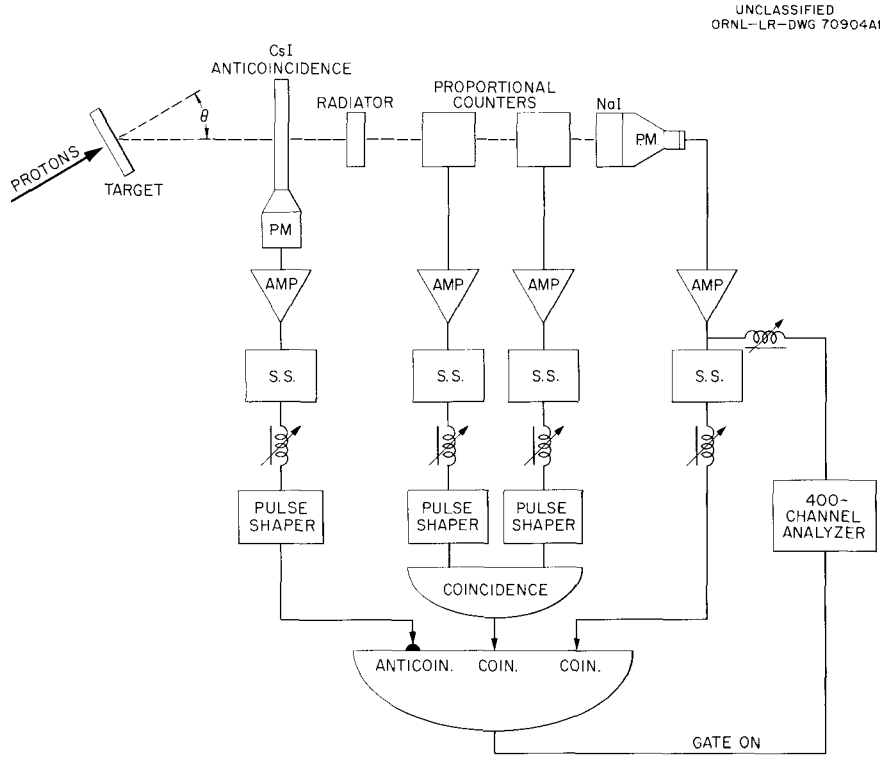

Fig. 8.2.1. Block Diagram of Proton-Recoil Telescope Proposed for Measurement of Neutron Spectra Over 8- to 50-Mev Range.

pulse-height analyzer that records the total energy deposited in the NaI crystal (see Fig. 8.2.1). A CsI crystal in front of the radiator is placed in anticoincidence with the other three counters and eliminates counts from protons present in the incident flux. Backgrounds are measured by replacing the polyethylene radiator with a carbon radiator containing the same amount of carbon as the polyethylene.

In the preliminary runs, adequate neutron counting rates were obtained and the single rates in the individual counters were reasonable. However, more than 60% of the triple coincidences representing neutron counts was background. On closer inspection it appeared that these counts were coming from high-energy (n,p) events in the structure of the proportional counters and surrounding material. The bodies of the proportional counters are now being rebuilt to reduce the mass of the counters and, hopefully, the background.

Spectral Measurements of 50- to 150-Mev Neutrons

The recoil telescope for the 50- to 150-Mev neutron range consists of a polyethylene radiator followed by two organic scintillators and an NaI crystal (see Fig. 8.2.2). All three crystals are placed in coincidence, and a coincidence pulse from these counters gates on the multichannel analyzer to analyze the pulse from the NaI crystal. An anticoincidence crystal is placed in front of the radiator to eliminate counts from protons in the incident flux.

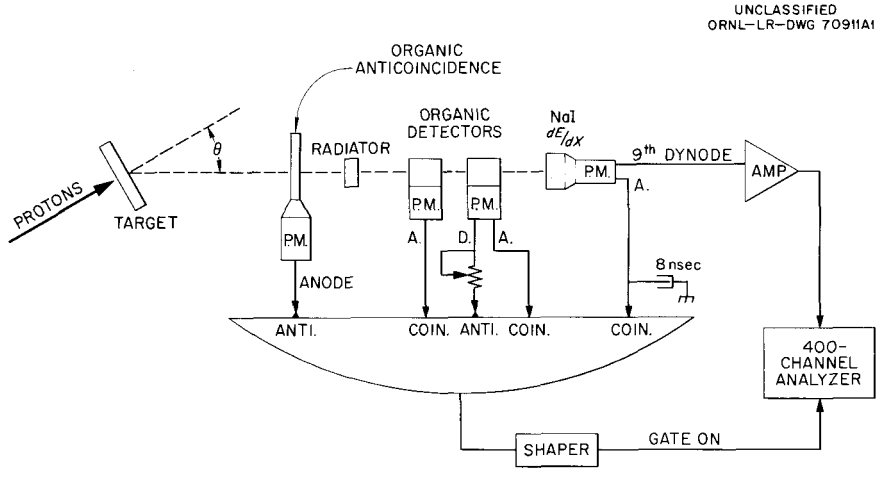

Fig. 8.2.2. Block Diagram of Proton-Recoil Telescope Proposed for Measurement of Neutron Spectra Over 50- to 150-Mev Range.

The NaI crystal is thin (1.5 g/cm^2) compared to the range of a 50-Mev proton and hence the dE/dx of the recoil proton is measured rather than its total energy.[3] The energy deposited in the crystal by the proton is calculated from the pulse height recorded by the multichannel analyzer. For protons which penetrate the NaI crystal, the energy deposited is a direct measure of the dE/dx of the recoil proton and

[3]G. L. Guernsey *et al.*, *Rev. Sci. Instr.* **23**, 476 (1952).

is a unique function of energy for proton energies below the minimum energy for ionization; hence the total energy of the proton is determined from the curves relating dE/dx to energy.

The two major disadvantages of an energy determination by a dE/dx measurement are:

1. For the higher energies the dE/dx changes only slowly with energy and therefore the error in determining the total energy of the proton is much larger than the error in measuring dE/dx.
2. Statistical fluctuations in the energy lost by protons as they pass through the thin NaI crystal (known as the Landau effect[4]) introduce a spread in the pulse-height spectrum obtained for a monoenergetic beam.

The width of the resolution function has been calculated for the crystal used on this telescope and the full widths at half maximum for 50- and 156-Mev protons are 6% and 18%, respectively. The resolution obtained experimentally on the 156-Mev beam supports the calculation.

The advantages of using a thin crystal are that the probability of nuclear interaction is reduced to a negligible value and the geometric effects introduced by a finite thickness crystal are small.

An NaI crystal was chosen rather than an organic scintillator for the dE/dx measurement because of the greater light output of the crystal and because its scintillation efficiency increases with increasing dE/dx below 10 Mev g^{-1} cm^{-2}.[5] Since the dE/dx decreases with increasing proton energy, the two effects add to accentuate the inverse relation between the light output of the crystal and the energy of the proton.

Figure 8.2.3 is a plot of the efficiency of the recoil telescope as a function of energy. The solid line is the efficiency for a continuously increasing radiator thickness and a 10% geometric energy resolution, and the dotted lines show the efficiency for radiators of constant thicknesses. The intrinsic resolution of the telescope is approximately 15%. That is, the radiators are chosen so that the lowest energy proton being analyzed loses 10% of its energy in passing through the thickness of the radiator, and the geometries are chosen so that 10% uncertainty in the energy is introduced by variations in the scattering angle of the recoil proton.

Figure 8.2.4 is a plot of pulse height as a function of the energy of the protons incident upon the NaI crystal. It is seen that a particular energy deposition in the crystal does not correspond to a unique incident proton energy, since a low-energy proton that just stops in the crystal will result in the same size pulse as that produced by a higher-energy proton passing through the crystal. The straight-line portion of the graph at low energies results from those protons that stop in the crystal.

To overcome this ambiguity, it is planned to place an upper level discriminator on the organic scintillator preceding the NaI crystal in order to identify the low-energy protons which will stop in the last crystal (the low-energy protons will have a larger dE/dx and therefore deposit more energy in the crystal preceding the NaI crystal than will the higher-energy protons).

Figure 8.2.5 shows the pulse-height spectrum from the dE/dx crystal with both the background and an estimated contribution from low-energy neutrons subtracted. Figure 8.2.6 is a graph of the neutron spectrum obtained by calculating the total energy of the recoil protons from the pulse-height spectrum

---

[4]Bruno Rossi, *High Energy Particles*, Prentice Hall, New York (1952), p 29.

[5]R. B. Murray and A. Meyer, *Phys. Rev.* **122**, 815 (1961).

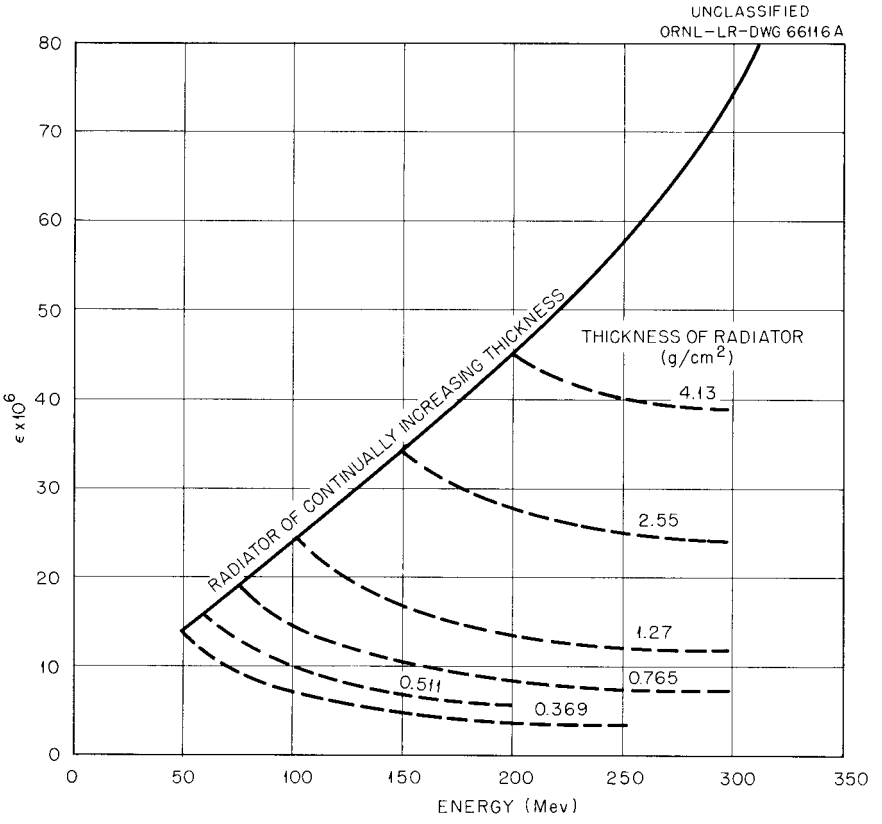

Fig. 8.2.3. Calculated Efficiency of High-Energy Proton-Recoil Telescope as a Function of Energy.

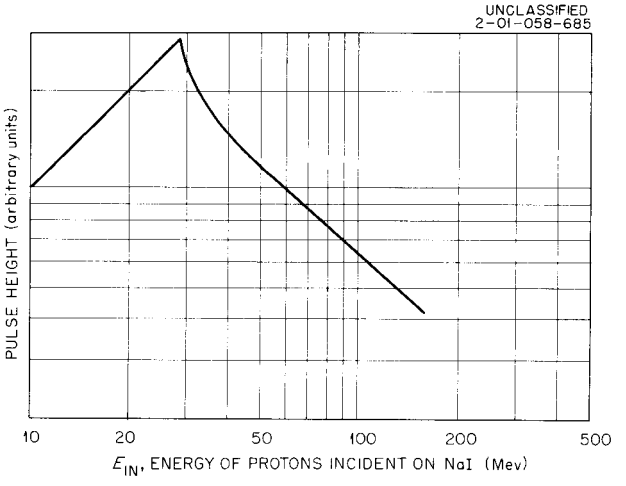

Fig. 8.2.4. Pulse Height, as a Function of Incident Proton Energy, for a 0.161-in.-Thick NaI Crystal in the Telescope Shown in Fig. 8.2.2.

of Fig. 8.2.5. Because of the uncertainty in estimating the low-energy neutron contribution and the large errors in the data, this curve is only indicative of the expected shape of the spectrum.

Since fast decay times are characteristic of organic scintillators, high counting rates were obtained and the operation of the telescope, except for the ambiguity introduced by the low-energy neutrons, was satisfactory. The background was about 10% of the foreground.

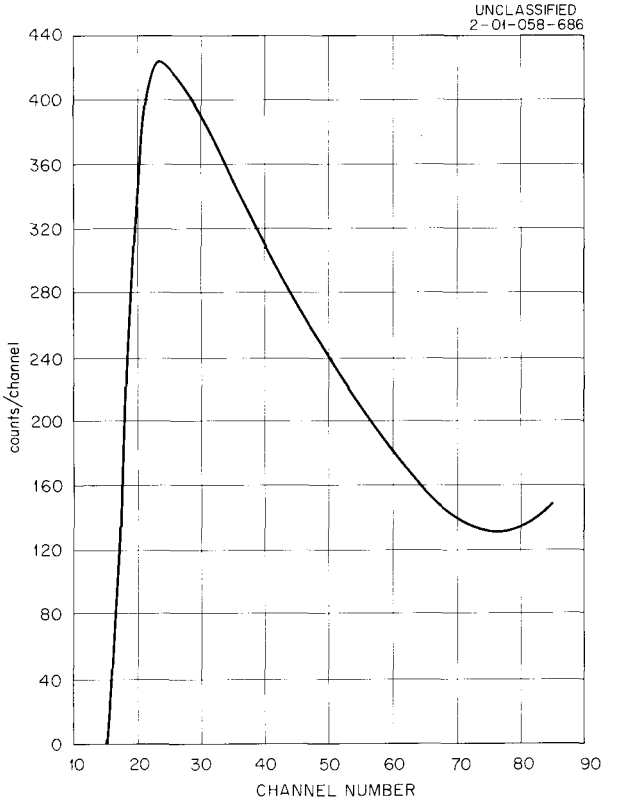

Fig. 8.2.5. Pulse-Height Distribution of Neutrons from 31.8-g/cm^2 Copper Target Bombarded by 156-Mev Protons. Curve corrected for background, and an estimated correction made for low-energy components.

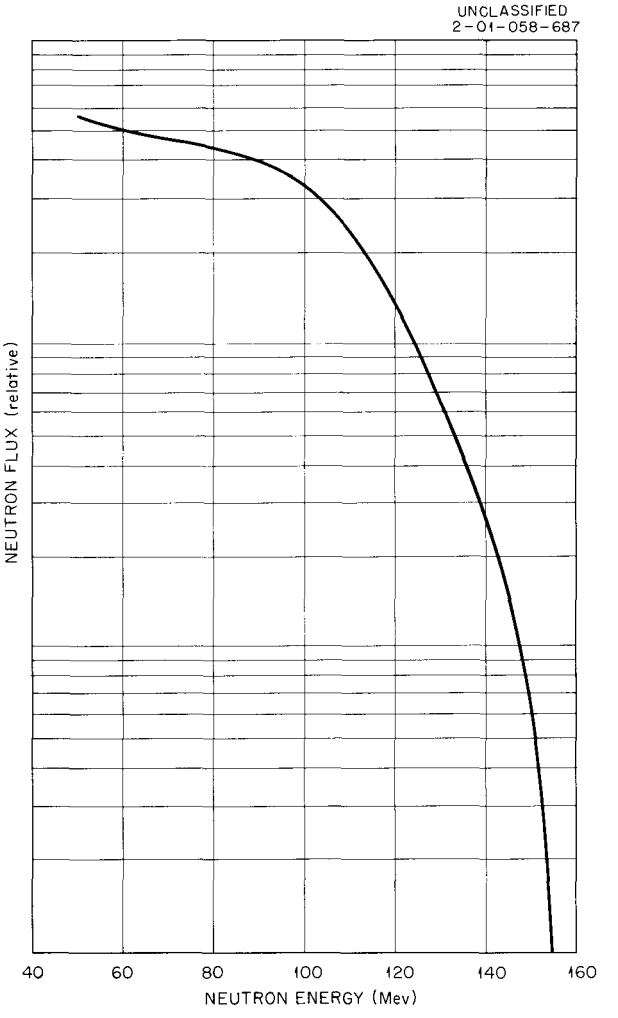

Fig. 8.2.6. Spectrum of Neutrons Emitted Forwardly from a 31.8-g/cm^2 Copper Target Bombarded by 156-Mev Protons. Computed from data of Fig. 8.2.5.

Spectral Measurements of Protons

The telescopes described will also be used for measurements of proton spectra, in which case the hydrogenous radiator and the anticoincidence crystal preceding the radiator will be removed and the telescopes will look directly at the target.

8.3. FLIGHT-TIME SPECTROSCOPY FOR NEUTRON AND PROTON YIELDS FROM NUCLEI BOMBARDED BY PROTONS

R. W. Peelle, T. A. Love, and G. A. Luce[1]

The deduction of energies of fast neutrons from measurements of their velocities is a common procedure for the energy region below 20 Mev, even for neutrons resulting from neutron-induced reactions. This "flight-time" method has also been used for very high energies, an example being its recent application at Harwell for neutrons produced in reactions of 143-Mev protons incident on nuclei.[2] Therefore, it was natural to consider flight-time spectroscopy for measuring thick-target yields and differential cross sections for interactions of 50- to 700-Mev protons with nuclei.

To measure the velocity of a secondary neutron in the Mev range, the time required for it to travel from the target to a fast-neutron detector, usually a plastic or liquid scintillator, is measured. Thus the pulse from the phototube attached to the scintillator determines one end of the flight-time interval. Either of two systems can be employed for timing the other end of the interval:

1. Particles in the beam can be bunched to an extent consistent with the required resolution, and the time that the entire group is incident upon the target can be determined by methods depending on the experiment in question. A neutron chopper is a simple example of this system.
2. The time of each individual incident particle can be determined, as in the associated-particle method in which a timing pulse representing an individual incident fast neutron is derived from a charged particle produced in the reaction with the neutron. For instance, the associated alpha particles may produce timing pulses for fast neutrons from the D(T,α)n reaction.

The first system was used at Harwell[2] by utilizing a natural phase bunch in the cyclotron internal beam once during each cycle of the modulation frequency. At least at the lower end of the range of interesting incident-proton energies, a like system could be used on an external beam provided that a special electrostatic deflection system could be employed to eliminate counts from most of the microstructure bursts. Since the time resolution of the proton burst probably could not be shorter than 4 nsec, a large target room would be required for such a method. Although with this system electronic timing problems would be simpler and there would be less stringent requirements on the detector and target thicknesses, it seems to be out of the question for the experiments required in this program since they must be conducted at other laboratories. Thus the second system has been adopted, and the time that each incident proton reaches the target is deducted from a pulse produced in a detector placed in the beam. This system leads to considerable difficulties with resolution and counting rates, but it is flexible enough that any available external proton beam which can be adjusted to the correct intensity can be used.

Experimental Method

Figure 8.3.1 shows a plan schematic of the detector apparatus required for neutron-producing reactions, along with a simplified block diagram of the associated electronic apparatus. Detector *A* consists of a

---

[1] On loan from General Dynamics Corp., Forth Worth, Texas.

[2] P. H. Bowen *et al.*, *Nucl. Phys.* **30**, 475 (1962).

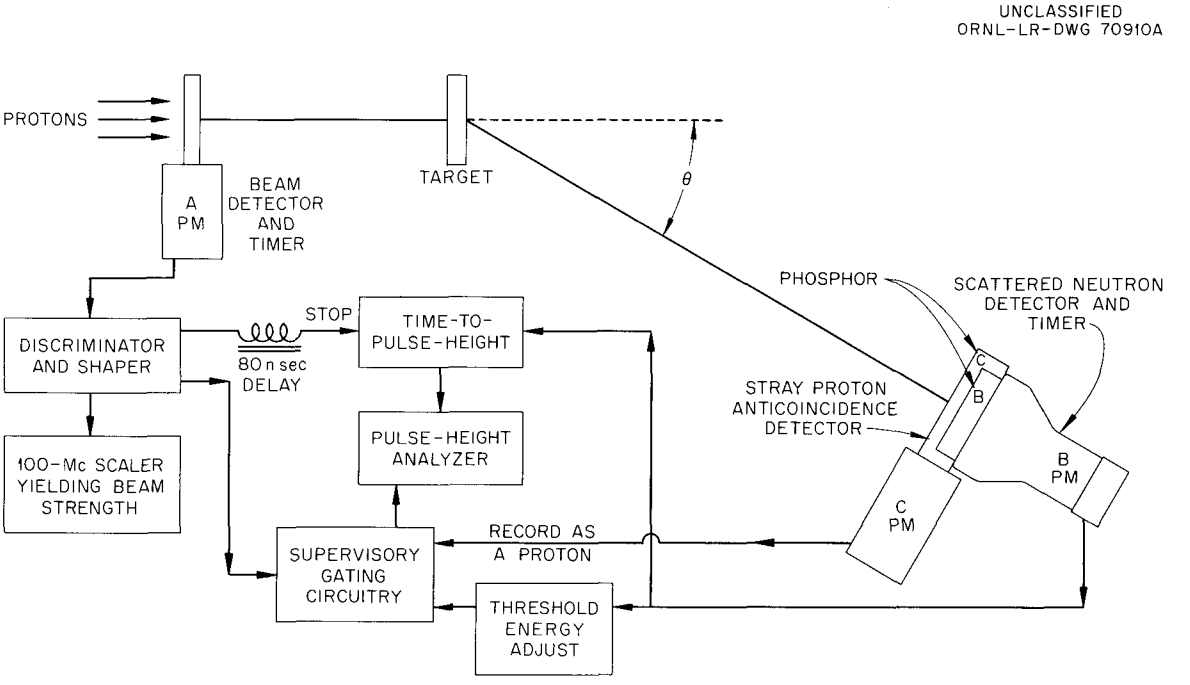

Fig. 8.3.1. Detector Plan View and Simplified Block Diagram for Neutron Time-of-Flight Spectrometer.

thin (1- or 2-mm) plastic scintillator placed a convenient distance from the target. Since the protons have essentially uniform velocity, the time the proton reaches the target can be inferred from the timing of the light flash in this scintillator. The 5-in.-diam detector *B*, generally 1 in. thick, is for detection of neutrons originating in the target. At energies below 10 Mev, detection is primarily by means of the recoil protons from *n-p* scattering, while above 20 Mev various charged-particle reactions with the carbon of the scintillator surely dominate. Detector *C*, which takes the form of a thin cup surrounding all but one side of detector *B*, is used in coincidence with the latter to label the detection of charged particles. Coincidences between detectors *B* and *C* cause the corresponding time measurement to be stored separately.

The simplified electronic diagram indicates several of the most important features required:

1. The strength of the incident beam, which must be known to put the experiment on an absolute basis, is determined by actually counting the individual protons detected. The time between the pulse from *B* and the delayed pulse from *A* is converted to a pulse amplitude and fed into a standard multichannel pulse-height analyzer for storage.
2. The time-to-pulse-height converters deemed appropriate for this experiment are of the general variety which measure the time between "start" and "stop" signals. Since the output of this converter is 1 μsec or so in length, the number of start signals must be as small as possible. For this reason the time scale is reversed by delaying the pulse from *A*.
3. At the beam strength corresponding to a reasonable counting rate, there will be an important ($\sim 10\%$) fraction of cases in which $B - A$ time intervals should not be recorded because two or more protons reach the target so closely spaced in time that it cannot be determined which proton produced the observed pulse in *B*. Control of such cases is a function of the supervisory circuitry.

4. Additional supervisory circuitry is required to set the lower energy threshold of detector *B* and to sort the true neutron-produced pulses from those which cause coincidences between detectors *B* and *C*. The *B* counting threshold is very important because it determines the neutron efficiency.

Two main types of background are likely to be encountered, assuming that detector *A* responds only to protons from the beam. Gamma rays that do not come from prompt reactions in the target can be detected in *B*. These lead to a flat background of time-interval measurements. The other important background arises from neutrons generated by the beam. The presence of the beam microstructure synchronizes this background to a certain extent with the protons observed in detector *A*, and so this background must be expected to be time dependent. The component that results indirectly from reactions in the target is virtually impossible to measure, but that from the floor and perhaps from the cyclotron shield can readily be measured by removing the target. Except for gamma rays from radioactivity in the target, the random gamma-ray background is also eliminated by subtracting the target-out counts from those obtained with the target in.

Some understanding of intensity problems can be gained by study of the estimated efficiency curve of Fig. 8.3.2 plotted for a scintillator thickness of about 1 in. and a detector bias of just over 1 Mev. If clumsy arrangements involving multiple *B* detectors are avoided and detector *B* is placed ~ 70 cm from the target, the scintillator subtends a fractional solid angle of $\sim 2 \times 10^{-3}$. If one neutron is produced in the target for every ten protons, then in the case of an isotropic yield there would be about one fast neutron detected for some flight time for each 10^5 incident protons. As is developed below, a plausible intensity

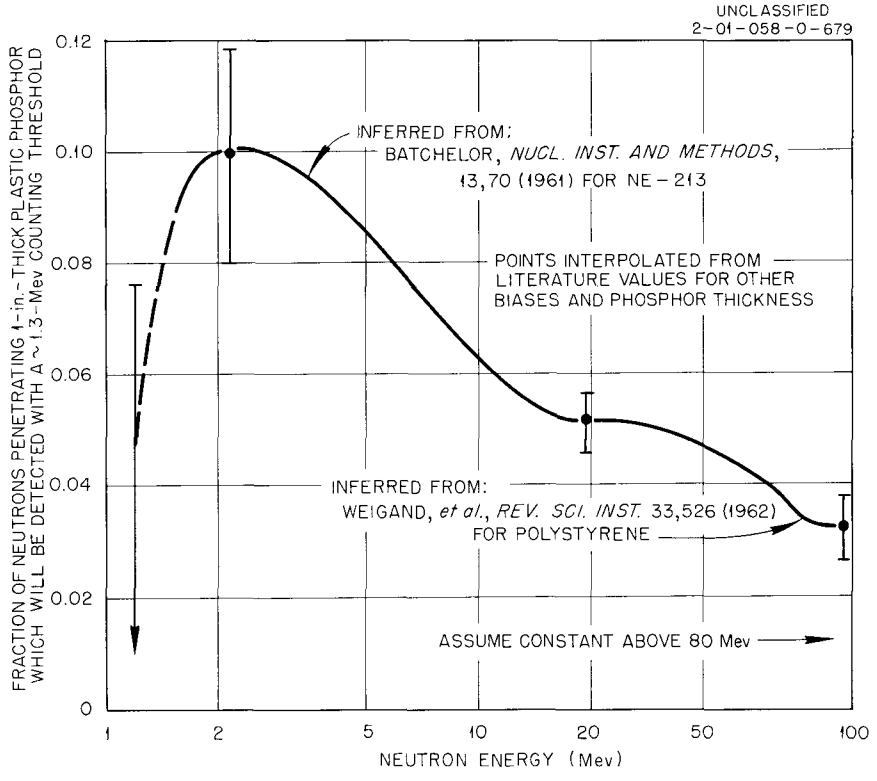

Fig. 8.3.2. Estimated Counting Efficiency of the Scattered-Neutron Detector.

is $2 \times 10^6 \times f$, where f is the gross duty factor, about 4% at the Harvard synchrocyclotron. Thus, in a typical case it can be anticipated that about 1 count/sec will correspond to some energy of interest. Rates actually observed in tests using a 25-g/cm^2 copper target were two or three times this value.

Table 8.3.1 will aid in understanding the time resolution problem. It shows the time required for a 70-cm flight by neutrons of various energies. For the assumed time-measuring system with resolution of about 1 nsec, the best available time resolution for a 50-Mev neutron is 12%, leading to an energy resolution of 25%. The target and detector thicknesses must also be considered. They typically limit energy resolution to 15% by making uncertain the precise length of the flight path. Thus with reasonable target-detector spacings, the equipment can be operated to detect neutrons over 50 Mev only for very low resolution work. Fortunately the efficiency of Fig. 8.3.2 does not seem to vary much in the higher energy region. Table 8.3.1 also indicates that at 70 cm the spectrum can be carried down to about 0.5 Mev if an 80-nsec period is allotted to each time measurement. If a 0.5-Mev bias is employed on detector B, efficiency will be reasonably well known for neutrons above 1 Mev. The considerations of this paragraph lead to the energy range limitation for secondary neutrons.

Table 8.3.1. Neutron Flight Time and Energy Resolution for a 70-cm Flight Path

Kinetic Energy of Secondary Neutron (Mev)	Neutron Velocity (cm/nsec)	Flight Time for 70-cm Path (nsec)	Energy Resolution for 1-nsec Time Resolution[a] (%)
0.5	0.98	71	3
1.0	1.38	51	4
2.0	1.95	36	6
4.0	2.76	25	8
8.0	3.89	18	11
16.0	5.46	13	15
30	7.4	9.5	23
60	10.2	6.8	32
100	12.8	5.5	40
150	15.2	4.6	50

[a]Energy resolutions quoted are for a limitingly thin target and detector and are based on a hypothetical 1.0-nsec time resolution of the system.

Since if two protons should arrive on the target during an 80-nsec period it is difficult to know which has generated a detected secondary particle, part of the supervisory circuitry is designed to eliminate such proton pairs from consideration. If in the macroburst (see Sec. 8.1) the intensity averages about 2.2×10^6 protons/sec, and if the microstructure is definite, there is an ~ 0.74 chance ($e^{-0.3}$) that a given pulse will

be adequately isolated from its neighbors. This probability would lead to a 25% correction by the supervisory electronics to a net counting rate of about 1.5×10^6 protons/sec during the macrobursts. Perhaps a gross microburst intensity as high as 3.3×10^6 protons/sec could be considered, which would give a net rate of 2.1×10^6 protons/sec after correction. It is doubtful if larger corrections by the supervisory circuitry should be allowed, and little counting intensity remains to be gained if the 80-nsec interval is maintained. If there were no microstructure, a clear time interval of ±80 nsec around each accepted proton would have to be provided, which has a probability per proton given by $\exp(-160 \times 10^{-9} \times 2.2 \times 10^6) = e^{-0.35} = 0.70$ for the case of a gross microburst intensity of 2.2×10^6 protons/sec. Therefore, the sharp microstructure helps slightly in utilizing the beam, provided that the amount of free time required is just less than an integral number of cyclotron r-f periods.

Preliminary Measurements

An apparatus of the type described above was tested in May 1962 with protons from the ~156-Mev external beam of the Harvard University synchrocyclotron (see Sec. 8.0). This section discusses very briefly the instrumentation used and shows some of the preliminary results obtained.

Detector *A* was a single 2-mm-thick polystyrene-based plastic scintillator which gave an ~40% pulse-height resolution from the ~1-Mev energy loss from a single proton. No protons produced pulses of less than one-half the average pulse height. The bias for pulses to be counted as part of the beam was set just below the half-average pulse-height level by use of a tunnel diode discriminator which fed an amplifier[3] capable of producing a pulse of appropriate shape for the 100-Mc scaler used. Detector *B* showed 14% resolution (on integrated pulses) for the ~15-Mev energy losses by the primary beam protons.

Light collection in detector *C* was inadequate, so the resolution for the 1-Mev energy loss from the full-energy beam was about 100%.

Integral lower-bias levels on *B* and *C* signal channels were set using conventional slow (1-μsec) electronic circuitry, and the necessary conditions for storage of a pulse were determined in a slow gating circuit.[4] This circuit was operated at much higher than design counting rates because of failure of some of the other supervisory circuitry. In practice, except for a few trial runs, mutally interfering events in the *A* channel were held to a minimum by operating at a beam strength during the macrobursts of about 0.5×10^6 protons/sec.

Timing signals were formed at the photomultiplier bases in the *B* and *C* signal channels by tunnel diode discriminators. The time-to-pulse-height converter formed a voltage pulse by integrating a fixed current during the time between the output signals from these discriminators.

Figure 8.3.3 indicates the timing resolution available under the ideal conditions of the full-energy proton beam traversing both the *A* and *B* detectors. Artificial delays account for the channel in which the peak

[3]Designed by N. L. Hill of the Instrumentation and Controls Division.

[4]Designed by F. M. Glass of the Instrumentation and Controls Division.

appears. For the broad spectrum of pulse heights resulting from a monoenergetic neutron incident on detector *B* the sharp resolution of the ideal case (~1.2 nsec) is not expected to exist. Figure 8.3.4 shows a typical calibration curve for the time-to-pulse-height converter; it was obtained by varying a delay line in the "start" signal channel. A nonlinearity is observable at small pulse heights. Velocity measurements were made by comparing the channel in which the pulse appeared against that in which was centered the full-energy proton peak with the target removed and the detector at 0°. Other distance and delay parameters were, of course, held constant.

Figure 8.3.5 shows a typical pulse-height spectrum, obtained at a 10° scattering angle from a copper target 25.2 g/cm^2 thick. The background with the target removed is plotted on the same scale and includes essentially the same random background as the target-in data. Figure 8.3.6 shows the same 10° data plotted on a neutron/Mev vs Mev basis. The data were reduced by a computing machine program[5] based on the detector efficiency illustrated in Fig. 8.3.2. The spectrum observed at 60° is shown on the same plot. The 120° data (not plotted) appear consistent with that shown for 60°, and the 30° spectrum falls between the

[5]The program was designed by R. Cowperthwaite, co-op student from Missouri School of Mines, Rolla, Missouri.

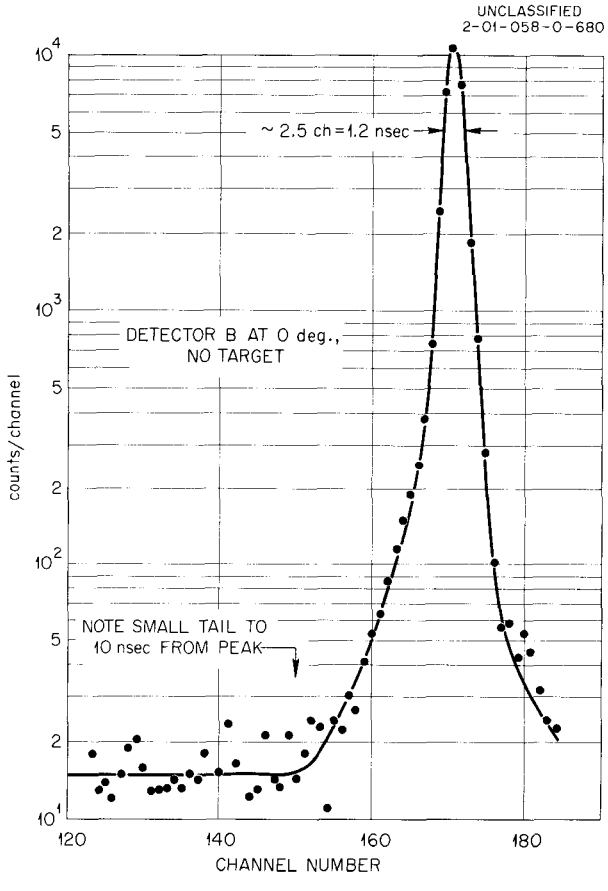

Fig. 8.3.3. Time Resolution of Spectrometer System at 0.45 nsec/channel.

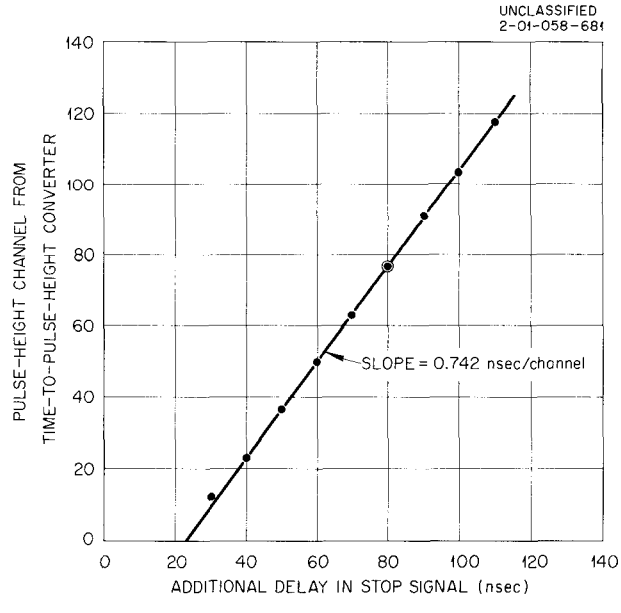

Fig. 8.3.4. Typical Calibration Curve of Time-to-Pulse-Height Converter.

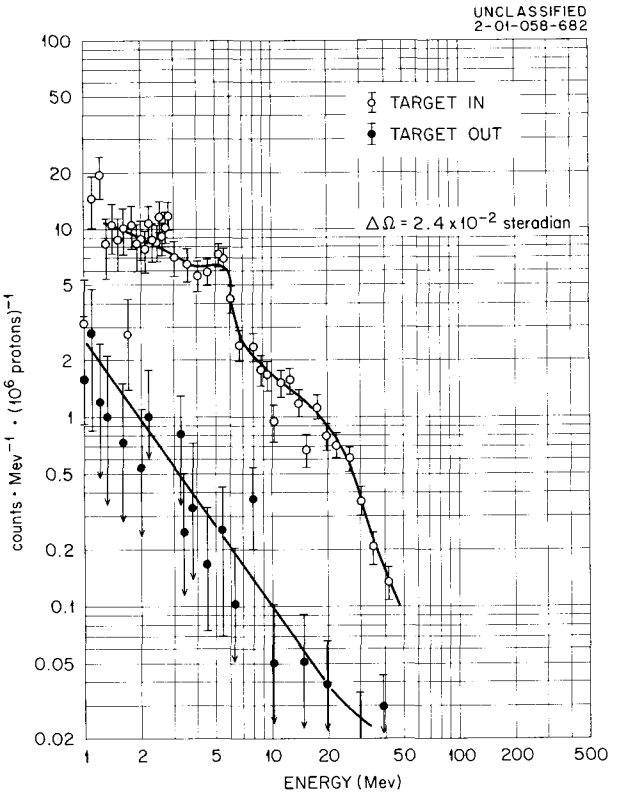

Fig. 8.3.5. Neutron Count Spectrum and Target-Out Background for 156-Mev Protons on 25.2-g/cm^2 Copper Target.

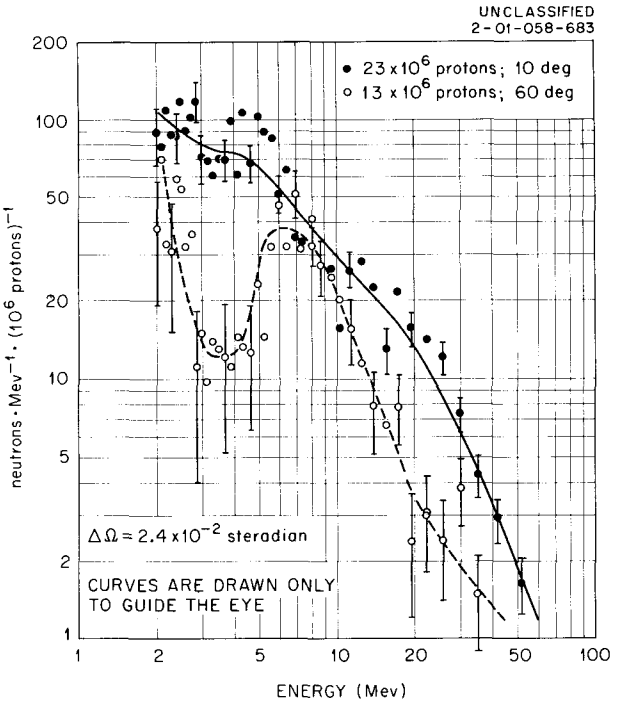

Fig. 8.3.6. Neutron Spectrum at Scattering Angles of 10 and 60° from a 25.2-g/cm^2 Copper Target.

two shown. The efficiencies used in reduction of the data should not be catastrophically in error at energies over 3 Mev. The peak in the neighborhood of 6 Mev, which appears at least at 60 and 120° is unexpected. Because of beam-counting and dead-time difficulties, absolute magnitudes are uncertain by at least 25% plus the undetermined percentage due to efficiency uncertainties.

While the apparatus automatically recorded "proton spectra" for each case studied, it was found that *BC* coincidences in the apparatus shown were inadequate to assure that the observed charged particles originated in the target. For this reason the proton spectra obtained are interesting but not helpful for estimating the actual proton spectra.

Table 8.3.2 gives gross observed counting rates during the entire series of short runs. The values should be helpful in estimating counting rates for future experiments, even though the present runs were too short to produce meaningful spectra. As indicated above, effective proton beam strengths of the order of 1.5×10^6 protons/sec are contemplated during future gross duty-cycle bursts; so at the Harvard cyclotron with a 4% gross duty cycle the apparatus can handle about 2×10^8 protons/hr. Adequate data should be obtainable at low resolution for a limited number of cases.

Table 8.3.2. Summary of Gross Counting Information

Copper Target Thickness (g/cm^2)	θ, Angle from Beam (deg)	Total Protons in Beam	Average Beam Strength (protons/sec)	Total Counts in Time-of-Flight Spectrum	Neutron Counts/10^6 Protons in Energy Bins Shown[a]				
					2–5 Mev	5–10 Mev	10–20 Mev	20–70 Mev	>70 Mev
		$\times 10^6$	$\times 10^3$						
25.2	10	22.7	14	1725	25 ± 1	14 ± 1	11 ± 0.6	9.5 ± 0.6	1.7 ± 0.3
8.6	10	8.1	16	1710[b]	15 ± 1	19 ± 1.5	7.6 ± 1	59[b]	19[b]
0	10	21.9	15	110	0.6 ± 0.1	0.6	0.5	1 ± 0.2	0.4
25.2	30	26.5	53	1690	10.7 ± 0.6	12.8	9.3 ± 0.5	8.8	0.5 ± 0.04
8.6	30	12.9	13	160	1.9 ± 0.4	2.2 ± 0.4	1.7	2.2	1.4
0	30	14.4	14	77	0.8	0.5	0.4 ± 0.2	0.8	0.2
25.2	60	13	13	510	6 ± 0.7	12 ± 1	4	3.5	3.0
8.6	60	8	16	83	3.5 ± 0.7	5.7 ± 0.8	4.0 ± 0.8	3.5	0.7
0	60	15	15	47	0.3	0.2	0.1	0.2	0.3
25.2	120	15	15	406	4.2 ± 0.6	9.8 ± 0.8	3.4	1.6	2.3 ± 0.4
8.6	120	8	16	73	1.2 ± 0.4	3.1	0.9	0.6	0.2 ± 0.1
0	120	16	16	46	0.2	0.3	0.2	0.1	0.1

[a] Representative errors shown are based on counting statistics.

[b] Many protons accidentally registered here as neutrons.

Development of Improved Instrumentation

In the period since the preliminary measurements, efforts have been made to improve the original apparatus in the following ways:

1. The ambiguity in the definition of the incident beam is to be resolved by using two *A* detectors in fast coincidence with each other.
2. All the electronics in the *A*-channel, dealing with the incident beam, will be fast.
3. The time isolation of the incident protons used will be more positively assured by using an "isolated signal detector" which yields output pulses for protons isolated from their neighbors by at least 60 nsec. The complementary logic was used during preliminary measurements.
4. Pulse-shape discrimination methods will be used to ensure that random gamma-ray backgrounds are not seriously large. To employ these methods, an NE-213 liquid scintillator[6] will be employed for the *B* detector.
5. Fast circuitry will be employed in the scattered particle detectors, *B* and *C*, so that measurements can be made at quite small angles with thin targets under conditions such that a substantial portion of the beam passes through these detectors.
6. A separate detection scheme will be employed to allow observation of proton spectra. The scheme includes an arrangement with minimum mass in the scattered beam path and a thin (0.5-mm) plastic detector (*C'*) placed about halfway between the target and the scattered-particle detector (*B'*) to create a telescope arrangement.
7. The anticoincidence detector, *C*, will be formed from thicker (4-mm) plastic, and an improved light pipe will be used so that effective anticoincidence action will be assured.

Figure 8.3.7 shows a block diagram of the equipment to be used in the next trial runs. It is expected that only minor changes will remain to be made to attain fully satisfactory operation after final testing of the arrangement shown.

Most of the fast circuits are in the final design or laboratory testing stage. The circuitry will be based largely on tunnel-diode univibrator designs similar to those described by Whetstone.[7] Adequately small propagation delays and rise and fall times can be attained, though some difficulty with dead times is anticipated. Only in the time-to-pulse-height converter will there be a problem caused by "walk" as a function of pulse amplitude from detector *B*.

If neutron spectra are to be measured over a range from 0.5 to 155 Mev, the light pulses in a 1-in.-thick plastic phosphor will have a dynamic range of 470:1. Since the minimum electronic pulse will be a few milliamperes at its peak, and since under the conditions of the experiment the 58 AVP photomultiplier is capable of producing maximum pulses of only about 0.5 amp, the dynamic range of electronic pulses will be smaller than that of the light pulses. Nevertheless, the electronic pulse range is usually large, and it is felt that this factor is the source of the major design problems in developing a time-to-pulse-height converter with 1-nsec resolution.

---

[6] Product of Nuclear Enterprises, Ltd., Winnipeg, Canada.

[7] A. Whetstone and S. Kounoso, *Rev. Sci. Instr.* **33**, 423 (1962).

UNCLASSIFIED
ORNL-LR-DWG 72860

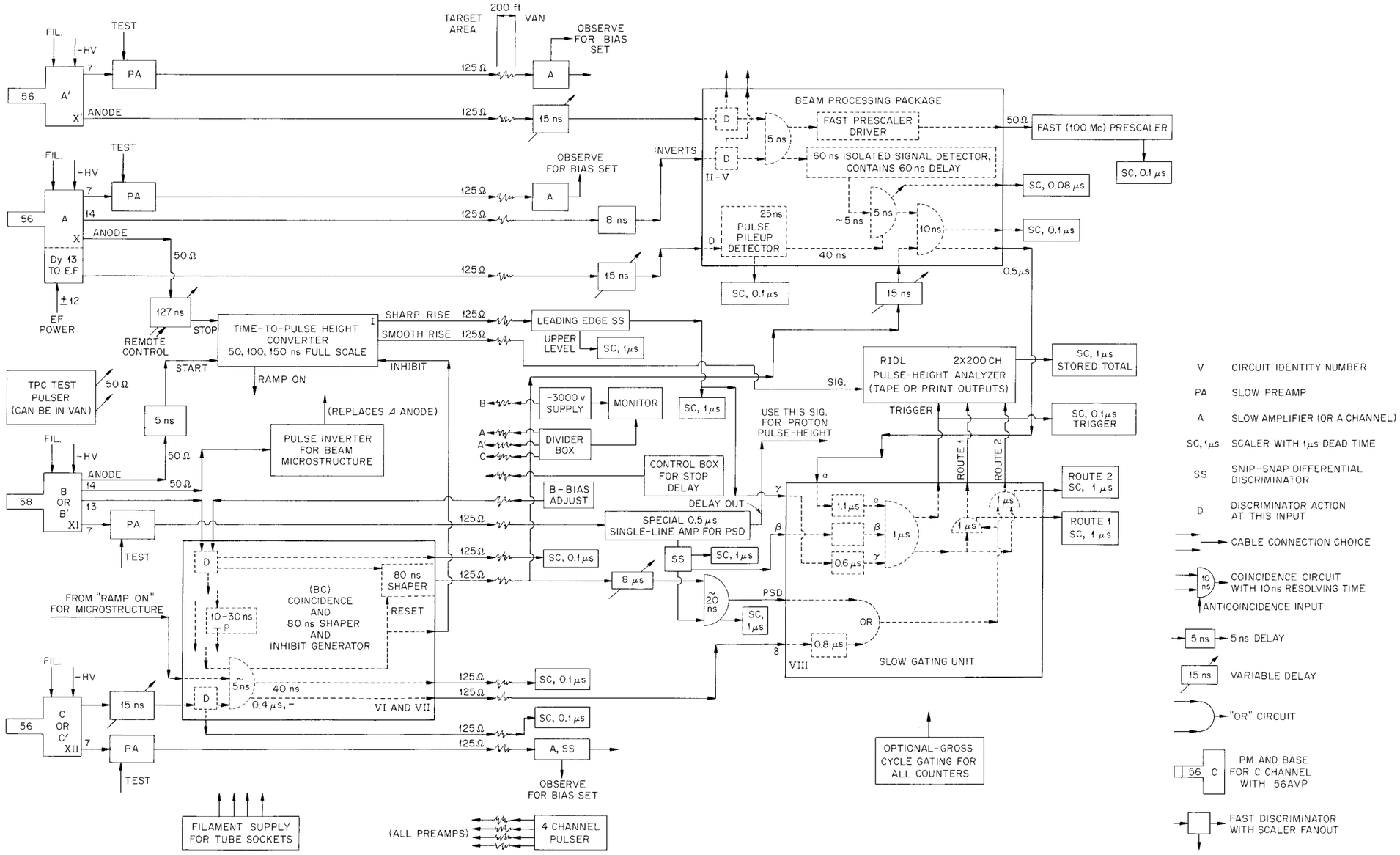

Fig. 8.3.7. Block Diagram of Neutron Time-of-Flight Spectrometer.

8.4. BONNER SPHERES AND THRESHOLD DETECTORS FOR NEUTRON SPECTROSCOPY

W. R. Burrus

The variety of neutron spectrometers required to encompass the wide range of energies considered in the space vehicle shielding problem is pointed out in Sec. 8.0. For neutron energies < 10 Mev, the use of so-called "Bonner spheres" has been investigated during preliminary experiments at the Harvard University synchrocyclotron, and the feasibility of augmenting the Bonner sphere data above 10 Mev by threshold detector techniques has been examined.

Experimental Procedure – Bonner Spheres

A Bonner sphere[1] basically consists of a thermal-neutron detector surrounded by a spherical mass of polyethylene moderator. For the present work the plans of Bonner have been followed as closely as possible, so that counting efficiency calibrations determined by him could be used. The thermal-neutron detector is a $Li^6I(Eu)$ scintillation crystal, essentially totally absorbing at thermal energies and "transparent" to energies > 100 ev. It is therefore predominantly sensitive to low-energy neutrons. As moderating material is added and the sphere diameter is increased, sensitivity to higher-energy neutrons is increased. Table 8.4.1 gives the counting efficiencies used, over a neutron energy range from 0.01 ev to 160 Mev, for spheres of five different diameters, as well as for the $Li^6I(Eu)$ detector both with and without a 30-mil-thick cadmium cover. The data from thermal energies to 15 Mev were compiled from large-scale graphs supplied by Bonner and are quoted to be accurate to about 6%. From 15 to 160 Mev, the data represent a crude extrapolation by the author.

A diagram of the simple experimental arrangement for the preliminary experiments is shown as Fig. 8.4.1.

Experimental Results – Bonner Spheres

Pulse-height distributions obtained with 2- and 8-in.-diam polyethylene spheres are shown in Figs. 8.4.2 and 8.4.3, respectively. In both cases the particles incident on the target were 156-Mev protons, and the Bonner sphere was located 40 cm from the target on a line 30° from the beam-target axis. The target in the case of the 2-in.-diam sphere was a copper disk with a hole punched through its center, while for the 8-in.-diam sphere it was a solid copper disk. Both targets had a thickness of 31.8 g/cm^2. A considerable background is evident in the data from the smaller sphere and punched-out target, mostly due to protons scattered from the primary beam. It should be possible to subtract the background satisfactorily by recording the entire pulse-height distribution and performing a least-squares analysis for the area of the thermal peak. Few pulse-height spectra were recorded in these tests since no significant background had been anticipated.

Net counts recorded for various sphere diameters are shown in Table 8.4.2. The values represent the total counts less background for $\sim 10^{10}$ protons incident on the copper target.

---

[1] R. L. Bramblett, R. I. Ewing, and T. W. Bonner, *Nuclear Instr. & Methods* **9**, 1 (1960).

Table 8.4.1. Counting Efficiencies for Bonner Spheres

Neutron Energy (ev)	Counting Efficiency (counts n^{-1} cm^{-2})						
	Bare Detector	Cd-Covered Detector	2-in.-diam Sphere	3-in.-diam Sphere	5-in.-diam Sphere	8-in.-diam Sphere	12-in.-diam Sphere
1.0 (−2)[a]	0.122	0.000	0.0820	0.0740	0.0420	0.0100	0.0040
1.6 (−2)	0.122	0.000	0.0850	0.0768	0.0448	0.0116	0.0041
2.5 (−2)	0.120	0.000	0.0880	0.0796	0.0476	0.0132	0.0043
4.0 (−2)	0.118	0.000	0.0930	0.0824	0.0504	0.0148	0.0044
6.3 (−2)	0.116	0.000	0.0960	0.0852	0.0532	0.0164	0.0045
1.0 (−1)	0.114	0.000	0.0980	0.0880	0.0560	0.0180	0.0046
1.6 (−1)	0.110	0.000	0.0990	0.0924	0.0600	0.0200	0.0047
2.5 (−1)	0.102	0.000	0.1000	0.0968	0.0640	0.0220	0.0048
4.0 (−1)	0.116	0.116	0.1000	0.1012	0.0680	0.0240	0.0050
6.3 (−1)	0.110	0.110	0.1008	0.1056	0.0720	0.0260	0.0051
1.0 (0)	0.084	0.084	0.1016	0.1106	0.0762	0.0282	0.0052
1.6 (0)	0.076	0.076	0.1020	0.1146	0.0806	0.0300	0.0054
2.5 (0)	0.068	0.068	0.1030	0.1194	0.0850	0.0318	0.0057
4.0 (0)	0.060	0.060	0.1040	0.1224	0.0896	0.0336	0.0059
6.3 (0)	0.052	0.052	0.1000	0.1262	0.0940	0.0354	0.0062
1.0 (1)	0.042	0.042	0.0940	0.1302	0.0986	0.0372	0.0064
1.6 (1)	0.036	0.036	0.0892	0.1338	0.1032	0.0390	0.0067
2.5 (1)	0.028	0.028	0.0862	0.1374	0.1076	0.0408	0.0070
4.0 (1)	0.020	0.020	0.0804	0.1410	0.1120	0.0426	0.0072
6.3 (1)	0.010	0.010	0.0776	0.1446	0.1164	0.0444	0.0075
1.0 (2)	0.002	0.002	0.0746	0.1482	0.1208	0.0462	0.0078
1.6 (2)	0.000	0.000	0.0712	0.1500	0.1258	0.0480	0.0080
2.5 (2)	0.000	0.000	0.0678	0.1520	0.1308	0.0498	0.0083
4.0 (2)	0.000	0.000	0.0646	0.1516	0.1358	0.0516	0.0085
6.3 (2)	0.000	0.000	0.0614	0.1510	0.1408	0.0534	0.0088
1.0 (3)	0.000	0.000	0.0582	0.1500	0.1458	0.0552	0.0090
1.6 (3)	0.000	0.000	0.0548	0.1478	0.1514	0.0574	0.0092
2.5 (3)	0.000	0.000	0.0516	0.1446	0.1570	0.0596	0.0095
4.0 (3)	0.000	0.000	0.0484	0.1412	0.1626	0.0618	0.0097
6.3 (3)	0.000	0.000	0.0452	0.1378	0.1682	0.0640	0.0100
1.0 (4)	0.000	0.000	0.0420	0.1346	0.1740	0.0660	0.0102
1.6 (4)	0.000	0.000	0.0386	0.1290	0.1798	0.0724	0.0116
2.5 (4)	0.000	0.000	0.0354	0.1236	0.1856	0.0790	0.0132
4.0 (4)	0.000	0.000	0.0322	0.1182	0.1914	0.0856	0.0148
6.3 (4)	0.000	0.000	0.0290	0.1126	0.1972	0.0920	0.0164
1.0 (5)	0.000	0.000	0.0258	0.1072	0.2032	0.0986	0.0180
1.6 (5)	0.000	0.000	0.0222	0.0986	0.2082	0.1148	0.0222
2.5 (5)	0.000	0.000	0.0180	0.0900	0.2136	0.1320	0.0274
4.0 (5)	0.000	0.000	0.0132	0.0780	0.2152	0.1578	0.0394
6.3 (5)	0.000	0.000	0.0098	0.0618	0.2118	0.2022	0.0618
1.0 (6)	0.000	0.000	0.0066	0.0596	0.1930	0.2240	0.0900
1.6 (6)	0.000	0.000	0.0044	0.0350	0.1580	0.2250	0.1360
2.5 (6)	0.000	0.000	0.0026	0.0230	0.1240	0.2120	0.1600
4.0 (6)	0.000	0.000	0.0016	0.0148	0.0880	0.1800	0.1650
6.3 (6)	0.000	0.000	0.0010	0.0092	0.0630	0.1640	0.1840
1.0 (7)	0.000	0.000	0.0008	0.0064	0.0420	0.1012	0.1252
1.6 (7)	0.000	0.000	0.0008	0.0056	0.0320	0.0800	0.1040
2.5 (7)	0.000	0.000	0.0008	0.0060	0.0260	0.0680	0.0880
4.0 (7)	0.000	0.000	0.0008	0.0060	0.0260	0.0600	0.0780
6.3 (7)	0.000	0.000	0.0008	0.0060	0.0260	0.0540	0.0720
1.0 (8)	0.000	0.000	0.0008	0.0060	0.0260	0.0520	0.0680
1.6 (8)	0.000	0.000	0.0008	0.0060	0.0260	0.0520	0.0660

[a]Digit in parentheses denotes power-of-ten multiplier.

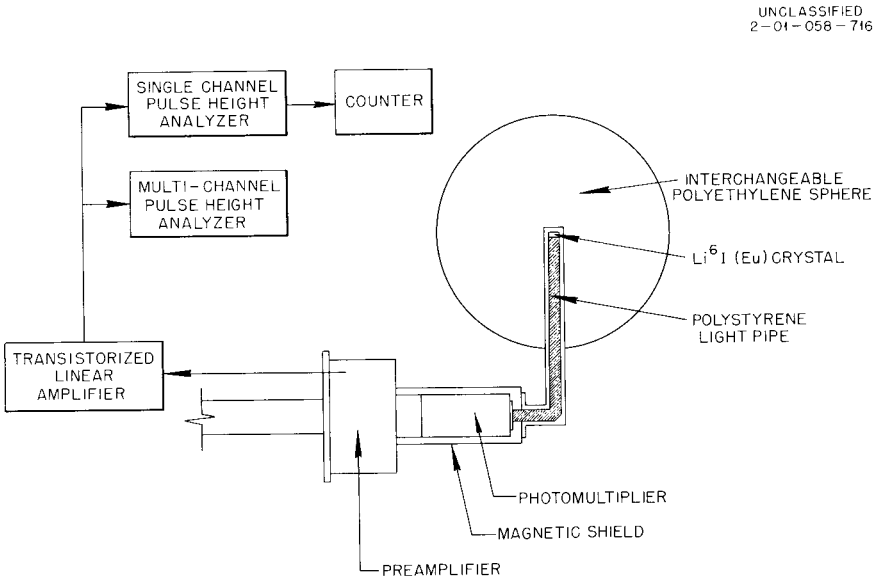

Fig. 8.4.1. Experimental Arrangement for Bonner Sphere Tests.

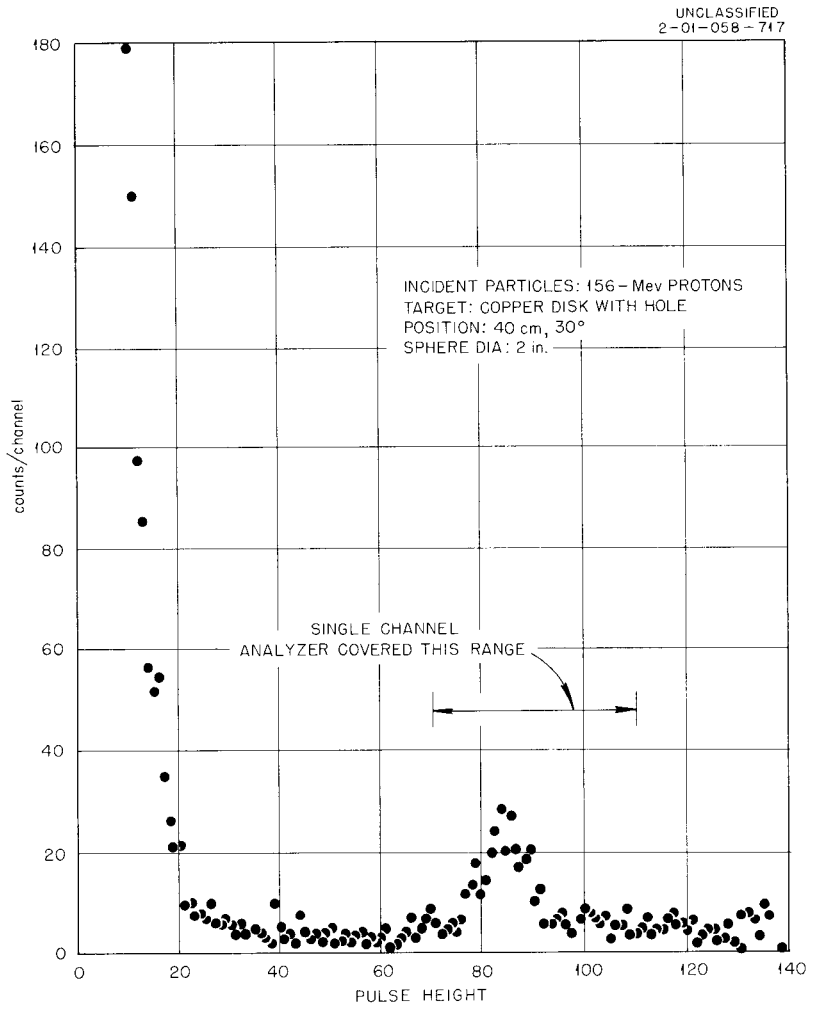

Fig. 8.4.2. Pulse-Height Distribution of Neutrons Resulting from 156-Mev Protons Incident Upon Copper, as Detected by a 2-in.-diam Bonner Sphere.

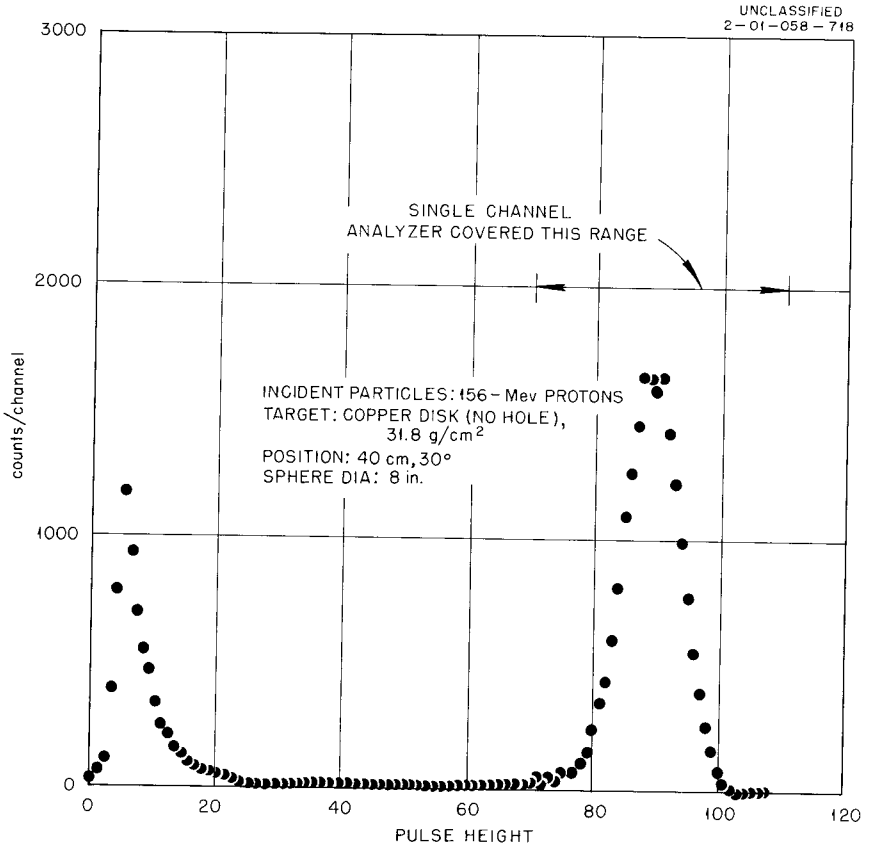

Fig. 8.4.3. Pulse-Height Distribution of Neutrons Resulting from 156-Mev Protons Incident Upon Copper, as Detected by an 8-in.-diam Bonner Sphere.

Table 8.4.2. Total Counts in Thermal Peak for Bonner Spheres of Various Diameters

Detector	Net Counts[a]
Bare $Li^6I(Eu)$	~ 200[b]
Cd-covered $Li^6I(Eu)$	~ 50[b]
2-in. sphere	300
3-in. sphere	1300
5-in. sphere	3800
8-in. sphere	4900
12-in. sphere	3400

[a] $\sim 10^{10}$ 156-Mev photons incident on 31.8-g/cm^2-thick copper target. Detector 40 cm from target and 30° from beam axis. Beam-off background and counting loss corrections negligible.

[b] Background estimated from similar experiments in which aluminum targets were used and pulse-height distributions recorded.

Experimental Procedure – Threshold Detectors

Three threshold detectors were tested to determine their usefulness for neutron energies > 10 Mev. Two were spiral fission chambers containing ~150 mg of U^{238} and ~150 mg of bismuth. A block diagram of the arrangement is shown in Fig. 8.4.4. The organic scintillator shown was used in anticoincidence with the fission chamber to discriminate against proton-induced fission.

The third threshold detector employed the $C^{12}(n,2n)C^{11}$ reaction, by measuring the 20.5-m β^+ activity induced in 2 by 2 in. cylinders of Polyfluor plastic scintillator. The cylinders, after exposure to the neutrons, were counted on a conventional pulse-height analyzer using a 6655A photomultiplier. Cross sections used to compute efficiencies for all detectors are given in Table 8.4.3.

Experimental Results – Threshold Detectors

The results obtained with the detectors described above are listed in Table 8.4.4. Because of the difficulty noted below, the fission chamber counts were taken without the anticoincidence guard. The

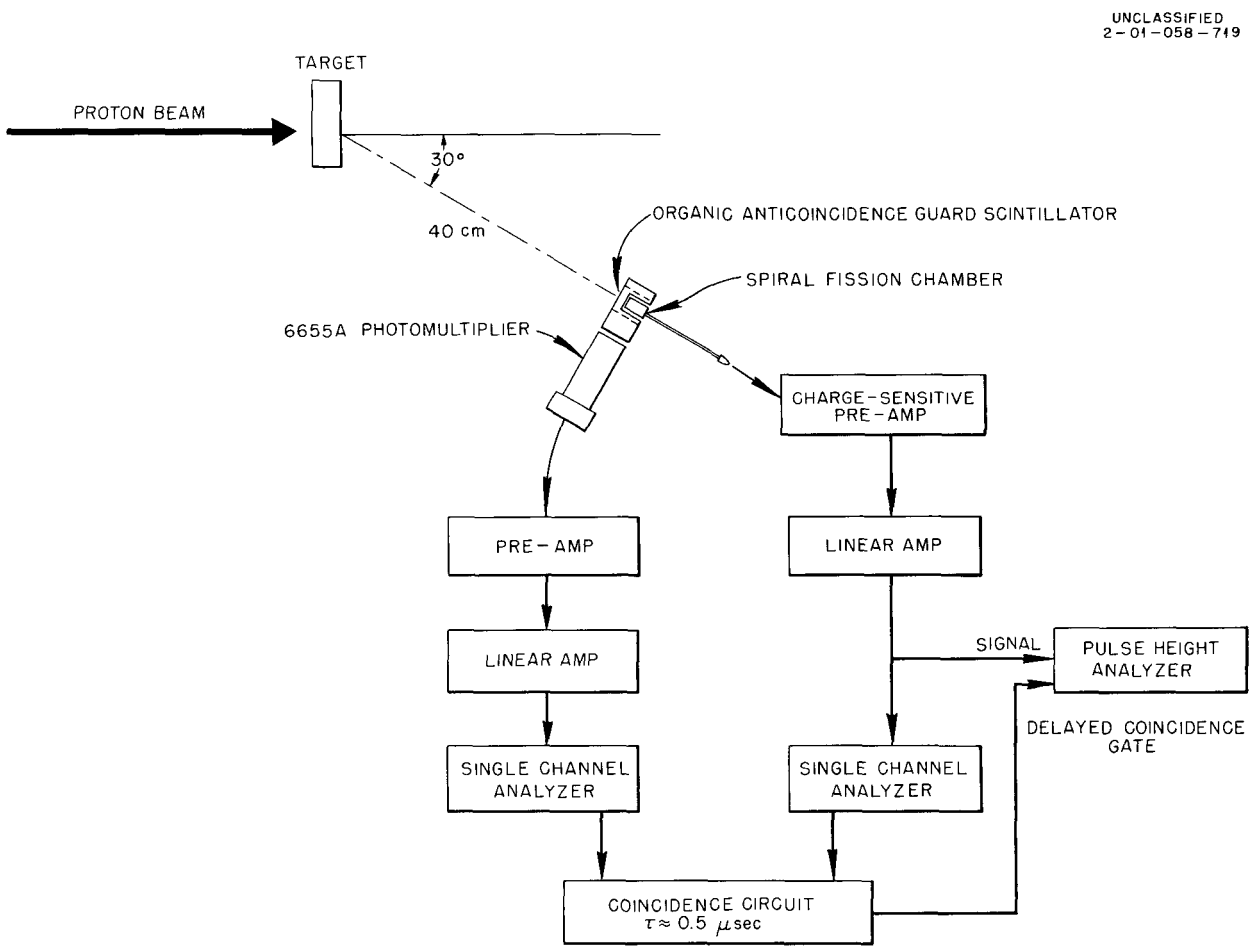

Fig. 8.4.4. Arrangement for Threshold Detector Experiments.

Table 8.4.3. Cross Sections Used for Threshold Detectors

Energy (Mev)	U^{238} (n,f) (barns)[a]	Bi (n,f) (barns)[b]	C $(n,2n)$ (barns)[c]
0.40	0.000		
0.63	0.001		
1.00	0.18		
1.6	0.30		
2.5	0.58		
4.0	0.56		
6.3	0.70		
10	1.01		
16	1.30		
25	1.60	0.000	0.000
40	1.60	0.007	0.025
63	1.60	0.022	0.030
100	1.60	0.095	0.033
160	1.60	0.150	0.033

[a]Accurate within 5% for energies below 16 Mev and probably within 20% for energies up to 160 Mev.

[b]Probably accurate within a factor of 2 for energies up to 100 Mev and within a factor of 3 for energies up to 160 Mev.

[c]Probably accurate within 30%.

Table 8.4.4. Experimental Results for Threshold Detectors

Detector	Number of Atoms in Sensitive Region	Number of Counts[a] per 10^{11} Incident Protons
U^{238} Spiral Fission Chamber (FS-110)	$N_U = 3.8 \times 10^{20}$	1250 ±80%
Bi Spiral Fission Chamber (FS-109)	$N_{Bi} = 3.66 \times 10^{20}$	25 ±40%
2 by 2 in. Polyfluor Cylinder	$N_C = 5.06 \times 10^{24}$	1.2×10^4 ±50%[b]

[a]Indicated errors include allowance for possible proton interaction. U^{238} data were not used in analysis.

[b]Value listed is total activation based on β^+ counting.

possibility of proton interaction is reflected in the large errors quoted. The U^{238} fission chamber data, of dubious value, were not used in the analysis of the data.

It was difficult to obtain satisfactory data with the threshold counters. If the primary proton beam intensity was adjusted so that a count rate of a few counts per second was obtained in the fission counters, then the anticoincidence guard crystal became jammed. Trouble was also encountered in using the $C^{12}(n,2n)C^{11}$ reaction because of the competing $C^{12}(p,pn)C^{11}$ reaction in the detector. Further development might eliminate these difficulties, but since the energy range above 10 Mev presumably will be adequately covered by other devices, the use of threshold detectors has been abandoned.

Calculation of Neutron Spectra

The raw material from which the neutron spectrum was calculated consisted of the efficiencies of Table 8.4.1, the cross sections of Table 8.4.3, and the experimental counting rates of Tables 8.4.2 and 8.4.4. It was known from published measurements and from theoretical calculations of the evaporation neutron spectrum that the neutron spectrum should be fairly slowly varying. This "regularity" of the spectrum was taken into account by assuming that the spectrum $\phi(u)$, where $u = \log_{10}(E/1\ \text{Mev})$, could be expressed as a positive combination of smooth functions,

$$\phi(u) = \sum_{k=1}^{m} q_k R_k(u) ,$$

where $q_k \geq 0$ and $R_k(u)$ are suitable slowly varying functions. Several typical $R_k(u)$ functions are shown in Fig. 8.4.5. Fifty-two such functions were used in the present calculation.

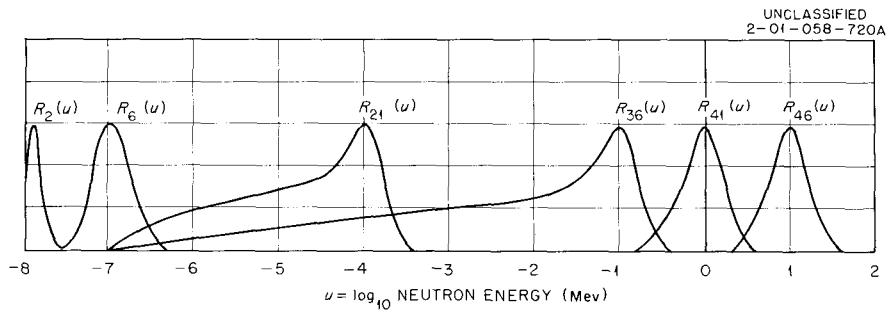

Fig. 8.4.5. Six Typical $R_k(u)$ Functions.

An approximate spectrum was then obtained by solving for the q_k's by the method of optimal combinations.[2] Briefly, the method consists of arbitrarily specifying the response function of a fictitious crude spectrometer and then trying to fit the response function with the counting efficiency functions of the actual detectors. The fictitious spectrometer chosen had a resolution (full width at half maximum) of 0.8 decade in energy.

[2]Although not specifically identified by this name, this is the method described by W. R. Burrus, *Neutron Phys. Div. Ann. Progr. Rept. Sept. 1, 1961*, ORNL-3193, p 44.

Results

The results of the present preliminary experiments have been analyzed in the manner described above to give the tentative differential neutron energy spectrum shown in Fig. 8.4.6. The choice of the fictitious spectrometer with its resolution of 0.8 decade is reflected in the resolution shown on the figure.

Having obtained the approximate spectrum, one may then calculate the biological dose resulting from such a spectrum. Alternatively, the biological dose may be calculated directly by the method of optimal combinations. It was decided to calculate the entire distribution function, or "importance function," for biological dose, that is, the fraction of the total biological dose due to neutrons with energy above E. The result is shown in Fig. 8.4.7. From this curve an idea as to which part of the spectrum is most important from a biological damage viewpoint can be obtained. Somewhat unexpectedly, the present work shows that one-half the dose comes from neutrons with energies > 20 Mev and that only ~20% is due to neutrons with energies < 4 Mev.

The relation between biological dose and neutron flux is fairly complicated. In calculating the dose due to the neutron spectrum of the present work, values were taken from NBS Handbook 63[3] for that part of the spectrum below 10 Mev. These values are based on the energy deposited in a 30-cm-thick slab of

[3] *Protection Against Neutron Radiation up to 30 Million Electron Volts,* NBS-63 (1957).

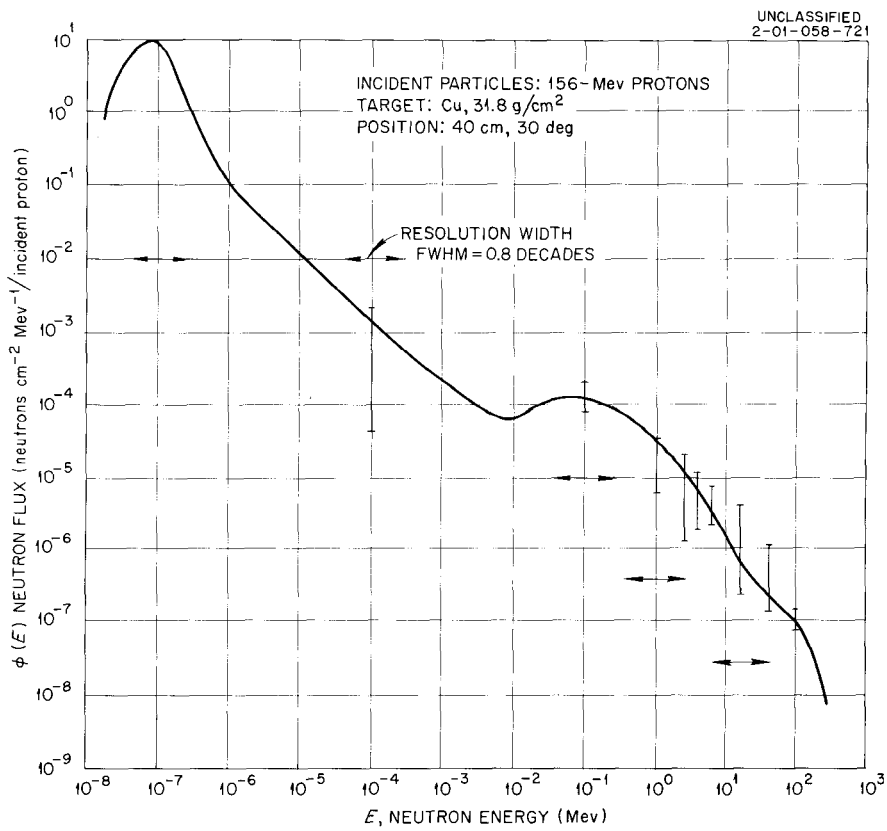

Fig. 8.4.6. Differential Neutron Energy Spectrum from 156-Mev Protons on Copper.

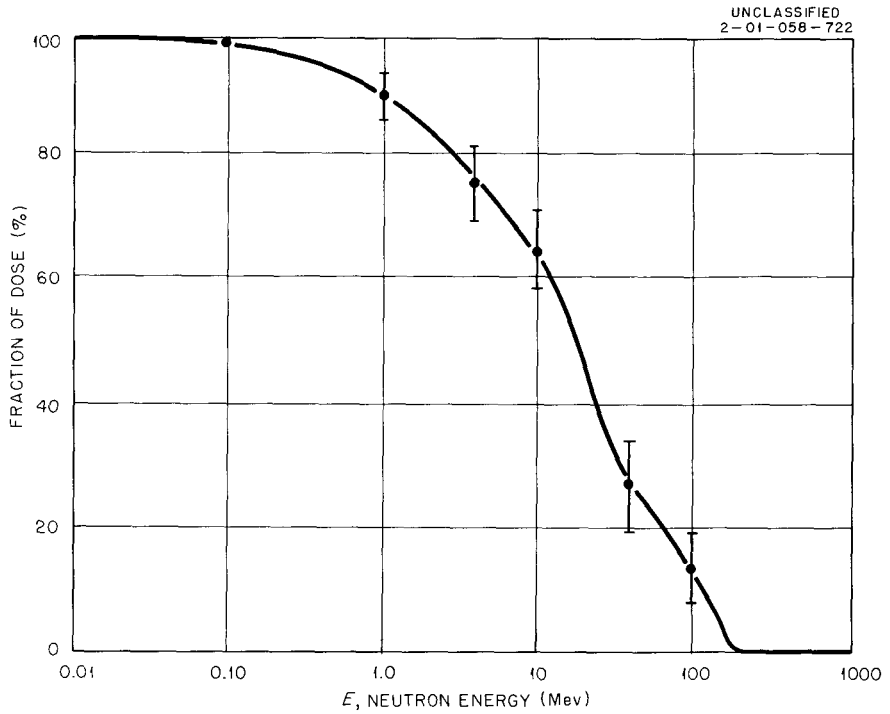

Fig. 8.4.7. Biological Dose Distribution.

tissue. They were weighted by a relative biological effectiveness (RBE) taken from NBS Handbook 69[4] and based on the linear energy transfer of the elementary event. Above 10 Mev the assumption was made that the product of the effective RBE and the effective buildup remained constant at the value of 6.5 found for 10 Mev, and the energy removal curve of Gibson[5] was used in lieu of the first-collision dose curve. The resulting curves for biological dose and first-collision dose are shown in Fig. 8.4.8. The data of Fig. 8.4.8, which result in an integrated dose rate of 1.8×10^{-12} ($\pm 40\%$) rem per incident proton, are probably reliable within a factor of ~3 at 160 Mev.

Problems Remaining in Use of Bonner Spheres

No measurements of the efficiencies of Bonner spheres in the energy region above 15 Mev are available. Efforts are under way to determine the sensitivity of results to errors in the efficiency in the region from 15 to 160 Mev. In the event that such errors are important, a Monte Carlo calculation of the high-energy response of the spheres appears feasible.

Although direct proton response may be subtracted from the thermal-neutron response peak, secondary neutrons produced within the moderator by *p,n* interactions are indistinguishable from target neutrons.

---

[4] *Maximum Permissible Body Burdens and Maximum Permissible Concentrations of Radionuclides in Air and Water for Occupational Exposure*, NBS-69 (1959).

[5] W. A. Gibson, *Energy Removed from Primary Proton and Neutron Beams by Tissue*, ORNL CF-61-6-48 (June 1961).

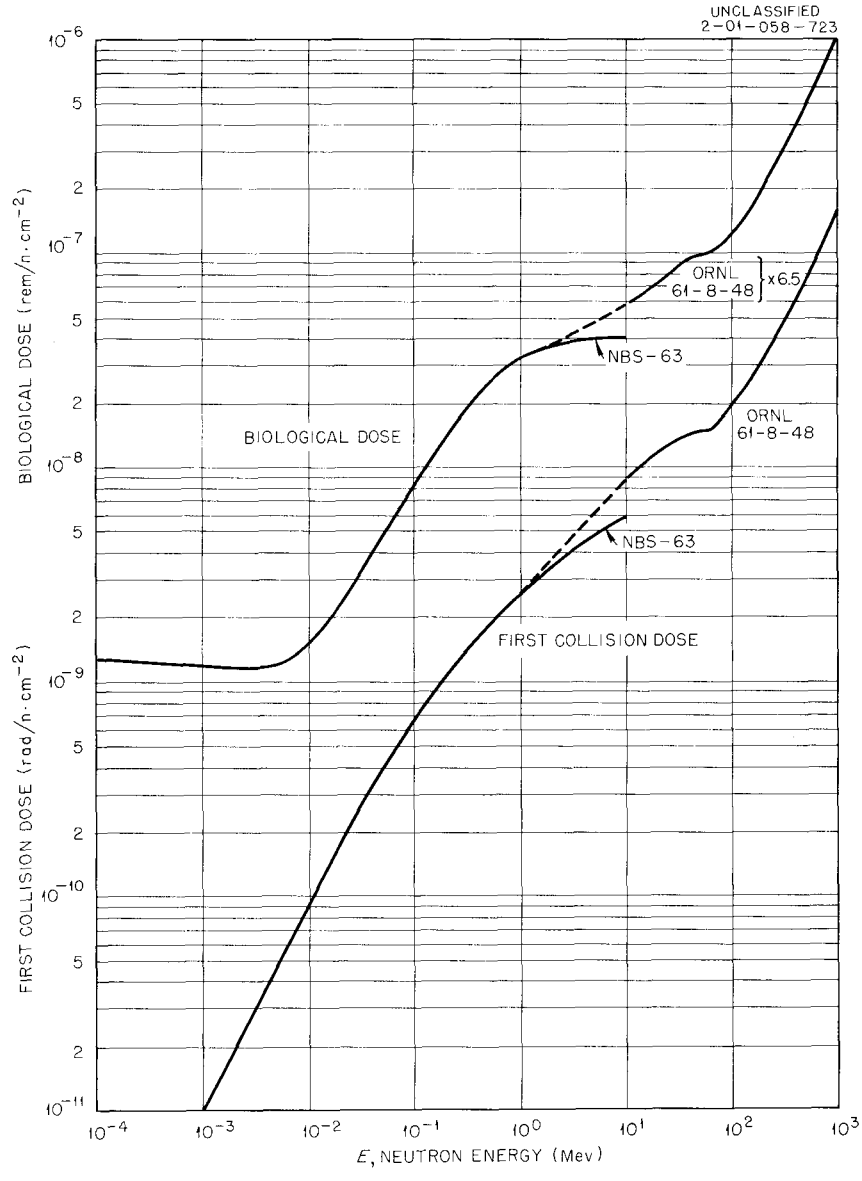

Fig. 8.4.8. Biological Dose and Removal Dose as a Function of Neutron Energy.

Additional experiments, with the proton beam directly incident on the sphere, are planned to estimate the importance of this effect.

Variations in the size of commercially furnished $Li^6I(Eu)$ crystals and small differences in techniques used to analyze the thermal-neutron peak cause slight discrepancies from published calibration values. Spheres to be used in future experiments will be calibrated against a recently obtained standardized Am-Be neutron source.

If dose distributions, such as the curve of Fig. 8.4.7, are to be important in future work, better values of flux-to-dose conversion ratios must be sought. It may be more plausible to base conversions on a tissue sphere rather than a tissue slab.

8.5. SPECTROMETRY FOR GAMMA RAYS FROM PROTON-BOMBARDED NUCLEI

W. Zobel

The spectrometer chosen for the preliminary measurements of secondary gamma rays produced by the bombardment of nuclei with ~156-Mev protons (see Sec. 8.0) was a multicrystal spectrometer. For low-energy (<2 Mev) photons it will be used as a total-absorption spectrometer, and for photons with energies above 2 Mev, as a pair spectrometer. Multicrystal spectrometers in use at ORNL have been described previously;[1] however, to improve the efficiency, the side crystals were redesigned so that the solid angle subtended by them at the center of the central crystal was greatly increased. The resulting configuration is shown in Fig. 8.5.1. Each side crystal is a frustum of a cone, with a base diameter of 4.000 in., a top diameter of 3.000 in., and a height of 1.871 in. A semicircular groove is cut into the base along a diameter. Both side crystals are mounted in a thin-walled aluminum can and are optically decoupled. A 3-in. photomultiplier tube, Du Mont Type K-1846, views each side crystal as shown. The central crystal, 1 in. in diameter and $1\frac{1}{2}$ in. in length, fits into the cylindrical hole formed by the semicircular grooves.

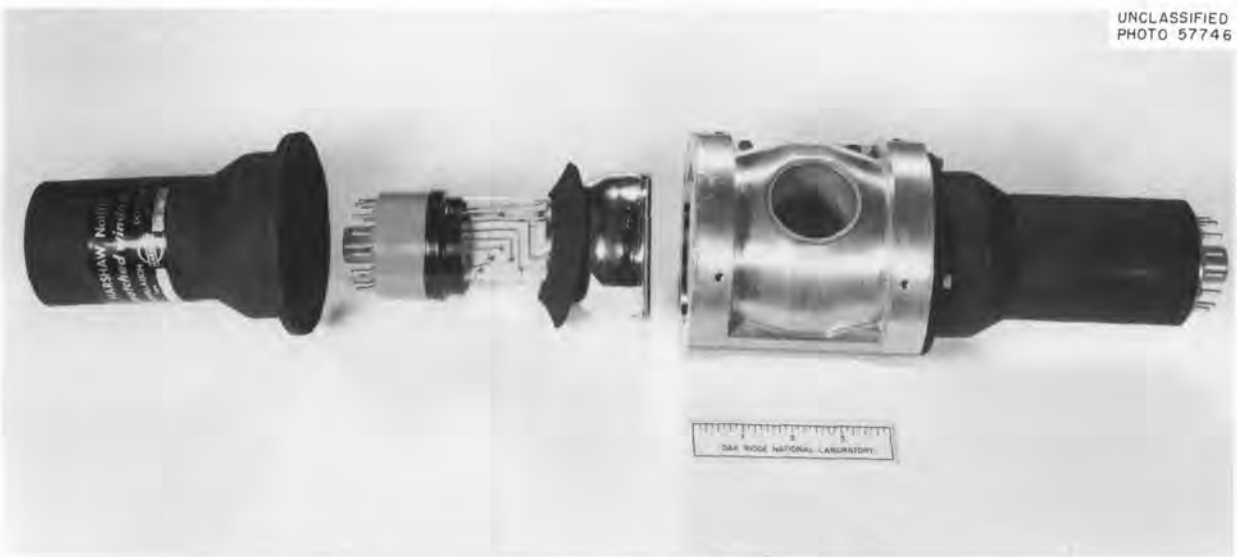

Fig. 8.5.1. Crystals and Photomultipliers of the Gamma-Ray Spectrometer.

A block diagram of electronics, as used for the pair configuration, is shown in Fig. 8.5.2. The central crystal is labelled *A*, the side crystals *B* and *C*. The amplifiers are Cosmic Radiation Labs., Inc., Model 901. The introduction of the snip-snap crossover pick-off single-channel analyzers eliminated the requirement for a slow coincidence circuit. The triple coincidence circuit used had a resolving time of ~130 nsec.

[1] T. A. Love, R. W. Peelle, and F. C. Maienschein, *Electronic Instrumentation for a Multiple-Crystal Gamma-Ray Scintillation Spectrometer*, ORNL-1929 (Oct. 25, 1955).

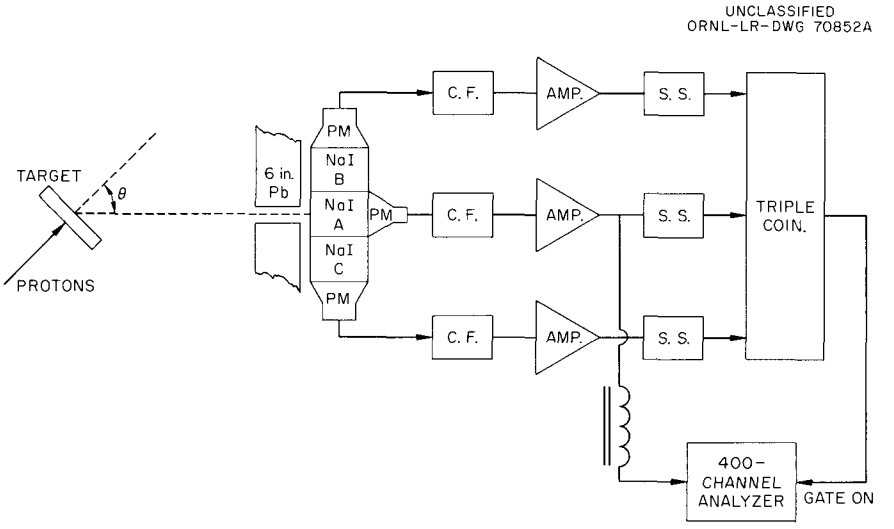

Fig. 8.5.2. Original Arrangement of Spectrometer Components in Pair Configuration.

For use as a total absorption spectrometer, the snip-snaps in the *B* and *C* channels are used as integral discriminators. Their outputs are placed in anticoincidence with the output of the *A* channel, and the resulting signal is used as the 400-channel analyzer gate.

The detectors are enclosed in a lead housing 6 in. thick on the side nearest the target and at least 4 in. thick on all other sides. During part of the preliminary runs an additional 8-in.-thick layer of lithiated paraffin, intended to reduce the neutron-induced background, surrounded the lead. A collimator through the target side of the housing permits radiation to fall on the central crystal only.

For the trial runs conducted thus far, only the pair spectrometer was used. During the initial runs, in which an aluminum target was used, it became apparent that a large background existed that was connected with radiation emanating from the target. The collimator was replaced by a solid lead plug and lithiated paraffin, but the coincidence counting rate was reduced only by about a factor of 2. Removal of the paraffin from the shield did not appear to influence the coincidence counting rate, but removal of the aluminum target reduced it by a factor of more than 10. Similar results were observed later when a copper target was used in the proton beam. The proper functioning of the spectrometer, however, was demonstrated by the data from a carbon target, shown in Fig. 8.5.3. It should be noted that these data are of a very preliminary nature, with no corrections of any type applied. Based upon a rough energy calibration, the very prominent peak appearing at about channel 136 corresponds to a gamma-ray energy of 4.5 Mev. This is in good agreement with the well-known 4.43-Mev gamma ray from carbon.

The results of the trials suggest that the large background is due to neutron-induced radiation. To verify this hypothesis and, if it is correct, to minimize the background, several modifications are being made. The shield around the spectrometer is being changed so that variable thicknesses of lead or lithiated paraffin may be used. It is felt that removal of mass from around the detectors will reduce the chance of neutron interaction and consequently reduce the background. Additionally, an attempt will be made to reduce the neutron-induced background by using time-of-flight techniques. A block diagram

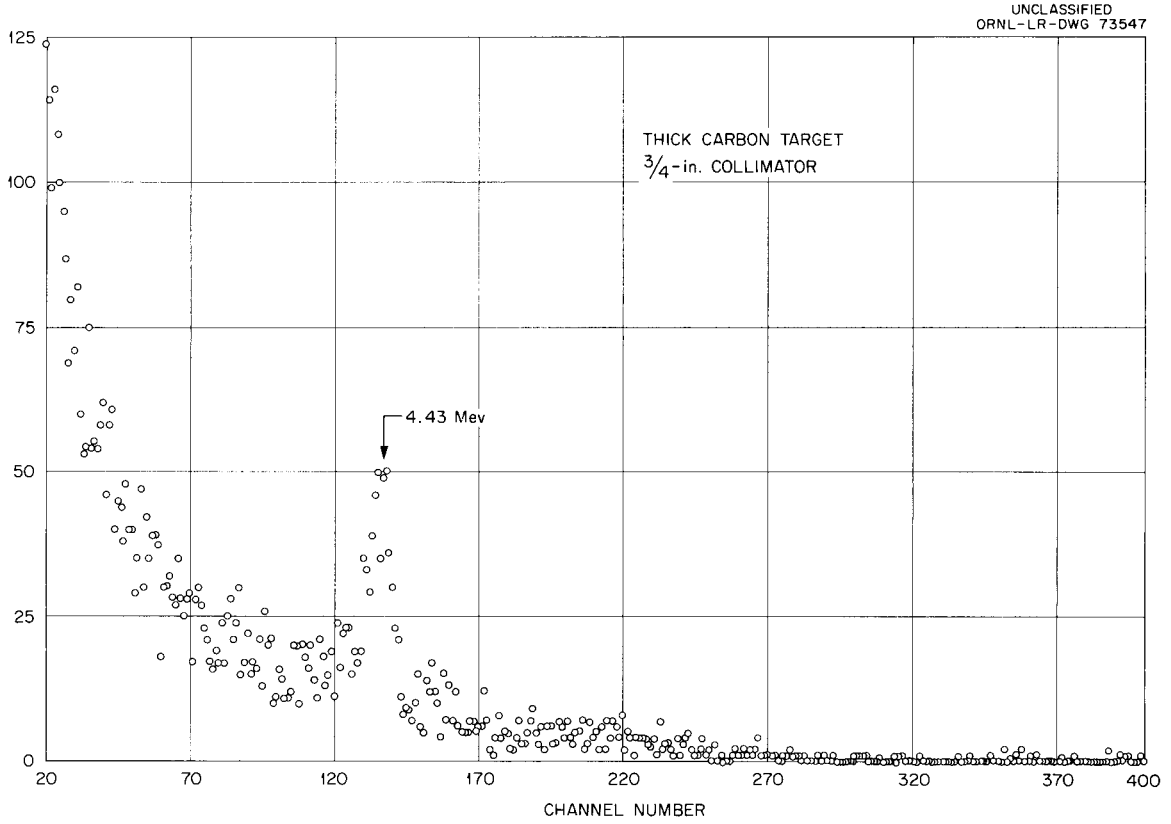

Fig. 8.5.3. Uncorrected Pulse-Height Spectrum of Gamma Rays Resulting from Bombardment of a Thick Carbon Target by ~156-Mev Protons.

of the revised electronics is shown in Fig. 8.5.4. The method depends on the experimental observation that the protons are produced in the machine in bursts, with a frequency depending on the rf of the accelerating voltage. A thin ($\sim$1 mm) plastic scintillator will detect the beam, and only those gamma rays detected in coincidence with the beam will be accepted. The distance from the target to the detectors will be so chosen that none but the most energetic neutrons can reach the detector prior to the end of each proton burst. The components have been designed and are presently being tested.

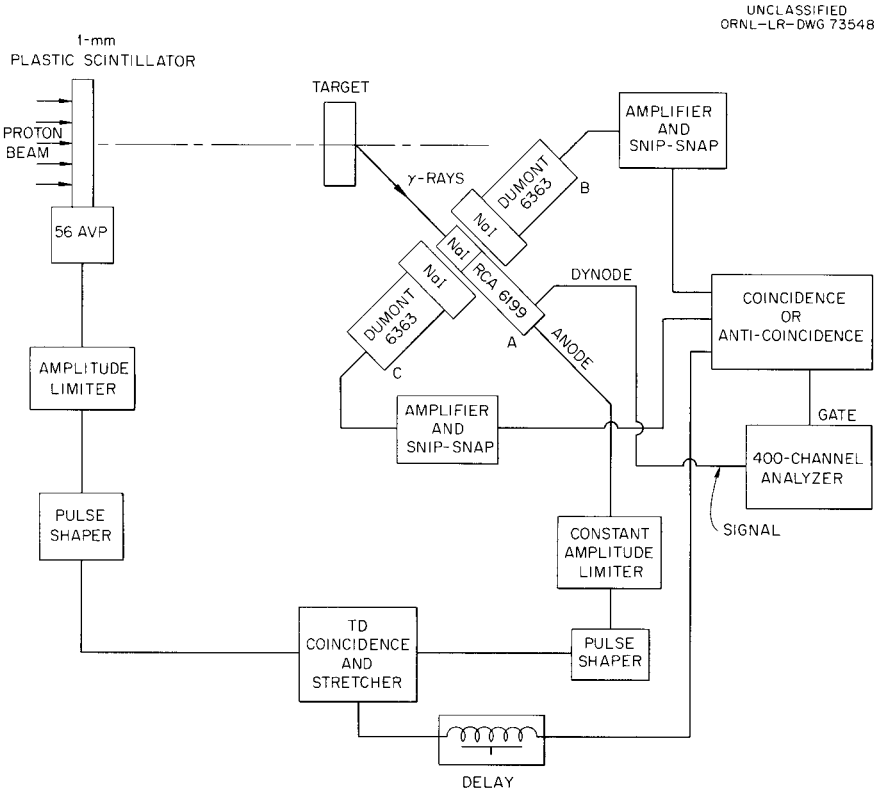

Fig. 8.5.4. Block Diagram of Modified Gamma-Ray Spectrometer.

8.6. DOSIMETRY

F. C. Maienschein and T. V. Blosser

Measurement of the physical dose resulting from the secondary particles from high-energy reactions would make additional demands upon the calculations. The proper conversion from flux to dose would be required, while for a large object, such as a man or phantom, the penetration through the object and integration over the incident angular distribution would have to be properly taken into account.

The instruments presently used to measure dose from reactor radiations are the result of lengthy development efforts. They measure either the total dose delivered to tissue or the separate contributions from neutrons and gamma rays to the dose.[1] Instruments of either type are not directly useful in the energy range of tens or hundreds of Mev, and another considerable development program will be required to provide dosimeters suitable for such energies. The present effort does not include such a program.

In one of the preliminary experiments (see Sec. 8.0) at the Harvard accelerator, however, an attempt was made to use dosimeters of the type developed for reactor use in order to obtain very approximate results. A RADSAN, which is a Hurst proton-recoil counter with pulse-height analysis,[2] was used as a neutron dosimeter, and a small, halogen-filled GM counter[3] was used as a gamma-ray dosimeter.[4] The GM counter gives only a single count for any charged particle passing through it, no matter how heavily ionizing, and thus discriminates against proton recoils. Unfortunately, both these instruments respond to high-energy protons with an undetermined efficiency. On a qualitative basis, the walls of the RADSAN were thick enough to stop protons with energies below about 35 Mev. For the relatively thin-walled GM tube, the pertinent parameter in considering the counting efficiency is the reciprocal of the energy loss per unit length, dE/dx. The dE/dx for a 150-Mev proton is roughly equal to that for a 60-kev electron, or three times the dE/dx for an electron in the energy range from $\sim$0.5 to $\sim$10 Mev. Therefore, the efficiency for high-energy protons should be only a few times less than that for recoil electrons produced by gamma rays.

Because of their nondirectional response and low-energy bias, the dosimeters are more responsive to background than are the spectrometers discussed in other sections of this report. Most of their use in the preliminary experiments at Harvard was in attempting to eliminate extraneous room background. As was noted in Section 8.1, backgrounds were reduced by using a slit to restrict the beam and by addition of lead shielding at the point where the beam pipe penetrated the cyclotron shield. The "target-out" background in the horizontal plane of the cyclotron beam was nevertheless very large for the gamma-ray dosimeter. This may be noted in Fig. 8.6.1. The target-out background increases rapidly as the angle between the beam axis and target-counter axis is decreased, that is, as the beam is approached. The effect of shielding

---

[1] G. S. Hurst *et al.*, *Measurement of Absorbed Dose of Neutrons, and of Mixtures of Neutrons and Gamma Rays*, NBS Handbook 75 (Sec. 3), 1961.

[2] E. B. Wagner and G. S. Hurst, *Rev. Sci. Instr.* **29**, 153 (1958).

[3] E. B. Wagner and G. S. Hurst, *Health Physics* **5**, 20 (1961).

[4] Appreciation is expressed to R. K. Abele, F. E. Gillespie, and R. E. Zedler, all of the Instrumentation and Controls Division, who constructed the counters in a very short time.

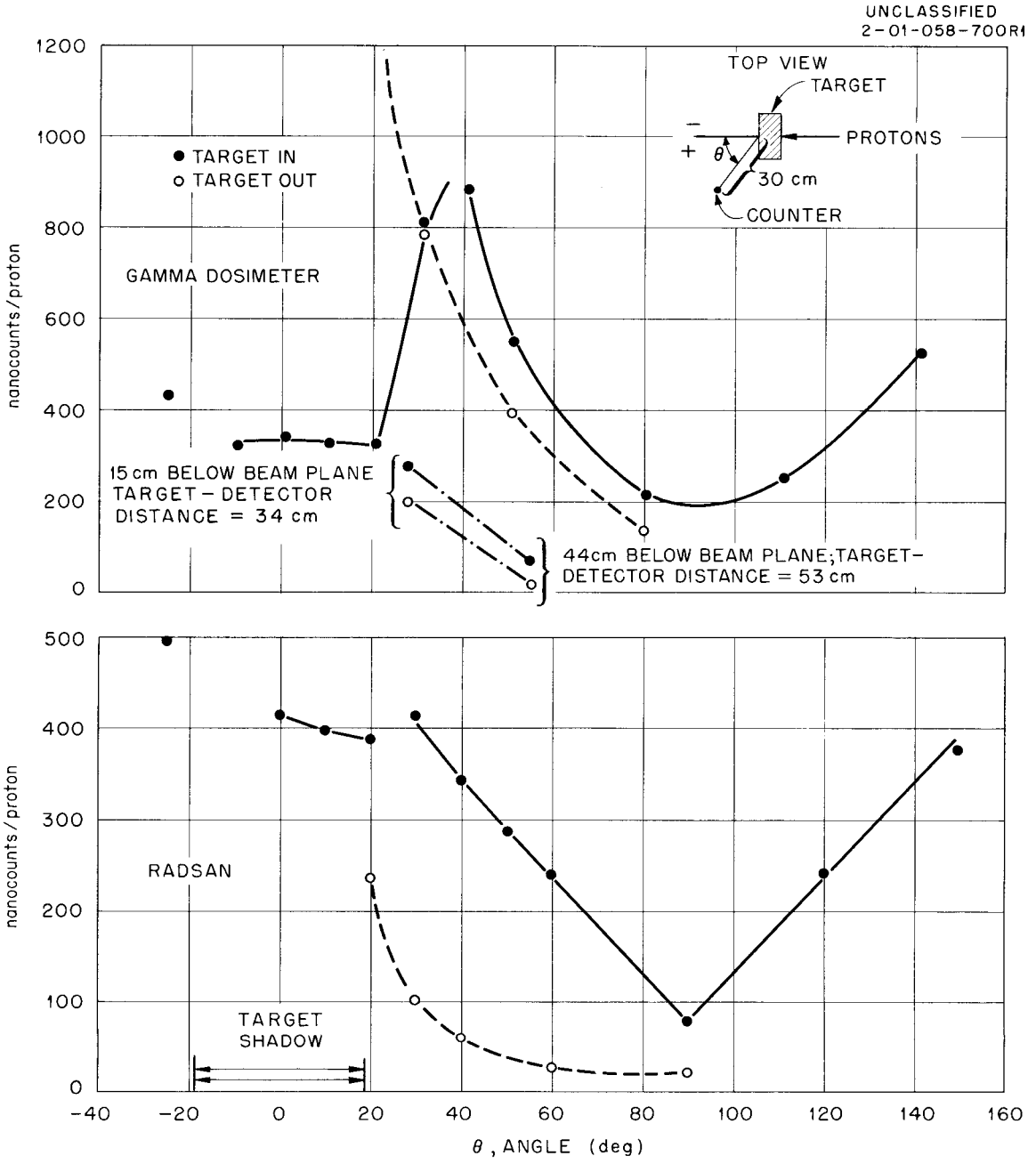

Fig. 8.6.1. Response of Gamma-Ray and RADSAN Dosimeters as a Function of Angle from Beam-Target Axis.

by the target at small angles may be seen in the target-in data. Background diminished rapidly as the detector was dropped below the plane of the beam.

In Table 8.6.1 are shown the results of measurements with the neutron and gamma-ray dosimeters at 40 cm from 20-cm-diam disk-shaped targets. The scattering angle was 40° for the neutron dosimeter and 50° for the gamma-ray instrument. The values listed, nominally in terms of tissue rad per incident proton, are quantitatively meaningless because of the proton background and are shown only to give an order of magnitude.

Table 8.6.1. Response of Dosimeters to Secondary Radiation from 156-Mev Protons Incident on Various Targets

Target	Thickness (g/cm^2)	Dose Rates (see text)	
		Neutrons	Gamma Rays
		$\times 10^{-14}$	$\times 10^{-14}$
H_2O	22.2	3.6	0.8
C	23.4	7.2	0.5
Al	26.5	8.9	2.0
Cu	29.4	16.0	2.8
Pb	44	28.0	1.0
None	0	3.8	5.3

Because of their high-energy proton response, the above dosimeters will not be used in future work. However, one dose measurement will be attempted. An ionization chamber will be used in a 42-cm-diam spherical water-filled phantom to determine the response due to all secondaries, regardless of type. The chamber will be moved throughout the phantom to determine the distribution in depth of the response of the ion chamber. The ionization current collected may be related to a physical dose, since the energy required to produce an ion pair depends but little on the type of particle or energy. Correlation with a biological dose, however, is clearly not possible unless the relative biological effectiveness is identical for all of the types of secondaries.

It is estimated that a 20-cc atmospheric-pressure ion chamber with polyethylene walls will yield about 10^{-11} to 10^{-12} amps, depending on position in the phantom, for a beam containing 10^{10} protons (150 Mev) per second. Such a current should be measurable with existing remote-reading electrometers. Determination of backgrounds will require "target-in," "target-out" subtractions. A serious additional background problem will be presented by reflection of secondaries from the laboratory floor.

9. ORNL Desalination Studies — Theoretical

9.1 ION EXCLUSION IN POROUS-BED SALT FILTERS[1,2]

Lawrence Dresner

For a long time it has been known that membranes of ion-exchange resins partly exclude ions of one sign from their interior. Because of this property, it has been suggested that these membranes be used as "salt filters" for the removal of dissolved salts from brackish waters by reverse osmosis.[3] The power cost involved in the use of ion-exchange membranes may be high, for in passing through an ion-exchange membrane, water is subject to a high flow resistance. A salt filter that may have much better flow properties than ion-exchange membranes has recently been suggested by K. A. Kraus. It consists of a porous bed of small particles to which ionizable groups are attached. When the bed is wetted by water, the ionizable groups go into solution, leaving the surfaces of the beads forming the bed electrically charged. The separation of charge thereby produced gives rise to high electric fields in the interstices of the bed. These electric fields are responsible for the partial exclusion from the interstices of ions of the same sign as the fixed charges on the bead surfaces (co-ions).

In the work being summarized here, this co-ion exclusion was studied at thermodynamic equilibrium in the hope of finding the properties that a porous-bed salt filter must have to be suitable for water desalination. In another paper, summarized in Sec. 9.2, a study of nonequilibrium situations in which there are flows of water and ions caused by pressure, concentration, and electrical gradients is reported.

The average concentrations of co- and counter-ions (ions of the same sign as the ionizable groups) at thermodynamic equilibrium in a bed in contact with an electrolytic solution can be determined from the conditions of thermodynamic equilibrium and electroneutrality to be

$$C_1 = C_0/2 + \left[(C_0/2)^2 + C^2 \left\langle e^{-\zeta} \right\rangle \right]^{1/2}, \tag{1a}$$

$$C_2 = -C_0/2 + \left[(C_0/2)^2 + C^2 \left\langle e^{-\zeta} \right\rangle \right]^{1/2}, \tag{1b}$$

where

C_0 = average concentration of fixed ions,
C_1 = average counter-ion concentration,
C_2 = average co-ion concentration,
C = electrolyte concentration in the contacting solution,
$\left\langle e^{-\zeta} \right\rangle$ = numerical factor accounting for the nonuniform spatial distribution of the fixed charges in the bed.

The factor $\left\langle e^{-\zeta} \right\rangle$ is related to the spatial variation of the ionic concentrations in the porous bed; the latter are obtained by solving the relevant form of the Poisson-Boltzmann differential equation. $\left\langle e^{-\zeta} \right\rangle$ is

---

[1]Work performed for the Office of Saline Water, U.S. Department of the Interior, at ORNL.

[2]A full report of this work has been written and submitted for publication in the *Journal of Physical Chemistry*.

[3]"Desalination Research and the Water Problem," *Report of the Desalination Research Conference Convened by the National Academy of Sciences – National Research Council at Woods Hole, Massachusetts, 19 June – 14 July 1961*, Publication 941, National Academy of Sciences – National Research Council, Washington, 1962

always greater than 1, except in the case of spatially uniform ion distributions in the bed, in which case it is equal to 1. Since C_2 is larger the larger that $\langle e^{-\zeta} \rangle$ is, the spatial nonuniformity of the ionic distribution always abets the invasion of the bed by co-ions.

In the case of good co-ion exclusion, that is, the case when $\langle C_2 \rangle \ll C$, explicit formulas for $\langle e^{-\zeta} \rangle$ can be obtained for two special models of the fixed-charge distribution:

1. The fixed charges are confined to a surface layer on the inner surface of cylindrical pores of radius R. Solution can only penetrate the interior of the pores; the rest of the bed is impenetrable.

2. The fixed charges are disposed in a square lattice of cylindrical charges with radius R_0 and spacing $R\sqrt{\pi}$; solution can penetrate all of the bed between them. The explicit solution of the Poisson-Boltzmann equation for this model requires the introduction of Wigner-Seitz cells of radius R.

Shown in Fig. 9.1.1 are values of $\langle e^{-\zeta} \rangle$ plotted vs dimensionless pore or cell radii ξ_R. These dimensionless radii are defined by

$$\xi_R^2 = \kappa^2 R^2 = \frac{e^2 C_0}{kT\epsilon} R^2 , \tag{2}$$

where e is the charge on the proton, kT is the product of Boltzmann's constant k and the absolute temperature T, and ϵ is the dielectric constant of the interstitial fluid. (When C_0 = 10 moles/liter, T = 15°C, and ϵ is the dielectric constant of water, κ = 0.741 Å^{-1}.)

The following approximate equivalence relation can be derived from the data in Fig. 9.1.1: The charge lattice with a dimensionless charge radius ξ_0 and a dimensionless cell radius ξ_R and the cylindrical pore of dimensionless radius ξ_R' given by

$$\xi_R'/\xi_R = (\sqrt{39}/2)(1 - \sqrt{\xi_0/\xi_R}) \tag{3}$$

have the same value of $\langle e^{-\zeta} \rangle$.

From Eq. 1*b* and the data in Fig. 9.1.1 it follows that to maintain an average co-ion concentration in the salt filter of 0.01 mole/liter the pore radius, R', must be about 42 Å for a 0.05-*M* feedwater, 21 Å for a 0.1-*M* feedwater, and 4 Å for a 0.5-*M* feedwater. R' is related to the dimensions of equivalent lattice cells through Eq. 3. These conclusions, moreover, are independent of the actual value of C_0, as long as it is large enough to guarantee that $C_2 \ll C$ and that $\xi_R' \gg 1$.

For feedwater salt concentrations of 0.5 mole/liter (approximately the NaCl concentration in sea water) the effective or actual pore radii are rather small and will produce large flow resistance to the passage of water through the filter. For lower salt concentrations, such as might be encountered in inland brackish waters, much larger pores or lattice spacings can be employed. Porous-bed salt filters will therefore be best for desalting waters of originally low salinity. It seems likely, moreover, that the particle size for a practical porous-bed salt filter must be so chosen that the interstitial channels have effective radii of around 50 Å or less.

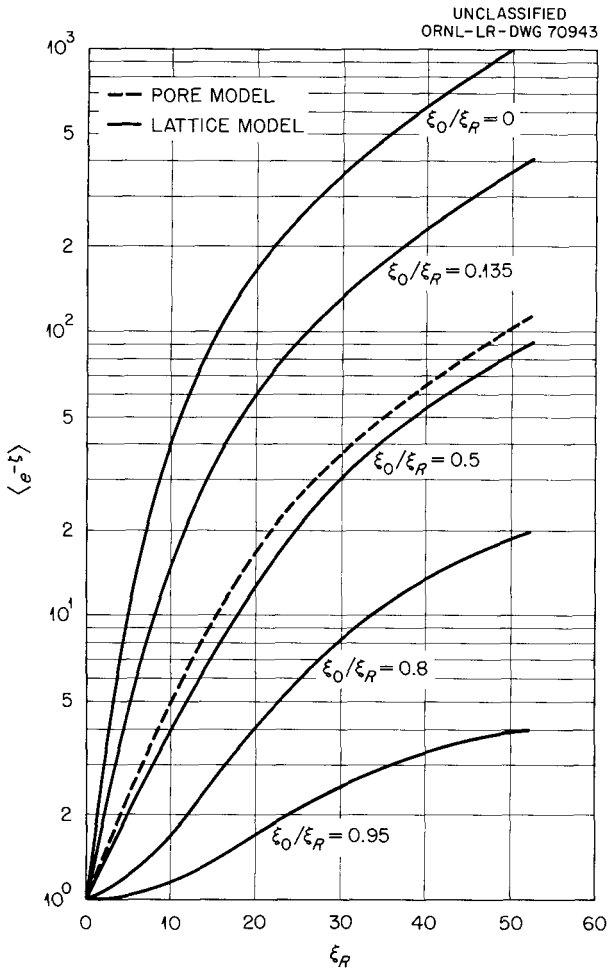

Fig. 9.1.1.1 The Factor $\langle e^{-\zeta} \rangle$ as a Function of ξ_R. $\langle e^{-\zeta} \rangle$ corrects the square of the salt concentration in the exterior solution for the nonuniform counterion distribution, and ξ_R is the dimensionless pore or cell radius. The ratios ξ_0/ξ_R attached to the lattice-model curves are the ratios of the dimensionless charge-cylinder radii ξ_0 to the dimensionless cell radii ξ_R.

9.2. ELECTROKINETIC PHENOMENA IN CHARGED MICROCAPILLARIES[1,2]

Lawrence Dresner

Electrokinetic phenomena have been known for more than a century and a half. The first theory of these phenomena was the work of Helmholtz,[3] who introduced the concept of the electrical double layer. Helmholtz's theory was later refined by the introduction of a diffuse double layer in the researches of Gouy,[4] Chapman,[5] and Stern.[6]

---

[1]Work performed for the Office of Saline Water, U. S. Department of the Interior, at ORNL.

[2]A full report of this work has been written and submitted for publication in the *Journal of Physical Chemistry.*

[3]H. Helmholtz, *Wiedemann's Annalen, N. F.*, **7**, 339 (1879).

[4]G. Gouy, *J. phys.* **9**, Ser. 4, 457 (1910); *Ann. Phys. (Paris)* **7**, Ser. 9, 129 (1917).

[5]D. L. Chapman, *Phil. Mag.* **25**(6), 475 (1913).

[6]O. Stern. *Z. Elektrochem.* **30**, 508 (1924).

In all these works the electrical charge density of the bulk fluid is nil, charge separation occurring only in a thin double layer near the wall. Recently, I have become interested in electrokinetic phenomena in charged fluids, such as may be found in surface-charged capillaries of very small diameter (microcapillaries). In the paper summarized here, these phenomena were studied.

The situation considered was the following: A long, cylindrical microcapillary on whose inner surface a uniform charge, $e\sigma$, resides has its ends immersed in two reservoirs of electrolyte. The reservoirs are kept at the same temperature, but concentration, pressure, and electrical gradients may exist between them. The surface ion density σ and capillary radius R are chosen so that ions of the same charge as the surface charge (co-ions) are nearly completely excluded from the capillary (see Sec. 9.1). The idealization of perfect co-ion exclusion is made in subsequent calculations.

The volumetric water flow q and current J of counter-ions (ions of the opposite sign to the surface charge) are assumed to be linearly related to the pressure difference Δp and the difference in electrochemical potential $\Delta\mu$ between the reservoirs:

$$q = L_{11}\Delta p + L_{12}\Delta\mu\,, \tag{1a}$$

$$J = L_{21}\Delta p + L_{22}\Delta\mu\,, \tag{1b}$$

$$L_{12} = L_{21}\,. \tag{1c}$$

Equation 1c is Onsager's relation.

The L-coefficients have been calculated explicitly on the basis of the following model:

1. The ionic diffusion with respect to the fluid caused by electrical and concentration gradients is described by the Planck-Henderson equation.

2. The water flow induced by the pressure gradient and the force transmitted to the water by the diffusing ions is described by the Navier-Stokes equation.

3. The electric potential and the ionic concentrations are related by Poisson's law.

4. The water and ion flows obey continuity equations.

5. When averaged over the capillary cross section, the ion concentrations and the surface charge must obey an equation of electroneutrality. The results of these calculations are

$$L_{11} = -\frac{\pi R^4}{8\eta d}, \tag{2a}$$

$$L_{12} = L_{21} = \frac{-2\pi R^2 C_0}{\eta d\kappa^2}\left[(1 + 8/\xi_R^2)\ln(1 + \xi_R^2/8) - 1\right], \tag{2b}$$

$$L_{22} = -\frac{\pi R^2 \mathbb{D}_1 C_0}{d} - \frac{2\pi C_0^2 R^2}{\kappa^2\eta d}\left[1 - (8/\xi_R^2)\ln(1 + \xi_R^2/8)\right], \tag{2c}$$

where

R = the capillary radius,

d = the capillary length,

η = the viscosity of water,

C_0 = the average fixed ion concentration in the capillary (= $2\sigma/R$),

$\kappa^2 = e^2 C_0 / kT\epsilon$,

e = the charge of the proton,

k = Boltzmann's constant,

T = the absolute temperature,

ϵ = the dielectric constant of water,

$\xi_R = \kappa R$,

$kT\mathbb{D}_1$ = the diffusion constant of the counter-ions.

The full report on which this summary is based contains a variety of numerical calculations of such electrokinetic effects and quantities as the electroviscous effect, the electroosmosis, the capillary resistivity, and the electroosmotic pressure. In addition, several velocity profiles occurring in reverse osmosis and electroosmosis have been calculated.

ORNL-3360
UC-34 – Physics
TID-4500 (17th ed., Rev.)

INTERNAL DISTRIBUTION

1. Biology Library
2–4. Central Research Library
5. Laboratory Shift Supervisor
6. Reactor Division Library
7–8. ORNL – Y-12 Technical Library, Document Reference Section
9–102. Laboratory Records Department
103. Laboratory Records, ORNL R.C.
104. L. S. Abbott
105. F. S. Alsmiller
106. R. G. Alsmiller, Jr.
107. H. W. Bertini
108–132. E. P. Blizard
133. T. V. Blosser
134. B. Bokari
135. G. E. Boyd
136. B. Buck
137. W. R. Burrus
138. V. R. Cain
139. A. D. Callihan
140. G. T. Chapman
141. F. H. Clark
142. C. E. Clifford
143. A. L. Colomb
144. R. R. Coveyou
145. R. L. Cowperthwaite
146. G. deSaussure
147. J. K. Dickens
148. L. Dresner
149. J. F. Ellis
150. M. B. Emmett
151. J. L. Fowler
152. R. M. Freestone, Jr.
153. W. A. Gibson
154. L. W. Gilley
155. R. Gwin
156. K. M. Henry
157. R. F. Hibbs (Y-12)
158. A. Hollaender
159. L. B. Holland
160. J. L. Hull
161. J. D. Jarrard
162. C. F. Johnson
163. E. B. Johnson
164. W. H. Jordan
165. L. Jung
166. F. B. K. Kam
167. J. D. Kington
168. W. E. Kinney
169. C. E. Larson
170. R. P. Leinius
171. T. A. Love
172. J. J. Lynn
173. W. S. Lyon
174. R. L. Macklin
175. R. E. Maerker
176. H. G. MacPherson
177. D. W. Magnuson
178–188. F. C. Maienschein
189. J. J. Manning
190. J. T. Mihalczo
191. J. M. Miller
192. H. S. Moran
193. K. Z. Morgan
194. F. J. Muckenthaler
195. J. E. Murphy (K-25)
196. J. P. Murray (K-25)
197. R. W. Peelle
198. S. K. Penny
199. F. Perey
200. E. R. Rohrer
201. R. T. Santoro
202. R. J. Scroggs
203. E. G. Silver
204. M. J. Skinner
205. R. D. Smiddie
206. A. H. Snell
207. J. A. Swartout
208. J. T. Thomas
209. H. A. Todd
210. D. K. Trubey
211. W. C. Tunnell
212. V. V. Verbinski
213. D. R. Ward
214. A. M. Weinberg
215. L. W. Weston
216. Gale Young
217. C. D. Zerby
218. W. Zobel
219. R. A. Charpie (consultant)
220. P. F. Gast (consultant)
221. R. F. Taschek (consultant)
222. T. J. Thompson (consultant)

EXTERNAL DISTRIBUTION

223. R. W. McNamee, Union Carbide Corporation, New York
224. Division of Research and Development, AEC, ORO
225–858. Given distribution as shown in TID-4500 (17th ed., Rev.) under Physics category (75 copies – OTS)